

AD-A269 616

(12)



**EDGEWOOD
RESEARCH,
DEVELOPMENT &
ENGINEERING
CENTER**

ERDEC-SP-006

**PROCEEDINGS OF THE 1992 SCIENTIFIC CONFERENCE
ON OBSCURATION AND AEROSOL RESEARCH**

**S DTIC
ELECTE
SEP 23 1993
A D**

Janice E. Rhodes

**BATTELLE EDGEWOOD OPERATIONS
Edgewood, MD 21040**

June 1993

Approved for public release; distribution is unlimited.

U.S. ARMY
CHEMICAL
AND BIOLOGICAL
DEFENSE AGENCY



Aberdeen Proving Ground, Maryland 21010-5423

93-22075



1 16-288

Disclaimer

The findings in this report are not to be construed as an official Department of the Army position unless so designated by other authorizing documents.

REPORT DOCUMENTATION PAGE

Form Approved
OMB No. 0704-0188

Public reporting burden for this collection of information is estimated to average 1 hour per response, including the time for reviewing instructions, searching existing data sources, gathering and maintaining the data needed, and completing and reviewing the collection of information. Send comments regarding this burden estimate or any other aspect of this collection of information, including suggestions for reducing this burden, to Washington Headquarters Services, Directorate for Information Operations and Reports, 1215 Jefferson Davis Highway, Suite 1204, Arlington, VA 22202-4302, and to the Office of Management and Budget, Paperwork Reduction Project (0704-0188), Washington, DC 20503.

1. AGENCY USE ONLY (Leave blank)	2. REPORT DATE 1993 June	3. REPORT TYPE AND DATES COVERED Final, 92 Jun - 92 Jun	
4. TITLE AND SUBTITLE Proceedings of the 1992 Scientific Conference on Obscuration and Aerosol Research			5. FUNDING NUMBERS PR-10161102A71A
6. AUTHOR(S) Janice E. Rhodes, Compiler			
7. PERFORMING ORGANIZATION NAME(S) AND ADDRESS(ES) Battelle Edgewood Operations 2113 Emmorton Park Road, Suite 200 Edgewood, MD 21040			8. PERFORMING ORGANIZATION REPORT NUMBER ERDEC-SP-006
9. SPONSORING/MONITORING AGENCY NAME(S) AND ADDRESS(ES) DIR, ERDEC, * ATTN: SCBRD-RT, APG, MD 21010-5423			10. SPONSORING/MONITORING AGENCY REPORT NUMBER
11. SUPPLEMENTARY NOTES POC: Dr. E. Stuebing, SCBRD-RTB, (410) 671-3089 *When this work was performed ERDEC was known as CRDEC and the Point of Contact was assigned to the Research Directorate.			
12a. DISTRIBUTION/AVAILABILITY STATEMENT Approved for public release; distribution is unlimited.			12b. DISTRIBUTION CODE
13. ABSTRACT (Maximum 200 words) In this report, 27 papers presented at the 1992 Scientific Conference on Obscuration and Aerosol Research are included under the headings of Aerosol Dynamics, Aerosol Characterization Methods, and Optical Properties of Aerosols.			
14. SUBJECT TERMS			15. NUMBER OF PAGES 471
Obscurants	Aerosols	Extinction	Transmission
Obscuration	Aerosol	Absorption	Infrared
Scatterings	Sizing	Smoke	(continued on page 2)
			16. PRICE CODE
17. SECURITY CLASSIFICATION OF REPORT UNCLASSIFIED	18. SECURITY CLASSIFICATION OF THIS PAGE UNCLASSIFIED	19. SECURITY CLASSIFICATION Of ABSTRACT UNCLASSIFIED	20. LIMITATION OF ABSTRACT UL

14. Subject Terms (Continued)

Electromagnetic scattering
Millimeter wave radiation
Submillimeter wave radiation
Visible radiation
Electromagnetic waves
Spherical particles
Mie scattering
Rayleigh scattering
Raman scattering
Concentration sampling
Particle dynamics
Diffusive mixing
Aerosol growth
Nucleation
Smoke generation
Aerosol generation
Photoionization
Conductivity
Chemical characterization
Phosphorus smoke
Fluorescence
Aerosol clusters
Spheres
Cylinders
Rough particles
Irregular particles
Nonspherical particles
Particle aggregates
Particle chains
Infrared emission
Cooperative scattering
Dependent scattering
Multiple scattering
Radiative transfer
Coagulation
Condensation
Liquid drop
Drop growth
Fog oil smoke
Diesel oil smoke
Particle mechanics
Atmospheric optics
Atmospheric dispersion
Cloud dynamics
Scavenging
Aerosol collectors
Aerosol elimination
Aerosol characterization
Particle sizing
Hygroscopic smokes
Particle size distribution
Particle orientation distribution
Optical constants
Optical properties
Anomalous diffraction
Attenuated total reflection
Reflection spectroscopy
ATR
Far-infrared
Refractive index
Index of refraction
Inversion
Inversion techniques
Gypsum
Natural minerals
Minerals
Metal
Metallic particles
Powdered minerals
Complex refractive index
Effective media
High energy laser
Particles
Aerosol particles
SERS
Surface Enhanced Raman Scattering
Dielectric particles
Conducting particles
Cylindrical particles
Fibers
Conducting fibers
Gas-aerosol reactions
Transport phenomena
Aerosol measurement
Spheroids
Laser pulses
Optical pulses
Pulse propagation
Clouds
Laser
Radiation transport
Fourier analysis
Plume mechanics
Light
Plumes
Properties

PREFACE

The 1992 U.S. Army Edgewood Research, Development and Engineering Center (Edgewood RDEC)* Scientific Conference on Obscuration and Aerosol Research was held 22 - 25 June 1992 at the Edgewood Area Conference Center of Aberdeen Proving Ground, MD. The Conference is held annually, the last full week in June, under the direction of Dr. Edward Stuebing, Research Area Coordinator, Aerosol Science. This report was authorized under project number 1O161102A71A, Research in CW/CB Defense.

The Conference is an informal forum for scientific exchange and stimulation among investigators in the wide variety of disciplines required for aerosol research, including a description of an obscuring aerosol and its effects. The participants develop some familiarity with the U.S. Army aerosol and obscuration science research programs and also become personally acquainted with the other investigators and their research interests and capabilities. Each attendee is invited to present any aspect of a topic of interest and may make last minute changes or alterations in his presentation as the flow of ideas in the Conference develops.

While all participants in the Conference are invited to submit papers for the proceedings of the Conference, each investigator, who is funded by the U.S. Army Research Program, is requested to provide one or more written papers that document specifically the progress made in his funded effort in the previous year and indicating future directions. Also, the papers for the proceedings are collected in the Fall to allow time for the fresh ideas that arise at the Conference to be incorporated. Therefore, while the papers in these proceedings tend to closely correspond to what was presented at the Conference, there is not an exact correspondence.

The reader will find the items relating to the Conference itself, photographs, the list of attendees, and the agenda in the appendixes following the papers and in the indexes pertaining to them. Please note, due to the recent reorganization of the Chemical Research, Development and Engineering Center, the terms CRDEC and Edgewood RDEC have been used interchangeably.

The use of trade names or manufacturers' names in this report does not constitute an official endorsement of any commercial products. This report may not be cited for purposes of advertisement.

*When this work was performed, Edgewood RDEC was known as the U.S. Army Chemical Research, Development and Engineering Center, and the Point of Contact was assigned to the Research Directorate.

This report has been approved for release to the public. Registered users should request additional copies from the Defense Technical Information Center; unregistered users should direct such requests to the National Technical Information Service.

Accession For	
NTIS CBANI	<input checked="" type="checkbox"/>
DTIC TAB	<input type="checkbox"/>
Unannounced	<input type="checkbox"/>
Justification	
By _____	
Dist. Status	
Availability Codes	
Dist	Availability Codes
A-1	

TABLE OF CONTENTS

	Page
I. AEROSOL DYNAMICS	9
THE EFFECT OF INTERPARTICLE FORCES ON POWDER SPRAYING H. Littman and M.H. Morgan III	9
ELECTROSTATIC SMOKE (FOG) CLEARING IN ENCLOSED CHAMBERS Z. Zhou, W. McLeod, R. Shaffer, D. Reidy, and G.O. Rubel	25
METASTABLE PHASES IN COMPRESSED 1-OCTADECANOL MONOLAYERS ON LEVITATED WATERDROPS M. Seaver and G.O. Rubel	31
ON FEASIBILITY OF FINITE ELEMENT SOLUTION OF THE MAXWELL EQUATIONS FOR ABSORPTION AND SCATTERING OF ELECTROMAGNETIC RADIATION BY A PARTICLE M.K. Choi and J.R. Brock	37
ON THE SIMILARITY OF LINE INTEGRATED CONCENTRATION FLUCTUATIONS ACROSS PLUMES DIFFUSING IN GRID-GENERATED TURBULENCE M. Poreh and J.E. Cermak	47
SOME FRACTAL PROPERTIES OF INTEGRATED CONCENTRATION FLUCTUATIONS A. Hadad, M. Stiassnie, M. Poreh and J.E. Cermak	55
II. AEROSOL CHARACTERIZATION METHODS	61
A. NEPHELOMETRY AND INVERSION	61
USE OF A NEW POLARIMETRIC OPTICAL BISTATIC SCATTEROMETER TO MEASURE THE TRANSMISSION AND REFLECTION MUELLER MATRIX FOR ARBITRARY INCIDENT AND SCATTER DIRECTIONS R.D. Kubik, E. Bahar and D.R. Alexander	61
INVERSION OF LIGHT SCATTERING MEASUREMENTS FOR PARTICLE SIZE AND OPTICAL CONSTANTS M.R. Jones, B.P. Curry, K.H. Leong and M.Q. Brewster	77
KRAMERS-KRONIG RELATIONS IN OPTIC DATA INVERSION M.H. Lee	91

	*MEASURED CHARACTERIZATION OF RANDOMLY ROUGH SURFACES BY IR MUELLER MATRIX SCATTERING	
	A.H. Carrieri, J.O. Jensen, J.R. Bottiger, D. Zeroka and H.F. Hameka	97
	ANGULAR MEASUREMENT OF THE FORWARD LIGHT SCATTERING FROM A QUARTZ FIBER	
	E.S. Fry, G.G. Padmabandu and C. Oh	103
	REMOTE DETECTION OF ISOTROPICALLY ANISOTROPICALLY, OR BIANISOTROPICALLY ENCAPSULATED BIOLOGICAL MATERIALS IN A CLOUD	
	O.I. Sindoni, N. Witriol, and D.K. Cohoon	115
B.	IMAGING OF MICROPARTICLES AND AEROSOLS	141
	MANIPULATION OF MICROPARTICLES IN MULTIPHASE LEVITATION TRAPS	
	E.E. Allison, B.R.F. Kendall, B.V. Bronk and D.S. Weyandt	141
C.	SPECTROSCOPY OF SINGLE PARTICLES AND AEROSOLS	145
	CW STIMULATED RAMAN SCATTERING IN MICRODROPLETS	
	J.D. Eversole, A.J. Campillo and H-B. Lin	145
	CAVITY-ENHANCED RHODAMINE 6-G SPONTANEOUS EMISSION RATES IN LEVITATED MICRODROPLETS	
	M.D. Barnes, W.B. Whitten, J.M. Ramsey and S. Arnold	155
	TIME AND WAVELENGTH DOMAIN ALGORITHMS FOR CHEMICAL ANALYSIS BY LASER RADAR	
	D.L. Rosen and J.B. Gillespie	173
	MICROPARTICLE-BASED FLUORESCENCE IMMUNOASSAY	
	W.B. Whitten, J.M. Ramsey and B.V. Bronk	177
	COMPUTERIZED FLUOROMETER ANALYSIS: AUTOMATED IDENTIFICATION OF PARTICLES	
	L. Reinisch	183
	UV LIDAR DETECTION OF BIOLOGICAL AEROSOLS	
	S. Christesen, M.S. DeSha, A. Wong, C. Merrow, M. Wilson and J. Butler	191
D.	INTERNAL STRUCTURE	199
	SUPPRESSION OF MORPHOLOGY DEPENDENT RESONANCE BY DROPLET SURFACE OSCILLATIONS	
	M. Essien, R.L. Armstrong and J.B. Gillespie	199

WORKSHOP

	CARBON PARTICLES FROM HYDROCARBON FEEDSTOCKS C.A. Clausen, P.W. Morgan, T.R. Racine and G. Hermann	219
III.	OPTICAL PROPERTIES OF AEROSOLS	239
	ANALYTIC APPROXIMATION TO RANDOMLY ORIENTED SPHEROID EXTINCTION B.T.N. Evans and G.R. Fournier	239
	OPTICAL PROPERTIES OF SPHERES CONTAINING A SPHERICAL ECCENTRIC INCLUSION F. Borghese, P. Denti, R. Saija and O.I. Sindoni	255
	ELECTROMAGNETIC FIELD CALCULATIONS FOR A BEAM FOCUSED ON A LAYERED PARTICLE J.P. Barton, S.A. Schaub and D.R. Alexander	277
	COMPARISONS BETWEEN THE DISCRETE DIPOLE APPROXIMATION AND THE EXACT SOLUTION FOR LIGHT SCATTERING BY TWO SPHERES P.J. Flatau and K.A. Fuller	289
	ABSORPTION AND SCATTERING CROSS SECTIONS OF CARBON DISPERSION AEROSOLS K.A. Fuller	297
	EXTINCTION AND ANGULAR SCATTERING BY ROUGH PARTICLES R.T. Wang	323
	A THEORY OF HEATING OF VOIGT SOLIDS AND FLUIDS BY EXTERNAL ENERGY SOURCES AND FLAME THEORY D.K. Cohoon	333
	GLOBALLY CONVERGENT HOMOTOPY, CONTINUED FRACTIONS AND THE EIGENVALUES OF SPIN WEIGHTED ANGULAR SPHEROIDAL HARMONICS D.K. Cohoon	359
	SCATTERING OF ELECTROMAGNETIC RADIATION BY NON- CONNECTED, HETEROGENEOUS BIANISOTROPIC STRUCTURES D.K. Cohoon	387
	FORWARD SCATTERING AND SIZE PARAMETER IN LAYERED SPHERICAL AEROSOL PARTICLES N.M. Witriol and O.I. Sindoni	423

QUASI-BINARY DECISION MAKING: AN UPDATE P.Hu and M. Lax	427
LIGHT SCATTERING FROM A SLICED TARGET USING THE INTERNAL FIELD OF INFINITE CYLINDERS: COMPARISON WITH MIE THEORY AND A SLICED SPHERE A. Cohen, R.D. Haracz, and L.D. Cohen	437

INDEXES FOR THESE PROCEEDINGS

A. Index of Authors'	453
B. Index of Author's Organizations	455

APPENDIXES FOR THESE PROCEEDINGS

A. Photograph of 1992 Conference Attendees	457
B. List of 1992 Attendees	459
C. Conference Agenda	467

I. AEROSOL DYNAMICS

The Effect of Interparticle Forces on Powder Spraying

by

H. Littman and M. H. Morgan III
Department of Chemical Engineering
RPI, Troy, N.Y. 12180-3590

A. Material properties relevant to transporting fine powders.

In all of our research, we have never had any difficulty transporting aeratable particles into a transport line from a hopper. However, when interparticle forces become large the material behavior can change from fluidized (behaving like a fluid) to solid (behaving like a solid). Solid type or cohesive behavior is apparent in Fig. 5 of the paper by Pacek and Nienow (Powder Tech., 1990) where lines of fracture can be observed in powders. For spraying particles, this cohesive behavior is undesirable because it makes it difficult if not impossible to obtain sprays consisting of individual particles.

The isostatic tensile stress, σ_0 , of an unconsolidated bulk powder of mono-sized spheres is related to the interparticle contact force F_0 , by the equation

$$\sigma_0 = \frac{1-\epsilon}{\pi} \frac{k(\epsilon) F_0}{d_p^2} \quad (1)$$

where $(1-\epsilon)$ is the solids fraction, $k(\epsilon)$ is the coordination number which is associated with the number of points of contact a particle has with neighboring particles and d_p is the particle diameter. F_0 is the cohesive force at particle contact points in the powder which can arise from a variety of causes, for example, chemical (van der Waal's) forces, electrostatic forces, etc. Clearly the larger the interparticle contact force the larger the isostatic (or apparent) tensile stress of the powder. Eqn (1) shows that σ_0 also increases with the solids fraction and as the particle diameter decreases. The fact that σ_0 varies inversely with the square of the particle diameter is quite important since changing from a 1 mm to a 1 μ m particle increases the apparent tensile stress by a factor of a million.

The material properties of a bulk powder involve σ_0 and the angle of internal friction, ϕ . These material constants are distinctive for every powder and relate the shear stress in the powder, τ_f , to the compressive stress on the powder, σ when the powder is just about to slide. Thus the yield locus of the powder is

$$\tau_f = \mu (\sigma + \sigma_0); \mu = \tan \phi; \sigma \geq 0 \quad (2)$$

where μ is the coefficient of friction. There are mechanical tests for measuring μ , and σ_0 is obtained by extrapolation of the τ_f vs σ measurements (Rietema, 1991 and Brown and Richards, 1970). For a non-cohesive powder, σ_0 is zero and, the classical law of friction is obtained between the shear stress and compressive loading as

$$\tau_f = \mu \sigma \quad ; \quad \mu = \tan \phi \quad ; \quad \sigma \geq 0 \quad (3)$$

An important fact of considerable importance practically is that prior history of the powder affects the material constants in Eqn (2). If, for example, the particles are compacted for storage or shipping they may not behave in the same way after the shipping container is opened. The flow behavior of a cohesive powder depends on its previous loading history.

Brown and Richards (1970) define a Coulomb powder as a rigid-plastic powder with a linear yield locus (Eqns 2 and 3). The term plastic is applied to the powder if sliding takes place when the shear stress applied equals the shear strength of the powder. The term elastic refers to a material which returns to its original shape after the load is removed.

B. Description of the stress field at a point in the powder (Mohr Circle).

The stress field at any point in a bulk powder is commonly presented in terms of a Mohr circle diagram. To keep the discussion as simple as possible, a planar stress field will be described. The Mohr circle diagram plots the tangential (or shear) stress

vs. the normal (compressive) stress at a particular point, P(x,y), in the bulk powder. These stresses vary with the orientation of the plane passing through P as seen in Figure 1a.

Consider an element of solid mass located at point P(x,y) in the bulk powder. The four faces of the planar element are located parallel and perpendicular to the Cartesian unit vectors \bar{i} and \bar{j} as shown in Figure 1b. On each face there are normal (compressive) and tangential (shear) stresses and Figure 1a shows a face of arbitrary orientation.

The stress tensor, $\bar{\sigma}$, can be represented relative to the \bar{i} and \bar{j} unit vectors for the case of plane stress as

$$\bar{\sigma} = \sigma_{xx} \bar{i}\bar{i} + \tau_{xy} \bar{i}\bar{j} + \tau_{yx} \bar{j}\bar{i} + \sigma_{yy} \bar{j}\bar{j} \quad (4)$$

where the tensor is symmetric, that is,

$$\tau_{xy} = \tau_{yx} \quad (5)$$

and we will assume that

$$\sigma_{xx} > \sigma_{yy} \quad (6)$$

The principal stresses are the eigenvalues of the matrix

$$\begin{pmatrix} \sigma_{xx} & \tau_{xy} \\ \tau_{yx} & \sigma_{yy} \end{pmatrix} \quad (7)$$

Following the method given in Kreyszig (1962), the principal stresses are

$$\lambda(1) \text{ and } \lambda(2) = \left(\frac{\sigma_{xx} + \sigma_{yy}}{2} \right) \pm \left\{ \left(\frac{\sigma_{xx} - \sigma_{yy}}{2} \right)^2 + \tau_{xy} \right\}^{1/2} \quad (8)$$

where $\lambda(1) > \lambda(2)$. Note from Eqn (8) that $\lambda(1) + \lambda(2) = \sigma_{xx} + \sigma_{yy}$.

Along the principal axes of stress there are no shear stresses so that

$$\bar{\sigma} = \lambda(1) \bar{i}'_p \bar{i}'_p + \lambda(2) \bar{j}'_p \bar{j}'_p \quad (9)$$

The matrix of this tensor is

$$\begin{pmatrix} \lambda(1) & 0 \\ 0 & \lambda(2) \end{pmatrix} \quad (10)$$

Comparing the matrices in Eqns (7) and (10), we see again that the sum of the elements along the diagonal is invariant [$\sigma_{xx} + \sigma_{yy} = \lambda(1) + \lambda(2)$].

The normal stress along a plane of arbitrary orientation (ac in Figure 1a) is obtained by well known tensor operations. Let σ'_{xx} represent the normal (compressive) stress along an arbitrary plane passing through P(x,y).. Then

$$\begin{aligned} \sigma'_{xx} &= \bar{i}' \cdot \bar{\sigma} \cdot \bar{i}' \\ &= \left(\frac{\sigma_{xx} + \sigma_{yy}}{2} \right) + \left(\frac{\sigma_{xx} - \sigma_{yy}}{2} \right) \cos 2\theta + \tau_{xy} \sin 2\theta \end{aligned} \quad (11)$$

The corresponding tangential stress τ'_{xy} is

$$\begin{aligned} \tau'_{xy} &= \bar{i}' \cdot \bar{\sigma} \cdot \bar{j}' \\ &= - \left(\frac{\sigma_{xx} - \sigma_{yy}}{2} \right) \sin 2\theta + \tau_{xy} \cos 2\theta \end{aligned} \quad (12)$$

where θ is the angle between \bar{i} and \bar{i}' as shown in Figure 1a.

Along the principal axes, τ'_{xy} is zero so that Eqn (12) gives for $\theta = \theta_p$

$$\tan 2\theta_p = \frac{2 \tau_{xy}}{(\sigma_{xx} - \sigma_{yy})} \quad (13)$$

Eqn (13) shows the principal axes are always 90° apart. The principal axes of stress have been obtained by simply rotating the \bar{i} and \bar{j} axes to the plane on which the shear stress, \bar{i}'_{xy} is zero.

Suitably squaring Eqns (12) and (13) and combining them, the following equation of a circle is obtained

$$\left[\sigma'_{xx} - \left(\frac{\sigma_{xx} + \sigma_{yy}}{2} \right) \right]^2 + \tau'_{xy} = \left[\left(\frac{\sigma_{xx} - \sigma_{yy}}{2} \right)^2 + \tau_{xy}^2 \right] \quad (14)$$

The center of the circle is $\left(\frac{\sigma_{xx} + \sigma_{yy}}{2}, 0 \right)$ and its radius $\left[\left(\frac{\sigma_{xx} - \sigma_{yy}}{2} \right)^2 + \tau_{xy}^2 \right]^{1/2}$.

This is the equation of the Mohr circle seen in Figure 2.

To understand the construction of the diagram note that τ'_{xy} is zero along the principal axes so that points A(1) and A(2) represent the principal stresses $\lambda(1)$ and $\lambda(2)$. The point, E, locates the center of the Mohr circle. The ray ED is the angle $(\theta_p - \pi/2)$. Passing from P1 to P2 on the Mohr circle must involve an angle change of in θ of $\pi/2$ because the principal axes are 90° apart (\bar{i}'_p to \bar{j}'_p). Thus points on the circle,

for example, C are located 2θ from the principal axis, $\theta_p - \frac{\pi}{2}$.

If we let the point, C, represent the normal and tangential stresses σ_{xx} and τ_{xy} on face 1 ($\theta = 0$) in Figure 1, the distance CD must be τ_{xy} and the distances on the EDC triangle related by the equation

$$\left[\left(\frac{\sigma_{xx} - \sigma_{yy}}{2} \right)^2 + \tau_{xy}^2 \right] = (ED)^2 + \tau_{xy}^2 \quad (15)$$

Therefore $ED = \frac{\sigma_{xx} - \sigma_{yy}}{2}$. The distance OD therefore represents the stress

$$\left(\frac{\sigma_{xx} + \sigma_{yy}}{2}\right) + \left(\frac{\sigma_{xx} + \sigma_{yy}}{2}\right) = \sigma_{xx} \quad (16)$$

In a similar fashion, it can be shown that the distance OF represents the stress τ_{xy} and the point G, the stresses on face 2 (a plane rotated 90° from the plane of face 1). Points on the circle counter-clockwise between C and G represent a rotation of the plane of arbitrary orientation by $\pi/2$. This coincides with conditions on face (4) in Figure 1b.

C Failure in a bulk powder

The Mohr circle diagram represents the state of stress in a powder at any point, P(x,y), along various directions through P. The powder will slide when τ_f equals τ'_{xy} . If the compression on the powder is raised, the radius of the Mohr circle increases. There is clearly some compressive stress where the conditions for sliding occur. Geometrically this is the state for which the yield locus is tangent to the Mohr circle at a particular point. Figure 3 shows that the powder cracks in shear along the plane θ equals θ_f where $\theta_f = [\theta_p - \pi/2 + \phi]$.

D Cohesive forces in a consolidated bulk powder

The cohesive force, F_0 , at a particle contact point in an unconsolidated powder arises as previously mentioned due chemical (van der Waal's), electrostatic, or other forces. Molerus (1975) has formulated the dependence of the cohesive force, F, at a contact point in a consolidated powder as a function of the compressive normal force causing the consolidation as

$$F = F_0 + \alpha N \quad (17)$$

where F_0 and α are material constants of the powder. The variation of F with N in Eqn (17) shows how the cohesive force increases as the normal stress at the contact point increases. One example of such behavior is seen in Figure 4.

The compressive force, C , at the contact point in the consolidated medium is therefore $N + F$ so that we can write

$$C = F_0 + (1 + \alpha) N \quad (18)$$

and by similarity with Eqn (2)

$$\tau_{fc} = \tan \phi \left\{ \left[\frac{(1-\epsilon)k(\epsilon)}{\pi d_p^2} \right] [N + (F_0 + \alpha N)] \right\} \quad (19)$$

where τ_{fc} is shear stress in a consolidated bulk powder when it is just about to slide.

There is an increase in the apparent tensile stress of the powder due to the αN term which is envisioned as being caused by changing the effective contact point area.

If the applied stresses to the bulk powder are compressive then from Eqn (11) we can write that along an arbitrary plane that the force at the contact point is

$$N(\theta) = F_M + F_R \cos 2\theta \quad (20)$$

where F_M and F_R are Mohr circle parameters. The shear force is

$$|T(\theta)| = |\sin 2\theta| \quad (21)$$

and thus the limiting condition for sliding is

$$F_R |\sin 2\theta| \leq (1 + \alpha)(F_M + F_R \cos 2\theta) \tan \phi \quad (22)$$

We can define the effective friction angle as

$$\tan \Theta_e = (1 + \alpha) \tan \phi \quad (23)$$

Thus we have presented a theory for a consolidated bulk powder such as would be obtained by compressing it for shipping and storage. The basic material parameters would have to be obtained experimentally.

E. Electrification of bulk powders and hazards

Bulk powders passing through transport pipes become triboelectrically charged due to frictional contacts of individual particles with the wall. High charge densities in the range of 1 to 100 $\mu\text{C}/\text{kg}$ are generated which cause effects that are generally undesirable. In bulk they cause individual particles to stick together making it difficult to feed them into the transport pipe. In the line, they cause increased pressure drop and make dispersion as individual particles difficult if not impossible. Finally, there are hazards of dust explosions and spark ignition in bulk powder piles within containers.

Charge generation and accumulation requires contact between electrically dissimilar surfaces and high electrical resistivity on one of the surfaces (Gibson, 1983). Moving bulk powders have much make and break interparticle and particle-wall contacts particularly in the feeder to our transport pipe. The detailed mechanism of charge generation is not fully understood, nor is the interparticle contact force predictable with any accuracy because particle shape and surface properties are important factors in determining this force. Whatever experiments are done with pure substances and clean surfaces, the fact remains that in practice one has to deal with the realities of surface contamination, impurities, and adsorbed or adsorbed species. The level of electrification in particular processes using particular equipment must in the end be determined by experiment or estimated from the literature (Gibson, 1983).

To limit charge buildup, conductors such as pipe walls are grounded. The earthing condition requires that the leakage resistance to earth be less than 100/charging current. The 100 constant arises from the fact that 100 V is the minimum potential at which an incendive discharge can occur. Since the maximum value of the charging current in industrial processes is 10^{-4}A , a resistance to earth of less than $10^6 \Omega$ will preclude dangerous charge accumulation (Gibson, 1983).

Grounding is not the answer when non-conducting materials such as plastics are used. The $27 \mu\text{C}/\text{m}^2$ figure at which air breakdown occurs (Blyth and Reddish, 1979) is reachable in practice. To minimize this problem, plastic surfaces should be located where substantial charge generation cannot occur and conducting plastic materials employed wherever possible.

Glor (1987), in agreement with Gibson (1983), states that within the transport pipe the charge on the powder is not hazardous but maintains that incendive sparks or brush discharges can occur due to charges on the pipe if the wall is non-conducting or conducting but ungrounded. In addition, a grounded conductive pipe can become hazardous if covered by an internal coating of high dielectric strength.

The charged bulk powder after passing through the transport pipe becomes hazardous in a pile within a container. Its bulk density has increased over that in the pipe and the powder is now charged. If the particles are non-conducting, the charge will be retained on them for a long period of time and the electrostatic energy within the pile will present a hazard. This energy, if released within a small volume by an electrostatic spark, may be hot enough to ignite the powder.

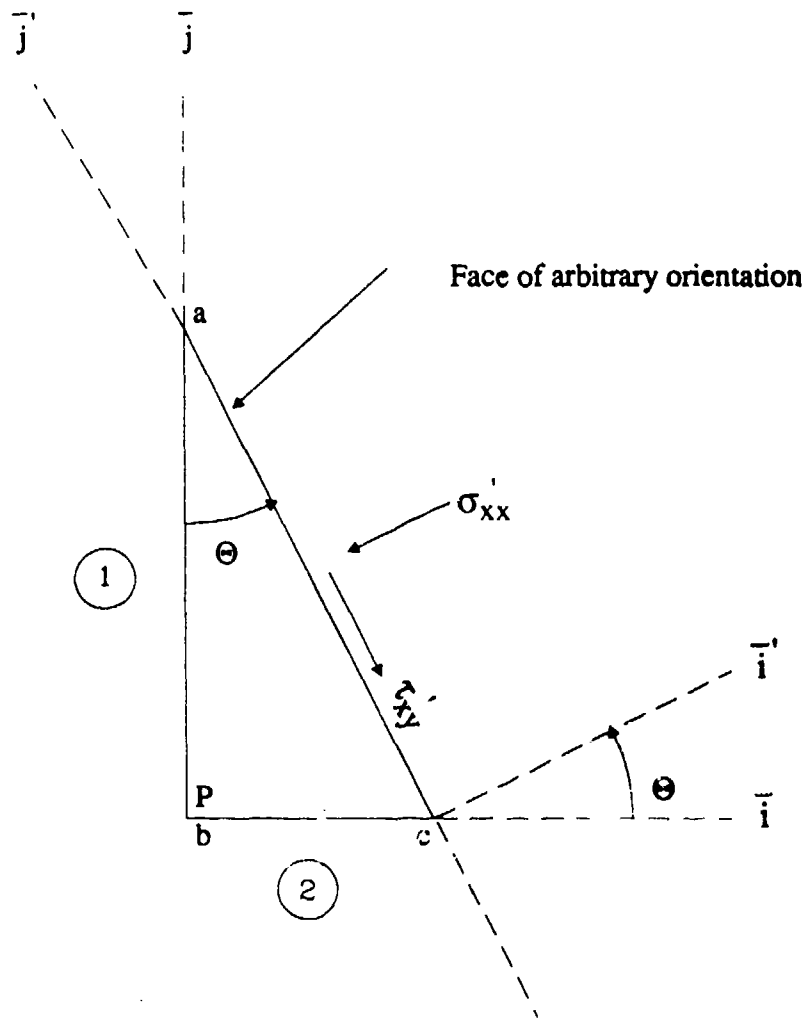
Charges can leak off through the pile by conduction, or through corona or brush discharges which neutralize charge through highly localized air breakdown followed by ionization of the gas (Jones and King, 1991). If the conduction is modeled as ohmic, the charge relaxation time $t_r = \kappa \epsilon_0 \gamma$ where κ is the dielectric constant ϵ_0 is the permittivity of free space and γ is the bulk resistivity in ohm-meters. A relaxation time of 1 second is considered safe. Polymer particles such as polyethylene have relaxation times of the order of 10^4 seconds. Charge leakage can be increased by raising the humidity above about 60% and by the use of thin grounded metal rods (< 3 mm in diameter) which promote corona discharges.

E. Electrostatic force on a particle

Electrostatically active powders such as starch and cabosil can produce about $10^3 \mu\text{C}$ of charge per kg of agitated powder (Eden, 1973). For a $20 \mu\text{m}$ sphere with a density of 3000 kg/m^3 , he calculates the charge per particle as about 10^{-14} C . The electrostatic force between the particle and the wall is $1.43 \times 10^{-8} \text{ N}$ which is 116 times the gravitational force. This indicates that the particle will stick on the wall.

References

- Pacek, A.W. and Nienow, A.W., Powder Tech. 60, 145-58 (1990).
- Rietema, K., "The Dynamics of Fine Powders", Elsevier, England, 1991.
- Brown, R.L. and Richards, J.C., "Principles of Powder Mechanics," Pergamon, England, 1970.
- Kreyszig, E., "Advanced Engineering Mathematics", John Wiley, U.S., 1962.
- Molerus, O., Powder Tech. 12, 259-75 (1975).
- Gibson, N., "Electrostatics 1983", S. Singh, Ed., Inst. of Physics, London, England, p. 1-11, 1983.
- Blythe, A.R. and Reddish, W., "Electrostatics 1979", Inst. of Physics, London, England, p. 107, 1979.
- Glor, M., "Electrostatics 1987", J.L. Sproston, Ed., Inst. of Physics, London, England, p. 207-16, 1987.
- Jones, T.B. and King, J.L., "Powder Handling and Electrostatics, Lewis, Chelsea, Michigan, 1991.



- Notes:
- $\Theta = 0$ is face 1 whose outward drawn normal is \bar{i}
 - $\Theta = \Theta$ is the face of arbitrary orientation whose outward drawn normal is \bar{i}'
 - $\Theta = \pi/2$ is face 4 in Fig 1b whose outward drawn normal is \bar{j}

Figure 1a Normal and Tangential Stresses in Bulk Powder on a Plane of Arbitrary Orientation through a Point P(x,y)

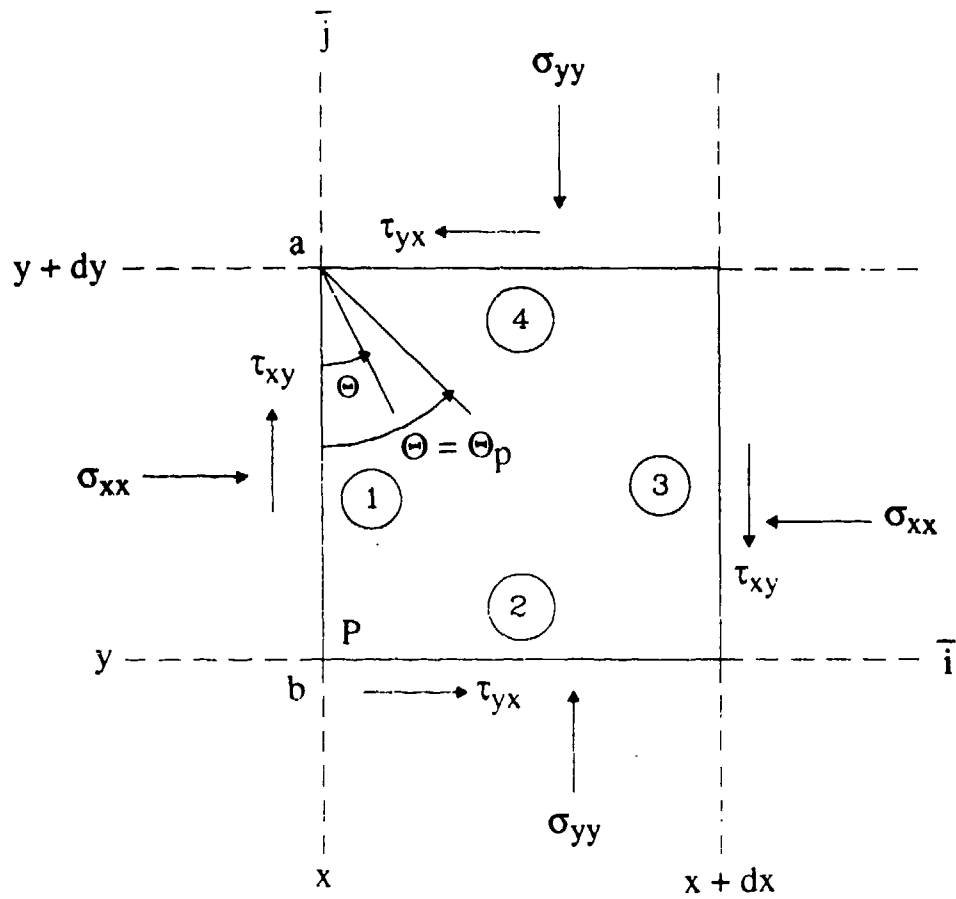


Fig 1b Stresses on Element of Bulk Powder Oriented Parallel and Perpendicular to the \bar{i} and \bar{j} Coordinate Axes Located at Point P.

Fig 2 Mohr Circle Diagram

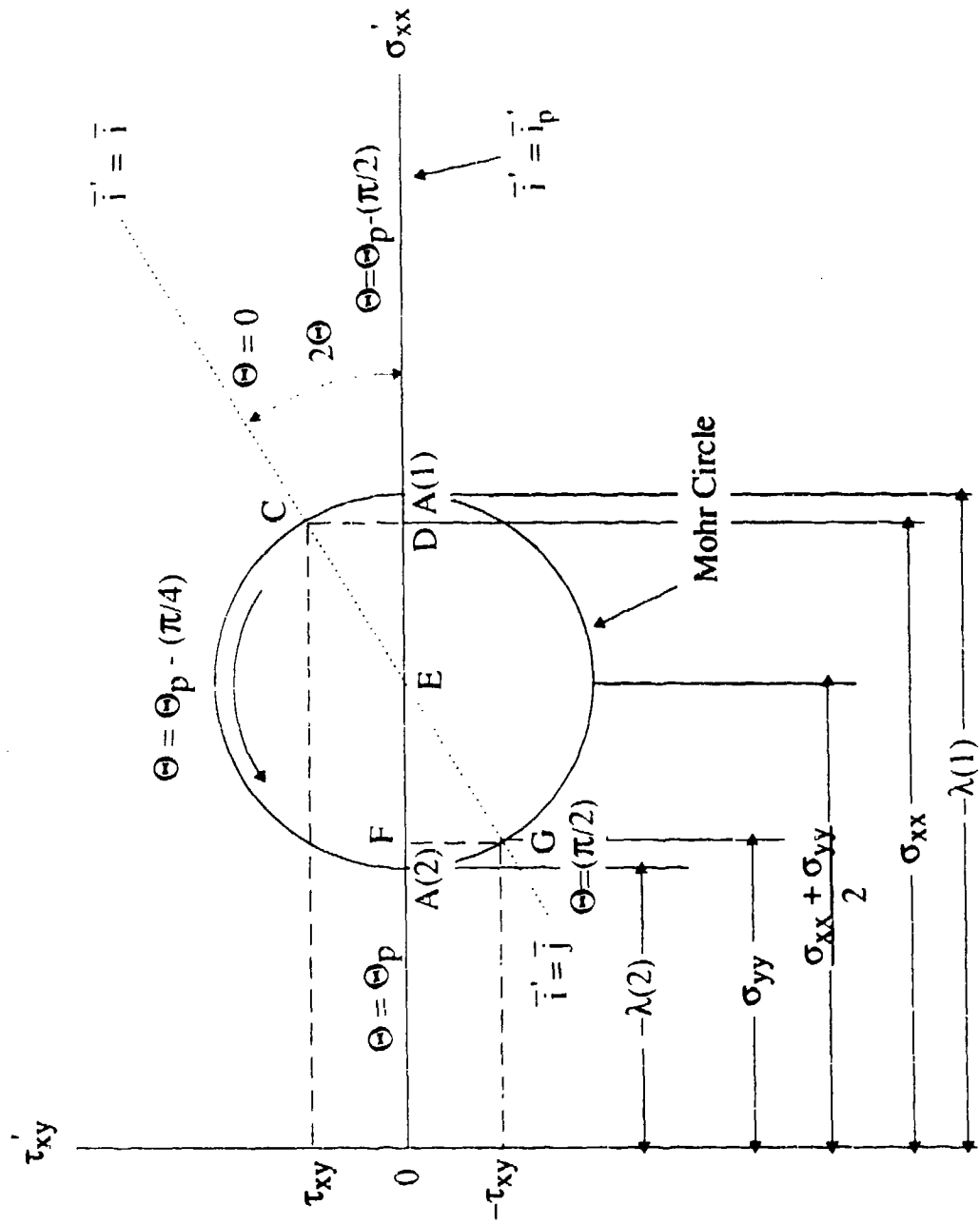


Fig 3 Fracture Condition at Point P in a Bulk Powder

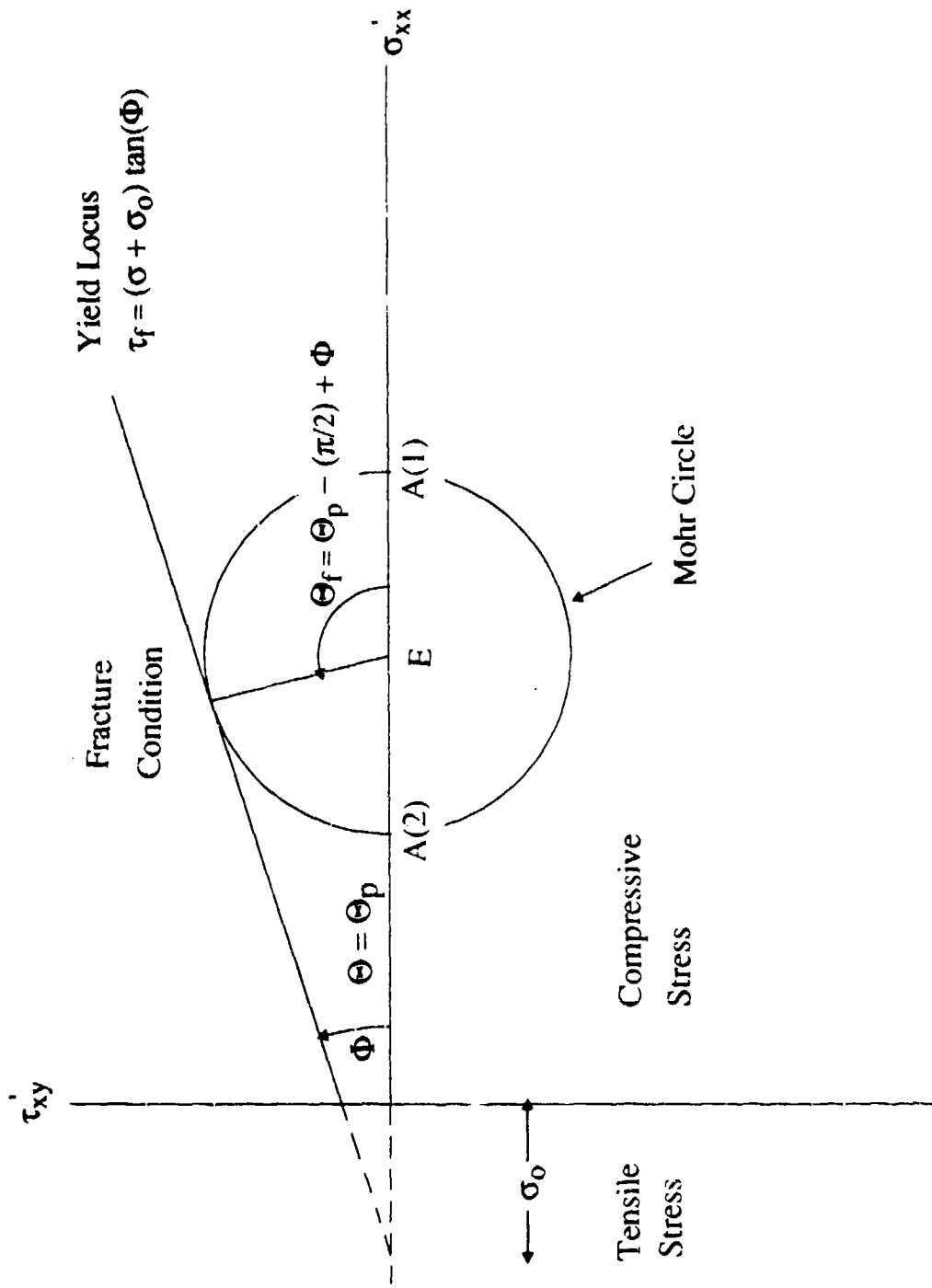
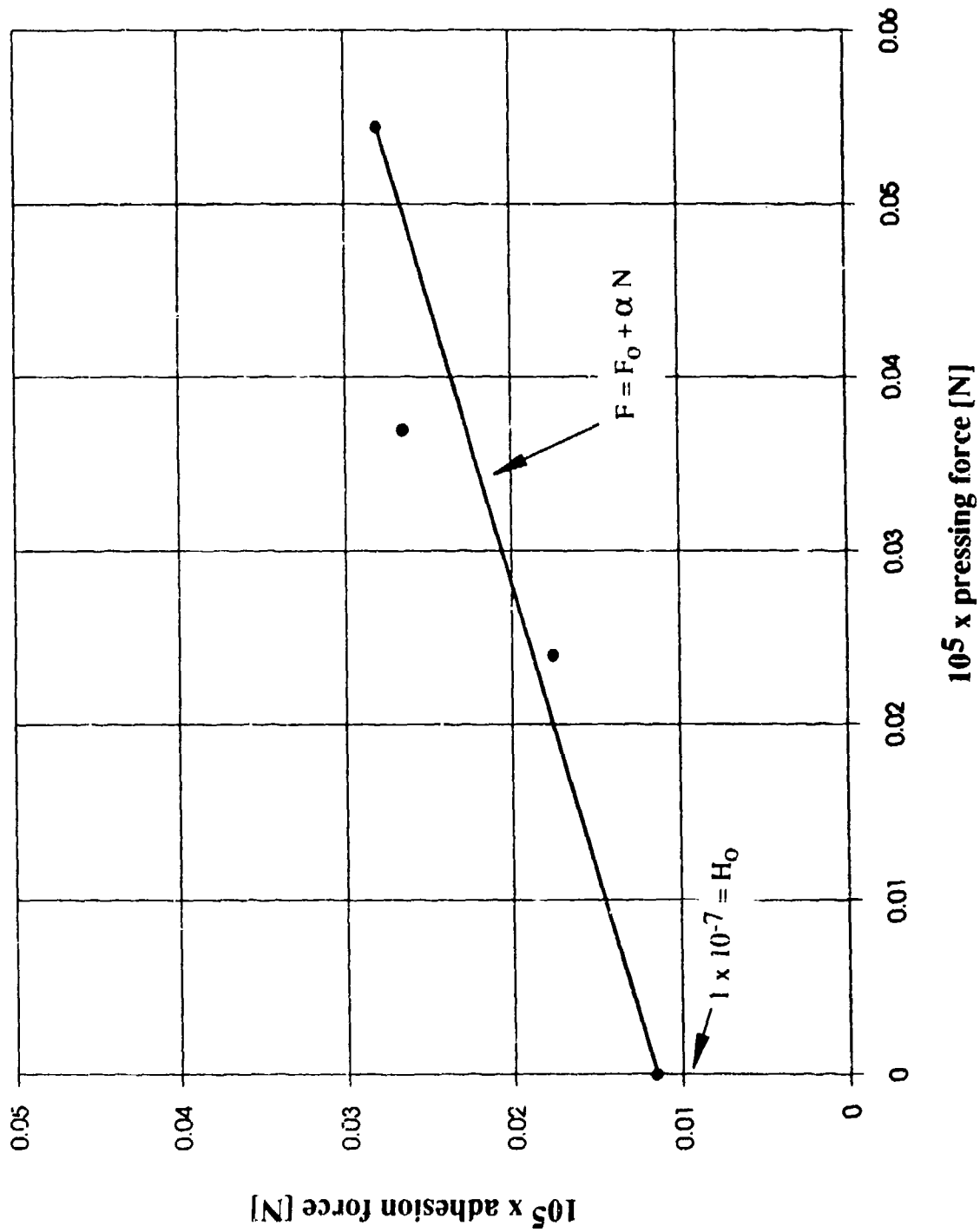


Fig. 4 Adhesive forces of limesione particles on a metal surface,
influence of previous pressing at low load level



Blank

**ELECTROSTATIC SMOKE (FOG) CLEARING
IN ENCLOSED CHAMBERS**

Z. Zhou, W. McLeod, R. Shaffer, and D. Reidy

GEO-CENTERS, INC.
7 Wells Avenue
Newton Centre, MA 02159

Glen Rubel
CRDEC
Edgewood, MD 21040

ABSTRACT

Smokes or fogs (aerosol clouds) have been cleared up using a method based on electrostatic precipitation in enclosed chambers. The visibility of the smoke or fog has been measured as a function of time before and after the electrostatic precipitation. The results show that electrostatic precipitation is effective in clearing smokes and fogs (aerosol clouds). Further work is needed to extend the chamber results to outdoor field tests.

INTRODUCTION

Some major accidents generate hazardous smokes or fogs (or aerosol clouds) which decrease visibility and thus present dangers. These smokes or fogs (aerosol clouds) need to be cleared up quickly. Currently, a variety of approaches exist to clear the smokes or fogs (aerosol clouds). They are generally classified into four categories: 1) direct removal of aerosol particles from the cloud, such as electrostatic precipitation, 2) coagulation and subsequent sedimentation, such as various agglomeration methods, 3) evaporation of droplets if the smoke is formed by liquid aerosols, such as light heating, and 4) dilution of smoke or aerosol clouds. Among these four general approaches, the first method based on electrostatic precipitation, is considered highly effective [1], [2]. Smoke or fog clearing experiments in enclosed chambers were conducted using electrostatic precipitation with a point source corona discharge.

EXPERIMENTAL

The experiments were conducted in a chamber of 13.4 M³ (3.4M x 2.1M x 1.9M) for red phosphorous smoke (RP smoke) and in a chamber of 0.7 M³ (1.2M x 0.76M x 0.76M) for a fog (liquid aerosol). The experimental set up is given schematically in Figure 1. The measurement equipment includes a helium-neon laser ($\lambda = 633 \text{ nm}$) at one side of the chamber and a photodiode at the other side. The laser light enters from one side of the chamber, passes through the smoke or aerosol cloud, comes out from the other side and there is detected by the photodiode. The intensity of transmitted light is quantified and fed into a personal computer for data processing. A corona discharge device (a point source) close to the chamber wall is used to generate ions inside the chamber. The ions collide with and attach themselves to the aerosols. Then, the charged aerosols drift and deposit onto the walls under the influence of an electrical field established between the corona discharge point and the ground.

CLEARING OF RED PHOSPHOROUS SMOKE

The red phosphorous smoke is generated inside the chamber by burning approximately 1.4 gram of red phosphor. After the burning, the chamber is filled with opaque red phosphorous smoke with transmissivity about 20%. A mixing fan is running all the time throughout the experiments to keep the smoke uniform inside the chamber. The smoke transmissivity increases slowly with time, typically at a rate below 3% over 1000 seconds, due to coagulation. After the ions are introduced in the chamber by corona discharge (rate of input electric charge is 43 μA), the smoke precipitates dramatically to the walls under the influence of the electric field. This is evidenced by the rise of smoke transmissivity inside the chamber and directly from the fact that the wall is covered with a thin layer of smoke particles after the precipitation.

The result is given in Figure 2. For 4 minute long introduction of ions into the smoke chamber, the light transmissivity of the smoke increases from 23% to 67%. Ten minutes after the introduction, the transmissivity increases to over 80%. For 2 minute long introductions, the light transmissivity increases from 21% to 47%. Ten minutes after the introduction, the transmissivity increases to 57%.

CLEARING OF LIQUID AEROSOLS (FOG)

Liquid aerosols (fog) are generated by the evaporation and condensation of a water-based glycol mixture, which is used for fog

generation. A ROSCO fog machine [3] is used in the experiments. A fog of approximately 0.5% transmissivity is generated inside the chamber for the experiments. The electrical corona current in electrostatic precipitation (rate of input electrical charge) is varied from 5 μA up to 28 μA while transmissivity of the smoke in the chamber is monitored constantly throughout the experiment.

A typical plot of smoke transmissivity in the chamber as a function of time is given in Figure 3 for $I = 10 \mu\text{A}$. An expanded view of smoke transmissivity as a function of time is given in Figure 4. The corona discharge starts at time 36.67 min. and ends at 41.67 min. The time it takes to clear the aerosol cloud in the chamber from 0.5% to 90% of transmissivity are 4.8 minutes at corona discharge current of 5 μA , 3.0 minutes at 10 μA , 1.8 minutes at 20 μA , and 1.8 minutes at 28 μA .

REFERENCES

1. Podzimek, J., "Survey of Techniques for Clearing Military Smoke Clouds", Contract Report ARGSL-CR-70-20, 1979.
2. White, J., "Industrial Electrostatic Precipitation", Addison-Wesley Publishing Co., Inc., 1963.
3. ROSCO Laboratories, Inc., 36 Bush Avenue, Port Chester, NY, 10573.

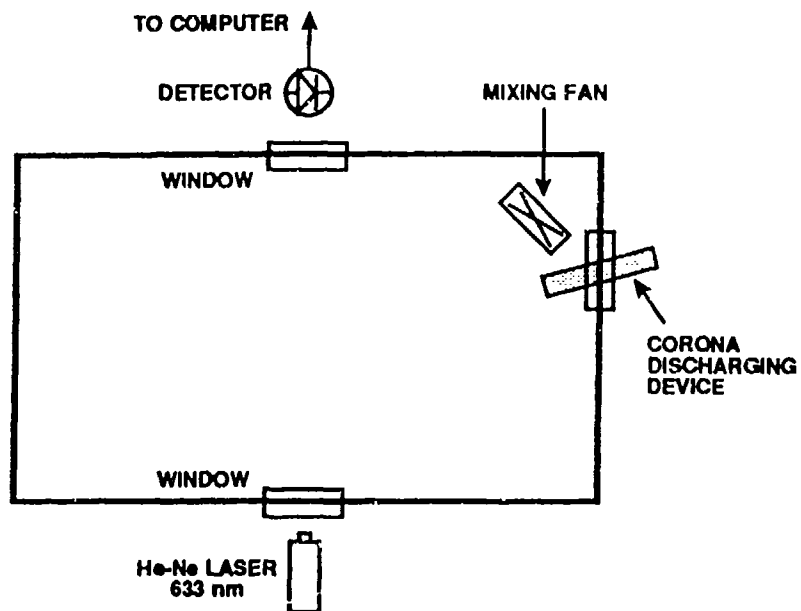


Figure 1. Smoke Chamber

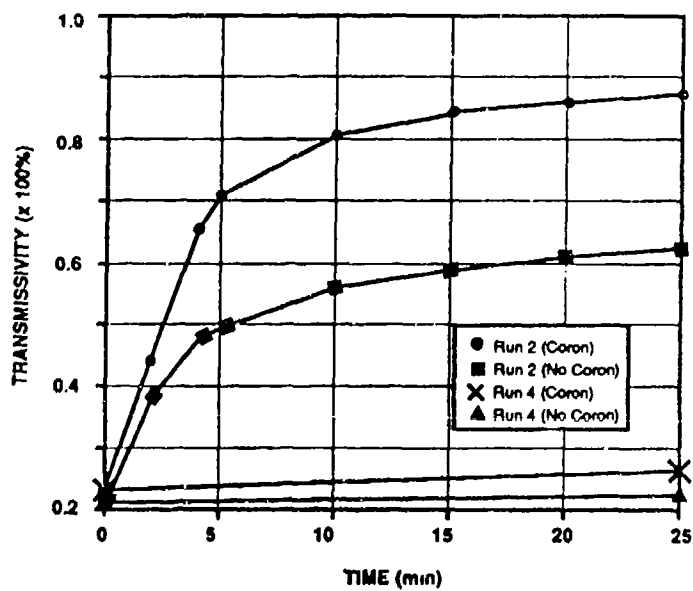


Figure 2. Transmissivity vs. Time

- Corona discharge begins at time zero
- For Run 2, the corona discharge lasts 4 minutes
- For Run 4, the corona discharge lasts 2 minutes

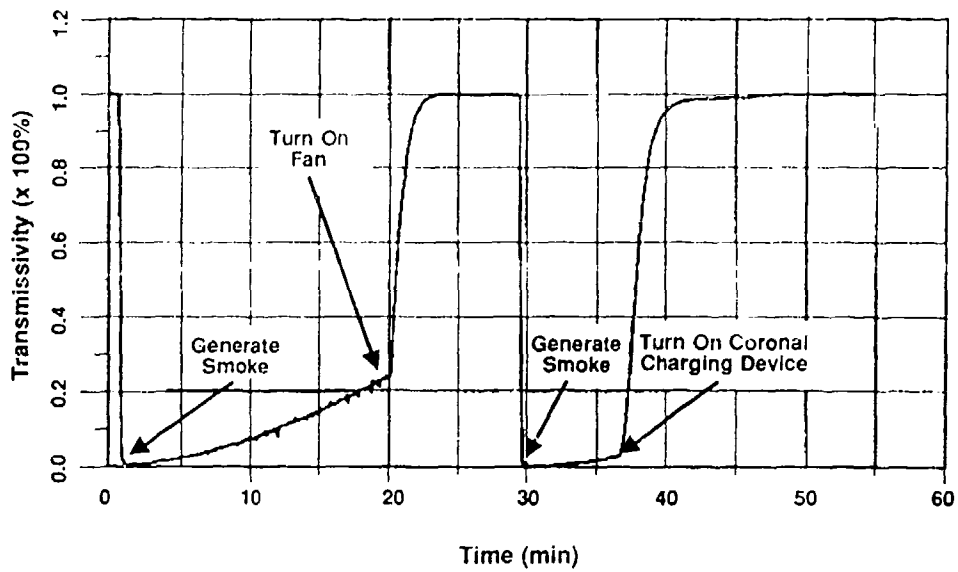


Figure 3. Transmissivity as a Function of Time ($I = 10A$)

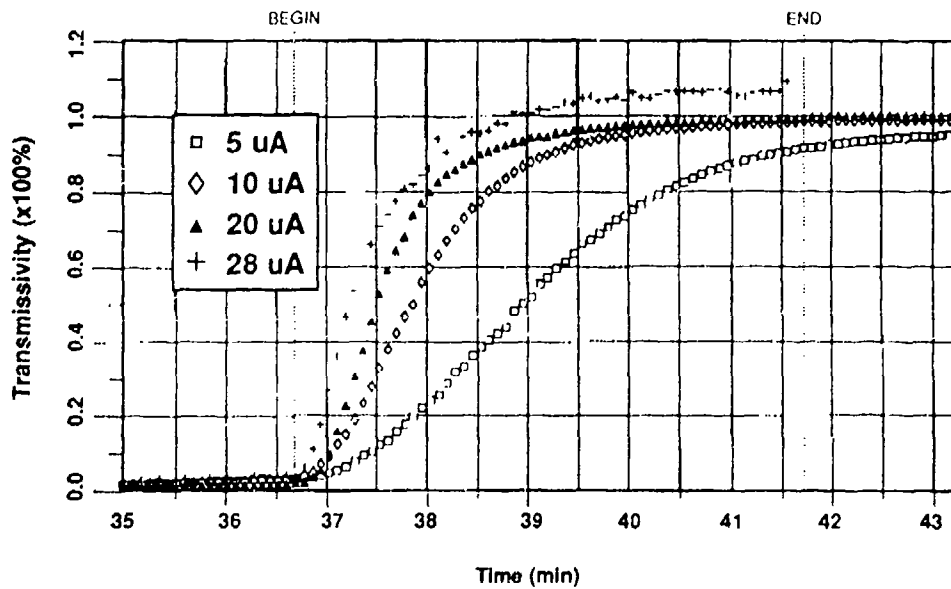


Figure 4. Transmissivity as a Function of Time.

(Corona Discharge Begins at 36.7 min. and Ends at 41.7 min)

Blank

**METASTABLE PHASES IN COMPRESSED 1-OCTADECANOL MONOLAYERS
ON LEVITATED WATERDROPS**

MARK SEAVER AND GLENN O. RUBEL

Code 6540, Naval Research Lab, Washington, DC 20375
and
U. S. Army Armament Munitions and Chemical Command, CRDEC,
Aberdeen Proving Ground, MD 21010-5423

RECENT PUBLICATIONS AND PRESENTATIONS:

Gas Scavenging of Insoluble Vapors: Condensation of Methyl Salicylate Vapor onto Evaporating Drops of Water, Mark Seaver, J. R. Peele, and G. O. Rubel, *Atmos. Environ.* **26**, 205 (1992).

Gas Scavenging of Simulated Pesticides by Evaporating Water Drops in an Acoustic Levitation Wind Tunnel, Mark Seaver and J. R. Peele, in "Precipitation Scavenging and Atmosphere-Surface Exchange, Vol. 1.", S. E. Schwartz and W. G. N. Slinn eds., (Hemisphere, Washington, 1992). p41.

Evaporation Kinetics of Ventilated Waterdrops Coated with Octadecanol Monolayers, Mark Seaver, J. R. Peele, T. J. Manuccia, G. O. Rubel, and George Ritchie, *J. Phys. Chem.* **96**, 6389 (1992).

Remote Thermometry of Evaporating Water Drops as an Octadecanol Monolayer Changes Phase, Mark Seaver and J. R. Peele, presented at 3rd Conference on Laser Applications to Chemical Analysis, Salt Lake City, UT. Jan 26-29, 1992.

Remote thermometry of evaporating water drops coated with fatty alcohol monolayers, George Ritchie, Mark Seaver, T. J. Manuccia, and J. R. Peele, presented at Laser Electro-Optical Society, San Jose, CA, Nov. 3-6, 1991.

ABSTRACT

In a Langmuir trough, the gas to liquid condensed (G/LC) phase change of 1-octadecanol monolayers occurs near 0.220 nm²/molecule. This phase change is also associated with a dramatic reduction in the transport of water through the monolayer. We use 0.220 nm²/molecule and the initial octadecanol concentration in a drop to predict the surface area (S_p) at which the change in

evaporation rate should occur. When we compare our measured values for the surface area at which the evaporation rate change occurs (S_m) with S_p , we see the G/LC phase change occur at S_m/S_p values between 0.1 and 0.3. As we add $\text{Eu}^{3+}(\text{EDTA})$ at concentrations between 1.0×10^{-6} and 2.0×10^{-4} M, we see the S_m/S_p ratios rise asymptotically to 0.6. Increasing the initial pH of a drop to 6.0 reduces S_m/S_p at all $\text{Eu}(\text{EDTA})$ concentrations. These results are accounted for in terms of multilayers of octadecanol on the drop surface created by a delayed G/LC phase change, and heterogeneous nucleation of the G/LC phase change by the $\text{Eu}(\text{EDTA})$.

INTRODUCTION

Studies of monolayer phases and their effects on mass transport are usually carried out with a Langmuir trough.^{1,2} The results of such studies are reported in terms of surface pressure-area (π -A) isotherms and/or monolayer resistivities (R). The results of Costin and Barnes link the resistivity increase in a pure octadecanol monolayer with the gas to liquid-condensed (G/LC) phase change³ which occurs at A values near $0.220 \text{ nm}^2/\text{molecule}$. The study by Marsden and Schulman⁴ shows that fatty alcohol monolayers are not affected by pH changes between pH=2-10.

In these experiments, we monitor the evaporation of an acoustically levitated waterdrop and use the change in evaporation rate to pinpoint the G/LC phase change. When we compare the measured drop surface area at the G/LC phase change with that predicted using $0.220 \text{ nm}^2/\text{molecule}$, we find that the phase change occurs at surface areas that are 1.5 to 10 times smaller than the predicted values. We also find that this number varies asymptotically with $\text{Eu}^{3+}(\text{EDTA})$ concentration and shows a pH dependence. In contrast to the drop results, we have obtained π -A isotherms for octadecanol on pure water and on water containing 2.0×10^{-5} M $\text{Eu}(\text{EDTA})$ and find them indistinguishable from the literature results.⁵

EXPERIMENTAL

The apparatus, which uses an acoustic standing wave to levitate ~2mm diameter drops in the jet of a wind tunnel has been described in detail.⁶ For these experiments the gas jet is dry nitrogen to which water vapor is added to produce ~30% relative humidity. The gas stream temperature is 20.3°C . Production and handling of the stock solutions has also been described previously.⁷ The working solutions all contain 1.2 mole% ethanol, 2.85×10^{-3} M octadecanol, and $\text{Eu}(\text{EDTA})$ between 0.0 and 2.0×10^{-4} M. Drops are placed in the acoustic trap with a syringe. Backlit drops are imaged with a video microscope whose output is digitized and analyzed at specified intervals to provide drop volume and surface area measurements.

RESULTS AND DISCUSSION

Figure 1 illustrates a typical drop evaporation history. In this figure, we see a drop whose evaporation is indistinguishable from pure water for the first 750s. At that time a sudden decrease in evaporation rate occurs. The Langmuir trough results suggest that this change in evaporation rate corresponds to the G/LC phase change. Thus, we associate the surface area measured at this time, S_m , with the area occupied by the octadecanol monolayer. Since the number of octadecanol molecules in this monolayer will depend on the octadecanol concentration and the initial drop volume, we report the ratio S_m/S_p , which is independent of our experimental parameters. The quantity S_p is calculated from the octadecanol concentration in the working solution (2.85×10^{-4} M), the initial drop volume, and $0.220 \text{ nm}^2/\text{molecule}$.

Figure 2 summarizes the drop history results. Here we see that the S_m/S_p ratios increase with Eu(EDTA) concentration and this increase tends toward an asymptote near 0.60. We also see that increased pH produces smaller S_m/S_p ratios at constant Eu(EDTA) concentration and that the data get very noisy as the Eu(EDTA) concentration vanishes.

There are three possible interpretations for S_m/S_p ratios less than unity. First, ratios less than one suggest that less than 100% transfer of the octadecanol in the stock solution to the drop surface. Such would be the case if octadecanol "comes out" of solution in the working mixture which is only 1.2 mole% ethanol. This explanation, however, does not account for the dependence in S_m/S_p on Eu(EDTA). Another possibility is that the Eu(EDTA) increases the solubility of the octadecanol. Were this true, we would expect a decrease in S_m/S_p with Eu(EDTA) concentration. Additional evidence against a change in solubility comes from our π -A isotherm measurements on ultrapure water and on 2.0×10^{-5} M Eu(EDTA)/water. For both substrates, the isotherms are indistinguishable from the results of Harkins and Copeland.⁵ The increase in S_m/S_p with Eu(EDTA) concentration could be explained if the inorganic complex gets incorporated into the monolayer. However, surface tension measurements for the ultrapure water and the 2.0×10^{-4} M Eu(EDTA) solution give 72 and 71 dyne/cm² respectively. This small change precludes surface activity. Also, >2% Eu(EDTA) in the monolayer would limit the evaporation rate change after the G/LC phase change. We see no increases in the final evaporation rates when drops containing Eu(EDTA) are compared with drops of pure water.

The second explanation postulates the formation of octadecanol micelles. In this scenario, the G/LC phase change occurs whenever micelle diffusion has brought enough octadecanol to the surface to produce a condensed monolayer. The addition of Eu(EDTA) would then reduce micelle size and increase the micelle diffusion rate. Our literature searches have uncovered no evidence for micelle formation by fatty alcohols.

The final hypothesis is that the G/LC phase change requires nucleation. In a levitated drop of pure water there are no walls or barriers to help orient the octadecanol molecules and act as heterogeneous nucleation sites. Thus, the phase change is delayed waiting for homogeneous nucleation events and we build up multilayers of octadecanol on the drop surface prior to the phase change. The addition of Eu(EDTA) provides heterogeneous nucleation sites which lie below the surfactant layer and therefore, expedite the G/LC phase change without effecting the monolayer's transport characteristics.

REFERENCES

- ¹A. W. Adamson, *Physical Chemistry of Surfaces*, 5th ed. (Wiley. Interscience, New York, 1990).
- ²G. L. Gaines, *Insoluble Monolayers at Liquid-Gas Interfaces*, (Interscience, New York, 1966).
- ³I. S. Costin and G. T. Barnes, *J. Colloid Interface Sci.* 25, 584 (1967).
- ⁴J. Marsden and J. H. Schulman, *Trans. Farad. Soc.* **34**, 748 (1938).
- ⁵W. D. Harkins and L. E. Copeland, *J. Chem. Phys.* **10**, 272, (1942).
- ⁶M. Seaver, A. Galloway, and T. J. Manuccia, *Rev. Sci. Instrum.* **60**, 3452 (1989).
- ⁷M. Seaver, J. R. Peele, T. J. Manuccia, G. O. Rubel, and George Ritchie, *J. Phys. Chem.* **96**, 6389 (1992).

Figure 1. Sample Drop Evaporation History

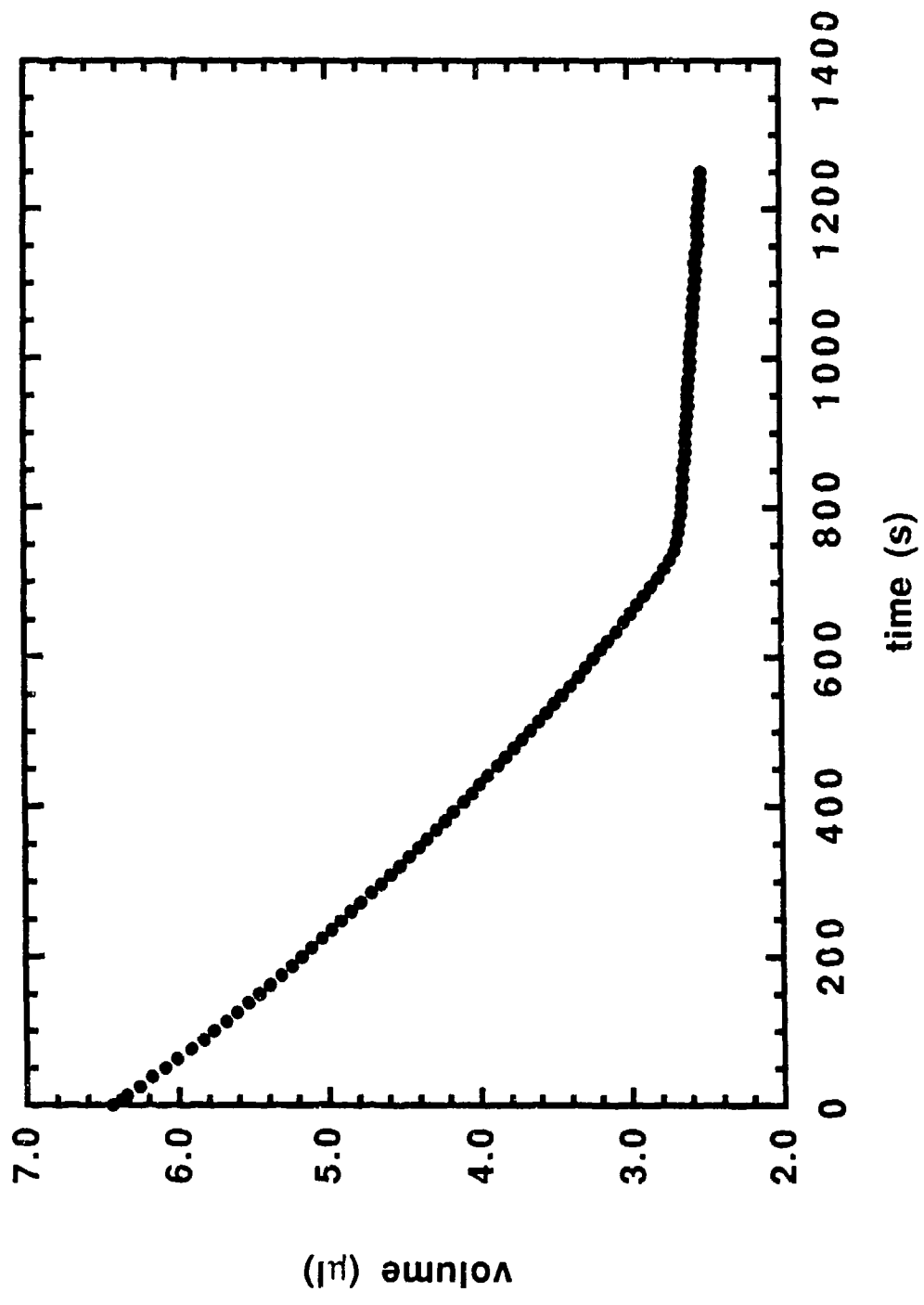
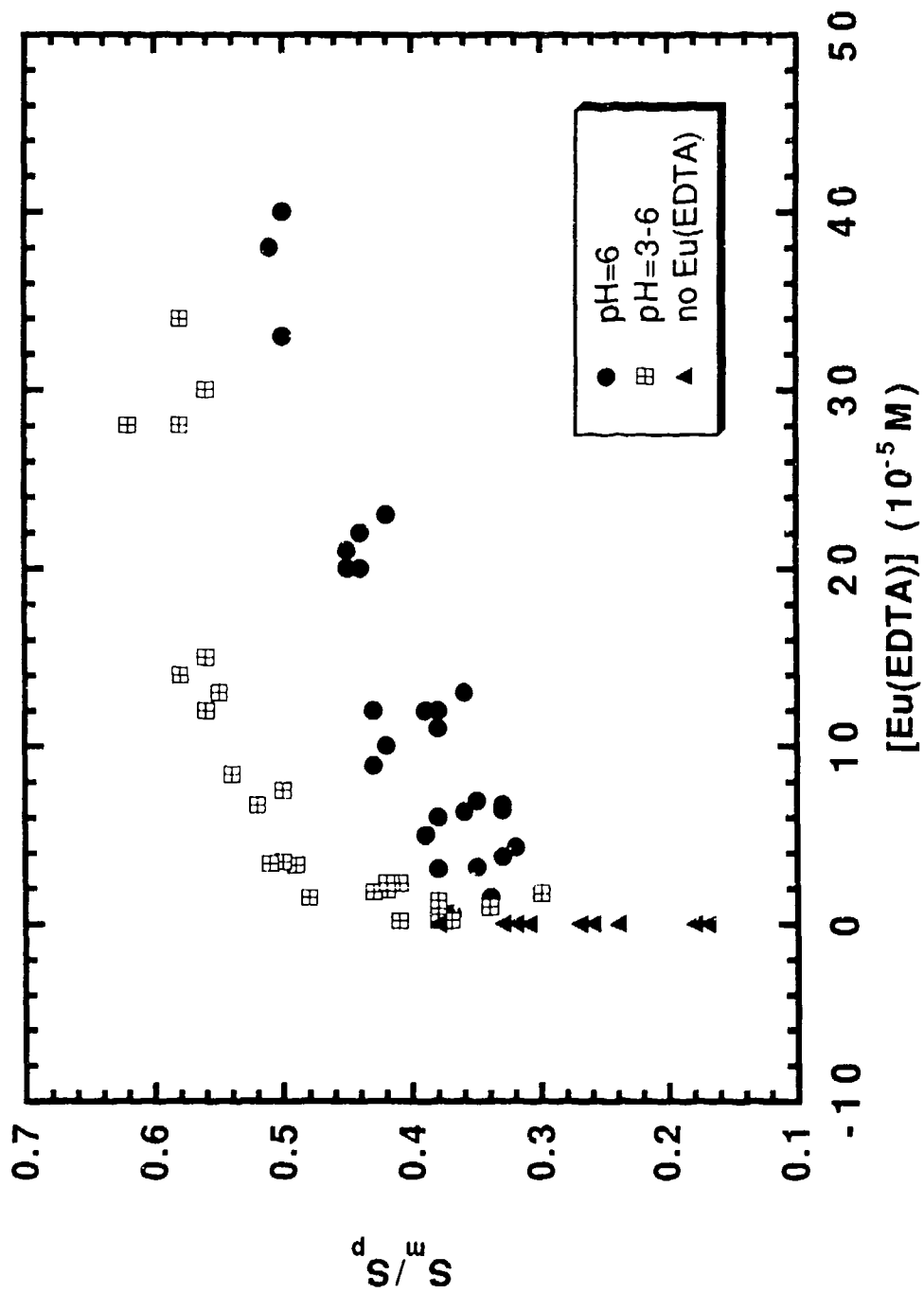


Figure 2. Monolayer Phase Change Results



ON FEASIBILITY OF FINITE ELEMENT SOLUTION OF THE MAXWELL EQUATIONS
FOR ABSORPTION AND SCATTERING OF ELECTROMAGNETIC RADIATION
BY A PARTICLE

M. K. Choi and J. R. Brock
Chemical Engineering Department
University of Texas, Austin, Texas 78712

RECENT PUBLICATIONS, SUBMITTALS FOR PUBLICATION AND PRESENTATIONS

- "Numerical simulation of particle formation and growth in rapidly expanding two dimensional flows", J. Phys. Chem. submitted (1992) (with B. J. Jurcik)
- "Time-resolved Raman spectroscopy from reacting optically levitated microdroplets", SPIE Proceedings, *Nonlinear Optics and Materials* 1497,(1991).(with J. C. Carls)
- "Attachment of TiO₂ powders to hollow glass microbeads:activity of the TiO₂-coated beads in the photoassisted oxidation of ethanol to acetaldehyde", J. Electrochem. Soc. 138, 3660 (1991) (with N. Jackson, C. Wang, Z. Luo, J. Schwitzgebel, J. Ekerdt, and A. Heller)
- "Simulation of plasma interactions in a resonant RF cavity for plasma chemistry processing", Proceedings of 33d Annual Meeting American Physical Society, Division of Plasma Physics, Nov.4, 1991.(with E. Montalvo, D. Booth, R. Carrera, J. Gallmeier and M. E. Oakes).
- "Collection optics of photocatalyst on hollow glass microbeads floating on oil slicks", J. Phys. Chem. 96 3423(1992) (with I. Rosenberg and A. Heller)
- "Plasma processing of hazardous materials", Proceedings of 1992 International Conference on Plasma Science", 1992. (with W. Booth, R. Carrera, J. Gallmeier)
- "A theoretical investigation of low pressure particle impaction in a highly underexpanded sonic impinging slit jet", J. Aerosol Sci. In Press, (1992) (with P. S. Chang and I. Trachtenberg)
- "A finite element solution of the Maxwell equations in the frequency domain for absorption and scattering of electromagnetic radiation by a dielectric particle", submitted (1992) (with L. Libberman)
- "Light-assisted liquid film etching", J. Appl. Phys., In Press (1992).(with P. Lim and I. Trachtenberg)
- "Particle formation by homogeneous nucleation in rapidly expanding flows" *Proceedings of the 1990 CRDEC Scientific Conference on Obscuration and Aerosol Research*, CRDEC, U. S. Army, 1991 (with B. J. Jurcik).
- "Particle formation by binary homogeneous nucleation in supersonic flows" *Proceedings of the 1991 CRDEC Scientific Conference on Obscuration and Aerosol Research*, CRDEC, U. S. Army, 1992 (with B. J. Jurcik).
- "Formation of graphite and diamond fibers in corona discharges" *Proceedings of the 1991 CRDEC Scientific Conference on Obscuration and Aerosol Research*, CRDEC, U. S. Army, 1992.
- "Finite element solutions of the Maxwell equations " *Proceedings of the 1991 CRDEC Scientific Conference on Obscuration and Aerosol Research*, CRDEC, U. S. Army, 1992.

ABSTRACT

The problem of scattering and absorption of electromagnetic radiation by particles can be solved analytically for only the simplest cases, but established numerical methods allow a straightforward extension to particles with arbitrary inhomogeneities, arbitrary shapes, and nonlinear response. In this paper a recently developed frequency domain method involving CFD techniques is reviewed and applied to the problem of a dielectric sphere of arbitrary size parameter. Numerical results showing good agreement with analytical solutions for size parameters over 20 are given. Results obtained suggest that finite element methods have promise for analytically intractable scattering/absorption problems and show that the Debye amplitude formulation of the problem offers great advantages in a numerical scheme and that, contrary to the naive view, as we show here, negligible error is introduced in going from the Debye amplitude formulation to field observables, such as the source function.

Mie theory exactly describes the absorption and scattering of a plane electromagnetic wave by an isotropic, dielectric sphere of arbitrary size and refractive index^{1,2}. This conceptually simple analytical solution is well known, but it involves cumbersome computations. However, many problems of interest do not readily admit analytical calculation. If a systematic numerical rather than an analytical approach is taken, the extension to particles with arbitrary inhomogeneities, arbitrary shapes, and nonlinear response is apparent since the general governing equations and the solution technique remain unchanged.

If one takes a numerical approach to solving the light scattering problem, the extension to particles with arbitrary inhomogeneities and arbitrary shapes is straightforward since the governing equations and the solution technique remain unchanged. For comparable electromagnetic wave scattering problems in radio and microwave engineering, differential methods have been used predominantly {Bates, 1975}. Finite difference methods and finite element methods are typical differential solution techniques, and both can be applied to the Maxwell equations in their time-domain or frequency-domain form. While these methods have been applied in various disciplines for some time {Taflove, 1988; Taflove, 1975; Taflove, 1989; Umashankar, 1982; Lynch, 1985; Lynch, 1990; Kerner, 1986 }, they have not been adapted to study the absorption and scattering of light by small particles.

In the majority of past work, the problems have been solved in terms of the vector field variables (\mathbf{E}, \mathbf{H}) that are oscillatory in nature over the infinite domain of the scattering problem. The difficulty of modeling these oscillations is removed in this study by reformulating the problem in terms of the Debye amplitude (DA) functions as described below. Another complication in scattering problems is the treatment of the particle interface and the determination of the internal fields. This issue has been considered in previous time-domain {Lynch, 1990} and frequency-domain {Lynch, 1985} solution methods, although many past investigations involved perfect conductors (no internal fields).

The preferential use of frequency-domain or time-domain methods has not been established. Frequency-domain approaches are generally more accurate and require less computation time, but time-domain methods typically require less memory and permit easier handling of material interfaces {Lynch, 1990; Taflove, 1975}. In this study the frequency-domain Maxwell equations are solved.

The advantage of finite element methods over finite difference techniques lies in geometrical flexibility; finite elements can better handle irregular domains {Lee, 1990}. Since one of the goals of this investigation is to allow for the extension to particles of arbitrary shape, a finite element method is used. No complete finite element analysis approach to this problem has been published previously (cf. Morgan and Mei, 1979).

Previously a finite difference method was applied to the problem of a linearly polarized plane electromagnetic wave scattered by a perfectly conducting sphere¹. The results demonstrated the applicability of computational fluid dynamics (CFD) methods to the basic scattering problem. This work differs importantly from this previous work in that the finite element method is consistently applied, and we use Galerkin's formulation to the whole domain of calculation, and dielectric particles are considered. Previously Morgan and Mei (1977) used a hybrid method with a Fourier expansion of the fields to get trial functions with expansion coefficients found by their so-called "unimoment" method. Theirs is not a true finite element formulation of the problem and extension of their method may not be straightforward and might prove to be problematic; it cannot apply to nonlinear problems. Our true finite element formulation is described, followed by presentation of results of comparisons between analytical and numerical solutions.

The problem to be solved consists of a plane polarized wave incident on a dielectric particle; only linear scattering is considered. Assuming $\exp(-i\omega t)$ dependence for all fields, the electric and magnetic fields, \mathbf{E} and \mathbf{H} , must satisfy the vector wave equations both inside and outside the particle, with a requirement that the tangential components of \mathbf{E} and \mathbf{H} must be continuous across the surface of the particle² and the Sommerfeld radiation condition³ requires that the scattered fields represent divergent traveling waves as $r \rightarrow \infty$.

By introducing two auxiliary scalar functions, the electric and magnetic Debye potentials, u and v , in the usual way^{4,5,6}, it is possible to reduce the vector wave equations to a set of uncoupled scalar wave equations.

Since the field variables are oscillatory in nature over the infinite domain it is advantageous to reformulate the problem once again, this time in terms of a generalized amplitude function which eliminates the oscillations due to the incident field⁷; use of these Debye amplitude functions(DAs) is an essential step in a numerical approach. We have found no important degradation in accuracy in recalculating the field observables, such as for example the source function. By making use of the superposition property of the fields, the Debye potentials outside the particle can be decomposed into incident and scattered components. The scattered components then are written as:

$$u^s = \frac{\cos \phi \sin \theta}{(kI)^2} f_1^s(r, \theta) \frac{e^{i k r}}{r} \quad (1)$$

$$v^s = \left(\frac{\epsilon^I}{\mu^I} \right)^{1/2} \frac{\sin \phi \sin \theta}{(kI)^2} f_2^s(r, \theta) \frac{e^{i k r}}{r} \quad (2)$$

where "I" denotes the exterior region and "II" will denote the interior region and $k^2 = \omega^2 \epsilon \mu$.

$f(r, \theta)$ is the DA. Similar expressions can be written for the potentials inside the particle. It should be noted that the formulation of equations (1) and (2) inherently restricts one to the consideration of only axisymmetric problems. For asymmetric cases the ϕ dependence of the Debye potentials can not be factored out explicitly and one must solve for $f(r, \theta, \phi)$.

By substituting equations (1) and (2) into their respective scalar wave equation, it can be shown that the problem to be solved is

$$-\nabla^2 (f_1 e^{i k t}) - \frac{2 \cot \theta}{r^2} e^{i k t} \frac{\partial f_1}{\partial \theta} + \frac{2}{r} e^{i k t} \left(\frac{\partial f_1}{\partial r} + i k f_1 \right) - e^{i k t} f_1 \left(k^2 - \frac{2}{r^2} \right) = 0 \quad (3)$$

$$\left(\frac{\epsilon}{\mu} \right)^{1/2} \left(-\nabla^2 (f_2 e^{i k t}) - \frac{2 \cot \theta}{r^2} e^{i k t} \frac{\partial f_2}{\partial \theta} + \frac{2}{r} e^{i k t} \left(\frac{\partial f_2}{\partial r} + i k f_2 \right) - e^{i k t} f_2 \left(k^2 - \frac{2}{r^2} \right) \right) = 0 \quad (4)$$

The boundary conditions are, in terms of f_1 and f_2 :

$$e^{i k t} \epsilon^{\Pi} f_1^{\Pi} - e^{i k t} \epsilon^I f_1^s = \frac{\epsilon^I W}{\sin \theta} \quad (5)$$

$$e^{i k t} \sqrt{\epsilon^{\Pi}} f_2^{\Pi} - e^{i k t} \sqrt{\epsilon^I} f_2^s = \frac{\sqrt{\epsilon^I} W}{\sin \theta} \quad (6)$$

$$e^{i k t} \left[\left(\frac{\partial f_1^{\Pi}}{\partial r} + i k f_1^{\Pi} \right) - \left(\frac{\partial f_1^s}{\partial r} + i k f_1^s \right) \right] = \frac{1}{\sin \theta} \frac{\partial W}{\partial r} \quad (7)$$

$$e^{i k t} \left[\left(\frac{\epsilon^{\Pi}}{\mu^{\Pi}} \right)^{1/2} \left(\frac{\partial f_2^{\Pi}}{\partial r} + i k f_2^{\Pi} \right) - \left(\frac{\epsilon^I}{\mu^I} \right)^{1/2} \left(\frac{\partial f_2^s}{\partial r} + i k f_2^s \right) \right] = \left(\frac{\epsilon^I}{\mu^I} \right)^{1/2} \frac{1}{\sin \theta} \frac{\partial W}{\partial r} \quad (8)$$

where

$$W(r, \theta) = \frac{e^{i k r} \cos \theta}{\sin \theta} - \cot \left(\frac{\theta}{2} \right) \frac{e^{i k r}}{2} - \tan \left(\frac{\theta}{2} \right) \frac{e^{-i k r}}{2} \quad (9)$$

and the radiation condition can be expressed as

$$\lim_{r \rightarrow \infty} \frac{\partial f_1}{\partial r} = 0 \qquad \lim_{r \rightarrow \infty} \frac{\partial f_2}{\partial r} = 0 \qquad (10)$$

Equations (5) through (9) are formulated for a spherical particle, with radius "a". For the general asymmetric problem, equations (5) through (9) must be satisfied at all (x,y) on the particle surface and the partial derivatives are given by $\nabla f \cdot \mathbf{n}$.

The system of equations is solved numerically on a Cray Y-MP8/864 by a finite element method with 9-node Lagrange quadrilaterals⁸ using the subroutine HCGBLE, part of the Boeing Computer Services mathematical library⁹. A multiplier method¹⁰ is used to enforce the jump in solution across the particle boundary, which must coincide with element boundaries. The radiation boundary condition is imposed at a finite artificial surface ($r \ll \infty$) with good accuracy by using a second-order approximation to the Sommerfeld condition¹¹. Both the radiation boundary condition and the jump in flux condition are incorporated into the weak formulation of the differential equations.

Initial investigations have been performed for a linearly polarized plane wave with a wavelength of 10.591 μm , incident on a spherical water particle that has a refractive index of 1.179+0.071i. The particle was isolated and surrounded by air, assumed to have a refractive index of 1.0. Size parameters that were studied range from 2.97, to 21, which correspond to water droplets having diameters of 10.0 μm to ~80.0 μm .

Results are presented for the 70.0 μm case in Fig. 1. These results were obtained using a 26x45 uniform mesh having a maximum grid radius of twice the particle radius and required ~55 seconds of CPU time (including output time for results, with a code that has not been fully vectorized) to determine both f_1 and f_2 over the entire domain. Fig. 1 depicts three-dimensional views of the numerical and analytical solutions of the real part of f_1 . In these graphs the incident wave propagates in the positive z-direction, from the left foreground to the right rear. The particle is centered at the origin which is at the center of the plot, and the x- and z-axes show distances in micrometers. By comparing the top and bottom pictures, the excellent agreement between the two solutions can be seen. Plots of the imaginary part of f_1 and the real and imaginary parts of f_2 show similar agreement.

It is not necessary to rely on subjective impressions of agreement between exact and numerical solutions; one quantitative measure of the error of the numerical solution over its domain is given by the mean-square, or L^2 , norm⁸, which is defined for complex functions as

$$L^2 = \left[\int_{\text{Area}} (e e^*) dA \right]^{1/2} \qquad (11)$$

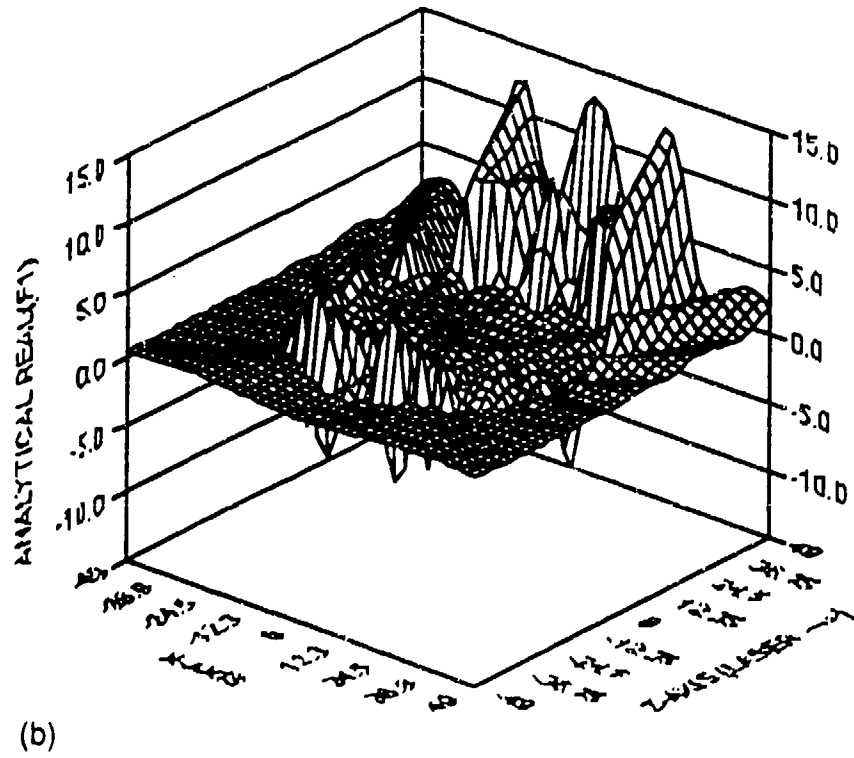
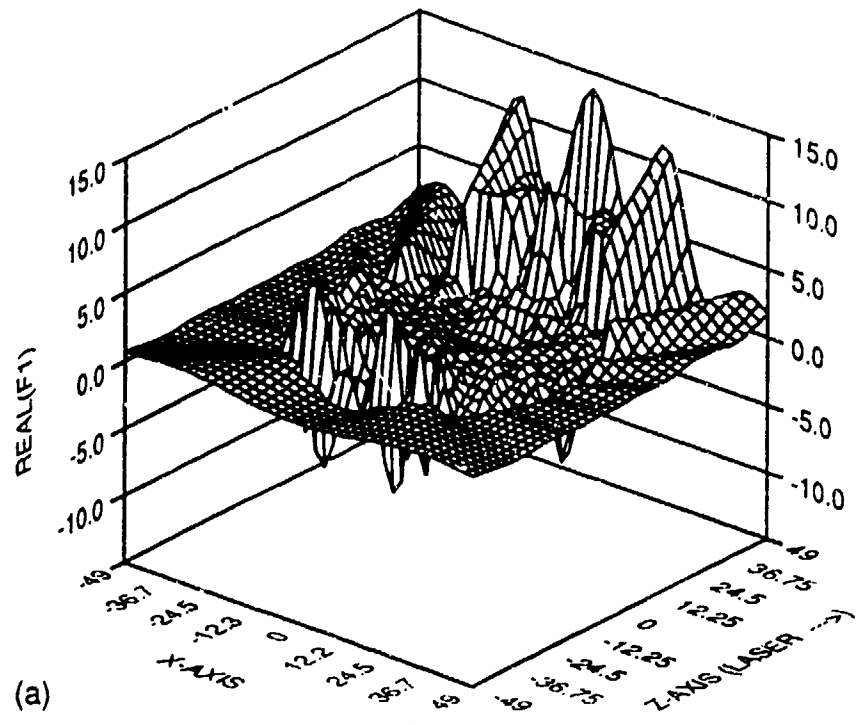


FIG 1

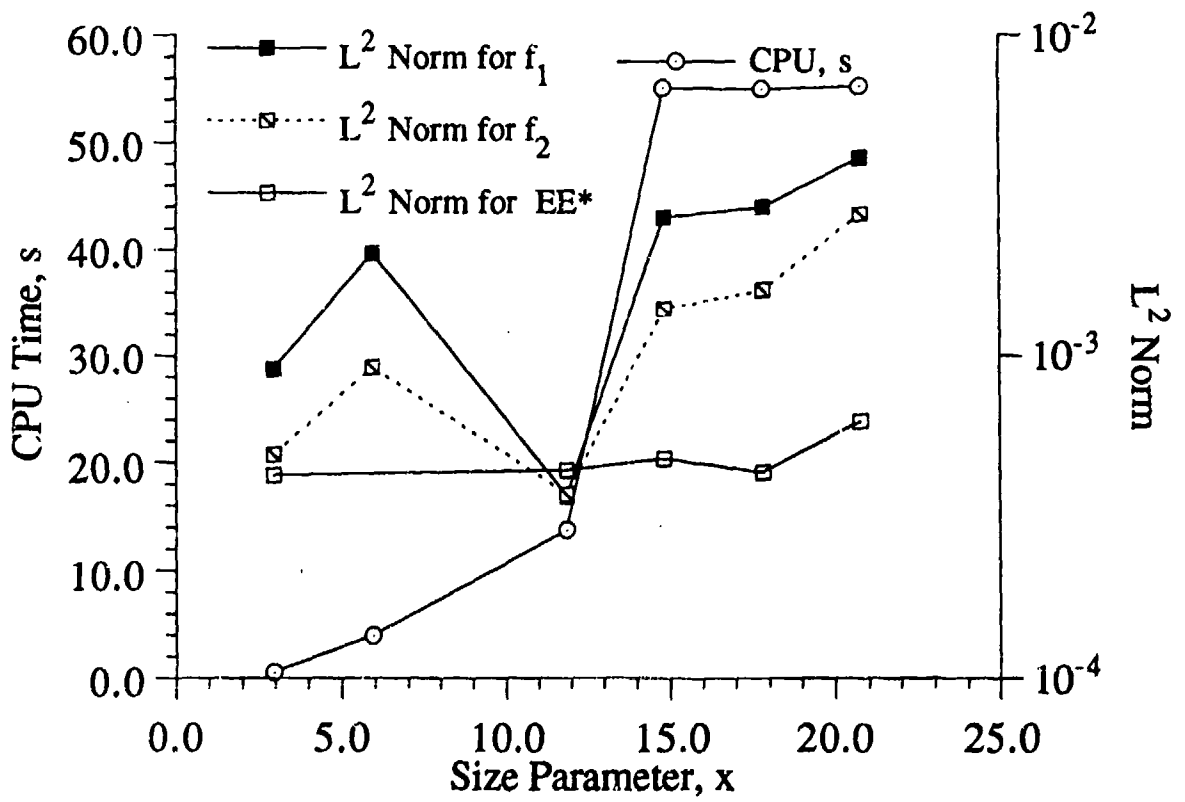


FIG. 2

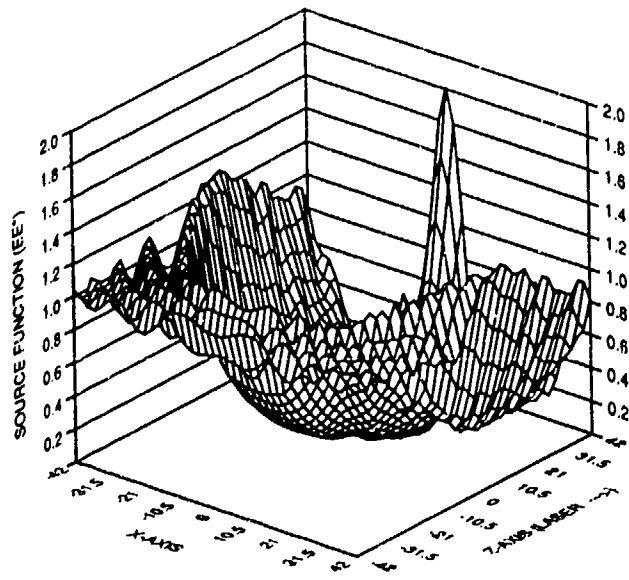
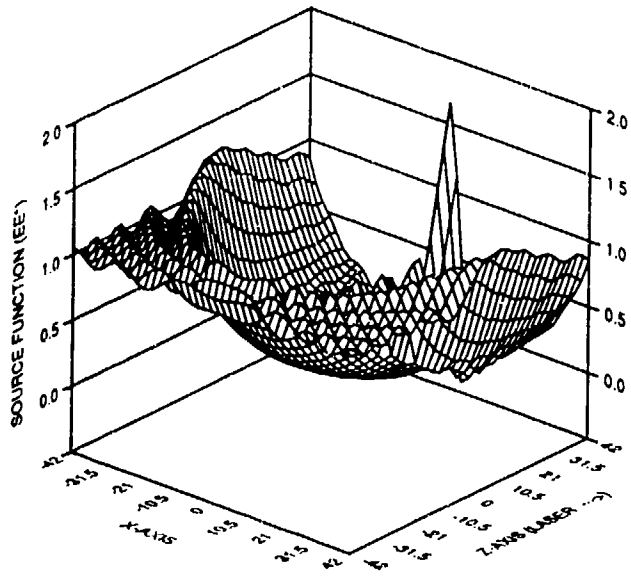


FIG.3

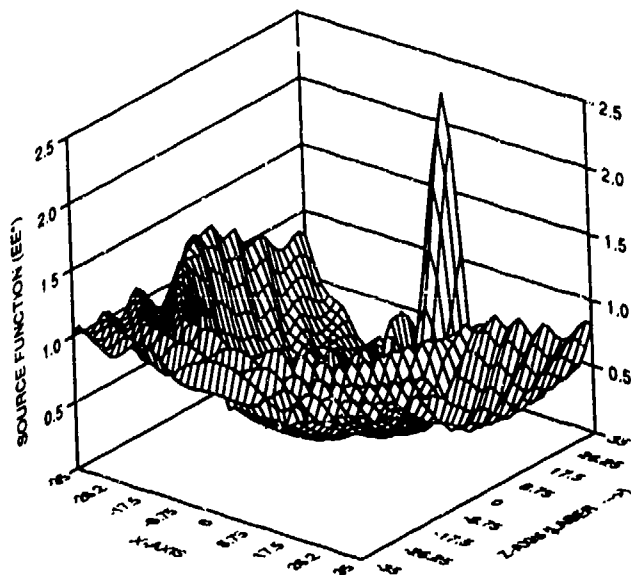
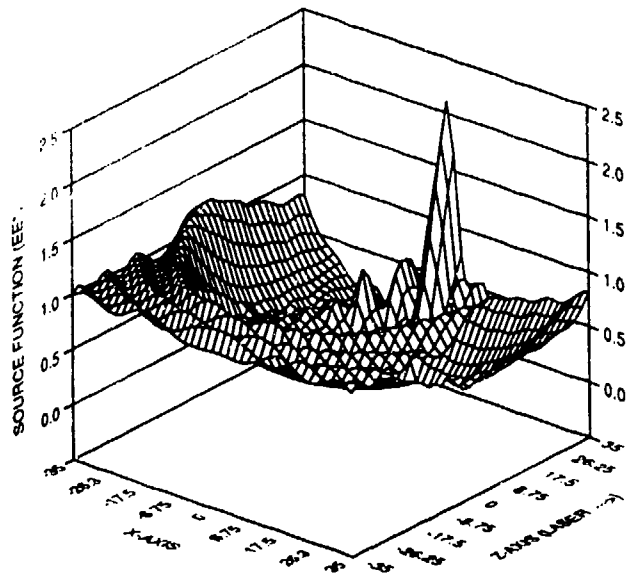


FIG.4

Blank

ON THE SIMILARITY OF LINE INTEGRATED CONCENTRATION FLUCTUATIONS ACROSS PLUMES DIFFUSING IN GRID-GENERATED TURBULENCE

M. Poreh and J. E. Cermak

Colorado State University
Fluid Dynamics and Diffusion Laboratory
Engineering Research Center
Ft. Collins, Colorado 80523 USA

RECENT PUBLICATIONS, SUBMITTALS FOR PUBLICATION, AND PRESENTATION:

Poreh, M. and Cermak, J. E., "Statistical properties and similarity of line integrated concentration fluctuations across plumes diffusing in grid-generated turbulence," CSU Report No. CER92-93MP-JEC3.

Poreh, M., Hadad, A. and Cermak, J. E., "Fluctuations of line integrated concentrations across plume diffusing in grid-generated turbulence," 1991, CSU Report CER91-92MP-AH-JEC2.

Hadad, A., Stiassnie, M., Poreh, M. and Cermak, J. E., "Fractal aspects of integrated concentration fluctuations," Proceedings of the 35th Ohalo Conference on Transport and Diffusion in Turbulent Fields, October 1991. Published by Kluwer Academic Publishers. Submitted to Boundary Layer Meteorology.

Poreh, M., Hadad, A. and Cermak, J. E., "Fluctuations of line integrated concentrations across plumes diffusing in grid-generated turbulence and in shear flows," Proceedings of the 35th Ohalo Conference on Transport and Diffusion in Turbulent Fields, October 1991. Published by Kluwer Academic Publishers. Submitted to Boundary Layer Meteorology.

ABSTRACT

The existence of similarity of the statistical properties of the fluctuations of line Integrated Concentrations (IC) across plumes diffusing in grid-generated turbulence is reevaluated using new data. It is shown that the lateral distributions of the mean values of IC, as well as those of the relative fluctuations and of the autocorrelation functions, are approximately similar at all distances from the source. The distributions of the rms/mean values of the fluctuations and those of the intermittency show, however, a dependence on the distance from the source, but appear to be approximately similar in the range $20 < x/M < 100$ where M is the grid mesh size. Based on these new data and findings, the development of a comprehensive model for IC fluctuation is planned.

INTRODUCTION

Interest in the dynamics of obscuration by aerosol plumes have led the authors to undertake a series of systematic studies [1-5] on the nature of line integrated concentration fluctuations across plumes from point sources diffusing in shear flows and in grid-generated turbulence. Perhaps the most surprising finding of these studies has been an observed approximate similarity of the

statistical properties of the IC fluctuations in the range $20 < x/M < 100$ downwind of an $M = 3$ in. grid. The main goal of this investigation was to further explore the existence of similarity of the statistical properties of integrated concentration fluctuations across plumes and to provide new data for the planned future development of an extensive model of IC fluctuations.

TYPICAL RESULTS

From measurements of IC downwind of a 3 in. grid and a 14 in. grid, the dimensionless parameter $IC^* = IC U M/Q$, where Q is the strength of the source and U is the mean velocity, was calculated. The lateral distributions of its mean value, $ICM^*(y)$, at different distances were found to be closely Gaussian: $ICM^*(y) = ICM^*(0) \exp[-y^2/(2\sigma^2)]$, where $\sigma(x)$ is the lateral length scale of the mean plume.

Typical variations of IC^* versus the dimensionless time $T^* = tU/M$, at approximately the centerline of the plume are shown in Figure 1. The figure depicts the increase of the time scale of the fluctuations with the distance. Typical probability distribution functions $P(a)$, which describe the probability that the ratio of the instantaneous value of IC to its mean is larger than a given value a , along the centerline of the plume are plotted in Figure 2. They show that the IC fluctuations at different distances are not similar. However, it is observed that at large distances from the source, the effect of the distance becomes milder. For example, the $P(a)$ curves at $x/M = 36$ and 102 are very close to each other.

Figure 3 shows the values of the intermittencies γ for the measurements downwind of the 14 in. grid and downwind of the 3 in. grid. It appears from the data that the distributions of γ at $x/M = 2.07, 4.215$ and 8.43 are approximately similar. The distributions of γ at $x/M = 36 - 102$ downwind of the 3 in. grid are also similar but much larger, and for $y/\sigma < 1$ the value of γ in this range is about 1. The measurements at $x/M = 17$ downwind of the 14 in. grid and those at $x/M = 20$ downwind of the 3 in. grid are quite scattered but appear, on the average, to be closer to those measured at larger values of x/M .

The distributions of the relative rms values of the fluctuations of the integrated concentrations, $ic^*(y/\sigma)/ic^*(0)$, at different distances from the source, are shown in Figure 4. The data exhibit a close similarity of the relative rms values. The distributions of ic^*/ICM^* , however, were found to depend on the distance.

Of great interest are the autocorrelation function $R(\tau)$ of the fluctuations of IC^* where τ is the time difference. Its value for $R(0)$ is always 1 and its limit for large τ is zero. Figure 5 shows the distributions of R at the centerline of the plume plotted versus the dimensionless time $\tau U/\sigma$. The figure demonstrates a remarkable similarity of the autocorrelation function at all distances, except at $x/M = 2.07$. It indicates that the time scale of the fluctuations at all distances is proportional to σ/U , namely to the time that a fluid parcel with a longitudinal dimension of σ passes a stationary point.

DISCUSSION

Similarity of dispersing plumes in turbulent flows is defined as the existence of similar dimensionless cross-wind distributions of the statistical properties of the concentration field at different distances which are independent of the distance from the source of the plume. Different levels of similarity may exist, from a similarity which is limited to the mean values of the concentration field, to a similarity of all the statistical properties of the fluctuating concentration field.

The existence and the level of similarity is of great theoretical and practical significance. Its theoretical significance is that it exhibits a moving equilibrium of the flow of the diffusing plume, in which the conditions upstream are mostly irrelevant, so that dimensionless distributions based on local velocity and length scales are similar or self preserving [6]. It also indicates that the various turbulent processes, which are expressed by the various terms in the equation for the mean and fluctuating quantities, are in equilibrium. The practical importance of similarity is that it permits formulation of simple prediction models. The advantage of such models is so great that a similar (Gaussian) model has been adopted for use in most air-pollution models, even though it is well recognized that the vertical mean concentration distributions in most cases are not similar and depend on the distance from the source.

When analyzing the dynamics of plumes diffusing in turbulent flow, one may distinguish between an instantaneous plume (typical lateral length scale σ_i) and a mean plume (typical length scale σ). The fluctuations of the concentrations at a point are viewed to be a result of the meandering of the instantaneous plume and the concentration fluctuations within the instantaneous plume. A similarity of concentration fluctuations within a certain range implies that the ratio σ_i/σ remains constant within that range. Theoretical considerations [7] suggest that σ_i and σ grow at different rates at different distances from the source, and that the relative role of the meandering reduces with the distance. Very close to the source, at least for ideally small sources, the fluctuations are primarily due to meandering caused by relatively large eddies. At very large distances, when the size of the instantaneous source becomes large compared to the size of the turbulent eddies in the flow, the effect of meandering decreases, the ratio σ_i/σ approaches one, and the relative magnitude of the fluctuations decrease.

Indeed, the measurements reported are consistent with such a model. The measured values of γ are smaller at small distances from the source. As seen from Figure 3, the value of γ at the center of the plume in the range $2.0 < x/M < 4$ is about 0.75. Namely, for 25% of the time the entire plume was at either side of the centerline of the plume. At larger distances from the source, $x/M > 20$, γ was 1 at the entire central region of the mean plume - $1 < y/\sigma < 1$, and intermittency due to meandering was noticed only at the edges of the plume. Clearly, this observation indicates that the fluctuations near the source are primarily due to the meandering of the instantaneous plume. It also indicates that the average ratio of σ_i/σ increases with the distance from the source and stays approximately constant for $20 < x/M < 100$.

Now, in spite of the lack of similarity of the probability density distributions of the IC fluctuations, the measurements exhibit a universal similarity of a few functions of the fluctuations. First, the distributions of the mean values $ICM(y)$ are always similar and can be described by a Gaussian function. Then, the

distributions of the rms of the fluctuations at all stations appear to be similar (Figure 2). On the other hand, the distributions of the ratio of the rms to the mean ic^*/ICM^* , was found to depend on the distance. These findings suggest that for $x/M > 20$, some of the instantaneous plumes are close to the size of the mean plume. Thus, they increase the mean value of IC without contributing to the rms of the fluctuations.

It was also surprising to find that in spite of the absence of similarity, the autocorrelations at all stations, except very very close to the source, were proportional to the local length scale σ and similar to each other. Since $R(\tau)$ is based on the correlation of the fluctuations, namely the deviations from the mean, the result is consistent with the existence of similarity of the rms values of the fluctuations.

We have concluded earlier that the autocorrelation curves suggest that the instantaneous plume disintegrates into patches with relatively high concentrations separated by entrained air with zero or small concentrations. The similar autocorrelation curves indicate that these patches pass a given line normal to the flow within a period of the order of $2\sigma/U$, at all distances from the sources. This observation also suggests that the break up of the instantaneous plume is caused by relatively large eddies, which also determine the meandering of the plume and its mean size. The dominant role of the large eddies in determining the meandering, or equivalently, the breakup of the instantaneous plume and its diffusion, is probably the reason for the observed similarity between the fluctuations of the Vertical Integrated Concentration across plumes diffusing in a boundary-layer flow and the fluctuation of IC across plumes diffusing in grid-generated turbulence [4].

Clearly, the investigation has yielded a detailed view of both the dispersion process and the characteristics of the fluctuations of integrated concentrations across plumes. Hopefully, a relatively simple model could be developed, using the data collected in this research, which would describe the dynamics of plumes diffusing in different types of flows. A development of such a model is planned.

REFERENCES

1. Poreh, M. and Cermak, J. E. (1987), "Experimental study of aerosol plume dynamics, Part III: Wind tunnel simulation of vertical integrated concentration fluctuations," CSU Report No. CER87-88MP-JEC4.
2. Poreh, M., Hadad, A. and Cermak, J. E. (1990), "Fluctuations of visibility through a ground level aerosol plume," Presented at the Ninth Symposium on Turbulence and Diffusion, Roskilde, Denmark, 30 April - 1 May 1990, published by the American Meteorological Society, Boston, MA.
3. Poreh, M., Hadad, A. and Cermak, J. E. (1991), "Fluctuations of line integrated concentrations across a plume diffusing in grid-generated turbulence," Final Report for U.S. Department of the Army, Aberdeen Proving Ground, MD, October, 1991, CER91-92MP-AH-JEC2.
4. Poreh, M., Hadad, A. and Cermak, J. E. (1991), "Fluctuations of line integrated concentrations across plumes diffusing in grid-generated turbulence and shear flows," Presented at the Ohalo Conference, October 1991. To be published in "Transport and Diffusion in Turbulent Flows," Kluwer Academic Publishers.

5. Poreh, M. and Cermak, J. E. (1992), "Statistical properties and similarity of line integrated concentration fluctuations across plumes diffusing in grid-generated turbulence," CSU Report No. CER92-93MP-JEC3.
6. Townsend, A. A. (1976), The structure of turbulent shear flow, 2nd Edition, Cambridge University Press.
7. Hinze, J. O. (1975), Turbulence, 2nd Edition, McGraw Hill.

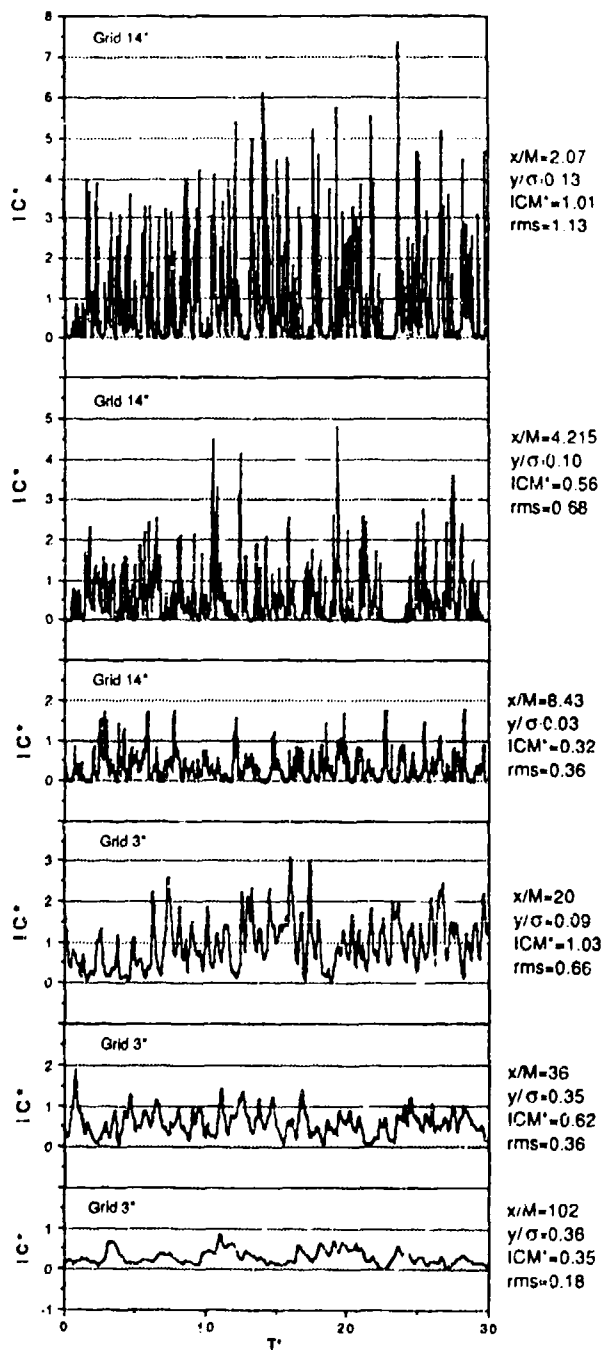


Figure 1. Typical IC^* fluctuations near the center of the plume at different distances downstream of the source ($M = 14$ in.).

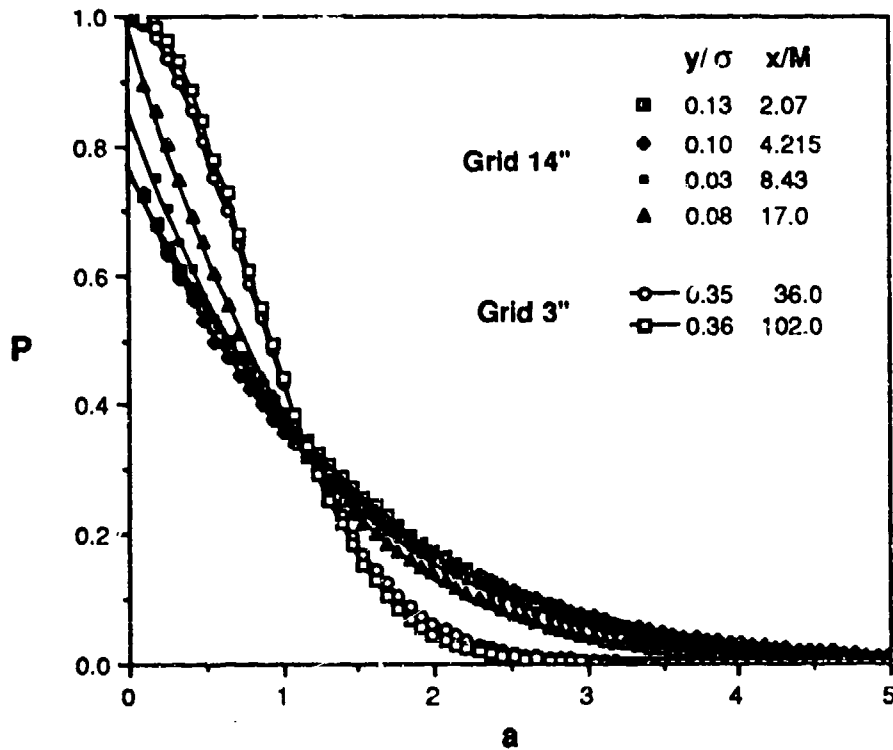


Figure 2. Typical distributions of the probability that IC^*/ICM^* exceeds the value a near the centerline of the plume at different distances from the source.

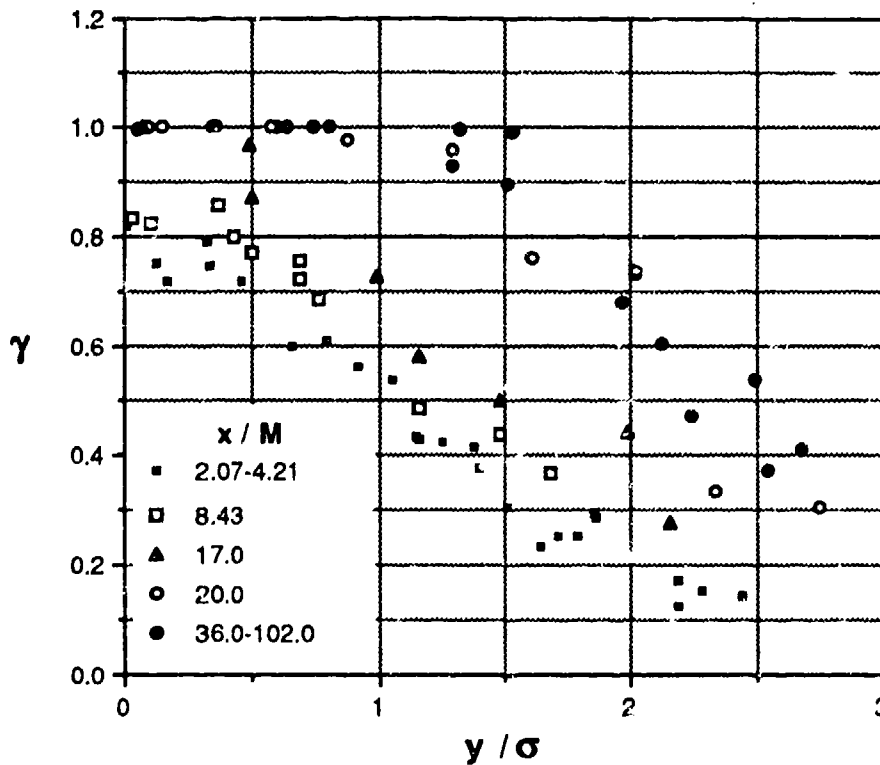


Figure 3. Lateral distribution of the intermittency γ .

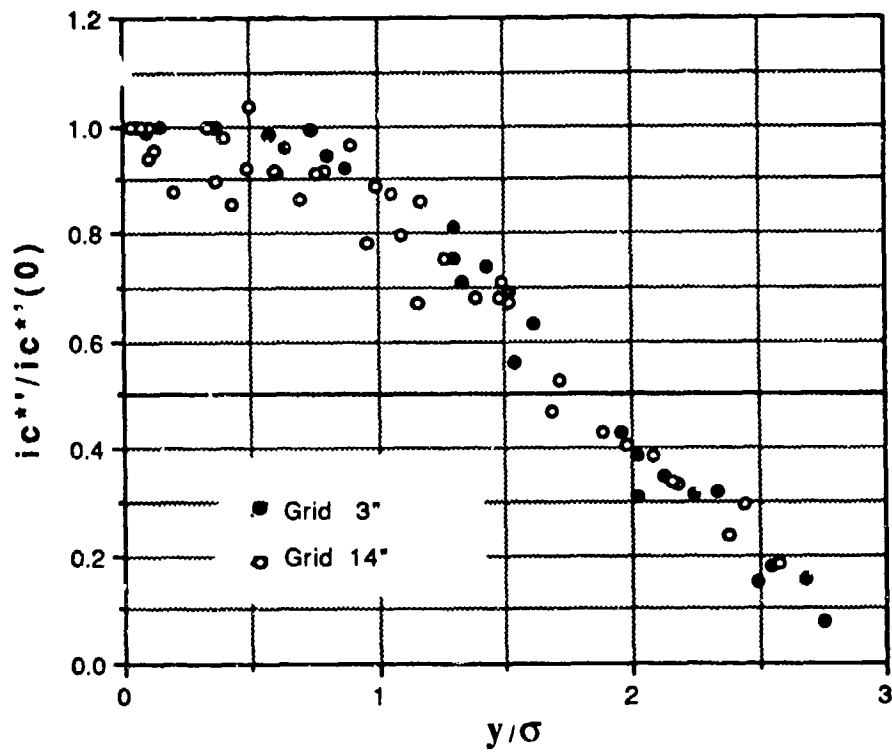


Figure 4. Comparison of the lateral distributions of the relative rms of the fluctuation, $ic^{**}/ic^{**}(0)$, downwind of the 14 in. grid ($2.07 \leq x/M \leq 17$) and the 3 in. grid ($20 \leq x/M \leq 102$).

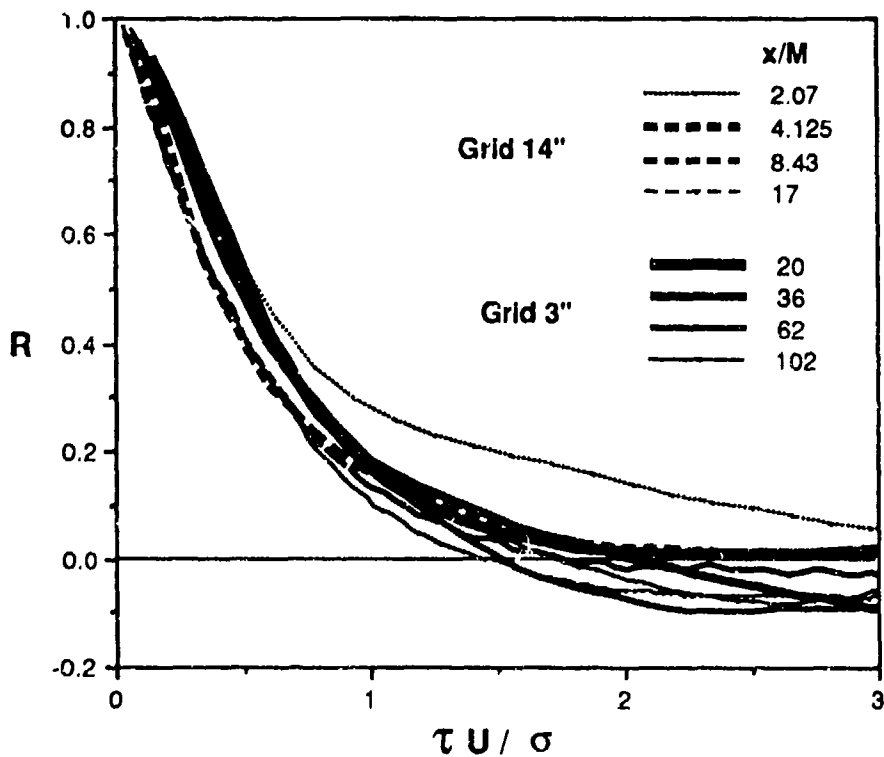


Figure 5. Plot of the autocorrelation of IC^* versus $\tau U/\sigma$ near the centerline of the plume.

Blank

SOME FRACTAL PROPERTIES OF INTEGRATED CONCENTRATION FLUCTUATIONS

A. Hadad, M. Stiassnie, M. Poreh
Department of Civil Engineering, Technion, Haifa 32000, Israel

and J. E. Cermak
Fluid Dynamics and Diffusion Laboratory,
Colorado State University, Ft. Collins, Colorado 80523, USA

RECENT PUBLICATIONS, SUBMITTALS FOR PUBLICATION, AND PRESENTATION:

Poreh, M., Hadad, A. and Cermak, J. E., "Fluctuations of line integrated concentrations across plume diffusing in grid-generated turbulence," 1990, CSU Report CER91-92MP-AH-JEC2.

Hadad, A., Stiassnie, M., Poreh, M. and Cermak, J. E., "Fractal aspects of integrated concentration fluctuations," Proceedings of the 35th Ohalo Conference on Transport and Diffusion in Turbulent Fields, October 1991. Published by Kluwer Academic Publishers. To be published in a special issue of Boundary Layer Meteorology.

Poreh, M., Hadad, A. and Cermak, J. E., "Fluctuations of line integrated concentrations across plumes diffusing in grid-generated turbulence and in shear flows," Proceedings of the 35th Ohalo Conference on Transport and Diffusion in Turbulent Fields, October 1991. Published by Kluwer Academic Publishers. To be published in a special issue of Boundary Layer Meteorology.

ABSTRACT

The fractal properties of integrated concentration fluctuations across a plume diffusing in grid-generated turbulence are analyzed. Two regions are identified in which a fractal process and a subfractal process of fluctuations exist, respectively. It is planned to compare the singularity spectrum and the fractal dimensions of simultaneous records of velocity and integrated concentration fluctuations and to simulate numerically the diffusion in a fractal velocity field.

INTRODUCTION

The fluctuations of physical properties in turbulent flows, such as local velocities, concentrations at a point or integrated concentrations along a line in space, are an inherent part of such flows and of great interest in many applications. Since turbulence has been shown to exhibit properties of fractals (Mandelbrot, 1974), fractal analysis has been used to explore measurements of such fluctuations in order to gain new insight and better understanding of their nature. Fractal analysis derives parameters which are related to the geometry of the fluctuating signals, such as the *Fractal Dimension* D_b , and has thus been used to study cloud structure, flame surfaces and velocity and concentration time series. In cases where the energy spectrum of time series is described by a power law with an exponent β , the value of β can be related through a *singularity spectrum* to the fractal dimension. Special attention was given to the

multifractal nature of energy dissipation rate (Meneveau and Sreenivasan, 1987) and scalar dissipation rate (Prasad et al., 1988) in various turbulent flows, using the formalism of the singularity spectrum $f(\alpha)$ that was suggested by Halsey et al. (1986).

Recently, Stiasnie (1991) proposed a somewhat different formulation of a singularity spectrum, which is designated by $F(\alpha)$. For a fluctuating signal $y(t)$, the value of α , the *singularity strength*, is associated with the rate at which the derivative of the signal tends to infinity. For a turbulent signal one expects $y(t)$ to have different values of α at different times. Thus, $y(t)$ may be viewed as a union of an infinite number of subsets, each having a typical singularity strength α with a singularity spectrum $F(\alpha)$. The Fractal Dimension D_b , is related to $F(\alpha)$ by

$$D_b = 1 - a_1 + F(a_1), \quad (1)$$

where a_1 may be defined by $F'(a_1) = 1$.

A multifractal process is an indication of spectral density power law $k^{-\beta}$, and it can be shown that the spectral exponent β is related to $F(a_1)$ by

$$\beta = 3 - 2D_b + 2F(a_1). \quad (2)$$

ANALYSIS OF INTEGRATED CONCENTRATION FLUCTUATIONS

We have examined measurements of Vertically Integrated Concentrations (VIC) across a plume from a continuous point source diffusing in grid-generated turbulence (Poreh et al., 1990).

A significant length scale of the dispersing plume is its lateral length scale, σ_y . As shown by Poreh et al. (1990), the fluctuating VIC signal exhibits an approximate similarity, within a large range of distances from the source. Namely, its statistical properties are functions of y/σ_y , and practically independent of the distance.

Figure 1 shows the dimensionless spectral energy density of the VIC fluctuations $S^* = S(n)U/[\sigma_{vic}^2 \sigma_y]$, where $S(n)$ is the spectral energy density plotted versus $m^* = n\sigma_y/U$. The spectral energy distribution suggests that the VIC spectrum is characterized by two regions. The transition between the two regions is around $m^* = n\sigma_y/U = 1$. In Region II, which corresponds to length scales between about σ_y and $5\sigma_y$ ($0.2 < n^* < 1$), one finds a negative spectral exponent close to $5/3$, similar to what is usually obtained in records of velocities and concentrations in the inertial subrange and between some bounds of wave numbers in measurements of cross-wind integrated concentrations of plumes in the atmospheric boundary layer by Bowers and Black (1985). The energy spectrum for these measurements was calculated by Hanna and Insley (1989). In Region I, that corresponds to length scales between $0.3\sigma_y$ (which corresponds to the Nyquist frequency of the measurement, and which is longer than both the IR beam diameter and the smallest eddy in the field) and σ_y , one observes a spectral exponent of $1/3$. One may conclude that in Region II, the spectral density of VIC fluctuations is the same as that of the concentration fluctuations at a point, since the line of integration crosses at each instant only one large eddy. In Region I, on the

other hand, the integration of the point concentrations with a spectral exponent 5/3 law is the cause for an attenuation of the spectral exponent to a (5/3+2) law.

As noted earlier, a spectral power law is an indication of a fractal nature. If our VIC record would have been a monofractal set, we would expect it to have a fractal dimension of $D = (5 + \beta)/2$, which yields a value of 2/3 in the Region I, and a value of 5/3 in the Region II. Similarly, one expects in our case to have a singularity or Lipschitz-Hölder (L-H) exponent $-\alpha = 2 - D$ which yields values of 4/3 in Region I, and 1/3 in Region II. But, since our VIC records are embedded in a two-dimensional space, its fractal dimension must be limited between the limits 1 and 2, and its L-H exponent between 0 and 1. Thus, we conclude that the process in Region I is *subfractal*, whereas the process in Region II is fractal.

Independent fractal analysis of the same signal shows that the fractal nature of the VIC fluctuations corresponding to Region II is characterized by $D_b = 1.62 (\pm 0.03)$, $\alpha_1 = 0.343$, $F(\alpha_1) = 0.963$ and, according to Eq. (2), $\beta = 1.693$, which is very close to the value of $\beta = 5/3 = 1.667$.

DISCUSSION

Analysis of VIC fluctuations across a plume diffusing in grid-generated turbulence identifies two subdomains. The first is related to integrated concentration fluctuations and may be described as a subfractal process, whereas the second one is related to point concentration fluctuations and may be described as a fractal process.

Our analysis indicates that the VIC fluctuations, in the range where they also describe concentration fluctuations, are multifractal and singular everywhere. These conclusions were derived from the singularity spectrum $F(\alpha)$ of the record. The $F(\alpha)$ spectrum is related to the scaling properties of the "statistical moments." The first two "moments" are related to the fractal box-dimension and to the spectral exponent, respectively. For the given VIC record, in the range which reflects concentration fluctuations, we found that $D_b = 1.62 \pm 0.03$ and $\beta = 1.69$. These values are in agreement with the corresponding results from the box-counting algorithm and from spectral analysis.

Figure 2 shows the singularity spectrum $f(\alpha)$ for the VIC data together with spectra of other turbulent variables in different flows. It shows that the calculated $f(\alpha)$ curves for VIC are more similar to the corresponding curves of velocity fluctuations, than with those of passive scalar fluctuations.

In the future we plan to compare $F(\alpha)$ curves from simultaneous records of velocity and VIC fluctuations. This will give a better understanding of the scaling nature of turbulent fluctuations in general and of passive scalar fluctuations in particular. It is also planned to simulate numerically the diffusion of particles in a fractal velocity field.

REFERENCES

- Bowers, J. F. and Black, R. B. (1985), "Test report-product improved M3A3 (M3A3E2) smoke generator (mobile applications)," U. S. Army Dugway Proving Ground, Dugway, UT 84022-5000.
- Frisch, U. and Parisi, G. (1985), "On the singularity structure of fully developed turbulence," *Turbulence and Predictability in Geophysical Fluid Dynamics and Climate Dynamics*, New York, 84-88.
- Halsey, T. C., Jensen, M. H., Kadanoff, L. P., Procaccia, I. and Shraiman, B. I. (1986), "Fractal measures and their singularities: The characterization of strange sets," *Phys. Rev. A* 33, 1141-51.
- Hanna, S. R. and Insley, E. M. (1989), "Time series analyses of concentration and wind fluctuations," *Boundary Layer Meteorology*, 47, 131-147.
- Mandelbrot, B. B. (1974), "Intermittent turbulence in self-similar cascades: Divergence of high moments and dimensions of the carrier," *J. Fluid Mech.*, 62, 331-358.
- Meneveau, C. and Sreenivasan, K. R. (1987), "The multifractal spectrum of the dissipation field in turbulent flows," *Nucl. Phys. B.*, 2, 49-76.
- Poreh, M. and Cermak, J. E. (1987), "Experimental study of aerosol plume dynamics-III, Wind-tunnel simulation of vertical integrated concentration fluctuations," CSU Project No. 5-3 2571, CER87-88MP-JEC4.
- Poreh, M., Hadad, A. and Cermak, J. E. (1990), "Fluctuations of line integrated concentrations across plume diffusing in grid-generated turbulence," CSU Project No. 5-3 8765, CER91-92MP-AH-JEC2.
- Prasad, R. R., Meneveau, C. and Sreenivasan, K. R. (1988), "Multifractal nature of the dissipation field of passive scalars in fully developed turbulent flows," *Amer. Phys. Soc.*, 61, 74-77.
- Sreenivasan, K. R. (1991), "Fractals and multifractals in fluid turbulence," *Annual Rev. Fluid Mech.*, 23, 539-600.
- Stiassnie, M. (1991), "The multifractal structure of the ocean surface," *Proceedings of the Nonlinear Water Waves Workshop, Bristol, 22-25 October 1991.*

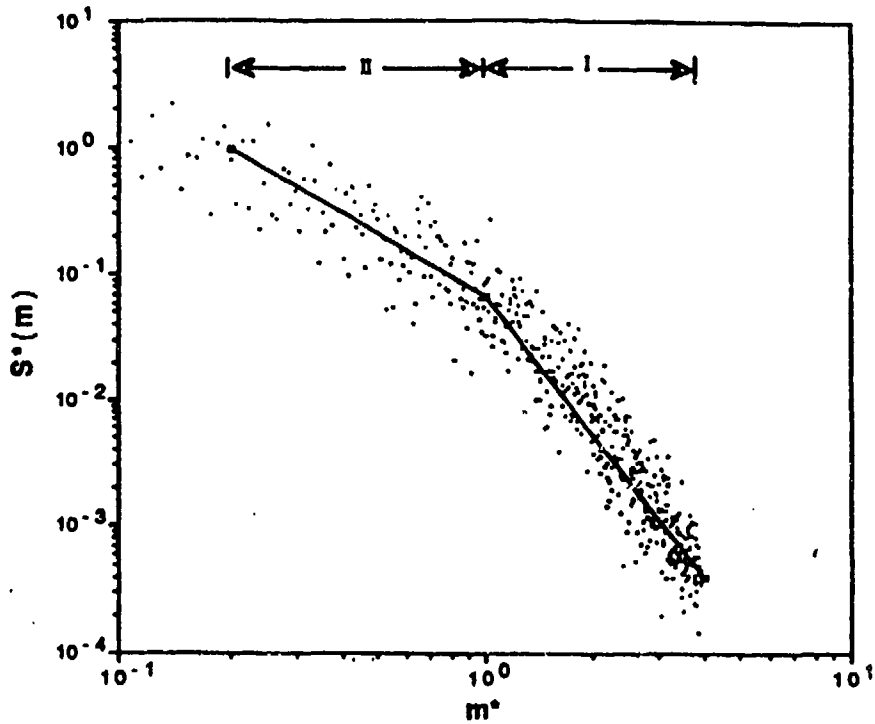


FIGURE 1. DIMENSIONLESS SPECTRAL ENERGY DENSITY OF THE VIC FLUCTUATIONS (7 SETS OF 1024 SAMPLING POINTS EACH).

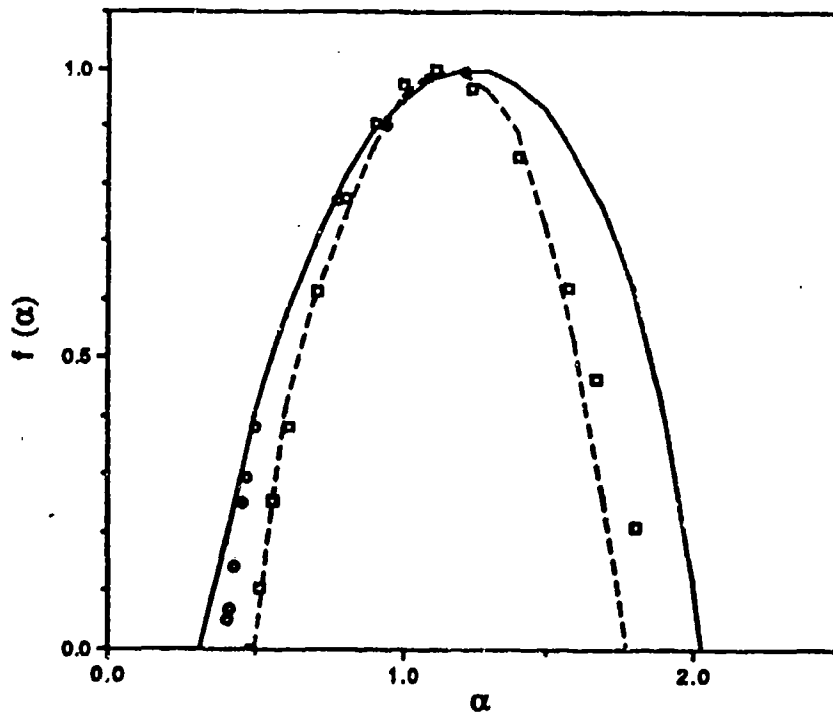


FIGURE 2. MEASURED SINGULARITY SPECTRA OF THE DISSIPATION RATE.
 (----) Velocity time series (Meneveau and Sreenivasan, 1987),
 (—) Spatial instantaneous concentrations (Prasad et al., 1988),
 (o) Temperature time series (Prasad et al., 1988), and
 (□) VIC fluctuations in Region II.

Blank

II. AFROSOI CHARACTERIZATION METHODS

A. NEPHELOMETRY AND INVERSION

Use of a new polarimetric optical bistatic scatterometer to measure the transmission and reflection Mueller matrix for arbitrary incident and scatter directions

Robert D. Kubik

Ezekiel Bahar

Electrical Engineering Department and the Center for Electro-optics
University of Nebraska-Lincoln
209N WSEC, Lincoln, Nebraska 68588-0511

Dennis R. Alexander

Mechanical Engineering Department and the Center for Electro-optics
University of Nebraska-Lincoln
248 WSEC, Lincoln, Nebraska 68588-0656

RECENT PUBLICATIONS

- A) E. Bahar and M. El-Shenawee, "Use of Supercomputers to Evaluate Singly and Multiply Scattered electromagnetic Fields from Rough Surfaces," *IEEE Trans. on Magnetics*, Vol. 27, No. 5, pp. 4287-4290, September, 1991.
- B) E. Bahar, "Examination of Full Wave solutions and 'Exact Numerical Results' for One-Dimensional Slightly Rough Surfaces," *Journal of Geophysical Research*, Vol. 96, No. C9, pp. 17123-17131, September 15, 1991.
- C) E. Bahar and S. M. Haugland, "Multiples Scattering of Electromagnetic Waves from Coated Rough Surfaces," *Proceeding of the 1990 Scientific Conference on Obscuration and Aerosol Research*, 1991.
- D) E. Bahar, S. M. Haugland, and A. H. Carrieri, "Polarized IR Scattering Used to Identify Contaminant Coatings Over Rough Surfaces," *Proceeding of the 1991 Scientific Conference on Obscuration and Aerosol Research*, June 1991.
- E) E. Bahar and R. D. Kubik, "Simulation of High Resolution Radar Polarimetric Images - Unified Full Wave Approach," *International Journal of Remote Sensing*, in press.
- F) S. M. Haugland, E. Bahar and A. H. Carrieri, "Identification of contaminant coatings over rough surfaces using polarized IR scattering," *Applied Optics*, Vol. 31, No. 19, pp. 3847-3852, July 1992.
- G) S. A. Schaub, D. R. Alexander, and J. P. Barton, "Glare Spot Image Calculations for a Spherical Particle Illuminated by at Tightly Focused Beam," *Journal of the Optical Society of America A*, 9, No. 2, pp. 316-330, February, 1992.
- H) J. Zhang and D. R. Alexander, "Hybrid Inelastic Scattering Models for Particle Thermometry: Unpolarized Emissions," *Applied Optics*, 31, No. 24, 1992.
- I) J. Zhang and D. R. Alexander, "Hybrid Inelastic Scattering Models for Particle Thermometry: Polarized Emissions," *Applied Optics*, 31, No. 24, 1992.

ABSTRACT

The Center for Electro-optics and electrical engineering department at the University of Nebraska-Lincoln recently acquired from TMA (Toomay, Mathis, and Associates) a TASC (True Angle Scatter Coordinate system) optical, polarimetric scatterometer. This instrument measures the 4×4 Mueller (Stokes) matrix as well as the Bidirectional Reflective Distribution Functions (BRDF) that completely characterize scattered light reflected from or transmitted through electromagnetic media with irregular boundaries. The incident and scatter directions can be chosen arbitrarily in 4π .

FUTURE WORK

The scatterometer in conjunction with a scanning tunneling/atomic force microscope will be used to validate different analytical/numerical solutions to a broad class of electromagnetic scattering problems by relating electromagnetic scattering data to ground truth measurements in controlled laboratory experiments.

1. INTRODUCTION

The Stokes vector polarimetrically characterizes light^{1,2}. The Mueller matrix relates the incident Stokes vector to the scattered Stokes vector. In most applications of light scatter only a few elements of the Mueller matrix are used to determine how light is modified upon interaction with electromagnetic material. For example, in ellipsometry³ only the relative intensity and the relative phase of the vertically and horizontally polarized specularly reflected light are measured, and usually in remote sensing only the four components of the modified Mueller matrix that relate to the vertically and horizontally polarized intensities are retained.

The TASC instrument produces six incident Stokes vectors and measures six corresponding reflected/transmitted Stokes vectors. Through combinations of these measurements all sixteen elements of the Mueller matrix are determined, the redundancy in the number of measurements is used to minimize errors. One of the unique aspects of this instrument is that the receiver can be rotated in and out of the plane of incidence (defined by the incident electromagnetic wave vector and the normal to the mean surface). Thus bistatic measurements can be made in 4π . Two coherent light sources ($\lambda = 0.6328 \mu\text{m}$ and $\lambda = 1.063 \mu\text{m}$) are currently used in the operation of the scatterometer. The instrument can be retrofitted to include additional light sources.

2. SYSTEM DESCRIPTION⁴

The system is designed such that the transmitter can rotate in an arc in a vertical plane while the receiver can rotate in both vertical planes and horizontal planes (with respect to the mean plane of the sample). The sample is at a distance of 50 cm from the receiver. It is oriented such that the normal to the mean plane of the sample is along the z-axis (see Figure 1). The sample holder can rotate the sample in the x-y plane to vary the azimuth angle (ϕ^i) of the incident wave vector. Variation of the incident wave vector in the y-z plane ($0^\circ \leq \theta^i \leq +135^\circ$ with respect to the z-axis, Figure 2) is achieved by rotating the optical table on which the sources are mounted. The receiver (in the scattered direction) can rotate in an 180° arc (measured from the z-axis), thus the elevation angle (θ^f) of the scattered wave vector is varied. The receiver is rotated in the x-y plane by the receiver arm

rotating in a 180° arc around the z-axis, thus the azimuth angle (ϕ^J) of the scattered wave vector is varied. The sources are aligned such that the beams have a common path upon exiting the beam combiner (Figure 3). The system is currently excited by 2 laser sources (see Table I).

	source #1	source #2
Laser type:	HeNe	Nd:Yag
Wavelength (μm):	0.6328	1.063
Power, mW (CW):	7	10

Table 1. Laser sources.

Upon transmission through the beam combiner, the beam encounters a calcite polarizer which is used to set the polarization state of the beam before it enters the source polarization optics. The beam is chopped (by an AC synchronous motor turning fan-like blades) in order to detect the scattered signal. The beam is partially deflected to a reference detector to account for laser power fluctuations. This reference power is also used as a synchronizing signal for the lock-in amplifier of the receiver. Upon reflection from the combined beam turning mirror, the laser beam is directed into the source polarization optic components. These components include a halfwave plate and a quarterwave plate. They are mounted in rotary stages that are computer controlled. Each laser beam has its own set of source polarization optics. The source polarization optics are controlled to produce six different polarization states: Vertical (p or electric field parallel to the plane of incidence), Horizontal (s or electric field perpendicular to the plane of incidence), Right circular, Left circular, linear polarizations +45° and -45° with respect to the plane of incidence. After the desired polarization state is generated the beam is passed through the optical table and down towards the sample (see Figure 2).

Mounted on the receiver arm is the receiver assembly. This assembly consists of a quarterwave plate, a polarizer, a preamplifier, and a detector. The detectors for both wavelengths are made of silicon. They consist of filters and other optical components which enhance operation at the selected wavelength. The receiver polarizer and quarterwave plate are mounted in rotary stages that are similar to those of the source polarization optics. This allows for computer control of the receiver polarization (the same six polarization states as for the transmitter). The whole system is controlled by a software package. The motorized stages currently operational in this machine are:

Source components:

- halfwave plate
- source quarterwave
- source incident angle

Receiver components:

- quarterwave plate
- halfwave plate
- receiver scattered angle (elevation)
- receiver scatter plane (azimuth)

Additional optional computer operated components consist of: sample xy and z translation, beam expansion, beam focus, and sample rotation. The instrument has the ability to operate in the retro (backscatter) mode by replacing the mirror that directs the laser beam down to the sample by a beam splitter (see Figure 3). The backscatter mode is the mode of operation most commonly associated with active remote sensing.

3. SAMPLE MEASUREMENTS

Figures 4a and 4b show scans of the incident beams with a receiver aperture of 1.07 mm. From these scans we estimate that the beam diameters are:

width	Nd:Yag	HeNe
1/e	3.24 mm	1.86 mm
1/e ²	5.04 mm	2.79 mm

Table II. Laser Beam widths.

In figures 5a and 5b the Mueller matrix elements are plotted for transmission through a polarizer. For an ideal polarizer with the angle α between the transmission axis of the polarizer (parallel to the transmitted electric field) and the x-axis (normal to the plane of incidence), the Mueller matrix is given by²

$$\frac{1}{2} \begin{bmatrix} 1 & \cos(2\alpha) & \sin(2\alpha) & 0 \\ \cos(2\alpha) & \cos^2(2\alpha) & \cos(2\alpha) \sin(2\alpha) & 0 \\ \sin(2\alpha) & \cos(2\alpha) \sin(2\alpha) & \sin^2(2\alpha) & 0 \\ 0 & 0 & 0 & 0 \end{bmatrix}. \quad (1)$$

The horizontal axes on the graphs is a measured in degrees. Notice that the element m_{11} is ideally 0.5 (this element relates the total incident power to the total transmitted power). It fluctuates slightly below 0.5 due to the non-ideal properties of the polarizer. Ideally the seven elements show in Figure 5b should be zero. They also exhibit a slight dependence on the rotation angle.

Since the Mueller matrix contains complete information about the intensities and the relative phases of polarized scattered light, it has very general applications. For example, in ellipsometry³ the measurement that is of interest is the ratio of the complex reflection coefficients r_{pp} and r_{ss} for specularly reflected light. This ratio (the so-called ellipsometric function) is commonly expressed as follows;

$$\rho = \frac{r_{pp}}{r_{ss}} = \left| \frac{r_{pp}}{r_{ss}} \right| \exp[j(\phi_{pp} - \phi_{ss})] = \tan(\Psi) \exp(j\Delta) \quad (2)$$

where Ψ and Δ are known as the ellipsometric angles or ellipsometric parameters. Following Azzam,⁵ assuming that the surface is perfectly flat and no depolarization occurs, the elements of Mueller matrix satisfy the special relationships $m_{11} = m_{22}$, $m_{12} = m_{21}$, $m_{33} = m_{44}$, and $m_{34} = -m_{43}$. In this case the ellipsometric angles can be obtained uniquely from the Mueller matrix elements

$$\Psi = \frac{1}{2} \text{Arccos} \left(\frac{-m_{12}}{m_{11}} \right) \quad (3a)$$

$$\Delta = \text{Arctan} \left(\frac{m_{34}}{m_{33}} \right) \quad (3b)$$

Care is taken in interpreting 3b so that Δ is set in the correct quadrant. In practice the assumption that the surface exhibits no depolarization is not strictly satisfied. The measurements taken off an isotropic gold reflector at the incident angle of 65 and wavelength of 0.6328 μm are⁵

$$M = \begin{bmatrix} 1.000 & -0.080 & -0.014 & -0.003 \\ -0.069 & 0.988 & -0.011 & -0.008 \\ 0.000 & 0.009 & -0.450 & 0.886 \\ 0.006 & -0.007 & -0.894 & -0.457 \end{bmatrix} \quad (4)$$

The corresponding ellipsometric angle Ψ ranges from 42.71° to 43.02° and Δ range from 116.69° to 117.28° depending on which elements of the Mueller matrix are used to compute these angles.

If there is some depolarization of the incident light by the target, the ellipsometric parameters should be extracted from the Mueller matrix as follows.

$$\Psi = \frac{1}{2} \text{Arccos} \left(\frac{-(m_{12} + m_{21})}{m_{11} + m_{22}} \right) \quad (5a)$$

$$\Delta = \text{Arctan} \left(\frac{m_{34} - m_{43}}{m_{33} + m_{44}} \right) \quad (5b)$$

As above, care should be taken in interpreting $\text{Arctan}(\cdot)$ to obtain Δ in the correct quadrant. For a relative smooth surfaces the most significant elements of the Mueller matrix used in conjunction with ellipsometry are (see results show in (4) above),

$$m_{11} = \langle r_{pp}r_{pp}^* \rangle + \langle r_{ss}r_{ss}^* \rangle + \langle r_{sp}r_{sp}^* \rangle + \langle r_{ps}r_{ps}^* \rangle \quad (6a)$$

$$m_{12} = \langle r_{pp}r_{pp}^* \rangle - \langle r_{ss}r_{ss}^* \rangle + \langle r_{sp}r_{sp}^* \rangle - \langle r_{ps}r_{ps}^* \rangle \quad (6b)$$

$$m_{21} = \langle r_{pp}r_{pp}^* \rangle - \langle r_{ss}r_{ss}^* \rangle - \langle r_{sp}r_{sp}^* \rangle + \langle r_{ps}r_{ps}^* \rangle \quad (6c)$$

$$m_{22} = \langle r_{pp}r_{pp}^* \rangle + \langle r_{ss}r_{ss}^* \rangle - \langle r_{sp}r_{sp}^* \rangle - \langle r_{ps}r_{ps}^* \rangle \quad (6d)$$

$$m_{33} = \Re \langle r_{pp}r_{ss}^* \rangle + \Re \langle r_{ps}r_{sp}^* \rangle \quad (6e)$$

$$m_{34} = \Im \langle r_{pp}r_{ss}^* \rangle + \Im \langle r_{sp}r_{ps}^* \rangle \quad (6f)$$

$$m_{43} = -\Im \langle r_{pp}r_{ss}^* \rangle + \Im \langle r_{sp}r_{ps}^* \rangle \quad (6g)$$

$$m_{44} = \Re \langle r_{pp}r_{ss}^* \rangle - \Re \langle r_{ps}r_{sp}^* \rangle \quad (6h)$$

in which $\langle \cdot \rangle$ denotes the statistical average, $*$ denotes the complex conjugate, $\Re(\cdot)$ and $\Im(\cdot)$ denotes the real and imaginary parts of the argument, respectively. Thus the ellipsometric angles (5) can be obtained as follows from the definition of the ellipsometric parameters:

$$-\cos(2\Psi) = \frac{\langle r_{pp}r_{pp}^* \rangle - \langle r_{ss}r_{ss}^* \rangle}{\langle r_{pp}r_{pp}^* \rangle + \langle r_{ss}r_{ss}^* \rangle} = \frac{-(m_{12} + m_{21})}{m_{11} + m_{22}} \quad (7a)$$

$$\tan(\Delta) = \frac{\Im \langle r_{pp}r_{ss}^* \rangle}{\Re \langle r_{pp}r_{ss}^* \rangle} = \frac{m_{34} - m_{43}}{m_{33} + m_{44}} \quad (7b)$$

Using his experimental data (4) Azzam⁵ obtains the following values for the ellipsometric angles; $\Psi = 42.85^\circ$ and $\Delta = 117.00^\circ$. Assuming that the gold is optically thick one can extract the complex index of refraction from these values for ρ (2) using the well know relation^{3,5}

$$N = n - jk = \sin(\theta) \sqrt{1 + \left(\tan(\theta) \frac{1 - \rho}{1 + \rho} \right)^2} \quad (8)$$

The corresponding value for the index of refraction is $N = 0.27 - j3.02$. The published values⁶ for the index of refraction of gold at $0.633 \mu\text{m}$ is approximately $N = 0.183 - j 3.09$.

In an experiment conducted at the University of Nebraska-Lincoln a silicon wafer was coated with a 1000 Angstroms layer of Nickel. A 1000 Angstroms layer of gold coated this surface. The sample was scanned (specularly) by the scatterometer between 1° to 85° in steps of 1° , the resulting values of Ψ , Δ , and N are shown in figure 6. For the same set of parameters used by Azzam⁵ the Mueller matrix obtained for the experiments with the scatterometer is as follows

$$M = 0.861 \begin{bmatrix} 1.000 & 0.042 & -0.022 & -0.002 \\ 0.048 & 0.998 & 0.014 & 0.016 \\ 0.007 & 0.014 & -0.559 & 0.824 \\ 0.022 & 0.009 & -0.827 & -0.558 \end{bmatrix} \quad (9)$$

The results given in (9) for the incident angle of 65° correspond to the ellipsometric parameters of $\Psi = 43.71^\circ$ and $\Delta = 124.08^\circ$. The complex index of refraction is computed as $N = 0.20 - j 3.54$.

Note that in reference 3 the second element (I_2) of the stokes vector is defined as

$$I_2 = \langle E_p E_p^* \rangle - \langle E_s E_s^* \rangle \quad (10)$$

while using the convention introduced by Born and Wolf¹ (and adopted by us) the second element of the Stokes vector is defined as

$$I_2 = \langle E_s E_s^* \rangle - \langle E_p E_p^* \rangle \quad (11)$$

As a result there are sign differences in the elements of the Mueller matrix m_{j2} and m_{2j} ($j=1,3,4$) as defined by Azzam³ and Born and Wolf¹.

4. CONCLUSION

Measurement of the Mueller matrix that characterize scattered light from surfaces can yield more information about the material and its surface than measurements taken by commonly used techniques. In this paper we have discussed the measurement of well know optical properties of a flat optically thick gold film and the complete characterization of a well know optical device, a linear polarizer. This optical polarimetric scatterometer will be used in conjunction with a scanning tunneling/atomic force microscope to validate coated and uncoated rough surface scattering theories in controlled experiments in order to felicitate the detection and identification of chemical contaminants of rough surfaces.

6. ACKNOWLEDGMENTS

The authors wish to thank Dr. A. H. Carrieri for his encouragement.

5. REFERENCES

- [1] M. Born and E. Wolf, *Principles of Optics*, third edition (Pergamon Press, London), Ch. 1.4, p. 30-32, Ch. 10.8.3, p. 554-555, 1965.
- [2] W. A. Shurcliff, *Polarized Light*, first edition (Harvard University Press, Cambridge, Massachusetts), Ch. 8, p. 109-123, 1966.
- [3] R. M. A. Azzam and N. M. Bashara, *Ellipsometry and polarized light*, first edition (North-Holland, Amsterdam), Ch. 3.4, p. 173-174, 1977.
- [4] *TMA TASC Polarimetric Scatterometer, Instrument operation manual*, (TMA Technologies, Inc., Bozeman, Montana), March 1992.
- [5] R. M. A. Azzam, K. A. Giardina, and A. G. Lopez, "Conventional and generalized Mueller-matrix ellipsometry using the four-detector photopolarimeter," *Optical Engineering*, vol. 30, no. 10, pp. 1583-1589, Oct. 1991.
- [6] E. D. Palik, *Handbook of optical constants of solids*, first edition (Academic Press, Orlando), part 2 subpart 4, p. 294, 1985.

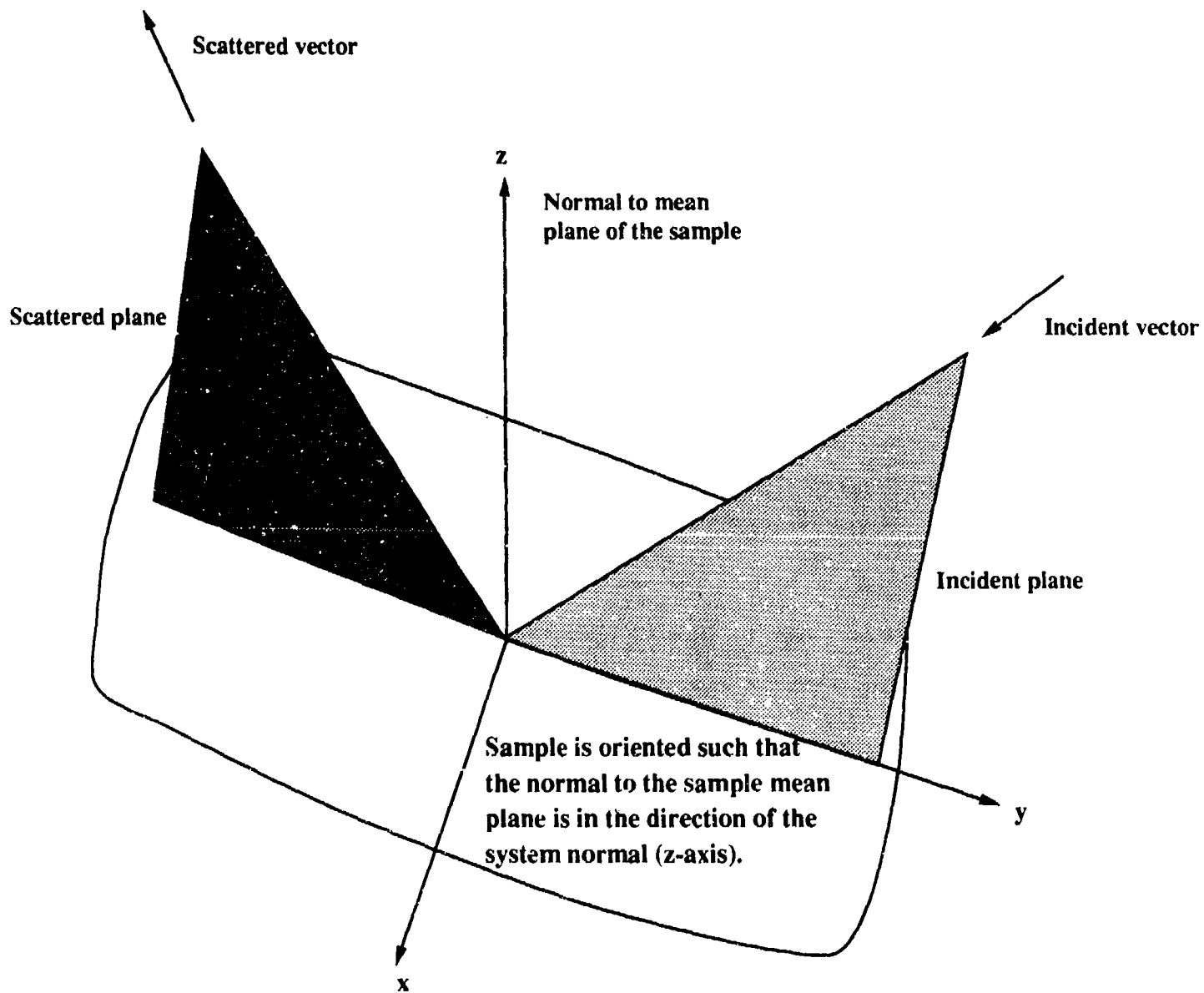


Figure 1. Planes of incidence and scatter.

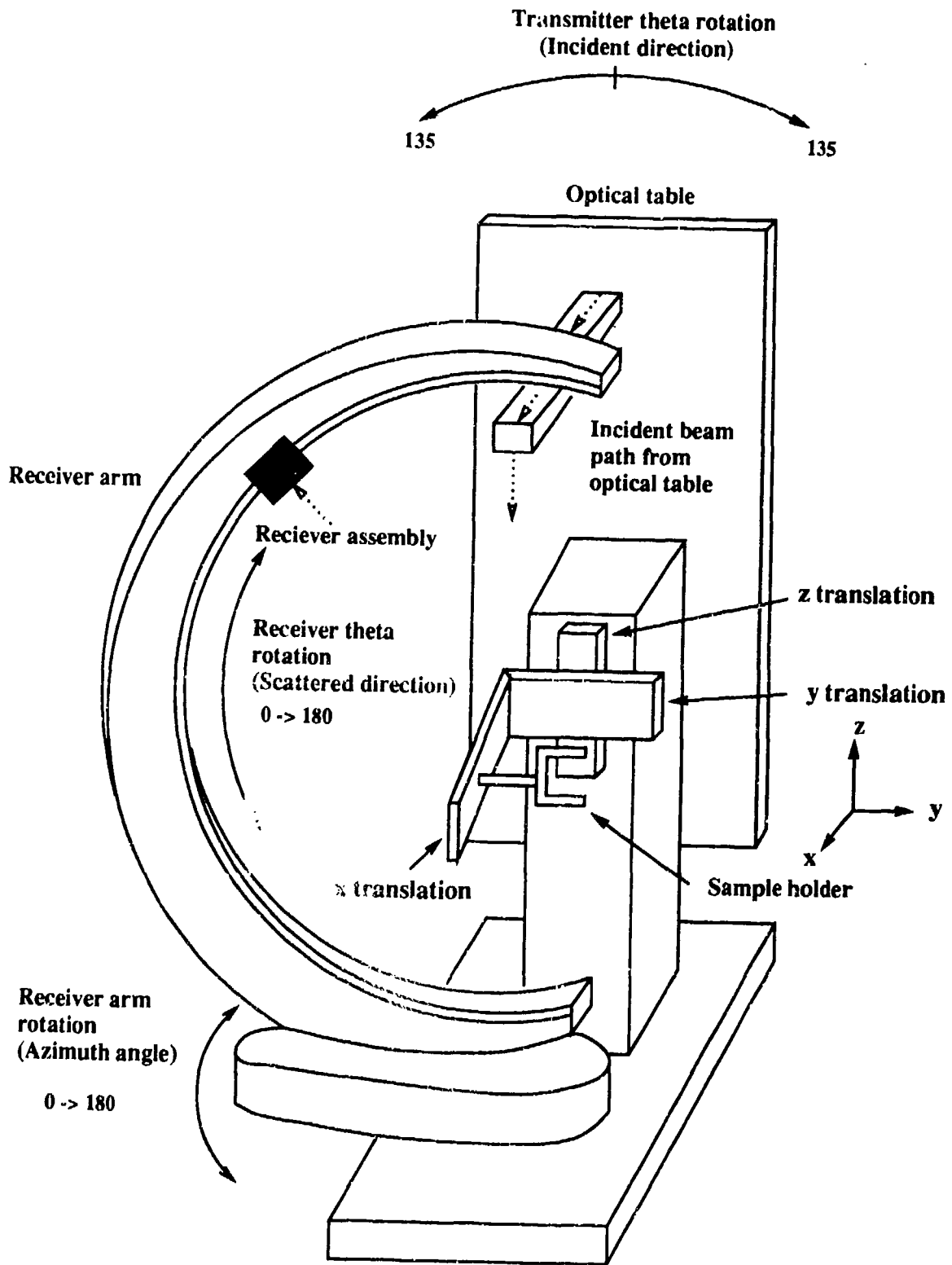


Figure 2. Schematic of the Optical Polarimetric Scatterometer.

Beam path is denoted by $\cdots \rightarrow$.

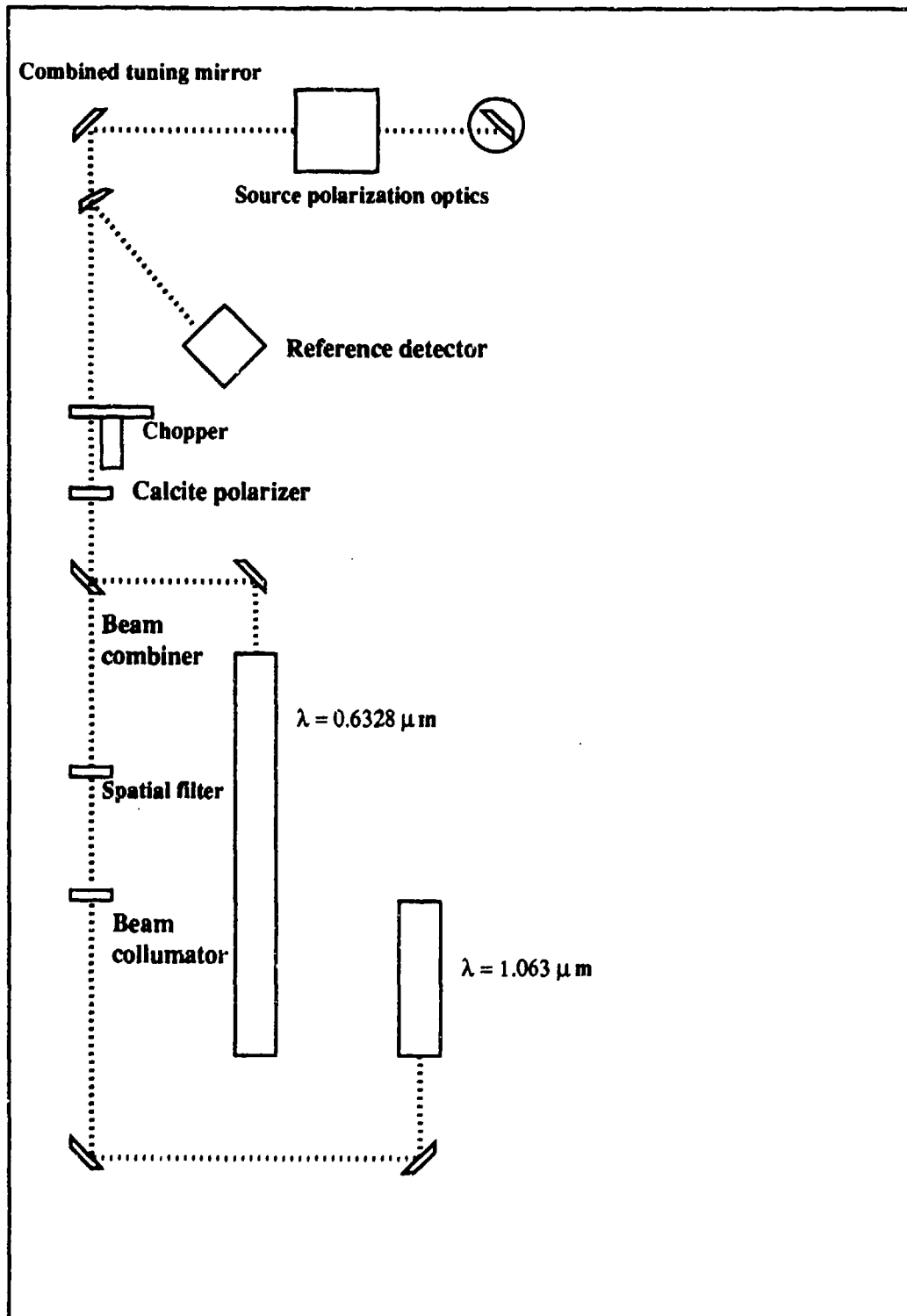


Figure 3. Optical table layout.

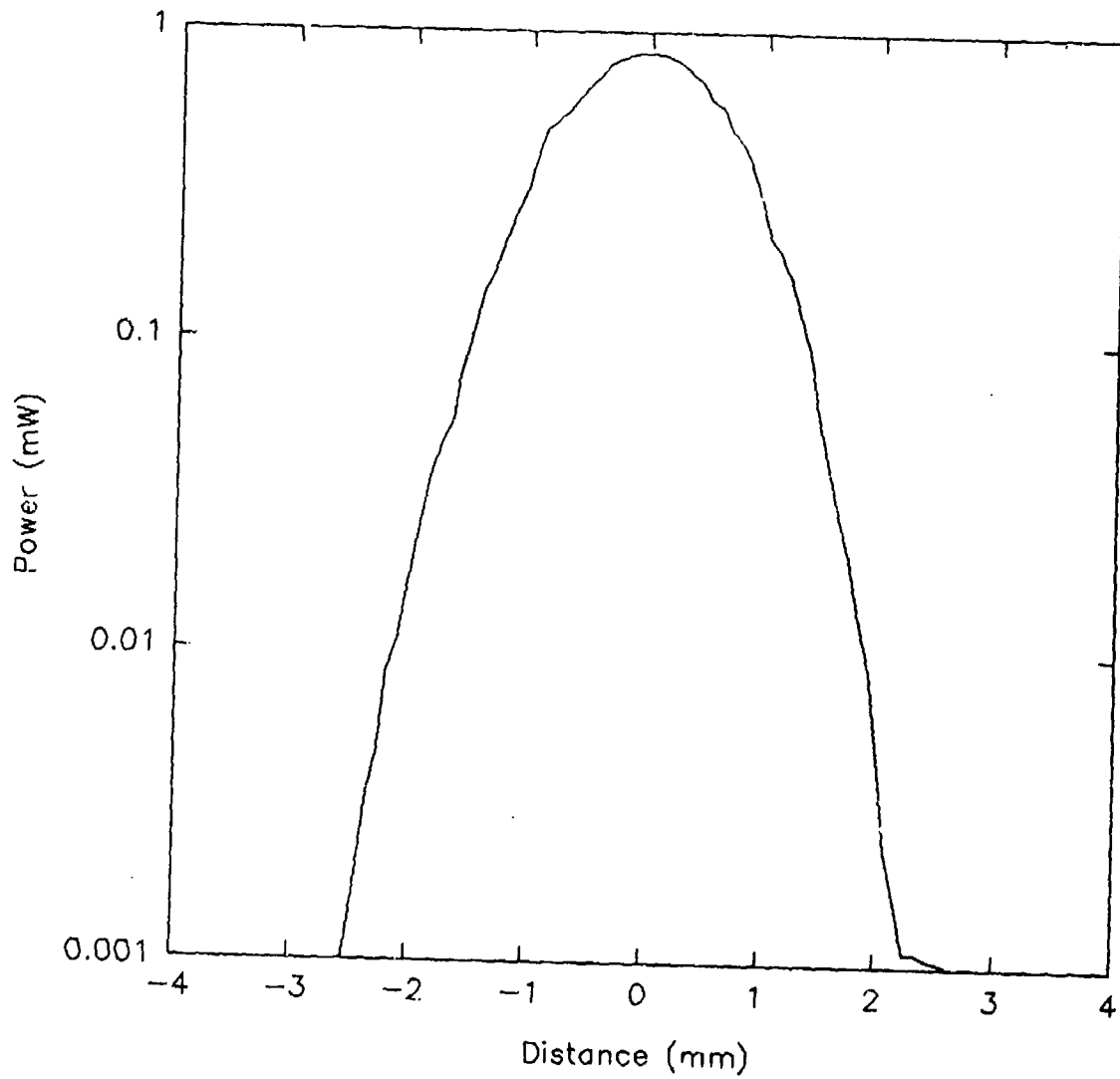


Figure 4a. Scan of the incident beam for a wavelength of $0.6328 \mu\text{m}$ and a receiver aperture of 1.07 mm.

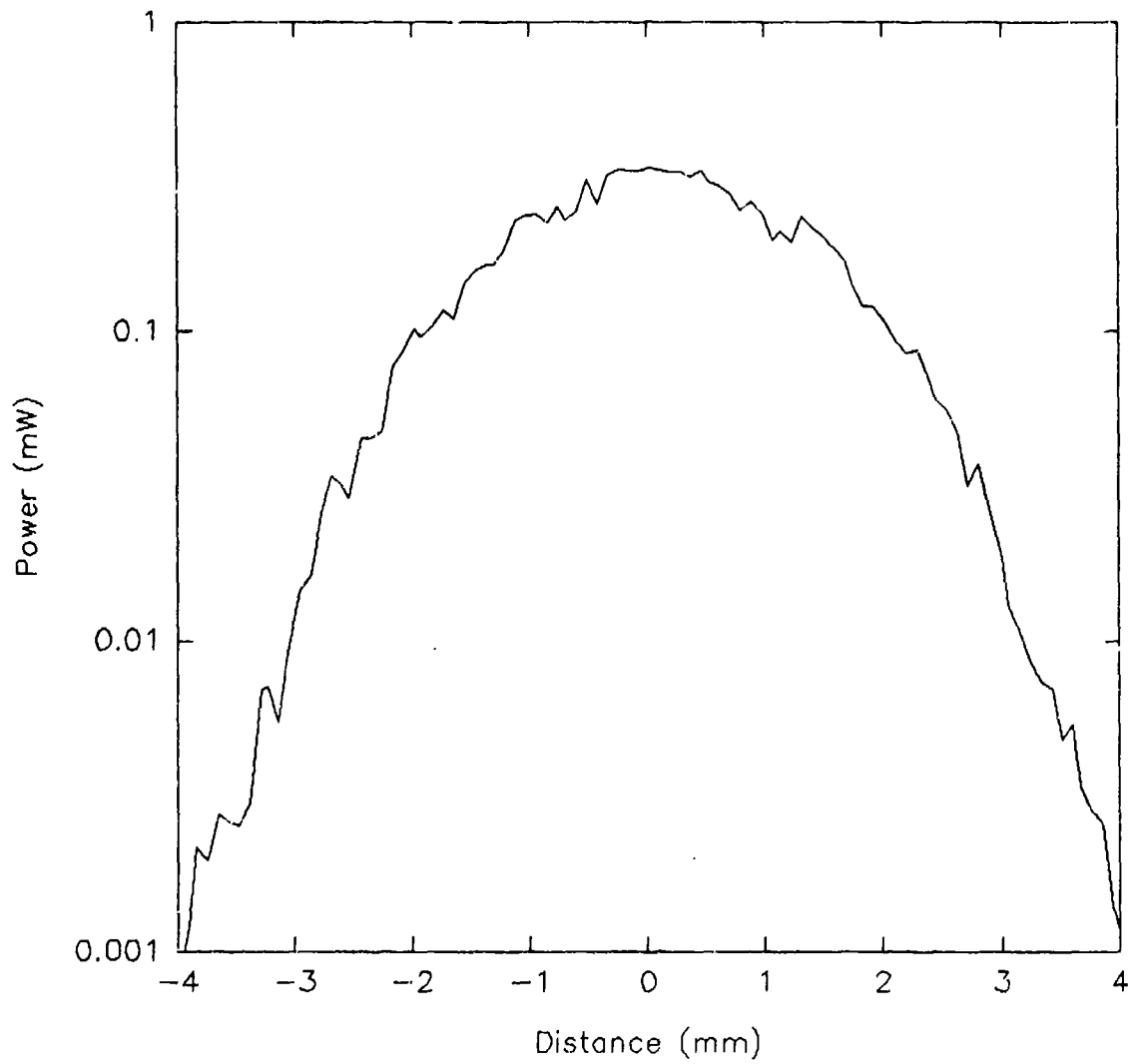


Figure 4b. Scan of the incident beam for a wavelength of $1.06 \mu\text{m}$ and a receiver aperture of 1.07 mm .

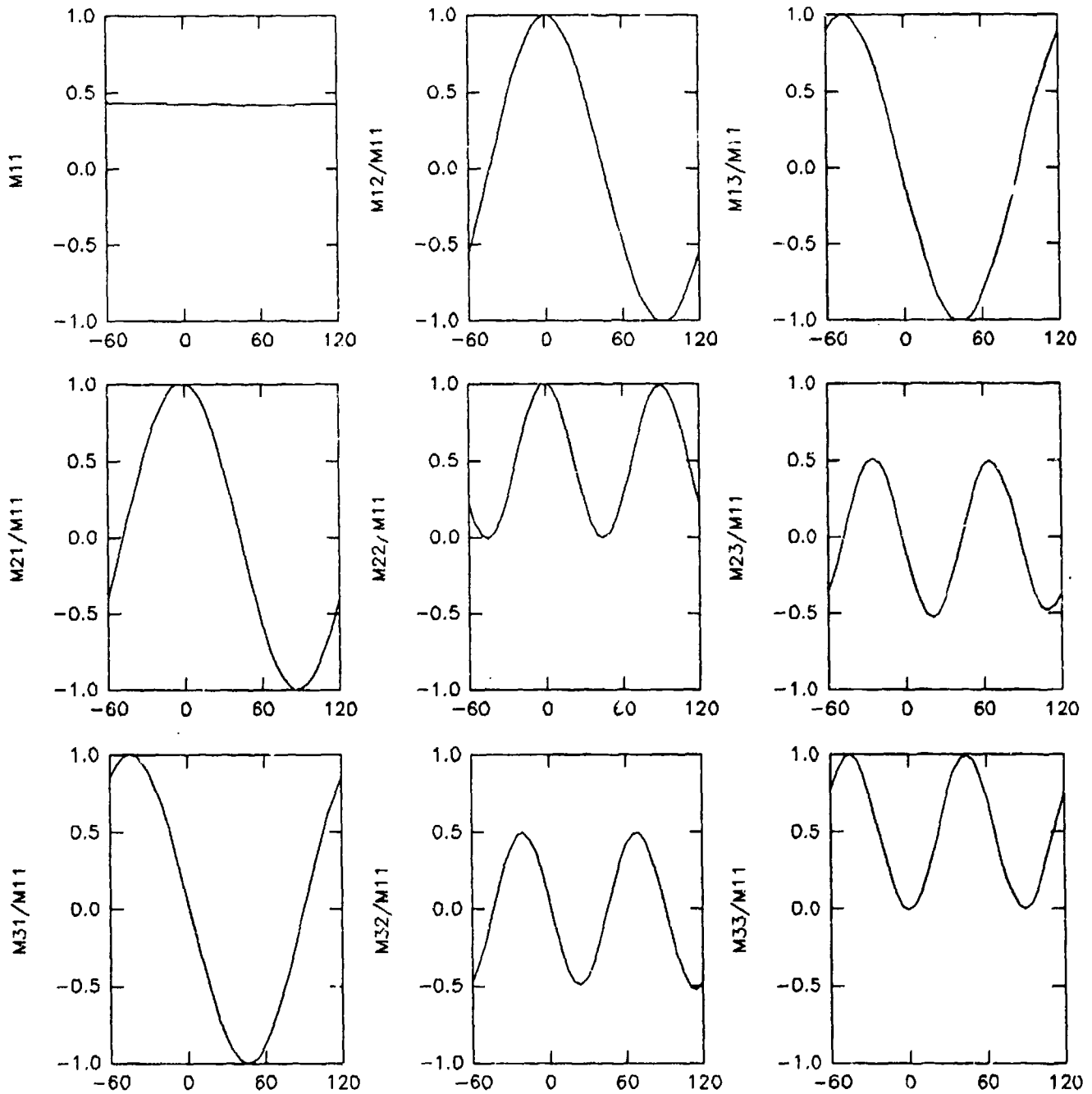


Figure 5a. Muller matrix elements for a polarizer
Horizontal axis is α (see Equation 1).

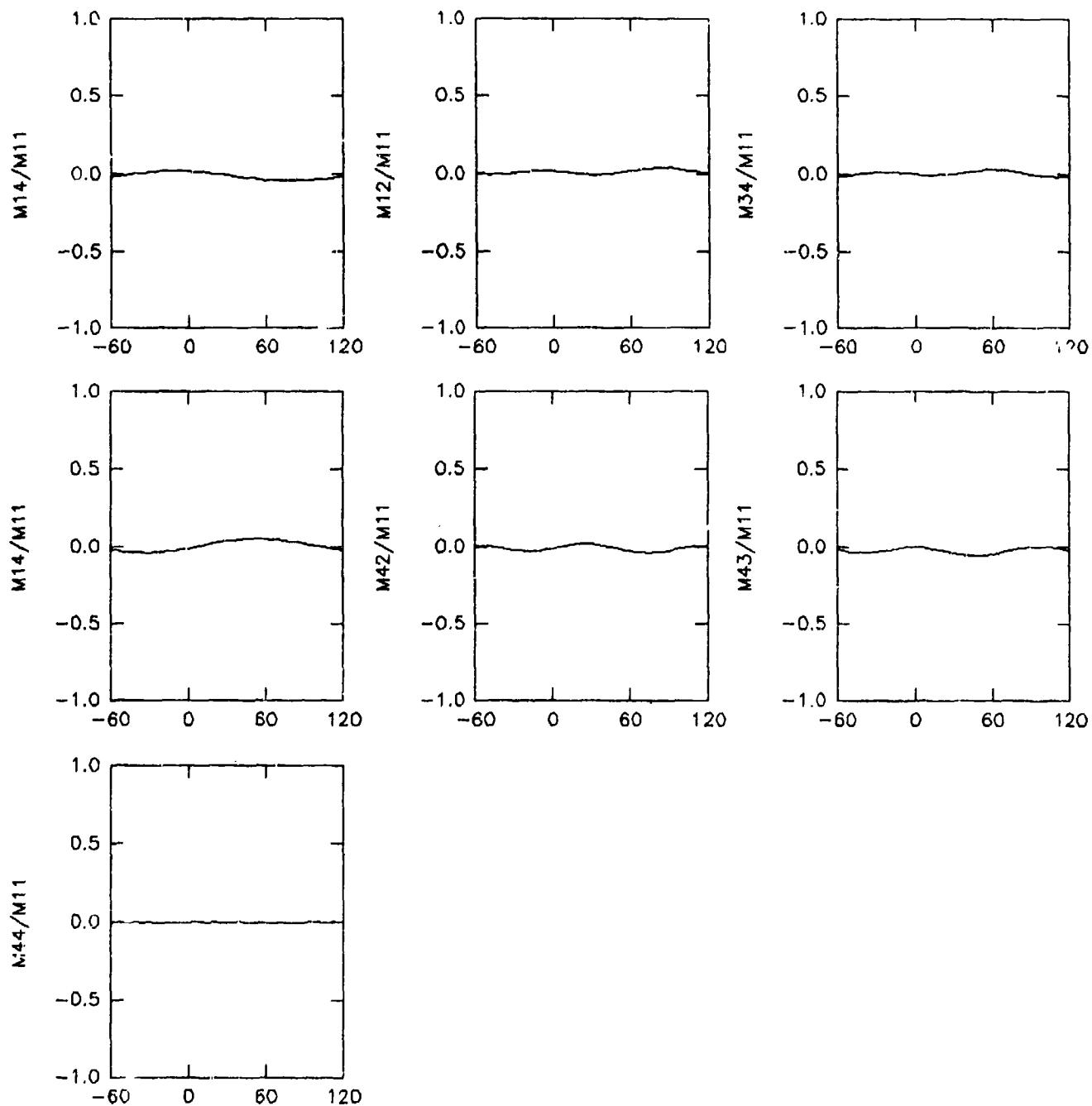


Figure 5b. Muller matrix elements for a polarizer
Horizontal axis is α (see Equation 1).

Gold coated silicon wafer (100 nm. thick)

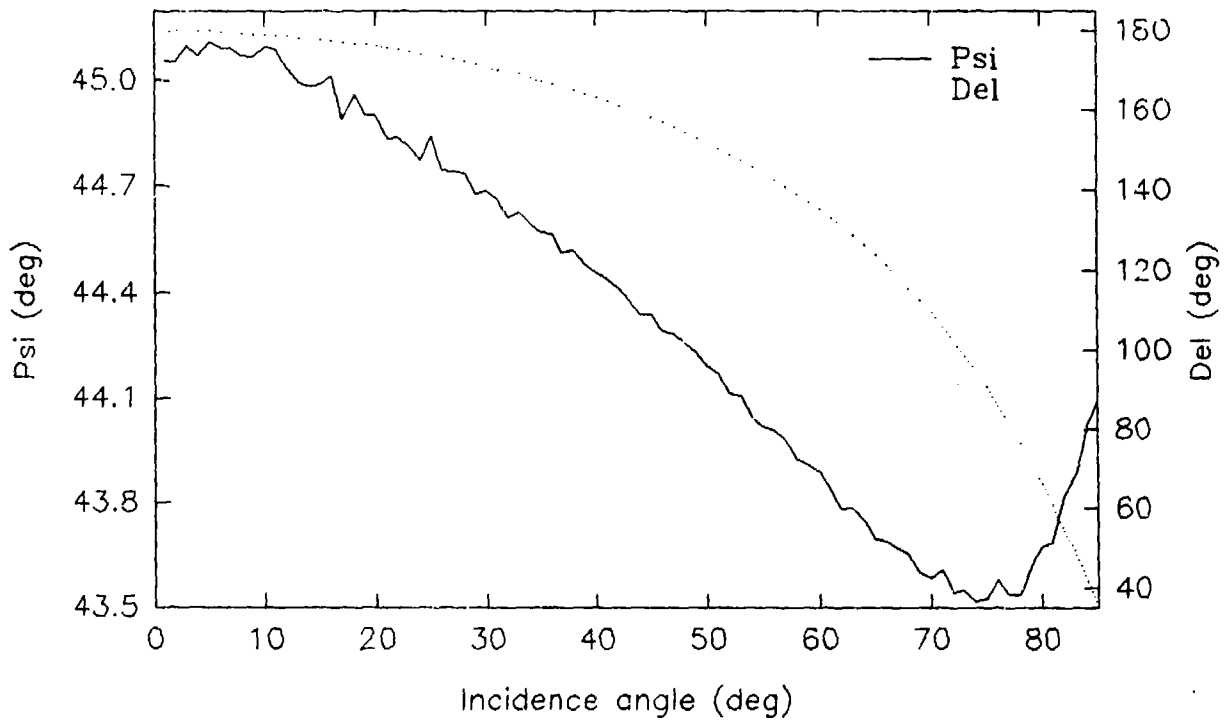


Figure 6a. Ellipsometric angles Psi and Del.

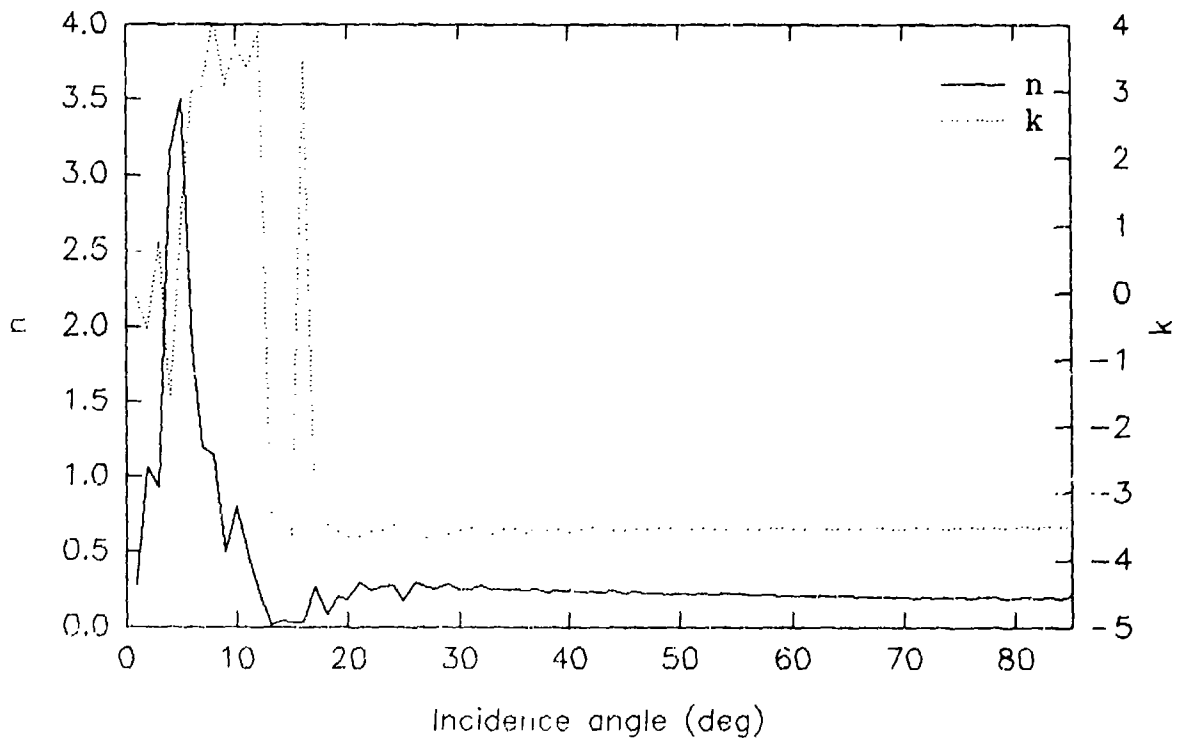


Figure 6b. Complex refractive index.

Blank

INVERSION OF LIGHT SCATTERING MEASUREMENTS FOR PARTICLE SIZE AND OPTICAL CONSTANTS

Matthew R. Jones*
Bill P. Curry*
Keng H. Leong*
M. Quinn Brewster**

*Argonne National Laboratory
9700 South Cass Avenue
Argonne, IL 60439

**University of Illinois at Urbana-Champaign
Department of Mechanical and Industrial Engineering
140 Mechanical Engineering Building
1206 West Green Street
Urbana, IL 61801

RECENT PUBLICATIONS, SUBMITTALS FOR PUBLICATION AND PRESENTATIONS

M.R. Jones, B.P. Curry, and M.Q. Brewster, "Constrained Linear Inversion of Light Scattered from Non-Absorbing, Nearly Identical Spherical Particles for Size and Real Refractive Index", Proceedings of the 1991 CRDEC Scientific Conference on Obscuration and Aerosol Research, In Preparation

M.R. Jones, B.P. Curry, and M.Q. Brewster, "Constrained Linear Inversion of Light Scattered from Non-Absorbing, Nearly Identical Spherical Particles for Size and Refractive Index", Submitted to Applied Optics

M.R. Jones, B.P. Curry, and M.Q. Brewster, "Constrained Linear Inversion of Light Scattering Measurements for the Determination of Al_2O_3 Particle Size Distribution and Optical Constants," Presented at the 23rd Fine Particle Society Meeting, Las Vegas, NV, July 13-17, 1992

M.R. Jones, B.P. Curry, K.H. Leong, and M.Q. Brewster "Inversion of Light Scattering Measurements for Particle Size and Optical Constants", Presented at the AAAR 1992 Annual Meeting, San Francisco, Oct. 12-16, 1992

ABSTRACT

The Fredholm equation representing the light scattered by a weakly absorbing spherical particle or a narrow distribution of spherical particles is inverted to obtain the particle size and refractive index. The solution is obtained by expanding the distribution function as a linear combination of a set of orthonormal basis functions. The set of orthonormal basis functions is composed of the Schmidt-Hilbert eigenfunctions and a set of supplemental basis functions which have been orthogonalized with respect to the Schmidt-Hilbert eigenfunctions using the Gram-Schmidt orthogonalization procedure. The orthogonality properties of the basis functions and of the eigenvectors of the kernel covariance matrix are employed to obtain the solution which minimizes the residual errors subject to a trial function constraint. The inversion process is described, and results from the inversion of several synthetic data sets are presented.

NOMENCLATURE

a_j	Expansion coefficients for the unconstrained solution.
a_j^c	Expansion coefficients for the constrained solution.
a_j^t	Expansion coefficients for the trial function.
C_{sca}^{avg}	Average of the angular scattering cross section (μm^2).
c_{sca}^{avg}	Average of the normalized and imprecision weighted angular scattering cross sections (μm^{-2}).
C_{sca}^j	Angular scattering cross sections (μm^2).
c_{sca}^j	Normalized and imprecision weighted angular scattering cross sections (μm^{-2}).
$\tilde{f}(x,n,k)$	Distribution function.
$f(x)$	Particle size distribution function
$f^t(x,n)$	Trial function
$h(k)$	Ratio of the scattering kernels evaluated at a finite value of k to the scattering kernels evaluated at k equal to zero.
k	Imaginary part of the refractive index.
k_i	Lower limit on the range of imaginary refractive indices.
k_f	Upper limit on the range of imaginary refractive indices.
k_s	Retrieved imaginary part of the refractive index.
$\frac{d\tilde{C}_j}{d\Omega}(\Omega,x,n,k)$	Differential scattering cross sections (μm^2).
$\frac{d\tilde{C}_j^{avg}}{d\Omega}(x,n,k)$	Differential scattering cross sections that have been averaged over the solid angle subtended by the detectors (μm^2).
$\frac{dC_j^{avg}}{d\Omega}(x,n,k)$	Imprecision weighted differential scattering cross sections.
m	Number of inputs
n	Real part of the refractive index.
n_i	Lower limit on the range of real refractive indices.
n_f	Upper limit on the range of real refractive indices.
n_s	Retrieved real part of the refractive index.
N_{ij}	Kernel covariance matrix.
p	Number of supplemental basis functions
u_j^i	The j^{th} element of the i^{th} eigenvector of the kernel covariance matrix.
x	Size parameter.
x_i	Lower limit on the range of size parameters
x_f	Upper limit on the range of size parameters
δC_{sca}^j	Experimental error in the j^{th} measurement (μm^2).
δc_{sca}^j	Normalized and imprecision weighted experimental errors (μm^{-2}).

$\delta(x)$	Dirac delta function.
ΔC_{sca}^j	Estimate of the imprecision in the j^{th} measurement (μm^2).
Δf	Relative error in the retrieved distribution function.
$\Delta\Omega$	Solid angle subtended by the detector (sr)
λ	Wavelength of the laser beam (μm).
λ_j	Eigenvalues of the kernel covariance matrix.
$\Phi_j(x,n)$	Basis functions.
$\phi_j(x,n)$	Supplemental basis functions.
$\tilde{\phi}_j(x,n)$	Orthogonalized supplemental basis functions.
Ω	Scattering direction.

INTRODUCTION

Techniques for solving inverse scattering problems have received considerable attention in the literature and are of great interest due to the wide range of potential applications in areas as diverse as combustion, meteorology, geology, and bioengineering. The wide variety of applications is primarily due to the fact that properties of a physical sample can be determined from the interaction of the sample with radiation from a known source. For instance, measurements of the light scattered by a particle provide an indirect way of determining the particle's size and optical properties. Twomey¹ and Bottiger² describe and compare most of the schemes currently used to invert light scattering or spectral extinction measurements for the particle size distribution function (PSDF). Recently, several techniques not described by Twomey or Bottiger have appeared in the literature³⁻⁸. Since the information content in a set of scattering or extinction measurements is quite limited^{1,9-11}, most inversion techniques require the use of *a priori* information regarding the PSDF and/or careful optimization of the inputs. Indeed, the primary difference between most inversion schemes is the way the *a priori* information is incorporated or the inputs are optimized. Also, other than the sequential gradient restoration algorithm⁷, all the techniques are limited by the fact that the complex refractive index of the particles must be known. This paper describes an inversion scheme that is capable of retrieving the size and optical properties of a weakly absorbing spherical particle or of a narrow distribution of non-absorbing spherical particles. A description of the inversion technique is given with an emphasis on the actual mechanics of the inversion process. The results from several inversions of synthetic data sets are also presented.

THE SCATTERING EQUATION

In the development of this inversion process, attention was focused on simulating an experiment in which a multi-channel polar nephelometer is used to measure the light scattered from weakly absorbing particles. The nephelometer uses an unpolarized red ruby laser ($\lambda = 0.67 \mu\text{m}$) as a light source and has detectors positioned every 4° from 20° to 160° . Therefore, the available set of measurements consists of measurements of the power scattered in 36 directions. The ratio of the power scattered in the direction of a particular detector to the incident irradiance is referred to as an angular scattering cross section. The angular scattering cross section measured by the j^{th} detector, C_{sca}^j , is related to the unknown distribution of sizes and optical properties by a Fredholm equation.

$$\begin{aligned}
C_{sca}^j &= \int_{\Delta\Omega} \int_{k_i}^{k_f} \int_{n_i}^{n_f} \int_{x_i}^{x_f} \tilde{f}(x,n,k) \frac{d\tilde{C}_j}{d\Omega}(\Omega,x,n,k) dx dn dk d\Omega + \delta C_{sca}^j \\
&= \Delta\Omega \int_{k_i}^{k_f} \int_{n_i}^{n_f} \int_{x_i}^{x_f} \tilde{f}(x,n,k) \frac{d\tilde{C}_j^{avg}}{d\Omega}(x,n,k) dx dn dk + \delta C_{sca}^j \quad (1)
\end{aligned}$$

The $\frac{d\tilde{C}_j}{d\Omega}(\Omega,x,n,k)$ are differential scattering cross sections and are often referred to as scattering kernels. Assuming the particles are spheres, the differential scattering cross sections can be calculated from Mie theory^{12,13}.

The following assumptions are made in order to simplify Equation 1. For weakly absorbing particles ($k \sim 10^{-3}$), the scattering kernels can be approximated by the product of a function that depends only on k and the scattering kernel with k set equal to zero.

$$\frac{d\tilde{C}_j^{avg}}{d\Omega}(x,n,k) \sim h(k) \frac{d\tilde{C}_j^{avg}}{d\Omega}(x,n,0) \quad (2)$$

It is assumed that if a distribution of particles is present, all the particles have the same optical properties.

$$\tilde{f}(x,n,k) = f(x) \delta(n-n_s) \delta(k-k_s) \quad (3)$$

Equation 1 now simplifies to

$$C_{sca}^j = \Delta\Omega h(k_s) \int_{n_i}^{n_f} \int_{x_i}^{x_f} f(x) \delta(n-n_s) \frac{d\tilde{C}_j^{avg}}{d\Omega}(x,n,0) dx dn + \delta C_{sca}^j \quad (4)$$

Neglecting the error in the measurements, the average of the measurements can be approximated by the the average of the right hand side of Equation 4.

$$\begin{aligned}
C_{sca}^{avg} &= \frac{1}{m} \sum_{j=1}^m C_{sca}^j \\
&\approx \frac{1}{m} \sum_{j=1}^m \Delta\Omega h(k_s) \int_{n_i}^{n_f} \int_{x_i}^{x_f} f(x) \delta(n-n_s) \frac{d\tilde{C}_j^{avg}}{d\Omega}(x,n,0) dx dn \quad (5)
\end{aligned}$$

The unknown function, $h(k)$, can be eliminated from Equation 4 by normalizing by the average of the measurements. Earlier investigations have also shown that it is beneficial to weight each measurement and scattering kernel by the corresponding imprecision estimate^{13,14}. These simplifications allow the Equation 4 to be rewritten as

$$C_{sca}^j = \frac{1}{C_{sca}^{avg}} \int_{n_i}^{n_f} \int_{x_i}^{x_f} f(x) \delta(n-n_s) \frac{dC_j^{avg}}{d\Omega}(x,n,0) dx dn + \delta C_{sca}^j \quad (6)$$

where

$$C_{sca}^j = C_{sca}^j / C_{sca}^{avg} \Delta C_{sca}^j \quad (7)$$

$$\delta C_{sca}^j = \delta C_{sca}^j / C_{sca}^{avg} \Delta C_{sca}^j \quad (8)$$

$$\frac{dC_j^{avg}}{d\Omega}(x,n,0) = \frac{d\tilde{C}_j^{avg}}{d\Omega}(x,n,0) / \Delta C_{sca}^j \quad (9)$$

$$C_{sca}^{avg} = \frac{1}{m} \sum_{j=1}^m \int_{n_i}^{n_f} \int_{x_i}^{x_f} f(x) \delta(n-n_s) \frac{dC_j^{avg}}{d\Omega}(x,n,0) dx dn \quad (10)$$

EXAMPLE INVERSION

A linear inversion procedure is used to invert Equation 9 and retrieve the real part of the refractive index. Constrained linear inversion is used to retrieve the PSDF. The value of the imaginary part of the refractive index is obtained by comparing the measured scattering pattern with the scattering pattern calculated using the retrieved real refractive index and PSDF. The value of the imaginary refractive index that results in the smallest residual errors is taken to be the retrieved imaginary refractive index. There are five major steps in the inversion process: preliminary analysis of the measurements, selection of the inputs from the available measurement set, retrieval of the real part of the refractive index using the unconstrained solution, retrieval of the PSDF using the constrained solution, and finally, retrieval of the imaginary part of the refractive index by matching the measured and calculated scattering patterns. An example inversion is described along with presentation of the mathematical formulation in order to illustrate the mechanics of the inversion process. An effort has been made to keep the description of the mathematics brief, but still provide the reader with all the equations needed to actually perform an inversion. Complete developments of the mathematics of inversion are available elsewhere¹.

PRELIMINARY ANALYSIS OF THE MEASUREMENTS

Angular scattering cross sections should be calculated for several different sizes and optical properties within the expected ranges before attempting to invert any measured values. Particular attention should be given to the value of the most forward angular scattering cross section available and the average of the angular scattering cross sections. These parameters will serve as a guide in selecting the trial function used in obtaining the constrained solution. The range of sizes and optical properties considered in the example inversion are listed in Table 1. Table 2 lists the average and 20° angular scattering cross sections for 12 different sizes and 3 sets of optical properties.

Table 1. Range of Sizes and Optical Properties

Diameter Range (μm)	Size Parameter Range	Real Refractive Index Range	Imaginary Refractive Index Range
0.1 - 10.1 μm	0.5 - 47.6	1.1 - 2.0	0.0 - 0.3

Table 2. Average and 20° Angular Scattering Cross Sections

Diameter (μm)	Size Parameter	Refractive Index					
		$1.1 + i 10^{-3}$		$1.5 + i 10^{-3}$		$2.0 + i 10^{-3}$	
		$C_{\text{sca}}^{\text{avg}} (\mu\text{m}^2)$	$C_{\text{sca}}^{20^\circ} (\mu\text{m}^2)$	$C_{\text{sca}}^{\text{avg}} (\mu\text{m}^2)$	$C_{\text{sca}}^{20^\circ} (\mu\text{m}^2)$	$C_{\text{sca}}^{\text{avg}} (\mu\text{m}^2)$	$C_{\text{sca}}^{20^\circ} (\mu\text{m}^2)$
0.1	0.5	3.3E-7	3.6E-7	7.2E-6	7.9E-6	2.2E-5	2.5E-5
0.5	2.3	3.1E-4	3.1E-3	1.2E-2	7.7E-2	3.5E-2	0.1
1.0	4.7	3.5E-3	0.1	0.7	0.4	0.1	0.3
2.0	9.4	1.1E-2	0.2	0.2	0.6	0.2	0.7
3.0	14.1	3.4E-2	0.6	0.3	1.7	0.4	1.1
4.0	18.8	0.1	0.9	0.5	2.2	0.6	1.9
5.0	23.4	0.1	1.9	0.6	3.8	0.9	3.5
6.0	28.1	0.2	2.3	1.1	4.6	1.1	4.5
7.0	32.8	0.3	4.1	1.1	6.2	1.5	4.8
8.0	37.5	0.3	3.9	1.7	7.7	1.7	6.6
9.0	42.2	0.6	8.0	1.7	9.8	2.2	9.8
10.0	46.9	0.6	6.6	2.4	11.0	2.8	11.5

Synthetic measurements representing the light scattered by a single spherical particle were calculated using Equation 1. The size and the optical properties of the particle were randomly selected from the ranges specified in Table 1, so the actual parameters of the distribution function were not known until after the inversion had been completed. Gaussian distributed random noise was added to each synthetic measurement in order to simulate actual experimental conditions. The angular scattering cross sections are plotted in Figure 1, and the imprecision estimates shown in the figure are equal to the standard deviation of the random noise. The standard deviation of the random noise was equal to 10% of the error free measurements. The average of these angular scattering cross sections is $0.67 \mu\text{m}^2$ and the 20° angular scattering cross section has a value of $2.6 \mu\text{m}^2$. Comparison of the 20° angular scattering cross section and the average of the angular scattering cross sections with the values in Table 2 indicates that the particle has a diameter of approximately 4 to 5 μm (a size parameter between 19 and 23).

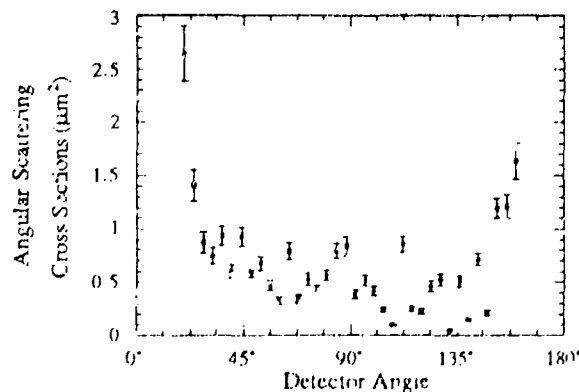


Figure 1. Synthetic Angular Scattering Cross Sections

INPUT SELECTION

The scattering kernels are not mutually orthogonal functions, so a large number of measurements may only contain a few measurements that are independent of the rest¹¹. Therefore, it is necessary to select a set of inputs from the available set of measurements. An algorithm similar to that used by Capps et al⁹ is used to determine which measurements to use in the inversion process. A kernel covariance matrix is calculated using the scattering kernels corresponding to the complete set of measurements, and the eigenvalues and eigenvectors of the kernel covariance matrix are calculated. The kernel covariance matrix is defined as

$$N_{ij} = \int_{n_i}^{n_f} \int_{x_i}^{x_f} \frac{dC_i^{avg}}{d\Omega}(x,n,0) \frac{dC_j^{avg}}{d\Omega}(x,n,0) dx dn \quad (11).$$

Once the eigenvalues are known, an expression derived by Twomey¹¹ for the relative error (the square root of the ratio of the square norm of the error in the distribution function to the square norm of the distribution function) is used to determine whether or not the selected inputs can be successfully used in an inversion process.

$$\Delta f = \frac{1}{m} \left\{ \sum_{j=1}^m \frac{1}{\lambda_j} \sum_{j=1}^m \lambda_j \sum_{j=1}^m (\Delta C_{sca}^j)^2 / \sum_{j=1}^m (C_{sca}^j)^2 \right\}^{1/2} \quad (12).$$

If the relative error given by Equation 12 is too large, the largest off diagonal element of the kernel covariance matrix is used to identify the two most nearly dependent measurements. The sum of the squares of the off diagonal matrix elements is calculated for each row corresponding to the two most redundant measurements. The largest of these sums identifies the measurement that is most nearly dependent on the rest of the measurements, and that measurement is eliminated from the set of inputs. A new kernel covariance matrix is then calculated, and the process is repeated until the relative error calculated from Equation 12 is small enough. In this study, the best results were obtained when the relative error is slightly less than 1. For the angular scattering cross sections shown in Figure 1, 27 to 30 of the 36 measurements were eliminated from the input set before a relative error less than 1 was achieved. The variation in the number of inputs was due to variations in the range of real refractive indices as discussed in the next section.

RETRIEVAL OF THE REAL PART OF THE REFRACTIVE INDEX

Once a set of inputs has been selected, an unconstrained solution is obtained by expanding the distribution function as a linear combination of the Schmidt-Hilbert eigenfunctions.

$$f(x) \delta(n-n_s) \approx \sum_{j=1}^m a_j \Phi_j(x,n) \quad (13)$$

The unconstrained expansion coefficients are calculated from

$$a_j = \sum_{i=1}^m g_i u_i^j / \sqrt{\lambda_j} \quad (14)$$

where the λ_j and u_i^j are the eigenvalues and eigenvectors of the kernel covariance matrix. The Schmidt-Hilbert eigenfunctions are obtained from

$$\Phi_j(x,n) = \frac{1}{\sqrt{\lambda_j}} \sum_{i=1}^m u_i^j \frac{dC_j^{avg}}{d\Omega}(x,n,0) \quad \text{for } 1 \leq j \leq m \quad (15)$$

The value of the real part of the refractive index and the unconstrained PSDF are calculated from the unconstrained solution.

$$W(n_S) = \int_{n_i}^{n_f} \int_{x_i}^{x_f} W(n) \sum_{j=1}^m a_j \Phi_j(x,n) dx dn / \int_{n_i}^{n_f} \int_{x_i}^{x_f} \sum_{j=1}^m a_j \Phi_j(x,n) dx dn$$

$$n_S = W^{-1}(W(n_S)) \quad (16)$$

$$f(x) = \int_{n_i}^{n_f} \sum_{j=1}^m a_j \Phi_j(x,n) dn \quad (17)$$

The weighting function, W , is used to increase the sensitivity of the unconstrained solution to changes in the real refractive index. A weighting function that proved to be useful in this study is the phase shift¹³ squared, $x^2[n-1]^2$. In practice, it is usually necessary to vary n_i and n_f to ensure that the retrieved refractive index is close to the actual value. When inverting the example data set, the entire range of refractive indices (1.1 - 2.0) was first considered, and the retrieved real refractive index was 1.47. The range of refractive indices was then narrowed to 1.3 - 1.6, and the retrieved refractive index was 1.43. This process was continued until the retrieved value of the real refractive index converged to 1.42. The unconstrained PSDF is shown in Figure 2.

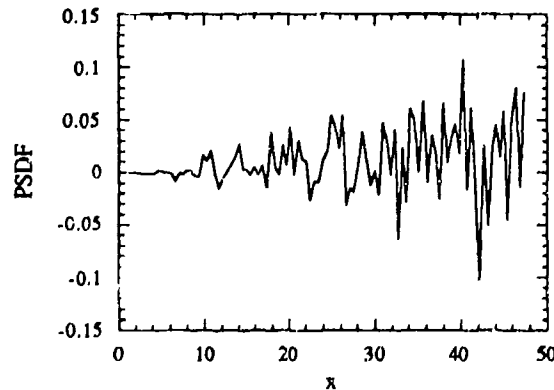


Figure 2. Unconstrained PSDF

RETRIEVAL OF THE PSDF

The unconstrained solution satisfies Equation 6 for the set of inputs, and therefore, is a mathematically correct solution. However, the PSDF obtained from the unconstrained solution displays characteristics such as high frequency oscillations and negative values which make it physically unrealistic. These characteristics are due to errors in the measurements and to the limited information content of the measurements. Although it is not possible to eliminate the error in the measurements, the difficulty associated with the limited information content can be dealt with through the introduction of *a priori* information in the form of a trial function constraint. Of course, the nature of the trial function will depend on the particular conditions under which the measurements are made, and can only be determined after careful consideration of the particular experiment. If measurements are made of the light scattered by a single particle or by an ensemble of nearly identical particles, the unconstrained solution and the preliminary analysis of the measurements provide enough information to successfully choose a trial function. In our example inversion, it is known that the measurements are of light scattered by a single particle. Based on this fact, the form of the trial function is chosen to be

$$f(x, n) = \delta(x - x_1)\delta(n - n_s) \quad (18)$$

Based on the preliminary analysis of the measurements, x_1 is expected to be in the range of 19 to 23. The exact value of x_1 is obtained by examining the unconstrained PSDF shown in Figure 2. In this case, there are no prominent peaks within the expected size range. However, the expected size range only serves as a rough guide in selecting the trial function, and there is a fairly prominent peak in the unconstrained PSDF at $x = 25.1$. Therefore, x_1 is chosen to be 25.1.

The imposition of the trial function constraint requires that the trial function and the unknown distribution function be expanded as linear combinations of a set of orthonormal basis functions. However, adequate representations of these functions cannot be obtained using the Schmidt-Hilbert eigenfunctions alone. Therefore, a set of supplemental basis functions or "pseudo-empirical eigenfunctions"¹⁰ must be introduced. The additional basis functions are obtained by orthogonalizing a set of orthonormal functions with respect to the Schmidt-Hilbert eigenfunctions. The supplemental orthonormal functions used in the example inversion were

$$\phi_j(x, n) = \delta(x - x_j)\delta(n - n_j) \quad \text{for } 1 \leq j \leq 101 \quad (19),$$

where the x_j are evenly spaced throughout the size range. The supplemental basis functions are calculated by orthogonalizing the $\phi_j(x, n)$ with respect to the Schmidt-Hilbert eigenfunctions using the Gram-Schmidt orthogonalization procedure. Some of the $\phi_j(x, n)$ will lie entirely in the space spanned by the lower order basis functions and will be eliminated by the orthogonalization procedure. Therefore, the number of supplemental basis functions, p , will be less than the number of $\phi_j(x, n)$. The number of supplemental basis functions used in the example inversion was 93.

$$\tilde{\phi}_j(x, n) = \phi_j(x, n) - \sum_{i=1}^{j-1} \phi_j(x, n) \int_{n_i}^{n_f} \int_{x_i}^{x_f} \phi_j(x', n') \Phi_i(x', n') dx' dn' \quad \text{for } 1 \leq j \leq 101$$

$$\Phi_j(x, n) = \tilde{\phi}_j(x, n) / \left\{ \int_{n_i}^{n_f} \int_{x_i}^{x_f} \tilde{\phi}_j^2(x', n') dx' dn' \right\}^{1/2} \quad \text{for } m < j \leq m+p \quad (20)$$

The trial function and the unknown distribution function can now be accurately expressed in terms of the basis functions.

$$f^l(x,n) = \sum_{j=1}^{m+p} a_j^l \Phi_j(x,n) \quad (21)$$

$$f(x) \delta(n-n_s) = \sum_{j=1}^{m+p} a_j^c \Phi_j(x,n) \quad (22)$$

The expansion coefficients for the trial function are obtained from

$$a_j^l = \int_{n_i}^{n_f} \int_{x_i}^{x_f} f^l(x,n) \Phi_j(x,n) dx dn \quad (23).$$

The constrained expansion coefficients are found by minimizing the residual errors subject to the trial function constraint. A performance function is defined as

$$Q = \sum_{j=1}^m \left[\frac{1}{c_{sca}^{avg}} \int_{n_i}^{n_f} \int_{x_i}^{x_f} \sum_{i=1}^m a_i \Phi_i(x,n) \frac{dC_j^{avg}}{d\Omega}(x,n_s,0) dx dn \right]^2 - c_{sca}^j \quad (24)$$

$$+ \gamma \int_{n_i}^{n_f} \int_{x_i}^{x_f} \left[\sum_{i=1}^m a_i \Phi_i(x,n) - \sum_{i=1}^m a_i^l \Phi_i(x,n) \right]^2 dx dn$$

The performance function is proportional to the residual errors in the retrieved solution and to the square norm of the difference between the unconstrained solution and the trial function. The weighting parameter, γ , determines the relative importance of the trial function constraint. Minimizing the performance function with respect to the expansion coefficients gives the following expression for the constrained expansion coefficients

$$a_j^c = \frac{a_j \lambda_j + \gamma a_j^l}{\lambda_j + \gamma} \quad \text{for } 1 \leq j \leq m$$

$$a_j^c = a_j^l \quad \text{for } m < j \leq m + p \quad (25).$$

Clearly, the value used for γ will be important in the inversion process. It can be shown that the square norm of the error introduced by applying the constraint is minimized if the parameter known as the residual relative variance (RRV)¹¹ is minimized with respect to γ . The partial derivative of the RRV with respect to γ is given by

$$\frac{\partial \text{RRV}}{\partial \gamma} = \sum_{j=1}^m \lambda_j \left[\gamma (a_j - a_j^t)^2 - (c_{\text{sca}}^{\text{avg}})^2 / (C_{\text{sca}}^{\text{avg}})^2 \right] / (\lambda_j + \gamma)^3 \quad (26).$$

The optimal value of γ is obtained by increasing γ until $\frac{\partial \text{RRV}}{\partial \gamma}$ is approximately zero. In the example inversion, at $\gamma = 86.3$, $\frac{\partial \text{RRV}}{\partial \gamma} = -5.0\text{E}-08$. Once the optimal value of γ is determined, the constrained solution can be calculated from Equation 21. The PSDF is then obtained by integrating the constrained solution over the range of refractive indices.

$$f(x) = \int_{n_i}^{n_f} \sum_{j=1}^{m+p} a_j^c \Phi_j(x, n) \, dn \quad (27)$$

The constrained PSDF for the example inversion is plotted in Figure 3.

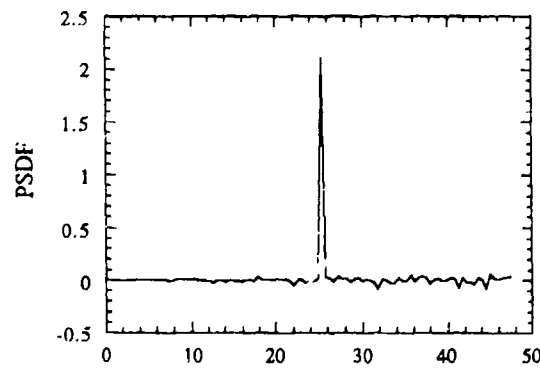


Figure 3. Constrained PSDF

RETRIEVAL OF THE IMAGINARY PART OF THE REFRACTIVE INDEX

A value for the imaginary part of the refractive index can now be obtained. An initial guess of the imaginary refractive index is made and the scattering pattern is calculated using Equation 1. The value of the imaginary part of the refractive index can be adjusted until the measured and calculated scattering patterns are in close agreement. If it is not possible to bring the measured and calculated scattering patterns into agreement by adjusting the value of the imaginary refractive index, the inversion process should be repeated using a different trial function. For the example inversion, the value of the imaginary part of the refractive index that gave the lowest rms residual error was 10^{-3} . The measured and calculated scattering patterns are compared in Figure 4. The relatively large discrepancy between the calculated patterns and measured 20° angular scattering cross section indicate that the size parameter selected for the trial function is too large. The relatively good agreement between the calculated and measured scattering cross sections in the 100° to 150° range indicate that the retrieved value of the real refractive index is close to the actual value. Figure 2 is again used to select a x_t value for a new trial function. The largest peak at a size parameter less than 25.1 is at $x = 20.1$. A new constrained solution is calculated as before. Using the new constrained solution, the closest agreement between the measured and calculated scattering patterns is obtained for an imaginary part of the

refractive index of 10^{-4} . The new calculated scattering pattern compares well with the measured scattering pattern as shown in Figure 5.

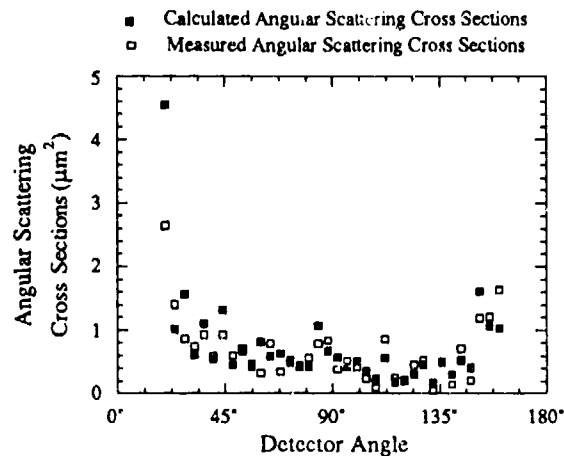


Figure 4. Comparison of the Measured and Calculated Scattering Patterns with $x_1 = 25.1$

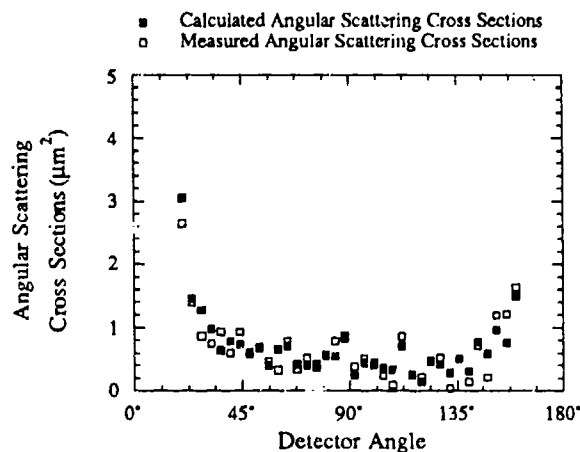


Figure 5. Comparison of the Measured and Calculated Scattering Patterns with $x_1 = 20.1$

SUMMARY OF THE EXAMPLE INVERSION

The retrieved and actual size and optical properties of the particle in the example data set are compared in Table 3.

Table 3. Comparison the Particle Size and Optical Properties with the Retrieved Values

Parameter	Actual Value	Retrieved Value
Diameter (μm)	4.5	4.3
Size Parameter	21.2	20.1
Refractive Index	$1.45 + i7.5E-5$	$1.42 + i1.0E-4$

INVERSION OF MORE SYNTHETIC DATA SETS

In order to further test the inversion process, J.R. Bottiger provided the authors with 6 sets of synthetic light scattering measurements. The authors were told that the measurements corresponded to the light scattered by narrow distributions of non-absorbing spheres, but no other information was given. The results of the inversions are shown in Table 4.

Table 4. Comparison of the Actual and Retrieved PSDFs and Refractive Indices

Case	Retrieved Mean Size Parameter	Actual Mean Size Parameter	Retrieved Geometric Standard Deviation	Actual Geometric Standard Deviation	Retrieved Refractive Index	Actual Refractive Index
1	10.1	10.0	1.08	1.11	1.33	1.33
2	19.7	20.0	1.11	1.11	1.46	1.45
3	23.2	20.0	1.09	1.35	1.45	1.45
4	48.9	35.0	1.03	1.11	1.56	1.55
5	47.4	35.0	1.04	1.22	1.56	1.55
6	55.0	55.0	1.03	1.02	1.33	1.33

The actual PSDFs are plotted in Figure 6 for all 6 cases. Although the PSDF for case 4 has the same geometric standard deviation as the PSDFs for cases 1 and 2, the PSDF for case 4 is actually broader than those for cases 1 and 2. These results show that the technique is successful when the distributions are narrow (cases 1, 2 and 6), but has difficulty when the distributions are broad (cases 3, 4, and 5). This is due to the fact that as the PSDFs become broader, the scattering pattern becomes smoother, and probability of finding another PSDF that will produce a similar scattering pattern increases. It is interesting to note that even when the retrieved distributions differed from the actual distributions, the refractive index was retrieved accurately.

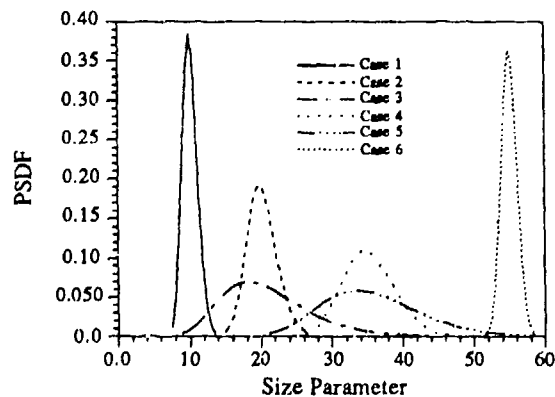


Figure 6. Particle Size Distribution Functions

CONCLUSIONS

An inversion technique that retrieves the particle size distribution function and the refractive index of weakly absorbing spherical particles from synthetic measurements of scattered light has been developed. The solution is obtained by expanding the distribution function as a linear combination of orthonormal basis functions. The orthogonality properties of the basis functions are used to find the expansion coefficients which minimize the residual errors subject to a trial function constraint. The technique is shown to be capable of retrieving the size and optical properties from noisy measurements of the light scattered by a weakly absorbing sphere. The technique was also used to retrieve the PSDF and refractive index from synthetic measurements of the light scattered by narrow log normal distributions of non-absorbing spheres in a blind test. Attempts to retrieve the PSDF were less successful when the distributions were not narrow, but the refractive index was still retrieved accurately.

ACKNOWLEDGEMENTS

This work was sponsored by the Army Chemical Research, Development, and Engineering Center, Aberdeen Proving Ground, MD. under the supervision of J. R. Bottiger.

REFERENCES

1. S. Twomey, *Introduction to the Mathematics of Inversion in Remote Sensing and Indirect Measurements* (Elsevier, Amsterdam, 1977).
2. J.R. Bottiger, "Intercomparison of Some Inversion Methods on Systems of Spherical Particles," in *Advances in Remote Sensing Retrieval Methods*, A. Deepak, H. Fleming and M. Chahine, Eds.(A. Deepak, Hampton, VA, 1985), pp.581-593.
3. M. Bertero and E.R. Pike, "Particle size distributions from Fraunhofer diffraction I. An analytic eigenfunction approach," *Opt. Acta* 30, 1043 (1983).
4. M. Bertero, P. Boccacci, and E.R. Pike, "Particle-size distributions from Fraunhofer diffraction: the singular-value spectrum," *Inverse Problems* 1, 111 (1985).
5. M. Bertero, C. De Mol, and E.R. Pike, "Particle size distributions from spectral turbidity: a singular-system analysis," *Inverse Problems* 2, 247 (1986).
6. S. Arridge, P van der Zee, D.T. Delpy, and M. Cope, "Particle sizing in the Mie scattering region: singular-value analysis," *Inverse Problems* 5, 671 (1989).
7. T.T. Lam and S. Lee, "Application of an Optimization Technique to the Inverse Determination of Particle Properties," AIAA 26th Thermophysics Conference, June 24-26, 1991, Honolulu, HA, AIAA 91-1432.
8. K. Shimizu and A. Ishimaru, "Differential Fourier transform technique for the inverse scattering problem," *Appl. Opt.* 29, 3428 (1990).
9. C.D. Capps, R.L. Henning, and G.M. Hess, "Analytic inversion of remote-sensing data," *Appl. Opt.* 21, 3581 (1982).
10. A. Ben-David, B.M. Herman, and J.A. Reagan, "Inverse problem and the pseudocempirical orthogonal function method of solution. 1: Theory," *Appl. Opt.* 27, 1235 (1988).
11. S. Twomey, "Information Content in Remote Sensing," *Appl. Opt.* 13, 942 (1974).
12. C.F. Bohren and D.R. Huffman, *Absorption and Scattering of Light by Small Particles* (John Wiley & Sons, New York, 1983).
13. H.C. van de Hulst, *Light Scattering by Small Particles* (Dover, New York, 1981), pp.131-134.
14. B.P. Curly, "Constrained eigenfunction method for the inversion of remote sensing data: application to particle size determination from light scattering measurements," *Appl. Opt.* 28, 1345 (1989).
15. M.D. King, D.M. Byrne, B.M. Herman, and J.A. Reagan, "Aerosol Size Distributions Obtained by Inversion of Spectral Optical Measurements," *J. Atmos. Sci.* 35, 2153 (1978).

KRAMERS—KRONIG RELATIONS IN OPTIC DATA INVERSION

M. Howard Lee

Department of Physics and Astronomy
The University of Georgia
Athens, GA 30602, USA

RECENT PUBLICATIONS:

M.H. Lee and O.I. Sindoni, Dynamic response function and bounds of the susceptibility of a semiclassical gas and Kramers—Kronig relations in optic data inversion, Phys. Rev. A 46, 3028 (1992).

ABSTRACT

The Gaussian model for the extinction coefficient is often made in optic data inversion. To obtain the frequency—dependent real refractive index therefrom via the Kramers—Kronig relations, it is necessary to overlook certain symmetry properties of the extinction coefficient. A precise measure of error for using the Gaussian model is derived. Also, a physical basis of the Gaussian model is presented by showing that the dynamic susceptibility of a semiclassical ideal gas has an identical structure. The Gaussian model therefore may be viewed as the scattering of light by a semiclassical ideal gas. The use of the Kramers—Kronig relations in nonlinear optical problems is being investigated.

INTRODUCTION

The Hilbert transforms are well known mathematical techniques for relating the real and imaginary parts of an analytic function. The transforms are found useful in a variety of physical problems. In these applications, one finds that functions of physical interest very often satisfy restrictive symmetry properties owing to the causality principle among others. The Hilbert transforms in these specialized applications are commonly referred to as the Kramers—Kronig relations. In optics one is interested in, e.g., the frequency—dependent complex refractive index. The Kramers—Kronig relations allow one to calculate the real refractive index from the measured extinction coefficient. This is an example of optic data inversion.

Let W be a physical quantity of interest depending on some physical parameter denoted by z , where the real part of z may denote the angular frequency ω , the energy ϵ , or the wavelength λ . Then one can decompose W into the real and imaginary parts:

$$W(z) = W_1(z) + i W_2(z). \quad (1)$$

The Kramers—Kronig relations assert that

$$W_1(z) = \frac{1}{\pi} P \int_{-\infty}^{\infty} \frac{W_2(z') dz'}{z - z'} \quad (2a)$$

and

$$W_2(z) = -\frac{1}{\pi} P \int_{-\infty}^{\infty} \frac{W_1(z') dz'}{z-z'} \quad (2b)$$

where P denotes the Cauchy principal value. In deriving the above relations, one assumes that $W(z)$ is analytic in the upper half of the complex z plane such that $W(z) \rightarrow 0$ as $|z| \rightarrow \infty$. In physical applications, one finds that $W_1(z)$ is an even function of real z and $W_2(z)$ is an odd function of real z , known as crossing symmetries. Observe that the "susceptibility" sum rule follows from (2a) by setting $z = 0$:

$$W_1(z=0) = -\frac{1}{\pi} \int_{-\infty}^{\infty} W_2(z) z^{-1} dz \quad (3)$$

where $W_2(z)$ is the scattering law, subject to detailed balance.

Now turning to optical applications, let z denote the angular frequency ω and W the complex frequency dependent refractive index n . In the customary notation,

$$n(\omega) = n_1(\omega) + i n_2(\omega). \quad (4)$$

The extinction coefficient $n_2(\omega)$ is measurable or at least modelable. Hence, given this input, one can in principle calculate the real refractive index $n_1(\omega)$ as a function of the real frequency ω . Physically the frequency ω is a real positive number. Hence, (2a) is unsuited to optical applications. Taking note of the crossing symmetries:

$$n_1(-\omega) = n_1(\omega) \quad (5a)$$

and

$$n_2(-\omega) = -n_2(\omega), \quad (5b)$$

one can rewrite (2a) as follows:

$$n_1(\omega) = -\frac{1}{\pi} P \int_0^{\infty} \frac{\omega' n_2(\omega') d\omega'}{\omega^2 - \omega'^2} \quad (6)$$

where now the measurable frequency ω' is limited to positive numbers only. It is important to recognize that (6) is valid strictly if $n_2(\omega)$ is an odd function of ω . What if $n_2(\omega)$ is not exactly an odd function, is Eq. (6) still applicable perhaps approximately? If so, what may be measures of the approximate validity of Eq. (6)? Our work provides answers to these practical questions, described briefly in the following two sections. For complete detail, we refer the reader to our original work.¹ Also the previous relevant references may be found therein.

DATA MODELING

In an experiment arranged to measure the extinction coefficient, it is desirable to express the measured values by some convenient function. That is, to find a function to fit the measured data.² Typically, the trial function $\tilde{n}_2(\omega)$ is a well-behaved function like a Gaussian:

$$\tilde{n}_2(\omega) = A e^{-B(\omega-\omega_0)^2} \quad (7)$$

where A and B are two adjustable parameters. The Gaussian trial function is evidently peaked at $\omega = \omega_0$. In such a fitting, one does not know a priori the significance of A, B and ω_0 . One hopes that the physical meaning can be deduced ultimately from some basic optical models of scattering.

It is known that the trial form represents the measured values of the extinction coefficient rather accurately for a large interval of the frequency in a number of optical systems. But can one obtain an accurate value of the real refractive index $n_1(\omega)$ therefrom using Eq. (6)? We observe that $\tilde{n}_2(\omega)$ is not an odd function of ω . It is neither even nor odd in the frequency. Strictly speaking, we are unable to use Eq. (6) since it requires an odd function for $n_2(\omega)$. The trial function $\tilde{n}_2(\omega)$, while evidently quite accurately representing the true function $n_2(\omega)$, fails to meet the fundamental condition of the true function. To overcome this difficulty, we consider a modification of the trial function:

$$\tilde{n}_2(\omega) \rightarrow \tilde{n}'_2(\omega) = A \left[e^{-B(\omega-\omega_0)^2} - e^{-B(\omega+\omega_0)^2} \right] \quad (8)$$

Now observe that $\tilde{n}'_2(\omega)$ is an odd function of ω , satisfying the fundamental requirement of the true but still unknown function $n_2(\omega)$. Also observe that if $B \gg 1$, then $\tilde{n}'_2(\omega) \approx \tilde{n}_2(\omega)$. Hence, if B is large enough, our new trial function (8) can accurately represent the true function $n_2(\omega)$ and at the same time it can also meet the fundamental requirement of the crossing symmetry. Hence, one can now use Eq. (6) and obtain the real refractive index therefrom.

To understand the accuracy of (8) as a function of B, we shall examine the new trial function for the entire range of ω : $-\infty < \omega < \infty$. The first term on the rhs of (8) is peaked at $\omega = \omega_0$, while the second term is negatively peaked at $\omega = -\omega_0$. The two terms overlap, the amount of overlapping depending on the size of the value B. If $B \rightarrow 0$, the overlap is maximal. If $B \rightarrow \infty$, there is no overlap. In fact, as $B \rightarrow \infty$ (also $A \rightarrow 0$), the rhs of (8) becomes two delta functions peaked at $\omega = \pm \omega_0$. If there is to be little or no overlap, then clearly $\tilde{n}'_2(\omega) \approx 0$ if $\omega \approx 0$. Thus, for practical purposes, if there is little overlap in a trial function, the required oddness of a trial function is of little practical significance. Thus, one could use $\tilde{n}_2(\omega)$ in place of $\tilde{n}'_2(\omega)$. It is possible to provide a quantitative measure for estimating errors for this replacement, described in the next section.

SCATTERING BY A SEMICLASSICAL GAS

We find that the extinction coefficient of the form (8) is exactly realized in the dynamic structure factor in the scattering of light by a semiclassical ideal gas, also known as a Boltzmann liquid in the thermal scattering theory. For this system, one can construct a complete dynamical theory by means of linear response theory. Hence, it is possible to provide a quantitative measure of errors in the trial functions for the extinction coefficient.

By a semiclassical ideal gas,¹ we mean an assembly of identical noninteracting particles of mass m each. The positions and momenta of particles, \mathbf{r}_i and \mathbf{p}_i , respectively, do not commute but obey the usual commutation relation: $[\mathbf{r}_i, \mathbf{p}_j] = i \hbar \delta_{ij}$. The equilibrium state of this assembly is to be described by the Boltzmann distribution. If scattered by light, each particle in the assembly acts as a free independent scatterer. When the particles become very massive, the model represents scattering from single fixed atoms or nuclei.

The total energy of the assembly is

$$H = \sum_{j=1}^N \mathbf{p}_j^2 / 2m \quad (9)$$

where N is the total number of particles in a unit volume. The system is assumed to be translationally invariant. Let $\rho(\mathbf{r})$ be the density operator at the position \mathbf{r} defined in the usual way

$$\rho(\mathbf{r}) = \sum_{j=1}^N \delta(\mathbf{r} - \mathbf{r}_j) \quad (10)$$

Then, for a wave vector \mathbf{k} , we can define

$$\hat{\rho}_{\mathbf{k}} = \int d^3r e^{i\mathbf{k} \cdot \mathbf{r}} \rho(\mathbf{r}) = \sum_{j=1}^N e^{i\mathbf{k} \cdot \mathbf{r}_j} \quad (11)$$

The time dependent susceptibility $X_{\mathbf{k}}(t)$ has the well-known definition in terms of the density operator:

$$\begin{aligned} X_{\mathbf{k}}(t) &= iN^{-1} \langle [\hat{\rho}_{\mathbf{k}}(t), \hat{\rho}_{-\mathbf{k}}] \rangle \text{ if } t > 0 \\ &= 0 \text{ if } t < 0, \end{aligned} \quad (12)$$

where the angular brackets mean the thermal average. For our model defined by (9), we have shown that

$$\begin{aligned} X_{\mathbf{k}}(t) &= 2 \sin(\omega_0 t) e^{-at^2} \text{ if } t > 0 \\ &= 0 \text{ if } t < 0, \end{aligned} \quad (13)$$

where $\omega_0 = \hbar k^2/2m$, the recoil frequency, $a = \omega_0/\beta \hbar$, β is the inverse temperature.

The frequency-dependent susceptibility $\hat{X}(\omega)$, now suppressing the k index, follows from (13):

$$\hat{X}(\omega) = \int_0^\infty dt e^{-i\omega t} X(t) = \hat{X}_1(\omega) + i \hat{X}_2(\omega), \quad (14)$$

$$\hat{X}_1(\omega) = (1/\sqrt{4a}) [D(\gamma_+) - D(\gamma_-)] \quad (15a)$$

$$\hat{X}_2(\omega) = \sqrt{\pi/4a} \left[e^{-\gamma_+^2} - e^{-\gamma_-^2} \right] \quad (15b)$$

where

$$\gamma_\pm = (\omega \pm \omega_0)/\sqrt{4a} \quad (16a)$$

and

$$D(y) = e^{-y^2} \int_0^y dx e^{x^2}. \quad (16b)$$

Here D is Dawson's integral. Observe that $\gamma_\pm(-\omega) = -\gamma_\mp(\omega)$ and $D(-y) = D(y)$. Hence, $\hat{X}_1(\omega)$ and $\hat{X}_2(\omega)$ are, respectively, even and odd functions of ω .

We observe that $\hat{X}_2(\omega)$ is exactly in the form of $\hat{n}_2'(\omega)$ given by (8) if we identify $A = -\sqrt{\pi/4a}$ and $B = 1/4a$. Referring to (15a,b), let us write:

$$\hat{X}_i(\omega) = \hat{X}_i^+(\omega) + \hat{X}_i^-(\omega), \quad i = 1 \text{ or } 2. \quad (17)$$

Then, $\hat{n}_2(\omega) = X_2^-(\omega)$. Hence, one can at once write down the measure for errors or the difference between $n_1(\omega)$ and $\hat{n}_1(\omega)$ as:

$$\begin{aligned} \Delta n(\omega) &\equiv n_1(\omega) - \hat{n}_1(\omega) = \hat{X}_1(\omega) - \frac{2}{\pi} P \int_0^\infty \frac{\hat{X}_2^-(\omega') \omega' d\omega'}{\omega^2 - \omega'^2} \\ &= \frac{2}{\pi} P \int_0^\infty \frac{\hat{X}_2^+(\omega') \omega' d\omega'}{\omega^2 - \omega'^2} = \hat{X}_1^+(\omega). \end{aligned} \quad (18)$$

Hence,

$$\Delta n_1(\omega) = \hat{X}_1^+(\omega) = \frac{1}{\sqrt{a}} D(\gamma_+). \quad (19)$$

The magnitude of $\Delta n_1(\omega)$ evidently depends on nonzero values of $\hat{X}_2^+(\omega)$ for $\omega > 0$. If a or B^{-1} is small, the magnitude of $\Delta n_1(\omega)$ becomes small. This is precisely what has been observed in some recent numerical studies.² The dynamical susceptibility of a semiclassical ideal gas thus provides an effective measure of accuracy for trial functions employed in practical use of the Kramers–Kronig relations.

CONCLUSION

We have shown that the Kramers–Kronig relations can be expressed to accommodate positive values of the frequency only. The frequency–dependent real refractive index can then be calculated therefrom, given the extinction coefficient. The extinction coefficient can be measured and it is often modeled by trial functions such as the Gaussian. If the measured values are sharply peaked at some nonzero frequency, one may ignore that the extinction coefficient must be an odd function of the frequency. If not very sharply peaked, the errors can be corrected. We have provided a particular correction formula if the extinction coefficient is modeled by a Gaussian.

We have found a theoretical basis for understanding the Gaussian model for the extinction coefficient. A semiclassical ideal gas gives rise to the dynamic susceptibility, whose imaginary part has precisely the trial form of the extinction coefficient. The semiclassical ideal gas model is a fluid model used in thermal scattering theory used for studying the scattering of light by fixed atoms or nuclei. The correspondence between the semiclassical gas and the Gaussian model for the extinction coefficient allows us to interpret the peak position as the recoil frequency in the light scattering. The other parameters A and B which occur in the Gaussian model of the extinction coefficient have similar interpretations. A further extension of the use of the Kramers–Kronig relations in nonlinear optical problems is in progress.

ACKNOWLEDGMENTS

This work has been supported in part by the ARO and CRDEC, also by the Office of the Vice President for Research at the University of Georgia. The author is grateful for their support.

REFERENCES

1. M.H. Lee and O.I. Sindoni, *Phys. Rev. A* **46**, 3028 (1992).
2. K.E. Peiponen and E.M. Vartiainen, *Phys. Rev. A* **44**, 8301 (1991).

MEASURED CHARACTERIZATION OF RANDOMLY ROUGH SURFACES
BY IR MUELLER MATRIX SCATTERING

Arthur H. Carrieri
James O. Jensen
Jerold R. Bottiger

U.S. Army Chemical Research, Development, and Engineering Center
Aberdeen Proving Ground, Maryland, 21010-5423

Daniel Zeroka
Lehigh University
Bethlehem, Pennsylvania 18015-3172

Hendrik F. Hameka
University of Pennsylvania
Philadelphia, Pennsylvania 19104

RECENT PUBLICATIONS AND SUBMITTALS FOR PUBLICATION

1. **Mid Infrared Polarized Light Scattering: Applications for the Remote Detection of Chemical and Biological Contaminations**, A.H. Carrieri, J.R. Bottiger, D. Owens, C.E. Henry, C.M. Herzinger, S.M. Haugland, J.O. Jensen, K.E. Schmidt, and J.L. Jensen. CRDEC-TR-318, Chemical Research, Development, and Engineering Center, Aberdeen Proving Ground, MD, January 1992.
2. **Calculations of the Structure and the Vibrational Infrared Frequencies of Some Methylphosphonates**, H.F. Hameka, A.H. Carrieri, and J.O. Jensen, *Phosphorus, Sulfur, and Silicon*, 66, 1-11 (1992).
3. **Identification of Contaminant Coatings Over Rough Surfaces Using Polarized IR Scattering**, S. Mark Haugland, Ezekiel Bahar, and Arthur H. Carrieri, *Appl. Opt.*, 31(19), July, 1992.
4. **Visualizing Infrared Mueller Matrix Elements of Absorbing Randomly Rough Surfaces**, Arthur H. Carrieri, Charles Jeffrey Schmitt, Craig M. Herzinger, and James O. Jensen, manuscript submitted for publication in *Applied Optics*, July, 1992.
5. **Theoretical Prediction of Vibrational Circular Dichroism Spectra of Hexoses in Linear Form**, Daniel Zeroka, James O. Jensen, Arthur H. Carrieri, and Janet L. Jensen, manuscript submitted for publication in *Carbohydrate Research*, July, 1992.

ABSTRACT

The non-zero elements of the 4×4 Mueller matrix were computer visualized over the mid infrared region of the electromagnetic spectrum where vibrational states of organophosphorous and simulant molecules (contaminant analyte) are excited, and over CO_2 laser beam backscattering angles (normal-to-oblique incidence) from randomly surfaces that contain these liquid contaminant organic layers. Predictions of the Mueller elements were computed from a *full wave* model of electromagnetic scattering reported by E. Bahar and co-workers. The non-zero elements were displayed and recorded in a multi-dimensional format, as geometry of the scattering surface changes from a specular to Lambertian-like reflector of infrared radiation. The surface may contain multiple contaminant layers that are targeted for detection by analyzing Mueller elements at beam energies tuned to vibrational resonances of the contaminant then off-resonance. In a related problem regarding standoff detection of biological simulants

we present measured Mueller matrices of a chiral amine, on and off vibrational resonance, emphasizing elements [1,4] and [4,1]; identifiers of Vibrational Circular Dichroism, and element pairs [1,2], [2,1] and [3,2], [2,3]. Together, these elements appear to be features of identification of chiral matter by elastic polarized scattering on-off beam energies of molecular resonance by the analyte molecules. Future work calls for refining this technology toward optimum solution of the chemical/biological standoff detection problem.

INTRODUCTION

We apply elastic polarized infrared (IR) scattering for the remote sensing of contaminant layers (analytes) spread across terrestrial and other (background interferent) scatterers. In one problem, the analyte is a liquid layered surface that is randomly rough on the micrometer scale. A *full wave* model of EM scattering is applied to predict elements of the Mueller matrix by scattering from an area of statistically derived mean-squared heights and spatial slopes. This model, in present form, provides closed form solutions of Maxwell's equations assuming single-scattering by isotropic surfaces of random geometry. The code RETRO(10) is a 10th version of numerical implementation of *full wave* theory.

Analytes of specific interest include DMMP⁽²⁾, DIMP⁽²⁾, SF96, and TBP, simulants of the chemical G and VX liquid agents. Absorption of IR radiation by the analyte is key for its detection. All these organophosphorous and silicon-based hydrocarbons exhibit fundamental IR vibration modes within primary atom groups. The phosphorous linkages P=O, P-CH₃, and P-O-C in DMMP, DIMP, and TBP are driven into normal modes of rocking, bending, and stretching vibrational states by tuning of energy of the incident ellipsometer beam source. In SF96, a silicon based hydrocarbon, Si-O-Si and Si-CH₃ are groups exhibiting normal IR vibrational modes.

The optical bandwidth of the ellipsometer instrument is 9 - 12.5 μm . The experiment is designed to excite at least one IR resonance, then rapidly detune to a non-resonant energy in the incident beam (an energy for establishing a reference Mueller matrix). We then ascertain those Mueller elements in backscattering most susceptible to the targeted analyte mass under resonance-reference beam energy irradiation conditions. We have and continue to develop mathematical algorithms^(1,3) that access the entire 16-element Mueller matrix field of elements (the non-susceptible elements themselves are information used in making detection decisions) and operate (map) into *feature-space*, where classification of the analyte is done.

In another remote detection problem of interest to us, chiral matter (crystalline and saturated in solution) is targeted for detection. (Chirality is *handedness* of the asymmetric molecule. Chiral molecules cannot be superimposed on their mirror image.) The chiral compounds of interest in our trial experiments include various amines and sugars that react differently to R- and L-circularly polarized IR radiations, as in some organisms which we are interested in screening. Important features for the detection of chiral molecules are Mueller elements [1,4] and [4,1]. These elements describe the transform between left \rightarrow right and right \rightarrow left circular polarizations between input beam and scattered radiance. This information correlates to dextro and levo optical rotational behavior by the chiral structure and is a direct measure of Vibrational Circular Dichroism (VCD), when the energy of the probe beams matches vibrational resonance of the molecule.⁽⁵⁾

VCD is a non-Born Oppenheimer phenomena caused by coupling of electronic and nuclear motions. Nuclear motion of parent atoms causes a slight asymmetry in the way left-handed and right-handed circular polarizations interact with the chiral molecule. Measurements on low-molecular weight chirals compliment the VCD quantum calculations now being performed by two of us (Zeroka and Jensen). These calculations provide a means to understand fundamental properties of VCD on molecular structures that are simpler but similar to some organisms; a basis to build on the more complex biological structures. Much of the work conducted in our laboratory involves selecting the proper basis wavefunction sets, optimizing scaled force fields, and determining the correction factors to the raw quantum

calculations on these molecules.

In addition to VCD Mueller elements [1,4] and [4,1], visual inspection of the raw experimental data suggest that element pairs [1,2], [2,1] and [3,2], [2,3] contain identification information on some chiral amine crystals under irradiation by the resonance-reference energy beams. We include experimental data on L-Alanine, a compound that exhibits these properties.

RESULTS

A presentation of *full wave* predictions from randomly rough substrates wetted by DMMP, DIMP, SF96, TBP, diesel oil, three fatty acids, soot pellets, and other contaminant layers are given in our previous work.^(1,3,4) Several conclusions were drawn: (1) as expected, the rougher the surface (the greater its spatial mean slope) the more diffuse it is a reflector of the IR beam, (2) on vibrational resonances of the analyte, the off-diagonal Mueller elements [1,2] and [3,4] exhibit strong signal intensities about $\approx 30^\circ$ beam incidence. This signal propagates through a polarity reversal as the surface roughness parameter of mean-squared slope increases. The peak in this signal also appears to shift slightly toward oblique incidence. This behavior was accurately tracked in visualization code applied to the *full wave* data base.⁽⁴⁾

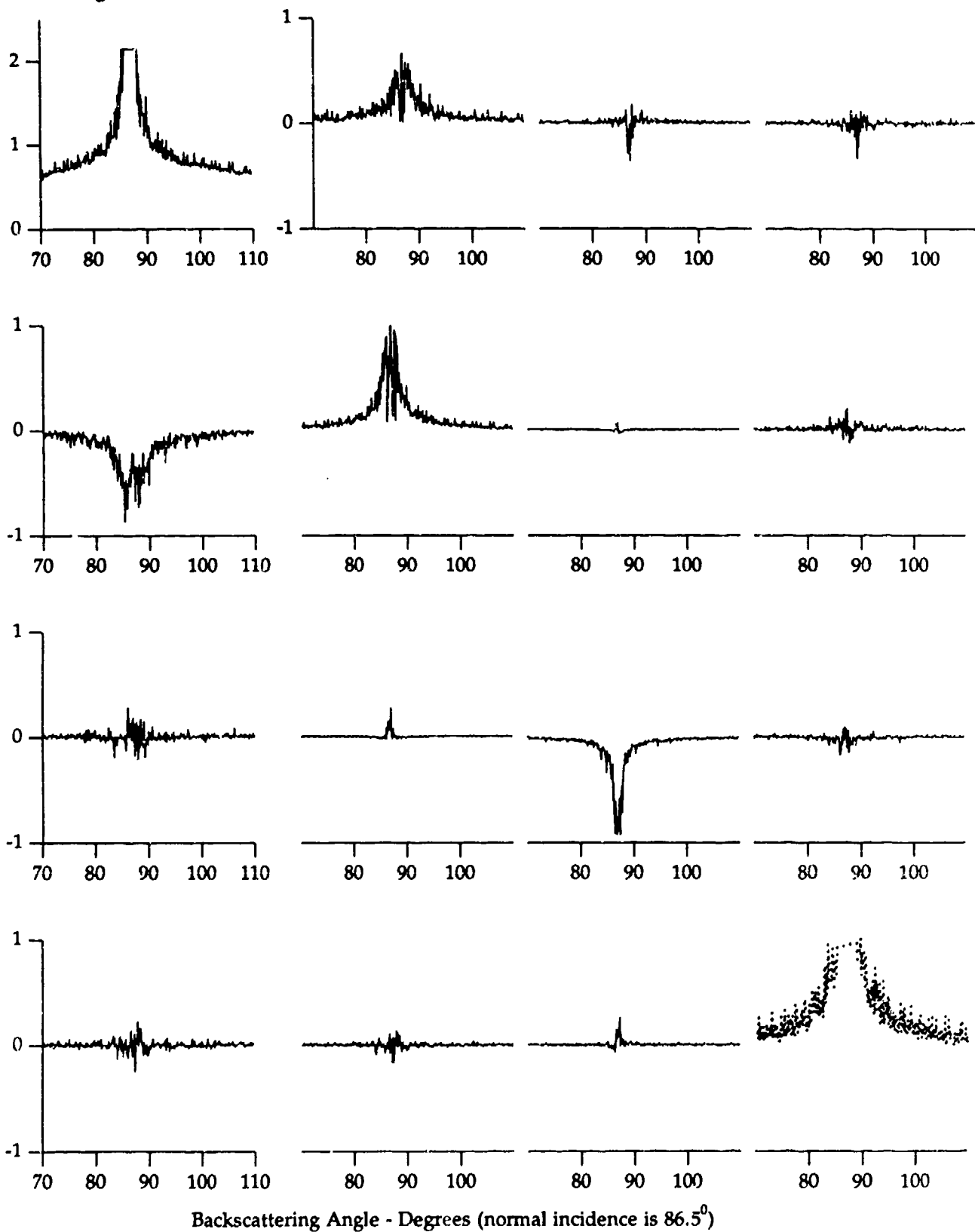
The Mueller matrix sensor built here at CRDEC is a 2-photoelastic modulator design with four tunable CO₂ laser of separate isotope and non isotope gas mixtures. It is a monostatic backscattering system automated by stepper-motor computer control. A full description of the ellipsometer sensor including optic design, electronic sub-assemblies, logic, data acquisition/reduction/analysis, and calibration is provided in Reference 1. We have made several matrix measurements on Arizona road dusts (soils of various particle size distributions) both dry and wetted by some of the above organic liquid analytes. We have yet to analyze these data and make comparisons with model predictions. These analyses will be reported at a later time.

The current data base consists mostly of matrix measurements in backscattering by various crystalline structures. These include (\pm) Tartaric, Glutamic, and Aspartic acids; Camphor, Glucose, Sorbose, Histidine, Mannose, Alanine, Tyrosine, and Serine wafers. The 16 element matrix field is measured at wavelengths on vibrational resonance of the molecule plus a reference wavelength of no vibrational excitation for comparison. Angular positioning of the sample is performed typically in tenth-degree resolution. Our interest with these materials is to seek out their chiral property inherent in elements [1,4] and [4,1], and others that react to the laser-driven molecular resonance conditions. These data also compliment theoretical work now being done at CRDEC that investigates the quantum properties of VCD.

Figures 1 and 2 are examples of raw data collected by the ellipsometer instrument. The L-Alanine wafer is two inches in diameter and quarter inch thick, area of beam surface irradiation is 0.8 in², and the collected radiance deviates from true backscattering by less than 0.5 degree. Figure 1 represents the Mueller matrix response to the 0.114 eV beam driving a stretching mode in the NH₂CHCH₂CO₂H molecules. Figure 2 is the same measurement after the laser was detuned to 0.130 eV, off the resonance band. Three pairs of active elements about normal incidence can be discerned, without mathematical filtering, viz; [1,4] and [4,1], [1,2] and [2,1], [2,3] and [3,2]. The non-active elements complete this 16-element binary map of L-Alanine. (One envisions a 16-node neural network with 6 firing neurons and 10 dormant neurons.)

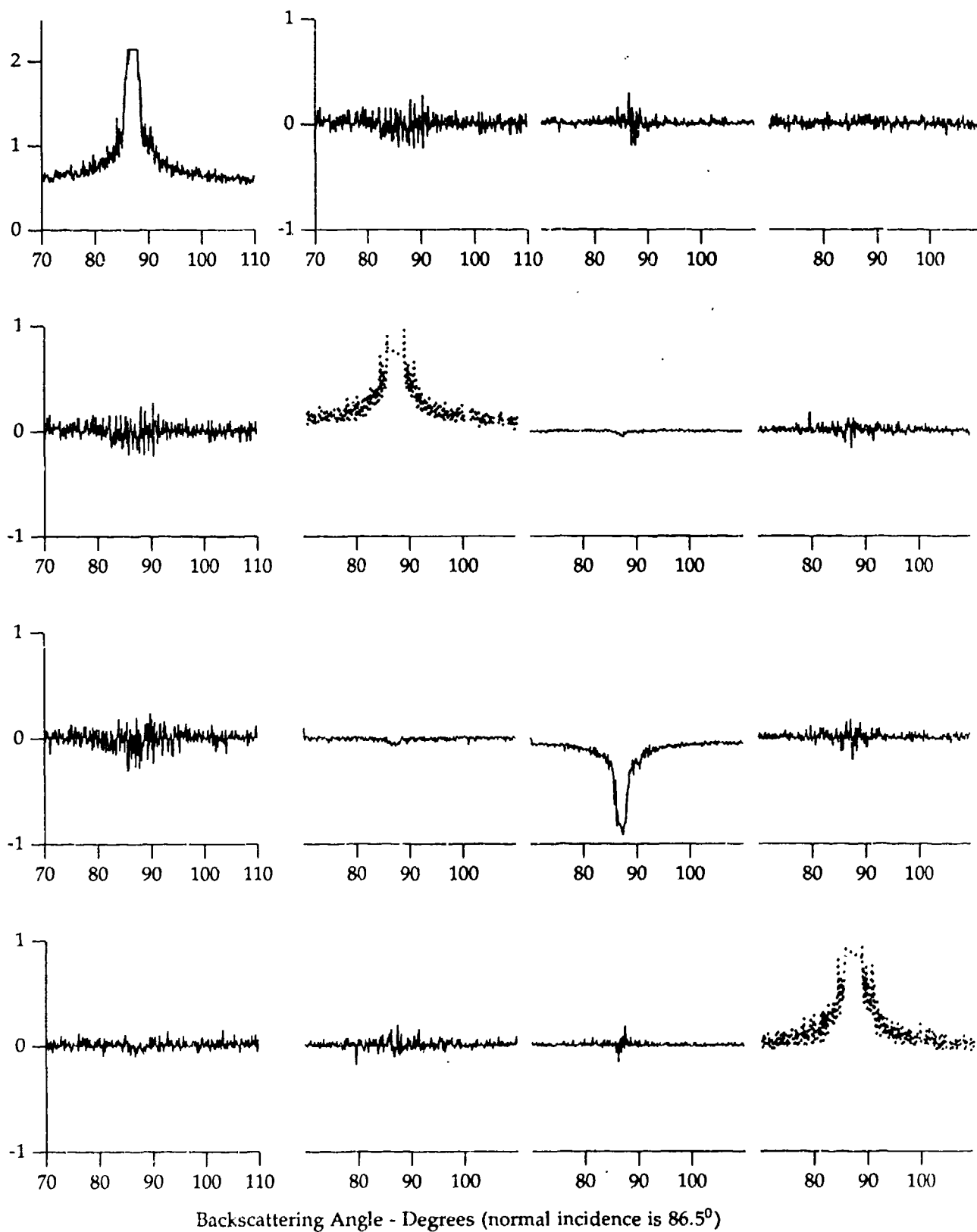
An initial inspection of the data base have shown few vibrational resonances in chiral sugar and amine compounds producing measurable activity in the corner [1,4] and [4,1] elements and associative elements. Much of the work in this laboratory investigates why this is and what are characteristic quantum effects that cause the slight asymmetry in circular polarizations on vibrational resonance in chirals.

Figure 1. On-Resonance Mueller Matrix Elements of L-Alanine, $\lambda = 10.88 \mu$ meters



Backscattering Angle - Degrees (normal incidence is 86.5°)

Figure 2. Off-Resonance Mueller Matrix Elements of L-Alanine, $\lambda = 9.52 \mu$ meters



Backscattering Angle - Degrees (normal incidence is 86.5°)

CONCLUSION

We use polarized scattering to study problems of remote sensing of chemical and biological contaminations in the field. Before a grand leap into field measurements and analysis is done, a better understanding of the information inherent in the Mueller matrix is needed through modeling and control experimentation.

At the macroscopic level, investigations were made on applying *full wave* theory to the detection problem. This physical optics model predicts Mueller matrix elements as a function of topographic mean height/slope and refractive index of the scatterer. The present form of this model restricts the surface as an isotropic medium, it does not incorporate multiple-scattering effects (depolarization), and cannot describe dichroism (scattering by chiral matter). We hope that *full wave* theory, or another analytical theory, can accurately encompass these phenomena.

At the microscopic level we singled-out elements [1,4] and [4,1] as candidate features for possible detection of biological compounds by driving the chiral molecule into vibrational resonance and detecting Vibrational Circular Dichroism. The VCD information was detected in only a few sugar and amine compounds over all vibrational modes. Moreover, it is interesting to note that those chirals exhibiting active [1,4] and [4,1] elements have associative element pairs, such as elements [1,2], [2,1] and [2,3], [3,2] in L-Alanine.

Both theory and experiment programs continue, with goals of determining if and how phase-sensitive light scattering can be successfully applied and developed into a remote sensing device.

ANGULAR MEASUREMENT OF THE FORWARD LIGHT SCATTERING FROM A QUARTZ FIBER

Edward S. Fry, G. G. Padmabandu, and Choonghoon Oh
Department of Physics
Texas A & M University
College Station, TX 77843-4242

RECENT PUBLICATIONS, SUBMITTALS FOR PUBLICATION, AND PRESENTATION:

A) G. G. Padmabandu, Choonghoon Oh, and Edward S. Fry, "Application of Beam Fanning in a Photorefractive BaTiO₃ Crystal; Measurement of Light Scattering at Zero Degrees by a Single Glass Fiber," in Technical Digest on Photorefractive Materials, Effects, and Devices, (Optical Society of America, Washington, D. C.), Vol. 14, pp. 314-316 (1991).

B) G. G. Padmabandu, Choonghoon Oh, and Edward S. Fry, "Measurement of Light Scattering at 0° by Micron-Size Quartz Fibers," *Opt. Lett.* Vol. 17, No. 3, pp. 169-171 (1992).

C) Edward S. Fry, George W. Kattawar, and Robin M. Pope, "Integrating Cavity Absorption Meter," *Appl. Opt.* Vol. 31, No. 12, pp. 2055-2065 (1992).

D) Edward S. Fry and G. G. Padmabandu, "Scattering at and Near 0° by Spheres and Quartz Fibers," Submitted to the Proceedings of the 1991 CRDEC Scientific Conference on Obscuration and Aerosol Research.

E) Edward S. Fry, G. G. Padmabandu, and Choonghoon Oh, "Measurements of Scattering At and Near 0° by Glass Fibers," Presented at the 1991 CRDEC Scientific Conference on Obscuration and Aerosol Research, Aberdeen, MD, June, 1991.

F) Choonghoon Oh, G. G. Padmabandu, and Edward S. Fry, "Measurement of the Forward Light Scattering from Polystyrene Spheres with a Barium

Titanate Crystal." Presented at Optical Society of America 1991 Annual Meeting, San Jose, CA, November, 1991.

G) Choonghoon Oh, G. G. Padmabandu, and Edward S. Fry, "Angular Measurement of the Forward Light Scattering from Quartz Fibers with a Barium Titanate Crystal," Presented at Optical Society of America 1992 Annual Meeting, Albuquerque, NM, September, 1992.

H) G. G. Padmabandu, Choonghoon Oh, and Edward S. Fry, "Measurement of Light Scattering at Zero Degrees by a Single Glass Fiber," Presented at the LEOS 91 Annual Meeting, San Jose, CA, November, 1991.

I) Edward S. Fry, "Angular Scattering At and Near Zero Degrees," Presented at the 1992 CRDEC Scientific Conference on Obscuration and Aerosol Research, Aberdeen Proving Ground, MD, June, 1992.

Abstract

Using a new technique based on the fanning of a coherent light beam in a photorefractive BaTiO₃ crystal angularly resolved forward light scattering from quartz fibers of radii from 15 μm to 30 μm have been successfully measured. Data have been obtained in the angular range, 0° to 0.3° and they are in good agreement with theory.

Introduction

Light scattering by small particles has been the subject of intense investigations for many decades. However, virtually all of the experimental work to date has been limited to angles from near forward to backward directions.^{1,2} The limiting experimental factor in the measurement of forward scattering is the unscattered incident wave which is superimposed

to the scattered wave. There has been little previous experimental success in attempts to separate the two waves in the forward direction.

Wang and Greenberg^{3,4} used the microwave analog method to measure light scattering in all directions including 0° . They used microwave radiation and artificially constructed targets to simulate light scattering by micron-size particles at optical frequencies. Spinrad⁵ used a special low-angle scattering meter to measure volume-scattering functions down to angles as small as 0.1° from the forward direction. Forward-scattering measurements from an isolated sphere have been made recently by using the Guoy phase shift that occurs at the waist of a focused Gaussian beam.⁶ However, that method is applicable only to particles so small that the scattering phase shift can be neglected in the analysis. By contrast, the present research is directed toward particles of all size, including larger ones for which there are appreciable scattering phase shifts.

The purpose of this research is to use a new technique based on the fanning of a coherent light beam in a photorefractive BaTiO_3 crystal⁷ and measure the forward light scattering from quartz fibers of radii from $15 \mu\text{m}$ to $30 \mu\text{m}$ as a function of angle.⁸

Photorefractivity

Photorefractivity is the ability of a crystal to change its index of refraction by interacting with incident light with energy less than the band gap. When a photorefractive crystal is exposed to a light beam the charge carriers (for example, electrons) from localized impurities (donors) are excited to the conduction band by photoionization process and diffuse or drift until they become retrapped by other impurities (traps). If the intensity of incident light is spatially modulated then the charge density of

the crystal is accordingly modulated by this process. This spatially modulated charge distribution induces a spatially modulated electric field. This static electric field modulates the refractive index of the crystal through the linear electro-optic effect and forms an index grating. In a diffusive medium like BaTiO_3 , this modulation of refractive index is spatially shifted relative to the modulation of the light intensity, which makes photorefractive energy coupling possible. The incident beam is diffracted by this grating and the intensity distribution is changed inside the crystal, which in turn changes the charge distribution. The whole process is repeated until a steady state is reached.

Beam fanning can be explained as a photorefractive amplification of the light scattered by medium inhomogeneities.^{6,9,10} When a photorefractive crystal is illuminated by a single pump beam some of the light is scattered by impurities of the crystal. Even though this scattered light is weak it can be amplified through photorefractive coupling with the incident beam. In a BaTiO_3 crystal, the photorefractive gain of the scattered light is especially large so that more than 90% of the incident light energy can be deflected through beam fanning process alone. The extinction ratio depends on a number of factors, such as the angle between the pump beam and the crystal c axis, the polarization of the pump beam, crystal geometry, crystal imperfections and aberrations in the pump beam.

To produce the photorefractive effect, photoinduced charges should migrate from regions of high optical intensity to regions of low optical intensity to eventually establish a static charge distribution.⁷ A finite time is required for the charges to migrate. This time τ is known as the photorefractive response time; it is inversely proportional to the intensity of the incident beam.¹¹ The response time becomes quite long at low

intensities (e.g., for BaTiO₃, it is of the order of 1 second at 1 mW/cm² incident intensity). If the spatial character or the phase of any part of the beam is perturbed rapidly compared to τ , then the perturbed portion does not undergo fanning and is transmitted without deviation. As a result, if the scattered light has time dependence which is faster than the response time of the crystal then it can pass through the crystal while the unscattered light is fanned out. This is the basis of our technique to separate the scattered and unscattered beams and could be applicable to suspensions of scatterers as well as to isolated scatterers.

Experimental Results

Fig. 1 schematically illustrates the experimental setup for the angular resolved measurement of forward scattering by a quartz fiber. The cw Ar⁺ laser beam (514.5 nm) is polarized in the plane of the figure, which also contains the *c* axis (illustrated with arrows) of two BaTiO₃ crystals. Both crystals are 0°-cut and approximately 5 mm × 5 mm × 5 mm cubes. To introduce a time dependence to the scattered light a quartz fiber is mounted on a 1 rpm synchronous motor that rotates it in a circle of radius 3 cm. Adjustable apertures A1, A2 and A3 shield the crystals and the detector from stray light. Most of the incident light is fanned out of its direct beam path by the first crystal. However, because of the asymmetric nature of beam fanning, some of the light is left on one side of the beam. This remaining light is fanned out by the second crystal leaving less than 1% of the incident light in the background. As the fiber crosses the laser beam a pulse of scattered light is generated in this dark background. The angular distribution of this pulse is measured with an optical multichannel analyzer

(OMA) which has 1024 detectors per inch. This signal is recorded in a computer and compared with the results of theoretical calculations.

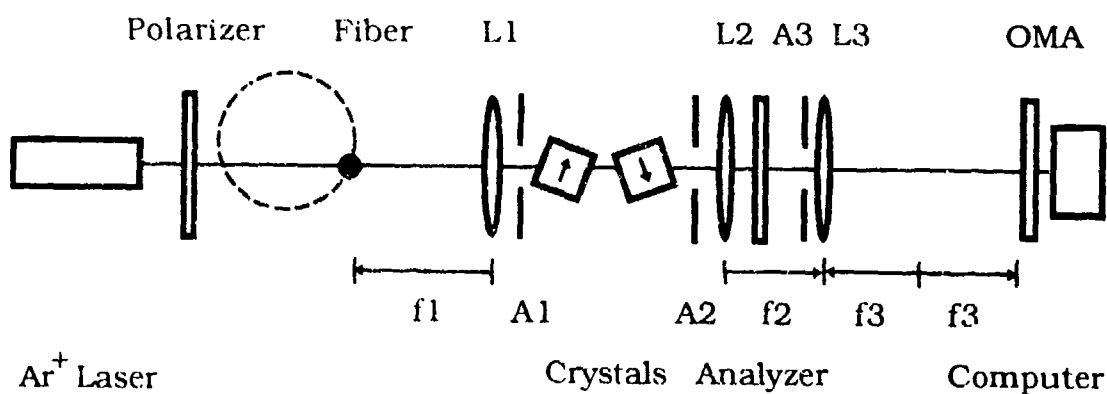


Figure 1. Experimental set-up to measure angular resolved forward scattering by a quartz fiber

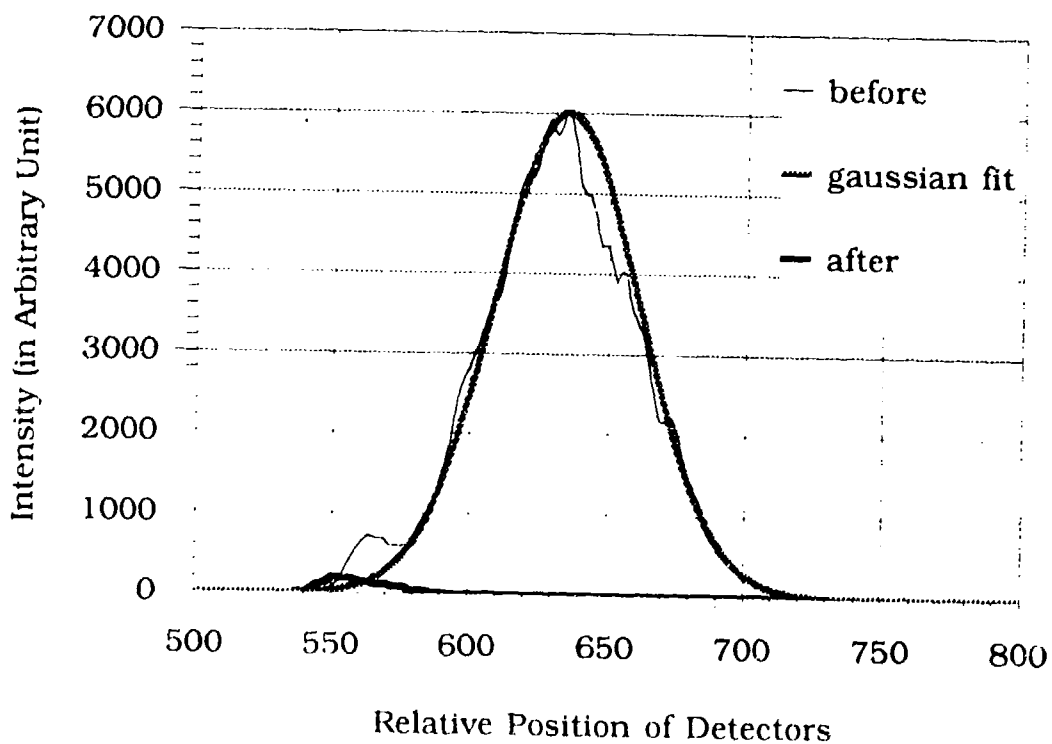


Figure 2. The profile of the background beam before and after beam fanning

Fig. 2 shows the profile of the background beam pattern before and after the beam fanning is established without a fiber. Before beam fanning is established the laser beam profile is measured for short period of time. Even though it was measured for relatively short period (< 1 sec) the measured profile shows a sign of beam fanning. Here we can see that 1) after the beam fanning the extinction of the background beam is so great that intensity of the background beam is almost zero and 2) even though the intensity of the background beam is very small it is not zero and the profile of the background beam is asymmetric. That is because this beam fanning process is an asymmetric photorefractive process.

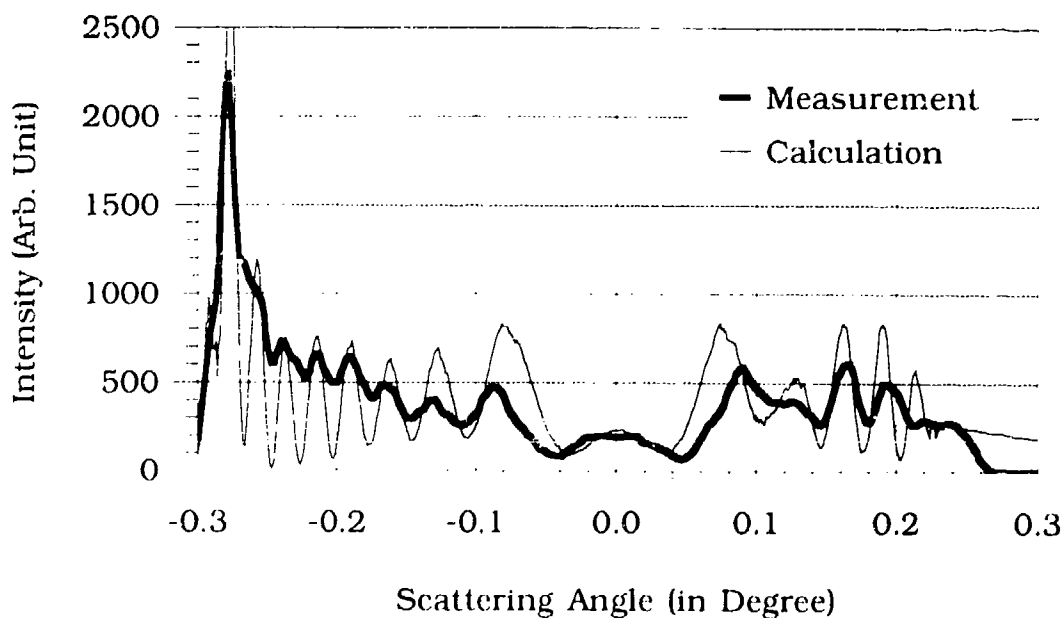


Figure 3. The interference pattern between the forward scattered beam and the background beam with weak beam fanning

Fig. 3 shows one of the typical measurements of the forward scattering from a quartz fiber. The horizontal axis is the scattering angle in degree and

the vertical axis is the intensity in arbitrary unit. The thick curve is the measurement and the thin curve is the calculation. Because the background intensity is finite what is measured here is the interference pattern between the background wave and the scattered wave. In this measurement the beam fanning is relatively weak and the background is comparable to the scattered signal. In calculating the interference pattern, two fitting parameters, the amplitude of the scattered field at 0° and the position of 0° , were used. The uncertainty of angle is about 0.005° . The measurement shows very good agreement with the calculation. In this graph we can see the most characteristic interference pattern of 0° scattering. The intensity distribution $I(x)$ at the detector plane is the result of the interference between the scattered field $E_s(x)$ and the background field $E_b(x)$ which is given by

$$I(x) = |\bar{E}_b(x)|^2 + |\bar{E}_s(x)|^2 + 2|\bar{E}_b(x)||\bar{E}_s(x)|\cos(\phi(x)) \quad (1)$$

Here $\phi(x)$ is the phase difference between two fields and x is the position at the plane which can be converted into the scattering angle. $I(x)$ is the interference between a plane wave and a cylindrical wave. As shown in Fig. 4, at precisely 0° the phase difference between the scattered field and the incident field is about $3\pi/4$ radian. So in the interference pattern there is local maximum at 0° and this small peak is the signature of 0° position.

Fig. 5 shows the forward scattering from a $24.2 \mu\text{m}$ fiber with strong beam fanning. Note that there is a strong interference on the left hand side of 0° while no clear interference on the other side. The reason is that the background on the right hand side of 0° is not the remaining incident beam after beam fanning but it is due to multiple reflection of fanned beam and is incoherent with the laser beam. Therefore, it does not interfere with the

forward scattered beam as in the measurement. However, in the calculation for the simplicity the coherent background is assumed and we have the interference.

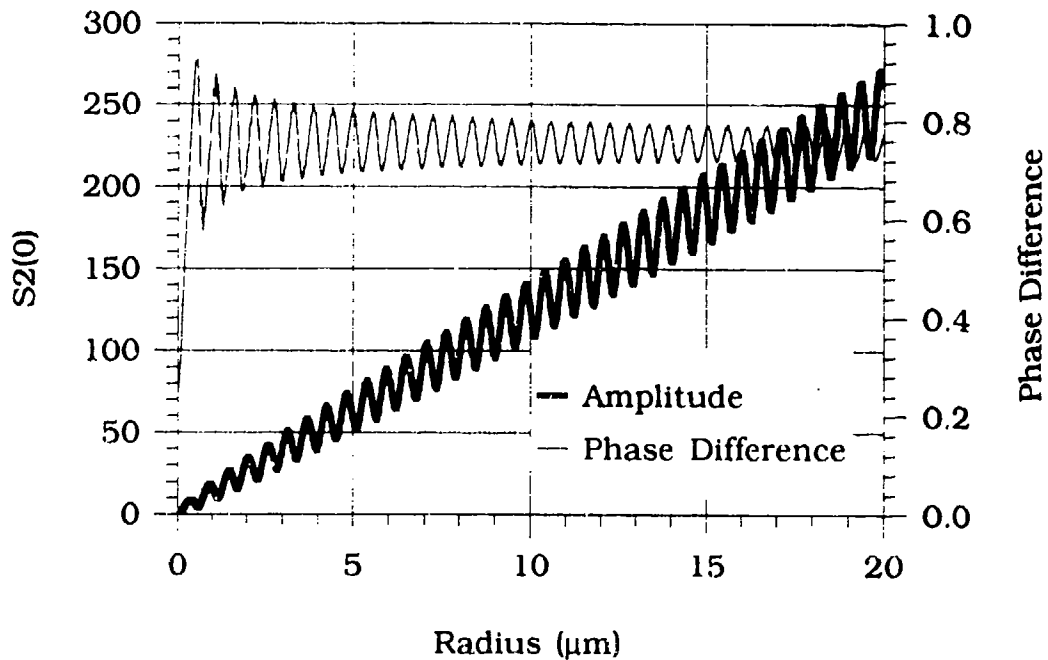


Figure 4. The phase difference ($\times \pi$) between the forward scattered beam and the background beam.

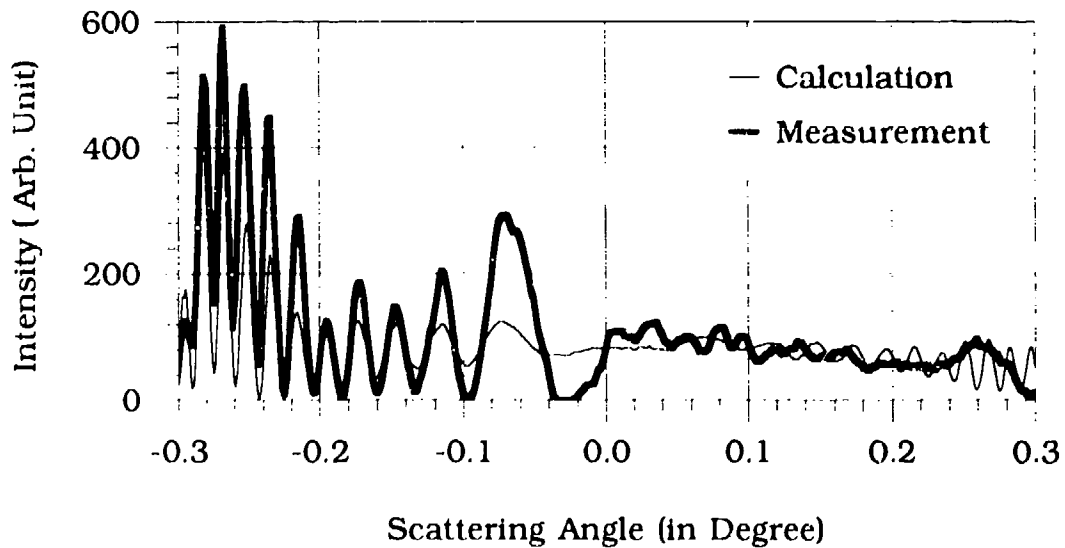


Figure 5. Measurement of forward scattering with strong beam fanning

Fig. 6 shows $S(0)*S(0)$ versus fiber radius. The 0° readings were made by producing Fig.5 for all different fibers. The rapidly oscillating curve is the result of Mie calculation. The data show good agreement with the theory.

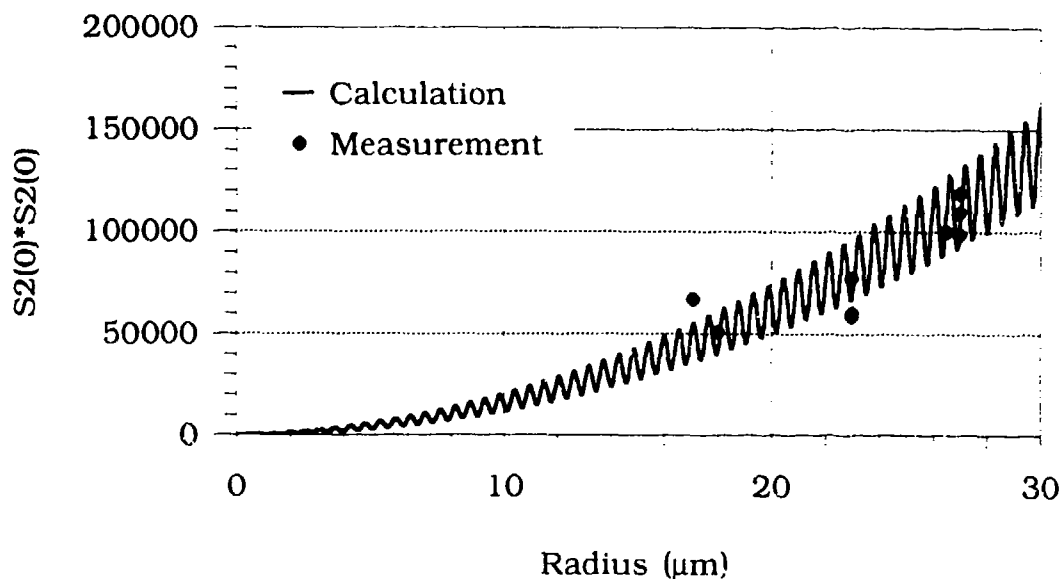


Figure 6. $S(0)*S(0)$ versus fiber radius.

Conclusions

In conclusion, we have successfully measured the 0° scattering from a quartz fiber. Angular distribution of forward scattered light has been successfully resolved including 0° using this technique. $BaTiO_3$ crystal has proved to be an excellent novelty filter.

Reference

1. Bohren, C. F. and D. R. Huffman, "Absorption and Scattering of Light by Small Particles," (Wiley Interscience, New York, 1981)
2. Chylek, P., J. T. Kiehl, and M. W. Ko, "Narrow Resonance Structures in the Mie Scattering Characteristics," *Appl. Opt.* 17, 3019 (1978).
3. A. C. Lind, R. T. Wang, and J. M. Greenberg, "Microwave Scattering by Nonspherical Particles," *Appl. Opt.* 4, 1555-1561 (1965).
4. R. T. Wang and J. M. Greenberg, "Scattering by Spheres with Nonisotropic Refractive Indices," *Appl. Opt.* 15, 1212-1217 (1976).
5. Petzold, T. J., "Volume Scattering Function for Selected Ocean Waters," (Scripps Institute of Oceanography, 1972).
6. George C. Valley, "Competition between Forward- and Backward-Stimulated Photorefractive Scattering in BaTiO₃," *J. Opt. Soc. Am. B* 4, 14-19 (1987).
7. J. Feinberg, "Asymmetric Self-defocusing of an Optical Beam from the Photorefractive Effect," *J. Opt. Soc. Am.* 72, 46-51 (1982).
8. G.G. Padmapabdu, C. Oh, and E. S. Fry, "Measurement of Light Scattering at 0° by Micrometer-size Quartz Fibers," *Opt. Lett.* 17, 169-171 (1992).
9. D. A. Temple and C. Warde, "Anisotropic Scattering in Photorefractive Crystals," *J. Opt. Soc. Am. B* 3, 337-341 (1986).
10. R. A. Rupp and F. W. Drees, "Light-induced Scattering in Photorefractive Crystals," *Appl. Phys. B* 39, 223-229 (1986).
11. S. Ducharme and J. Feinberg, "Speed of the Photorefractive Effect in a BaTiO₃ Single Crystal," *J. Appl. Phys.* 56, 839-842 (1984).

Blank

Remote Detection of Isotropically, Anisotropically, or Bianisotropically Encapsulated Biological Materials in a Cloud

Orazio Sindoni
Norman Witriol
D. K. Cochon

October 17, 1992

Contents

1 INTRODUCTION	1
2 The Problem of Noisy Data	2
2.1 Noise Removal	2
2.2 Fibonacci Optimization	3
3 Bioagents Placed in the Core of a Layered Sphere	4
3.1 Spherical Harmonics and Orthogonality Relations	4
3.2 Representation of the Electric Vector	6
3.3 Determination of Expansion Coefficients	13
3.4 Recovering the Properties of a Layered Sphere	14
4 Layering Detection on Structures with a General Shape	14
4.1 Surface Integral Equations	15
4.2 Recovery of Layering in Objects with a General Shape	18
5 Computer Code Validation	18
5.1 Energy Balance Checks	18

1 INTRODUCTION

What is the difference between a droplet of water in a cloud and a layered structure whose core contains a germ warfare agent which is from the choice of coating made to appear to ordinary visual interrogation to be a drop of water or to as a group blend in

with a cloud of water droplets so as to be difficult to see with ordinary multiple scattering experiments? We give in this paper a method of telling the difference between an encapsulated germ warfare agent and an ordinary droplet.

We describe in this paper a method of determining when a cloud is likely to contain biological warfare agents. Normally materials in a cloud that are not man made do not have a carefully layered structure. We show in particular how to use scattered electromagnetic radiation to discriminate between layered spheres and unlayered spheres, and proceed to discuss the general problem of layered particles with an arbitrary shape.

The basic idea is to separate a potentially highly complex problem into the two simpler problems of (i) finding the expansion coefficients of the scattered radiation which produced the measurements, and (ii) using the redundancy of droplet parameter information embodied in these expansion coefficients to discriminate between encapsulated materials and naturally occurring cloud droplets. We suppose that for an N layered sphere that there is a transition matrix \overline{Q} relating expansion coefficients representing the electric and magnetic vectors in the biological warfare agent core to the expansion coefficients representing the electric and magnetic vectors in the region surrounding the sphere. The representation of the electric and magnetic vectors of the scattered radiation becomes more and more rapidly convergent as you move away from the spherical cloud droplet, while the known electric vector of the incoming radiation becomes more and more slowly convergent.

2 The Problem of Noisy Data

Measurements always have error, and the more dimensions you have in an optimization problem, the longer it takes to solve. Do you try to find the best fit of parameters for a one or two layer structure to a limited number of measurements or to a large number of measurements, solving the entire problem at once or do you try to decompose the problem. We shall suggest using a very large number of measurements, and breaking up the problem into two smaller parts. A cloud consists of many particles of differing sizes and multiple scattering must be taken into account. To test the feasibility of the theory, we consider the simpler problem of scattering from a single cloud droplet and attempt to determine whether or not that droplet is a single layered structure or an encapsulated biological warfare agent. In the first part we obtain, independent of the nature of the spherical particle that produced the scattered radiation, a representation, in terms of spherical harmonics, of the electric vector of the scattered radiation that produced the measurement. The fact that the coefficients needed in this representation redundantly represent the layered structure and electromagnetic properties of the scattering body then enables us to tell what kind of a scatterer produced the measurements.

2.1 Noise Removal

Whatever set of measurements we take, it is important to have enough of them that we can remove unsystematic noise from these measurements. If the noise is unsystematic

or white, then even if the pure signal were a small fraction of the measurements, it could then be removed by an integration procedure or a local averaging procedure. The local time average is

$$\int_{\tau=0}^{\tau=t+T_p} S(\tau) d\tau = \int_{\tau=0}^{\tau=t+T_p} [S(\tau) + N(\tau)] d\tau \quad (1)$$

2.2 Fibonacci Optimization

We use a kind of higher dimensional Fibonacci optimization using planes perpendicular to the hyperplane of values that are needed to represent the electric vector of the scattered radiation. The measurement is determined by the electric vector of the scattered radiation plus the system noise which we assume we can nearly remove by averaging or filtering processes. We consider hyperplanes each defined by keeping one of the parameters of interest constant. We use normalized variables such as the one obtained by replacing the permittivity ϵ by its ratio ϵ/ϵ_0 to free space permittivity. Assume that we move along lines normal to these hyperplanes. For the j th hyperplane we move from our initial starting point $\vec{x}^{(0)}$ given by the equation

$$\vec{x}^{(0)} = (x_1^{(0)}, x_2^{(0)}, \dots, x_n^{(0)}) \quad (1)$$

along the vector

$$\vec{e}_j = (\delta_{(1,j)}, \delta_{(2,j)}, \dots, \delta_{(n,j)}) \quad (2)$$

a distance of r giving us a function of a single variable. We estimate the partial derivative of the reciprocal of the nonnegative function to be minimized in this direction given by equation (2). We use these estimates of the partial derivatives to give us an estimate of the gradient of the of this function. If we move in the direction of the gradient we will be moving in the direction of the greatest increase of the function. So far this is almost like the conjugate gradient method. We intersperse now Fibonacci optimization by in this direction finding the location of the minimum of the function of a single variable that moves along the line defined by the estimation of the gradient. Said differently, if \vec{v} is the estimated direction of the gradient of the reciprocal of the function to be minimized, then we attempt to minimize the function

$$g(r) = f(\vec{x}^{(0)} + r \cdot \vec{e}_j)$$

We at this stage have the problem of minimizing a function of a single variable. We wish to carry out this minimization without any computation of gradients. Basically we imagine that we know the value of the function at points r_1 and r_2 and that the value at r_1 is larger than the value at r_2 . We then move to the point r^* given by adding $s * (r_2 - r_1)$ to r_1 , where s is a positive fraction. We then compare the values at $r_2^{(1)}$ and r^* and rename the point in the set

$$S = \{r_2^{(1)}, r^*\}$$

at which g is larger $r_1^{(2)}$ and the point in this set S at which g is smaller $r_2^{(2)}$. We proceed until the difference between points becomes smaller than our error tolerance. This

then becomes our new point for starting the multidimensional minimization process. This method is a combination of the multidimensional conjugate gradient method and the one dimensional Fibonacci optimization.

3 Bioagents Placed in the Core of a Layered Sphere

We show in this section how to detect a biological agent in a cloud when the agent is stored in the core of a layered sphere. The sphere materials may be *isotropic* in the sense that the electromagnetic properties of each layer are the same in every direction. The sphere properties may be *anisotropic* in the sense that the properties are permittivity and permeability only and these properties are different in different directions. One of the easiest of the anisotropic spheres to deal with is the *uniaxial* anisotropic material which has one property as you go in the radial direction and another property as you move tangentially to the sphere. This is of practical concern as you might have a bioagent core encapsulated by an oriented molecular layer designed to make it difficult by ordinary means to discriminate between this and an ordinary droplet. The same result may be theoretically achieved for a bioagent encapsulated by a full tensor material. Bianisotropic encapsulations of biological agents would present another level of difficulty. Bianisotropic materials might be created using molecular layers with a twisted and intertwined molecular structure. The Faraday (the one with curl of the electric vector) and Ampere (the equation with curl of the magnetic vector) Maxwell equations both have the form of a tensorially bilinear function of the electric and magnetic vectors being equal to the curl of either the electric or magnetic vector.

3.1 Spherical Harmonics and Orthogonality Relations

In order to understand how to solve the inverse problem systematically when you know that that the scatterer is a single or multiple layered spherically symmetric structure, we need to have some understanding of the orthogonality of vector spherical harmonics which dramatically reduces the dimensionality of the problem of detecting an encapsulated sphere containing biological materials.

The basic idea of the code is that the induced and scattered electric and magnetic vectors can be, for (i) isotropic, (ii) uniaxial, (iii) full tensor anisotropic, (iv) uniaxially bianisotropic, and (v) full tensor bianisotropic spherically symmetric structures be expressed in terms of

$$\vec{A}_{(m,n)} = \left[im \frac{P_n^m(\cos(\theta))}{\sin(\theta)} \vec{c}_\theta - \frac{d}{d\theta} P_n^m(\cos(\theta)) \vec{c}_\phi \right] \exp(im\phi), \quad (1)$$

$$\vec{B}_{(m,n)} = \left[\frac{d}{d\theta} P_n^m(\cos(\theta)) \vec{c}_\theta + im \frac{P_n^m(\cos(\theta))}{\sin(\theta)} \vec{c}_\phi \right] \exp(im\phi), \quad (2)$$

and

$$\vec{C}_{(m,n)} = P_n^m(\cos(\theta)) \exp(im\phi) \vec{c}_r, \quad (3)$$

where \vec{e}_r , \vec{e}_θ , and \vec{e}_ϕ are the unit vectors perpendicular, respectively, to the $r = 0$, $\theta = 0$, and $\phi = 0$, coordinate planes, and where $P_n(\cos(\theta))$ is the ordinary Legendre function defined by Rodrigues's formula

$$P_n(z) = \frac{1}{2^n n!} \left(\frac{d}{dz} \right)^n (z^n - 1)^n \quad (4)$$

The associated Legendre functions P_n^m are given by

$$P_n^m(z) = (1 - z^2)^{m/2} \left(\frac{d}{dz} \right)^m P_n(z) \quad (5)$$

It is obvious that even without integrating over a sphere that the dot product of either of $\vec{A}_{(m,n)}$ or $\vec{B}_{(m,n)}$ with $\vec{C}_{(m,n)}$ is zero. The orthogonality of the functions $\exp(im\phi)$ and $\exp(i\tilde{m}\phi)$ on the unit circle for $m \neq \tilde{m}$ show that if as in ([5]) we define the inner product of two vector valued functions $\vec{U}(\theta, \phi)$ and $\vec{V}(\theta, \phi)$ defined on the unit sphere by,

$$\langle \vec{U}, \vec{V} \rangle = \int_0^{2\pi} \int_0^\pi \vec{U}(\theta, \phi) \cdot \vec{V}(\theta, \phi)^* \sin(\theta) d\theta d\phi \quad (6)$$

with two different values of m are orthogonal. If we take the dot product of two distinct members of the collection

$$\mathcal{S} = \{ \vec{A}_{(m,n)}, \vec{B}_{(m,n)}, \vec{C}_{(m,n)} : m \in \mathbb{Z}, \text{ and } n \in \{ |m|, |m| + 1, \dots \} \}, \quad (7)$$

with the same values of m and make use of ([1], p 333) the negative index relationship

$$P_\nu^{-\mu}(z) = \frac{\Gamma(\nu - \mu + 1)}{\Gamma(\nu + \mu + 1)} \left[P_\nu^\mu(z) - \frac{2}{\pi} \exp(-i\mu\pi) \sin(\mu\pi) Q_\nu^\mu(z) \right] \quad (8)$$

we find that any two members with different values of n are orthogonal with respect to the inner product defined by equation (6). For example, to see that

$$\langle \vec{A}_{(m,n)}, \vec{B}_{(m,r)} \rangle = 0 \quad (9)$$

for all n and r we note that this dot product reduces to

$$im(2\pi) \int_0^\pi \frac{d}{d\theta} [P_n^m(\cos(\theta)) P_r^m(\cos(\theta))] d\theta = im(2\pi) \int_{-1}^1 \frac{d}{dx} \{ P_n^m(x) P_r^m(x) \} dx \quad (10)$$

The details of the remaining orthogonality relations are found in ([5]) or can be derived from properties of the Legendre functions described in Jones ([22]).

Plane waves in free space can be represented using the functions described above by carrying out the expansion (Bell, [4] page 51 and Jones [22], page 490, equation 94)

$$\exp(-ik_0 r \cos(\theta)) = \sum_{n=0}^{\infty} a_n P_n(\cos(\theta)) j_n(k_0 r) \quad (11)$$

where the expansion coefficients a_n are given by (see Jones [22], page 490)

$$a_n = (-i)^n (2n + 1). \quad (12)$$

These coefficients are determined by letting $z = k_0 r$, carrying out a Taylor series expansion in z , and making use of the orthogonality relationships

$$\int_0^\pi P_n(\cos(\theta))P_m(\cos(\theta))\sin(\theta)d\theta = \begin{cases} 2/(2n + 1) & \text{if } n = m \\ 0 & \text{if } n \neq m \end{cases} \quad (13)$$

This equation is based on the relation (Bell [4], page 61)

$$\int_{-1}^1 (z^2 - 1)^n dz = \int_{-1}^1 (z - 1)^n (z + 1)^n dz = \frac{2^{2n+1}(n!)^2}{(2n + 1)!} \cdot (-1)^n \quad (14)$$

which follows from integration by parts in the left side of equation (13). This relationship can be proven using the Rodrigues definition (equation 4). By using the notion that the algebraic structure formed by linearly combining these vector fields in a ring of radial functions is invariant under the curl operation also enables one to get an exact solution to the scattering problem for isotropic, anisotropic, or bianisotropic spheres.

3.2 Representation of the Electric Vector

The key to the solution of the remote sensing problem is to decompose a potentially numerically intractable problem into two much simpler problems by using the measured observations of the scattered radiation to find the expansion coefficients used to represent the electric vector of the scattered radiation as a sum of multiples of the vector spherical harmonics given by equations (1), (2), and (3) by functions of the distance r from the center of the sphere. Noise is removed by multiple measurements for each sensor. Ultra high order quadrature can be used to obtain an accurate representation of the electric vector of the scattered radiation by precise placement of sensors at quadrature points located on a section of a sphere. In this way we can obtain an expansion in spherical harmonics using the orthogonality of the vector valued functions given by equations (1) and (2) by integrating only over a small (in terms of steradians) portion of the sphere.

If we put in general functions of the radial variable as multiples of the orthogonal functions given by (1), (2), and (3) and substitute into the Maxwell equations we derive equations such as

$$\begin{aligned} & \left(\frac{1}{r} \left(\frac{\partial}{\partial r} \right)^2 \right) (r Z_n^{(b)}(kr)) \\ & + \left[(k_a^2 + \alpha\beta) - \frac{n(n+1)\zeta_b}{r^2} \right] Z_n^{(b)}(kr) = 0 \end{aligned} \quad (1)$$

For the simple uniaxially bianisotropic material the radial functions are solutions of

$$\begin{aligned} & -\frac{\mu n(n+1)}{\mu_r r^2} Z_n^{(a)} + \frac{1}{r} \left(\frac{\partial}{\partial r} \right)^2 (r Z_n^{(a)}(r)) = \\ & -k_a^2 Z_n^{(a)}(r) - \alpha\beta \zeta_n^{(a)}(r) \end{aligned} \quad (2)$$

where the ordinary uniaxially anisotropic sphere propagation constant is

$$k_a^2 = \omega^2 \mu \epsilon - i \omega \mu \sigma \quad (3)$$

If we introduce the variable

$$\zeta_n = \frac{\mu}{\mu_r} \quad (4)$$

and the propagation constant k is given by

$$k^2 = \omega^2 \mu \epsilon - i \omega \mu \sigma + \alpha \beta \quad (5)$$

the ordinary differential equation (2) satisfied by $Z_n^{(a)}(kr)$ is simply

$$\frac{1}{r} \left(\frac{\partial}{\partial r} \right)^2 (r Z_n^{(a)}(kr)) + \left[k^2 - \zeta_n \frac{n(n+1)}{r^2} \right] Z_n^{(a)}(kr) = 0 \quad (6)$$

which is easily seen to be a form of Bessel's differential equation whose solution is simply a Bessel function with a complex index and argument.

One of the radial functions used as a multiplier involves the reciprocal of the radial variable r times the partial derivative with respect to r of a Bessel function with complex index given by

$$W_{(n,p)}^{(a,j)}(k_p r) = \frac{1}{k_p r} \left(\frac{\partial}{\partial r} \right) (r Z_{(n,p)}^{(a,j)}(k_p r)) \quad (7)$$

and a corresponding equation for the radial functions of type b satisfying equation (1).

When we substitute the suggested representations of the electric and magnetic vectors into the Faraday Maxwell equation (the one involving $\text{curl}(\vec{E})$) and Ampere Maxwell equation, the one involving $\text{curl}(\vec{H})$, we obtain consistency conditions relating the expansion coefficients in any region. As we impose the boundary conditions across the layers, namely the continuity of tangential components of electric and magnetic vectors across a separating sphere, we get relations between the coefficients in the core and the region surrounding the sphere. For a simple uniaxially bianisotropic material the propagation constant in layer p is given by

$$k_p^2 = \omega^2 \mu^{(p)} \epsilon^{(p)} - i \omega \mu^{(p)} \sigma^{(p)} + \alpha^{(p)} \beta^{(p)} \quad (8)$$

where $\epsilon^{(p)}$ is the permittivity, $\mu^{(p)}$ is the permeability, $\sigma^{(p)}$ is the conductivity, and $\alpha^{(p)}$, and $\beta^{(p)}$ are complex coupling constants giving respectively the contribution of the electric vector on the right side of the Faraday Maxwell equation and the contribution of the magnetic vector on the right side of the Ampere Maxwell equation. In the p th layer of the sphere the magnetic vector has the form,

$$\vec{H} = \sum_{(m,n) \in I} \left[\left(\frac{i}{\omega \mu_r^{(p)}} \right) \left\{ a_{(m,n)}^{(p)} \frac{Z_{(n,p)}^{(a,1)}(k_p r) n(n+1)}{r} + \right. \right. \\ \left. \left. \alpha_{(m,n)}^{(p)} \frac{Z_{(n,p)}^{(a,3)}(k_p r) n(n+1)}{r} + (-i) \left(\alpha_r^{(p)} \zeta_n n(n+1) b_{(m,n)}^{(p)} \frac{Z_{(n,p)}^{(b,1)}(k_p r)}{k_p r} + \right. \right. \right.$$

$$\begin{aligned}
& \left. \alpha_r^{(p)} \zeta_b n(n+1) \beta_{(m,n)}^{(p)} \frac{Z_{(n,p)}^{(b,3)}(k_p r)}{k_p r} \right\} \bar{C}_{(m,n)} + \\
& \frac{i}{\omega \mu^{(p)}} \left\{ a_{(m,n)}^{(p)} k_p W_{(n,p)}^{(a,1)}(k_p r) + \alpha_{(m,n)}^{(p)} k_p W_{(n,p)}^{(a,3)}(k_p r) \right\} \bar{B}_{(m,n)} + \\
& \left(\frac{-i}{\omega \mu^{(p)}} \right) \left\{ \alpha^{(p)} b_{(m,n)}^{(p)} (W_{(n,p)}^{(b,1)}(k_p r)) + \alpha^{(p)} \beta_{(m,n)}^{(p)} (W_{(n,p)}^{(b,3)}(k_p r)) \right\} \bar{B}_{(m,n)} + \\
& \left(\frac{i}{\omega \mu^{(p)}} \right) [-k_p] \left\{ b_{(m,n)}^{(p)} Z_{(n,p)}^{(b,1)}(k_p r) + \beta_{(m,n)}^{(p)} Z_{(n,p)}^{(b,3)}(k_p r) \right\} \bar{A}_{(m,n)} + \\
& \left(\frac{i}{\omega \mu^{(p)}} \right) \left\{ \alpha^{(p)} a_{(m,n)}^{(p)} Z_{(n,p)}^{(a,1)}(k_p r) + \alpha^{(p)} \alpha_{(m,n)}^{(p)} Z_{(n,p)}^{(a,3)}(k_p r) \right\} \bar{A}_{(m,n)} \quad (9)
\end{aligned}$$

Equation (9) implies, upon equating tangential components of \vec{H} , on each side of the boundary $r = R_p$, by taking the dot product of both sides of (9) with respect to $\vec{B}_{(m,n)}$ and integrating over the sphere $r = R_p$ that

$$\begin{aligned}
& \frac{i}{\omega \mu^{(p)}} \left\{ a_{(m,n)}^{(p)} k_p W_{(n,p)}^{(a,1)}(k_p r) + \alpha_{(m,n)}^{(p)} k_p W_{(n,p)}^{(a,3)}(k_p r) \right\} + \\
& \left(\frac{-i}{\omega \mu^{(p)}} \right) \left\{ \alpha^{(p)} b_{(m,n)}^{(p)} (W_{(n,p)}^{(b,1)}(k_p r)) + \alpha^{(p)} \beta_{(m,n)}^{(p)} (W_{(n,p)}^{(b,3)}(k_p r)) \right\} = \\
& \frac{i}{\omega \mu^{(p+1)}} \left\{ a_{(m,n)}^{(p+1)} k_{p+1} W_{(n,p+1)}^{(a,1)}(k_{p+1} r) + \alpha_{(m,n)}^{(p+1)} k_{p+1} W_{(n,p+1)}^{(a,3)}(k_{p+1} r) \right\} + \\
& \left(\frac{-i}{\omega \mu^{(p+1)}} \right) \left\{ \alpha^{(p+1)} b_{(m,n)}^{(p+1)} (W_{(n,p+1)}^{(b,1)}(k_{p+1} r)) + \alpha^{(p+1)} \beta_{(m,n)}^{(p+1)} (W_{(n,p+1)}^{(b,3)}(k_{p+1} r)) \right\} \quad (10)
\end{aligned}$$

Again using the continuity of tangential components of the magnetic vector given by (9) on opposite sides of a delimiting boundary we deduce by orthogonality of the vector functions given by (1) that

$$\begin{aligned}
& \left(\frac{i}{\omega \mu^{(p)}} \right) [-k_p] \left\{ b_{(m,n)}^{(p)} Z_{(n,p)}^{(b,1)}(k_p r) + \beta_{(m,n)}^{(p)} Z_{(n,p)}^{(b,3)}(k_p r) \right\} \\
& \left(\frac{i}{\omega \mu^{(p)}} \right) \left\{ \alpha^{(p)} a_{(m,n)}^{(p)} Z_{(n,p)}^{(a,1)}(k_{p+1} r) + \alpha^{(p)} \alpha_{(m,n)}^{(p)} Z_{(n,p)}^{(a,3)}(k_{p+1} r) \right\} = \\
& \left(\frac{i}{\omega \mu^{(p+1)}} \right) \left\{ b_{(m,n)}^{(p+1)} [-k_{p+1}] Z_{(n,p+1)}^{(b,1)}(k_{p+1} r) \right. \\
& \quad \left. + \beta_{(m,n)}^{(p+1)} [-k_{p+1}] Z_{(n,p+1)}^{(b,3)}(k_{p+1} r) \right\} \\
& \left(\frac{i}{\omega \mu^{(p+1)}} \right) \left\{ \alpha^{(p+1)} a_{(m,n)}^{(p)} Z_{(n,p+1)}^{(a,1)}(k_{p+1} r) + \alpha^{(p+1)} \alpha_{(m,n)}^{(p+1)} Z_{(n,p+1)}^{(a,3)}(k_{p+1} r) \right\} \quad (11)
\end{aligned}$$

We now attempt to develop transition matrices which will relate expansion coefficients in one layer to expansion coefficients in another layer. We start with equation (10); we find,

after multiplying both sides of this equation by $\mu^{(p)}$ and dividing both sides of equation (10) by k_p , that

$$\begin{aligned} & \left\{ a_{(m,n)}^{(p)} W_{(n,p)}^{(a,1)}(k_p r) + \alpha_{(m,n)}^{(p)} W_{(n,p)}^{(a,3)}(k_p r) \right\} + \\ & \left\{ \left(-\frac{\alpha^{(p)}}{k_p} \right) b_{(m,n)}^{(p)} (W_{(n,p)}^{(b,1)}(k_p r)) + \left(-\frac{\alpha^{(p)}}{k_p} \right) \beta_{(m,n)}^{(p)} (W_{(n,p)}^{(b,3)}(k_p r)) \right\} = \\ & \left(\frac{\mu^{(p)} k_{p+1}}{\mu^{(p+1)} k_p} \right) \left\{ a_{(m,n)}^{(p+1)} W_{(n,p+1)}^{(a,1)}(k_p r) + \alpha_{(m,n)}^{(p+1)} W_{(n,p+1)}^{(a,3)}(k_p r) \right\} + \\ & \left(\frac{-\mu^{(p)} \alpha^{(p+1)}}{\mu^{(p+1)} k_p} \right) \left\{ b_{(m,n)}^{(p+1)} (W_{(n,p+1)}^{(b,1)}(k_p r)) + \beta_{(m,n)}^{(p+1)} (W_{(n,p+1)}^{(b,3)}(k_p r)) \right\} \end{aligned} \quad (12)$$

Multiplying both sides of equation (9) by $\vec{A}_{(m,n)}(\theta, \phi)$ and observing that

$$\begin{aligned} & \lim_{r \rightarrow R_p^-} \int_{S_p(r)} \vec{H} \cdot \vec{A}_{(m,n)}(\theta, \phi) dA = \\ & \lim_{r \rightarrow R_p^+} \int_{S_p(r)} \vec{H} \cdot \vec{A}_{(m,n)}(\theta, \phi) dA \end{aligned} \quad (13)$$

we derive equation (11). From this, after multiplying all terms by $-i\omega\mu^{(p)}k_p$ and dividing all terms by k_p^2 , where k_p is defined by (8), we derive the relation that

$$\begin{aligned} & \left(\frac{\alpha^{(p)}}{k_p} \right) \left\{ a_{(m,n)}^{(p)} Z_{(n,p)}^{(a,1)}(k_p r) + \alpha_{(m,n)}^{(p)} Z_{(n,p)}^{(a,3)}(k_p r) \right\} + \\ & \left\{ b_{(m,n)}^{(p)} Z_{(n,p)}^{(b,1)}(k_p r) + \beta_{(m,n)}^{(p)} Z_{(n,p)}^{(b,3)}(k_p r) \right\} = \\ & \left(\frac{\mu^{(p)} \alpha^{(p+1)}}{\mu^{(p+1)} k_p} \right) \left\{ a_{(m,n)}^{(p+1)} Z_{(n,p+1)}^{(a,1)}(k_{p+1} r) + \alpha_{(m,n)}^{(p+1)} Z_{(n,p+1)}^{(a,3)}(k_{p+1} r) \right\} + \\ & \left[-\frac{\mu^{(p)} k_{p+1}}{\mu^{(p+1)} k_p} \right] \cdot \left\{ b_{(m,n)}^{(p+1)} Z_{(n,p+1)}^{(b,1)}(k_{p+1} r) + \beta_{(m,n)}^{(p+1)} Z_{(n,p+1)}^{(b,3)}(k_{p+1} r) \right\}. \end{aligned} \quad (14)$$

where k_p and k_{p+1} are defined by (8).

We now define parameters which appear in the matrix relating expansion coefficients in one layer to those in an adjacent layer. We obtain these by considering terms appearing in equation (14)

$$\rho_{(b,3)}^{(p+1)} = \left(\frac{\mu^{(p)}}{\mu^{(p+1)}} \right) \left[-\frac{k_{p+1}}{k_p} \right] \quad (15)$$

Also

$$\rho_{(a,3)}^{(p+1)} = \left(\frac{\mu^{(p)} \alpha^{(p+1)}}{\mu^{(p+1)} k_p} \right) \quad (16)$$

with k_p and k_{p+1} being defined by (8). A similar term appearing in the inner shell matrix is

$$\rho_{(a,1)}^{(p)} = \left(\frac{\alpha^{(p)}}{k_p} \right) \quad (17)$$

A term in the second row of the outer shell matrix is

$$\rho_{(a,2)}^{(p+1)} = \left(\frac{\mu^{(p)} k_{p+1}}{\mu^{(p+1)} k_p} \right) \quad (18)$$

Another term appearing in second row of the matrix is

$$\rho_{(b,2)}^{(p+1)} = \left(\frac{-\mu^{(p)} \alpha^{(p+1)}}{\mu^{(p+1)} k_p} \right) \quad (19)$$

The corresponding term in the inner shell matrix is

$$\rho_{(b,2)}^{(p)} = \left(\frac{-\alpha^{(p)}}{k_p} \right) \quad (20)$$

With the special functions $Z_{(n,p)}^{(a,j)}$, defined by (6), and $Z_{(n,p)}^{(b,j)}$, defined by (1), and the derivative terms defined by equation (7) being evaluated at the separating spherical boundary $r = R_p$, we see that the matrix equation relating expansion coefficients in layer p to those in layer $p + 1$ is given by

$$\begin{bmatrix} Z_{(n,p)}^{(a,1)} & Z_{(n,p)}^{(a,3)} & 0 & 0 \\ W_{(n,p)}^{(a,1)} & W_{(n,p)}^{(a,3)} & \rho_{(b,2)}^{(p)} W_{(n,p)}^{(b,1)} & \rho_{(b,2)}^{(p)} W_{(n,p)}^{(b,3)} \\ \rho_{(a,3)}^{(p)} Z_{(n,p)}^{(a,1)} & \rho_{(a,3)}^{(p)} Z_{(n,p)}^{(a,3)} & Z_{(n,p)}^{(b,1)} & Z_{(n,p)}^{(b,3)} \\ 0 & 0 & W_{(n,p)}^{(b,1)} & W_{(n,p)}^{(b,3)} \end{bmatrix} \begin{bmatrix} a_{(m,n)}^{(p)} \\ \alpha_{(m,n)}^{(p)} \\ b_{(m,n)}^{(p)} \\ \beta_{(m,n)}^{(p)} \end{bmatrix} = \begin{bmatrix} Z_{(n,p+1)}^{(a,1)} & Z_{(n,p+1)}^{(a,3)} & 0 & 0 \\ W_{(n,p+1)}^{(a,1)} & W_{(n,p+1)}^{(a,3)} & \rho_{(b,2)}^{(p+1)} W_{(n,p+1)}^{(b,1)} & \rho_{(b,2)}^{(p+1)} W_{(n,p+1)}^{(b,3)} \\ \rho_{(a,3)}^{(p+1)} Z_{(n,p+1)}^{(a,1)} & \rho_{(a,3)}^{(p+1)} Z_{(n,p+1)}^{(a,3)} & \rho_{(b,3)}^{(p+1)} Z_{(n,p+1)}^{(b,1)} & \rho_{(b,3)}^{(p+1)} Z_{(n,p+1)}^{(b,3)} \\ 0 & 0 & W_{(n,p+1)}^{(b,1)} & W_{(n,p+1)}^{(b,3)} \end{bmatrix} \begin{bmatrix} a_{(m,n)}^{(p+1)} \\ \alpha_{(m,n)}^{(p+1)} \\ b_{(m,n)}^{(p+1)} \\ \beta_{(m,n)}^{(p+1)} \end{bmatrix} \quad (21)$$

This equation can be written more compactly in the form

$$T_n^{(p)}(k_p R_p) \begin{bmatrix} a_{(m,n)}^{(p)} \\ \alpha_{(m,n)}^{(p)} \\ b_{(m,n)}^{(p)} \\ \beta_{(m,n)}^{(p)} \end{bmatrix} = T_n^{(p+1)}(k_{p+1} R_p) \begin{bmatrix} a_{(m,n)}^{(p+1)} \\ \alpha_{(m,n)}^{(p+1)} \\ b_{(m,n)}^{(p+1)} \\ \beta_{(m,n)}^{(p+1)} \end{bmatrix} \quad (22)$$

To compute the inverse of the matrix $T_n^{(p)}$ we need its transpose which is given by

$$\begin{bmatrix} Z_{(n,p)}^{(a,1)}(k_p R_p) & W_{(n,p)}^{(a,1)}(k_p R_p) & \rho_{(a,3)}^{(p)} Z_{(n,p)}^{(a,1)}(k_p R_p) & 0 \\ Z_{(n,p)}^{(a,3)}(k_p R_p) & W_{(n,p)}^{(a,3)}(k_p R_p) & \rho_{(a,3)}^{(p)} Z_{(n,p)}^{(a,3)}(k_p R_p) & 0 \\ 0 & \rho_{(b,2)}^{(p)} W_{(n,p)}^{(b,1)}(k_p R_p) & Z_{(n,p)}^{(b,1)}(k_p R_p) & W_{(n,p)}^{(b,1)}(k_p R_p) \\ 0 & \rho_{(b,2)}^{(p)} W_{(n,p)}^{(b,3)}(k_p R_p) & Z_{(n,p)}^{(b,3)}(k_p R_p) & W_{(n,p)}^{(b,3)}(k_p R_p) \end{bmatrix} = (T_n^{(p)})^{(transpose)'} \quad (23)$$

Wronskian relations will show that we can define a new matrix $Q_n^{(p)}$ by the rule

$$Q_n^{(p)} = T_n^{(p)}(k_p R_p)^{-1} T_n^{(p+1)}(k_{p+1} R_p). \quad (24)$$

Using equations (22) and (24) we see that the expansion coefficients in the core are related to the expansion coefficients in the outer shell by the rule,

$$\begin{bmatrix} a_{(m,n)}^{(1)} \\ 0 \\ b_{(m,n)}^{(1)} \\ 0 \end{bmatrix} = Q_n^{(1)} Q_n^{(2)} \dots Q_n^{(N)} \begin{bmatrix} a_{(m,n)}^{(N+1)} \\ \alpha_{(m,n)}^{(N+1)} \\ b_{(m,n)}^{(N+1)} \\ \beta_{(m,n)}^{(N+1)} \end{bmatrix} \quad (25)$$

This gives us four equations in four unknowns, since we assume that the expansion coefficients $\alpha_{(m,n)}^{(N+1)}$ and $\beta_{(m,n)}^{(N+1)}$ are determined; these expansion coefficients could define a complex source such as a radar or laser beam in the near field (Barton [2] and [3], Pinneck et al [27] and Pinnick and Pendleton [26]). Solving equation (25) we find values of $a_{(m,n)}^{(1)}$ and $b_{(m,n)}^{(1)}$ and assuming that $\alpha_{(m,n)}^{(1)}$ and $\beta_{(m,n)}^{(1)}$ are both zero, we can easily obtain the expansion coefficients in every layer of the structure. If we define the matrix $\mathcal{R}_n^{(p)}$ by the rule,

$$\mathcal{R}_n^{(p)} = T_n^{(p+1)}(k_{p+1} R_p)^{-1} T_n^{(p)}(k_p R_p) \quad (26)$$

We see that the definition of $\mathcal{R}_n^{(p)}$ by equation (26) implies the relationship

$$\mathcal{R}_n^{(p)} \begin{bmatrix} a_{(m,n)}^{(p)} \\ \alpha_{(m,n)}^{(p)} \\ b_{(m,n)}^{(p)} \\ \beta_{(m,n)}^{(p)} \end{bmatrix} = \begin{bmatrix} a_{(m,n)}^{(p+1)} \\ \alpha_{(m,n)}^{(p+1)} \\ b_{(m,n)}^{(p+1)} \\ \beta_{(m,n)}^{(p+1)} \end{bmatrix} \quad (27)$$

between expansion coefficients in adjacent layers of the spherical structure.

These computations using equation (27) are facilitated by the fact that we have exact formulas for the determinant and inverses of the 4 by 4 matrices $T_n^{(p)}$. Let the determinant of $T_n^{(p)}$ be defined by

$$\begin{aligned} \Delta_p &= Z_{(n,p)}^{(a,1)}(k_p R_p) W_{(n,p)}^{(a,3)}(k_p R_p) \\ &\quad \{ Z_{(n,p)}^{(b,1)}(k_p R_p) W_{(n,p)}^{(b,3)}(k_p R_p) - W_{(n,p)}^{(b,1)}(k_p R_p) Z_{(n,p)}^{(b,3)}(k_p R_p) \} + \\ &\quad (-1) \{ Z_{(n,p)}^{(a,3)}(k_p R_p) W_{(n,p)}^{(a,1)}(k_p R_p) \} \\ &\quad \{ Z_{(n,p)}^{(b,1)}(k_p R_p) W_{(n,p)}^{(b,3)}(k_p R_p) - W_{(n,p)}^{(b,1)}(k_p R_p) Z_{(n,p)}^{(b,3)}(k_p R_p) \} \end{aligned} \quad (28)$$

which means that the determinant Δ_p is the product of two Wronskians $\mathcal{W}_{(n,p)}^{(a)}$ and $\mathcal{W}_{(n,p)}^{(b)}$ where

$$\mathcal{W}_{(n,p)}^{(b)} = Z_{(n,p)}^{(b,1)}(k_p R_p) W_{(n,p)}^{(b,3)}(k_p R_p) - W_{(n,p)}^{(b,1)}(k_p R_p) Z_{(n,p)}^{(b,3)}(k_p R_p) \quad (29)$$

We find that equation (28) and the Wronskian relationship,

$$\mathcal{W}_{(n,p)}^{(a)}(k_p R_p) = \frac{-i}{(k_p R_p)^2} \quad (30)$$

enables us to compute determinants with no roundoff error. This enables us to get exact formulas for the entries of the inverse of this matrix. If $(T_n^{(p)}(k_p R_p)^{-1})_{(i,j)}$ denotes the entry in the i th row and j th column of the inverse of the matrix $T_n^{(p)}$, then the entry in row 1 and column 1 of the inverse is

$$(T_n^{(p)}(k_p R_p)^{-1})_{(1,1)} = W_{(n,p)}^{(a,3)}(k_p R_p) \mathcal{W}_{(n,p)}^{(b)}(k_p R_p) / \Delta_p, \quad (31)$$

The (1,2) entry is

$$(T_n^{(p)}(k_p R_p)^{-1})_{(1,2)} = -Z_{(n,p)}^{(a,3)}(k_p R_p) \mathcal{W}_{(n,p)}^{(b)}(k_p R_p) / \Delta_p, \quad (32)$$

The (1,3) term is

$$(T_n^{(p)}(k_p R_p)^{-1})_{(1,3)} = 0 \quad (33)$$

The (1,4) term is

$$(T_n^{(p)}(k_p R_p)^{-1})_{(1,4)} = -Z_{(n,p)}^{(a,3)}(k_p R_p) \left(\frac{-\alpha^{(p)}}{k_p} \right) \mathcal{W}_{(n,p)}^{(b)}(k_p R_p) / \Delta_p, \quad (34)$$

Equations (31), (32), (33), and (34) define the first row of the transition matrix. The entry in row 2 and column 1 of the inverse is

$$(T_n^{(p)}(k_p R_p)^{-1})_{(2,1)} = -W_{(n,p)}^{(a,1)}(k_p R_p) \mathcal{W}_{(n,p)}^{(b)}(k_p R_p) / \Delta_p, \quad (35)$$

The entry in row 2 and column 2 of the inverse is

$$(T_n^{(p)}(k_p R_p)^{-1})_{(2,2)} = Z_{(n,p)}^{(a,1)}(k_p R_p) \mathcal{W}_{(n,p)}^{(b)}(k_p R_p) / \Delta_p, \quad (36)$$

The entry in row 2 and column 3 of the inverse is

$$(T_n^{(p)}(k_p R_p)^{-1})_{(2,3)} = 0 \quad (37)$$

The entry in row 2 and column 4 of the inverse is

$$(T_n^{(p)}(k_p R_p)^{-1})_{(2,4)} = Z_{(n,p)}^{(a,1)}(k_p R_p) \left(\frac{-\alpha^{(p)}}{k_p} \right) \mathcal{W}_{(n,p)}^{(b)}(k_p R_p) / \Delta_p, \quad (38)$$

Equations (35), (36), (37), and (38) define the second row of the transition matrix. The (3,1) entry is

$$(T_n^{(p)}(k_p R_p)^{-1})_{(3,1)} = W_{(n,p)}^{(b,3)}(k_p R_p) \left(\frac{-\alpha^{(p)}}{k_p} \right) \mathcal{W}_{(n,p)}^{(b)}(k_p R_p) / \Delta_p, \quad (39)$$

The (3,2) entry is

$$(T_n^{(p)}(k_p R_p)^{-1})_{(3,2)} = 0 \quad (40)$$

The (3,3) entry is

$$(T_n^{(p)}(k_p R_p)^{-1})_{(3,3)} = W_{(n,p)}^{(b,3)}(k_p R_p) \mathcal{W}_{(n,p)}^{(a)}(k_p R_p) / \Delta_p, \quad (41)$$

The (3,4) entry is

$$(T_n^{(p)}(k_p R_p)^{-1})_{(3,4)} = -Z_{(n,p)}^{(b,3)}(k_p R_p) \mathcal{W}_{(n,p)}^{(a)}(k_p R_p) / \Delta_p, \quad (42)$$

Equations (39), (40), (41), and (42) define the third row of the matrix. The (4,1) entry is given by

$$(T_n^{(p)}(k_p R_p)^{-1})_{(4,1)} = -W_{(n,p)}^{(b,1)}(k_p R_p) \left(\frac{-\alpha^{(p)}}{k_p} \right) \mathcal{W}_{(n,p)}^{(a)}(k_p R_p) / \Delta_p, \quad (43)$$

The (4,2) entry is

$$(T_n^{(p)}(k_p R_p)^{-1})_{(4,2)} = 0 \quad (44)$$

The (4,3) entry is

$$(T_n^{(p)}(k_p R_p)^{-1})_{(4,3)} = -W_{(n,p)}^{(b,1)}(k_p R_p) \mathcal{W}_{(n,p)}^{(a)}(k_p R_p) / \Delta_p, \quad (45)$$

Finally, the (4,4) entry of the inverse of $T_n^{(p)}$ is

$$(T_n^{(p)}(k_p R_p)^{-1})_{(4,4)} = Z_{(n,p)}^{(b,1)}(k_p R_p) \mathcal{W}_{(n,p)}^{(a)}(k_p R_p) / \Delta_p, \quad (46)$$

We have therefore obtained round-off error free expressions for the entries of the inverse of $T_n^{(p)}(k_p R_p)$. Thus, except for the expression relating the expansion coefficients in equation (25), all computations are carried out by exact formulas. The matrix inverse computation requires no subtractions or additions and consequently there is no round off error if the Bessel and Hankel functions of complex index and their derivatives can be computed precisely.

3.3 Determination of Expansion Coefficients

Let us suppose that we have an N layer sphere subject to plane wave radiation. By multiplying the inverse of $T_n^{(p)}$ evaluated at $k_p R_p$ by the matrix $T_n^{(p+1)}$ evaluated at $k_{p+1} R_p$ we obtaining the matrix

$$\mathcal{T}_n^{(p)} = T_n^{(p)}(k_p R_p)^{-1} T_n^{(p+1)}(k_{p+1} R_p) \quad (1)$$

relating the expansion coefficients in layer p to those in layer $p + 1$. We then multiply all of these matrices (1) obtaining a matrix

$$\mathcal{T} = \mathcal{T}_n^{(1)} \cdot \mathcal{T}_n^{(2)} \cdot \dots \cdot \mathcal{T}_n^{(N)} \quad (2)$$

where N is the number of layers of the sphere which relates the expansion coefficients in the core to the expansion coefficients in the space surrounding the sphere. This gives four equations in four unknowns. But it is really simpler than that. Using the second and fourth rows of this matrix equation, we can relate the expansion coefficients of the scattered radiation to the known expansion coefficients of the incoming radiation. We then have in the first and third rows of this equation a formula for the expansion coefficients in the inner core.

3.4 Recovering the Properties of a Layered Sphere

We now consider a set of equations which may be used to recover the properties of either a layered isotropic sphere or a layered uniaxially anisotropic sphere. Imagine that you have a matrix \bar{Q} relating the expansion coefficients representing the electric and magnetic vectors in the inner core to the expansion coefficients representing the electric and magnetic vectors in the region surrounding the layered sphere. By eliminating the unknown expansion coefficients in the core we get for each spherical harmonic index equations relating the two complex, a priori unknown but measurement determined expansion coefficients giving the radiation emanating from the layered sphere to the a priori known expansion coefficients defining the known interrogating radiation. For the different types of spheres there are repeated sets of equations that should give the same answers for sphere properties. If these sets of equations do all indicate that the sphere is homogeneous and isotropic, then we conclude that the droplet is not encapsulated. If these are not satisfied, then we conclude that the droplet is something else and if we prove that the equations that are satisfied are consistent with a layered sphere assumption we conclude that the particles are man made.

When the scattering sphere is isotropic and homogeneous like an ordinary cloud water droplet the only unknowns are (i) the radius R (ii) the real permittivity ϵ , (iii) the conductivity σ , (iv) the real part and (v) the imaginary part of the complex permeability μ which for water may be assumed to be that of free space so that in any case there are at most 5 real variables to solve for. For each Legendre function index n for the vector spherical harmonics given by equations (1), (2), and (3), we see that there are four equations, given by the real and imaginary parts of the equations

$$\alpha_{(m,n)}^{(N+1)} = \left(- \left[Q_{(2,1)}^{(m,n)} \cdot a_{(m,n)}^{(N+1)} \right] \cdot \left(1/Q_{(2,2)}^{(m,n)} \right) \right) \quad (1)$$

and with R denoting the 2 by 2 matrix relating the b and β coefficients in the core to those in region $N + 1$ outside the droplet, we have

$$\beta_{(m,n)}^{(N+1)} = \left[- \left(R_{(2,1)}^{(m,n)} \cdot b_{(m,n)}^{(N+1)} \right) / \left(R_{(2,2)}^{(m,n)} \right) \right] \quad (2)$$

If we keep getting the same values for the radius and permittivity, conductivity and complex permeability, for different combinations of 5 equations for different values of the index n , then we conclude that we have a nonlayered structure, not an an encapsulated biological agent.

4 Layering Detection on Structures with a General Shape

There is no exact solution to the problem of describing the scattering of electromagnetic radiation from an aerosol particle with a general shape. Surface and volume integral equations are one way of attacking the problem on existing computers. In the next section

we describe surface integral equations give a way of treating a complex of homogeneous structures each with different properties that are glued together to form an aerosol particle with a complex shape. If you can imagine a structure that by molding as modeling clay you could change into the interior of a sphere, the interior of a torus (doughnut), the interior of a two handled sphere (two doughnuts that have been cooked together) et cetera, these are the structures that are allowed. For example a cube is allowed because if you imagine that a cube was made of soft putty, it could be changed into a spherical shape.

4.1 Surface Integral Equations

A surface integral equation formulation based on a specialization of a vector calculus identity which says that

$$\begin{aligned}
 & \frac{1}{4\pi} \int_{\Omega} \left[-k^2 \vec{V} \Phi + \operatorname{div}(\vec{V}) \cdot \operatorname{grad}(\Phi) \right] dv \\
 & - \frac{1}{4\pi} \int_{\Omega} \left[\operatorname{grad}(\Phi) \times \operatorname{curl}(\vec{V}) \right] dv + \\
 & \frac{1}{4\pi} \int_{\partial\Omega} \left[\vec{V} (\vec{n} \cdot \operatorname{grad}(\Phi)) - \vec{n} (\vec{V} \cdot \operatorname{grad} \Phi) \right] da + \\
 & \frac{1}{4\pi} \int_{\partial\Omega} \left[(\vec{V} \cdot \vec{n}) \operatorname{grad}(\Phi) \right] da \\
 & = \begin{cases} \vec{V}(r) & r \in \Omega \\ \vec{0} & r \in \mathbf{R}^3 - \bar{\Omega} \end{cases} \quad (1)
 \end{aligned}$$

where the distribution Φ in the above equation is the fundamental solution of the scalar Helmholtz operator

$$L = \Delta + k^2 \quad (2)$$

that is temperate and rotationally invariant. New codes can be developed that would permit the description of interaction of radiation with bodies covered with different types of tensor material (e.g. bianisotropic, biisotropic, anisotropic, gyroelectric, uniaxial, et cetera). The surfaces are those surrounding homogeneous regions. The layered bianisotropic sphere code that I have developed can be used to check out the layering aspect of the surface integral equation formulation of the interaction of electromagnetic radiation with the first detailed model of general aerosol particles in a complex electromagnetic field. I have included a careful description of my unique exact finite rank integral equation) approach which is the only method for solving volume or surface integral equations that can give computing machine precision.

Consider a set Ω in \mathbf{R}^3 with boundary surface $\partial\Omega$ on which are induced electric and magnetic surface currents \vec{J}_j and \vec{M}_j . If we have a simple $N + 1$ region problem, where we have N inside and a region outside all N bounded homogenous aerosol particles corresponds to the region index j being equal to 1 and the region inside corresponds to j values ranging from 2 to $N + 1$, then if the propagation constant k_j in region j is defined also by a function k_j , naturally defined on a Riemann surface as the square root of,

$$k_j^2 = \omega^2 \mu \epsilon - i \omega \mu \sigma \quad (3)$$

For a Debye medium (Daniel, [13]) the branch cuts are along the imaginary ω axis. For a Lorentz medium particle (Brillouin, [6], [28]) the branch cuts are in the upper half of the complex ω plane parallel to the real axis. where μ , ϵ , and σ are functions of frequency that assure causality and that the radiation does not travel faster than the speed of light in vacuum. There are two Helmholtz equations, one for the interior of the particle and the other for the exterior, defined by

$$(\Delta + k^2)G_r = 4\pi\delta \quad (4)$$

where G_j is the temperate, rotationally invariant, fundamental solution ([21]) of the Helmholtz operator. We let

$$J_1 = J = -J_2 \quad (5)$$

and

$$M_1 = M = -M_2 \quad (6)$$

where we assume that the surface $S_{(1,2)}$ separates region 1 and region 2. We generalize equations (5) and (6) inductively by saying that for any surface $S_{(j,\tilde{j})}$ separating region j from region \tilde{j} where

$$j < \tilde{j} \quad (7)$$

we have

$$J_j = J = -J_{\tilde{j}} \quad (8)$$

and

$$M_j = M = -M_{\tilde{j}} \quad (9)$$

We define

$$\mathcal{I} = \{(j, \tilde{j}) : S_{(j,\tilde{j})} \text{ is a separating surface}\} \quad (10)$$

where j is less than \tilde{j} . We get a single coupled, combined field integral equation which describes the interaction of radiation with the conglomerate aerosol particle or cluster given by

$$\begin{aligned} \vec{n} \times \vec{E}^{inc} = & \vec{n} \times \sum_{(j,\tilde{j}) \in \mathcal{I}} \left\{ \left(\frac{i\omega}{4\pi} \right) \int_{S_{(j,\tilde{j})}} \int \vec{J}(\vec{r}) (\mu_j \cdot G_j(r, \vec{r}) + \mu_{\tilde{j}} \cdot G_{\tilde{j}}(r, \vec{r})) da(\vec{r}) \right. \\ & + \frac{i}{4\pi\omega} grad \left\{ \int_{S_{(j,\tilde{j})}} \int (div_s \cdot \vec{J}) \left[\frac{G_j(r, \vec{r})}{\epsilon_j} + \frac{G_{\tilde{j}}(r, \vec{r})}{\epsilon_{\tilde{j}}} \right] da(\vec{r}) \right\} + \\ & \left. \left(\frac{1}{4\pi} \right) curl \left(\int_{S_{(j,\tilde{j})}} \int \vec{M}(\vec{r}) \cdot (G_j(r, \vec{r}) + G_{\tilde{j}}(r, \vec{r})) da(\vec{r}) \right) \right\} \quad (11) \end{aligned}$$

In addition to equation (11) we need equation involving the magnetic vector H^{inc} of the stimulating electromagnetic field which is given by

$$\vec{n} \times \vec{H}^{inc} = \vec{n} \times \sum_{(j,\tilde{j}) \in \mathcal{I}} \left\{ \left(\frac{i\omega}{4\pi} \right) \int_{S_{(j,\tilde{j})}} \int \vec{M}(\vec{r}) (\epsilon_1 \cdot G_j(r, \vec{r}) + \epsilon_2 \cdot G_{\tilde{j}}(r, \vec{r})) da(\vec{r}) \right\}$$

$$\begin{aligned}
& + \left(\frac{i}{4\pi\omega} \right) \text{grad} \left\{ \int_{S_{(i,i)}} \int (\text{div}_s \cdot \vec{M}) \left[\frac{G_j(r, \vec{r})}{\mu_j} + \frac{G_j^*(r, \vec{r})}{\mu_j} \right] da(\vec{r}) \right\} + \\
& \left. \frac{1}{4\pi} \text{curl} \left(\int_{S_{(i,j)}} \int \vec{J}(\vec{r}) \cdot (G_j(r, \vec{r}) + G_j^*(r, \vec{r})) da(\vec{r}) \right) \right\} \quad (12)
\end{aligned}$$

Once the coupled combined field system (11) and (12) is solved for \vec{J} and \vec{M} , the surface electric and magnetic currents respectively and we define the surface electric charge density by ([15], p 7)

$$\rho^e(\vec{r}) = \frac{i}{\omega} [\text{div}_s \cdot \vec{J}(\vec{r})] \quad (13)$$

and the surface magnetic charge density

$$\rho^m(\vec{r}) = \frac{i}{\omega} [\text{div}_s \cdot \vec{M}(\vec{r})] \quad (14)$$

where div_s is the surface divergence. Now for each region index j we define

$$\mathcal{J}(j) = \{ \vec{j} : (j, \vec{j}) \in \mathcal{I} \} \quad (15)$$

where \mathcal{I} is the set of all indices of separating surfaces defined by (10). We now need to be able to express the electric and magnetic fields inside and outside the scattering body. We first define the vector potentials \vec{A}_j and \vec{F}_j by the rules, ([15] [24])

$$\vec{A}_j = \sum_{\vec{j} \in \mathcal{J}(j)} \left[\frac{\mu_j}{4\pi} \int_{S_{(j,\vec{j})}} \int \vec{J}_j(\vec{r}) \cdot G_j(r, \vec{r}) da(\vec{r}) \right] \quad (16)$$

$$\vec{F}_j = \sum_{\vec{j} \in \mathcal{J}(j)} \left[\left(\frac{\epsilon_j}{4\pi} \right) \int_{S_{(j,\vec{j})}} \int \vec{M}_j(\vec{r}) \cdot G_j(r, \vec{r}) da(\vec{r}) \right] \quad (17)$$

The scalar potentials are defined in terms of the electric charge density (13) and magnetic charge density (14) by the rules,

$$\Phi_j(\vec{r}) = \sum_{\vec{j} \in \mathcal{J}(j)} \left[\left(\frac{1}{4\pi\epsilon_j} \right) \int_{S_{(j,\vec{j})}} \int \rho_j^e(\vec{r}) G_j(r, \vec{r}) da(\vec{r}) \right] \quad (18)$$

and

$$\Psi_j(\vec{r}) = \sum_{\vec{j} \in \mathcal{J}(j)} \left[\left(\frac{1}{4\pi\mu_j} \right) \int_{S_{(j,\vec{j})}} \int \rho_j^m(\vec{r}) G_j(r, \vec{r}) da(\vec{r}) \right] \quad (19)$$

We now can define the electric and magnetic vectors inside the region j in terms of these potentials (16), (17), (18), and (19) by the rules,

$$\vec{E}_j = -i\omega\vec{A}_j(r) - \text{grad}(\Phi_j(r)) + \frac{1}{\epsilon_j} \text{curl}(\vec{F}_j)(r) \quad (20)$$

and

$$\vec{H}_j = -i\omega\vec{F}_j(r) - \text{grad}(\Psi_j(r)) + \frac{1}{\mu_j} \text{curl}(\vec{A}_j)(r) \quad (21)$$

Similar equations apply outside the body, by there the fields represented are the differences \vec{E}_1^s and \vec{H}_1^s between the total electric and magnetic vectors and the electric vector \vec{E}^{inc} and the magnetic vector \vec{H}^{inc} of the incoming wave that is providing the stimulation. Thus ([15]) we see that outside the body,

$$\vec{E}_1^s = -i\omega\vec{A}_1(r) - grad(\Phi_1(r)) + \frac{1}{\epsilon_1}curl(\vec{F}_1)(r) \quad (22)$$

and

$$\vec{H}_1^s = -i\omega\vec{F}_1(r) - grad(\Psi_1(r)) + \frac{1}{\mu_1}curl(\vec{A}_1)(r) \quad (23)$$

These equations generalize the formulation of Glisson ([15]) to a three dimensional structure whose regions of homogeneity are diffeomorphisms of the interior of the sphere or a torus in \mathbf{R}^3 . If the scattering structure is not a body of revolution, then the region may be a diffeomorph of an N handled sphere.

4.2 Recovery of Layering in Objects with a General Shape

The encapsulation of a spherical structure is probably from a manufacturing standpoint, the easiest thing to do, but the once this is known the theoretical problems of recovering the interior structure of a layered sphere are easily handled. In theory one can do the same thing for a particle with a completely general shape. We use the fact that each component of the electric vector is real analytic in a connected open set Ω and that if in an open subset U of the connected open set Ω the function is known, then it can be extended to all of Ω . By carrying out spatial Fourier transforms on orthogonal spatial hyperplanes which avoid the scatterer, we recover the integrand which gives us not only the a priori unknown generated current densities but also their support when regarded as distributions. This automatically gives us the layering in the general shape aerosol particle.

5 Computer Code Validation

How does one know that a computer code is giving accurate answers. There are several methods. These are (i) reciprocity methods, (ii) boundary condition checks, and (iii) energy balance checks.

5.1 Energy Balance Checks

One can calculate the total absorbed power in two different ways. One method is to use Gaussian quadrature to integrate the power density distribution over the interior of the scattering body. Another method is to use a Poynting vector analysis on the surface of the organ, a kind of energy balance bookkeeping which says that the the total power going in minus the total power scattered away is the integral of the Poynting vector of the

total field outside dotted with the inward directed normal minus the Poynting vector of the total scattered field dotted with the inward directed normal integrated over the surface of the aerosol particle. This check was applied to a six layer model of the human head exposed to 10^9 Hertz radiation, and possessing the properties described in the table:

I	R	ϵ/ϵ_0	σ
1	.0527	60.0	0.90
2	.0547	76.0	1.70
3	.0552	45.0	1.00
4	.0580	8.5	0.11
5	.0590	5.5	0.08
6	.0600	45.0	1.00

The propagation constants for this head model are listed in the table below:

layer no	propagation constant
1	163.78... - $i \cdot (21.69 \dots)$
2	186.23... - $i \cdot (36.03 \dots)$
3	143.26... - $i \cdot (27.55 \dots)$
4	61.51... - $i \cdot (7.06 \dots)$
5	49.56... - $i \cdot (6.37 \dots)$
6	143.26... - $i \cdot (27.55 \dots)$

This code has been augmented with a kind of inverse scattering procedure to use the scattered radiation in a simple way to see inside a potentially layered sphere and determine the number of layers, the electromagnetic properties of these layers and the radius of the outer sphere bounding these layers; The expansion coefficients of the scattered radiation have an infinite number of copies of redundant information which characterize the properties of the multiple layered sphere which produced the scattered radiation. The Poynting vector analysis, which tells us that the total power going into the sphere minus the total power scattered away is the total absorbed power is embodied in the equation,

$$\left(\frac{1}{2}\right) \cdot \int_{-\pi}^{\pi} \int_0^{\pi} [(\vec{E} \times (\vec{H})^*) \cdot (-\vec{n}) - (\vec{E}^s \times (\vec{H}^s)^*) \cdot \vec{n}] R^2 \sin(\theta) d\theta d\phi$$

$$= 1.45324 \times 10^{-5} \text{ Watts} \quad (1)$$

A completely different approach based on the Gauss divergence theorem and obtained by taking the divergence of the Poynting vector and using information about the conductivity σ_j of the material filling the j th layer and the radius R_j of the outermost sphere bounding the j th layer and using the *multiple layered sphere* computer program generated electric field vectors at Gaussian quadrature points within the layers tells us that

$$\sum_{j=1}^6 \int_0^{2\pi} \int_0^{\pi} \int_{R_{j-1}}^{R_j} \left(\frac{1}{2} \sigma \mid \vec{E} \mid^2\right) r^2 \sin(\theta) dr d\theta d\phi$$

$$= 1.453240960 \times 10^{-5} \text{ Watts}$$

This together with the fact that the spherical harmonic representation of the plane wave had full machine precision on the surface and the fact that the series converged on the inside of the spheres would tell us that the accuracy of the internal fields is at least 6 digits, the number of digits of agreement between the two answers. This idea when generalized to arbitrary surfaces and used along with boundary condition verification, reciprocity validation and local verification of the Maxwell equations will give us a measure of the accuracy with which the internal fields are being computed.

Part of the problem associated with electromagnetic pulse analysis, particularly for bodies with a general shape has been the number of different frequencies for which the interaction problem must be solved for time harmonic incident plane waves to see the electromagnetic pulse effect. There are two types of electromagnetic pulse effects. The geometry of the scattering body can cause the pulse to continue to resonate back and forth, particularly in a low loss material like bone, long after the pulse has passed by. Another effect is the dispersive effect based on the dependence of the tissue electromagnetic properties on frequency.

There is an economical way to see geometrical pulse effects by initially assuming that the electromagnetic properties, the permittivity ϵ and conductivity σ , did not depend on frequency. Integral equation formulations and even finite difference equation formulations require the solution of large systems of linear equations. If we have the inverse of the associated matrix for incoming radiation of one frequency, then by an N^2 homotopy process as we know the dependence of the filled matrix on frequency we would solve for the inverse matrix as the answer to an initial value problem. Another N^2 steps would take care of the multiplication of the inverse matrix by the vector giving us the representation of the incoming field. To understand this simple idea suppose that L_0 was the original matrix to be inverted and that the inverse of this matrix was R_0 . Suppose that the filled matrix at the new frequency was L_1 . It is easy to see that a noncommutative product rule holds for matrix derivatives. We know that if y_0 is the vector representation of the incoming radiation, then the vector representation x_0 of the internal fields is given by $R_0 \cdot y_0$. We suppose that $R(s)$ is the inverse of the matrix $L(s)$. The matrix product rule tells us that

$$L(s) \cdot R'(s) + L'(s) \cdot R(s) = \bar{0}$$

where $\bar{0}$ represents the derivative of the identity matrix. Since we know $L(s)$ and $L'(s)$ we can solve for the new inverse $R(s)$ of the matrix $L(s)$ by solving the matrix differential equation

$$R'(s) = -R(s) \cdot L'(s) \cdot R(s)$$

With an N^{2+} matrix multiplication, we in essence have a matrix inversion scheme of the same order.

We use the fact that we can multiply a an N by N matrix by a column vector in N^2 steps to get an inversion scheme that is guaranteed to be of order N^{2+} for arbitrarily small ϵ . We suppose that by some effort we have obtained an inverse for the matrix L_0 giving a solution vector x solving the equation,

$$L_0 \cdot x = y$$

by the rule

$$x = R_0 \cdot y$$

If we wished to know the response of the body to radiation of another frequency represented by a vector y_1 We would therefore consider the equation

$$L(s) \cdot x(s) = y_1$$

But if we write the inverse of $L(s)$ as $R_0 \cdot S$, then

$$[L_0 + (L(s) - L_0)] \cdot R_0 \cdot S = I$$

where I is the identity and this relationship becomes

$$[I + (L(s) - L_0) \cdot R_0] S = I$$

so that if $L(s)$ is fairly close to $L(0)$ we can write

$$S = \sum_{k=0}^{\infty} [(-1)^k ([L(s) - L_0] \cdot R_0)^k]$$

which means that we have a local power series representation of $R(s)$ and that in view of the fact that

$$x'(s) = R'(s) \cdot y_1$$

we get an ordinary differential equation for the solution vector given by

$$x'(s) = - R_0 \cdot \left\{ \sum_{k=0}^{\infty} [(-1)^k ([L(s) - L_0] \cdot R_0)^k] \right\} \cdot L'(s) \cdot x(s)$$

This means that we can just use R_0 and move along a solution path from the solution vector x_0 to the solution vector x_1 which will give the electric and magnetic vectors at the next frequency needed for the Fourier inversion. If we limit the number of terms in the series and always multiply matrix products by the column vectors first so that for example if A, B, and C were matrices and x were a column vector then

$$A \cdot B \cdot C \cdot x = A \cdot (B \cdot (C \cdot x))$$

can be carried out with less than $6 \cdot N^2$ multiplications and additions. This procedure is also valid for dispersive materials, and means that we do not need a separate matrix inversion, an N^3 process for each new frequency that is needed to represent the electromagnetic pulse.

Another concept is that if we can, in a highly accurate manner, represent the incoming radiation field with a small number of frequencies, then by inverting the integral operators we can solve for the induced internal electric fields at these frequencies, add them up and get the pulse response. I plan to adapt this sound idea by using a novel method of frequency partitioning that I developed under an effort concerning modeling the swimming motions of unflagellar microorganisms. The first graph shows the microscope slide data

and the graph below shows the very small number of frequencies needed to describe the oscillations perpendicular to the path along which this single celled creature is heading.

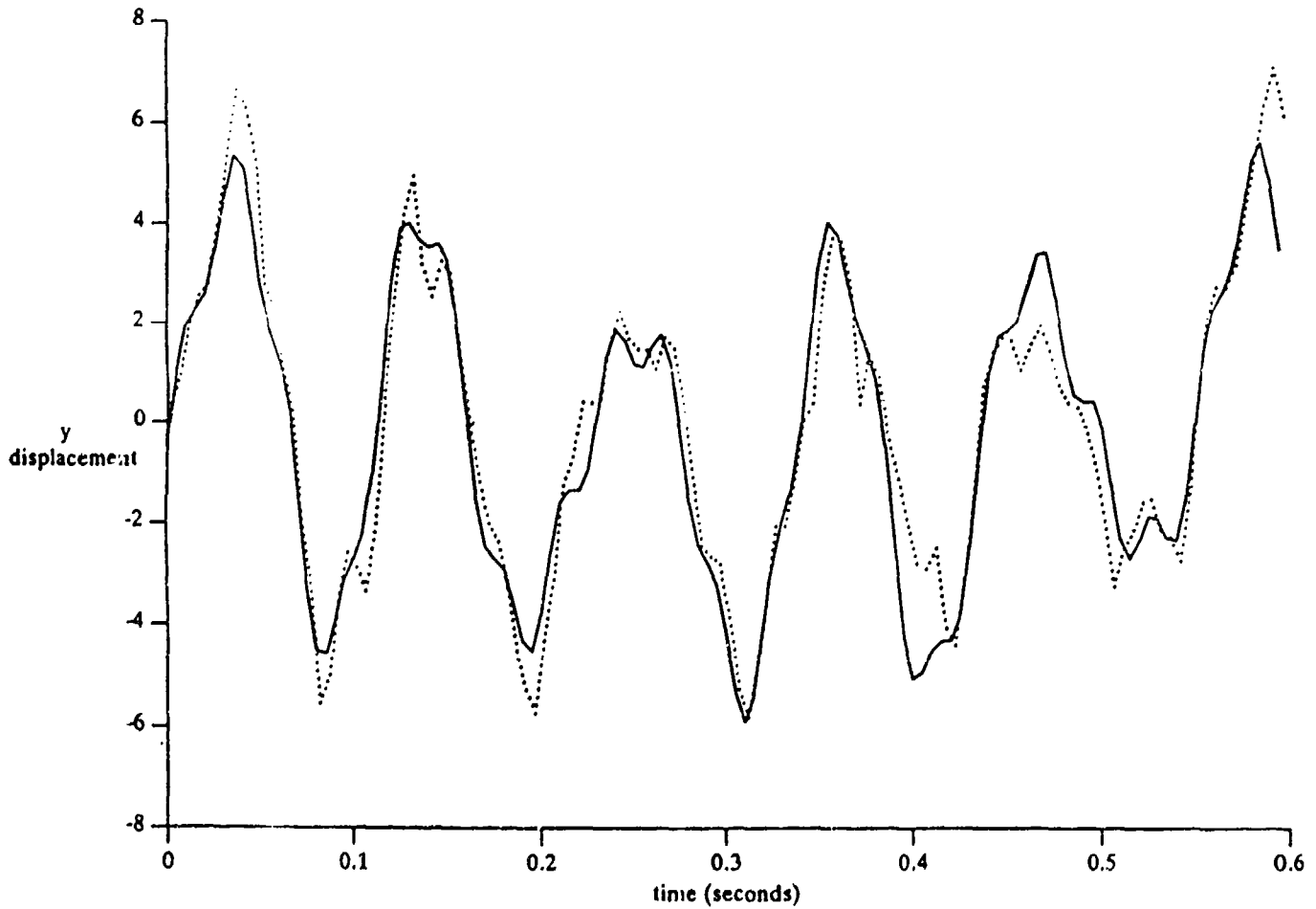
Cross track motion

A = -.7450419, B = 3.6563991, ω = 57.499979

A = 1.0479472, B = .65366872, ω = 1248.0990

A = -.56414504, B = -.80276769, ω = 80.815101

A = -.059328814, B = .66970221, ω = 217.76566



Note that in these two figures only four seemingly unrelated frequencies are significant, but if you tried a naive Fourier analysis using a base frequency ω_0 and its harmonics $2 \cdot \omega_0, 3 \cdot \omega_0, \dots$ then after a thousand terms you would be little better off than when you had started. I would therefore propose to model the incoming pulse using this same type of frequency partitioning that was so successful in my bihydrodynamics modeling. By the way, this same method could be used in computer speech recognition, handling spatial frequencies in a manner that would permit a satellite to remotely positively identify relocatable objects on the ground or in the air.

References

- [1] Abramowitz, Milton, and Irene Stegun. *Handbook of Mathematical Functions with Formulas, Graphs and Mathematical Tables. NBS Applied Math Series 55* Washington, D.C.: U.S. Government Printing Office (1972)
- [2] Barton, J. P., D. R. Alexander, and S. A. Schaub. "Internal fields of a spherical particle illuminated by a tightly focused laser beam: focal point positioning effects at resonance." *Journal of Applied Physics. Volume 65 No. 8* (April 15, 1989) pp 2900-2906
- [3] Barton, J. P., D. R. Alexander, and S. A. Schaub. "Internal and near surface electromagnetic fields for a spherical particle irradiated by a focused laser beam" *Journal of Applied Physics. Volume 64, no 4* (1988) pp 1632-1639.
- [4] Bell, Earl L., David K. Cohoon, and John W. Penn. *Mic: A FORTRAN program for computing power deposition in spherical dielectrics through application of Mic theory. SAM-TR-77-11* Brooks AFB, Tx 78235: USAF School of Aerospace Medicine (RZ) Aerospace Medical Division (AFSC) (August, 1977)
- [5] Bell, Earl L., David K. Cohoon, and John W. Penn. *Electromagnetic Energy Deposition in a Concentric Spherical Model of the Human or Animal Head SAM-TR-79-6* Brooks AFB, Tx 78235: USAF School of Aerospace Medicine (RZ) Aerospace Medical Division (AFSC) (December, 1982).
- [6] Brillouin, Leon. *Wave Propagation and Group Velocity*. New York: Academic Press (1960).
- [7] Burr, John G., David K. Cohoon, Earl L. Bell, and John W. Penn. Thermal response model of a Simulated Cranial Structure Exposed to Radiofrequency Radiation. *IEEE Transactions on Biomedical Engineering. Volume BME-27, No. 8* (August, 1980) pp 452-460.
- [8] Cohoon, D. K. "Uniqueness of electromagnetic interaction problems associated with bianisotropic bodies covered by impedance sheets" Rassius, George (Ed) *Heritage of Gauss* Singapore: World Scientific Publishing (1991)

- [9] Cohoon, D. K., J. W. Penn, E. L. Bell, D. R. Lyons, and A. G. Cryer. *A Computer Model Predicting the Thermal Response to Microwave Radiation SAM-TR-82-22* Brooks AFB, TX 78235: USAF School of Aerospace Medicine. (RZ) Aerospace Medical Division (AFSC) (December, 1982).
- [10] Cohoon, D. K. "An exact solution of Mie Type for Scattering by a Multilayer Anisotropic Sphere" *Journal of Electromagnetic Waves and Applications, Volume 3, No. 5* (1989) pp 421-448
- [11] Cohoon, D. K. "Free commutative semi-groups of right invertible operators with decomposable kernels" *Journal of Mathematical Analysis and Applications, Vol 19, Number 2* (August, 1967) pp 274-281.
- [12] Cohoon, D. K. "An exact formula for the accuracy of a class of computer solutions of integral equation formulations of electromagnetic scattering problems" *Electromagnetics Volume 7, Number 2* (1987) pp 153-165.
- [13] Daniel, Vera V. *Dielectric Relaxation* New York: Academic Press (1967).
- [14] Friedman, Avner. *Foundations of Modern Analysis* New York: Holt, Reinhart, and Winston (1970)
- [15] Glisson, A. K. and D. R. Wilton. "Simple and Efficient Numerical Techniques for Treating Bodies of Revolution" University of Mississippi: University, Mississippi USA 38677 *RADC-TR-79-22*
- [16] Gohberg, I. C. and I. A. Feldman. *Convolution Equations and Projection Methods for their Solution* Providence: American Mathematical Society (1974)
- [17] Guru, Bhag Singh and Kun Mu Chen. "Experimental and theoretical studies on electromagnetic fields induced inside finite biological bodies" *IEEE Transactions on Microwave Theory and Techniques, Volume MTT-24, No. 7* (1976).
- [18] Hagmann, M. J. and O. P. Gandhi. "Numerical calculation of electromagnetic energy deposition in man with grounding and reflector effects" *Radio Science Volume 14, Number 6* (1979) pp 23 -29
- [19] Hagmann, M. J. and O. P. Gandhi. "Numerical calculation of electromagnetic energy deposition for a realistic model of man." *IEEE Transactions on Microwave Theory and Techniques Volume MTT-27, Number 9* (1979) pp 804-809.
- [20] Hagmann, M. J. and R. L. Levin. "Nonlocal energy deposition - - problem in regional hyperthermia" *IEEE Transactions on Biomedical Engineering, Volume 33* (1986) pp 405 - 411.
- [21] Hörmander, Lars. *Linear Partial Differential Operators* New York: Academic Press (1963)
- [22] Jones, D. S. *Theory of Electromagnetism* Oxford: Pergamon Press(1964)

- [23] Kronsjo, Lydia. *Algorithms: Their Complexity and Efficiency, Second Edition* New York: John Wiley (1979)
- [24] Mautz, J. R. and R. F. Harrington. "Radiation and Scattering from bodies of revolution" *Applied Science Research. Volume 20* (June, 1969) pp 405-435.
- [25] Pan, Victor. "How can we speed up matrix multiplication" *SIAM Review. Volume 26, Number 3* (July, 1984) pp 393-415.
- [26] Pinnick, R. G. and J. D. Pendleton. *Applied Optics. Vol 29* (1990) page 918
- [27] Pinnick, R. G., P. Chylek, M. Jarzembki, E. Creegan, and V. Srivastava, G. Fernandez, J. D. Pendleton, and A. Biswas. "Aerosol induced laser breakdown thresholds wavelength dependence" *Applied Optics. Vol 27, No. 5* (March 1, 1988) pp 987-996
- [28] Sherman, George C. and Kurt Edmund Oughston. "Description of pulse dynamics in Lorentz media in terms of energy velocity and attenuation of time harmonic waves." *Physical Review Letters, Volume 47, Number 20* (November, 1981) pp 1451 - 1454.
- [29] Strassen, Volker. "Gaussian Elimination is not Optimal" *Numerical Math. Vol 19* (1969) pp 184-204.
- [30] Whittaker, E. T. and G. N. Watson. *A Course of Modern Analysis* London: Cambridge University Press (1986).

Blank

MANIPULATION OF MICROPARTICLES IN MULTIPHASE LEVITATION TRAPS

E.E. Allison, B.R.F. Kendall, B.V. Bronk*, and D.S. Weyandt

Department of Physics
The Pennsylvania State University
University Park, PA 16802

*U.S. Army CRDEC
Aberdeen Proving Ground, MD 21010

RECENT PUBLICATIONS, SUBMITTALS FOR PUBLICATION, AND
PRESENTATIONS

B.R.F. Kendall, D.S. Weyandt, and M.F. Vollero, "Multiphase Electrodynamic Trapping and Manipulation of Microparticles", Proceedings of the 1991 CRDEC Scientific Conference on Obscuration and Aerosol Research.

ABSTRACT

Electrodynamic levitation traps are used to suspend and electrically manipulate charged microparticles. Isolation of a particle from a group, transfer of particles from one trap to another, and the merging of suspended aerosols of opposite charge are described. Future work involving particle isolation and the suspension of microparticles in a gas flow is previewed.

INTRODUCTION

Electrodynamic levitation traps were originally developed by Wuerker¹, et al, in connection with fusion research in the late 1950's. Under the simplest condition of a single particle in an evacuated trap, particle motion is described by a set of Mathieu differential equations. If the magnitude and frequency of the AC drive voltage to the trap are in the stable range for a given particle charge-to-mass ratio, stable levitation will occur. When a group of particles is levitated, particle-to-particle interaction (due to like electrical charge) causes the particles to form an array distributed about the geometric center of the trap. If the trap is not evacuated the stability limits for levitation are extended due to the damping effect of the air on particle motion.

In general, levitated particles are held in orbits within the trap with the diameter of the orbit increasing as the average distance between the particle and the geometric center of the trap increases. Thus, a particle becomes nearly stationary at the center of the trap. Due to the effects of gravity and particle to particle interaction, a particle will not normally be at the trap center. DC cross-fields may be added to the AC

levitation fields to position particles within the trap as desired.

EQUIPMENT DESCRIPTION

A cubical trap geometry with six planar electrodes and 2ϕ AC drive as described by Kendall², et al, was used for this work. The inside dimension of the trap was 3.2 cm on a side. The sides were constructed of Plexiglas with small holes at their centers for particle illumination and observation. The top and bottom were made from aluminum disks with holes at their centers through which particles could be injected. The electrodes were mounted to the inside of the cube and were made of a fine wire mesh. Two traps were joined together with a common mesh electrode to form a dual chamber trap for particle transfer work.

AC drive on the order of 2 kV rms 2ϕ (60°) from 50 to 200 Hz was used to drive the trap. Three DC cross-fields were used to position the particles along the X, Y, and Z axes. A 5 watt argon laser operating at about 2.5 watts was used to illuminate the trap through the bottom mesh electrode. A beam spreader was used to expand the laser beam for more complete illumination of the trap.

Particles were injected into the top of the trap in all cases. Glass beads of a nominal 20 μm diameter were used for solid particles. They were launched from an aluminum cup, with a small hole in the bottom, which was elevated to 20 kV. Aerosol particles of approximately 50 μm diameter were produced by two modified perfume sprayers with their metallic atomizers connected to high voltage power supplies.

ISOLATION OF A PARTICLE

A single levitated particle can be isolated from a group of levitated particles. This is done by positioning the desired particle at the center of the trap with DC cross-fields and then momentarily switching off the AC drive to the trap. Since the desired particle is at the center of the trap it is nearly stationary while all other particles have velocities dependant upon their position within the trap. Thus, when the AC is switched off all the particles but the desired one tend to fly off and be lost. This process may have to be repeated several times to clear the trap of undesired particles.

Further experimentation with particle isolation is planned. At present, successful isolation depends upon a skilled operator and all particles but the desired one are lost. Feedback control methods might be employed to hold the desired particle at the trap center while the AC drive is switched off. Also, an isolation method which allows a desired particle to be removed from a group, without particle loss, might be possible by using a small capture trap within a larger trap containing the group of particles under study.

TRANSFER OF PARTICLES BETWEEN TRAPS

Two levitation traps were joined together with a common wire mesh electrode as previously described. DC cross-fields were then used to force the particles from one trap into the other where they were recaptured.

AC drive was applied to each of the traps in parallel by connecting corresponding side electrodes together. The top, common, and bottom electrodes were operated at AC ground. The top and bottom electrodes were electrically connected together. DC cross-fields were then produced by applying a DC potential between the common electrode and the top and bottom electrodes. This arrangement made it possible to force levitated particles from one trap into the other by controlling the DC cross-field magnitude and polarity during the transfer.

Charged particles were first launched into the top trap with the DC cross-field adjusted to neutralize gravity and aid in particle capture. The cross-field was then reversed and increased in magnitude to expel the particles from the top trap into the lower one. At this point, the DC cross-field had to be quickly reversed to its previous value to permit levitation in the lower trap. This method worked better when the particles were moved from the upper trap to the lower than in the reverse direction. This difficulty was overcome by using independent cross-fields for the upper and lower traps but the equipment became more difficult to operate. Particle transfer was also done horizontally by similar techniques.

MERGING OF SUSPENDED AEROSOLS

Charged aerosol particles were produced by the modified perfume sprayers previously discussed. Two sprayers were used. The first was filled with a water and glycol mixture (20% glycol by volume) and was operated with a 20 kV charging potential. The second was filled with water, glycol, and Rhodamine B dye and was operated at -100 V charging potential.

Aerosol particles from the first sprayer were levitated first. Then, a lightly charged aerosol of the opposite charge was injected into the trap from the second sprayer. Since the charge-to-mass ratios of the particles in the second aerosol were very low, they did not levitate but were attracted to the levitated particles of the first aerosol (due to opposite charge) causing the particles to merge.

The merging of particles was easily detected since the levitated particles became dyed as they merged with injected particles which contained the dye.

Since the dyed particles were lightly charged and had similar masses to the levitated ones, particles produced from a merger had only about half the charge-to-mass ratio of the

original levitated ones. Despite this, the stable range of the particle trap was sufficient to permit the merged particles to remain in levitation.

PARTICLE LEVITATION IN A GAS FLOW

A levitation trap is presently being used to levitate microparticles in a laminar gas flow. The object of this work is to create an environment for studying the microphysical and chemical behavior of particles typical of the lower stratosphere.

A DC cross-field is used to balance the force of the gas upon the particles. Testing to date has used 20 μm glass beads in gas flows up to 20 cm/s.

Additional tests are planned using submicron aqueous particles in reagent gas flows up to 10 cm/s. Gas temperature and pressure will then be controlled within the trap to simulate lower stratospheric conditions.

REFERENCES

1. R. F. Wuerker, H. Shelton and R. V. Langmuir, *Journal of Applied Physics* Vol. 30, 342 (1959).
2. B. R. F. Kendall, D. S. Weyandt and M. F. Vollero, *Proceedings of the 1991 CRDEC Scientific Conference on Obscuration and Aerosol Research*.

CW STIMULATED RAMAN SCATTERING IN MICRODROPLETS

J. D. Eversole
Potomac Photonics Inc.
Lanham, MD 20706

A. J. Campillo and H-B. Lin
Naval Research Laboratory
Washington, D. C. 20375-5000

Recent Journal Papers (7/91-6/92)

This work:

* H-B. Lin, J. D. Eversole and A. J. Campillo, "Continuous-wave stimulated Raman scattering in microdroplets", *Optics Lett.*, **17**, 828-30 (1992).

Related cavity QED work:

* A. J. Campillo, J. D. Eversole and H-B. Lin, "Cavity quantum electrodynamic enhancement of stimulated emission in microdroplets", *Phys. Rev. Lett.* **67**, 437-40 (July 22, 1991).

* H-B. Lin, J. D. Eversole and A. J. Campillo, "Spectral properties of lasing microdroplets", *JOSA B*, **9**, 43-50 (1992).

* H-B. Lin, J. D. Eversole, C. D. Merritt and A. J. Campillo, "Cavity-modified spontaneous emission rates in liquid microdroplets" *Phys. Rev. A* **45**, 6756-60 (1992).

* A. J. Campillo, J. D. Eversole and H-B. Lin, "Cavity quantum electrodynamic enhancement of spontaneous and stimulated emission in microdroplets", *Mod. Phys. Lett. B*, **6**, 447-457 (1992).

Other related work:

* P. Chýlek, H-B. Lin, J. D. Eversole and A. J. Campillo, "Absorption effects on microdroplet resonant emission structure", *Opt. Lett.* **16**, 1723-25 (November 15, 1991).

* J. D. Eversole, H-B. Lin and A. J. Campillo, "Cavity mode identification of fluorescence and lasing in dye doped microdroplets", *Appl. Optics*, **31**, 1982-1991 (1992).

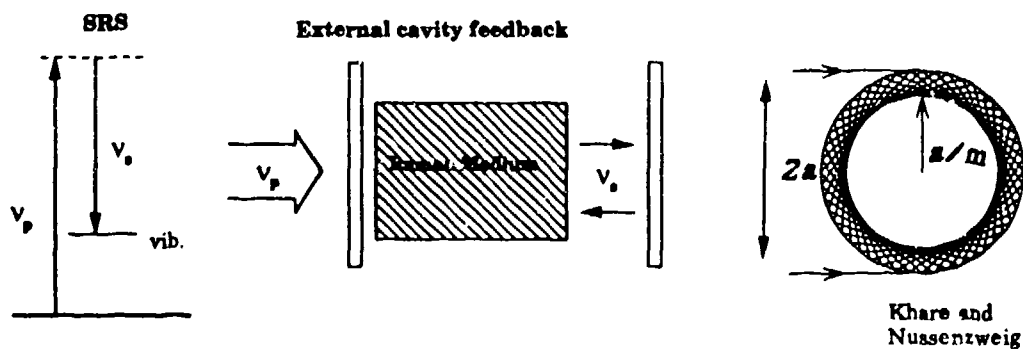
* H-B. Lin, A. L. Huston, J. D. Eversole, A. J. Campillo and P. Chýlek, "Internal scattering effects on microdroplet resonant emission structure", *Opt. Lett.*, **17** (July 15, 1992).

Abstract

Continuous wave stimulated Raman scattering was observed in 11 to 13 μm diameter benzene and toluene microdroplets at pump intensities as low as 8 kW/cm^2 and 24 kW/cm^2 , respectively. Low thresholds were achieved by exploiting : (1) simultaneous pump and Stokes wave resonance in the droplets and (2) Raman gains that were cavity QED enhanced $\approx 50 \text{ X}$ with respect to bulk liquid values. Based on a photon state conservation argument, the cavity gain enhancement factor may be approximated by the ratio of spectral spacing between resonant modes of the same order to that of the homogeneous Raman linewidth. This relation appears to be consistent with the relative experimental behavior of benzene, ethanol and toluene.

Introduction

Cross sections for spontaneous Raman scattering are typically quite small, and those for stimulated Raman (SRS) are correspondingly much lower, which is why SRS is normally reported using high peak power pulsed laser pumps. Most of the comparatively few reports of cw SRS employed an external cavity to enhance the pump and SRS signal intensities. Figure 1 contains a schematic energy level diagram of the SRS process and external cavity arrangement for a bulk medium, and also introduces the idea of a sphere (liquid droplet) as a natural optical cavity¹. Radiation may be trapped in this type of geometry by the mechanism of total internal reflection.



There are two advantages of using a cavity resonator

Fig. 1.

1. Concentration of pump radiation
2. Redistribution of density of final photon states

In addition to multiplying the pump intensity, a cavity also causes redistribution of the photon final states in phase space compared to the free space environment for a radiating molecule. Such redistribution can result in an apparent enhancement in the stimulated Raman cross section (also referred to as QED enhancement) and will be discussed later.

Radiation becomes trapped at particular resonance values of the ratio of the droplet circumference $2\pi a$ to the incident wavelength λ (known as the size parameter x). Referred to as morphology dependent resonances (MDR's), their positions can be calculated from Lorenz-Mie theory², and each has a unique internal field distribution (cavity mode) which can be cataloged by integers n (mode number) and l (mode order). Each resonant mode is either transverse electric or magnetic (TE or TM) and has a characteristic quality factor $Q = x_{nl}/\Delta x$, where Δx is the width of the resonance. In Fig. 2 typical plots are shown of the calculated internal field distributions for the particular modes indicated across the equatorial plane of the droplet^{3,4}. Emission spectra are also shown recorded as a function of wavelength in dye-doped droplets⁵. Intensity peaks occur at MDR positions due to the increased density of photon states. Below the spectra, computed positions are indicated by arrows pointing up (down) for TE (TM) polarization and are offset vertically to indicate mode order. The lowest order modes have the highest theoretical Q's. In the cw SRS study, the pump radiation is fixed and the droplet size is varied to achieve resonance conditions.

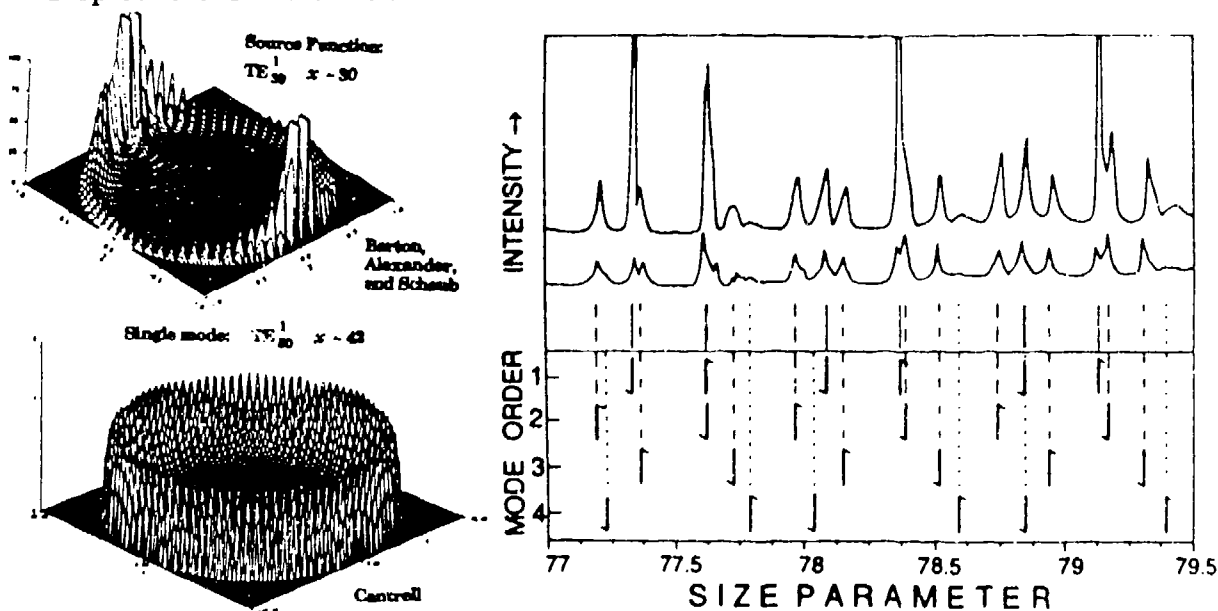


Fig. 2. Cavity Mode Properties

Experimental

To study the optical properties of droplets, a monodisperse stream of either benzene, toluene or ethanol droplets tunable in diameter from 11 to 13 μm was produced using a vibrating-orifice droplet generator with a 5 μm diameter orifice⁶. Droplets were optically pumped as they fell through a 514.5 nm wavelength cw argon-ion laser beam focused to a 40 μm spot diameter. The droplet size and refractive index were determined by matching the measured fixed-angle elastic laser scattering near 90° as a function of the generator frequency (see Fig. 3a) to the computed scattering intensities as previously described^{5,6,7}. Spectral composition of radiation emitted by the droplet at $\approx 120^\circ$ scattering angle was examined using a 1 meter double monochromator with a resolution of $\approx 2.25 \text{ cm}^{-1}$ and equipped with a cooled photomultiplier and photon counting system (see Fig. 4b).

Fig. 3a shows a typical 514.5 nm elastic scattering spectrum from a benzene droplet stream. Figure 3b is the corresponding frequency plot of the total Raman signal at $542 \pm 1 \text{ nm}$ due to the 992 cm^{-1} C-C stretch vibrational mode. One large peak and several smaller ones appear in the orifice frequency spectrum. Fig. 4a shows the spectral dependence of the 992 cm^{-1}

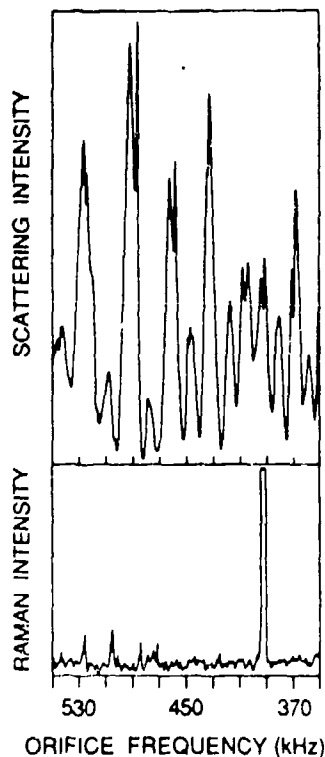


Fig. 3. SRS Observed As A Double Resonance Effect

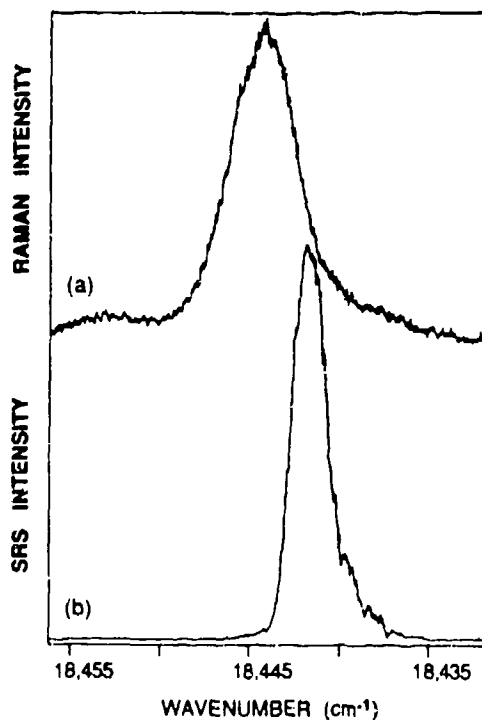


Fig. 4. Spontaneous and Stimulated Raman Spectra

spontaneous Raman emission (width $\approx 2.5 \text{ cm}^{-1}$) from a 1 cm long sample of benzene. Fig. 4b shows the spectral dependence of the Raman emission from the droplet stream under conditions (droplet radius, $a \approx 6.4 \mu\text{m}$) corresponding to the large peak at 390 kHz in Fig. 3b. These size droplets lead to the fortuitous placement of high Q cavity modes very nearly coincident with both pump and Raman wavelengths. As shown in Fig. 4b, shifts of several cm^{-1} from line center were common. We calculate that for droplets of this size, first and second order² TE and TM output modes have theoretical Q's in excess of 10^7 and there are 3 orders of input TE and TM modes having Q's $> 5 \times 10^4$. The experimentally achievable Q's, however, may be limited to values lower than 10^7 by laser induced droplet heating/distortion. The spectral spacing $\Delta\nu$, between modes of the same order and polarization is approximated² by: $(\arctan[(m^2-1)^{1/2}])/2\pi a(m^2-1)^{1/2}$, where m is the index of refraction; for $a \approx 6.4 \mu\text{m}$, $(\Delta\nu) \approx 190 \text{ cm}^{-1}$

Observed nonlinear power dependence of the emission (Fig. 5) is indicative of SRS oscillation with a pump threshold of ca. 50 mW for benzene (open circles). A second Stokes SRS signal at 1984 cm^{-1} , having an amplitude about an order of magnitude lower than that of the first Stokes, was also observed. Up to 14 orders of Stokes waves have previously been observed in pulsed experiments⁸ in larger droplets where the probability of aligning appropriate modes within the respective narrow Stokes gain profiles was more favorable. The 50 mW threshold power corresponds to an incident intensity I_0 of only 8 kW/cm^2 . The intensity of the resonant pump within the cavity I_p has been shown⁹ to be greater by a factor of $f/[4\pi^2 a m \delta\nu_L]$ when $Q > \nu/\delta\nu_L$. Here $\delta\nu_L$ is the spectral width of the argon ion laser, measured with a scanning Fabry-Perot interferometer to be about 0.3 cm^{-1} . Therefore, the intensity inside the droplet when the pump is resonant with a high Q mode is $\approx 0.3 \text{ MW/cm}^2$.

Note that the effective intensity may vary due to partial spatial overlap between the input and output modes represented as f and taken to be ≈ 0.5 here. Assuming an output mode Q of 10^7 , a benzene Raman gain of 3 cm/GW , and a resonant mode located on the shoulder of the Raman line (i.e. $1/2$ gain as in Fig. 2), the SRS pump threshold intensity should be at least a factor of 70 higher than actually observed.

These results and conclusions for the benzene experiment are summarized in Table 1. The apparent enhancement of the stimulated Raman gain is denoted as κ , and can be explained in terms of QED effects discussed below.

Table 1
cw SRS in Benzene

- Measured SRS threshold: $I \approx 8 \text{ kW/cm}^2$
- $I_p \approx I_0 f/4\pi^2 m \delta\nu a \approx 0.3 \text{ MW/cm}^2$,
since $a \approx 6 \mu\text{m}$, $\delta\nu \approx 0.3 \text{ cm}^{-1}$ and $f \approx 0.5$.
- At threshold, gain = loss: $g_c I_p \geq 2\pi m/Q\lambda$
for $Q \approx 10^7 \rightarrow g_c \approx 210 \text{ cm/GW}$,
but bulk gain $g_0 \approx 3 \text{ cm/GW}$.

Therefore: $K_{\text{exp.}} = g_c/g_0 \approx 70$

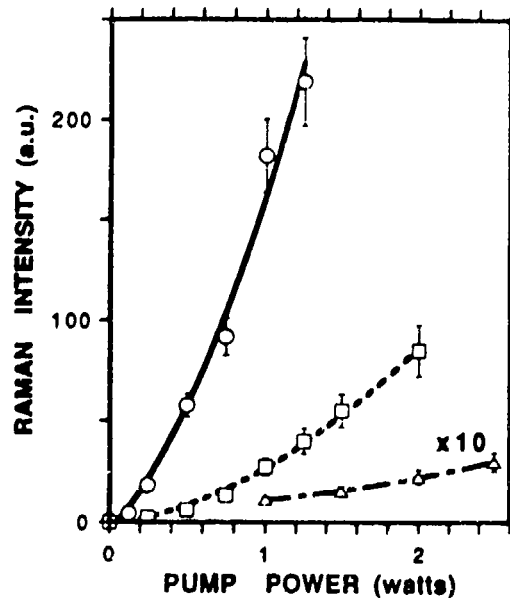


Fig. 5. SRS Nonlinear Pump
Dependence

QED Effects

A simple heuristic model which conveys a physical idea of how transition rates are affected by electromagnetic boundary conditions inside a cavity can be presented in terms of the density of final photon states $\rho(\nu)$. The radiative transition probability for a quantum system (molecule) as given by Fermi's Golden rule includes a factor of $\rho(\nu)$. In free space this quantity is easily shown to be proportional to ν^2 which is nearly constant (ρ_0) over a given narrow range (emission bandwidth) as shown in Fig. 6a. When a molecule is introduced to a cavity the total number of final states is conserved, but the density is redistributed so the emission probability at resonant frequencies is increased while emission at nonresonant frequencies is inhibited. The cavity state distribution can be approximated by Lorentzian lineshapes centered at resonant frequencies with appropriate widths as shown in Fig. 6b. For regular periodic spacing of resonances $\Delta\nu_{\text{MDR}}$, the conserved number of states, $\rho_0\Delta\nu_{\text{MDR}}$, is indicated by the shaded areas in Figs. 6a and 6b. The gain profile is characteristic of the molecule and in free space the observed emission profile simply reflects the shape of the molecular profile since $\rho(\nu)$ is flat (Fig. 6c). The actual gain will be proportional to the total number of photon states available to the molecule under its gain profile and in free space is just $g_0 = \rho_0 \Gamma$ (where Γ is the profile width), while in the cavity: $g_c = \rho_0\Delta\nu_{\text{MDR}}$. Thus the QED enhancement: $\kappa = g_c / g_0 = \Delta\nu_{\text{MDR}} / \Gamma$.

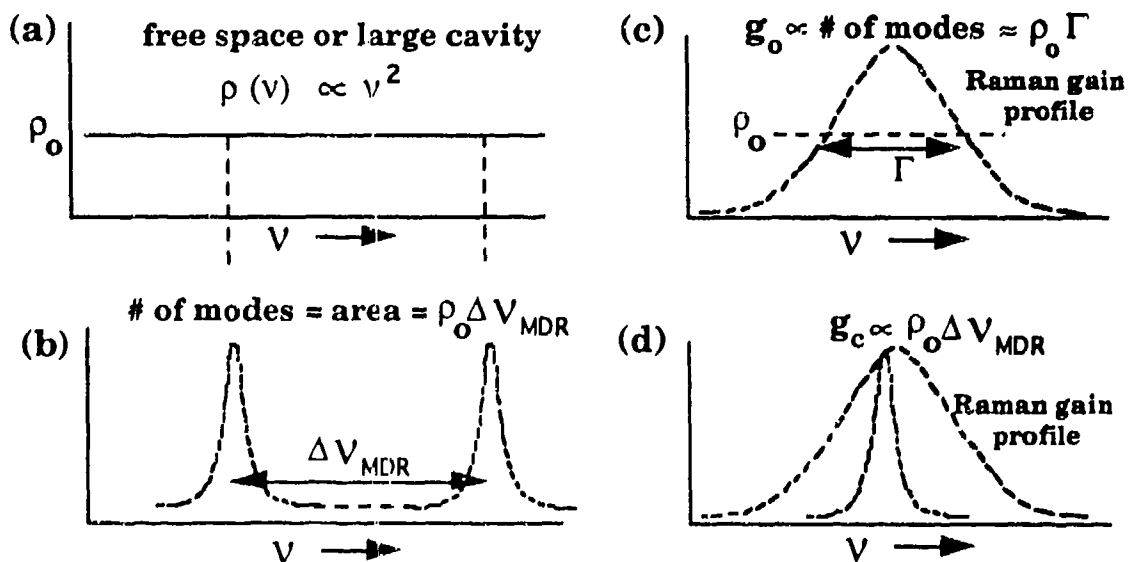


Fig. 6 QED Gain Enhancement

Conclusion

To see if this simple model is valid for the case of benzene, we have: $\Gamma \approx 2 \text{ cm}^{-1}$ and for $6 \mu\text{m}$ droplet radii, $\Delta\nu_{\text{MDR}} \approx 190 \text{ cm}^{-1}$ resulting in a predicted κ of ≈ 95 consistent with the experimentally observed enhancement of 70. To further test the model, other liquids (toluene and ethanol) with different Raman linewidths were studied in similar sized droplets under identical experimental conditions. Toluene possesses a Γ similar to benzene but has a 2.3X lower free space Raman gain. Ethanol has a free space SRS gain equal to toluene (1.3 cm/GW) but has a Γ that is significantly broader than either benzene or toluene. The homogeneous bandwidth is inversely proportional to the dephasing time of the vibrational modes¹⁰. These lifetimes have been estimated to be 2.6 psec and 0.25 psec for toluene¹⁰ and ethanol¹¹, respectively, and so $(\Gamma)_{\text{EtOH}}/(\Gamma)_{\text{Tol}} \approx 10$. The growth curves of the emission output with pump intensity for toluene and ethanol droplets are plotted in Fig. 5 with open squares and triangles respectively. The emission from ethanol was weak spontaneous Raman scattering as its SRS threshold was not achieved at the maximum pump intensity of 2.5 W. This result is consistent with the predicted lower QED enhancement of Raman gain due to the much broader linewidth of ethanol. Toluene has the same bulk Raman gain as ethanol but since its linewidth is a factor of 10 narrower, it was observed to have an SRS threshold at 150 mW. The expected threshold for ethanol at $\approx 1.5 \text{ W}$ was not observed because at high pump intensities the effective Q of the mode will be degraded by thermal perturbations. Table 2 summarizes the results of the three liquids investigated, listing their bulk Raman gain g_o , Raman linewidth Γ , predicted cavity gain g_c (assuming $Q \approx 10^7$), and observed SRS threshold I_p .

Table 2

	g_o (cm/GW)	Γ (cm^{-1})	g_c (cm/GW)	I_p (mW)
Benzene	3.0	2	300	50
Toluene	1.3	2	130	150
Ethanol	1.3	>20	<10	>2500

The significant points of this paper may be summarized as follows:

- **First observation of cw SRS in microdroplets**
- **pump radiation or "input" resonant with droplet necessary**
- **gains appear enhanced by $\approx 100\times$ consistent with simple mode density model of:**
$$g_c \propto g_o \left\{ \frac{\Delta v_{MDR}}{\Gamma} \right\}$$
- **relative experimental behavior of benzene, toluene, and ethanol consistent with model**

References

1. V. Khare and H. M. Nussenzweig, "Theory of the glory", *Phys. Rev. Lett.* **38**, 1279-82 (1977).
2. S. C. Hill and R. E. Benner, "Morphology-Dependent Resonances," in *Optical Effects Associated with Small Particles*, P. W. Barber and R. K. Chang, ed. (World Scientific, New Jersey, 1988) p.3-61.
3. J. P. Barton, D. R. Alexander, and S. A. Schaub, *J. Appl. Phys.* **65**, 2900 (1989).
4. C. D. Cantrell, *J. Opt. Soc. Am. B* **8**, 2181 (1991).
5. J. D. Eversole, H-B. Lin and A. J. Campillo, *Appl. Opt.* **31**, 1982 (1992).
6. H-B. Lin, J. D. Eversole and A. J. Campillo, *Rev. Sci. Instrum.* **61**, 1018 (1990).
7. J. D. Eversole, H-B. Lin, A. L. Huston and A. J. Campillo, *J. Opt. Soc. Am. A*, **7**, 2159 (1990).
8. S-X. Qian and R. K. Chang, *Phys. Rev. Lett.*, **56**, 926 (1986).
9. H-B. Lin, A. L. Huston, J. D. Eversole and A. J. Campillo, *J. Opt. Soc. Am. B*, **7**, 2079 (1990).
10. W. R. L. Clements and B. P. Stoicheff, *Appl. Phys. Lett.*, **12**, 246 (1968).
11. D. von der Linde, A. Laubereau and W. Kaiser, *Phys. Rev. Lett.*, **26**, 924 (1971); **27**, 802 (1971); **28**, 1162 (1972).

Blank

CAVITY-ENHANCED RHODAMINE 6-G SPONTANEOUS EMISSION RATES
IN LEVITATED MICRODROPLETS

M. D. Barnes, W. B. Whitten, and J. M. Ramsey
Analytical Chemistry Division,
Oak Ridge National Laboratory
Mail Stop 6142
Oak Ridge, Tennessee 37831

S. Arnold
Microparticle Photophysics Laboratory
Polytechnic Institute of New York
333 Jay Street, Brooklyn, New York 11201

RECENT/SUBMITTED PUBLICATIONS

(1) M. D. Barnes, W. B. Whitten, S. Arnold, and J. M. Ramsey, "Homogeneous Linewidths of Rhodamine 6G at Room Temperature from Cavity-Enhanced Spontaneous Emission Rates", *J. Chem. Phys.*, submitted August 1992.

ABSTRACT

Fluorescence decay kinetics of Rhodamine 6-G molecules in levitated glycerol microdroplets (4 -20 microns in diameter) have been investigated to determine the effects of spherical cavity resonances on spontaneous emission rates. For droplet diameters greater than 10 microns, the fluorescence lifetime is essentially the same as in bulk glycerol. As the droplet diameter is decreased below 10 microns, bi-exponential decay behavior is observed with a slow component whose rate is similar to bulk glycerol, and a fast component whose rate is as much as a factor of 10 larger than the bulk decay rate. This fast component is attributed to cavity enhancement of the spontaneous emission rate and, within the weak coupling approximation, a value for the homogeneous linewidth at room temperature can be estimated from the fluorescence lifetime data.

1. INTRODUCTION

The ability to modify emission rates from atoms or molecules in an excited state is of great importance since experimental control over the pathway for excited state deactivation can be obtained. For example, inhibition of spontaneous emission can be used to direct excited state chemical reactions and multi-photon processes. Alternatively, enhancement of spontaneous emission rates could lead to increased sensitivity in low-level fluorescence applications such as DNA sequencing or effluent tracing requiring single-molecule detection limits.[1,2] Recently, both enhancement and inhibition of spontaneous emission have been demonstrated for chelated ions.[3] However, whether such effects could be observed for polyatomic dye molecules was uncertain principally because it was assumed[4,5] that large homogeneous linewidths (taken to be approximately equal to the fluorescence spectral width) would result in, at best, only a small emission rate enhancement. In this paper, we show that a dramatic increase in fluorescence emission rate occurs in glycerol microdroplets, implying that the homogeneous linewidth is actually only a fraction of the fluorescence spectral width.

Fermi's "Golden Rule", given Eqn. 1, provides a basic understanding of how emission rates can be modified by the geometrical structure of the matrix in which the atom or molecule is solvated. The transition rate from state i to state j may be expressed as, [6]

$$A_{i \rightarrow j} = \frac{1}{\hbar^2} \langle i | H_{ij} | j \rangle^2 \rho(\nu) \quad (1)$$

where \hbar is Planck's constant, $\langle i | H_{ij} | j \rangle$ is the volume-normalized Hamiltonian matrix element representing the atom-field interaction, and $\rho(\nu)$ is the density of final photon states. Placing the emitter inside an optical cavity whose dimension is on the same order as the transition wavelength causes the emitted light to be coupled into discrete cavity modes rather than into the continuum of vacuum states. Since the density of states is large when ν corresponds to an allowed cavity mode, and small when ν is non-resonant, the emission rate will be modified (enhanced or inhibited) depending upon whether

the emission frequency corresponds to a particular allowed cavity mode.[7]

Modification of spontaneous emission rates was first observed by Drexhage and co-workers[8] by measuring emission rates from europium ions layered in Langmuir-Blodgett films above a reflective surface. Using a waveguide structure as a linear micro-cavity, Kleppner and co-workers[9] were able to demonstrate inhibited spontaneous emission of Rydberg atoms at microwave frequencies. De Martini and co-workers[10] demonstrated both enhancement and inhibition of spontaneous emission at optical frequencies using a linear tunable Fabry-Perot cavity. However, with the exception of the work of Drexhage and co-workers, these investigations all involved linear micro-cavities where, despite the simple geometry, exact calculations of internal fields are not possible. The spherical cavity offers a geometry which is much more amenable to theoretical modeling since all fields and modes are exactly calculable from Lorenz-Mie theory.[11]

It has been known for some time that micrometer sized dielectric spheres act as high Q resonators, where photons propagate around the sphere near its edge. Spherical cavity modes in these microspheres arise from so-called "morphology dependent resonances", or MDRs, which occur at specific values of the size parameter, X, where $X = 2\pi a/\lambda$, a is the radius of the sphere, and λ is the wavelength of light. Cavity effects such as stimulated emission[12] and lasing[13,14] from liquid microdroplets have been reported. Recently, Campillo and co-workers have demonstrated cavity enhanced spontaneous emission of chelated Europium ions in a stream of falling ethanol droplets[15] and observed an increase in the spontaneous emission rate of a factor of 2.5 above the bulk value. These authors argue that, in the regime where the cavity mode spacing ($\Delta\nu_C$) > homogeneous linewidth (Γ_{HB}) > cavity mode bandwidth (δ_C), the enhancement can be approximated by the ratio

$$\xi = \Delta\nu_C / \Gamma_{HB} \quad . \quad (2)$$

If Γ_{HB} is much narrower than $\Delta\nu_C$, large enhancements similar to those predicted by the Purcell equation[7] should be observed. Conversely, if Γ_{HB} is larger than $\Delta\nu_C$, no enhancement should be observed. Thus, the cavity mode spacing is an extremely important parameter in determining the magnitude of enhancement in these microdroplets. Because the cavity mode spacing can be estimated based on a knowledge of the droplet diameter, it is possible to

determine the homogeneous linewidth of a fluorescing molecule by measuring the fluorescence lifetime.

In this paper, we present the results of fluorescence lifetime measurements of Rhodamine 6-G in glycerol droplets with diameters ranging from 4 - 20 microns. The enhancement is large (10 x) for the smallest droplets and decreases with increasing droplet diameter, and does not appear to be attributable to droplet lasing or stimulated emission. Modeling the variation of decay rate enhancement using Eqn. 2 with different values of Γ_{HB} suggests a value of about 100 cm^{-1} for the homogeneous linewidth of R6G in glycerol at room temperature.

2. EXPERIMENTAL

Spontaneous emission rates of Rhodamine 6-G in levitated microdroplets were measured using a time-correlated photon counting technique.[16] The experimental setup is shown schematically in Figure 1. Briefly, a glycerol droplet with a concentration of R6G ranging from 10^{-7} to 10^{-5} M is levitated in an electrodynamic trap. A mode-locked Ar^+ laser (Spectra Physics 171) supplies the short (150 ps fwhm) 514 nm excitation pulses and the repetition rate was reduced to 4 MHz using an acousto-optic cavity dumper (Spectra Physics 344) as an extra-cavity pulse selector. The laser beam was focused to a $50 \text{ }\mu\text{m}$ waist giving a peak intensity at the droplet of about 70 KW/cm^2 with pulse energies of about 100 pJ.

The droplet generator and electrodynamic trap have been described in detail elsewhere.[17] Rhodamine 6G solutions in glycerol were diluted in ultrapure water (Carolina Biological Supply Co.) by a factor of 20 - 100. Approximately 100 μL of this solution was drawn into the tip of a microdroplet generator and a voltage pulse applied to a piezoelectric transducer in the generator produces an acoustic wave which forces a droplet out of the tip. Initially, the droplet diameter is about the same as the tip orifice ($40 \text{ }\mu\text{m}$) but rapid evaporation of water leaves a nominal diameter between 5 and $15 \text{ }\mu\text{m}$ depending on the relative amount of glycerol added to the solution.

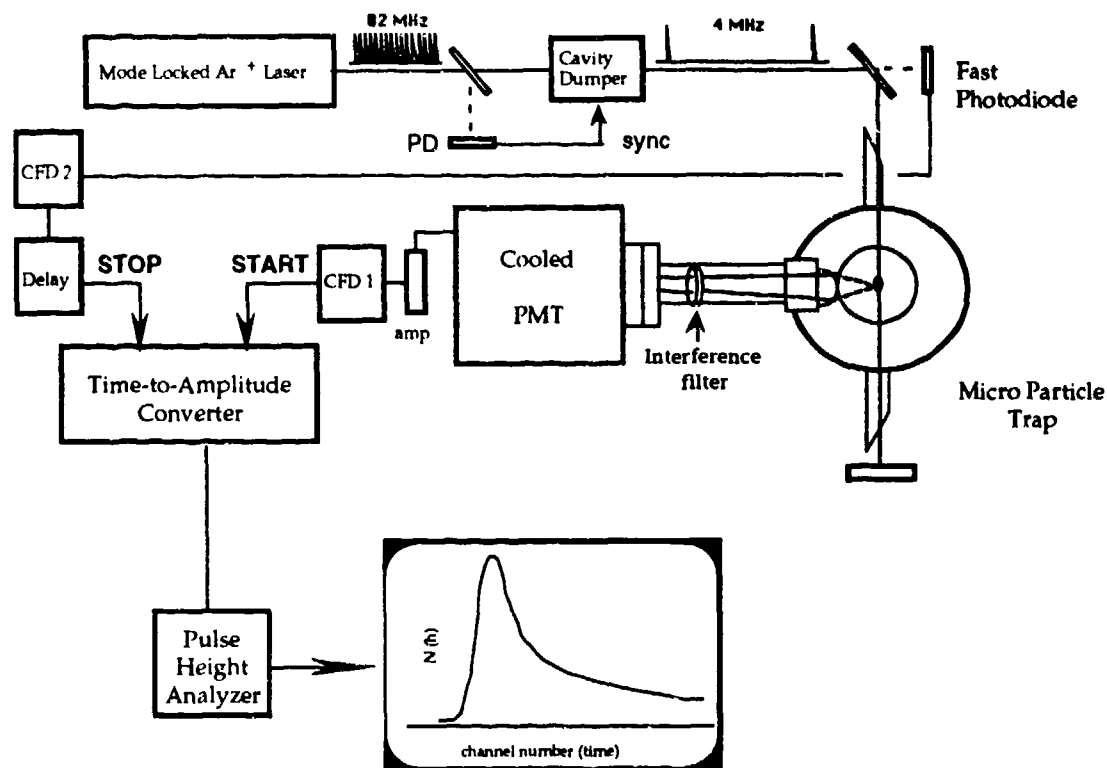


Figure 1. Schematic of experimental apparatus used to measure R6G fluorescence lifetimes in levitated microdroplets.

Fluorescence from the droplet is collected by a 3 mm diameter GRIN lens with 0.25 pitch and a 20X microscope objective focuses the image through a 1.5 mm spatial filter onto a cooled photomultiplier tube (Hamamatsu R943-02). An interference filter centered at 575 nm with 26 nm bandwidth (Omega Optical 575 DF26) spectrally filters the fluorescence and two Corning 3-66 long pass filters are also used to ensure that no elastically scattered photons are detected during a fluorescence lifetime measurement. In these experiments, a 16 nanosecond time window divided into 512 channels was used, with each channel having a width of about 33 picoseconds.

In a time-correlated single photon counting experiment, it is essential that only one photon is detected per excitation pulse as multiple START pulses

encountered during the voltage ramp can cause distortions in the timing spectrum.[18] For most of the fluorescence lifetime measurements, the laser intensity was sufficiently low enough so that no additional attenuation of the input beam was necessary. Typical fluorescence count rates were between 0.1 and 10 KHz; thus the probability of two photons arriving during a single scan is about 10^{-4} . Characterization of the instrument response function was performed by detecting elastically scattered light from a blank droplet (no R6G added) with the interference filter removed, and the laser intensity attenuated to give approximately 10 KHz count rate. For lifetime measurements made on bulk glycerol solutions, the upper end cap electrode was removed and a 1 cm square cuvette was placed inside the trap. All other experimental parameters were identical for droplet and bulk measurements. In the following section, the results of fluorescence lifetime measurements performed on droplets of varying size and R6G concentration are discussed.

3. RESULTS AND ANALYSIS

Fluorescence decay kinetics of R6G was investigated for droplets varying from 4 to 25 microns in diameter, and with concentrations varying from 1×10^{-7} to 2×10^{-5} M in glycerol. Figure 1 shows the instrument response function and normalized fluorescence data for 4, 6, and 11 μm droplets (10^{-6} M/glycerol), as well as for 10^{-6} M bulk glycerol solution. The full width-half maximum instrument response is 0.85 ns,[19] and decay components with lifetimes as short as 5 ps can be deconvoluted reliably.[20] The bulk fluorescence decay is described well by a single exponential decay with $\tau = 3.65 \pm 0.05$ ns. Fluorescence from the 11 μm droplet also follows single exponential decay with the same decay rate as observed in bulk solution. For diameters between 4 and 8 μm , the fluorescence decay becomes increasingly non-exponential, where the relative amplitude of the fast decay component increases with decreasing diameter. Because the density of states (and therefore the enhancement) should vary according to the radial position of the molecule within the droplet,[21] a distribution of decay rates was expected to provide a more accurate representation of the system than a simple biexponential decay function. Using a Laplace inversion technique,[22,23] decay rate probability distributions were extracted from the fluorescence lifetime data to determine the emission rate enhancement.

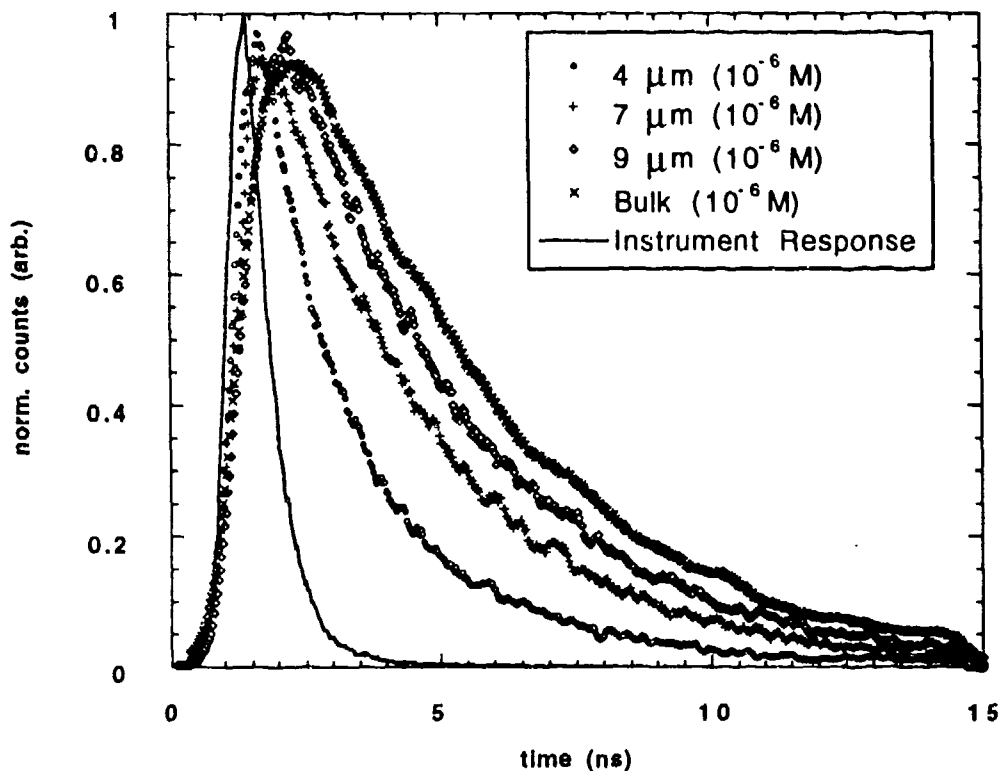


Figure 2. R6G fluorescence decay data in 4, 7, and 9 μm glycerol droplets as well as bulk glycerol solution. Dye concentrations for each data set shown was 10^{-6} M. The data has been smoothed by a five-point running average.

The observed fluorescence decay data, $C(t)$, can be represented by a convolution of the instrument response function and a sum of exponentials expressed as

$$C(t) = \text{IRF}(t) * \sum_n \lambda_i \alpha_i \exp(-\lambda_i t) \quad (3)$$

where $\text{IRF}(t)$ is the instrument response function, λ_i is the i th decay rate, and α_i is the probability that a photon will be emitted at rate λ_i . If the sum in Eqn. 3 is replaced by an integral, it can be seen that the function $\lambda\alpha(\lambda)$ is the inverse Laplace transform of $C(t)$, where $\alpha(\lambda)$ is a decay rate

probability distribution function. Thus, Laplace inversion of the measured data $C(t)$ yields the function $\alpha(\lambda)$ which contains the decay rate and probability amplitude information.

In a simplified view, determination of the function $\alpha(\lambda)$ from $C(t)$ is performed as follows. The solution space is defined by specifying the initial and final decay rates, λ_0 and λ_{n-1} , and the number of grid points, n . Values used for λ_0 and λ_{n-1} were 0.1 and 15 ns^{-1} respectively, with $n = 75$. The array, $\alpha(i)$, represents a decay rate probability distribution and is determined by singular value decomposition, where the values are subject to the following constraints: (1) all values are non-negative; (2) χ^2 parameter is minimized; and (3) the value of a *regularizer*, or 2nd derivative smoothness function, is minimized. In principle, a large number of decay components can be resolved[24] using this technique, making it a powerful tool for analyzing multiexponential decays.

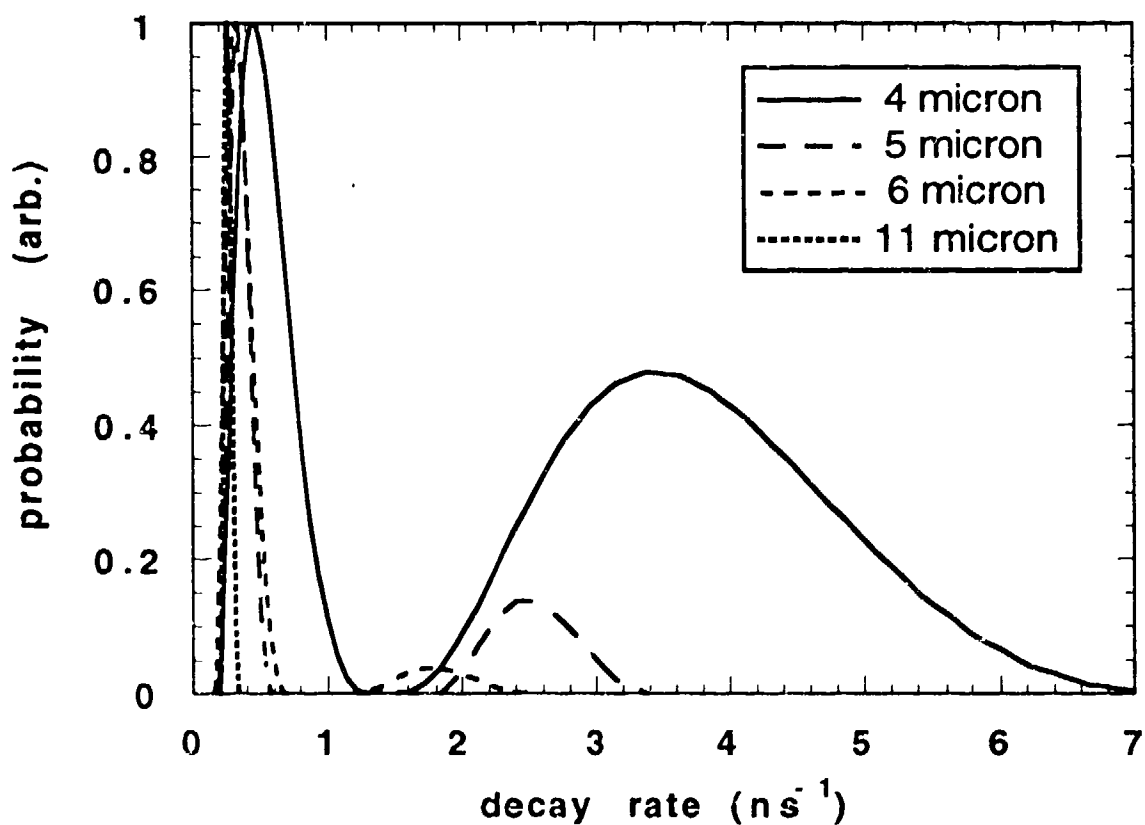


Figure 3. Decay rate probability distributions from fluorescence decay data for 4, 5, 6, and 11 μm droplets.

Figure 3 shows decay rate probability distribution functions obtained from R6G fluorescence lifetime data in 4, 5, 6, and 11 μm droplets. Each distribution shows a strong peak centered around the bulk fluorescence decay rate (0.27 ns^{-1}). However, distributions for the 6, 5, and 4 μm droplets show a fast decay component whose rate and maximum probability amplitude increases with smaller droplet diameter. The degree of enhancement of this fast component for the smallest droplets is as much as a factor of 10 larger than the bulk decay rate and, as shown in Figure 4, falls off sharply with increasing droplet diameter. In the decay rate probability distributions obtained from our experimental data, the width of the enhanced rate feature arises primarily from the limited sampling (512 points) and the noise in the data. The non-zero probability for photon emission at extremely large rates near the edge of the solution grid is probably not physically significant.

Since it is well known that stimulated emission and lasing can occur in microdroplets, the question arises as to whether the enhanced decay rate can be attributed to stimulated emission. The possibility of lasing was estimated using an expression given by Lin, et al. [14] as

$$2\pi mX/Q_{\text{ext}}kg_0 < 1 - L/kg_0 \quad (4)$$

where m is the refractive index, X is the size parameter, Q_{ext} is the cavity Q , k is the enhancement in lasing gain, g_0 is the round trip gain, and L represents the transmissive and internal losses. Laser oscillation may occur when the above equation is satisfied. Substituting values appropriate for our experimental conditions, it was concluded that, even at the highest dye concentration and pulse power, the threshold for lasing would not be exceeded. Although it is almost certain that the enhanced decay rate component is not due to droplet lasing, the possibility still exists that we are observing stimulated emission. An estimate of the probability of stimulated emission was made using values for photon lifetime in the cavity, γ_c , and an estimate of the number of excited states formed per pulse. This calculation suggests that the probability of stimulated emission is on the order of 10^{-4} .

As an experimental confirmation that we are indeed observing enhanced spontaneous emission, the characteristics of small droplet fluorescence decay

were examined as a function of pulse energy. The laser intensity was varied using neutral density filters and several measurements were made on each droplet. Figure 4 shows the ratio of amplitudes for the two (fast and slow) most probable decay rates for 4 and 5 μm droplets at 1×10^{-6} and 2×10^{-5} M concentrations respectively. No significant differences in decay rates or relative amplitudes were observed for pulse energies ranging from 45 to 190 picojoules. Since the maximum intensity used in these experiments is well below saturation level, if the fast decay component were due to stimulated emission, the number of photons emitted with an enhanced decay rate relative to the number of photons emitted with bulk rate should increase with increasing pulse energy. This should be reflected in the lifetime spectrum by an increase in the relative probability amplitude of the fast decay component. Because no such dependence is observed, our conclusion is that a modification in the *spontaneous* emission rate is taking place.

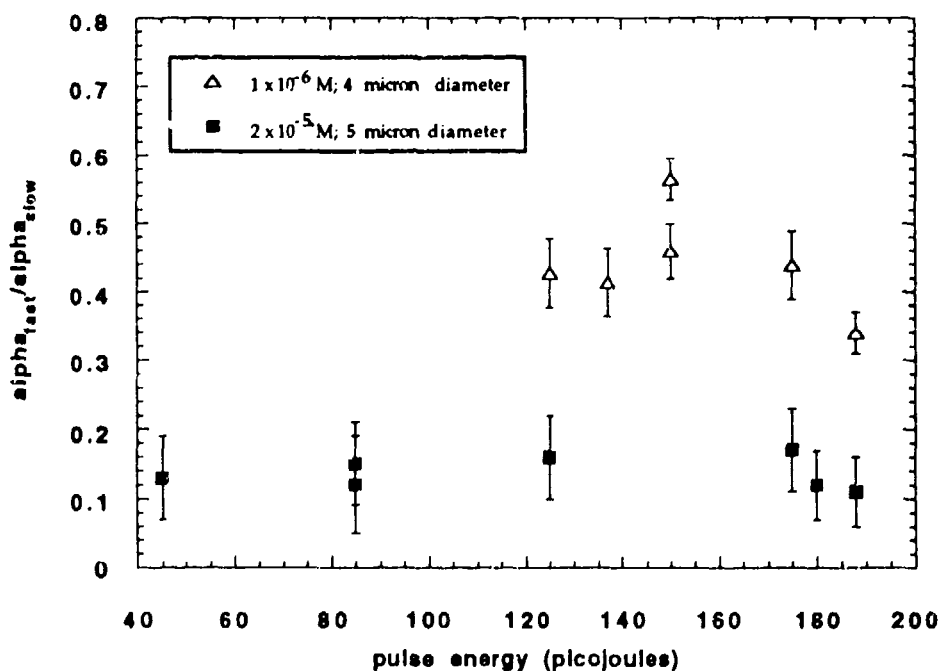


Figure 4. Ratio of amplitudes corresponding to the most-probable decay rates (bulk and enhanced) of the two components for 4 and 5 μm droplets.

Observation of decreased fluorescence lifetimes in the smaller droplets, however, does not guarantee that the effect is due to cavity enhancement. For example, dye fluorescence is known to be self-quenched at large ($\geq 10^{-3}$ M) concentrations.[25] However, this effect should not be significant at R6G concentrations used for these experiments. Other (unknown) quenching processes can also be effectively ruled out since the fluorescence yield per molecule is at least as large for the smaller droplets as it is for the larger ones. On this basis, it appears that the increased spontaneous emission rate is indeed due to a cavity enhancement.

4. DISCUSSION AND CONCLUSIONS

Examination of R6G fluorescence decay kinetics in microdroplets has revealed a striking dependence on droplet size. For droplet diameters ≥ 10 μm , the decay behavior is identical to that observed in bulk glycerol. As the droplet diameter is decreased below 10 μm , increasingly non-exponential decay behavior is seen where the enhancement and relative probability amplitude of a fast decay component increase as the diameter is decreased. This biexponential decay behavior can be qualitatively explained by considering how the 'mode volume' and degree of enhancement change as the droplet size is varied.

Light waves which propagate near the surface of the sphere in the high-Q cavity modes occupy a certain volume which is defined as the mode volume. Most of the molecules will be unaffected by the presence of cavity modes near the surface and emit at a rate similar to that of bulk medium. However, molecules located in the mode volume will have their emission coupled into cavity modes and their decay rate will be enhanced or inhibited depending on whether the emission is resonant with a cavity mode. For a 4 μm diameter glycerol droplet, V_m/V is about 0.1 and falls off roughly as $1/X^{1/2}$, where X is the size parameter. Thus, a larger percentage of molecules interact with a cavity mode in the smaller droplets which will be reflected in the lifetime spectrum as an increase in the relative probability amplitude of the enhanced rate component.

The second factor responsible for the observed trends in the decay rate probability distributions is the variation of enhancement with droplet diameter. Since the mode spacing, Δ_c , is approximately equal to $f(n)/2\pi r$, [26] where $f(n)$ is a function of the index of refraction, and r is the radius of

the sphere, experimentally measured rate enhancements can be used to estimate the homogeneous linewidth of a molecule such as R6G in glycerol at room temperature from Eqn. 2. Figure 5 shows the average decay rate enhancement for droplet diameters ranging from 4 to 10 μm along with the variation of enhancement expected from Eqn. 2 for three different homogeneous linewidths. The experimental rate enhancements are in good qualitative agreement with this simple model, however, the enhancement falls off much more sharply with droplet diameter than is predicted using this model. We are currently developing a more detailed theoretical model for decay rate enhancement in these small droplets which should approach quantitative agreement with experimental results, giving a clearer physical picture of the interaction of fluorescent molecules with cavity modes in these microdroplets. However, within the context of this simple model, the experimental data suggest a value of about 100 cm^{-1} for the homogeneous linewidth of R6G in glycerol at room temperature.

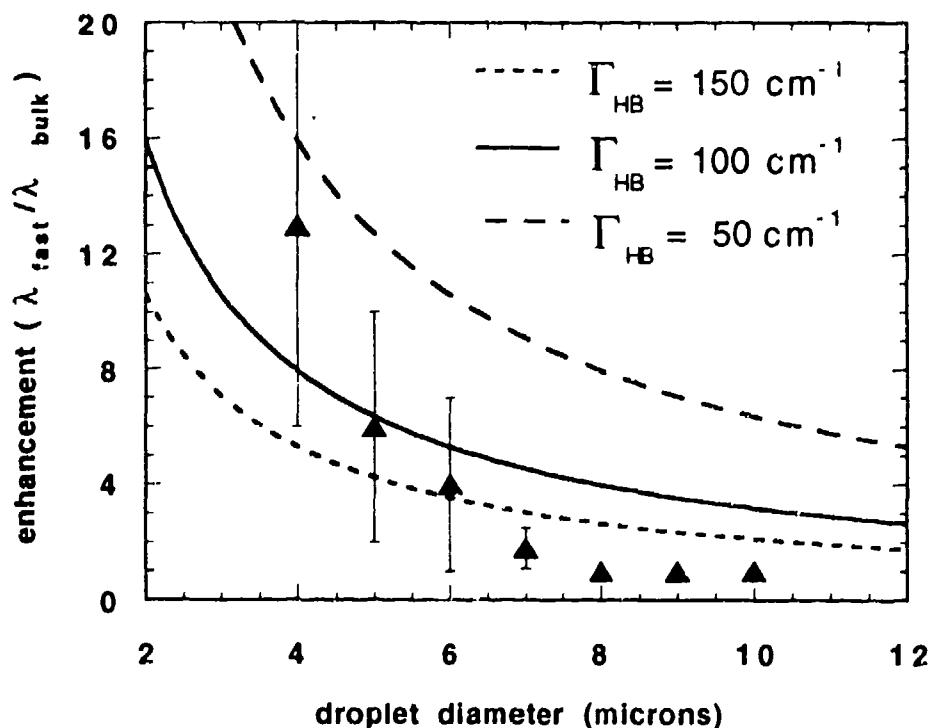


Figure 5. Enhancement (most-probable enhanced decay rate divided by bulk emission rate) vs. droplet diameter. Error bars represent $\pm 1\sigma$.

The narrow homogeneous linewidth for R6G in glycerol suggested by our experiments is supported by spectral hole burning data. Brito Cruz et al.[27] measured dephasing times for different dyes in an ethylene glycol dye jet using a femtosecond pump-probe technique. Similar dephasing times (≈ 80 femtoseconds) were measured for the dyes cresyl violet, Nile red and HITC, corresponding to a homogeneous linewidth of 140 cm^{-1} . Extrapolation from hole burning data on porphyrin molecules in cold (80° K) polymer matrices[28] suggest homogeneous linewidths at 300° K on the order of 50 cm^{-1} . It is therefore reasonable to expect that the homogeneous linewidth for R6G is narrower than the cavity mode spacing for droplet diameters less than 10 microns and that such a narrow linewidth could produce the large emission rate enhancements which have been observed experimentally.

The data presented in this paper shows that no significant spontaneous emission enhancement is observed until the droplet diameter reaches $7 - 8 \mu\text{m}$, while the work of Campillo[3] on Eu^{3+} shows about $2.5\times$ enhancement for a droplet diameter of about $10 \mu\text{m}$. Assuming that the homogeneous linewidths and cavity mode spacings are similar for the two cases, the apparent difference between the two sets of data can be rationalized in terms of differences in which the measurements were made. The work of Campillo involved dispersion of broadband emission at successive time frames where bulk and enhanced rate emission could be more clearly distinguished. In the work presented here, a measurement was made only of the number of photons arriving at the detector as a function of time following an excitation pulse. In our experiment, for larger droplets where the enhancement is smaller, the signal is dominated by emission at the free space rate which effectively diminishes the contrast between the two decay components.

Another important difference between these two sets of results is that no significant inhibited emission was observed in our work. In some cases, emission rates smaller than that of bulk glycerol were seen, however it is unclear as to whether this was a QED effect since residual water in the droplet[29] (bulk lifetime 4.5 ns) could result in a longer bulk emission rate. Also, because the time window for photon counting was only 16 ns , the long-time decay kinetics are not as clear.

4. SUMMARY

The fluorescence decay kinetics of R6G in levitated glycerol microdroplets have been investigated as a function of droplet size and shows a striking transition from single exponential to bi-exponential decay as the droplet size is decreased. An enhanced rate component becomes apparent at a droplet size of about 7 and 8 μm whose magnitude and relative probability amplitude increase as the droplet diameter is decreased. Examination of decay behavior as a function of input pulse energy suggest that this fast rate component is due to cavity-enhanced *spontaneous* emission. Within the context of a weak coupling model, the homogeneous linewidth for R6G can be estimated from this fluorescence lifetime measurements and a value of about 100 cm^{-1} is suggested from this data.

This research was sponsored by the U.S. Department of Energy, Office of Basic Energy Sciences, under contract DE-AC05-84OR21400 with Martin Marietta Energy Systems, Inc. Prof. S. Arnold gratefully acknowledges support from the National Science Foundation, grant ATM-89-175871. The authors would also like to thank Prof. Roger Gregory of Kent State University for use of the CONTINP2 program which was used to perform the Laplace inversion analysis.

- (1) W. B. Whitten, J. M. Ramsey, S. Arnold, and B. V. Bronk, *Anal. Chem.* **63**, 1027 (1991).
- (2) K. C. Ng, W. B. Whitten, S. Arnold, and J. M. Ramsey, *Anal. Chem.* submitted.
- (3) H-B. Lin, J. D. Eversole, C. D. Merrit, and A. J. Campillo, *Phys. Rev. A* **45**, 6756 (1992).
- (4) S. D. Druger, S. Arnold, and L. M. Folan, *J. Chem. Phys.* **87**, 2649 (1987).
- (5) P. T. Leung, and K. Young, *J. Chem. Phys.* **89**, 2894 (1988).
- (6) A. Yariv, *Quantum Electronics, 2nd Ed.*, (Wiley and Sons, Inc., New York, 1967).
- (7) E. M. Purcell, *Phys. Rev.* **69**, 681 (1946).
- (8) K. H. Drexhage, M. Fleck, H. Kuhn, F. P. Schafer, and W. Sperling, *Ber. Bun. Ges.* **70**, 1179 (1966).
- (9) D. Kleppner, *Phys. Rev. Lett.* **47**, 233 (1981); R. G. Hulet, E. S. Hilfer, and D. Kleppner, *Phys. Rev. Lett.* **55**, 2137 (1985).
- (10) F. De Martini, G. Innocenti, G. R. Jacobovitz, and P. Mataloni, *Phys. Rev. Lett.* **59**, 2955 (1987).
- (11) S. C. Hill, and R. E. Benner, in "Optical Effects Associated With Small Particles", P. W. Barber and R. K. Chang, eds., (World Scientific, Singapore, 1988).
- (12) A. J. Campillo, J. D. Eversole, and H-B. Lin, *Phys. Rev. Lett.* **67**, 437 (1991).

- (13) H-M. Tzeng, K. F. Wall, M. B. Long, and R. K. Chang, *Optics Letters* **9**, 499 (1984).
- (14) H-B. Lin, J. D. Eversole, and A. J. Campillo, *J. Opt. Soc. Am. B.* **9**, 43 (1992).
- (15) H-B. Lin, J. D. Eversole, C. D. Merritt, and A. J. Campillo, *Phys. Rev. A.* **45**, 6756 (1992).
- (16) S. K. Poultney, in *Advances in Electronics and Electron Physics*, L. Marton, ed. (Academic Press, New York, 1972), Vol. 31.
- (17) S. Arnold, and L. M. Folan, *Rev. Sci. Instrum.* **57**, 2250 (1986).
- (18) D. V. O Connor, and D. Phillips, *Time-Correlated Single Photon Counting*, (Academic Press, 1984).
- (19) The FWHM instrument response is much longer than the 150 ps pulse duration of the mode-locked laser pulse principally because of the variation in transit times during electron multiplication in the PMT.
- (20) K. G. Spears, L. E. Cramer, and L. D. Hoffland, *Rev. Sci. Instrum.* **49**, 255 (1978).
- (21) H. Chew, *Phys. Rev. A* **36**, 3410 (1988); H. Chew, *Phys. Rev. A* **37**, 4107 (1988).
- (22) R. B. Gregory, and Y. Zhu, in *Proc. 3rd Intl. Workshop on Positron and Positronium Chemistry*, edited by Y. C. Jean (World Scientific, Singapore 1990).
- (23) R. W. Wijnaendts van Resandt, K. H. Vogel, and S. W. Provencher, *Rev. Sci. Instr.* **53**, 1392 (1982).
- (24) The limit on the number of decay components which can be resolved is determined by the Shannon number (see Ref. 22), which is a function of the

width of the instrument response function, the number of individual points, and the signal-to-noise ratio.

(25) P. Pringsheim, *Fluorescence and Phosphorescence*, (Interscience Publishers, New York, 1949).

(26) P. Chylek, *J. Opt. Soc. Am.* **66**, 285 (1976).

(27) C. H. Brito Cruz, R. L. Fork, W. H. Knox, and C. V. Shank, *Chem. Phys. Lett.* **132**, 341 (1986).

(28) A. Furusawa, and K. Horie, *J. Chem. Phys.* **94**, 80 (1991).

(29) All water is assumed to have evaporated from the droplet, however some non-zero mole fraction (determined by Raoult's law) of water will be present according to the relative humidity.

Blank

Time and Wavelength Domain Algorithms for Chemical Analysis by Laser Radar

David L. Rosen and James B. Gillespie
U.S. Army Atmospheric Sciences Laboratory
White Sands Missile Range, NM 88002-5501

INTRODUCTION

Laser-induced fluorescence (LIF) is a promising technique for laser radar applications. Laser radar using LIF has already been applied to algae blooms and oil slicks.¹ Laser radar using LIF has great potential for remote chemical analysis because LIF spectra are extremely sensitive to chemical composition. However, most samples in the real world contain mixtures of fluorescing components, not merely individual components. Multicomponent analysis of laser radar returns from mixtures is often difficult because LIF spectra from solids and liquids are very broad and devoid of line structure. Therefore, algorithms for interpreting LIF spectra from laser radar returns must be able to analyze spectra that overlap in multicomponent systems.

Factor analysis-rank annihilation (FARA) is an eigenanalysis technique²⁻⁵ for analyzing two-dimensional data. FARA usually analyzes excitation-emission matrices (EEM). EEM are matrices where the rows (or columns) are emission spectra at fixed excitation wavelengths and the columns (or rows) are excitation spectra at fixed emission wavelengths. FARA is insensitive to the presence of unknown compounds if there is no energy transfer between constituents. This insensitivity would be useful for laser radar applications where not every compound in a natural environment can be known in advance. Although the measurement of EEM requires a wavelength tunable light source, laser sources strong enough for laser radar applications are usually not wavelength tunable. Therefore, scientists have not previously considered FARA a suitable method for analyzing laser radar returns.

This paper analyzes the possibility of using FARA to analyze emission-time matrices (ETM) from laser radar returns instead of EEM. The authors here define ETM as matrices where the rows (or columns) are emission spectra at fixed times and the columns (or rows) are temporal profiles for fixed emission wavelengths. Laser radar usually uses pulsed lasers for ranging purposes, which are suitable for measuring temporal profiles. Laser radar targets are hard instead of diffuse; that is, a definite surface emits the fluorescence instead of an extended volume. A hard target would not broaden the temporal profiles as would a diffuse target. Both fluorescence lifetimes and emission spectra are sensitive to chemical composition. Therefore, temporal profiles can be used instead of excitation spectra in FARA analysis of laser radar returns. The resulting laser radar returns would be ETM instead of EEM.

THEORY

This section describes an FARA algorithm, developed by Ho^{2, 3} for calculating nonzero concentrations. The calculation requires an ETM, D , from an unknown and another ETM, N_k , from a calibrant of known concentration. The subscript k designates the constituent one is looking for in the unknown, that is, the

component of interest. D and N_k are ETM in this paper, but can either be EEM or ETM. The laser radar return could come from an unknown, while the calibrant can be a sample of the component of interest especially prepared in a laboratory. This algorithm calculates the relative concentration, c_k , which is the ratio of the concentration of a constituent in an unknown to the concentration of the constituent in a known laboratory standard. The algorithms discussed in this paper are not valid if c_k is zero. Algorithms for deciding whether c_k is zero are available but will not be discussed in this paper.

The concentration, c_k , can be calculated in four steps. First, calculate the effective rank, r , of the matrix D . The effective rank is the number of fluorescence centers (that is, components with bilinear spectra) in the unknown. Complicated methods of choosing the effective rank are available,⁴ but beyond the scope of this paper. Second, calculate the residual matrix $E(c_k')$, defined as:

$$E(c_k') = D - c_k' N_k \quad (1)$$

where c_k' is a dummy variable that spans over a range of possible concentrations. Note that eq. (1) requires a calibrant only from the component of interest. Third, calculate the eigenvalues, $S_j(c_k')$, of $E(c_k')E(c_k')^t$. The superscript t designates transpose, while the subscript j designates the particular eigenvalue. The subscript j is ordered so that if $j > j'$, then $S_j > S_{j'}$. Finally, find the minimum of $S_r(c_k')$. The value at c_k' where the minimum occurs is the actual relative concentration, c_k , of the component. Another algorithm uses an analytical formula, developed by Lorber,⁵ to find the minimum of $S_r(c_k')$. However, the authors will show the functional form of $S_r(c_k')$ to clarify the discussion.

One can easily show that the shape of the laser pulse profile cannot affect the calculated values of concentration if the same laser pulse shape with the same time delay generates both the calibrant ETM and the laser radar return. Therefore, FARA also may serve as a type of deconvolution algorithm if both the laser pulse shape and electronic triggering are reproducible.

SIMULATION AND RESULTS

The ETM's of three hypothetical compounds (I, II, and III) were generated. The emission spectra of these compounds are shown in figure 1. Only relative decay times and relative shapes of emission bands affect the calculations. For ease of visualization, this paper will refer to the time units as nanoseconds (nsec) and wavelength units as nanometers (nm). For calculational ease the authors assumed a laser pulse shape to be a double-sided exponential with a decay constant of 0.5 nsec. The fluorescence decay times of the three compounds (I, II, and III) were 2.0 nsec, 6.0 nsec, and 10.0 nsec, respectively. The authors repeated the calculations using a Dirac delta function for the laser pulse profile.

The ETM of compounds I, II, and III were added to create a linear combination with effective concentrations (that is, coefficients) of 1.0, 2.0, and 3.0, respectively. This linear combination was defined as the ETM of the hypothetical mixture.

FARA analyzed both the linear combination and the calibrant EEM to find the nonzero concentrations, c_k . The calculated concentrations for the three compound profiles (I, II, and III) from the ETM are shown in table 1. The values of c_k calculated by FARA were the same as the actual concentrations in the hypothetical mixture. The calculated values were independent of the laser pulse shape, as expected.

The eigenvalue, $S(c_1')$, for the ETM of compound I is plotted in figure 2. The eigenvalue, S , shows a clear minimum at $c_1' = 1.0$, which is the true value of c_1 . Note that calculating the value of c_1 did not require laboratory standards from compound II or III.

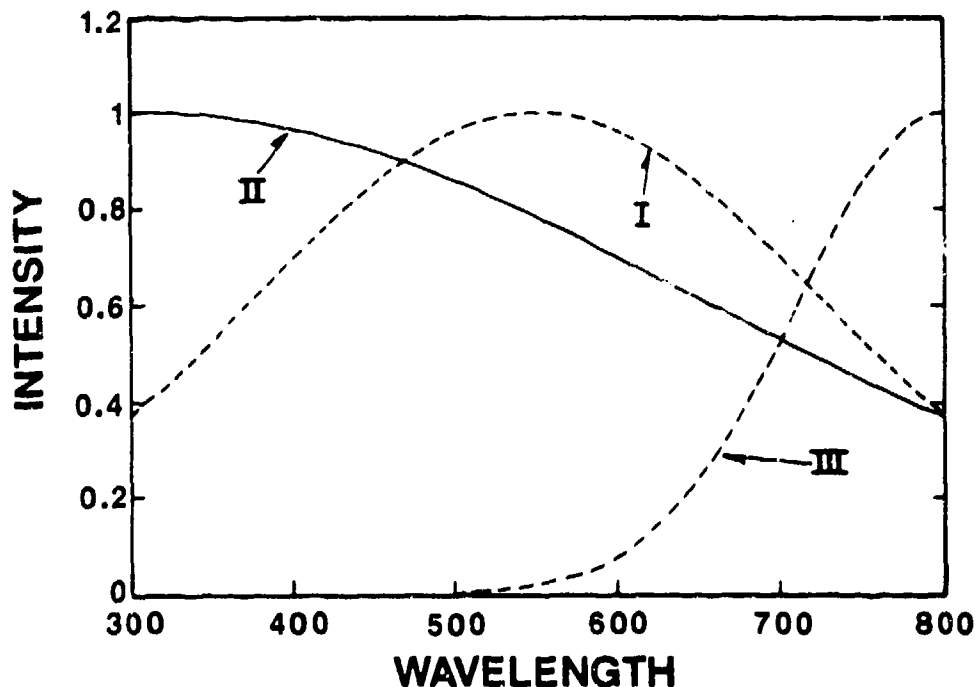


Figure 1. Normalized emission spectra of hypothetical compounds I, II, and III.

TABLE 1. CALCULATIONS FOR CONCENTRATION

Compound	I	II	III
Actual	1.00	2.00	3.00
FARA	1.00	2.00	3.00

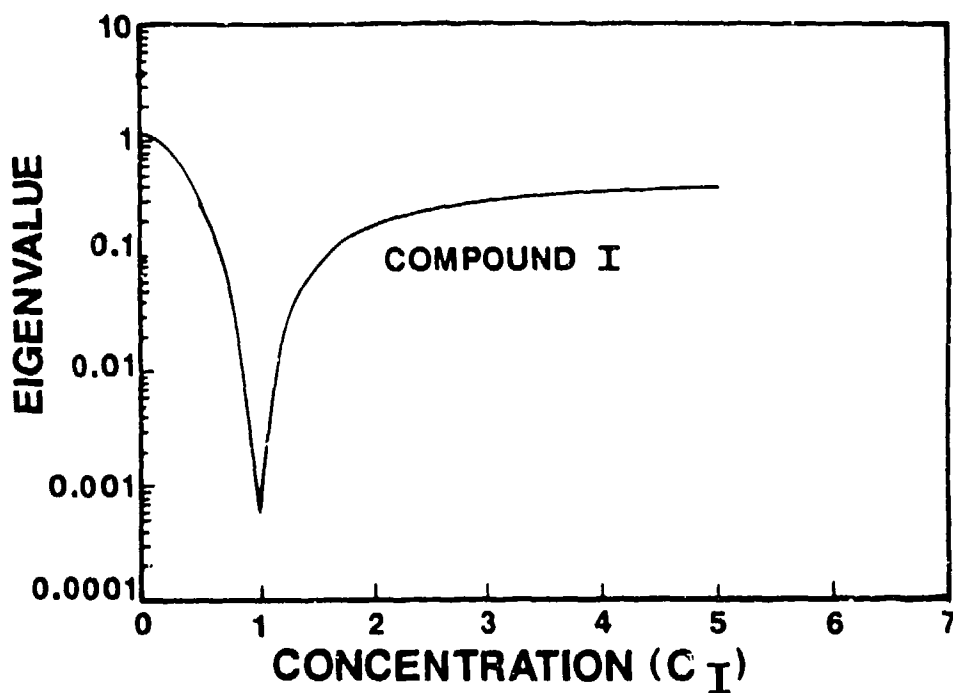


Figure 2. The functional dependence of the appropriate eigenvalue, S , on the hypothetical concentration c_I' for the ETM of compound I.

DISCUSSION AND CONCLUSIONS

FARA has potential as a method for interpreting laser radar returns. FARA can be applied to matrices consisting of fluorescence intensity as a function of emission wavelength and time. The authors have shown that it can calculate the nonzero concentration of a constituent in an unknown without having every laboratory standard from every constituent in the unknown. FARA also can serve as a deconvolution method for laser radar if the temporal profile of the laser pulse is reproducible.

REFERENCES

1. Measures, R., 1984. Laser Remote Sensing, New York: John Wiley and Sons.
2. Ho, C. -N., G. D. Christian, and E. R. Davidson, 1980. Anal. Chem., 52:1071-1078.
3. Ho, C. -N., G. D. Christian, and E. R. Davidson, 1978. Anal. Chem., 50:1108-1113.
4. Malinowski, E. R., and D. G. Howery, 1980. Factor Analysis in Chemistry, New York: John Wiley and Sons.
5. Lorber, A., 1986. Anal. Chem., 58:1167-1172.

MICROPARTICLE-BASED FLUORESCENCE IMMUNOASSAY

W. B. Whitten, J. M. Ramsey
Oak Ridge National Laboratory
Oak Ridge, Tennessee 37831-6142

and B. V. Bronk
U.S. Army CRDEC
Aberdeen, Maryland 21010

RECENT PUBLICATIONS, SUBMITTALS FOR PUBLICATION, AND PRESENTATIONS

- A) J. M. Dale, W. B. Whitten, and J. M. Ramsey, "Laser Ablation Mass Spectrometry of Levitated Microparticles", Proceedings of the 1991 CEC Scientific Conference on Observation and Aerosol Research, in preparation.
- B) J. M. Dale, W. B. Whitten, and J. M. Ramsey, "Chemical Characterization of Microparticles by Laser Ablation in an Ion Trap Mass Spectrometer", 32nd ORNL/DOE Conference on Analytical Chemistry in Energy Technology, Gatlinburg, TN Oct. 1-3, 1991.
- C) J. M. Ramsey, W. B. Whitten, S. Arnold, and B. V. Bronk, "Single Molecule Detection in Microdroplets", Federation of Analytical Chemistry and Spectroscopy Societies Meeting, Anaheim, CA, Oct. 6-11, 1991.
- D) S. Arnold, C. T. Liu, W. B. Whitten, and J. M. Ramsey, "A Microparticle-Based Spectral Hole Burning Memory", *Optics Lett.* **16** 420 (1991).
- E) J. M. Dale, W. B. Whitten, and J. M. Ramsey, "Chemical Characteristics of Microparticles by Laser Ablation in an Ion Trap Mass Spectrometer", Proceedings of 39th ASMS Conference on Mass Spectrometry and Allied Topics, Nashville, TN, 1991, p. 534.
- F) J. M. Dale, W. B. Whitten, and J. M. Ramsey, "Detection of Explosives Materials on Single Microparticles", FAA Symposium on Explosives Detection Technology, Atlantic City, NJ, November 13-15, 1991.
- G) J. M. Ramsey, "Advanced Techniques for the Chemical Characterization of Microparticles", U.S. Dept. of Energy EXPO '91 on Special Operations, Albuquerque, NM, Nov. 19-21.
- H) J. M. Dale, W. B. Whitten, and J. M. Ramsey, "Laser Desorption from Single Microparticles in an Ion Trap Mass Spectrometer", ASMS 4th Sanibel Conference on Mass Spectrometry, Sanibel Island, FL, Jan. 25-28, 1992.
- I) J. M. Ramsey, W. B. Whitten, S. Arnold, and K. C. Ng, "An Ultrasensitive Fluorescence Detector for Capillary Electrophoresis", 4th Intl. Symp. on High Performance Capillary Electrophoresis '92, Amsterdam, The Netherlands, Feb 9-13, 1992.
- J) W. B. Whitten, J. M. Ramsey, K. C. Ng, and S. Arnold, "Digital Molecular Detection", Institute for Spectrochemistry and Analytical Spectroscopy, Dortmund, Germany, Feb. 18, 1992.

- K) S. Arnold, J. Comunale, W. B. Whitten, J. M. Ramsey, and K. A. Fuller, "Room-Temperature Microparticle-Based Persistent Hole-Burning Spectroscopy", *J. Opt. Soc. Am.* **B9**, 819 (1992).
- L) W. B. Whitten, J. M. Dale, and J. M. Ramsey, "Detection of Explosives Material on Single Microparticles", Proceedings of FAA 1st Intl. Symp. on Explosives Detection Technology, Atlantic City, NJ, 1991.
- M) K. C. Ng, W. B. Whitten, J. M. Ramsey, and S. Arnold, "Digital Chemical Analysis of Dilute Microdroplets", submitted to *Anal. Chem.*
- N) J. M. Dale, W. B. Whitten, and J. M. Ramsey, "Laser Ablation from Microparticles in an Ion Trap Mass Spectrometer", ACS Symposium on Laser Materials Interactions, San Francisco, CA, April 5-10, 1992.
- O) W. B. Whitten, J. M. Ramsey, and S. Arnold, "Room Temperature Persistent Spectral Hole Burning", Computer Systems Policy Project Materials Track Meeting with DOE Labs, Albuquerque, NM, April 15-16, 1992.
- P) W. B. Whitten and J. M. Ramsey, "Photocount Probability Distributions for Single Fluorescent Molecules", *Appl. Spectrosc.* in press.

ABSTRACT

Techniques are being explored to combine the chemical specificity of the antibody-antigen reaction with the high sensitivity of fluorescence detection. Antibodies to the target analyte are labeled with strongly fluorescing tags. Microspheres with attached antibodies are used in a correlation approach to discriminate against unattached fluorescent labels.

We have recently shown that it is possible to detect single molecules of highly fluorescent dyes (1). However, there is a large number of compounds of practical interest that are either nonfluorescent or if fluorescent, the emission spectrum is not sufficiently distinctive to give useful analytical specificity. One way to achieve very high sensitivity and selectivity is to attach a fluorescent label to the analyte molecule via an antibody-antigen reaction. We have undertaken some experiments to explore the utility of immunofluorescence techniques in conjunction with our microparticle fluorescence measurements for the detection of biologically important substances.

The technique used for our initial experiments has been called by others a sandwich fluorescence immunoassay. Antibodies specific for the analyte molecule are covalently bound to carboxyl groups on the surface of microspheres about 10 μm in diameter. When a suspension of these treated particles is incubated with a solution containing the analyte antigen, analyte molecules will be extracted from the solution and become attached to the microparticles. The particles are subsequently incubated with a solution of the antibody to which a fluorescent tag has been bound. The microspheres thus become fluorescent in proportion to the original analyte concentration. The main problems now are how to distinguish between bound and free labeled antibodies and how to minimize nonspecific binding, i.e., the blank signal.

One way to minimize the signal from unbound antibodies is to perform a physical separation - by filtration or centrifugation, for example. The separated microspheres will no longer be in chemical equilibrium if maintained in suspension so measurement time will be governed by the dissociation rate constant for the immune reaction. Alternatively, an optical correlation technique can be employed restricting the number of valid measurements to those small volumes that contain microspheres. Saunders et al. (2) have achieved detection limits of 10^{-14} M in a flow cytometer in this way. In our experiments, both methods are used, with the fluorescent microspheres first separated by centrifugation, then analyzed by confocal fluorescence microscopy (3) correlated with the presence of a microsphere in the probe volume.

The experiments were performed with the apparatus shown in Fig. 1. Light from an argon ion laser is focused through a microscope objective onto the sample, an ensemble of microspheres in suspension on a slide. The laser focus has been adjusted so that the excitation volume is somewhat larger than the microspheres. With the laser beam blocked, the stage is manipulated manually until a microsphere is centered in the field of view and in the focal volume of the laser. When this is accomplished, the laser is switched on and the fluorescence signal is measured until the fluorescent tags have photolyzed. A fresh microsphere is then found and the process repeated until enough measurements have been made.

The first experiment was to determine the dissociation rate constant of a typical antibody-antigen pair. A monoclonal antibody (mouse) to horseradish peroxidase (HRP) was covalently attached to carboxylated 10- μm spheres using a carbodiimide reaction (3). The anti-HRP is the antigen in this experiment. The suspension was incubated over night with a solution of rabbit anti-mouse antibodies that were labeled with R-phycoerythrin, a highly fluorescent protein molecule obtained from algae. After washing by centrifugation, the spheres were resuspended in storage buffer. Confocal fluorescence correlation measurements were made on from 20 to 40 spheres at various times after the initial separation to observe the antibody-antigen dissociation. A portion of a typical run is shown in Fig. 2. The photomultiplier signal saturates while the particles are being observed with white light, then the fluorescence-photolysis decay is obtained for each sphere.

A plot of the average signal obtained as a function of time after separation is shown in Fig. 3. After an approximately exponential decay, the fluorescence signal reaches a steady state as chemical equilibrium is reached anew. The dissociation rate constant for the initial decay is $k_d = 1.5 \times 10^{-5} \text{ s}^{-1}$. The results of these determinations imply that reliable measurements could still be made within a few hours of the initial separation.

We also made a sandwich assay with the same mouse anti-HRP coated microspheres. The analyte antigen was in this case rabbit anti-mouse and the sandwich was completed with goat anti-rabbit labeled again with R-phycoerythrin. The antigen and labeled antibodies were incubated simultaneously with the antibody-coated spheres. A portion of a fluorescence measurement for the separated spheres is shown in Fig. 4. The fluorescence signal is now much stronger than the signal when the white light is on and there was visual evidence of coagulation. The measurement at 755 nm was on a probe volume with no sphere present.

An estimation of the ultimate sensitivity of the technique will require measurements on a blank, where the labeled antibodies are incubated with antibody-coated spheres and no antigen present, as well as with incubations in solutions of known antigen concentration. We are also studying the possibility of using morphological resonances of the microspheres to enhance the sandwich fluorescence relative to the solution fluorescence and Raman background.

REFERENCES

1. K. C. Ng, W. B. Whitten, J. M. Ramsey, and S. Arnold, *Anal. Chem.* submitted.
2. G. C. Saunders, J. H. Jett, and J. C. Martin, *Clin. Chem.* 31, 2020 (1985).
3. X. C. Huang, M. A. Quesada, and R. A. Mathies, *Anal. Chem.* 64, 967 (1992).

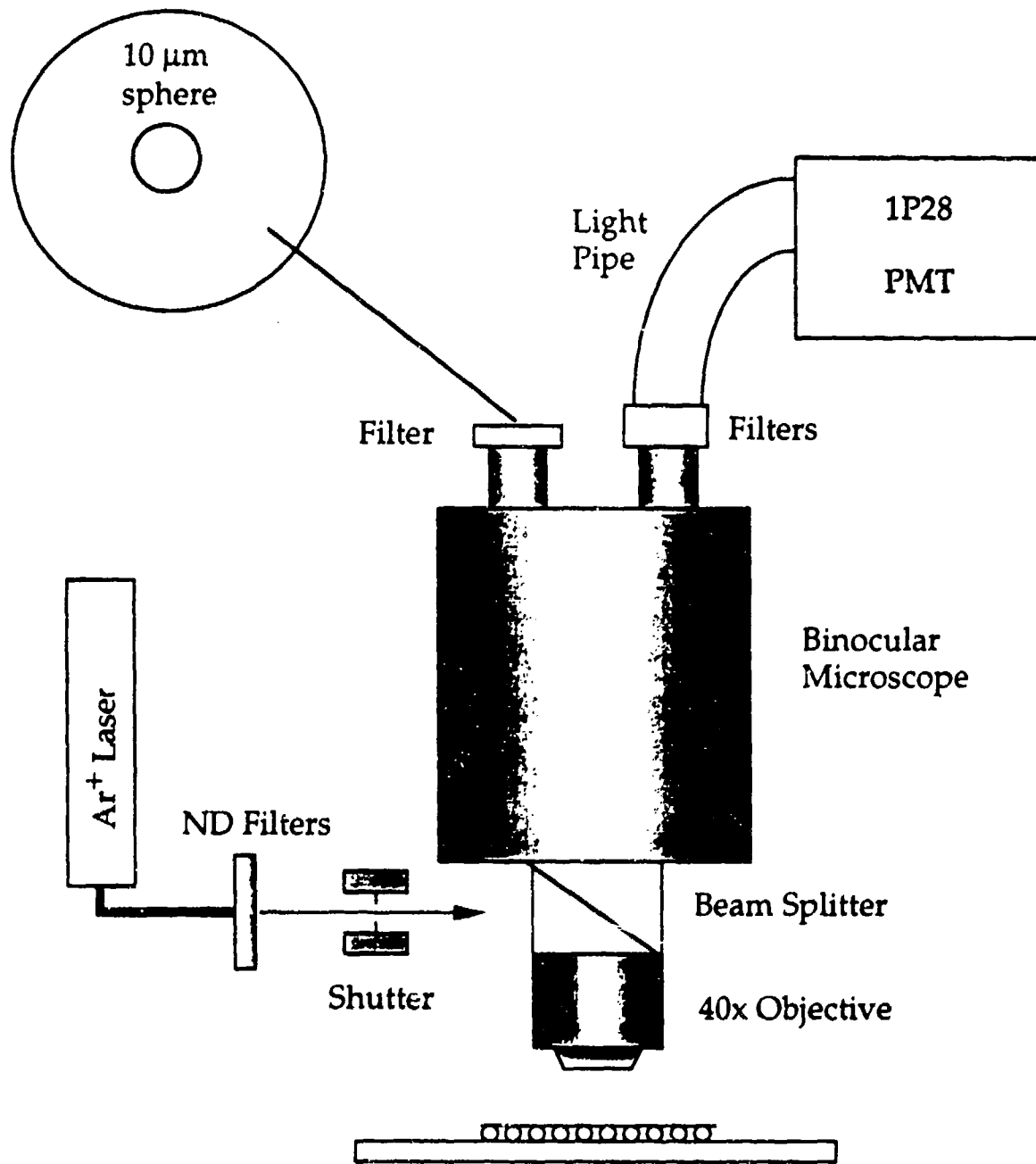


Fig. 1. Apparatus for measuring fluorescence of individual microspheres.

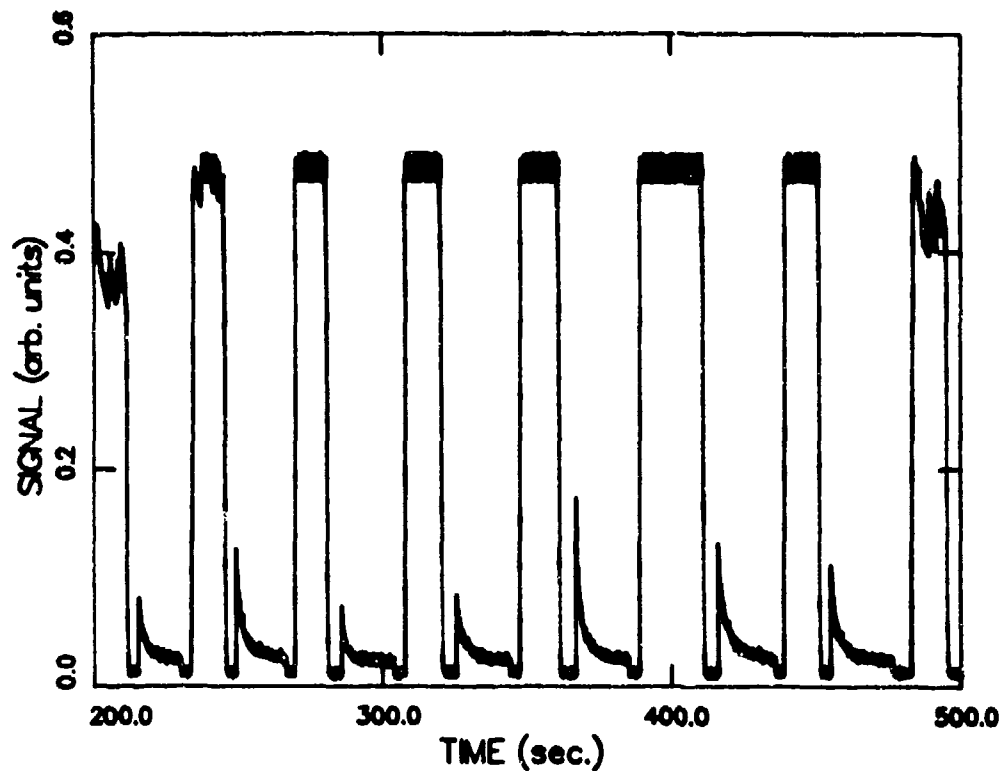


Fig. 2. Fluorescence measurements on individual microspheres. The large signals are when the particles are being visually centered in the field of view with white light illumination. The decaying curves are the fluorescence signals from microspheres when the laser is switched on. The decay of the fluorescence is due to photolysis of the antibody labels.

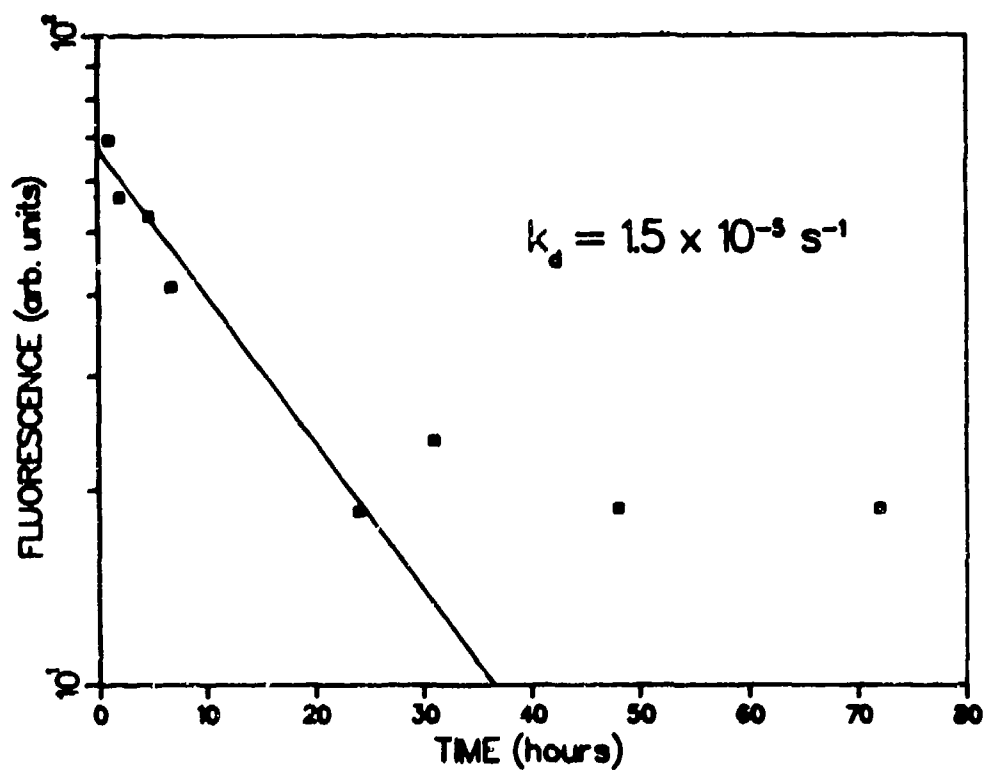


Fig. 3. Average fluorescence per microsphere versus time after separation from the unbound labeled antibodies.

**Computerized Fluorometer Analysis:
Automated Identification of Particles**

Lou Reinisch

*Department of Otolaryngology and Physics
S-2100 MCN, Vanderbilt University
Nashville, TN 37232*

Abstract

We have measured the fluorescence emission spectra as a function of the excitation wavelength for several bacteria in suspension. The *in vitro* samples consisted of the washed bacteria, centrifuged and then suspended in sterile, phosphate buffered saline at room temperature. The fluorometer measured the emission spectra at 90° in a 1 cm quartz cuvette in 2 nm steps. The excitation wavelength was scanned from 200 to 700 nm in 25 nm steps. The data were smoothed with a sum of Gaussians, least squares fit to the measured data. The smoothed data were presented as a contour plot and stored as a 21 x 21 matrix. The 21 x 21 square matrix was subsequently treated as a 441 element linear array. The linear array from a collection of 4 known bacteria could be "fit" using a linear least squares fitting routine to the measured spectrum of an unknown bacterium. As long as the unknown bacterium was in the collection of known spectra, the unknown could be identified, unambiguously. Work is in progress to limit the range of the fluorescence data required for the identification process. This will speed the data collection and reduce the time needed for the calculations of the least squares fit program.

Introduction

We are developing a fluorescence technique to investigate biological samples, in particular, bacteria and bacterial spores (Reinisch *et al.*, 1992). The fluorescence from bacteria and bacterial spores is due to the emissions of intrinsic fluorophores. These emissions are influenced by the number and the environment of the fluorophores. Thus, the fluorescence probes the interior and the composition of the biological samples. On the other hand, light scattering techniques (e.g., quasi-elastic or polarized) probe the exterior shape and size of the particle. Light scattering has been very effective in monitoring the shape and size changes of bacteria (Cummins, 1976). We have recently used a cross correlation method of quasi-elastic

light scattering to measure subtle changes in the shape of bacterial membranes as ions are pumped across the membrane (Czégé and Reinisch, 1990).

Fluorescence is a valuable tool in probing different materials. The emissions from intrinsic fluorophore are influenced by the surrounding material. Subtle differences in the emission spectra can, therefore, be used to identify the environment of the fluorophore. When studying bacteria, these environmental differences can be linked to the species of the microbes, or the growth stages of the bacteria (Chou-pong *et al.*, 1987; Coburn *et al.*, 1985; Shelly *et al.*, 1980).

There are several reasons to use fluorescence spectroscopy to detect and identify bacteria. The fluorescence technique is fast (Rossi and Warner, 1985). There is no need to grow the bacteria in the presence of antigens to determine the species. This traditional method of identification generally takes several hours or more. It is possible to measure a fluorescence spectrum in less than 1 s with a small f-number monochromator and a diode array detector. Fluorescence spectroscopy can also be used in remote detection. This has obvious military applications, especially in the event of bacterial warfare.

Fluorescence spectroscopy is a resonance phenomenon. This means that a small sample size can be used and it is still possible to achieve a good signal to noise ratio. The small sample size also decreases risk to laboratory personnel during the development and testing of the technique.

Fluorescence has a large number of parameters (*e.g.*, excitation wavelength, emission wavelength, and fluorescence lifetime). This affords several possibilities to tailor the technique to the problem. One can also use double or multiple discrimination techniques in the separation and identification of samples (Shelly *et al.*, 1980).

In earlier studies, several species of bacteria and bacterial spores were studied with fluorescence excitation and emission spectroscopy (Reinisch *et al.*, 1991). With dilute room temperature suspensions, reproducible characteristics in the fluorescence spectra from several different species of bacteria were found. These characteristics are generally independent of the conditions of growth and thought to be useful as a rapid mean of species identification. In general, there is an excitation peak near 280 nm with a strong emission peak near 340 nm. This peak is primarily due to tryptophan (Dalterio *et al.*, 1986, 1987; Munro *et al.*, 1979). However, the exact shape and size of this peak change with the environment of the tryptophan. These characteristic changes in the environment are the key to the species differentiation with fluorescence spectroscopy.

The consistency in the fluorescence emission spectrum from a single bacterial strain has also been probed (Reinisch *et al.*, 1991). The fluorescence emission spectra from *E. coli* B/r at different stages along the growth curve was specifically checked. Also the fluorescence emission

spectra of the *E. coli* B/r in different growth media was probed. There were minor differences in the measured fluorescence spectrum found. These differences, in part, resemble the emission spectra of the different growth media.

We present here an automated technique to identify fluorescence spectra from suspensions of bacteria from a short list of possible species. The data handling is automated and does not require operator judgment. The technique has been successful with several trials under many different conditions.

Materials and Methods

Bacillus subtilis (strain *Bacillus globigii*) ATCC 9372 was obtained from the U.S. Army and used without further purification. *Haemophilis influenzae*, type B, ATCC 33533, and *Branhamella catarrhalis* ATCC 25240 were obtained from American Type Culture Collection, Rockville, MD, and used without further purification. All bacteria were grown in Luria broth (10.0 g NaCl, 10.0 g tryptone (Difco 0123), and 5.0 g yeast extract (Difco 0127) with the pH adjusted to 7.0 in 1.0 l distilled water) or trypticase broth (30.0 g trypticase soy broth (BBL 11768) in 1.0 l distilled water). Samples were grown in a shaker bath at 37°C with moderate shaking. A flask containing the broth without inoculation was also placed in the shaker bath to check that the broth was not contaminated. Additionally, a small fraction of each growth was streaked on agar plates to confirm a single culture of bacteria present in the medium. The bacteria were grown to the stationary phase, and centrifuged. The bacteria were washed with sterile saline, and then resuspended in phosphate buffered sterile saline. The concentration was adjusted for 0.1 OD in a 1 cm cuvette measured at 600 nm.

The tympanic membrane was removed from a fresh frozen head of a chinchilla. The chinchilla head was gift of Robert Doyle, M.D. at the Department of Otolaryngology, University of Pittsburgh. The fluorescence spectrum was measured within 24 hours of harvesting.

The fluorescence spectra were measured on a Gregg 200 Lifetime Fluorometer (ISS, Urbana, IL). The monochromators had 10 nm bandwidth fixed slits. The fluorescence was measured at 90° to the excitation in the steady state mode. The excitation was stepped from 200 to 700 nm in 25 nm steps. The emission wavelength range was from the excitation wavelength plus 10 nm to 10 nm short of the twice the excitation wavelength. The emission monochromator was stepped every 2 nm.

Each measured emission was smoothed using a sum of Gaussians. Each Gaussian was represented by

$$P_i(x) = A_i \exp [-(x - x_{oi})^2 / 2 \sigma^2]$$

The Gaussians were equally spaced (x_{0i}), 4 nm apart on the emission wavelength axis. The width of each Gaussian (σ) was fixed at 4 nm. The amplitudes (A_i) were determined using a linear least squares fit from Mathematica (Wolfram Research, Urbana, IL). This smoothing technique avoided unwanted oscillations, preserved narrow Raman emission bands in the fluorescence spectrum, and extrapolated to a zero intensity at wavelengths beyond the measured region.

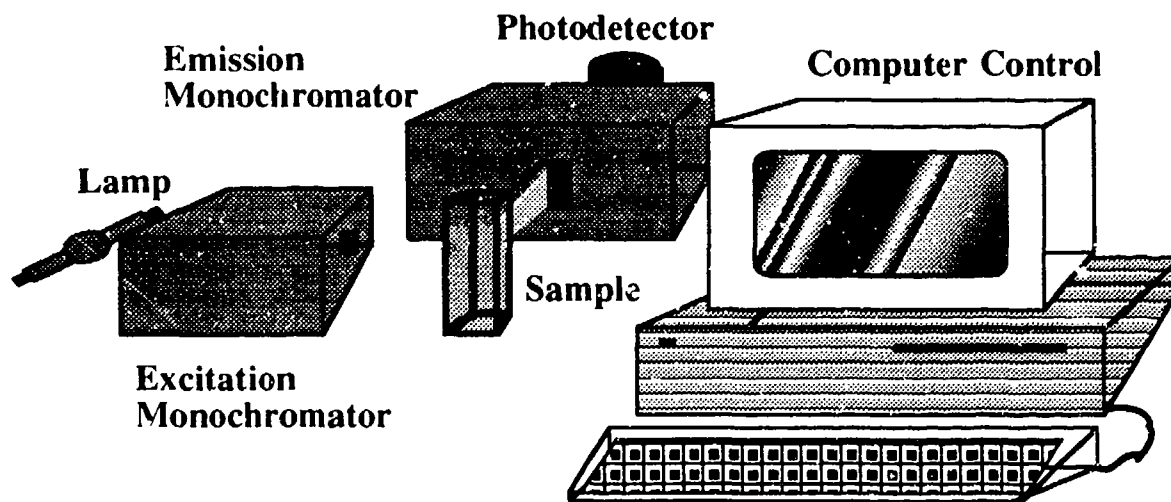


Figure 1: Experimental set-up. The light is from a continuous xenon arc lamp. The excitation wavelength is selected by a monochromator with a 10 nm bandwidth. This light is imaged onto the bacterial suspension in a quartz cuvette. The fluorescence is collected at 90° and passes through a second monochromator with 10 nm bandwidth. The fluorometer and subsequent data analysis is all under computer control.

The resulting smoothed curves were then combined into a contour plot using Mathematica. The fluorescent intensities from the contour plot were stored as a 21 x 21 matrix. This was transformed into a 441 element linear array and could be fit using a linear least squares technique.

Results and Discussion

The fluorescence spectra of the three bacteria and the tympanic membrane are shown in Fig. 2. The contours are often referred to as fluorescence finger prints. It is typical to see the excitation wavelength plotted on one axis and the emission wavelength plotted on the other axis. Instead, we have chosen to plot the excitation wavelength on one axis and a ratio of the emission wavelength divided by the excitation wavelength on the other axis. This unitless number from

1.0 to 2.0 gives a better presentation of the data, since the fluorescence spectrum is measured at wavelengths longer than the excitation wavelength and generally the spectrum is terminated at twice the excitation wavelength. At longer wavelengths, the second order transmission of the grating in the monochromator will distort the measurement. The fluorescence intensity is normalized to 1.00 at the peak. The contours are equally spaced along the intensity axis of the fluorescence.

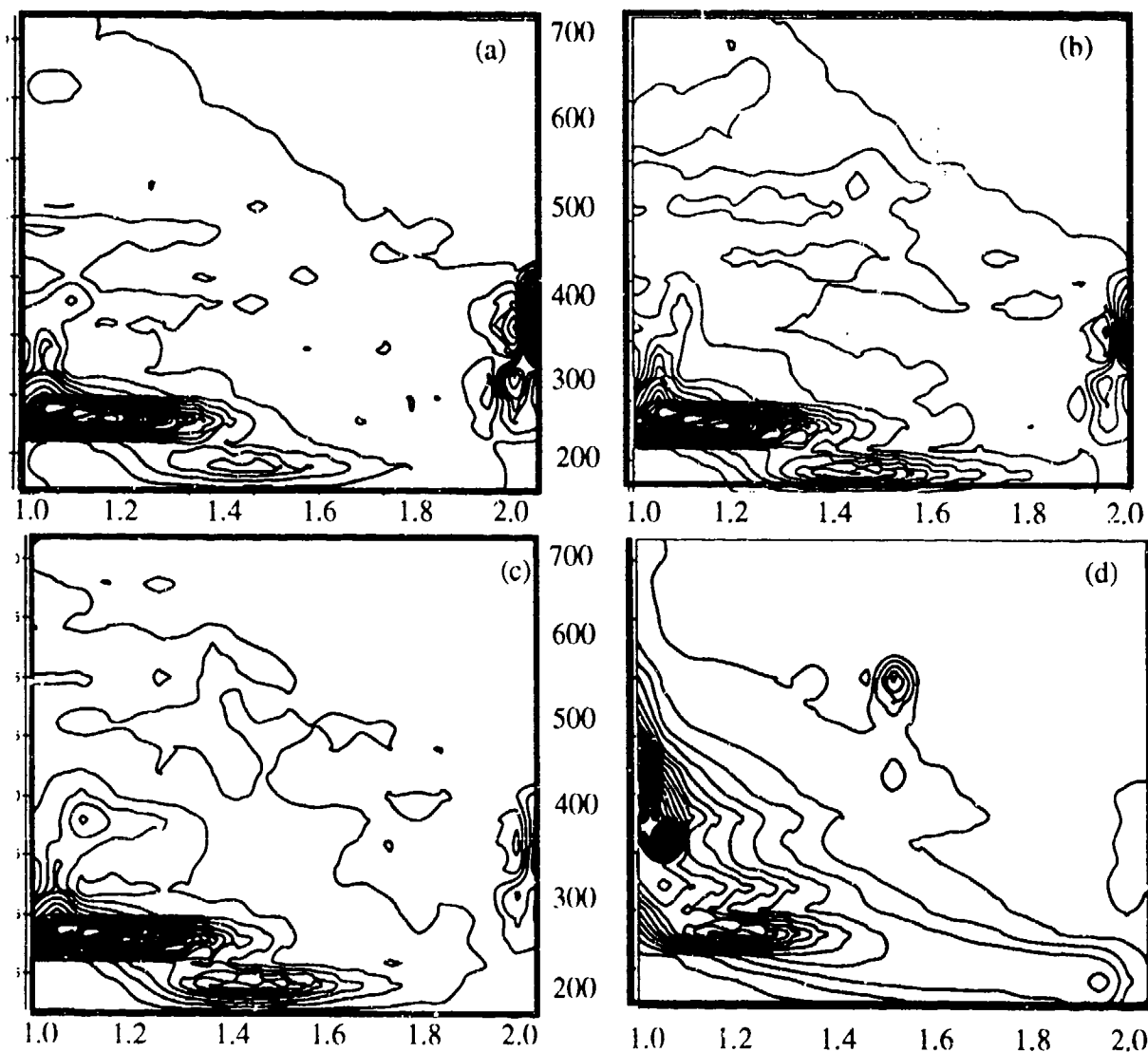


Figure 2 a-d: Fluorescence finger prints from four biological samples. (a) is *B. subtilis* grown in trypticase broth; (b) is *H. Influenzae* grown in trypticase broth; (c) is *Branhamella catarrhalis* in trypticase broth; (d) tympanic membrane from a fresh frozen chinchilla. The vertical axis is the excitation wavelength from 200 to 70 nm. The horizontal axis is the ratio of the emission wavelength divided by the excitation wavelength. The contours represent changes in the fluorescence intensity.

The fluorescence finger print of *H. influenzae* was measured from a sample grown in Luria broth (shown in Fig. 3). In all the fluorescent finger prints from bacteria, we see the strong fluorescence at 340 nm with a peak excitation wavelength near 280 nm.

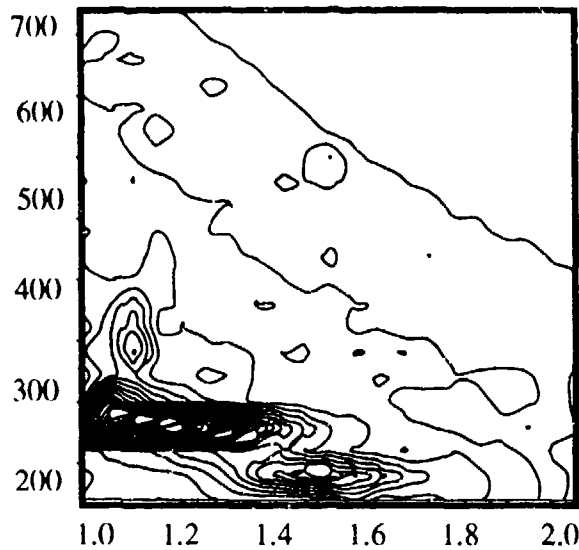


Figure 3: Fluorescence finger print from *H. influenzae* grown in Luria broth. The vertical axis is the excitation wavelength from 200 to 700 nm. The horizontal axis is the ratio of the emission wavelength divided by the excitation wavelength.

We treat this second measurement of *H. influenzae* as the unknown. The identification of the bacteria is not obvious upon visual inspection of the fluorescence finger print. We have therefore used a linear least squares technique. We use the measured the fluorescence finger prints of four different bacteria from above. We then use a linear least squares fit to "fit" the measured fluorescence profile of the unknown (designated $\text{data}(x_i)$) to the four known spectra (designated $f_j(x_i)$). In this notation, j is from 1 to 4 for the four different bacteria. The subscript i is for the individual data points that compose the fluorescence finger print. The least squares fit minimizes

$$\sum_i [\text{data}(x_i) - \sum_j A_j f_j(x_i)]^2$$

Where A_j is the coefficient for each of the known spectra to "fit" the measured spectrum. The coefficients, A_j can be found from

$$A_j = \sum_{ik} [V_{jk} f_k(x_i) \text{data}(x_i)]$$

and

$$(V_{jk}^{-1}) = \sum_i [f_j(x_i) f_k(x_i)]$$

Using the above data, the coefficients from fitting *H. influenzae* grown in Luria broth, the A_j 's, are: A (*Branhamella catarrhalis*) = 0.055; A (*H. influenzae* grown in trypticase broth) = 0.901; A (*B. subtilis*) = 0.085; and A (tympanic membrane) = 0.005. The match is easy to see.

The measured data that matches the known spectra typically has a fit coefficient 3 to 6 times larger than any other coefficient. We have used our technique with several different bacteria and combinations of known bacteria. To minimize the computer requirements and increase the speed of the fitting, we are currently trying to find what regions of the fluorescence fingerprint are characteristic of the fingerprint. Data from regions that are not characteristic can then be dropped. This will also allow us to make measurements with lasers. For example, a nitrogen pumped dye laser is not tunable from 200 to 700 nm without an expensive frequency doubling laser system. If the data at excitation wavelengths shorter than 337 nm are not essential, this technique will prove invaluable for remote detection and identification using small, portable nitrogen laser systems. Also, we are attempting to make the measurements using optical fibers to deliver the exciting light and to couple the fluorescence back into the fluorometer. Since scattering of the shortest wavelengths of light in the best optical fibers limits the transmission near 200 to 300 nm, we again want to determine the importance of this data in the fingerprint. The optical fibers will permit point detection of fluorescence from samples that cannot be placed into the fluorometer (e.g., a contaminated hand).

Acknowledgements

We thank Burt V. Bronk for his many helpful discussions and encouragement with this work. This work has been supported by a grant from the SDIO through the Office of Naval Research as part of the Medical Free Electron Laser Program, Grant # N00014-87-C-0146.

References

- Chou-pong, P. G. Patonay, C.W. Moss, D. Hollis, G.M. Carlone, B.D. Plikaytis and I.M. Warner (1987). Comparison of Flavobacterium and Shpingobacterium species by enzyme profiles, with use of pattern recognition of two dimensional fluorescence data. Clin. Chem. **33**:377-380.
- Coburn, J.T., F.E. Lytle and D.M. Huber, (1985). Identification of Bacterial Pathogens by Laser Excited Fluorescence. Anal. Chem. **57**, 1669-1673.
- Cummin, H.Z. 1976. NATO Adv. Study Inst. Ser. Ser. B **B23**:200-225.

- Czégé, J. and L. Reinisch, Cross-correlated Photon Scattering During the Photocycle of Bacteriorhodopsin. *Biophys. J.* **58**:721-729.
- Dalterio, R.A., W.H. Nelson, D. Britt, J.F. Sperry, J.F. Tanguay, and S.L. Suib. (1986). Steady state and decay characteristic of protein tryptophan fluorescence from live bacteria. *Appl. Spec.* **40**:86-90.
- Dalterio, R.A., W.H. Nelson, D. Britt, J.F. Sperry, J.F. Tanguay, and S.L. Suib. (1987). The steady state and decay characteristics of primary fluorescence from live bacteria. *Appl. Spec.* **41**:234-241.
- Munro, I., I. Pecht and L. Stryer (1979). Subnanosecond motions of tryptophan residues in proteins. *Proc. Natl. Acad. Sci. USA* **76**:56-60.
- Reinisch, L., W.P. Van De Merwe, and B.V. Bronk (1991) Comparative fluorescence spectra from bacteria and spores in different stages of growth. *Biophys. J.* **59**, 161a
- Reinisch, L., J. Tribble, J.A. Werkhaven and R.H. Ossoff, (1992). Non-invasive Optical Diagnosis of Bacteria Causing Otitis Media, *Laryngoscope* (submitted).
- Rossi, T.M. and I.M. Warner (1985) in *Rapid Detection and Identification of Microorganisms*, W.H. Nelson, ed. Verlag Chemie, 1-50.
- Shelly, D.C., J.M. Quarles and I.M. Warner (1980). Identification of fluorescent *Pseudomonas* species. *Clin. Chem.* **26**:1127-1132.
- Shelly, D.C., J.M. Quarles and I.M. Warner (1980). Multiparameter approach to the "fingerprint" of fluorescent *Pseudomonas*. *Clin. Chem.* **26**:1419-1424.

UV LIDAR DETECTION OF BIOLOGICAL AEROSOLS

Steven Christesen, M. Scott DeSha, and Anna Wong, CRDEC
Clifton Merrow, Mark Wilson, and John Butler, STC Corp.

I. INTRODUCTION

UV laser induced fluorescence detection of biological agents was investigated from approximately 1980 to 1986. As a result of these studies, both the strengths (relatively high sensitivity) and weaknesses (difficulty in discriminating between different agents) are well known, if not well characterized. The recent conflict in Southwest Asia provided the impetus to revisit fluorescence detection of biologicals, and to design and construct the UV fluorescence lidar system described herein. Technological advances in lasers, digital oscilloscopes, and gated detectors (photomultipliers and detector arrays) that have occurred since the mid 1980's were incorporated into the design of this system to yield a capability that was not available during the time of the previous studies.

II. LIDAR SYSTEM

In designing the lidar system, our primary goal was to take advantage of all the information available from the interaction of the UV laser with the bioaerosol cloud. To this end, a three channel detection system was designed. The first channel comprised a solar blind photomultiplier tube (PMT) to collect the elastically scattered radiation at 266 nm. This channel was sensitive to the presence of any aerosol cloud, fluorescing or nonfluorescing.

The second channel, a gated PMT with a UG-1 filter, detected the total fluorescence in the 300-400 nm region. A dispersed fluorescence spectrum was obtained in the third channel via a spectrograph and gated intensified charge coupled device (ICCD) array detector. The lidar system is shown in Figures 1 and 2, and a list of components is provided in Table 1.

III. LIDAR TESTS

The UV lidar tests took place at Dugway Proving Ground, Utah in September and October of 1991. *Bacillus subtilis* var *niger* sp. *globiggi* (BG) spores were disseminated at ranges of 600, 1000, 2000, and 3000 meters. Tests were run both predawn (no solar background) and after sunrise (solar background present). The outputs from the three detectors are shown in Figure 3. The right hand peaks visible on the 266 nm scatter and the UV fluorescence plots are return from a white poster board used as a hard target for aligning the lidar system. The CCD intensifier gate delay and width were adjusted to overlap the fluorescence return as observed on the oscilloscope. This adjustment was crucial to maximizing the fluorescence signal and minimizing the solar background detected by

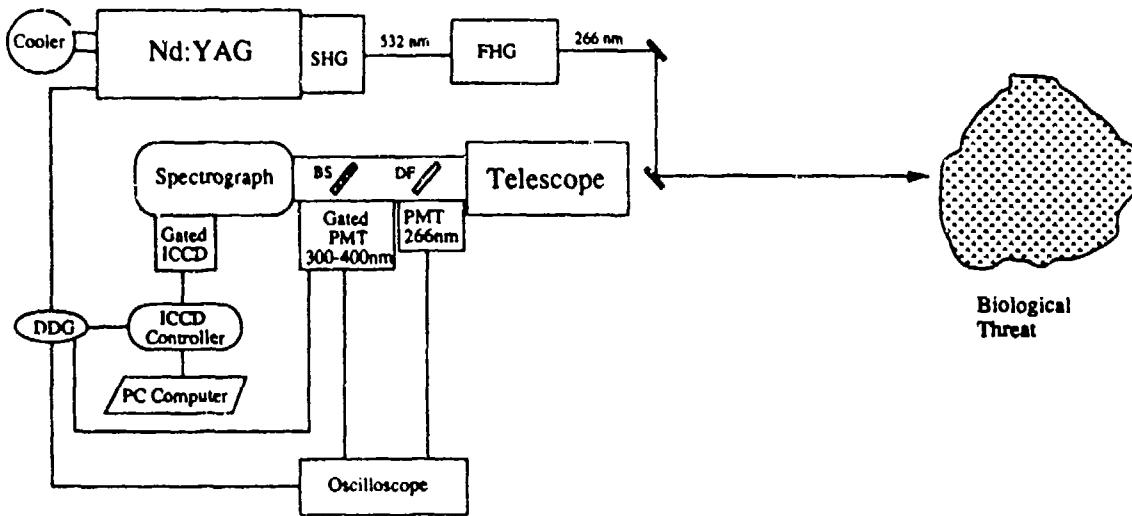


FIGURE 1: UV Fluorescence Lidar System

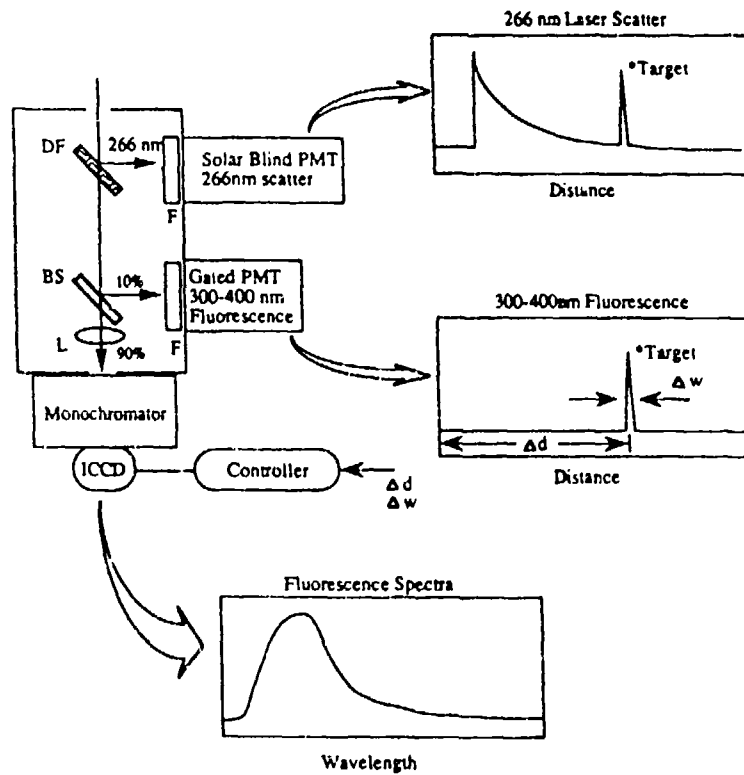


FIGURE 2: UV Fluorescence Lidar Detector Layout

the CCD. It should be pointed out that the system has not been calibrated, and that the dependence of the sensitivity on wavelength for the spectrograph/CCD has not been determined. These calibrations will be performed in the near future and the corrected spectra will be included in a subsequent publication.

DRY BG - [2000m, 6:50am, 190mJ]

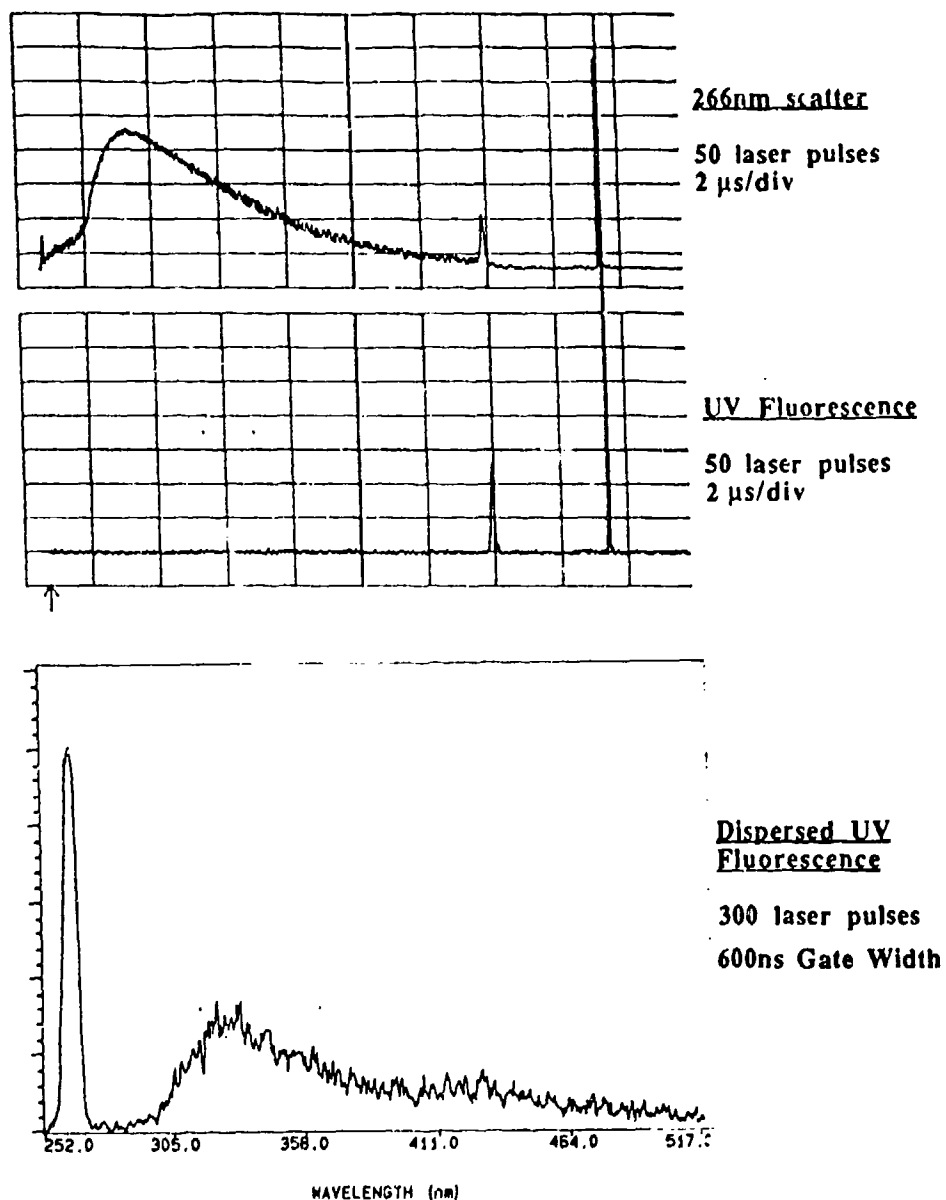


FIGURE 3: Outputs from 3 detector channels. Top: 266nm scatter, Middle: Total fluorescence 300-400nm, Bottom: Dispersed spectrum from ICCD.

TABLE 1: Lidar Components

COMPONENT	DESCRIPTION
Laser	Spectra-Physics Nd:YAG 4 th harmonic (266nm) 10Hz; 170-210mJ
Telescope	16" Casagrain
Gated PMT	Hamamatsu R955
Solar Blind PMT	Hamamatsu R166UH
Dichroic Filter (DF)	ARC Full Reflector 248-FR-45-2D-FL (98.5% ref.@248nm)
Beamsplitter (BS)	Fused Silica Uncoated Window
Filter (F)	ARC Interference Filter 266-S-2D (17% T, 90Å FWHM)
Filter (F')	Schott UG-1, 1mm Thick
Spectrograph	Thermo Jarrell Ash; Monospec 18, .18m FL
Intensified CCD (ICCD)	Princeton Instruments Model ICCD-576G/RB with UV-NIR response; 576x384 elements
Oscilloscope	LeCroy Model 7200

For all three detection channels, data were collected with the laser on followed by a background data collection with the laser blocked. The background signal was subtracted from the signal + background to produce the oscilloscope traces and spectra shown. An example of the subtraction process for the CCD data is shown in Figure 4. Even having to collect a background spectrum, it was possible to collect BG fluorescence spectra in real time as shown in Figure 5. The times of day for the data collection are listed to the right of the curve. This spectrum also contains the Raman scattering from atmospheric N₂ at approximately 284 nm. After calibrating the lidar system, we expect to be able to use this signal as a reference for calculating the BG concentration.

An Aerodynamic Particle Sizer (APS) was also located approximately along the laser line of sight providing time resolved measurements of particle concentrations and size distributions. Typical peak concentrations were on the order of 1000 to 3000 particles/cc with mass median particle diameters of 8 to 9 μm. The high particle concentrations appeared to yield large aggregates of the BG spores. It was not possible to correlate a specific lidar test result with a corresponding APS measurement, however, the highest particle count registered for the trial shown in Figure 5 was 2400 particles/cc.

Dry BG [600m; 200mJ; 8:47am]

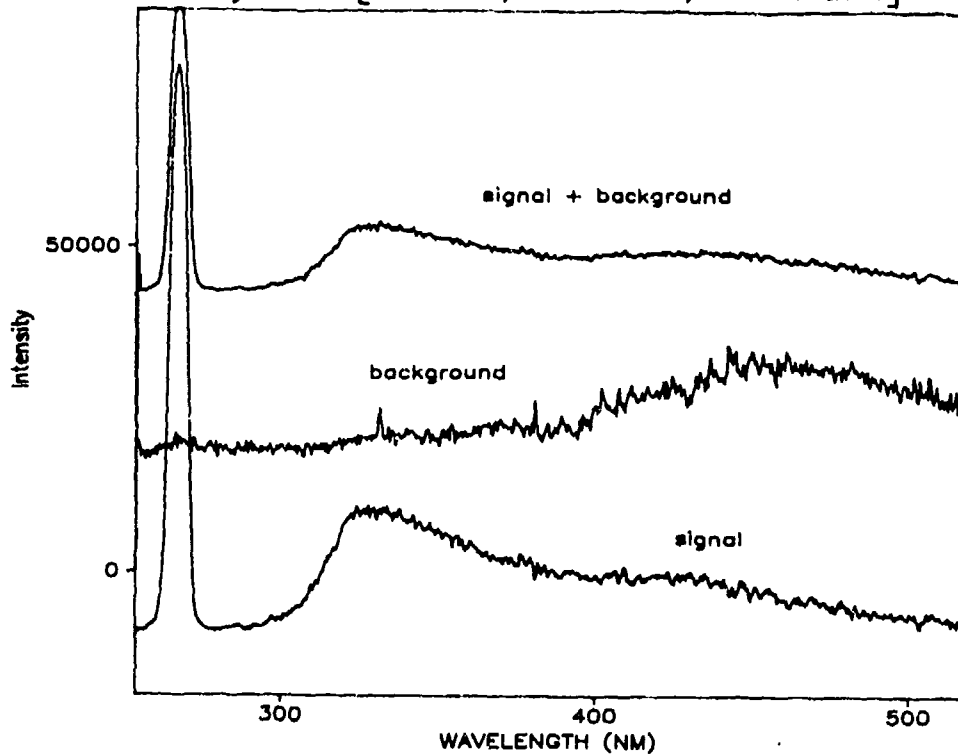


FIGURE 4: Subtraction of solar background

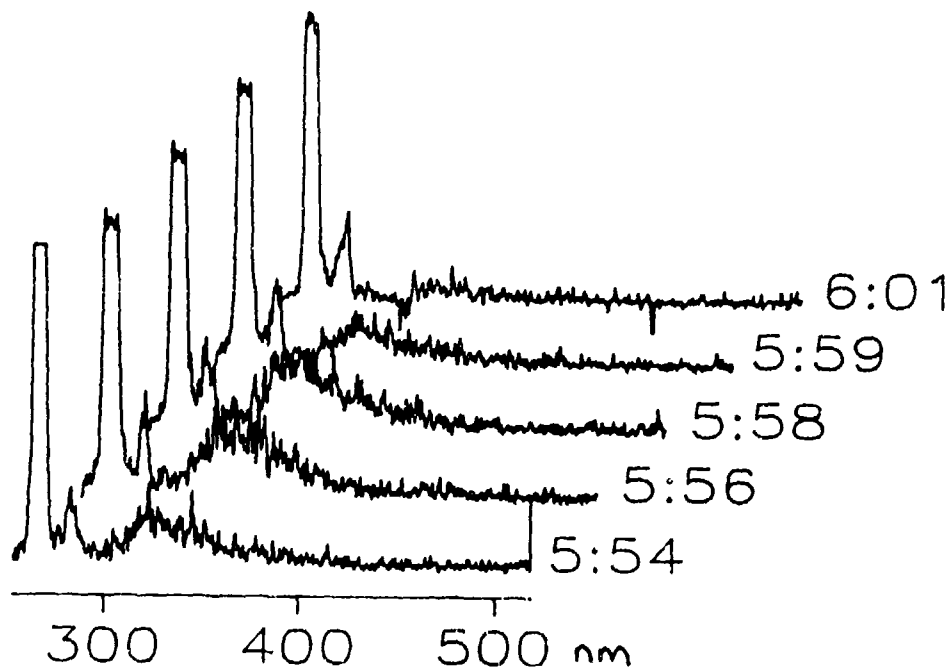


Figure 5: Dry BG at 3000m, 9/21/91. Times listed to right.

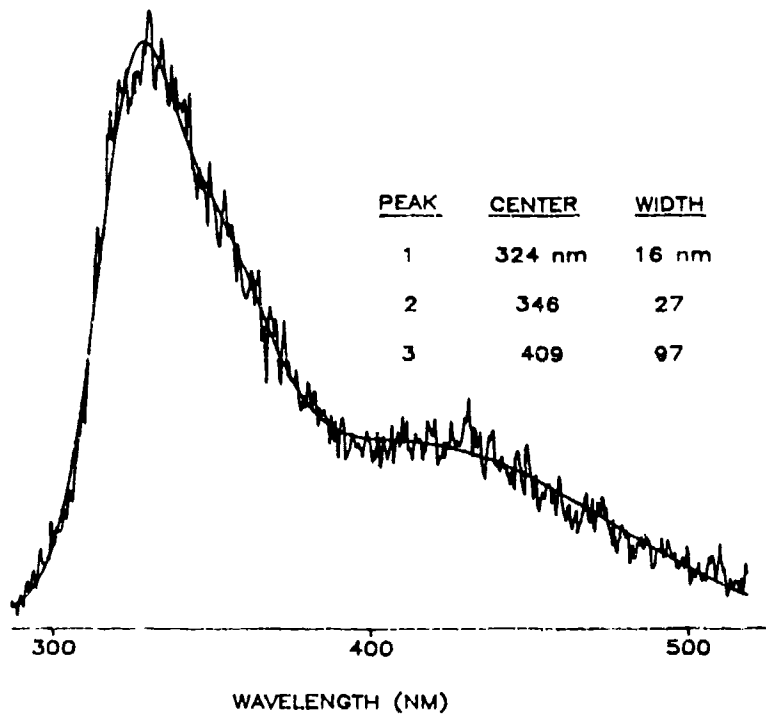


FIGURE 6: Fit of BG spectrum showing 3 peaks. Data from 9/23/91, range = 1000m.

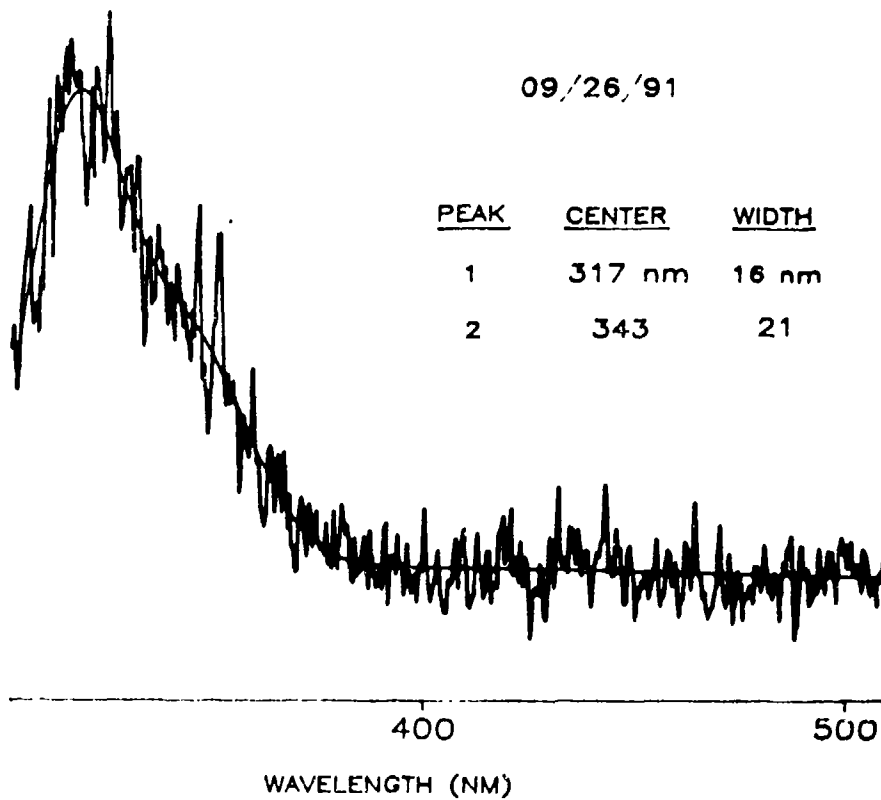


FIGURE 7: Fit of BG spectrum showing 2 peaks. Data from 9/26/91, range = 600m.

III. BG FLUORESCENCE SPECTRA

An interesting phenomenon observed during the tests was the apparent transformation of the BG spectrum. Spectra collected early in the testing exhibited a superposition of 3 peaks centered at 324nm, 346nm, and 409nm as determined by a least squares curve fitting routine (Figure 6). In the later tests (Figure 7), the long wavelength peak had disappeared and the spectra contained only 2 peaks; at 317nm and 343nm. These changes appear not to be correlated to time of day or attributable to incomplete subtraction of solar background. It will be important to understand the variability of the BG fluorescence spectrum (and by analogy the agent spectra) if a useful biofluorescence detector, either point or remote, is to be designed.

IV. SUMMARY

A biofluorescence lidar system has been built and tested and has demonstrated a capability to detect biological aerosols at ranges up to 2000 m in full sunlight and 3000 m at night. The ability to obtain dispersed fluorescence spectra in real time proved to be a great asset during the tests. This option does, however, limit sensitivity and might not be practical in a fielded system. The ability to predict the overall sensitivity of the lidar to actual agents hinges on the laboratory measurement of quantitative agent and simulant fluorescence spectra. It is also important to determine whether the spectra and/or cross sections change with particle size. The atmospheric nitrogen Raman signal provides an internal standard for calculating agent concentrations.

Blank

SUPPRESSION of MORPHOLOGY DEPENDENT RESONANCES by DROPLET SURFACE OSCILLATIONS

M. Essien, R. L. Armstrong, and J. B. Gillespie

M. Essien and R. L. Armstrong are with the Department of Physics, New Mexico State University, Las Cruces NM. 88003. J. B. Gillespie is with the U.S. Army Atmospheric Sciences Laboratory, White Sands Missile Range, New Mexico 88002

RECENT PUBLICATIONS: M. Essien, J. B. Gillespie, and R. L. Armstrong, "Observation of suppression of morphology-dependent resonances of singly levitated micrometer-sized droplets," *Appl. Opt.* **31**, 2148-2153 (1992).

ABSTRACT

Suppression of morphology-dependent resonance of the light elastically scattered by a laser-illuminated, micrometer-sized droplet is observed. A single nonabsorbing droplet is levitated using an electrodynamic quadrupole trap. The scattered light is monitored as the droplet slowly evaporates. Suppression is believed to be due to droplet surface oscillations which we model using an effective imaginary refractive index. Good agreement is obtained between the experimental curves and theoretical Mic computations.

5.1 INTRODUCTION

The characteristic resonance spectrum of a microsphere illuminated by plane, monochromatic radiation has been studied extensively.^{1,2,3} The

resonances arise when the incident radiation couples to the cavity modes of the sphere, and are denoted as TE (transverse electric) or TM (transverse magnetic). Resonances are also labelled by a mode number n and a mode order l . The mode number represents the order of the Ricatti-Bessel function that describes the radial part of the field, while the mode order denotes the l^{th} occurrence of a resonance with mode number n . For incident light polarized perpendicular to the scattering plane, the intensity of the scattered field is given by

$$i_s = \left| \sum_{n=1}^{\infty} \frac{2n+1}{n(n+1)} (a_n \pi_n(\cos\theta) + b_n \tau_n(\cos\theta)) \right|^2 \quad 1$$

where π_n and τ_n are angular dependent functions related to the Legendre polynomials, θ is the scattering angle, and n is the mode number of a particular resonance.

Suppression of morphology-dependent resonances of a single dye-doped microdroplet has recently been reported.⁴ The amount of suppression of an experimentally observed resonance was quantified by computing the contribution to the intensity of the same resonance of the theoretical curve providing the closest fit to the experimental data. The quality factor, Q , of the resonance is given by

$$Q = \frac{x}{\Delta x} \quad 2$$

where x is the size parameter and Δx is the full-width at half of the maximum resonance intensity. Experimental curves were obtained for a non-absorbing

droplet and for two absorbing droplets. Theoretical computations have shown that the suppression effect is greatest in narrow (high-Q) resonances.^{5,6} A similar result is obtained in our experimental observations. However, each of the curves of the absorbing droplets show more suppression than that predicted by Mie theory. Similarly, the non-absorbing droplet also shows suppression of the resonances with $Q > \sim 10^4$. An explanation for this additional suppression is presented in this report.

Suppression of MDR's by Surface Oscillations

Oscillations of the droplet surface caused by thermal fluctuations may cause suppression of MDR's. Lai et. al.⁷ have estimated this fluctuation to typically have an amplitude of about 0.1 nm and reports that the effect of these fluctuations is to lift the degeneracy of a particular mode, with the splitting given by

$$\langle \Delta\omega^2 \rangle = \delta^2 \omega_0^2 \quad 3$$

where ω_0 is the unperturbed frequency. The parameter δ is given by

$$\delta^2 = \frac{k_b T}{\gamma_s a^2} C_1 \quad 4$$

where $C_1 = 0.04$ for n (the mode number) $\gg 1$, k_b is the Boltzman constant, T is the temperature, and γ_s is the surface tension. Equation 3 then becomes

$$\langle \Delta\omega^2 \rangle = \frac{\omega_0^2 k_b T C_1}{\gamma_s a^2} \quad 5$$

The temperature is given by

$$T = T_0 + \Delta T \quad 6$$

where T_0 is the ambient temperature and ΔT is the increase in temperature that the droplet undergoes as it traverses a resonance. To determine ΔT , consider the two mass flux equations

$$m = \frac{DLMY_0}{RT_0^2(1-Y_0)} \frac{\Delta T}{a} \quad 7$$

$$Lm = \frac{K\Delta T}{a} = \frac{Q_a I}{4} \quad 8$$

where K is the thermal conductivity, D is the diffusion coefficient, L is the latent heat, M the molecular weight, and Y_0 the mass fraction. ⁸ Eliminating m and solving for ΔT ,

$$\Delta T = \frac{Q_a I a}{4(\Gamma + K)} \quad 9$$

Now Q_a may also be written as

$$Q_a = \frac{2\pi n}{\lambda \alpha_s} \quad 10$$

where α_s is the linear absorption coefficient.

Substituting $Q = \Delta\omega/\omega_0$, α_s becomes

$$\alpha_s = \frac{2\pi n}{\lambda} \frac{\Delta\omega}{\omega_0} \quad 11$$

The absorption coefficient α is related to the imaginary refractive index by

$$k = \frac{4\pi\alpha}{\lambda} \quad 12$$

Substituting equation 11 for α and using equation 5, equation 12 becomes

$$k_s = \frac{n}{2} \sqrt{\frac{k_b T C_1}{\gamma_s a^2}} \quad 13$$

Substituting for T, k_s becomes

$$k_s = \frac{n}{2} \sqrt{\frac{k_b C_1}{\gamma_s a^2} \left(T_0 + \frac{Q_a I_a}{4(\Gamma + K)} \right)} \quad 14$$

Therefore the effect of the surface oscillation is to increase the effective imaginary refractive index by an amount given by equation 14.

5.3 Results

The experimental apparatus is shown in Figure 1. Figures 2 through 4 show the transparent droplet experimental scattering curves ($\lambda = 0.488 \mu\text{m}$) along with the theoretical curves with a real refractive index $n=1.4722$ and imaginary refractive index $k=0$, for three ranges of droplet radii. The curves show scattered intensity vs size parameter as the droplet evaporates through the ranges from approximately 15.41 to $15.37 \mu\text{m}$, 15.35 to $15.31 \mu\text{m}$, and 14.71 to $14.68 \mu\text{m}$. Each range will subsequently be referred to as case 1, case 2, and case 3. Resonances in the experimental curves were labelled by noting the positions of the resonances in the theoretical curves and comparing these positions to positions obtained from a resonance location code.⁹ The

resonances in case 1 are, from the sharpest to broadest resonance, TE^{14}_{209} , TE^{15}_{205} , and TE^{16}_{201} . The case 2 resonances are TE^{14}_{208} , TE^{15}_{204} , and TE^{16}_{200} , while the case 3 resonances are TE^{13}_{201} , TE^{14}_{197} , TE^{15}_{193} . In each case the sharpest resonance (highest Q) is significantly less intense than the corresponding resonance predicted by theory. A check of these identifications was performed by modifying the Mie code of Bohren and Huffman¹⁰ so that the contribution from a specific resonance is omitted from the sum of equation 2. In this modification a loop is placed in the code so that the contribution due to a specified mode number n is neglected. If the identification is correct, the resonance associated with n will be absent from the scattering curve. The resulting curves for case 3 are shown in Figure 5. Similar curves were obtained for cases 1 and 2, confirming the resonance identification. Equation 14 shows that the effect of droplet surface oscillation is to increase the effective imaginary refractive index. For a non-absorbing droplet in thermal equilibrium with its surroundings, $k_s \approx 2.5 \times 10^{-6}$, so that an effective background suppression is present, even for the case of a transparent droplet. Figures 6-8 show the Mie theoretical calculations for a non-absorbing droplet with $k_s \approx 2.4 \times 10^{-6}$, 2.5×10^{-6} , and 2.6×10^{-6} , and the experimental curves of the droplet evaporating through the same size parameter ranges as in cases 1, 2, and 3. The effective k's that fit the experimental curves are determined with an accuracy of about 5%, about 0.1×10^{-6} for $k=2.5 \times 10^{-6}$. The theoretical curves show good agreement with the experimental curves.

5.4 Discussion and Conclusions

The total Q of the droplet may be written as

$$\frac{1}{Q} = \frac{1}{Q_0} + \frac{1}{Q_{\text{pert}}} \quad 15$$

where Q_0 is the Q of the non-absorbing droplet, and Q_{pert} arises from additional suppression mechanisms. In this case, Q is taken to be equal to the ratio, $x/\Delta x$, of the resonance peak of the theoretical curve that provides the best fit to the experimental curve. Therefore $1/Q_{\text{pert}}$ is given by

$$\frac{1}{Q_{\text{pert}}} = \frac{1}{Q} - \frac{1}{Q_0} \quad 16$$

It has been established that the principle mechanism contributing to Q_{pert} is suppression due to droplet surface oscillations. The effect of surface oscillations is quantified for three different values of the droplet radius by analyzing the theoretical curves that provided the closest fit to the experimental curves. This analysis was made by modifying the Mie scattering code so that only the contribution due to a specific resonance is included in the sum of equation 1. Figures 9-11 show intensity vs. size parameter for the narrowest resonances of cases 1, 2, and 3. The magnitude of Q_{pert} is calculated from these curves for each resonance and is listed in Table 5.1.

Table 5.1: Q_{pert} for the resonances effected by surface oscillations.

resonance	radius (μm)	k_s	Q_{pert}
TE ¹⁴ ₂₀₉	15.402	2.4×10^{-6}	2.2×10^5
TE ¹⁴ ₂₀₈	15.343	2.5×10^{-6}	2.8×10^5
TE ¹³ ₂₀₁	14.699	2.6×10^{-6}	3.2×10^5

The three values of the effective imaginary refractive index, k_s , listed in Table 5.1 were determined using equation 14 for the radii of the droplet at the resonances in question. The suppression effect believed to be due to surface oscillations is quantified by determining Q_{pert} at each resonance. Surface oscillations have been found to reduce the Q of the TE¹⁴₂₀₉ resonance by ~ 20%, the TE¹⁴₂₀₈ resonance by ~ 24%, and the TE¹³₂₀₁ resonance by ~ 25%. The error in a measurement of Q_{pert} was determined by varying the effective refractive index around the value of k_s determined from equation 13 until the theoretical curve no longer matched the experimental curve. This method yielded an error of about 12 % for each case. No detectable effect is noted for the moderate and broad resonances of cases 1-3.

REFERENCES

- 1 H. C van de Hulst , "Light Scattering by Small Particles", Dover, pp. 103-104, (1957).
- 2 R. Fuchs and K. L. Kliewer , "Optical modes of vibration in an ionic crystal sphere," J. Opt. Soc. Am. **58**, 319-330 (1968).
- 3 P. Chylek, "Partial-wave resonances and the ripple structure in the Mie normalized extinction cross section," J. Opt. Soc. Am. **66**, 285-287, (1976).
- 4 M. Essien, J. B. Gillespie, and R. L. Armstrong, "Observation of suppression of morphology-dependent resonances of singly levitated micrometer-sized droplets," Appl. Opt. **31**, 2148-2153 (1992).
- 5 P. Chylek, H. -B. Lin, J. D. Eversole, and A. J. Campillo , "Absorption effects on microdroplet resonant emission structure," Opt. Lett. **16**, 1723-1725 (1991).
- 6 B. A. Hunter, M. A. Box, and B. Maier, " Resonance Structure in Weakly Absorbing Spheres," J. Opt. Soc. Am A **5**, 1281-1286 (1988).
- 7 H. M. Lai, C. C. Lam, P. T. Leung, and K. Young, "Effect of perturbations on the widths of narrow morphology-dependent resonances in Mie Scattering," J. Opt. Soc. Am. B **8**, 1962-1973 (1991).
- 8 R. L. Armstrong , "Aerosol heating and vaporization by pulsed light beams," App. Opt. **23**, 148-155 (1984).
- 9 S. C. Hill (1992), private communication.
- 10 C. F. Bohren and D. R. Huffman, *Scattering of Light by Small Particles* (Wiley, New York) (1983).

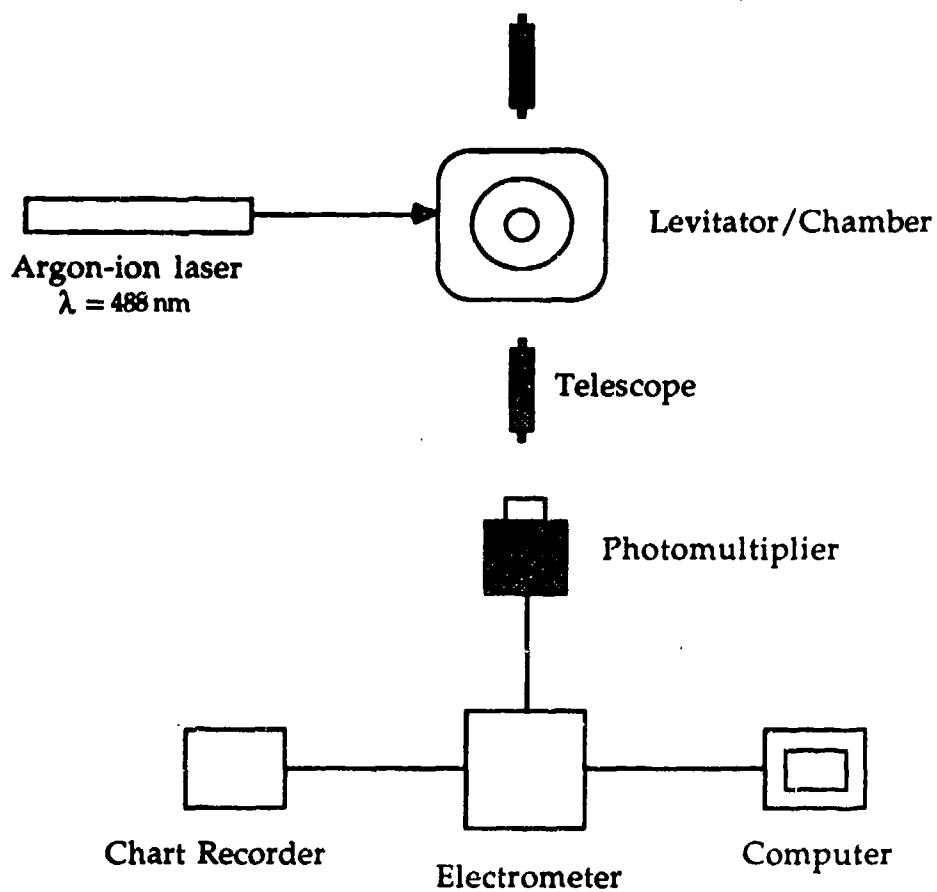


Figure 1. Experimental apparatus used to detect suppression of MDR's in microdroplets

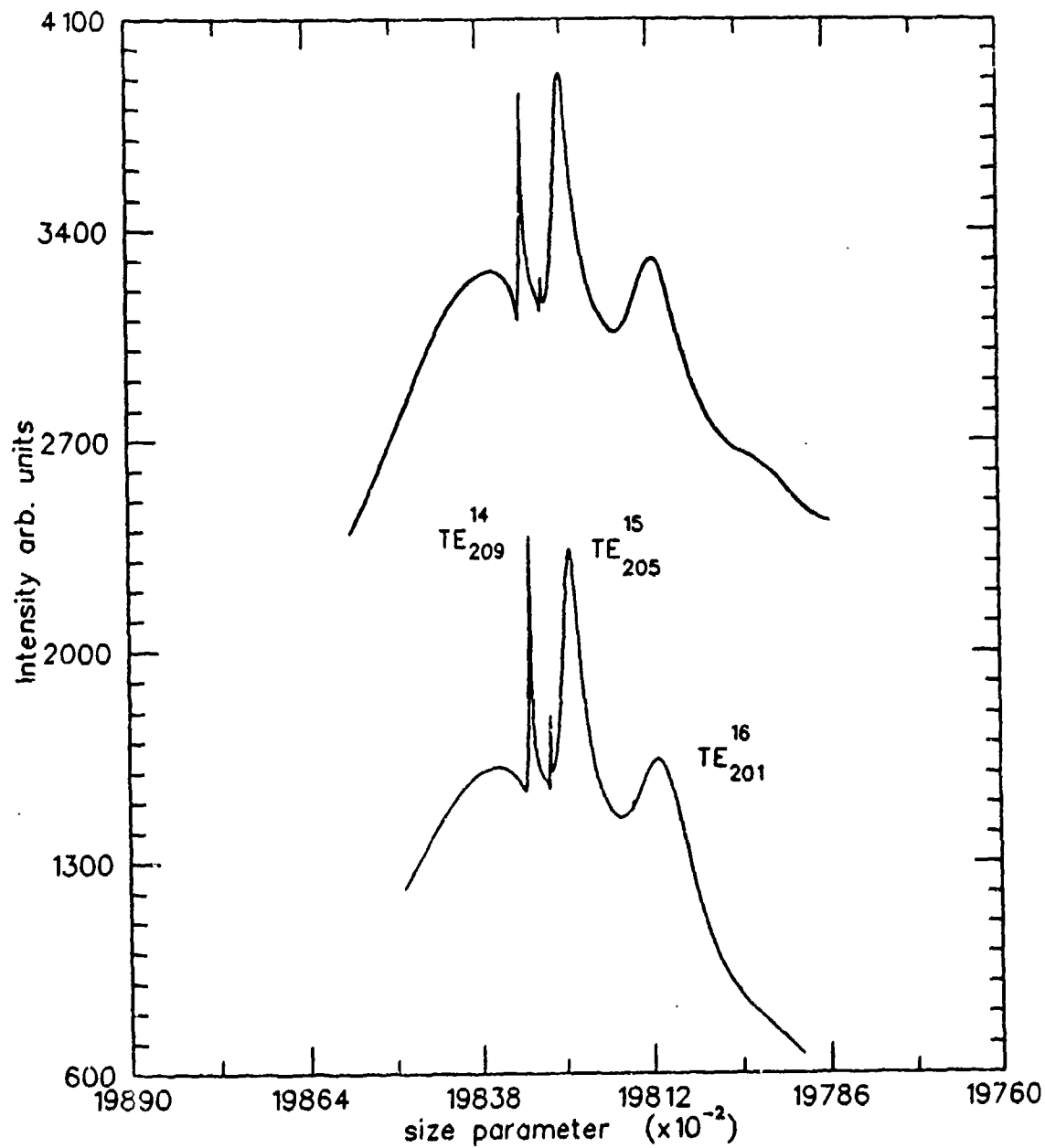


Figure 2. Experimental scattering curve of a glycerin/methanol droplet evaporating from $r = 15.41$ to $15.37 \mu\text{m}$ (top) along with the corresponding theoretical curve for $n=1.4722$ and $k=0.0$ (bottom).

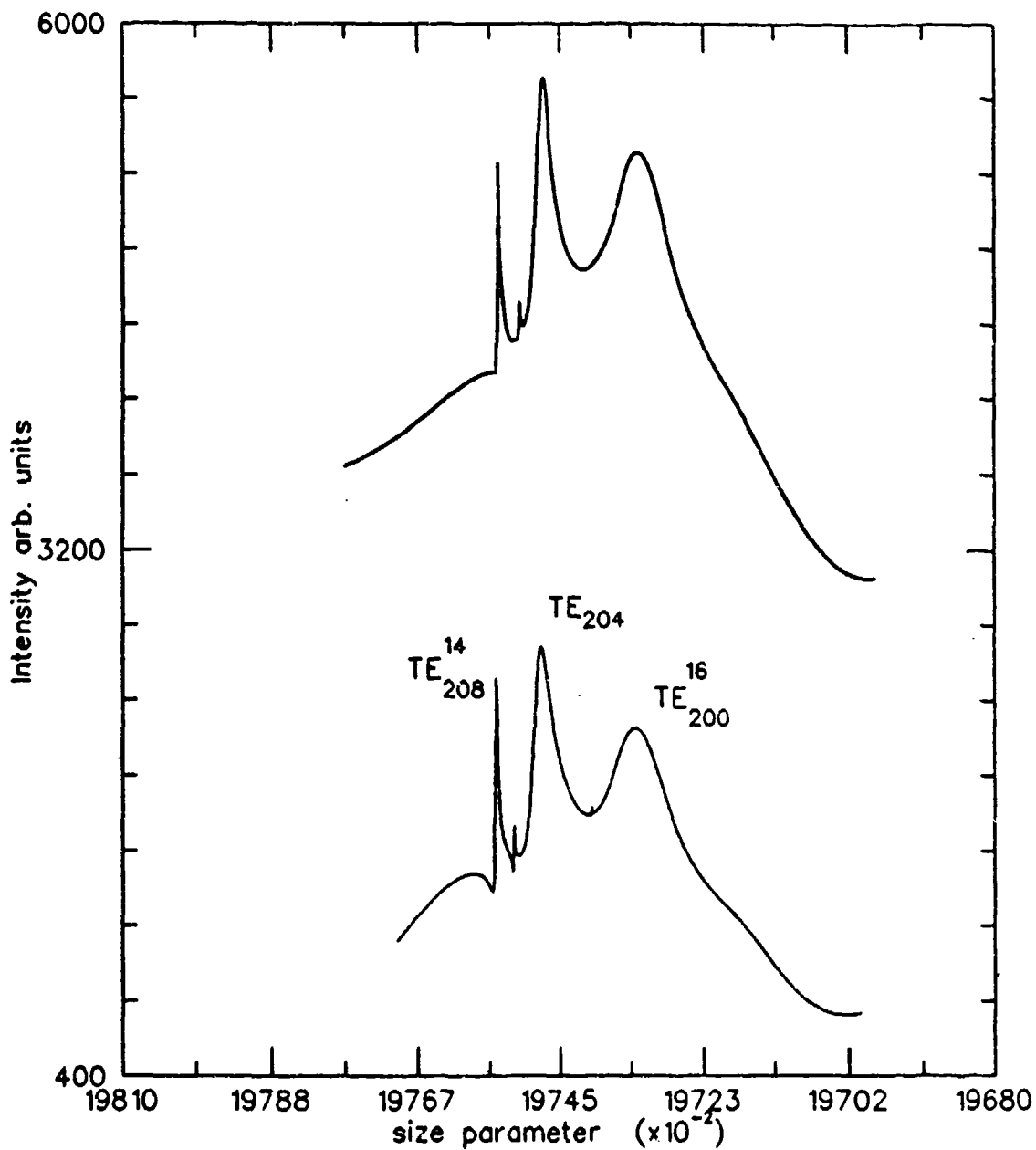


Figure 3. Experimental scattering curve of a glycerin/methanol droplet evaporating from $r = 15.35$ to $15.31 \mu\text{m}$ (top) along with the corresponding theoretical curve for $n=1.4722$ and $k=0.0$ (bottom).

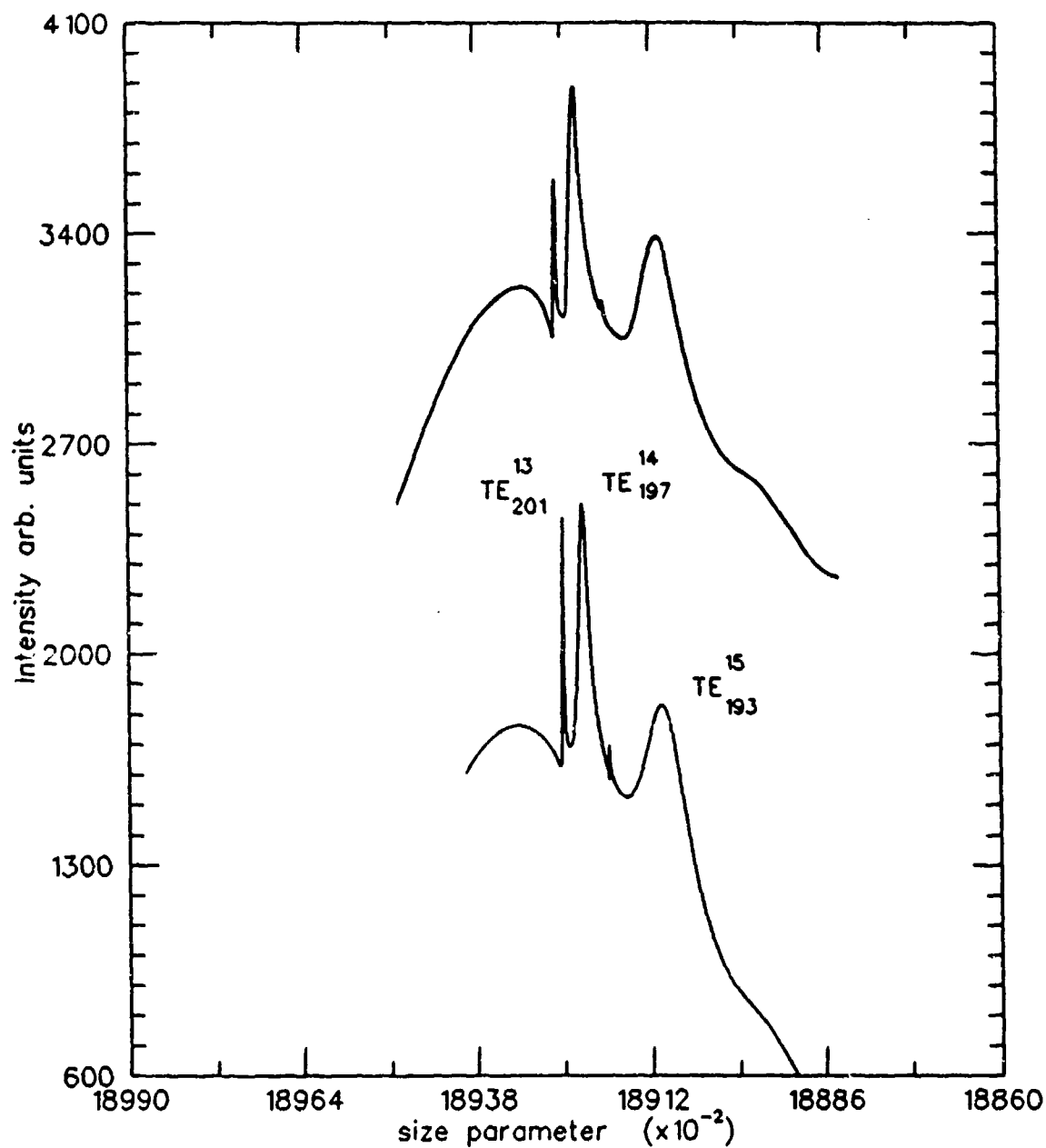


Figure 4 . Experimental scattering curve of a glycerin/methanol droplet evaporating from $r = 14.71$ to $14.68 \mu\text{m}$ (top) along with the corresponding theoretical curve for $n=1.4722$ and $k=0.0$ (bottom).

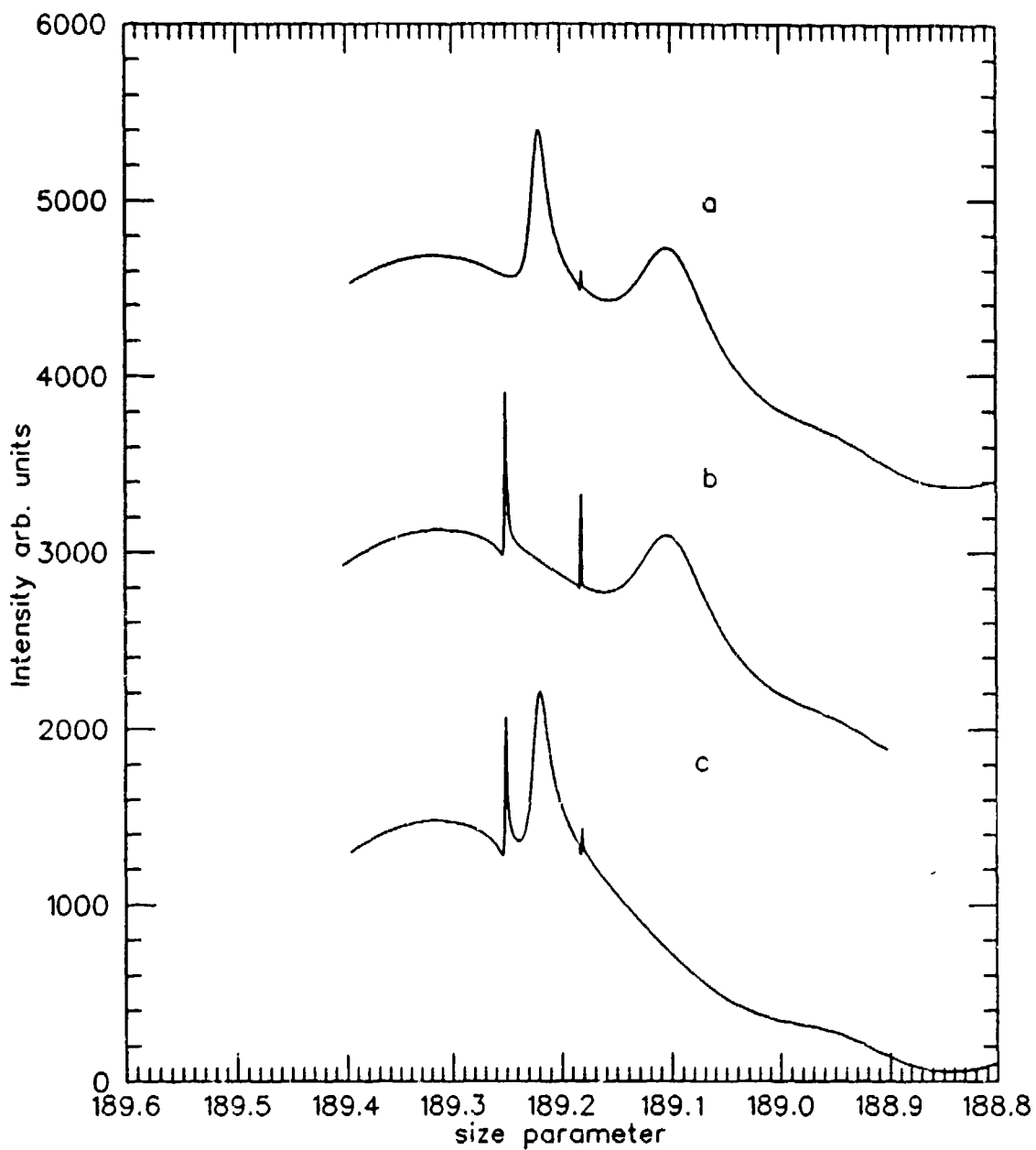


Figure 5. Check of the droplet resonance identification. The curves were generated by omitting the contribution to the scattered intensity from $n=201$ (a), 197 (b), and 193 (c).

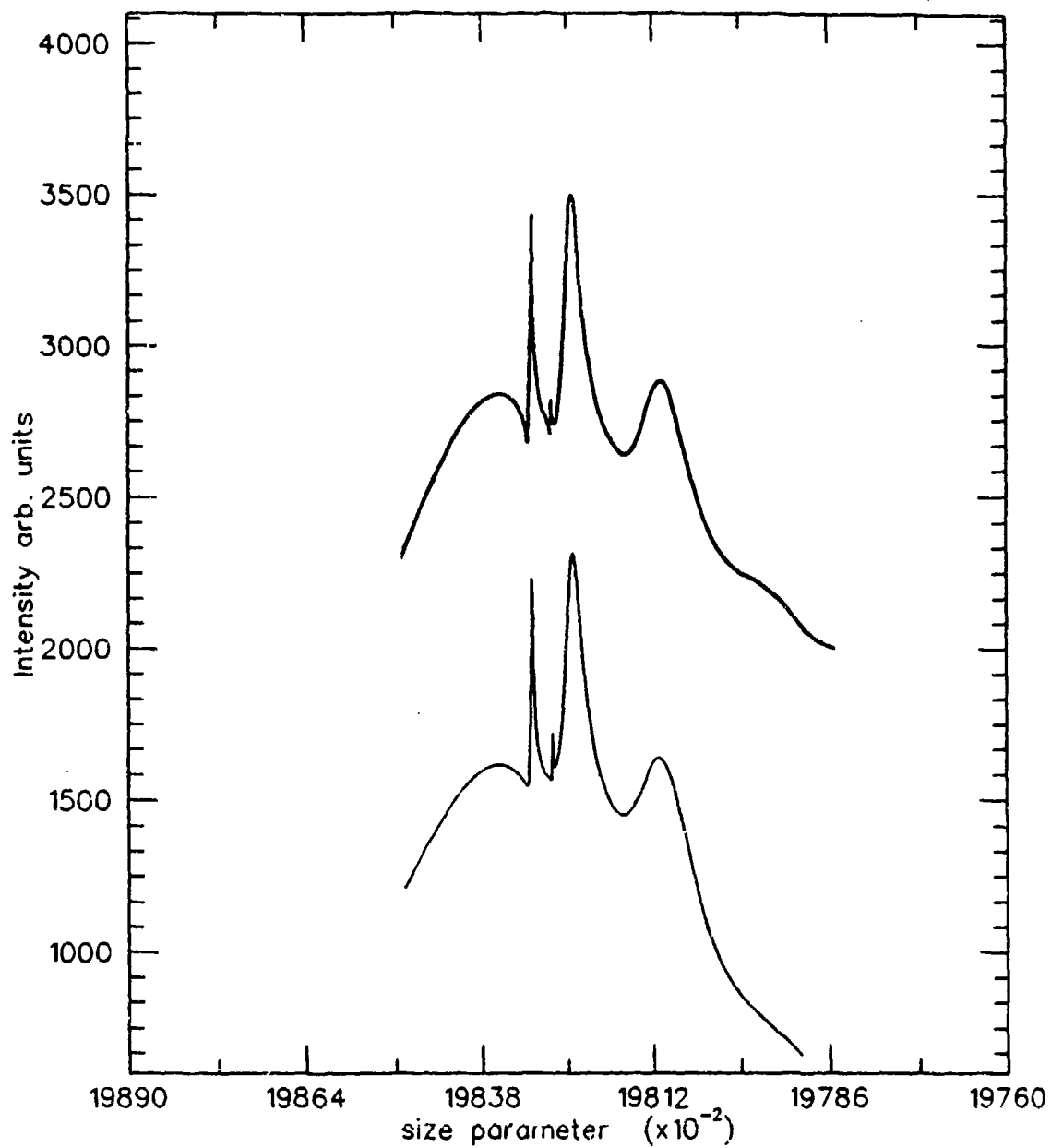


Figure 6. Experimental scattering curve of a glycerin/methanol droplet evaporating from $r = 15.41$ to $15.37 \mu\text{m}$ (top) along with the corresponding theoretical curve for $n = 1.4722$ and $k = 2.4e-6$ (bottom).

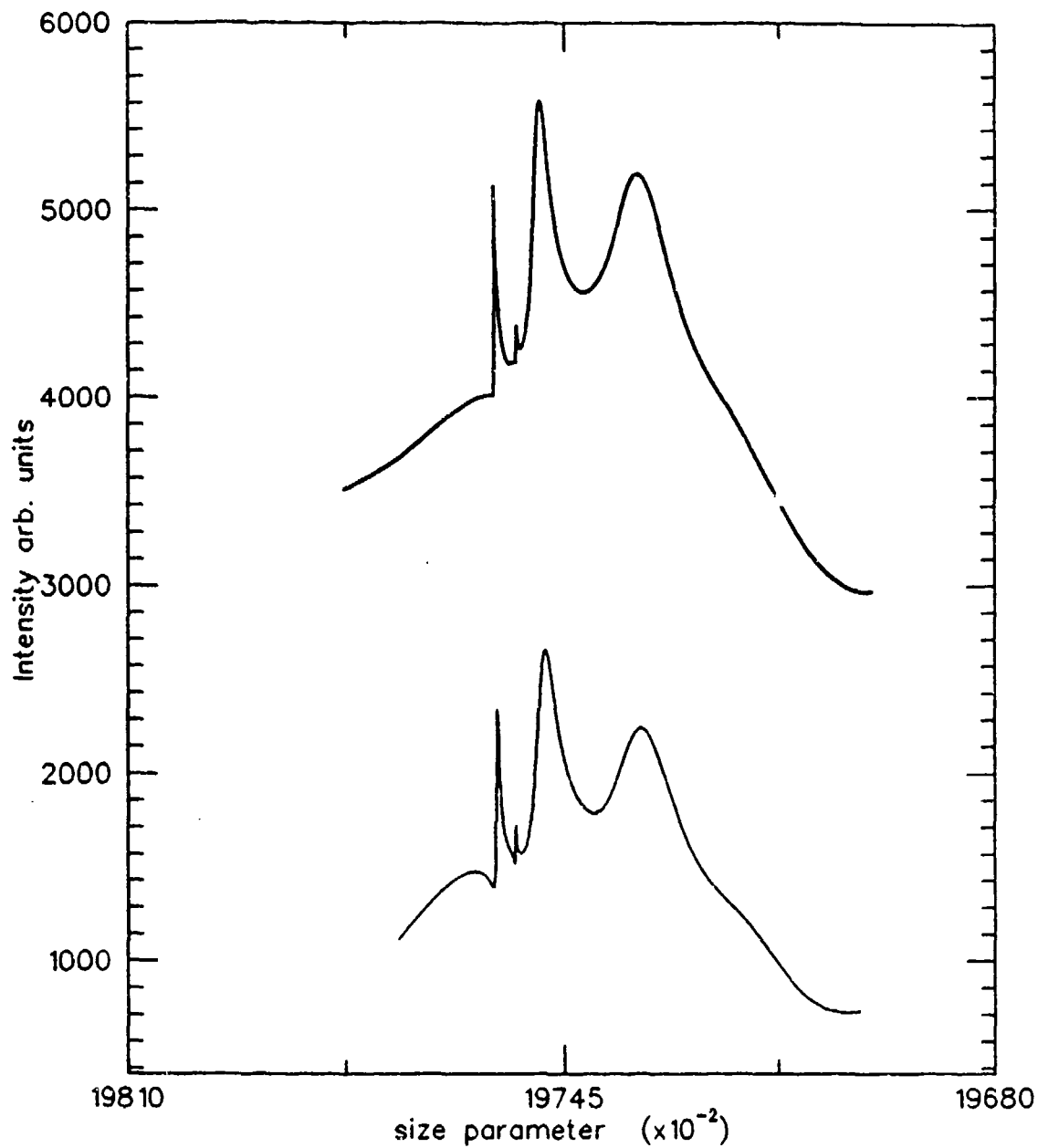


Figure 7. Experimental scattering curve of a glycerin/methanol droplet evaporating from $r = 15.35$ to $15.31 \mu\text{m}$ (top) along with the corresponding theoretical curve for $n=1.4722$ and $k=2.5e-6$ (bottom).

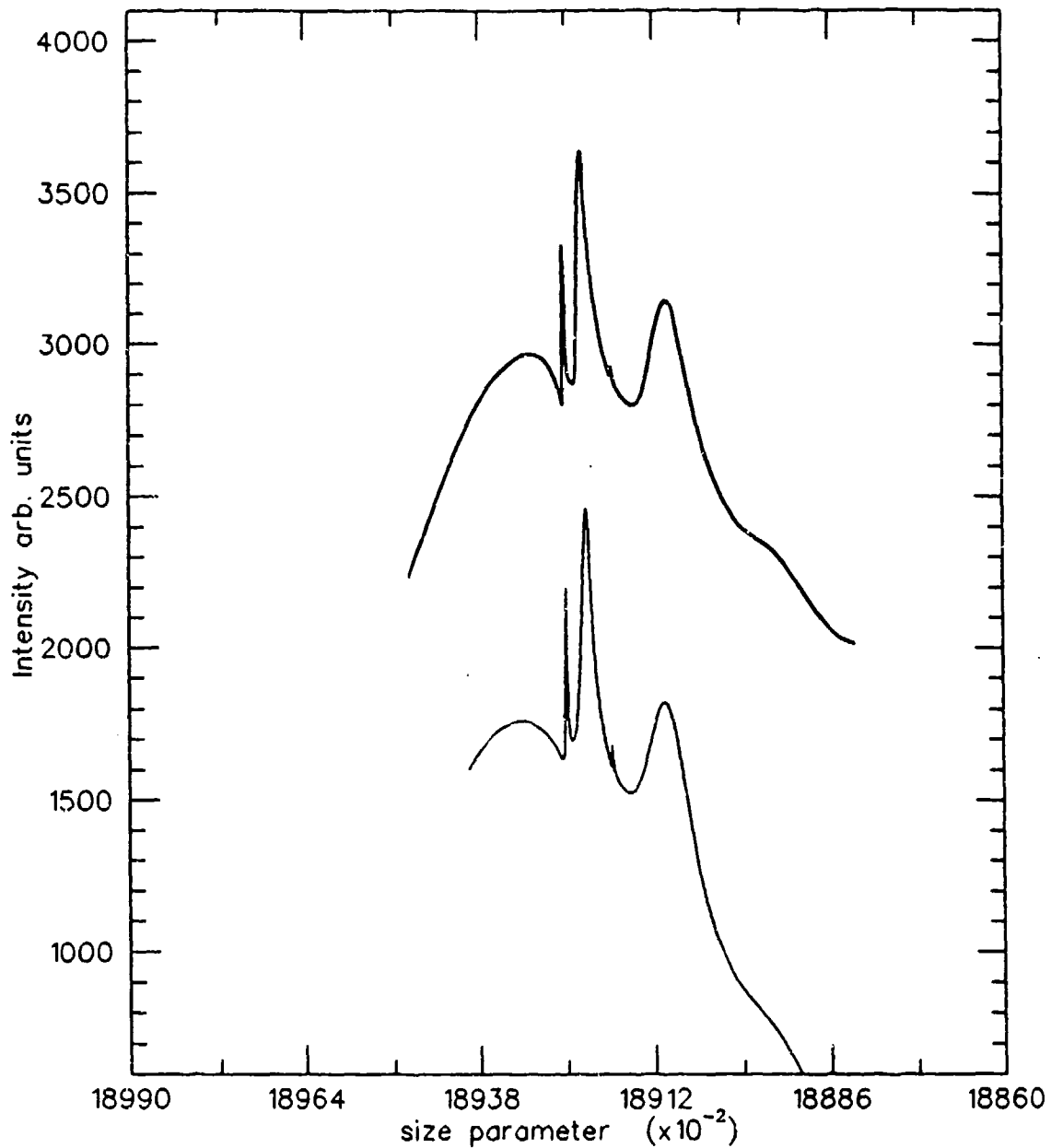


Figure 8. Experimental scattering curve of a glycerin/methanol droplet evaporating from $r = 14.71$ to $14.68 \mu\text{m}$ (top) along with the corresponding theoretical curve for $n=1.4722$ and $k = 2.6e-6$ (bottom).

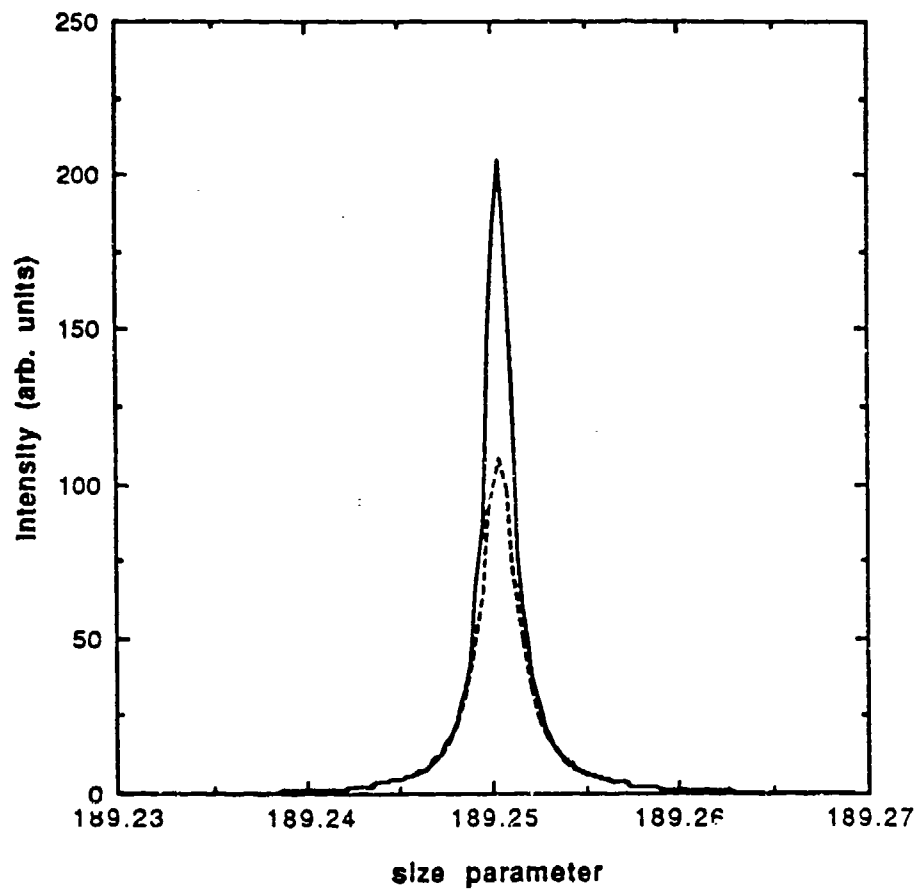


Figure 9. Contribution to the scattered intensity due to the TE_{13}^{201} resonance for $k=0.0$ (solid curve) and $k=2.6 \times 10^{-6}$ (dashed curve).

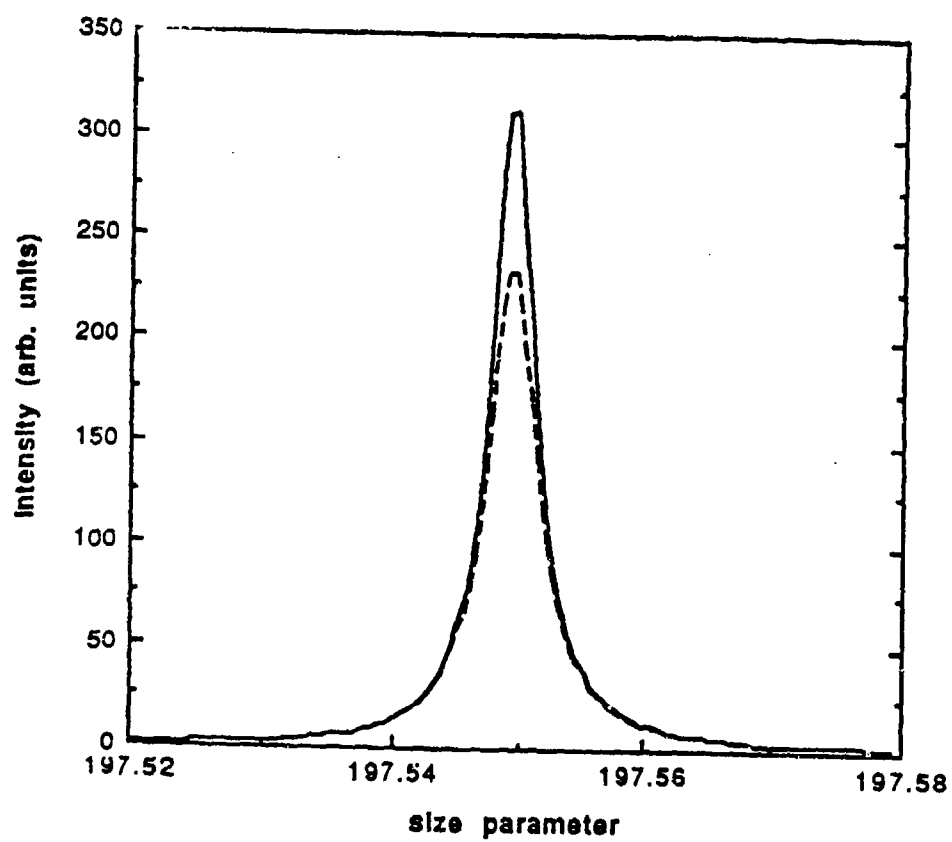


Figure 10 . Contribution to the scattered intensity due to the TE_{14}^{208} resonance for $k=0.0$ (solid curve) and $k=2.5e-6$ (dashed curve).

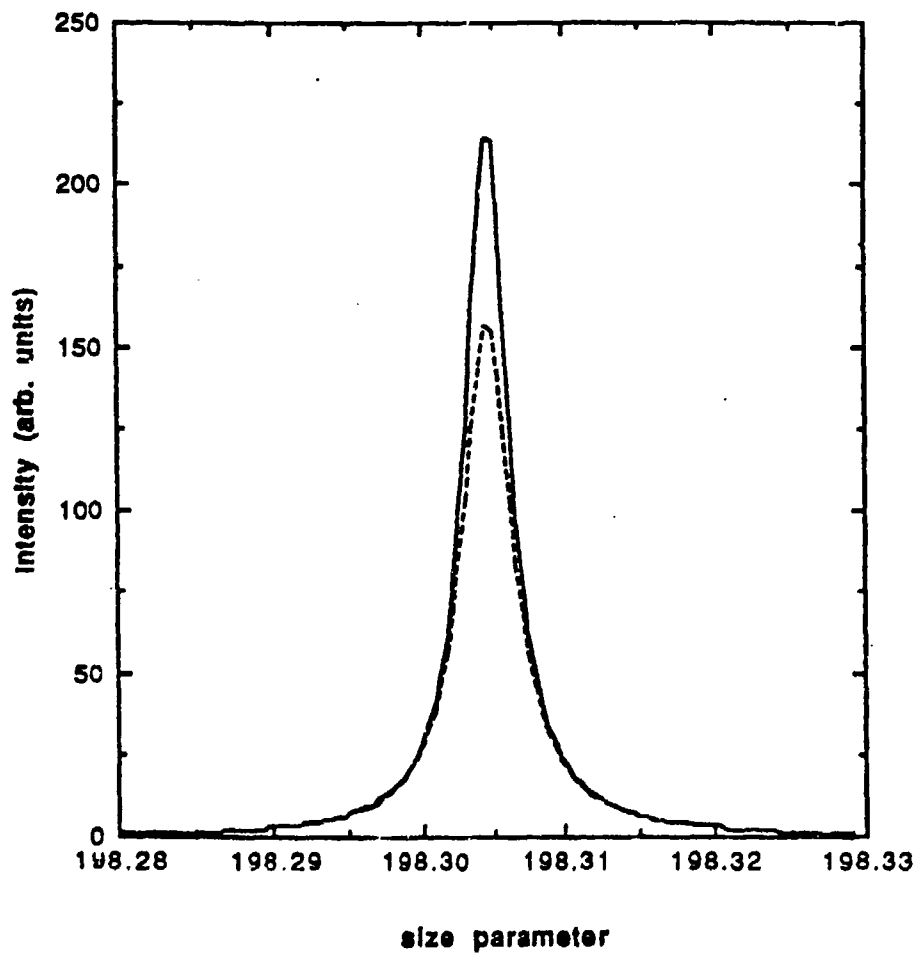


Figure 11 . Contribution to the scattered intensity due to the TE^{14}_{209} resonance for $k=0.0$ (solid curve) and $k=2.4e-6$ (dashed curve).

CARBON PARTICLES FROM HYDROCARBON FEEDSTOCKS

Christian A. Clausen
University of Central Florida
Orlando, FL 32816

Paul W. Morgan
Engineering Technology, Inc.
Orlando, FL 32826

Theresa Resetar-Racine and Gary Hermann
U.S. Army Chemical Research,
Development and Engineering Center
Aberdeen Proving Ground, MD 21010-5423

ABSTRACT

This paper describes the results of a series of studies that have been conducted to determine if multispectral screening materials can be generated from JP-8 or diesel fuel under battlefield achievable conditions. The work that is discussed demonstrates that carbon particles and filaments with desirable screening dimensions can be produced from either JP-8 or diesel fuel without the use of exotic co-reactants and within temperature and pressure limits that could be achieved under battlefield conditions. The investigations discussed show that carbon particles formed from JP-8 or diesel fuel feedstock exhibit superior screening clouds as compared to their droplet aerosols. In the infrared region, extinction coefficients exceeding $0.8 \text{ m}^2/\text{g}$ at 10 micrometers have been obtained from the JP-8 or diesel fuel feedstock. In addition, it has been demonstrated that carbon filaments with diameters in the range of 0.05 to 5.0 micrometers and lengths from 1.0 micrometer to 1.0 centimeter can be generated from a JP-8 feedstock under reducing conditions over a nickel, iron, or iron oxide catalyst. Conductivity and dissemination studies demonstrate that the carbon filaments generated from JP-8 exhibit attenuation properties in the microwave spectral region.

1.0 INTRODUCTION

The practice of using smoke screens for both offensive and defensive military operations has been a part of battle theater operations for hundreds of years. The earliest application of screening smokes most assuredly had as its objective the creation of a visual obscuring cloud. These smoke screens were generated by burning various types of combustible materials, quite often being what was available on the battlefield. As time progressed, battlefield equipment and operations improved and so did the types and applications of screening smokes. New materials such as phosphorus, titanium tetrachloride, fog oil, etc. were developed

for the purpose of producing more effective visual screening smoke clouds. Each of these materials in its own application was very effective in producing aerosols that exhibited very large extinction coefficients in the visible region of the electromagnetic spectrum. Some of these new materials could also be used to generate very large screening clouds. For example, fog oil, when subjected to a vaporization condensation procedure for generating aerosol particles can be used to generate visual screening clouds that are thousands of square meters in area. These large scale smoke screens have proven to be very effective in minimizing equipment and personnel losses on the battlefield. However, with the development of new weapon systems that operate in regions of the electromagnetic spectrum outside the visible band, a need has been created for screening smokes that attenuate in those regions outside of the visible window.

Another problem that has arisen with the use of fog oil to generate screening smokes is a result of changes in procedures and philosophy relative to logistic material support to the battlefield. The philosophy is to minimize the number of different types of items that must be supplied to the battlefield. Thus, fog oil, which is supplied in drum quantities becomes a logistic problem. The desire to simplify the logistical supply system to the battlefield is so strong that the military has decided that only one fuel will be used and that this fuel will be JP-8. Thus, with the Army's multispectral screening need being what it is and the possibility that the only potential material for generating a screening smoke is a JP-8 type hydrocarbon, it is an important issue to determine if in fact JP-8 can be used to generate an effective multispectral screening smoke.

Many methods have been investigated to accomplish the seemingly simple task of replacing the visual screening feedstock (fog oil) with more readily available feedstocks such as diesel fuel (DF) and JP-8. These schemes have thus far been impractical because of their demand for sophisticated apparatus (i.e. chemical plants, etc.) and/or special materials (i.e. high pressure gases, fuels, etc.). These requirements are incompatible with insitu generation in an operational theater. The problems as well as the potential pay offs increase when extension is made to IR and millimeter obscuration.

The objective of this paper is to summarize several studies that the authors have conducted that have been concerned with the development of methodologies for generating carbon particles and filaments from hydrocarbon feedstocks such as diesel fuel and JP-8. The primary operational guideline that the studies were conducted under is that the generation conditions be maintained within a range that could be produced in a battlefield environment.

2.0 TECHNICAL DISCUSSION

One of the primary purposes of the efforts described in this paper was to develop an understanding of the variables in the process required to maximize the production of carbon particles and filaments when using JP-8 or diesel fuel as the carbon source. These guidelines were developed by applying an experimental approach to a partial combustion process by using a systematic variation of air/fuel ratio, residence time, reaction zone temperature, and different types of catalysts. In addition to carbon yield measurements, extinction coefficients were determined for the airborne particles and filaments in the visual, infrared, and millimeter wavelength regions. Measurements were also made of the particle size distribution, evaporation rates, and settling times. In addition, comparison studies were conducted between droplet aerosols and particle aerosols.

2.1 THE GENERATION OF CARBON PARTICLE AEROSOLS

Hydrocarbon feedstocks have been used for many years to produce various carbon particulate products that have industrial value, with carbon black production being a primary example. Two important methods have been used industrially to produce carbon particulate products. One method is based upon the pyrolysis of a hydrocarbon feedstock, while the other method relies upon the partial oxidation of a hydrocarbon feed to strip hydrogen atoms off of molecules leaving behind a product that has a chemical composition corresponding approximately to C_6H . In the studies that are discussed in this paper, the partial oxidation method was used because it was determined that the equipment and operational demands that are required for this methodology could be achieved more readily under battlefield conditions.

The experimental apparatus constructed to generate carbon particles in the first laboratory study consisted of a heated isothermal reaction zone into which preheated air and vaporized diesel fuel or JP-8 was injected. A flow schematic of this research reactor is shown in fig. 1. The reaction zone temperature was set by a surrounding furnace and the air/fuel ratio varied by independent control of the air and fuel injected into the reaction zone. Residence time in the reaction zone was varied by air flow rate and by the relative location of the fuel introduction points. Initial studies in the use of the laboratory scale reactor to produce carbon particles from a hydrocarbon feed were conducted to establish operational procedures and to select process variables for parametric studies to maximize carbon particle yield from the partial combustion of diesel fuel or JP-8^{1,2}. The parametric matrix included variations of: 1) reaction zone temperature, 2) air/fuel mass ratio, 3) reaction zone residence time, 4) fuel preheat temperature, and 5) additives mixed with the hydrocarbon feed.

A summary of the major results is provided in Figs. 2, 3 and 4. The carbon particle yield proved to be a strong function of reaction zone temperature, Fig. 2. A maximum temperature of 1,150°C

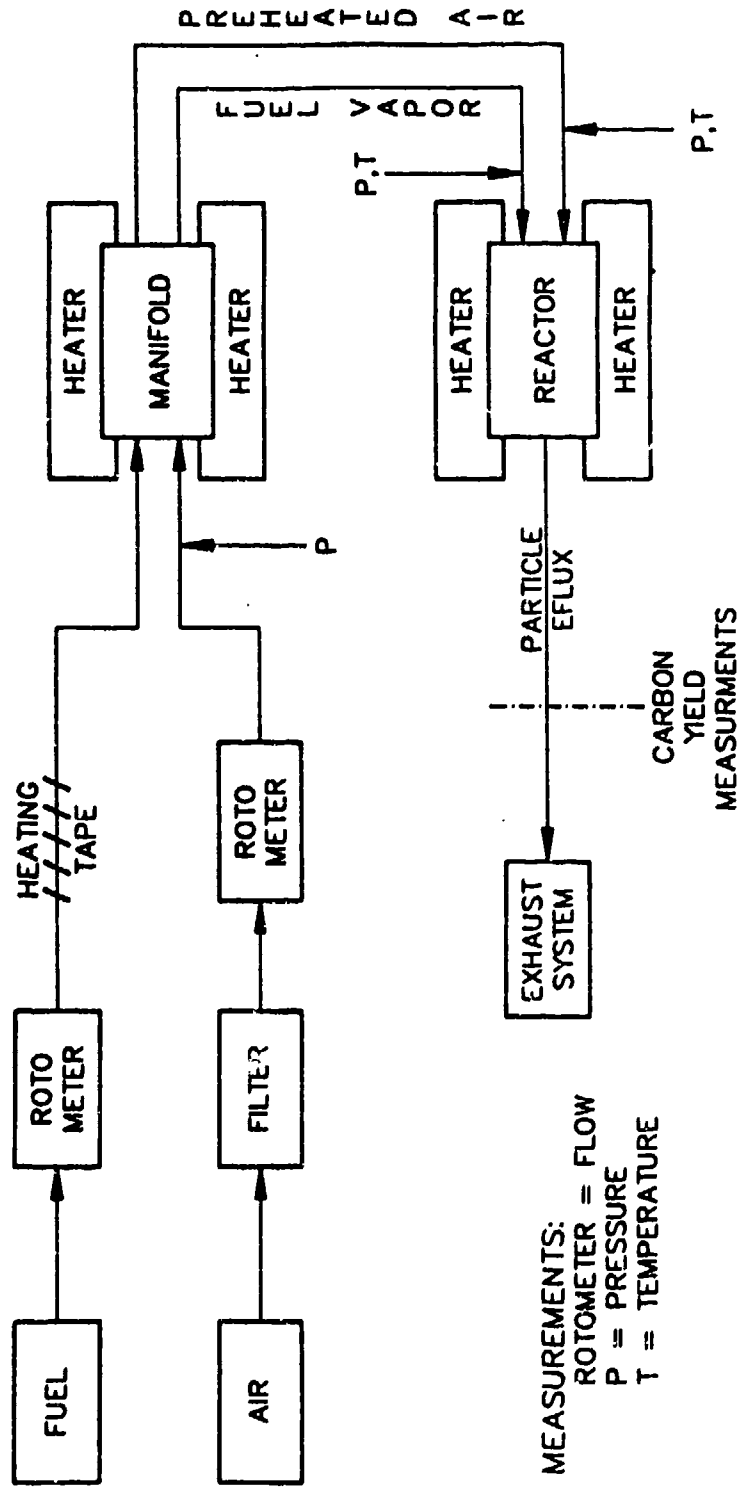


Figure 1. Schematic of research reactor.

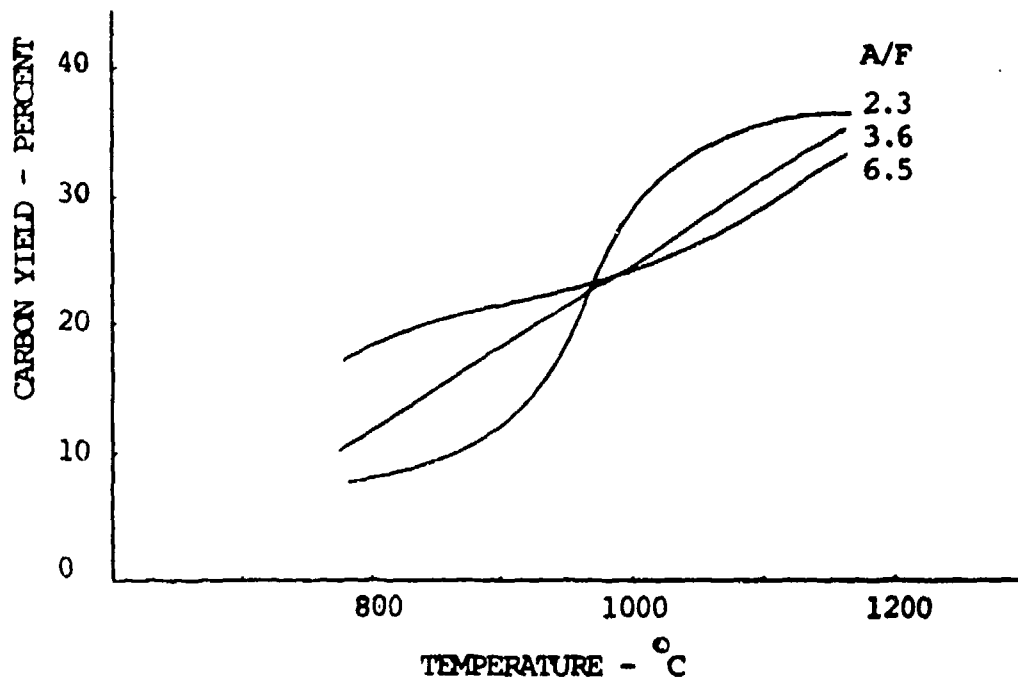


Figure 2. Effect of temperature on carbon yield.

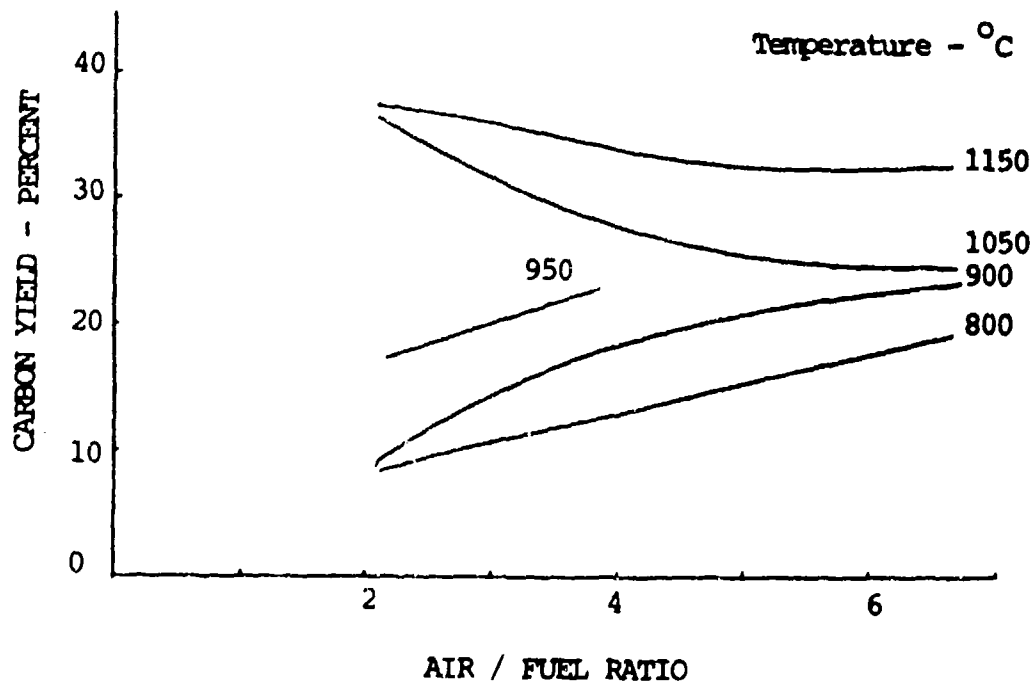


Figure 3. Effect of air/fuel ratio on carbon yield.

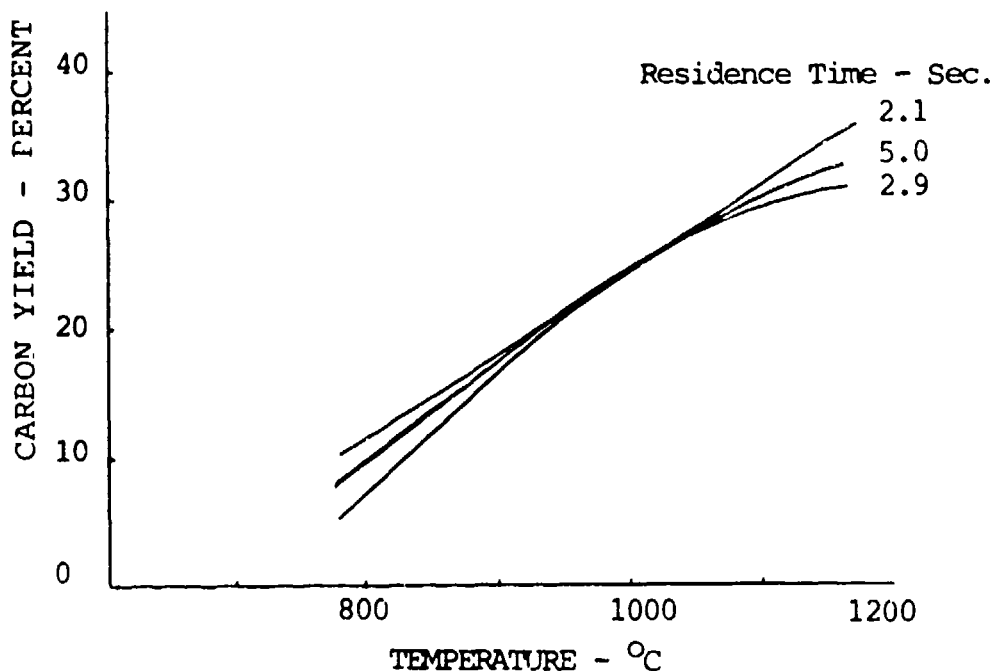


Figure 4. Effect of residence time on carbon yield.

was observed in order to respect practical temperature limits of field smoke generators. The carbon yield was a much weaker function of air/fuel ratio in the range from 2 to 6, Fig. 3. The differences noted in yield due to changes in reaction zone residence time from 1 to 5 seconds were not significant compared to uncertainty in the data, Fig. 4.

Based upon the results that were obtained with the laboratory scale reactor, a larger scale prototype reactor was designed and built. The schematic for this reactor is shown in fig. 5. The preheat air for this carbon particle generator was obtained from a turbocombustor that was matched to the particle generator.

The scaled up generator was capable of processing 0.1 gpm of diesel fuel or JP-8 while maintaining a carbon particulate yield of approximately 40%. A photograph detecting the quality of the carbon particle aerosol produced by this generator is shown in fig. 6.

The results of these initial studies demonstrated that it is possible to produce carbon particle aerosols from diesel fuel and JP-8 feedstocks by using the partial oxidation method. While these initial studies established the feasibility of this technology, they also served to uncover several areas where further work is required before a full field scale size carbon particle generator can be designed and built. For example, one area that must be addressed concerns the relative large size of the reactor that is required to process high hydrocarbon feed rates. Scale up of the

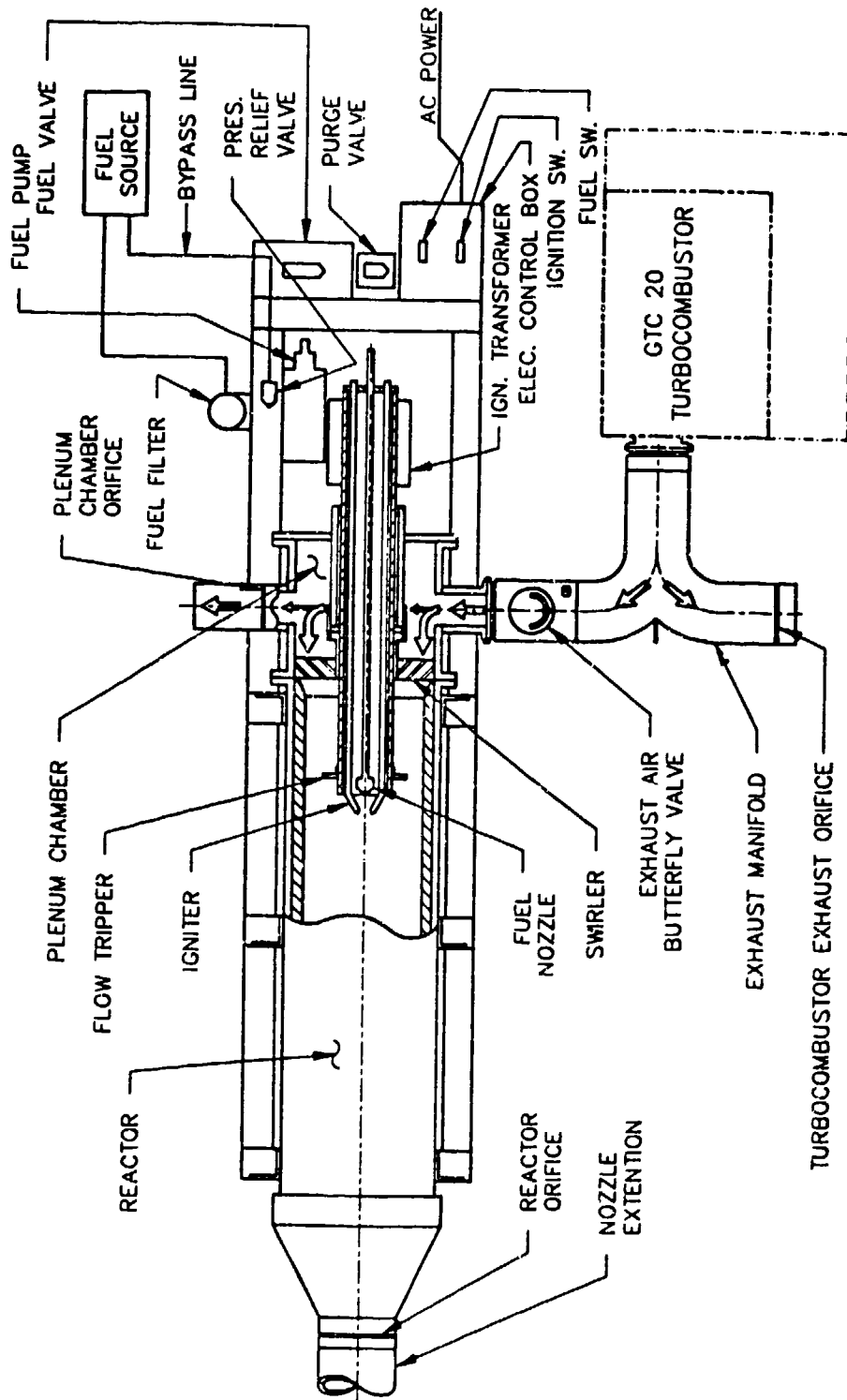


Figure 5. Integrated turbocombustor/prototype carbon particle generator.



Figure 6. Carbon Particulate aerosol produced by scaled-up prototype generator.

prototype generator would result in a reactor diameter of approximately 17 inches to achieve 0.5 gpm of diesel or JP-8 feed. Therefore, these and other unique methodologies need to be investigated further in order to reduce the size of the equipment. One potential method might be to operate the reactor at higher pressures, thus increasing the carbon yield per reactor volume ratio. Other methods include the use of flame containment and reaction quenching devices.

2.2 PROPERTIES OF CARBON PARTICLE AEROSOLS

The carbon particulate aerosols that were produced by the generators described in Section 2.1 were subjected to a series of tests in order to characterize them both chemically and physically. In addition, numerous tests were conducted in order to establish the attenuation properties of the particle aerosols.

Extinction coefficients in both the visible and infrared spectral regions were determined for carbon particle aerosols produced at selected particle generator conditions. Measurements were made in the Engineering Technology, Inc. 10 m³ test chamber located at the University of Central Florida and in the 190 m³ test chamber located at CRDEC. Agreement between the facilities was excellent and is shown in the data in Fig. 7 and Table I.

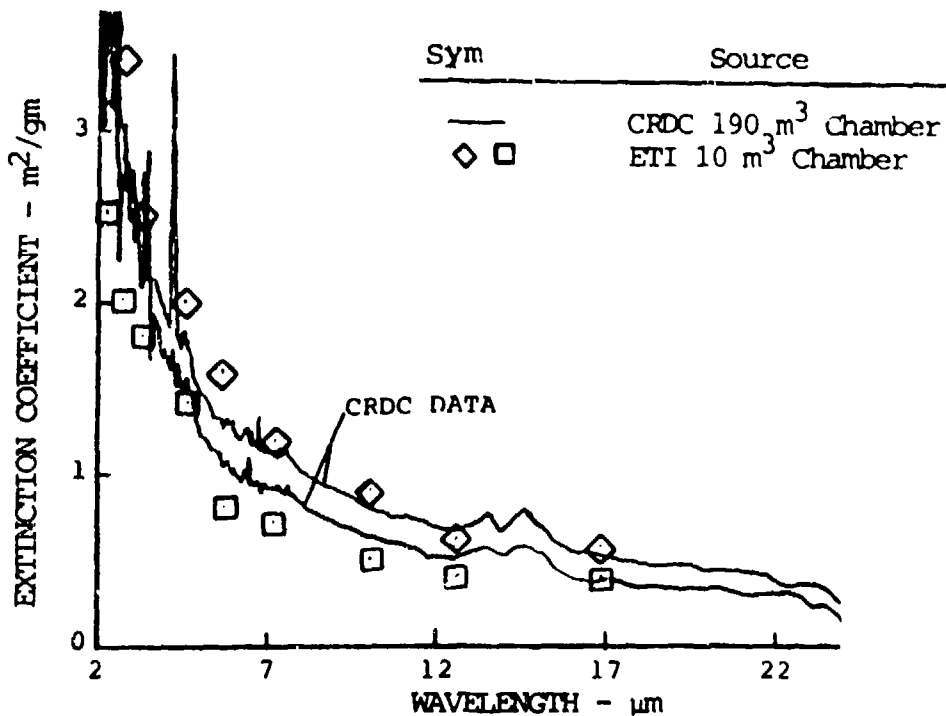


Figure 7. Comparison of extinction coefficients obtained in the ETI and CRDEC aerosol test chambers.

TABLE 1. EXTINCTION MEASUREMENTS FOR CARBON PARTICLE AEROSOLS AT A WAVELENGTH OF 0.63 MICRONS

Facility	Aerosol Concentration g/m ³	Extinction Coefficient m ² /gm
ETI Chamber -10 m ³	0.180	8.2
	0.0943	8.0
	0.0379	7.1
CRDEC Chamber -190 m ³	0.0476	6.1
	0.0098	8.7

The spectral data in the infrared region were obtained at both laboratories by the use of a Fourier Transform Spectrometer. The data at a wavelength of 0.63 micrometers were obtained using a helium-neon laser light source. Generally, because the extinction in the visible spectrum was much greater than in the infrared, the visible attenuation measurements were taken at a much lower value of airborne mass concentration. Typically, the chambers were charged with particles until visual transmission was reduced to 40 to 60 percent. After visible attenuation and particle concentration measurements were taken, charging continued until similar values of attenuation in the infrared were reached.

The data show that the carbon particles exhibit extinction coefficients of approximately $0.85 \text{ m}^2/\text{g}$ at a wavelength of 10 microns. This is significantly higher than what is exhibited by the droplet aerosols (i.e. extinction at 10 microns being less than $0.05 \text{ m}^2/\text{g}$).

Micrographs of carbon particles collected from the particle generator are shown in Figs. 8 through 10. The micrographs show that the carbon particles generated by the partial combustion and thermal decomposition of diesel fuel or JP-8 of the quality used in these experiments consist of small spheroids fused together to form chains and aggregates of various lengths and diameters. In general, the carbon spheroids vary in diameter between 0.1 and 0.5 micrometers. However, depending upon the concentration of particles in the agglomeration zone, the chains of spheroids can grow to lengths of several millimeters as shown in fig. 10.

Even though the use of carbonaceous particulate matter dates back to thousands of years before Christ³, only recently are advanced techniques being used to probe the nature of carbon particulates such as the soot produced by the partial oxidation of hydrocarbon fuels. Surprisingly, the detailed molecular structure of soot is not known. To account for the spherical morphology of particles, older models have proposed that polynuclear aromatic molecules are arranged with their planes tangential to concentric spherical annuli⁴. However, recently, Zhang, O'Brien, Heath, Liu, Curl, Kroto, and Smalley (abbreviated herein as ZOHLCCKS) have related soot to three dimensional carbon clusters, suggesting that because of dehydrogenation reactions "the polycyclic aromatic molecules known to be present in high concentrations in sooting flames may therefore, adopt pentagonal rings as they grow, so as to generate structures which maximize the number of c-c linkages⁵". While ZOHLCCKS did not propose that soot would contain pure carbon clusters ("buckminsterfullerene"), they suggested "the result of such a process would be a soot nucleus consisting of concentric, but slightly imperfect spheres"⁵.

A paper published by Ebert, Scanlon and Clausen (abbreviated herein in as ESC) described structural and chemical studies that were conducted on the carbon particulate (i.e. soot) produced by the laboratory scale reactor described in Section 2.1 while diesel fuel was being used as the hydrocarbon feedstock⁶. The purpose of



Figure 8. Carbon particles generated from diesel fuel (magnified 10,000x).



Figure 9. Carbon particles generated from diesel fuel (magnified 10,000x).



Figure 10. Carbon particles generated for diesel fuel (magnified 35X).

the study was to in part address the ZOHCKS proposal, and in part to generate data to compare the diesel fuel and JP-8 soots to other carbonaceous materials. The soot was characterized by x-ray diffraction and chemical reduction studies.

Microanalysis of several soot samples collected from diesel fuel based carbon particulate aerosols established that the weight percent carbon in the particulate averaged 92.06 ± 0.08 , while the hydrogen composition averaged 1.11 ± 0.13 percent. This results in an atomic H/C ratio of 0.14. Other analyses were for % S (0.46), % N (0.30, and % O (6.11). The average mass balance observed was 100.04%

Figure 11 gives the x-ray diffraction pattern of a typical diesel fuel soot over the range $2\theta = 15 - 105^\circ$. The appearance of diffraction peaks at 351, 208, 174, and 120 pm can be reconciled with a model involving stacked, planar benzenoid carbon arrays. The line widths of the diffraction peaks suggest correlation lengths on the order of 2 nm.

Chemically, the diesel fuel and JP-8 soot were observed to react with potassium naphthalenide¹ in THF to the extent of 1 K^o consumed for every 4.8 carbon atoms. The "soot anion" can be alkylated by methyl iodide to yield products containing methyl groups. Examination of both "THF solubles", and "THF insolubles" following alkylation with CD₃ groups via D NMR shows first order quadrupolar split as well as isotopic lines in each sample.

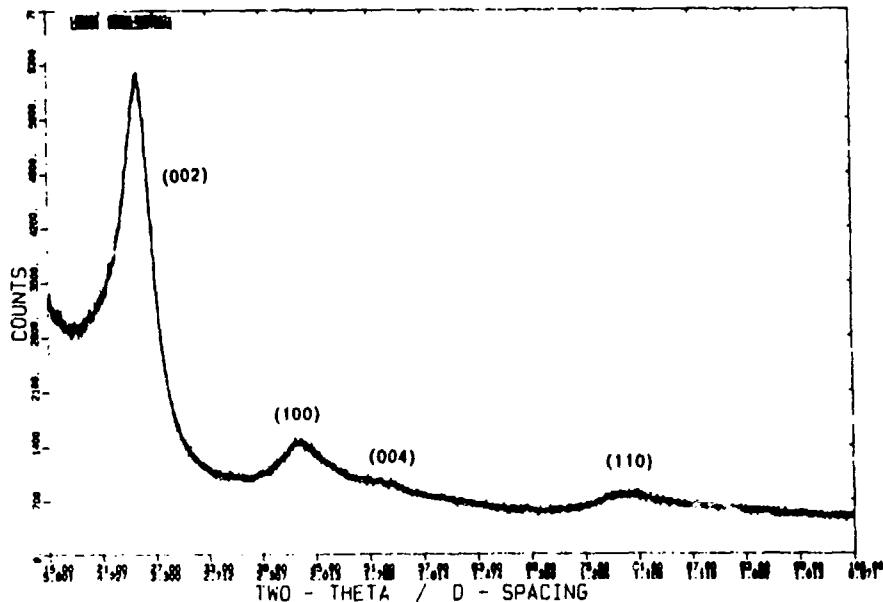


Figure 11. X-ray diffraction pattern of diesel fuel soot (Cu K α , $2\theta = 15 - 105^\circ$, Bakelite sample holder).

The insoluble material shows a greater fraction of quadupolar split deuterium nuclei. Soot does not intercalate potassium metal under conditions for which either graphite or petroleum coke will intercalate potassium.

The results of the ESC study can be reconciled with a model of diesel fuel originated soot as consisting of collections of large polynuclear aromatic hydrocarbons and heterocycles as schematically depicted in fig 12. One does not need to invoke C_{60} clusters or open spiraling clusters as models for the majority of the soot. In fact, x-ray diffraction simulation suggest that such clusters cannot account for the details of the experimentally observed diffraction patterns.

2.3 CATALYTICALLY PRODUCED FILAMENTOUS CARBON

In order to produce effective attenuation in the millimeter wavelength region, it is necessary to use conductive filaments with length to diameter ratios in the range of 200 to 500. The carbon particles that are produced by the partial oxidation process discussed in the previous two sections do not possess aspect ratios in this range even though they may chain together as shown in fig 10. Part of the reason is that the filaments are not conductively continuous. Currently, the commercially available carbon and graphite filaments used by the Army as millimeter screening agents are produced by the carbonization and graphitization of fibers made

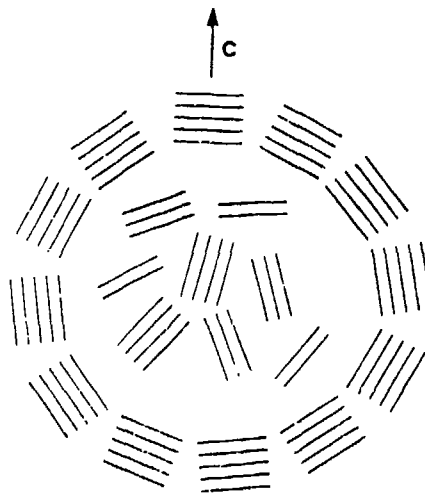


Figure 12. Schematic model for soot showing arrangement of polynuclear aromatics tangential to spherical annuli.

from either polymer precursors such as polyacrylonitrile or pitch precursors from petroleum or coal tar residues. However, it has been shown that carbon filaments can be produced by metal catalyzed pyrolysis of hydrocarbons such as methane, heptane, benzene, etc.⁷. These vapor-grown carbon filaments have a unique structural morphology that exhibits a greater degree of graphite perfection than pitch or PAN fibers produced at comparable temperatures. In addition, the vapor-grown filaments can be made in such a way that they possess a hollow central core.

The method by which vapor-grown filaments are produced is by heating small particles of transition metals, especially iron or nickel, in an atmosphere of hydrocarbon vapors, often with hydrogen being an accompanying co-reactant. At temperatures greater than 600°C the iron particles begin extruding long slender filaments of fairly graphitic carbon which may grow as rapidly as several millimeters per minute. Metallic crystals are often found at the end of the filament. These metallic crystals are believed to be analytically active for carbon deposition and are called "growth" crystals.

Based on the accumulated information from controlled experiments, a model has been proposed to account for the growth of filamentous carbon produced on metal particles. The key steps in the mechanism are believed to be the diffusion of carbon species through the particle from the hotter leading surface, to the cooler

rear faces at which carbon is precipitated from solution. It has been suggested that the driving force for carbon diffusion is the temperature gradient created in the particle by the exothermic decomposition of the hydrocarbon at the exposed front faces and endothermic deposition of carbon at the rear faces. Excess carbon which accumulates at the exposed face is transported by surface diffusion around the peripheral surfaces of the particle to form the graphite skin of the filament. Eventually, growth ceases when the leading face is encapsulated by a layer of carbon preventing further hydrocarbon decomposition.

A number of factors affect the growth of filamentous carbon. For example, temperatures in the range of 500 to 900°C have been reported while pressures between 1 and 760 torr have been used. Several different hydrocarbon feedstocks have been studied with the resulting carbon filaments appearing to be the same no matter what feedstock was used. However, the type of catalyst has a tremendous effect on the filament growth rate as well as on the characteristics of the filament. Both pure and combinations of metals have been studied. In general, transition metals provide the most active catalysts.

The purpose of the project described in this paper was to determine the conditions that are necessary to produce hollow carbon filaments under field realistic conditions from JP-8 and to evaluate their potential as screening agents.

The major part of the project that was described in Clausen et al's paper was concerned with studying the conditions that are necessary to produce carbon filaments under batch process conditions⁷. Several different batch reactors were designed, built, and tested. Basically, the batch reactor consists of a 2.5 cm i.d. quartz tube that is heated by an electric Lindberg furnace. The filament catalyst is contained inside ceramic boats maintained within the heated zone. The inlet to the quartz reactor tube is equipped with the capability of feeding gases, vapors, and liquids. The outlet of the reactor is fitted with a filament trap and a gas bubbler. Gas feed to the reactor is monitored and controlled through a series of rotometers and flow controllers.

When it is desired to crack (i.e. break larger molecules into smaller molecules) the feed stream, then the system is equipped with a reactor containing a cracking catalyst. The cracking catalyst consists of 1/8 inch pellets of faujasite molecular sieves. The catalyst bed is normally heated to 750°C.

The liquid feed (e.g. JP-8, diesel fuel) is injected into the heated zone of the cracking reactor, where it is vaporized and carried over the cracking catalyst by a stream of hydrogen or carbon monoxide gas. The cracked hydrocarbon stream is then passed over a bed of catalyst where the filaments grow.

Because it is desirable to use the filaments in an environment where personnel will come into contact with the filaments, relatively safe metal catalysts were chosen for these studies. In particular, metallic iron and iron compounds were used in the first series of filament growth studies. These were chosen because previous studies had suggested that small metallic iron particles are effective in promoting the formation of filamentous carbon. However, later experiments determined that iron oxide catalysts were more effective at growing the carbon filaments. The initial set of test conditions for growing carbon filaments was established by using low molecular weight feedstocks like ethylene, acetylene, and pentane. These experiments were conducted by passing the gas or vaporized liquid hydrocarbon over a bed of iron oxide catalyst. The filaments were then collected from the catalyst bed.

Experiments testing the effectiveness of vaporized hydrocarbons with chain lengths greater than five carbon atoms, demonstrated that the longer chain molecules had a tendency to foul the metal catalysts and thus, reduce the yield of filamentous carbon. The results of these experiments documented that if the use of long chain hydrocarbons is desirable as the feed source, then it will be necessary to break this feed stock into smaller molecules. It was determined at this point in the project that a cracking catalyst would be required to condition long chain hydrocarbon feed stocks such as JP-8 prior to reaction over the filament forming catalyst. Accordingly, a set of experiments were conducted and representative results of the type of filaments that were produced are shown in Figs. 13 and 14 where filamentous carbon was generated from cracked JP-8 feedstocks over iron oxide and metallic nickel catalysts.

The micrographs shown in Figs. 13 and 14 demonstrate that carbon filaments can be generated from long-chain hydrocarbons under field achievable conditions. This is achieved by passing the long-chain hydrocarbon feedstock (i.e. JP-8, diesel fuel, etc.) in a hydrogen or carbon monoxide atmosphere over a molecular sieve cracking catalyst at a temperature of approximately 700°C. At this time, additional studies are being conducted in order to determine what is the most effective filament growth catalyst. However, it has been demonstrated that the smaller the particle size of the catalyst, the greater the yield of the reaction. Some of the most effective iron oxide catalysts that were used in this study were in the range of 100 nanometers. With particles of this size, carbon to filament conversion on a weight basis as high as 30 percent was observed.

In order for filaments to exhibit effective attenuation properties in the millimeter wavelength region, they must be conductive in addition to possessing the necessary length to diameter ratios. Conductivity measurements for small filaments are typically performed by using the four-point probe technique. In order to use this technique on very small filaments, it is necessary to press the filaments into the form of a pellet. For the measurements conducted in this study, the filaments were

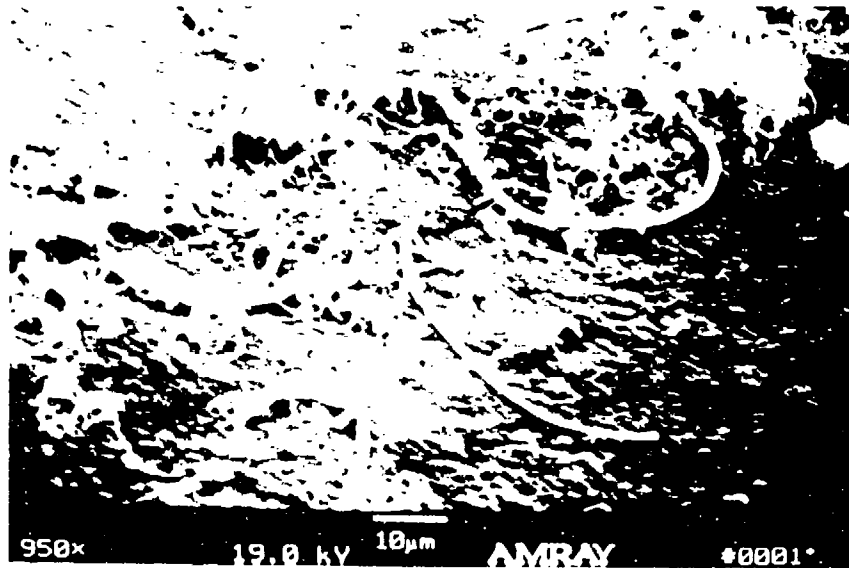


Figure 13. Carbon filaments generated from the reaction of cracked JP-8 over a Fe₃O₄ catalyst.

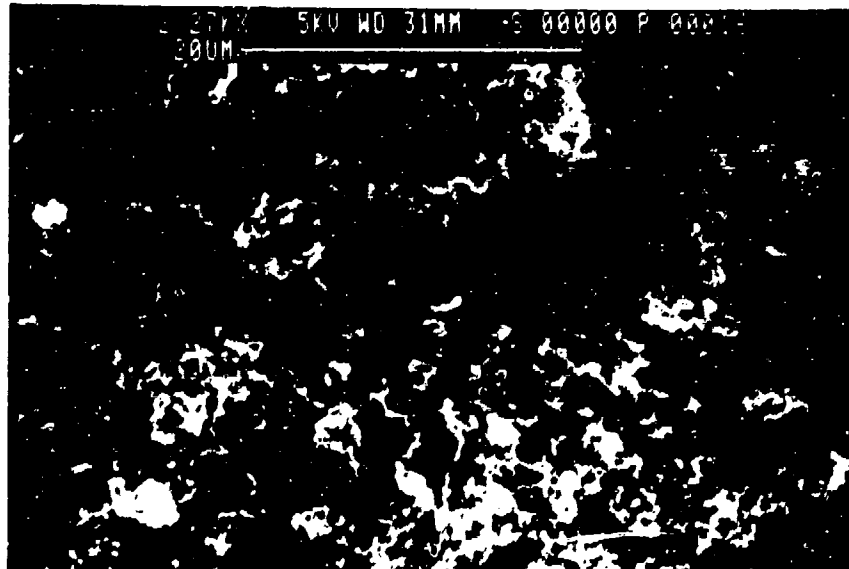


Figure 14. Carbon filaments generated from the reaction of cracked diesel fuel over an iron particle catalyst.

pressed into pellets at a pressure of 7,000 kg cm². The pellets were then measured for their conductivity by using the four-point probe method. Typical values were in the range of 10 to 40 Scm⁻¹. This suggests that if the filaments can be dispersed effectively into an aerosol cloud, their extinction coefficients in the millimeter wavelength region as comparable to those of graphite filaments should be similar.

As shown in the previous figures, when filamentous carbon is grown from a batch process, the filaments form clumps with the individual filaments being tangled together. This entanglement makes it very difficult to disperse the material in an airborne monofilament state. Attempts were made to break the clumps apart by passing them through high shear forces generated in a high velocity gas stream through a high speed set of rotating blades. The material was disseminated into a 3.6 m³ aerosol test chamber. The path-length for attenuation measurements was 2.4 m and extinction coefficients were measured at the He-Ne laser wavelength (0.63 microns) and in the millimeter wavelength region at 35 GHz and 94 GHz. Table II shows the extinction coefficients that were measured for carbon filaments generated over iron and nickel catalysts while using a mixed hydrocarbon feed. The values that were obtained are less than those observed for 1/8 inch length chopped 8-micrometer graphite in the millimeter wavelength region, but greater than the graphite filaments in the He-Ne region. The reason for the low values in the millimeter region is due to the inefficiency in disseminating the carbon filaments to a monodispersed state.

The ultimate goal of the filament project is to generate carbon filaments on a continuous basis. Generating the filaments by this procedure should help to minimize the birdnesting problem that is experienced when the filaments are generated in a batch process. This should lead to the production of carbon filament aerosols that are much more effective in the millimeter wavelength region.

3.0 CONCLUSIONS AND RECOMMENDATIONS

The work that was presented in this paper was the result of a series of studies designed to explore the potential for using JP-8 and diesel fuel as a feedstock to generate multispectral screening smokes. These studies demonstrated that JP-8 and diesel fuel can be converted into carbon particles by a thermal hydrogen stripping process that produces particulates that are effective screening agents both in the visible and infrared regions. Recent work has demonstrated that by cracking JP-8 and diesel fuel over a molecular sieve catalyst and then mixing the product stream with an iron oxide powder produces carbon filaments that are conductive and possess aspect ratios that make them effective attenuators in the millimeter wavelength region. Thus, it is theoretically possible to produce a mixed multispectral cloud of particles and filaments from JP-8 and diesel fuel under battlefield conditions. The next phase should be to build a prototype unit to evaluate and document any scale-up problems that might occur in the use of these processes.

TABLE II. ATTENUATION PROPERTIES OF CARBON AND GRAPHITE FILAMENTS

Sample	α ($\text{m}^2 \text{g}^{-1}$)		
	He-Ne (0.63 μ)	94 GHz	35 GHz
Filaments generated from cracked JP-8 over a Fe_3O_4 catalyst	0.21	0.19	0.40
Filaments generated from cracked JP-8 over a nickel catalyst	0.18	0.22	0.50
1/8 inch 8-micron graphite filaments	0.02	0.32	1.7

4.0 REFERENCES

1. Clausen, C.A. and Morgan, P.W., December 1988, A Laboratory Study of Infrared Obscuration by Black Smoke, ETI-TR-445-01, Engineering Technology, Inc., Orlando, FL.
2. Clausen, C.A. and Morgan, P.W., Leonare R.L., January 1988, A Comparison of JP-8 Aerosols to Diesel Fuel and Fog Oil Aerosols, CRDEC-CR-88031, Chemical Research Development and Engineering Center, Aberdeen Proving Ground, MD
3. Schwob, Y.; In Chemistry and Physics of Carbon; Dekker: New York, 1989\0; Vol. 15, pp 109-219.
4. Donnet, J.B.; Carbon 1982, 20, 266-282.
5. Zhang, Q.L., O'Brien, S.C., Heath, J.R., Liu, Y., Curl, R.F., Droto, H.W., Smalley, J.R.; J. Phys. Chem. 1986, 90, 525-528.
6. Ebert, L.B.; Scanden, J.C., and Clausen, C.A., J. Energy and Fuels, 1988, 2, 438.
7. Clausen, C.A., Racine T., Hermann, G., 1991, "The Formation of Filamentous Carbon From Hydrocarbon Feedstocks," Proceedings of the Smoke/Obscurants Symposium XV, Vol. 1 pp 123

Blank

ANALYTIC APPROXIMATION TO RANDOMLY ORIENTED SPHEROID EXTINCTION

by

B.T.N. Evans and G.R. Fournier
Defense Research Establishment Valcartier
Courcellette, Quebec G0A 1R0 Canada

RECENT/SUBMITTED PUBLICATIONS

- A) B.T.N. Evans and G.R. Fournier, "Simple Approximation to Extinction Efficiency Valid Over All Size Parameters", *Applied Optics*, **29**, 4666-4670 (1990).
- B) G.R. Fournier and B.T.N. Evans, "An Approximation to Extinction Efficiency for Randomly Oriented Spheroids", *Applied Optics*, **30**, 2042-2048 (1991)
- C) B.T.N. Evans and G.R. Fournier, "A Procedure for Obtaining An Algebraic Approximation to Certain Integrals", DREV R-4653/91
- D) G.R. Fournier and B.T.N. Evans, "Bridging the Gap Between the Rayleigh and Thomson Limits for Various Convex Bodies", Proc. of the 1991 CRDEC Scientific Conference on Obscuration and Aerosol Research.

ABSTRACT

An analytic semi-empirical approximation to the extinction efficiency, Q_{ext} , for randomly oriented spheroids, based on an extension of the anomalous diffraction formula, is given and compared to the extended boundary condition method or T-matrix method. Using this formula, Q_{ext} can be evaluated over 10^4 times faster than by previous methods. This approximation has been verified for complex refractive indices $m = n - ik$, where $1 \leq n \leq \infty$ and $0 \leq k \leq \infty$ and aspect ratios from .2 - 5. We believe that the approximation is uniformly valid over all size parameters and aspect ratios. It has the correct Rayleigh, refractive index and large particle asymptotic behaviours. The accuracy and limitations of this formula are extensively discussed.

1. INTRODUCTION

We have previously presented¹ a numerical approximation to Q_{ext} for randomly oriented spheroids. This work was applicable to particles with $1.01 \leq n \leq 2$ and $0 \leq k \leq 1$ for arbitrary sizes and aspect ratios. The required angular integration was carried out by a 64-point Gaussian quadrature. Since many materials have optical properties beyond the above limits, we have, in the present work, extended the refractive index range to $1 \leq n \leq \infty$ and $0 \leq k \leq \infty$. Furthermore, large optical sizes produce high frequency oscillations in the kernel of the angular integral. These integrals are very difficult and time consuming to estimate numerically. We have replaced this numerical integral with an approximate analytic expression that overcomes this difficulty.

The basic approach is to orthogonalize as much as possible the scattering physics into well defined regimes. For small physical and optical sizes, the electrostatics (Rayleigh) approximation is used. For larger and very large optical sizes we still use the electrostatics approximation but with the optical constants transformed² to include the effects of the magnetic dipole. In the large physical size regime we split the physics into a diffraction (anomalous diffraction) component and, what can be loosely described as edge effects. The diffraction component is modeled by the anomalous diffraction approximation as developed by Van de Hulst³. The edge effect (Fock theory) component is modeled by extending a technique introduced by Jones^{4,1}. In this report, this component is further generalized to have proper behaviour at small optical sizes and for large indices. The gap between the large and small particle regimes is bridged by a binomial form¹ similar to the generalized mean (Ref. 5, page 10).

The report is organized as follows: Section 2 develops the extinction formula. This includes section 2.1, small particle scattering, section 2.2 anomalous diffraction, 2.3 the edge effects and 2.4 the binomial bridging function. Section 3 contains comparisons of this approximation to the T-matrix method⁶. The final section, Section 4, gives the conclusions and remaining limitations.

2. DEVELOPMENT OF THE EXTINCTION FORMULA

2.1 Small Particle Term

For a physically and optically small particle, all applied electric field gradients disappear and the particle begins to respond to a homogeneous field. The electrostatics approximation then holds giving rise to the Rayleigh scattering formula for randomly oriented spheroids⁷. If the particle is still geometrically small but optically large the magnetic dipole field becomes significant. We have found² that one can use the electrostatics approximation but with the optical constants transformed. This transform correctly describes the full field. It is exact for spheres and approximate for randomly oriented spheroids. The following formulas for the extinction efficiency from small particles, Q_{small} are derived in Ref. 2:

$$Q_{small} = Q_{sca} + Q_{abs} \quad [1]$$

with

$$Q_{sca} = \frac{16 b^4 r^2}{9 \bar{A}} \{ |\tilde{\eta}_1|^2 + |\tilde{\eta}'_1|^2 + 2(|\tilde{\eta}_2|^2 + |\tilde{\eta}'_2|^2) \} \quad \text{and} \quad [2]$$

$$Q_{abs} = \frac{8 br}{3 \bar{A}} \text{Re} \{ i [\tilde{\eta}_1 + \tilde{\eta}'_1 + 2(\tilde{\eta}_2 + \tilde{\eta}'_2)] \}$$

where

$$\tilde{\eta}_i = \frac{1}{3(L_i + \frac{1}{\epsilon_{i,-1}})}, \quad \tilde{\eta}'_i = \frac{1}{3(L_i + \frac{1}{\mu_{i,-1}})} \quad [3]$$

The optical constants transform is

$$\epsilon_{1i} = \epsilon \left[\frac{2 \psi_1(\bar{z}_i)}{\bar{z}_i \psi'_1(\bar{z}_i)} \right]^\zeta, \quad \text{and} \quad \mu_{1i} = \mu \left[\frac{2 \psi_1(\bar{z}_i)}{\bar{z}_i \psi'_1(\bar{z}_i)} \right]^\zeta, \quad [4]$$

where $\psi_1(z)$ is the first Ricatti-Bessel function and,

$$\begin{aligned} \bar{z}_1 &= \sqrt{\epsilon\mu} b (1 + \chi(1 - 1/r^2)) && \text{prolates} \\ &= \sqrt{\epsilon\mu} b (r^2)^\chi && \text{oblates} \end{aligned} \quad [5]$$

$$\begin{aligned} \bar{z}_2 &= \sqrt{\epsilon\mu} b (1 + \chi^{1/3}(1 - 1/\sqrt{r})) && \text{prolates} \\ &= \sqrt{\epsilon\mu} b (\sqrt{r})^{\chi^{1/3}} && \text{oblates} \end{aligned} \quad [6]$$

where $\chi \approx \sqrt{3}/10$ and $\zeta \approx \{(91|m-1| - 64)/155 \mid 0 \leq \zeta \leq 1\}$.

The normalization factor is,

$$\begin{aligned} \bar{A} &= 1 + \frac{r^2}{\sqrt{r^2-1}} \sin^{-1} \left(\frac{\sqrt{r^2-1}}{r} \right) && \text{for prolates,} \\ &= 1 + \frac{r^2}{\sqrt{1-r^2}} \ln \left(\frac{1 + \sqrt{1-r^2}}{r} \right) && \text{for oblates.} \end{aligned} \quad [7]$$

The form factors are defined, for prolates as

$$L_1 = \frac{(1-g^2)}{g^2} \left\{ -1 + \frac{1}{2g} \ln \left(\frac{1+g}{1-g} \right) \right\}, \quad L_2 = \frac{1-L_1}{2}, \quad g^2 = 1 - \frac{1}{r^2} \quad [8]$$

and for oblates,

$$L_1 = \frac{1+f^2}{f^2} \left\{ 1 - \frac{\tan^{-1} f}{f} \right\}, \quad L_2 = \frac{1-L_1}{2}, \quad f^2 = \frac{1}{r^2} - 1. \quad [9]$$

The above set of equations is identical to that found in Ref. 2 apart from the exponent ζ in [4]. This exponent is introduced for the following reason. The exact solution of the scattering problem can be expressed in terms of scattering coefficients (for spheres these are the Mie coefficients). For small physical sizes the first scattering coefficient is dominant and can be expanded as an infinite power series in the size parameter x . The first term of this series is dominant only when $|m-1|$ is small. If we transform the optical constants then the first scattering coefficient can still be expressed as an infinite series in x but this time the first term dominates only when $|m-1|$ is large. For intermediate values of $|m-1|$, more terms of the power expansion of the scattering coefficients are required. Since the resulting expression would be cumbersome we have decided to modify the first term of the transformed series in such a way as to empirically model the scattering behaviour from small to large $|m-1|$. A simple and robust way to achieve this is to gradually turn on the transform by using the exponent ζ . Thus when $\zeta = 0$ the Rayleigh expression results and when $\zeta = 1$ the fully transformed expression results. Note that $\zeta = 0$ when $|m-1| \leq 64/91 \approx 0.7$ and $\zeta = 1$ when $|m-1| \geq 219/91 \approx 2.4$.

2.2 Large Particle Term

In this section we discuss the extinction efficiency of large particles Q_{large} . We separate the physics into two parts, one which corresponds to the anomalous diffraction, Q_{ad} and the other, which can be considered due to edges effects, Q_{ed} .

2.2.1 Extended Anomalous Diffraction

The anomalous diffraction formula is derived^{1,8}, by assuming that the incident plane wave is not significantly skewed in passing through the scattering object and that, to first order, the effect of the scatterer is to locally retard the phase of the wave and attenuate its amplitude⁹. The strict limit of validity of the formula is therefore the region where $(n-1) \ll 1$. The scattering object is in effect treated as an irregular disc normal to the incident wave and possessing a spatially dependent phase and amplitude. The Fraunhofer pattern at infinity is then derived and Q_{ext} evaluated from the standard relations. For a spheroidal scatterer, this procedure leads immediately to the following formula :

$$Q_{ad} = \text{Re} \left\{ 2 + 4 \frac{e^{-\omega}}{\omega} + 4 \frac{(e^{-\omega} - 1)}{\omega^2} \right\} \quad [10]$$

where ω is given by

$$\omega = i\Delta\psi, \quad \Delta\psi = 2(m-1) \frac{rb}{p} \quad [11]$$

and

$$p = \sqrt{\cos^2 \theta + r^2 \sin^2 \theta}, \quad a = 2\pi\alpha/\lambda, \quad b = 2\pi\beta/\lambda, \quad m = n - ik. \quad [12]$$

Where $r = a/b$ is the aspect ratio (for prolates $r > 1$ and for oblates $r < 1$), α is the length of the semi-axis of rotation, β is the other axis of the spheroid, θ is the angle between the incident radiation and the α or a axis, λ is the wavelength of the scattered radiation. Hence a and b are the two size parameters associated with the spheroid and p can be considered a projection operator of the penumbral ellipse (the ellipse defined by the shadow line on the surface of the spheroid) onto the plane perpendicular to the direction of the incoming radiation. When compared to exact results this formulation is satisfactory

for all oblate spheroids. However for prolates, significant phase differences appear due to deviation of the central ray.

To account for the refraction of the central ray we have in Ref.1, modified slightly the anomalous diffraction approximation. Now the deviation of the central ray is taken into account when computing its phase difference.

The extended anomalous diffraction $\Delta\psi$ is found to be

$$\begin{aligned} \psi &= i\Delta\psi = ib \left\{ \frac{\lambda r}{p} \left[\frac{p^2 \cos(\phi) + s \sin(\phi)}{p^2 \cos^2(\phi) + q^2 \sin^2(\phi) + 2s \cos(\phi) \sin(\phi)} \right] \right\} (m - \cos(\phi)) \\ \cos(\phi) &= \frac{s^2 + p^2 \Delta}{m(p^4 + s^2)} \\ \sin(\phi) &= \frac{s(\Delta - p^2)}{m(p^4 + s^2)} \\ \Delta &= [m^2(p^4 + s^2) - s^2]^{1/2} \\ s &= \sqrt{p^2 q^2 - r^2} \\ q &= [r^2 \cos^2(\theta) + \sin^2(\theta)]^{1/2}. \end{aligned} \quad [13]$$

In the limiting cases of $r \rightarrow \infty$ $\Delta\psi$ becomes:

$$\Delta\psi = 2b\{(m^2 - \cos^2 \theta)^{1/2} - \sin \theta\}. \quad [14]$$

For random orientations the angular averaging is carried out as follows:

$$\bar{Q}_{ad} = \frac{\int_0^{\pi/2} Q_{ad} p \sin \theta d\theta}{\int_0^{\pi/2} p \sin \theta d\theta} \quad [15]$$

The integration in the numerator of [15] can be readily computed numerically if the kernel is not too oscillatory. However, [15] can be analytically approximated by the technique described in Ref. 9. This eliminates numerical difficulties and leads to a more efficient algorithm. Following the procedure of Ref. 9, [15] becomes:

$$\bar{Q}_{ad} = 2 + 4(I_1 - I_2)/j(0) \quad [16]$$

with

$$I_1 = A \left[e^{-C} \left\{ \left(1 + \frac{1}{C}\right) \frac{F_2(C)}{C} - \left(1 + \frac{2}{C}\right) \frac{F_1(C)}{C^2} \right\} + \left(1 + \frac{2}{C}\right) \frac{F_1(0)}{C^2} + \frac{F_2(0)}{C^2} \right] \quad [17]$$

and

$$I_2 = \frac{j(0)}{C^2} + \frac{A}{C^2} \left(\frac{1}{\omega(0)} - \frac{1}{\omega(\pi/2)} \right) + \frac{2A}{C^3} \ln \left[\frac{B\omega(\pi/2)}{(B + j(0))\omega(0)} \right] \quad [18]$$

where

$$\begin{aligned} A &= \gamma B [B + j(0)], & B &= \frac{\omega(0) - \omega(\pi/4)}{\gamma + [\omega(\pi/4) - \omega(\pi/2)]/j(\pi/4)}, \\ C &= \omega(0) - \gamma B, & \gamma &= \frac{\omega(\pi/2) - \omega(0)}{j(0)}, \end{aligned} \quad [19]$$

and

$$\begin{aligned} j(\theta) &= -\frac{1}{2} \left[\cos(\theta) \sqrt{1 - g^2 \cos^2(\theta)} - \frac{\sin^{-1}(g \cos(\theta))}{g} \right], & \text{for prolates,} \\ &= \frac{r}{2} \left[\cos(\theta) \sqrt{1 + f^2 \cos^2(\theta)} + \frac{\ln(f \cos(\theta) + \sqrt{1 + f^2 \cos^2(\theta)})}{f} \right], & \text{for oblates.} \end{aligned} \quad [20]$$

Also,

$$F_n(C) \equiv \frac{E_n(\omega(0) - C)}{(\omega(0) - C)^{n-1}} - \frac{E_n(\omega(\pi/2) - C)}{(\omega(\pi/2) - C)^{n-1}}, \quad [21]$$

where E_n is the n th order exponential integral⁵. And finally for prolates (considering deviated rays),

$$\begin{aligned} \omega(0) &= 2bi \left[\frac{\sqrt{m^2 - 1}(m-1)}{(1-\alpha)(m-1) + \alpha\sqrt{m^2 - 1}/r} \right], \\ \omega(\pi/4) &= 2bi \left[g^2(\sqrt{m^2 - 1}/2 - 1/\sqrt{2}) + \frac{m-1}{r^2} \right], \\ \omega(\pi/2) &= 2bi(m-1), \\ \frac{1}{\alpha} &= 1 - rc \frac{(1-r)}{(1-rc)}, \quad rc = \sqrt{\left| \frac{m-1}{m+1} \right|}, \end{aligned} \quad [22]$$

for oblates (undeveloped rays),

$$\begin{aligned} \omega(0) &= 2bri(m-1), \\ \omega(\pi/4) &= 2bri(m-1)\sqrt{\frac{2}{1+r^2}}, \\ \omega(\pi/2) &= 2bri(m-1). \end{aligned} \quad [23]$$

As a consequence of the analytic integration technique, [13] is approximated by [22] at three values of θ whereas [11] exactly reduces to [23] at the same three values. Note that Equation [16] can be shown to reduce to the anomalous diffraction formula of Van de Hulst for the sphere.

2.2.2 Edge Effects

For a particle whose typical size is much larger than the wavelength, the edge cannot be treated as sharp and the effect of the curvature of the object must be included. Jones⁴ has shown how to estimate these edge effects for three dimensional convex bodies. In Ref. 1 we showed that

$$\begin{aligned} Q_{edge} &= \frac{2Dr^{2/3}}{p^{2/3}} {}_2F_1(-2/3, 1/2; 1; (1-1/p^2)) \quad (\text{prolates}) \\ &= \frac{2Dr^{2/3}}{p^2} {}_2F_1(-2/3, 1/2; 1; (1-p^2)) \quad (\text{oblates}), \end{aligned} \quad [24]$$

$$\begin{aligned} {}_2F_1(-2/3, 1/2; 1; z) &\approx \frac{.999947 - 2.19081z + 1.51871z^2 - .325449z^3}{1 - 1.85884z + .947705z^2 - .0847327z^3}, \quad |z| \leq 1, \\ D &= c_e/b^{2/3}. \end{aligned} \quad [25]$$

It can be shown for convex bodies, randomly oriented or illuminated by a randomly polarized beam, that c_e is a universal function of m . As $|m-1| \rightarrow 0$, $c_e \rightarrow c_0 = 0.996130$ and as $|m-1| \rightarrow \infty$, $c_e \rightarrow c_\infty = 0.0659708$ ^{1,11,12}. This universal function is not known. It is therefore necessary to model it. Since c_e is shape independent, this can be accomplished by studying the sphere alone. An added complication to D arises, however, when we consider spheroids with small phases, i.e. $\Delta\psi \ll 1$. This occurs since, what we have been calling an edge effect is really the field distortion around the boundaries of the particle, and hence its behaviour for small $\Delta\psi$ is quite different than for large $\Delta\psi$. As before, we have modelled this effect in our expression for D by using the sphere. Our empirical model of the above two behaviours is:

$$\begin{aligned} D &= \frac{c_0}{[b^{2\beta/3} + 1/|m-1|^\beta]^{1/\beta}} \\ \beta &= \frac{4/25}{|m-1|^3 + 8/125} + \left| \frac{c_0 - c_\infty}{\ln|m-1|} \right|, \quad |m| \leq 1.95 \quad \text{or} \quad |m| \geq 2.05 \\ &= 20, \quad 1.95 < |m| < 2.05 \end{aligned} \quad [26]$$

In the above, the special case for β with $m \approx 2$ is to avoid the obvious singularity in the main expression. At this point we require only a relatively large value for β .

The large particle limit for the spheroid becomes

$$Q_{ext} \rightarrow 2 + Q_{edge}. \quad [27]$$

We now wish to produce a term T which, when it multiplies [10], gives the same limit as [27] without diverging as the size parameter goes to zero. We have found that¹ an adequate expression for our purposes is:

$$T = 2 - e^{-Q_{edge}/2} \quad [28]$$

For random orientations the angular averaging is carried as in [15] but with T replacing Q_{ad} :

$$\bar{T} = \frac{\int_0^{\pi/2} T p \sin \theta d\theta}{\int_0^{\pi/2} p \sin \theta d\theta} \quad [29]$$

Using the same integration technique to obtain an analytic approximation to [29] we obtain:

$$\bar{T} = 2 - e^{-\delta C'} A' F_2' / j'(0) \quad [30]$$

where

$$A' = \gamma' B' [B' + j'(0)], \quad B' = \frac{1 - v(\pi/4)}{\gamma' + [v(\pi/4) - v(\pi/2)]/j'(\pi/4)}, \quad [31]$$

$$C' = 1 - \gamma' B', \quad \gamma' = \frac{v(\pi/2) - 1}{j'(0)}, \quad \delta = Dr^{2/3}.$$

and

$$F_2' \equiv \frac{E_2(\delta)}{\delta} - \frac{E_2(\delta v(\pi/2))}{\delta v(\pi/2)}. \quad [32]$$

Here E_2 , is the 2nd order exponential integral. For prolates,

$$j'(\theta) = rj(\theta),$$

$$v(\pi/4) = {}_2F_1\left[-\frac{2}{3}, \frac{1}{2}; 1; (r^2 - 1)/(r^2 + 1)\right] [2/(r^2 + 1)]^3 \quad [33]$$

$$v(\pi/2) = {}_2F_1\left[-\frac{2}{3}, \frac{1}{2}; 1; 1 - 1/r^2\right] / r^{2/3}$$

and for oblates,

$$j'(\theta) = -j(\theta),$$

$$v(\pi/4) = {}_2F_1\left[-\frac{2}{3}, \frac{1}{2}; 1; 1 - r^2/2\right] / r \quad [34]$$

$$v(\pi/2) = {}_2F_1\left[-\frac{2}{3}, \frac{1}{2}; 1; 1 - r^2\right] / r^2$$

2.2.3 Total Contribution to Q_{large}

The total contribution to Q_{large} for a given orientation is¹:

$$Q_{large} = Q_{ad} T. \quad [35]$$

For random orientation the angle averaging would give:

$$\bar{Q}_{large} = \frac{\int_0^{\pi/2} Q_{ad} T p \sin \theta d\theta}{\int_0^{\pi/2} p \sin \theta d\theta}. \quad [36]$$

Due to their complementary nature, $Q_{ad} \approx 2 = \text{constant}$ for large $|\omega|$, while $T \approx \text{constant}$ for small to medium $|\omega|$. Therefore, to a good approximation, we can separate the kernel of the above integral to get:

$$\bar{Q}_{large} = \bar{Q}_{ad} \bar{T}. \quad [37]$$

An extensive comparison between [37] and the numerical computation of \bar{Q}_{large} from [36] provides definitive evidence for the above argument. Some examples of this are shown in the next section.

2.3 Bridging Function

\bar{Q}_{small} is a good approximation to \bar{Q}_{ext} when the semi-major axis is less than 1. For larger values of the semi-major axis it overestimates \bar{Q}_{ext} . Similarly, \bar{Q}_{large} is a good approximation to \bar{Q}_{ext} when the semi-major axis is greater than 2 - 5 depending on $|m - 1|$. For smaller values of the semi-major axis it overestimates \bar{Q}_{ext} . In order to obtain \bar{Q}_{ext} , in the transition region, from \bar{Q}_{large} and \bar{Q}_{small} we need a bridging function that smoothly goes between the two. The form must have \bar{Q}_{small} as the first term in its series expansion and asymptotically go to \bar{Q}_{large} .

A quite general form that can do this is the confluent hypergeometric function or Kummer function which has the general form ${}_1F_1[a; b, cz^\nu]$ where a, b, c, ν are arbitrary parameters and z is the variable⁵. From the basic properties of this function

$$\begin{aligned} \lim_{z \rightarrow 0} \frac{\Gamma(b-a)}{\Gamma(b)} c^a z^{a\nu} {}_1F_1[a; b, -cz^\nu] &\rightarrow \frac{\Gamma(b-a)}{\Gamma(b)} c^a z^{a\nu} \left\{ 1 - \frac{caz^\nu}{b} + \frac{ba(a+1)z^{2\nu}}{2!b(b+1)} - \dots \right\} \\ \lim_{z \rightarrow \infty} \frac{\Gamma(b-a)}{\Gamma(b)} c^a z^{a\nu} {}_1F_1[a; b, -cz^\nu] &\rightarrow 1 + \frac{a(1+a-b)}{cz^\nu} + \dots \end{aligned} \quad [38]$$

With the small particle and large particle limits considered the bridging function B becomes:

$$\begin{aligned} B &\equiv \bar{Q}_{small} {}_1F_1[1/\nu; b, -(cz)^\nu] \quad \text{with} \\ c &= \Gamma(b)/\Gamma(b-1/\nu), \quad \text{and} \quad z = \bar{Q}_{small}/\bar{Q}_{large} \end{aligned} \quad [39]$$

which has the correct limits, i.e.

$$\begin{aligned} \lim_{z \rightarrow 0} B &\rightarrow \bar{Q}_{small} \\ \lim_{z \rightarrow \infty} B &\rightarrow \bar{Q}_{large} \end{aligned} \quad [40]$$

We now need to determine ν and b . We should expect these parameters to be insensitive to aspect ratio since most of the shape effects are already accounted for by \bar{Q}_{small} and \bar{Q}_{large} . This supposition has been confirmed by numerical evidence. Assuming these parameters are shape independent, we can, for each of an array of m values find the 'best' set of values of ν and b by considering the sphere only. We did this by using a nonlinear fitting routine. The results of this fit, for the vast majority of cases made b very large (> 10). When b becomes very large, B goes confluent (see Ref. 13 for more details). This means that the function simplifies dramatically to a binomial function, thus:

$$\lim_{b \rightarrow \infty} B \rightarrow \frac{\bar{Q}_{small}}{[1+z^\nu]^{1/\nu}} \quad [41]$$

This can be rearranged in a form similar to a generalized mean as:

$$\frac{1}{\bar{Q}_{ext}^\gamma} = \frac{1}{\bar{Q}_{small}^\gamma} + \frac{1}{\bar{Q}_{large}^\gamma} \quad [42]$$

We now must model the values for γ . We have modelled this parameter in previous papers^{1,14}. This previous modelling is not useful to the current approach since \bar{Q}_{small} and \bar{Q}_{large} have changed, the formula for \bar{Q}_{ext} has been extended to all $n \geq 1$ and angle averaging has been carried out.

In [42] it is clear that if one of either \bar{Q}_{small} or \bar{Q}_{large} is much smaller than the other then, to a good approximation, \bar{Q}_{ext} is this value provided that $\gamma > 0$. Larger values of γ will drive \bar{Q}_{ext} to the smallest value between \bar{Q}_{small} and \bar{Q}_{large} more than smaller values. Hence, when the physical size of the particle is small, \bar{Q}_{small} is equal to or smaller than \bar{Q}_{large} , γ should be large. Conversely, when the physical size of the particle is large, \bar{Q}_{small} is much larger than \bar{Q}_{large} and we then merely require that γ be positive. The real difficulty in modelling γ is thus in the intermediate ranges of physical sizes. Most of the behaviour of γ in the large particle regime can be determined by considering first the real axis, in the refractive index plane, and then by varying the imaginary component. Considering, first the real axis, the behaviour can be described by the sum of two asymptotic terms, one as $n - 1 \rightarrow 0$, and the other as $n \rightarrow \infty$. The behaviour of γ as k increases is well modelled by a single term. The sum of these terms we will call γ_1 . As the physical size of the particle changes from small to large, γ must go smoothly from some large value to γ_1 . This transition is most sensitive, and hence best modelled, where the Rayleigh scattering and absorption are roughly equal. This occurs since the Rayleigh absorption term and the anomalous diffraction absorption term are close to or may be equal while the scattering terms are usually quite different. This can play significantly on the balance between \bar{Q}_{small} and \bar{Q}_{large} as the physical size varies. This has been taken into account by an additional term dependent on the physical size. This size is represented by the volume equivalent sphere radius of the spheroid.

From an empirical fit on the above terms, γ becomes:

$$\begin{aligned} \gamma &= \gamma_1 + \frac{(54 - \gamma_1)}{1 + (\alpha r^{1/3} b)^4}, & \alpha &= \frac{5}{2} + \frac{3k_c}{k_c + k}, & k_c &= \frac{(n^2 - 1)^2}{66n} \\ \gamma_1 &= 1 + \frac{n - 1}{[(n - 1)^{1/3} + 1]^3} + 4 \left[\frac{4n}{\sqrt{16 + n^2}} - 1 \right]^2 + \frac{16u^2}{\sqrt{u^4 + 1}}, & u &= \frac{k}{[2(n - 1)]^2} \end{aligned} \quad [43]$$

We have verified that none of the above modelling of γ changes the empirical fact that B goes confluent in the best fit and hence [42] still remains valid. It should also be pointed out that the bridging function is not necessary if \bar{Q}_{ext} is only required outside the transition region. In this case $\bar{Q}_{ext} = \bar{Q}_{small}$ or $\bar{Q}_{ext} = \bar{Q}_{large}$, depending on the region of interest.

3. RESULTS

The complete formula, as given in the previous section, is guaranteed to give correct asymptotic behaviour for both large and small $|m - 1|$ and b . Thus, in studying the error behavior of the approximation, mid ranges of $|m - 1|$ and b are of greatest interest. In this section we will compare the analytic approximation with the T-matrix method as implemented by Barber⁶ or the Mie theory.

Figures 1 and 2 show the comparison of Q_{ext} vs b for aspects 2 and 1/2 respectively. The refractive index is $n = 1.3$, close to that of water. It is clear that the error decreases at either extreme of b . (The deviation seen in Fig. 1 for $b > 23$ is caused by ill conditioning in the T-matrix code). The largest errors are near and around the first two peaks. This occurs here since much more of the scattering physics must be considered to obtain better accuracy.

Figures 3 and 4 are contour graphs of the percent error between the analytic approximation and the T-matrix computation. The refractive index varies as $1 \leq n \leq 2$ and $10^{-5} \leq k \leq 10$. Figure 3 is for an oblate spheroid of aspect 1/2 and Fig. 4 is for a prolate spheroid of aspect 2. There are three features of note. One is the increase of the error for small k and large n . This error is shown well in Fig. 5 for the case of a sphere and index $m = 1.8 - 0i$. This feature is simply due to resonant surface waves that are not modelled. Note that for aspect 1/2 and 2, these errors are significantly smaller since the surface waves are damped by the asphericity. The remaining errors arise from inaccurate modelling of the bridging region—that is between the Rayleigh region and the first peak. The second feature occurs approximately when $2 < k < 10$. Here, for large particles, the coherence effect of the internal refracted wave is significant, and has not been properly modelled¹⁵. This is shown in Fig. 6 for an oblate particle with aspect ratio 1/2 and $m = 1 - 3i$. This becomes insignificant for larger k since the particle becomes reflective. The remaining error at these large values of k and $b \approx 1$ is again due to difficulties in the bridging function attempting to model the electromagnetic field on the surface. The third significant

feature occurs when the Rayleigh scattering and absorption are roughly equal. This occurs since the Rayleigh absorption term and the anomalous diffraction absorption term are close to or may be equal while the scattering terms are usually quite different. This was included in the modelling of γ in the previous section by k_c , [43]. Residual errors can still be seen in Figs. 3 and 4 due to imperfect modelling following curves $k \propto (n^2 - 1)^2/n$.

For large n , body resonances can occur. These are sometimes referred to as morphology dependent resonances (MDR). For spheres these occur near $nx = l\pi$, where l is a natural number. Figure 7 shows an example of an incipient MDR on the first diffraction peak of Q_{ext} . Here, $m = 3 - 0i$ and $r = 2$. Note that, despite the significant perturbation in the transition region due to the MDR, the approximation is excellent. Only the first, and hence simplest MDRs are modelled (by $\bar{\epsilon}_1$, [5] and $\bar{\epsilon}_2$, [6]). To show the accuracy of the approximation, the T-matrix was low pass filtered for $b \geq 1$ and is graphed in Fig. 8. Since by far the main contribution is now from the diffraction peaks, the underlying accuracy of the approximation is apparent.

The next example is a model of extinction by randomly oriented copper flakes in the infrared ($m = 35 - 35i$). An oblate spheroid with an aspect ratio of 0.333 was used. For this index, lower aspect ratios could not be considered since the T-matrix will not produce usable results and hence no comparison could be made. Q_{ext} for this case is shown in Fig. 9. Caution is required since the T-matrix for $b > .25$ begins to decrease rapidly and will go negative for larger b . This shows an advantage of the approximation. It can estimate Q_{ext} for combinations of n , k , b and r when the T-matrix cannot. Figures 10 and 11 are examples of Q_{ext} for water prolate and oblates spheroids at 9.4 GHz, respectively. Both are difficult cases since the T-matrix is almost ill conditioned and several MDRs are becoming apparent. In Fig. 10, the first MDR is reasonably well modelled while the second is not. However the latter only introduces an error of about 20%. Again Fig. 11, the first MDR is well modelled and the second is not. But in contrast to Fig. 10 it introduces a smaller error since it is coincident with the first diffraction peak. Note that at the highest b shown the T-matrix has become ill conditioned.

Extensive computations have been carried out to indicate the error of the approximation over the complete range of stability of the T-matrix method.

All our approximate Q_{ext} diagrams in this section were produced at a rate of greater than 10^4 times faster than by the T-matrix code. Since the T-matrix scales as the cube of the optical size whereas the analytic approximation is optical size independent, larger size parameters or larger refractive indices lead to larger speed-up factors.

4. CONCLUSIONS AND LIMITATIONS

We have presented an approximation to Q_{ext} for randomly oriented spheroids which is valid for all size parameters, aspect ratios and refractive indices $n \geq 1$ and $k \geq 0$ and $\mu = 1$.

Extensive computations have been carried out to indicate the error of the approximation over the complete range of stability of the T-Matrix method.

If high precision is not required, the formula is far more economical in computer time than the T-matrix method for obtaining Q_{ext} . When both the range of demonstrated validity and the accuracy are taken into account, this formula is superior to all other approximations known to the authors.

Several limitations of the previous numerical approach¹ have been removed. The remaining limitations, that for $n < 1$ and/or $k < 0$, are not modelled since new and significant physics arises (e.g. total internal reflections, optical gain). Even n modestly less than 1 can cause problems. Another limitation occurs for $2 \leq k \leq 10$ and large particles. In this region the absorption is not well modelled. If this effect was properly accounted for then Q_{abs} and hence Q_{sca} could be globally and readily obtained by using the same approach.

5. ACKNOWLEDGEMENT

The authors would like to thank Dr. Peter Barber of the Clarkson College of Technology for generously making available his T-matrix spheroid code without which this work could not have been carried out.

6. REFERENCES

1. Fournier, G.R. and Evans, B.T.N., "Approximation to Extinction Efficiency for Randomly Oriented Spheroids", *Applied Optics*, Vol. 30, No. 15, p. 2042, 1991.
2. Fournier, G.R. and Evans, B.T.N., "Bridging the Gap Between the Rayleigh and Thomson Limits for Various Convex Bodies", DREV R-4692/92, 1992.
3. Van de Hulst, H.C., "Light Scattering by Small Particles", Wiley, New York, 1957.
4. Jones, D.S., "High-Frequency Scattering of Electromagnetic Waves," *Proc. R. Soc. London, Ser. A* 240, p. 206, (1957).
5. Abramowitz, M., Stegun, I.A., Eds., "Handbook of Mathematical Functions (Dover, New York, 1972).
6. Barber, P.W. and Hill, S.C., "Light Scattering by Particles: Computational Methods", World Scientific, New Jersey, 1990.
7. Kerker, M., "The Scattering of Light and Other Electromagnetic Radiation," Academic Press, New York, 1969.
8. Greenberg, J.M. and Meltzer, A.S., "The Effect of Orientation of Non-Spherical Particles on Interstellar Extinction", *Astrophys. J.*, Vol. 132, p. 667, 1960.
9. Evans, B.T.N. and Fournier, G.R., "A Procedure for Obtaining an Algebraic Approximation to Certain Integrals", DREV R-4653/91, 1991.
10. Wolfram, S., "Mathematica: A System for Doing Mathematics by Computer", Addison -Wesley, New York, 1989.
11. Nussenzveig, H.M. and Wiscombe, W.J., "Efficiency Factors in Mie Scattering", *Phys. Rev. Lett.*, 45, 1490, 1980.
12. Beckmann, V.P. and Franz, W., "Berechnung der Streuquerschnitte von Kugel und Zylinder unter Anwendung einer modifizierten Watson-Transformation," *Z. Naturforschg.*, 12a, 533, 1957.
13. Luke, Y.L., "The Special Functions and Their Approximations", Vols. I and II, Academic Press, New York, 1969.
14. Evans, B.T.N. and Fournier, G.R., "A Simple Approximation to Extinction Efficiency Valid Over All Size Parameters", *Applied Optics*, Vol. 29, 1 Nov. 1990.
15. Cohen, A. and Tirosh, E., "Absorption by a Large Sphere with an Arbitrary Complex Refractive Index", *Journal of the Optical Society of America A*, Vol. 7, No. 2, p 323-325, 1990.

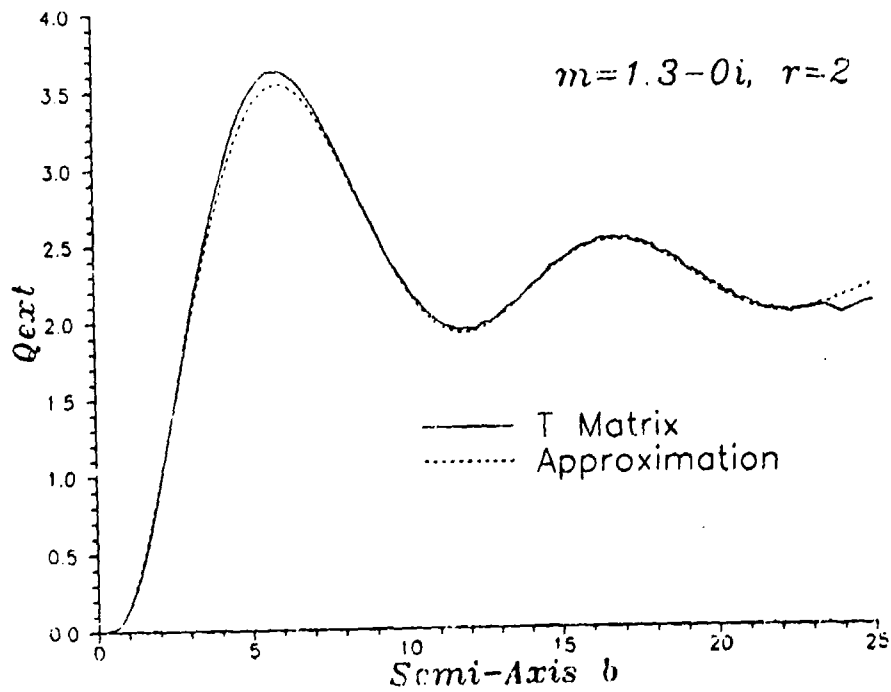


Fig.1 Comparison between approximation and T-matrix method for an index of 1.3 and an aspect ratio of 2.

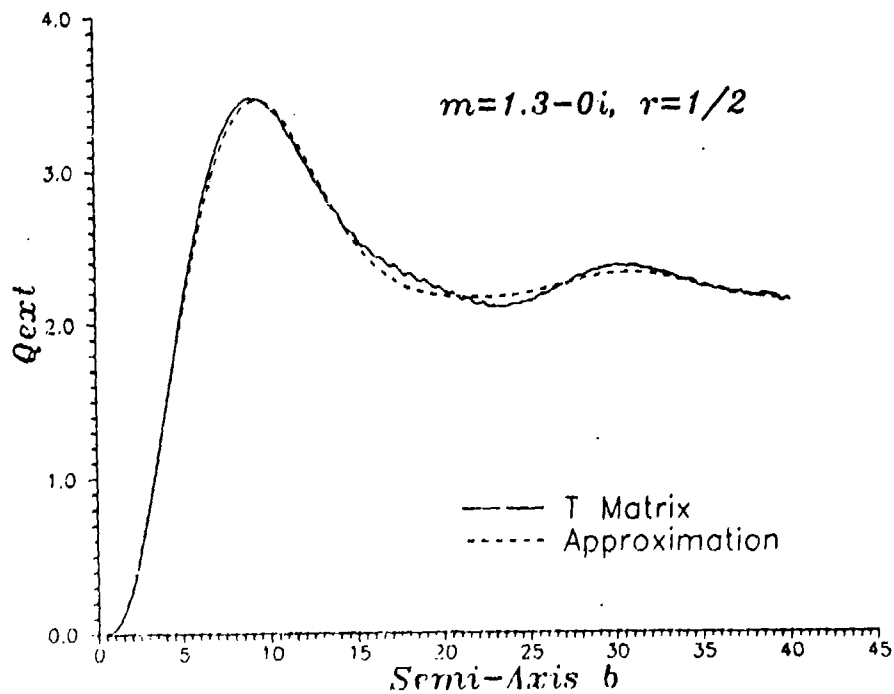


Fig.2 Comparison between approximation and T-matrix method for an index of 1.3 and an aspect ratio of 1/2.

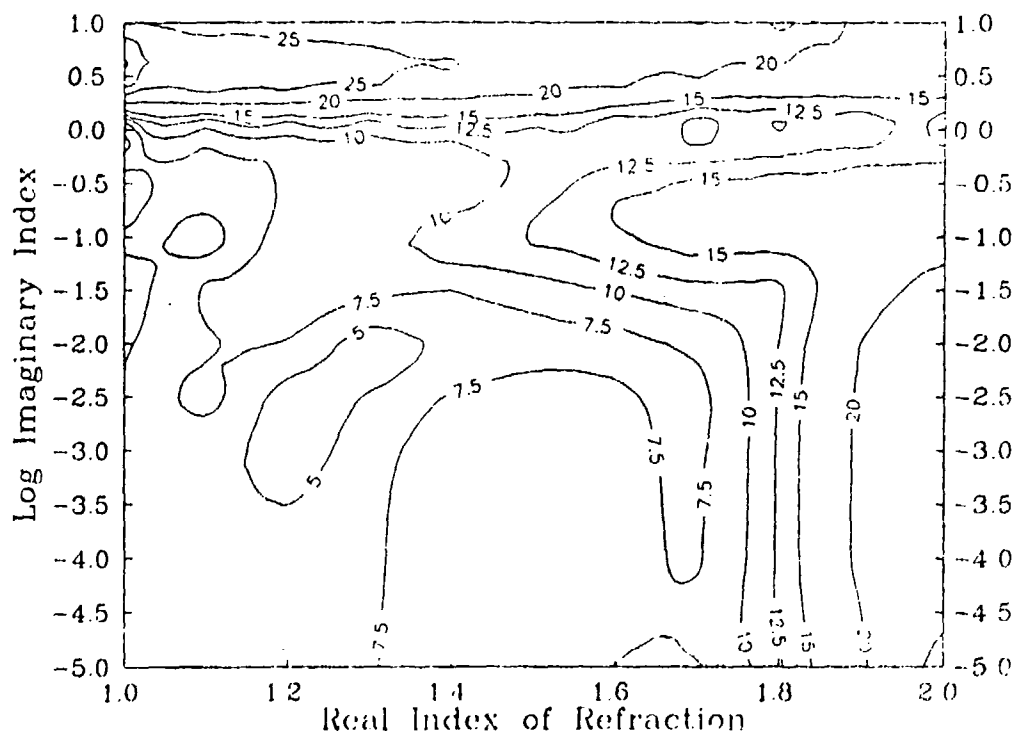


Fig.3 Maximum relative error, in percent, between analytic approximation and T-matrix $r = 1/2$.

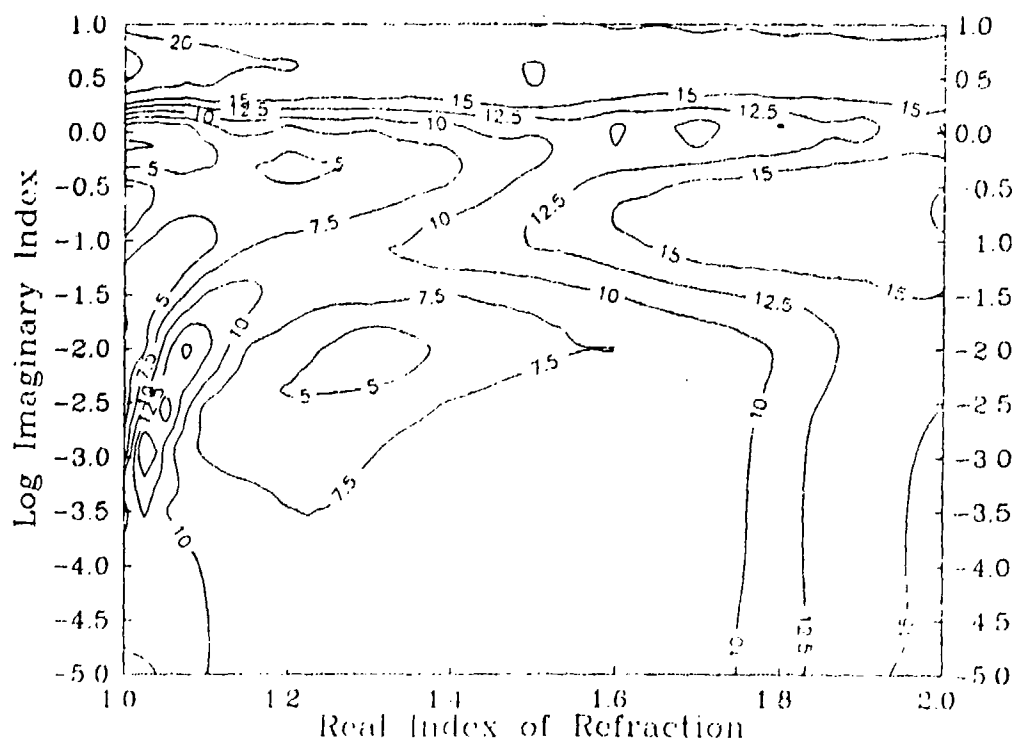


Fig.4 Maximum relative error, in percent, between analytic approximation and T-matrix $r = 2$.

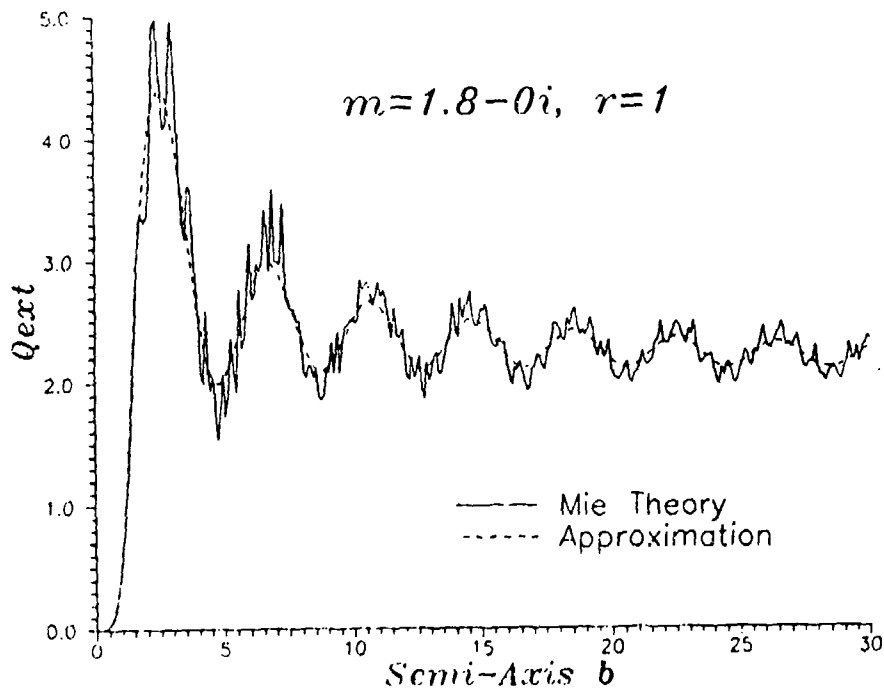


Fig.5 Comparison between approximation and Mie theory for an index of 1.8 and an aspect ratio of 1. Significant surface waves.

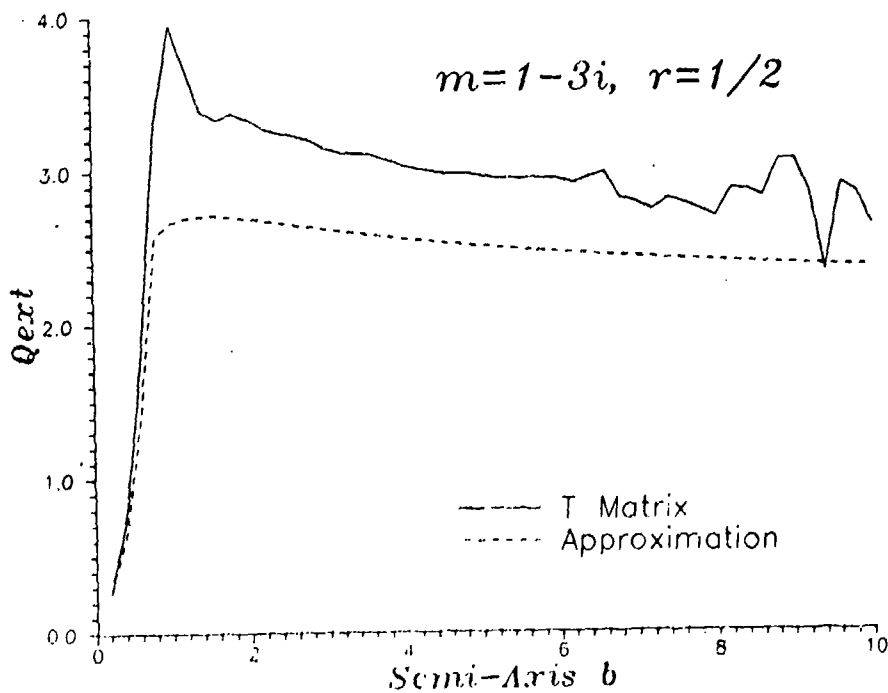


Fig.6 Comparison between approximation and T-matrix method for an index of $1-3i$ and an aspect ratio of $1/2$. Significant internal wave coherence effect.

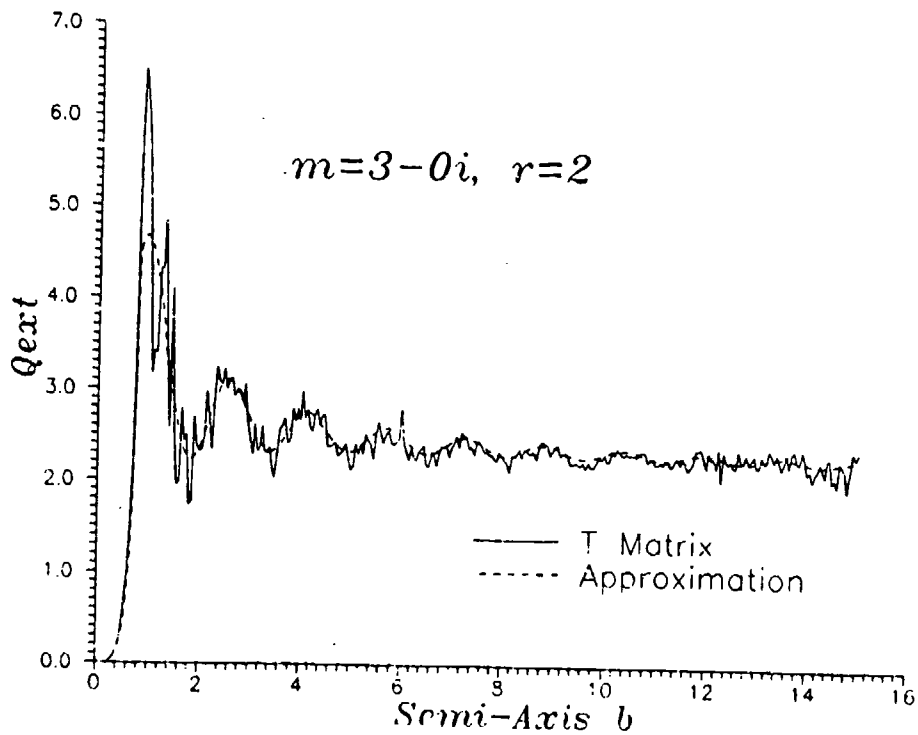


Fig.7 Comparison between approximation and T-matrix method for an index of $3 - 0i$ and an aspect ratio of 2. Incipient MDR at $b \approx 1$

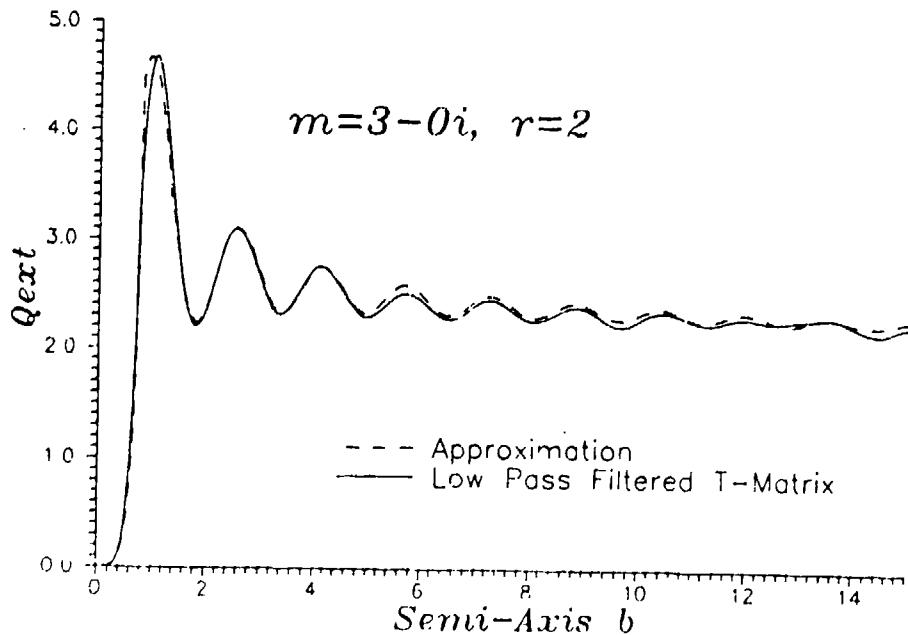


Fig.8 As Fig. 7 but T-matrix results low pass filtered for $b > 1$.

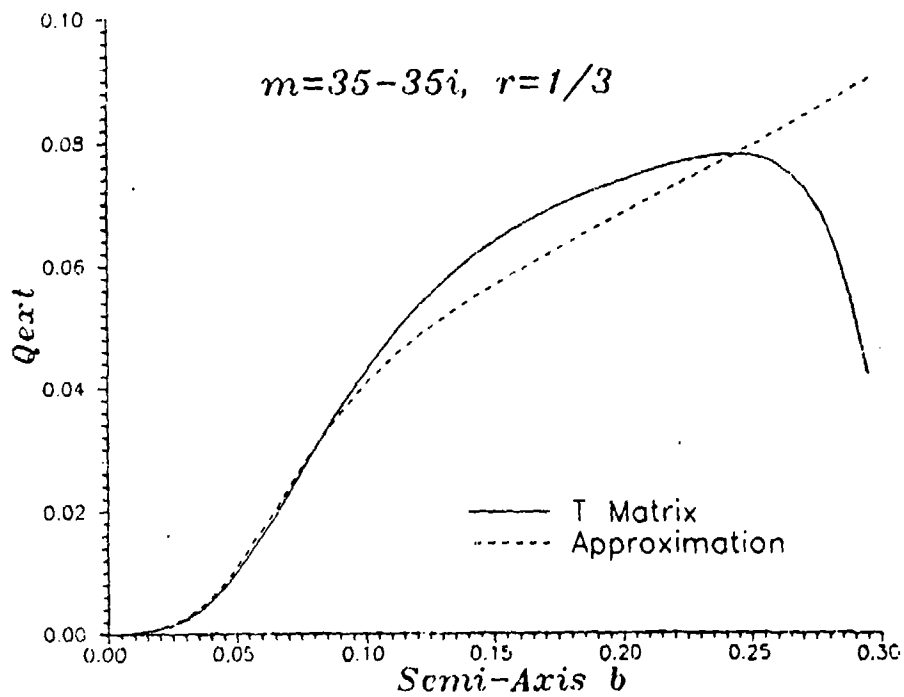


Fig.9 Comparison between approximation and T-matrix method for an index of $35 - 35i$ and an aspect ratio of $1/3$.

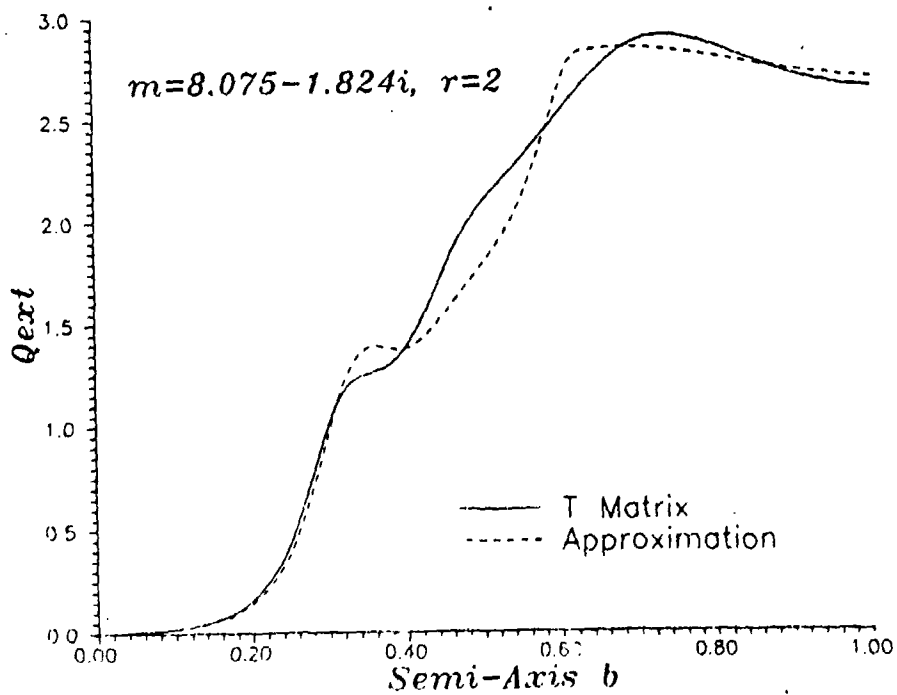


Fig.10 Comparison between approximation and T-matrix method for an index of $8.075 - 1.824i$ and an aspect ratio of 2 . Water at 9.4 GHz.

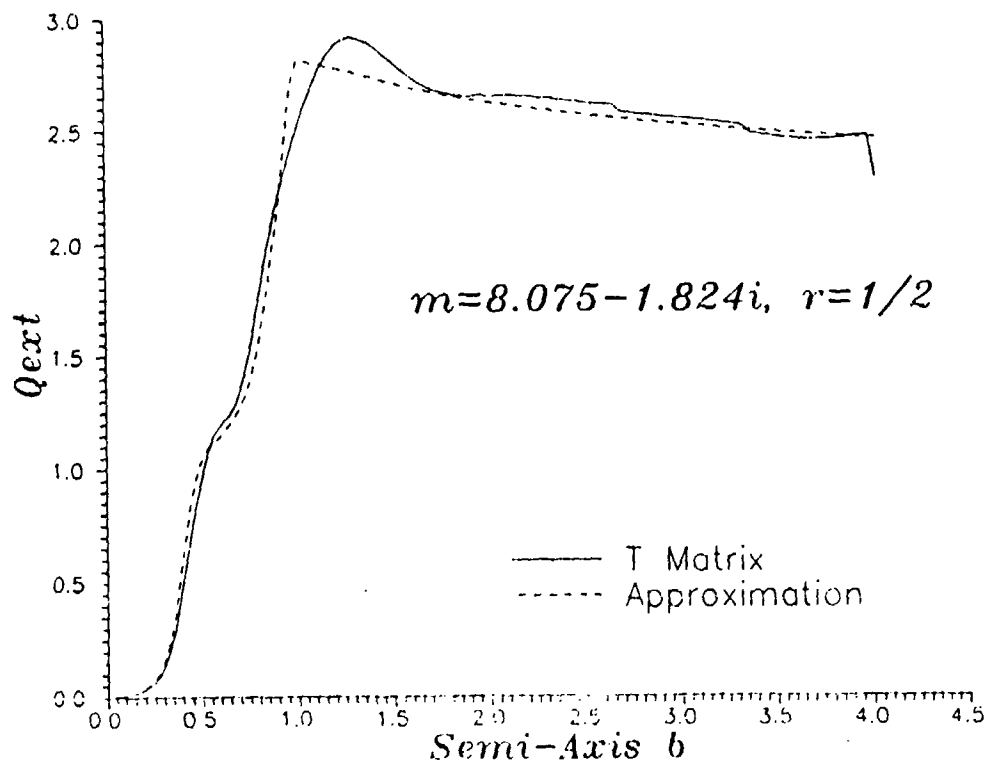


Fig.11 Comparison between approximation and T-matrix method for an index of $8.075 - 1.824i$ and an aspect ratio of $1/2$. Water at 9.4 GHz.

Optical properties of spheres containing a spherical eccentric inclusion.

F. Borghese†, P. Dent†, R. Saijat, O. I. Sindon††

†Universita' di Messina, Istituto di Struttura della Materia, Messina 98050, Italy

††CRDEC, Aberdeen Proving Ground, Maryland 21010-5423

ABSTRACT

Fikioris and Uzunoglu few years back presented a formalism to describe the electromagnetic scattering by homogeneous spheres containing an eccentric spherical inclusion. We have extended our previous formalism which is designed to account for the dependant scattering by aggregated spheres, to the case of spheres containing more than one inclusion. Our results are compared with those of Fikioris and Uzunoglu and the existing differences are explained in terms of the approximations that were used by Fikioris and Uzunoglu. We also show results for the case of dielectric spheres containing either a metallic or dielectric inclusion with parameters that could not be considered under the approximation of Fikioris and Uzunoglu. It will be shown how the scatterers response depends on the direction of incidence and on the polarization of the field, therefore making possible to distinguish from both a sphere with concentric inclusion and an homogeneous sphere.

1. Introduction

The theory of electromagnetic scattering known as Mie theory was originally developed to describe the properties of homogeneous spherical scatterers [1]. In time, it has been modified and improved to extend its applicability to radially nonhomogeneous spheres either composed of several homogeneous concentric layers or possessing a refractive index continuously varying along the radius [2]. The layered spheres are dealt with by imposing the appropriate boundary conditions across the surfaces separating each pair of contiguous layers; the case of continuously varying refractive index requires, instead, to replace the spherical Bessel functions, that are appropriate for homogeneous spheres, with the numerical solutions of a pair of radial equations. This latter approach applies, in particular, to spheres with a so-called soft surface [3] and proved to be adaptable to deal also with stratified spheres [4]. Obviously, the theory for stratified spheres is appropriate to deal with a sphere containing a concentric spherical inclusion but, when the inclusion is nonconcentric, or when more than one inclusion is present, a different approach is in order.

A sphere with an eccentric inclusion, in spite of its external symmetric appearance, is intrinsically anisotropic so that its scattering properties are expected to evidence effects that cannot be present for a truly spherical object. One could also expect that these effects influence in turn the macroscopic optical properties of a dispersion of such objects. Therefore, in

this paper we investigate the scattering properties of a homogeneous sphere containing a spherical eccentric inclusion with the specific purpose of assessing whether the effects due to the eccentricity make such an object easily distinguishable from a truly spherical scatterer. To this end we present a formalism designed to deal also with the macroscopic optical constants of a low-density dispersion of these anisotropic scatterers and discuss the results of its application to a few significant cases. Our approach can be easily extended to the case of spheres containing more than one inclusion, but, since these objects require a substantial increase of the computational effort, we resolved to defer their treatment to a forthcoming paper.

As far as we know, the only preceding formalism devised to study the scattering properties of the same kind of objects we deal with in this paper is that of Fikioris and Uzunoglu [5], whose approach is rather similar to the one we are going to describe. Nevertheless, the results presented by these authors were not obtained through the exact formalism but rather by means of an approximatinal procedure that is applicable only when the difference of the refractive indices of the inclusion and of the external sphere is sufficiently low. As will be discussed later, the results yielded by our formalism when applied just to the same scatterer dealt with by Fikioris and Uzunoglu, show that the range of the applicability of their approximatinal procedure is narrower than one would expect at first sight. The formalism we present in this paper arises as an extension of the one we devised a few years ago to deal with the external anisotropy of clusters of spheres, i. e. of objects built by aggregating several spherical scatterers [6]. As the approach we refer to is based on the expansion of the electromagnetic field in a series of spherical multipoles [7] and on the imposition of the appropriate boundary conditions at the surface of each spherical component of the cluster, the amount of calculation required to get reliable results may grow rather big. In spite of this inevitable feature of all the approaches based on the multipolar expansion of the electromagnetic field, our formalism proved effective not only to study single aggregates, even with rather complicated structure [8], but also, through use of the transformation properties of the multipoles under rotation, to calculate the macroscopic optical properties of a low-density dispersion of clusters with random orientation [9]. The scattering properties of a number of clusters with various geometries were investigated in this way and the predictions of our calculations proved to be in excellent agreement with the available experimental data for single clusters [10,11].

Also the treatment of the scattering from spheres with an eccentric inclusion that we present here is based on the boundary conditions approach and on the expansion of the fields in terms of spherical multipoles. As will be shown in the next section, even in this case we are able to calculate the properties of single objects as well as the macroscopic optical constants of a low-density dispersion of randomly oriented scatterers of this kind. All our calculations were performed with no approximation but the truncation of the multipole expansions of the field to such an order as to ensure the convergence of the results. The refractive indices and the size parameters of the scatterers we dealt with were chosen well beyond the limits of applicability of the approximatinal procedure of Fikioris and Uzunoglu [5]. The notation is a development of the one we used in our previous papers on clusters and has been designed to be immediately extended to the case in which more than one inclusion is present. The underlying mathematics is sketched in section 2; in section 3, after an analysis of the results yielded by the approximate approach of Fikioris and Uzunoglu [5], we discuss our specific results and in section 4 we make some conclusive remarks; the definition of the quantities occurring in our formalism is completed in Appendix A.

2. Theory

To study the scattering properties of a homogeneous sphere containing a spherical inclusion we partition the space into the three regions sketched in fig. 1; the external region, that is assumed to be filled by a homogeneous, non-dispersive, non-absorbing medium with refractive index n (typically the vacuum); the interstitial region, centered at \mathbf{R}_0 and of radius ρ_0 , that is filled with a homogeneous medium, possibly absorbing and/or dispersive, with

refractive index n_0 ; the region within the inclusion, centered at \mathbf{R}_1 and of radius ρ_1 , characterized by a refractive index n_1 that may be absorbing and/or dispersive. For the sake of simplicity, the theory in this section will refer to homogeneous inclusions only, on account that the resulting formulas are easily extended to the case of radial nonhomogeneity.

We assume that all the fields depend on time through the factor $e^{-i\omega t}$ and define the propagation constants

$$K = kn, \quad K_0 = kn_0, \quad K_1 = kn_1$$

in each of the regions mentioned above, respectively, with $k=\omega/c$. It is also convenient to define the size parameters of the external sphere and of the inclusion as

$$x_0 = k\rho_0, \quad x_1 = k\rho_1$$

respectively. Our aim is to determine the response of a sphere when excited by the plane wave field

$$\mathbf{E}_{\text{inc}} = E_0 \hat{\mathbf{e}} e^{i\mathbf{k}_{\text{inc}}\mathbf{r}_0}$$

where E_0 is the amplitude at \mathbf{R}_0 , $\hat{\mathbf{e}}$ is the (unit) polarization vector and $\mathbf{K}_{\text{inc}}=K \hat{\mathbf{k}}_{\text{inc}}$ is the incident wavevector. As anticipated in the preceding section, we expand the field in each region in terms of spherical multipole fields [7]. To this end we define the multipole fields \mathbf{H} as

$$\mathbf{H}_{LM}^{(1)}(K, \mathbf{r}) = h_L(Kr) \mathbf{X}_{LM}(\hat{\mathbf{r}}), \quad \mathbf{H}_{LM}^{(2)}(K, \mathbf{r}) = \frac{1}{K} \nabla \times \mathbf{H}_{LM}^{(1)}(K, \mathbf{r}), \quad (1)$$

where the \mathbf{X}_{LM} 's are vector spherical harmonics [12] and, on account of the chosen time dependence of the fields, the h_L 's are spherical Hankel function of the first kind; the superscripts 1 and 2 are the values of the parity index that are appropriate to the magnetic multipoles and to the electric ones, respectively. We also need to define the multipole fields \mathbf{J} that are identical to the \mathbf{H} 's, eq. (1), but for the substitution of the spherical Bessel functions, j_L , to the h_L 's. Accordingly, the field in the external region can be written as

$$\mathbf{E} = E_0 \sum_{\rho lm} \left\{ A_{lm}^{(\rho)} \mathbf{H}_{lm}^{(\rho)}(K, \mathbf{r}_0) + W_{lm}^{(\rho)} \mathbf{J}_{lm}^{(\rho)}(K, \mathbf{r}_0) \right\}, \quad (2)$$

whereas in the interstitial region

$$\mathbf{E} = E_0 \sum_{\rho lm} \left\{ P_{lm}^{(\rho)} \mathbf{J}_{lm}^{(\rho)}(K_0, \mathbf{r}_0) + P_{lm}^{(\rho)} \mathbf{H}_{lm}^{(\rho)}(K_0, \mathbf{r}_1) \right\}, \quad (3)$$

and within the inclusion

$$\mathbf{E} = E_0 \sum_{\rho lm} C_{lm}^{(\rho)} \mathbf{J}_{lm}^{(\rho)}(K_1, \mathbf{r}_1). \quad (4)$$

In the equations above the $A_{lm}^{(\rho)}$'s are the multipole amplitudes of the field scattered by the whole object and the $W_{lm}^{(\rho)}$ are the (known) multipole amplitudes of the incident planewave field that, according to their definition in Appendix A, encompass all the information on the direction of incidence and on the polarization; the $P_{lm}^{(\rho)}$ and the $P_{lm}^{(\rho)}$ are the amplitudes of the interstitial field and the $C_{lm}^{(\rho)}$ are those of the field within the inclusion. The A 's are, therefore, the main unknowns of the problem as all the relevant quantities can be expressed in terms of them. As an example, the normalized scattering amplitude, that is the quantity we are mainly interested in, can be written as [9]

$$\mathbf{f} = \frac{1}{K} \sum_{lm} (-i)^{l+1} \left[A_{lm}^{(1)} \mathbf{X}_{lm}(\hat{\mathbf{k}}_{\text{sca}}) + i A_{lm}^{(2)} \hat{\mathbf{k}}_{\text{sca}} \times \mathbf{X}_{lm}(\hat{\mathbf{k}}_{\text{sca}}) \right], \quad (5)$$

$\mathbf{K}_{\text{sca}} = K\hat{\mathbf{k}}_{\text{sca}}$ being the scattered wavevector, and the dependence on the polarization as well as on the wavevector of the incident plane wave, \mathbf{K}_{inc} is contained in the A 's. To calculate these latter we have to impose the appropriate boundary conditions at the surface of the inclusion as well as at the surface of the external sphere. According to eq. (3), not all the multipoles of the interstitial field are referred to the same origin, so that we have to use an appropriate addition theorem [13] to express the whole field with respect to a single origin, before the boundary conditions are applied. Then, the procedure we found more convenient to calculate the A 's is a two-step one: in the first step, by eliminating the C 's, and the A 's as well, by means of the equations that express the boundary conditions, we are confronted with a system of linear non-homogenous equations for the P 's only; then, we get the A 's from their relations with the P 's. The system for the P 's can be written matrixwise as

$$\begin{vmatrix} (\mathbf{R}_1)^{-1} & \mathbf{I}_{1 \rightarrow 0} \\ \mathbf{R}_W \mathbf{l}_{0 \rightarrow 1} & (\mathbf{R}_0)^{-1} \end{vmatrix} \begin{vmatrix} \mathbf{P}_1 \\ \mathbf{P}_0 \end{vmatrix} = \begin{vmatrix} \mathbf{O} \\ \mathbf{W} \end{vmatrix}, \quad (6)$$

or, in more compact form,

$$M P = W,$$

with obvious correspondence of the symbols. The elements of all the submatrices appearing in eq. (6) as well as those of all the submatrices that will appear hereafter are explicitly given in Appendix A. The analogy of eq. (6) with the one we obtained for the case of a cluster is quite evident [6]. In particular, the present equation contains terms which account for the scattering power of the inclusion and of external sphere (the diagonal submatrices \mathbf{R}_1 and \mathbf{R}_0 , respectively) as well as terms that account for the multiple scattering processes between the inclusion, and the external sphere (the submatrices $\mathbf{I}_{1 \rightarrow 0}$ and $\mathbf{R}_W \mathbf{l}_{0 \rightarrow 1}$). We notice that the submatrices \mathbf{l} arise from the addition theorem of reference [13] and effect the translation of the spherical multipoles from the origin to the center of the inclusion ($\mathbf{l}_{1 \rightarrow 0}$) and viceversa ($\mathbf{l}_{0 \rightarrow 1}$).

To solve the system, eq. (6), we have to invert the matrix M , but the actual calculation of the P 's, on account of the particular form of the vector W , that contains a subvector of zeros, involves only the rightmost columns of the inverted matrix. So, if we write M^{-1} in the partitioned form

$$M^{-1} = \begin{vmatrix} \mathbf{Z}_1 & \mathbf{Z}_{01} \\ \mathbf{Z}_{01} & \mathbf{Z}_0 \end{vmatrix},$$

where all the submatrices are of the same order as the corresponding ones appearing in M , and define the rectangular submatrix

$$Z = \begin{vmatrix} \mathbf{Z}_{10} \\ \mathbf{Z}_0 \end{vmatrix},$$

the P 's are given by the equation

$$P = ZW,$$

The A 's are then given by the equation

$$A = TP = SW, \quad (7)$$

where T is the rectangular matrix

$$T = \begin{vmatrix} \mathbf{M}_W \mathbf{l}_{0 \rightarrow 1} & \mathbf{M}_0 \end{vmatrix},$$

The rightmost form of eq. (7) evidences that the multipole amplitudes of the scattered field are obtained by operating on the amplitudes of the incident field with the matrix $S=TZ$ that includes all the information on the geometrical structure and on the scattering power of our

scatterers.

The matrix M is in principle of order $4L_M(L_M+2)$, if L_M is the highest value of l retained in the multipolar expansions of the fields, eq. (2)-(4), and its inversion is thus responsible for the main bulk of our calculations. Nevertheless, since the scatterers we deal with in this paper have a cylindrical symmetry, group theoretical techniques can be used to factorize M [14,15]: the maximum order of the matrices to be inverted reduces, in this case, to $4L_M$; only. It is well known, however, that this factorization can be achieved without using the machinery of the group theory simply by choosing the cylindrical axis as the z -axis (16).

As anticipated in the preceding section, we are also able to calculate the macroscopic optical constants of a medium formed by a low-density dispersion of inclusion-containing spheres identical to each other and with random orientations. In general, the macroscopic optical constants for the propagation of a plane wave through a low-density dispersion of anisotropic particles are given by the matrix of the refractive index [17]

$$N_{\eta\eta'} = n \left[\delta_{\eta\eta'} + \frac{2\pi}{K^2} \int \rho(\Theta) f_{\eta\eta'}(\Theta) d\Theta \right], \quad (8)$$

where $\rho(\Theta)$ is the number of particles per unit volume with orientation Θ , this latter being a shorthand for the Euler angles that individuate the orientation of each particle. In eq. (8) the indices $\eta, \eta' = 1, 2$ refer to a pair of unit vectors, \hat{e}_1 and \hat{e}_2 , orthogonal to each other and to \hat{k}_{inc} with respect to which we analyze the state of polarization both of the incident and of the scattered wave. Accordingly

$$f_{\eta\eta'}(\Theta) = f_{\eta}(\Theta) \cdot \hat{e}_{\eta'}$$

is the component along $\hat{e}_{\eta'}$ of the *forward-scattering* amplitude of a particle with orientation Θ when excited by a plane wave with $\hat{e} \equiv \hat{e}_{\eta}$. In particular, the macroscopic refractive index and the extinction coefficient of the dispersion are related to the diagonal elements of $N_{\eta\eta'}$, according to

$$n_{\eta} = \text{Re}[N_{\eta\eta}], \quad \gamma_{\eta} = 2k \text{Im}[N_{\eta\eta}],$$

respectively. Equation (8) is valid provided that the density of the dispersion is so low that the fields scattered by the whole medium can be approximated by the superposition of the fields scattered by the single isolated objects. Although this amounts to neglect the multiple scattering processes that may occur among different particles, the approximation is fairly acceptable for sufficiently tenuous media. To calculate the integral in eq. (8) one has to recall that the multipole fields transform under rotation according to the representations of the three-dimensional rotation group [18]. As fully explained in ref. (9), this implies that once f is known for a scatterer with orientation Θ_0 it is immediately known for any other identical scatterer with orientation Θ . Therefore, assuming that the scatterers are uniformly distributed on the orientations, the integral can be performed analytically with the result

$$N_{\eta\eta'} = n \left[\delta_{\eta\eta'} + \frac{2\pi\rho}{K^2} \bar{f}_{\eta\eta'} \right],$$

where ρ is the total number of the scatterers per unit volume and

$$\bar{f}_{\eta\eta'} = \bar{f}_{\eta} \cdot \hat{e}_{\eta'}$$

where \bar{f}_{η} must be calculated as $f_{\eta}(\Theta)$, eq. (5), but with

$$A_{lm}^{(p)} = \frac{1}{2l+1} \sum_{p'm'} S_{lm',lm'}^{(p,p')}(\Theta_0) W_{lm}^{(p')}$$

It is to be borne in mind that the definition of $\bar{f}_{\eta\eta'}$ turns out to be independent of the orientation Θ_0 one chooses to calculate the matrix elements of S .

3. Results and discussion

As far as we know, no experimental data are presently available on the scattering properties of the kind of objects we deal with in this paper. Therefore, we felt necessary to perform extensive and careful tests on the results yielded by our formalism. First of all, we verified that the scattering amplitude conforms to the symmetries that, as shown by van de Hulst [1], it must display. Secondly, we dealt with the properties that our scatterers must have when all the refractive indices are real; in particular the coincidence of the extinction cross section and of the scattering cross section was checked. Then, the limiting case of a concentric inclusion with the consequent identification of the scattering properties with those of a stratified sphere was also considered. At last, we dealt with the limiting cases that occur for particular values of the refractive indices. For instance, we followed the vanishing of the scattering when $n_0=n$ and $n_1=n$ as well as the coincidence of the results with those for the bare inclusion centered off the origin when n_1 is held fixed and $n_0=n$. All these tests were positive for any choice of the parameters and confirmed that some of the features we noticed in our preceding studies on aggregated spheres [19] persist even in the present case. The test that reduces the eccentric inclusion to a bare sphere off the origin is particularly significant for it involves the matrices $I_{1 \rightarrow 0}$ and $I_{0 \rightarrow 1}$ that effect the transfer of origin of the multipole fields according to the addition theorem of ref. [13]. The numeric results coincide fairly well with those that can be obtained directly for the bare sphere off the origin, but as a consequence of the intervention of the transfer matrices *the multipole expansion must be extended to higher values of l* in order to ensure the convergence to the same precision. This is a very general condition that occurs in all our calculations not only in the present paper but also in our previous studies of the scattering properties of aggregated spheres. In fact, we systematically found that, whenever dependent scattering occurs so that the use of the transfer matrices is necessary, the value of L_M that guarantees the convergence of the results is larger than the values of all the L_M 's that ensure the same convergence for all the individual spheres. We give here also a further result from our studies on dependent scattering: the value of L_M that ensures both the fulfilment of the due symmetry properties and the coincidence of the extinction and scattering cross sections when the refractive indices are real is smaller than the one that insures the convergence. As a consequence, *the fulfilment of the symmetry properties does not guarantee the accuracy of the results.*

Our successive step has been the application of our formalism just to the same scatterer dealt with by Fikioris and Uzunoglu and the comparison of our results with those reported by these authors. We recall that the object we refer to is a sphere of refractive index $n_0=1.3$ and size parameter $x_0=2$, centered at the origin, containing a sphere with $n_1=1.7$ and $x_1=1$, with the center on the x-axis. The external medium is assumed to be the vacuum ($n=1$). In our opinion, the most significant comparison is the one we effected in fig. 2 between the back-scattering efficiencies for incidence along the symmetry axis vs. the *eccentricity*, $x_E=kz$, where z is the coordinate of the center of the inclusion. It is quite evident at first glance that the general shape of the curves is similar but that the numerical values are quite different. To explain the origin of this discrepancy we remark that the curves do not completely agree neither when the inclusion is centered. In fact, with reference to our present notation, Fikioris and Uzunoglu expand the terms $(R_1)^{-1}$, eq. (6), as well as the amplitudes of the interstitial field, $P_{lm}^{(p)}$, in powers of $(n_1-n_0)x_1=0.4$, according to their choice of the parameters, and retain terms up to the second order only. Unless the expansion is completely convergent, this procedure alters the scattering power of the inclusion, and this alteration is always effective, even when the inclusion is concentric. Of course, when the inclusion is off center the effect of the expansion becomes more visible, as expected, for expanding the P 's alters also the strength of the coupling between the inclusion and the external sphere. These considerations should explain why the curves in fig. 2 tend to diverge with increasing x_E and suggest that the power series expansion of Fikioris and Uzunoglu is not completely convergent. A close examination of the values for the expanded amplitudes reported in Table I of ref. [5] shows that this is, indeed, the case. For all values of l the first and second order terms in the expansion of the P 's are of the same order of magnitude, so that there is no guarantee that

the third order terms are truly negligible. Furthermore, we found that neither the multipole expansion of Fikioris and Uzunoglu is perfectly convergent: according to our previous considerations one expects that their value of $L_M=4$ be quite adequate for the bare inclusion, but from our calculations $L_M=6$ seems at least necessary to achieve an accuracy of $\approx 1\%$. As a consequence, the fact that the calculations of Fikioris and Uzunoglu fulfil the symmetry properties implies only that $L_M=4$ is sufficient to achieve this effect and that the power series expansion, as often occurs, does not affect these properties.

As for the angular dependence of the scattered intensity, the curves from our calculations, apart from vertical shifts, compare fairly well with those in fig. 5 of ref. [5], so that this comparison does not deserve, in our opinion, a specific figure. The similarity of the angular behavior is in no way surprising, indeed, as an examination of the formalism shows that the dependence on the polarization and on the direction of incidence is contained in the vector \mathbf{W} , eq. (6), while the dependence on the direction of observation is contained in the vector spherical harmonics in \mathbf{f} , eq. (5): both these quantities are untouched by the series expansion. On the other hand, the vertical shifts are easily accounted for because the amplitudes $A_{lm}^{(p)}$ that appear in \mathbf{f} do are affected by the series expansion.

Considerations very similar to the ones reported above can explain any further difference between our results and those of ref. (5). Ultimately, we are lead to conclude that the range of applicability of the approximational procedure of Fikioris and Uzunoglu is narrower than one could expect so that, in general, it is wise to resort to the exact procedure.

Our specific calculations are performed with reference to the same geometry referred to above: the external sphere is centered at the origin and the center of the inclusion always lies on the z-axis. The incident field is a plane wave whose wavevector is individuated by the polar angles θ_{inc} and ϕ_{inc} ; in turn the wavevector of the scattered wave is individuated by the polar angles θ_{sca} and ϕ_{sca} . Our calculations were performed with $\theta_{inc}=0, \pi/4, \pi/2$, and $\phi_{inc}=0$, and, indicating by $\theta(0 \leq \theta \leq \pi)$ the angle of scattering,

$$\begin{aligned} \theta_{sca} &= \theta_{inc} + \theta, \phi_{sca} = 0 \quad \text{for } \theta_{inc} + \theta < \pi, \\ \theta_{sca} &= 2\pi - (\theta_{inc} + \theta), \phi_{sca} = \pi \quad \text{for } \theta_{inc} + \theta > \pi, \end{aligned}$$

Therefore the scattering plane coincides with the x-z plane; the polarization vector both of the incident and of the scattered field is always parallel ($\hat{\mathbf{e}} \equiv \hat{\mathbf{e}}_1$) or orthogonal ($\hat{\mathbf{e}} \equiv \hat{\mathbf{e}}_2$) to that plane.

The scattering properties are described through the normalized scattering amplitude: more precisely, we report the quantities [10]

$$P_\eta(\theta) = \frac{4}{K\rho_0^2} \text{Re}[f_\eta(\theta)], \quad Q_\eta(\theta) = \frac{4}{K\rho_0^2} \text{Im}[f_\eta(\theta)]$$

that, on account of the definition of f_η , eq. (5), are adimensional and independent of the radius of the spheres. We also report the quantities P^- and Q^- that are meaningful for forward scattering only ($\theta=0$) and are identical to $P(0)$ and $Q(0)$, respectively, but for the substitution of \mathbf{f}^- $\mathbf{f}(0)$. According to the preceding section, P^- and Q^- give information on the macroscopic optical properties of a low-density dispersion of the scatterers we deal with.

Since the objects we are interested in have a size parameter $x_0 > 1$, the value of L_M that is necessary to get fully converged results turns out to be rather large and the factorization of M referred to in the preceding section is, therefore, very useful to reduce the computational effort. As a criterion of full convergence we required that, with respect to the any increase of L_M , our results be stable at least to 4 significant digits; this accuracy is by far higher than required for any graphical display. It may be interesting to notice that, in agreement with the remarks by other workers dealing with dependent scattering from aggregated spheres, we met the slowest convergence when the surfaces of the inclusion and of the external sphere touch each other (20).

Hereafter we present the results of our calculations for a dielectric external sphere with refractive index $n_0 \equiv n_D = 1.61 + i0.004$ – this value describes satisfactorily the optical properties of spheres of acrylic in a large frequency range [10] – containing either a metallic inclusion (sect. 3.0.1) or an empty cavity (sect. 3.0.2). In both cases the external medium is assumed to be the vacuum ($n = 1$).

3.0.1. Metallic inclusion in a dielectric sphere

The size parameter of the dielectric sphere and of the inclusion are $x_D = 3$ and $x_M = 1$, respectively, so that the ratio of their radii is $\rho_D/\rho_M = 3$. The eccentricity of the inclusion can range from $x_E = 0$, when the inclusion is concentric, to $x_E = \pm 2$, when it is tangent to the surface of the external sphere. In our calculations of $f(0)$, *i. e.* when forward scattering is considered, the z -coordinate of the center of the inclusion assumes both positive and negative values. However, since our scattering amplitude rigorously fulfil the due symmetry properties [1], we will report only the results for $x_E \geq 0$. The dielectric properties of the metallic inclusion are assumed to be well described by the free electron Drude function,

$$\epsilon_M = 1 - \frac{1}{\nu(\nu + i\gamma)},$$

where $\nu = \omega/\omega_p$, ω_p being the plasma frequency. In our calculations we assume $\gamma = 0.01$ and choose $\nu = 0.1$ because for most metals this value of ν corresponds to a frequency in the visible or in the infrared range [21]: the resulting refractive index of the inclusion is $n_1 \equiv n_M = \sqrt{\epsilon_M} = 0.4994 + i9.9126$. The results we are going to discuss required at most $L_M = 10$ to reach full convergence in the sense explained above.

The quantities $P(0)$ and $Q(0)$ as a function of x_E for the three directions of incidence referred to above and for polarization both parallel and orthogonal to the scattering plane are reported in figs. 3a and 3b, respectively. In the same figures we also report the averages \bar{P} and \bar{Q} that, according to the discussion of the preceding section, are independent both of the direction and of the polarization of the incident wave. Of course, also $P(0)$ and $Q(0)$ are independent of the polarization when the direction of incident wavevector lies along the symmetry axis ($\theta_{inc} = 0$), but, when $\theta_{inc} = \pi/4$ and $\theta_{inc} = \pi/2$, they become strongly dependent on the polarization. A further interesting remark is at hand in the results of figs. 3. If we consider only one state of polarization, either parallel or orthogonal, the curves for \bar{P} and \bar{Q} not always lie within the curves for the various incidences, contrary to what would be expected of averaged quantities. This effect is due to the contributions to \bar{P} and \bar{Q} , coming from scatterers so oriented that their symmetry axis do not lie in the scattering plane. These contributions are never explicitly computed but are automatically accounted for by our analytic averaging procedure. Indeed, the response of a scatterer with its symmetry axis not lying in the scattering plane is easily recognized as identical to the response of a scatterer with its axis in that plane when this latter object is excited by a wave with an appropriate state of polarization that, in general, is neither parallel nor orthogonal. Therefore the above mentioned response must be a linear combination of the responses for parallel and orthogonal polarization and, since the scattering properties of the objects we are dealing with here show a noticeable sensitivity to the state of polarization, we got the seemingly anomalous behavior of \bar{P} and \bar{Q} described above.

As a reference we also calculated $P(0)$ and $Q(0)$ for a homogeneous dielectric sphere either with the same radius of the external sphere ($P_h(0) = 1.3173$ and $Q_h(0) = 3.9117$) or containing the same quantity of dielectric material as the sphere with the inclusion ($P_c(0) = 1.3151$ and $Q_c(0) = 3.9044$). Indeed, a comparison of these values with those of the curves in figs. 3a and 3b will give a better insight into the effect of the very presence of the inclusion and of its eccentricity as well. Let us remark, first of all, that $P_h(0)$ and $P_c(0)$ as well as $Q_h(0)$ and $Q_c(0)$ differ very little from each other because the ratio of the volumes of the homogeneous spheres defined above is $27/26$ on account of our choice $\rho_D/\rho_M = 3$. Moreover, the values of $P(0)$ and $Q(0)$ for a sphere with a centered inclusion ($x_E = 0$) are remarkably different from the corresponding values for the homogeneous

dielectric spheres of both sizes considered above. When x_E increases the difference of \bar{P} and $P_h(0)$ and, specially, that of \bar{Q} and $Q_h(0)$, tend to decrease while the behavior of the difference of $P(0)$ and $P_h(0)$ as well as that of $Q(0)$ and $Q_h(0)$ depends on the direction of incidence and, in general, also on the polarization. In fact, the spread of the curves of $P(0)$ and $Q(0)$ is rather large and reaches its maximum at $x_E = 2$ (fig. 3a) and for $x_E = 1.15-1.35$ (fig. 3b), respectively.

In figs. 4 we show $Q(\theta)$ vs. $P(\theta)$ for parallel polarization and for $\theta_{inc} = 0$ (fig. 4a), $\theta_{inc} = \pi/4$ (fig. 4b) and $\theta_{inc} = \pi/2$ (fig. 4c). In each figure we report the curves for the extreme values of the eccentricity ($x_E = 2$ and $x_E = -2$) as well as the curve for the centered inclusion ($x_E = 0$); as a reference, the curve of $P_h(\theta)$ vs. $Q_h(\theta)$ is also reported. Of course, both the curves for the centered inclusion and for the homogeneous sphere do not depend on the incidence and are thus the same in all these figures. It is easily seen that the curves for the spheres with an eccentric inclusion are rather different from each other and differ also from those both for the sphere with a centered inclusion and for the homogeneous sphere. For forward scattering ($\theta = 0$), the curves for the two eccentric positions stick together as expected on account of the symmetry properties of the scattering amplitude. At all incidences the position of the inclusion within the external sphere has an evident effect on the shape of the P - Q curves, although the general behavior remains unchanged. When the incidence is orthogonal to the symmetry axis ($\theta = \pi/2$) the curves for $x_E = 2$ and for $x_E = -2$ stick together not only for forward scattering ($\theta = 0$) but also at backscattering ($\theta = \pi$) as required by an obvious symmetry property of the matrix of the scattering amplitude (fig. 4c).

We do not report the curves we calculated for orthogonal polarization because, although the values we obtained are numerically rather different from those for parallel polarization, the general shape and properties of the curves are identical to those reported in figs. 4 and do not deserve, in our opinion, a separate comment.

3.0.2. Empty cavity in a dielectric sphere

The size parameter of the dielectric external sphere and of the empty cavity ($n_1 = n_c = 1$) are $x_D = 4.3410$ and $x_C = 2.1705$, respectively, and the ratio of their radii is $\rho_D/\rho_C = 2$. As a consequence, the eccentricity can range from $x_E = 0$ to $x_E = \pm 2.1705$. Our choice of $n_D = 1.61 + i0.004$ and of $x_D = 4.341$ is due to the fact that, as noted above, the experimental scattering properties of a solid dielectric sphere with these features are known, so that we used such an object as a reference scatterer to test the reliability of our calculations. In the present case the convergence of the results required at most $L_M = 8$.

The main body of our results is displayed in figs. 5a and 5b that are analogous to figs. 3a and 3b, respectively. As compared with the results of the preceding subsection the present results show a less strong dependence on the polarization and in particular this dependence is rather weak for $Q(0)$ (fig. 5b). As an immediate consequence of this weak dependence we notice that the curves of \bar{P} and \bar{Q} always lie within the curves of $P(0)$ and $Q(0)$ for a single polarization although those latter refer only to orientations with the symmetry axis in the scattering plane. The results both for the solid dielectric sphere with radius equal to that of the external sphere (the reference sphere mentioned above) and of the sphere containing the same quantity of dielectric material as the sphere with the inclusion are $P_h(0) = -0.9238$, $Q_h = 3.8373$ and $P_c = -0.7796$, $Q_c = 4.1082$, respectively. In the present case these values are noticeably different from each other since the ratio of the radii $\rho_D/\rho_C = 2$ implies that the ratio of the volumes is 8/7. Furthermore, the relative positions of these values show that $P(0)$ and $Q(0)$ for a homogeneous sphere are, in this range, decreasing functions of the size parameter. Both figs. 5a and 5b show that even in the present case, \bar{P} and specially \bar{Q} as the eccentricity increases, tend to reduce their difference both from $P_h(0)$ and $Q_h(0)$ and from $P_c(0)$ and $Q_c(0)$. The spread of the values for the different incidences we considered reaches a rather large maximum at the highest value of the eccentricity.

Although we performed also calculations analogous to those displayed in figs. 4a-c, we resolved not to report the results because they do not evidence any new significant feature worth of a separate comment.

4. Conclusions

The results we described in the preceding section are only a small sample of the large body of calculations that could be performed on the cases of interest. They were, in fact, chosen as representative examples of the physical situations one can meet in dealing with scatterers of this kind. By comparing the results for the two kinds of inclusion we dealt with in this paper it is quite clear that the evidence of the effects we described tend to vanish when the difference of the dielectric function of the external sphere and of the inclusion becomes small. The tests we discussed in the preceding section, strongly suggest that even in this limiting case any approximation procedure should be carefully checked, on account of the transfers effected by the matrices l and of the consequent complicated couplings among the equations for the multipolar amplitudes.

In our opinion the results we showed in the preceding section succeeded in proving that the presence of an eccentric inclusion within an otherwise spherical object is quite detectable. The eccentricity, in fact, introduces polarization effects, that are absent in homogeneous spheres as well as in spheres with concentric inclusions, *i. e.* when a true spherical symmetry is present; furthermore, the eccentricity itself changes the response both in the forward as well as in the non-forward scattering. We are not able to present experimental data against which the reliability of our results can be compared. Nevertheless, the magnitude of the effects we evidenced may encourage specific experimental research on the subject.

Appendix A

In this appendix we will go through the formulae of sect. 2 and give the explicit expression of the elements of the submatrices we used in this paper. The multipole amplitudes of the incident plane wave, $W_{lm}^{(p)}$, are the elements of the one-column submatrix W , eq.(6), and are defined as

$$W_{lm}^{(1)}(\hat{\mathbf{k}}_{\text{inc}}) = 4 \pi i^l \hat{\mathbf{e}} \cdot \mathbf{X}^*_{lm}(\hat{\mathbf{k}}_{\text{inc}}), \quad W_{lm}^{(2)}(\hat{\mathbf{k}}_{\text{inc}}) = 4 \pi i^l (\hat{\mathbf{k}}_{\text{inc}} \times \hat{\mathbf{e}}) \mathbf{X}^*_{lm}(\hat{\mathbf{k}}_{\text{inc}}),$$

Next, it is convenient to introduce the notation

$$n_{-1} = \frac{n_0}{n_1} - 1, \quad n_{+0} = \frac{n}{n_0} - 1,$$

and the functions

$$u_l(x) = x j_l(x), \quad w_l(x) = x h_l(x),$$

that help to write in compact form the elements of the matrix \mathbf{R}_1 , that characterizes the single inclusion we consider in this paper, as well as the matrices \mathbf{R}_0 , \mathbf{R}_W , \mathbf{M}_0 and \mathbf{M}_W , that characterize the sphere containing the inclusion. The matrices \mathbf{R}_1 , \mathbf{R}_0 and \mathbf{R}_W are diagonal with elements

$$R_{lm,lm}^{(p,p)} = \delta_{pp} \delta_{ll} \delta_{mm} R_l^{(p)},$$

$$R_{l'm',l'm'}^{(p,p')} = \delta_{pp'} \delta_{ll'} \delta_{mm'} R_{l'}^{(p)},$$

$$R_{l'm',l'm'}^{(p,p')} = \delta_{pp'} \delta_{ll'} \delta_{mm'} R_{l'}^{(p)},$$

where

$$R_{l'}^{(p)} = \frac{(1 + n_1^- \delta_{p1}) u_l(K_1 \rho_1) u'_l(K_0 \rho_1) - (1 + n_1^- \delta_{p2}) u'_l(K_1 \rho_1) u_l(K_0 \rho_1)}{(1 + n_1^- \delta_{p1}) u_l(K_1 \rho_1) w'_l(K_0 \rho_1) - (1 + n_1^- \delta_{p2}) u'_l(K_1 \rho_1) w_l(K_0 \rho_1)}$$

$$R_{l'}^{(p)} = i [(1 + n_0^- \delta_{p1}) u_l(K_0 \rho_0) w'_l(K \rho_0) - (1 + n_0^- \delta_{p2}) u'_l(K_0 \rho_0) w_l(K \rho_0)]^{-1},$$

$$R_{l'}^{(p)} = -i [(1 + n_0^- \delta_{p1}) w_l(K_0 \rho_0) w'_l(K \rho_0) - (1 + n_0^- \delta_{p2}) w'_l(K_0 \rho_0) w_l(K \rho_0)],$$

respectively. $R_{l'}^{(1)}$ and $R_{l'}^{(2)}$ coincide with the Mie coefficients b_l and a_l , respectively, for the scattering by a homogeneous sphere of radius ρ_1 and refractive index n_1 embedded in a homogeneous medium of refractive index n_0 . Also the matrices M_W and M_0 are diagonal with elements

$$M_{l'm',l'm'}^{(p,p')} = \delta_{pp'} \delta_{ll'} \delta_{mm'} M_{l'}^{(p)}$$

and

$$M_{l'm',l'm'}^{(p,p')} = \delta_{pp'} \delta_{ll'} \delta_{mm'} M_{l'}^{(p)},$$

where

$$M_{l'}^{(p)} = i [(1 + n_0^- \delta_{p1}) w_l(K_0 \rho_0) u'_l(K \rho_0) - (1 + n_0^- \delta_{p2}) w'_l(K_0 \rho_0) u_l(K \rho_0)]$$

and

$$M_{l'}^{(p)} = i [(1 + n_0^- \delta_{p1}) u_l(K_0 \rho_0) u'_l(K \rho_0) - (1 + n_0^- \delta_{p2}) u'_l(K_0 \rho_0) u_l(K \rho_0)]$$

respectively. Finally, we define the elements of the matrix $I_{1 \rightarrow 0}$, that, as explained in sect. 2, effects the transfer of origin of the multipole fields R_0 R_1 :

$$I_{l'm',l'm'}^{(p,p')} = \left[\delta_{pp'} - i \sqrt{\frac{2l+1}{l}} (1 - \delta_{pp'}) \right] \sum_{\mu} C(1, l+1-\delta_{pp'}, l; -\mu, m+\mu) \times$$

$$\times G_{l+1-\delta_{pp'}, m+\mu; l', m'+\mu}(K_0, R_{10}) C(1, l', l'; -\mu, m'+\mu),$$

where $R_{10} = R_0 - R_1$ and

$$G_{l'm',l'm'}^{(p,p')}(K, R) = 4\pi \sum_{\lambda} i^{l-l'-\lambda} I_{\lambda}(l, m; l', m') j_{\lambda}(K, R) Y_{\lambda, m-m'}^*(\hat{R}).$$

In the preceding equations the C 's are the Clebsch-Gordan coefficients and the quantities I_λ are the Gaunt integrals [7] that are defined as

$$I_\lambda(l, m; l', m') = \int Y_{lm} Y_{l'm'}^* Y_{\lambda, m'-m} d\Omega$$

The elements of the matrix $\mathbf{I}_{0 \rightarrow 1}$, that effect the transfer from the site R_1 to the site R_0 can be obtained from the expressions given above by substituting R_{01} to R_{10} .

As the last item of this appendix we make a comparison between the definition of the scattering amplitude we adopted in our formalism with the corresponding definitions assumed in some authoritative textbooks. According to Jackson (12), we assume that the phase of the incident plane wave field propagating through a homogeneous medium is

$$\phi^{(+)} = i(n^{(+)} \mathbf{k} \cdot \mathbf{r} - \omega t) ,$$

where $n^{(+)}$ is the (in general complex) refractive index defined as

$$n^{(+)} = n' + in'' .$$

For the normalized scattering amplitude f we use just the definition of Jackson

$$\mathbf{E}_{sc}^{(+)} = E_0 \frac{e^{in^{(+)}kr}}{r} \mathbf{f} ,$$

where $\mathbf{E}_{sc}^{(+)}$ is the scattered field. Bohren and Huffman [22] as well as Bayvel and Jones [23] assume different definitions for the scattering amplitude that are related to that of Jackson through the relations

$$f = \frac{i}{n^{(+)}k} S_{BH} = \frac{1}{n^{(+)}k} S_{BJ} .$$

van de Hulst makes a different choice of the phase:

$$\phi^{(-)} = -i(n^{(-)} \mathbf{k} \cdot \mathbf{r} - \omega t) ,$$

with

$$n^{(-)} = n' - in'' .$$

Therefore,

$$n^{(-)*} = n^{(+)} ,$$

and

$$\mathbf{E}_{inc}^{(-)*} = \mathbf{E}_{inc}^{(+)} , \quad \mathbf{E}_{sc}^{(-)*} = \mathbf{E}_{sc}^{(+)} ,$$

whence the relation of his normalized scattering amplitude with the f defined above follows:

$$S^{(-)*} = -in^{(+)}kf .$$

References

- [1] H. C. van de Hulst, *Light scattering by small particles* (Wiley, New York, 1957).
- [2] M. Kerker, *The scattering of light* (Academic Press, New York, 1969).
- [3] R. Ruppin, "Optical Properties of Metal Spheres with a Diffuse Surface," *J. Opt. Soc. Am.* 66, 449-453 (1976).
- [4] F. Borghese, P. Denti, R. Saija, G. Toscano and O. I. Sindoni, "Extinction coefficients for a random dispersion of small stratified spheres and a random dispersion of their binary aggregates," *J. Opt. Soc. Am. A4*, 1984-1991 (1987).
- [5] J. G. Fikioris and N. K. Uzunoglu, "Scattering from an eccentrically stratified dielectric sphere," *J. Opt. Soc. Am.* 69, 1359-1366 (1979).
- [6] F. Borghese, P. Denti, R. Saija, G. Toscano and O. I. Sindoni, "Multiple electromagnetic scattering from a cluster of spheres. I. Theory," *Aerosol Sci. Technol.* 3, 227-235 (1984).
- [7] R. M. Rose, *Multipole Fields* (Wiley, New York, 1955).
- [8] F. Borghese, P. Denti, R. Saija, G. Toscano and O. I. Sindoni, "Optical absorption coefficient of a dispersion of clusters composed of a large number of spheres," *Aerosol Sci. Technol.* 6, 173-181 (1987).
- [9] F. Borghese, P. Denti, R. Saija, G. Toscano and O. I. Sindoni, "Macroscopic optical constants of a cloud of randomly oriented nonspherical scatterers," *Nuovo Cim.* 81, 29-50 (1984).
- [10] R. T. Wang, J. M. Greenberg and D. W. Schuerman, "Experimental results of the dependent light scattering by two spheres," *Optics Lett.* 11, 543-545 (1981).
- [11] F. Borghese, P. Denti, R. Saija and O. I. Sindoni, "Reliability of the theoretical description of electromagnetic scattering from non-spherical particles," *J. Aerosol Sci.* 20, 1079-1081 (1989).
- [12] J. D. Jackson, *Classical electrodynamics* (Wiley, New York, 1975).
- [13] F. Borghese, P. Denti, G. Toscano and O. I. Sindoni, "An addition theorem for vector Helmholtz harmonics," *J. Math. Phys.* 21, 2754-2755 (1980).
- [14] F. Borghese, P. Denti, R. Saija, G. Toscano and O. I. Sindoni, "Use of group theory for the description of electromagnetic scattering from molecular systems," *J. Opt. Soc. Am. A1*, 183-191 (1984).

- [15] O. I. Sindoni, F. Borghese, P. Denti, R. Saija and G. Toscano, "Multiple electromagnetic scattering from a cluster of spheres. II. Symmetrization," *Aerosol Sci. Technol.* 3, 237-243 (1984).
- [16] K. A. Fuller and G. W. Kattawar, "Consummate Solution to the Problem of Classical Electromagnetic Scattering by an Ensemble of Spheres. I: Linear Chains," *Optics Lett.* 13, 90-92 (1988).
- [17] R. Newton, *Scattering theory of waves and particles* (McGraw-Hill, New York, 1966).
- [18] E. M. Rose, *Elementary Theory of Angular Momentum* (Wiley, New York, 1957).
- [19] See, for instance, ref. [4] and references therein.
- [20] K. A. Fuller, "Recent Progress in the Study of the Optical Resonances of Two-sphere Systems," in *Proc. 2nd Int. Conf. On Optical Particle Sizing*, 65-68 (University of Arizona, Tempe, 1990).
- [21] C. Kittel, *Introduction to Solid State Physics* (Wiley, New York, 1976).
- [22] C. F. Bohren and D. R. Huffman, *Absorption and Scattering of Light by Small Particles* (Wiley, New York, 1983)
- [23] L. P. Bayvel and A. R. Jones, *Electromagnetic Scattering and its Applications* (Applied Science, London, 1981).

5. Figure Captions

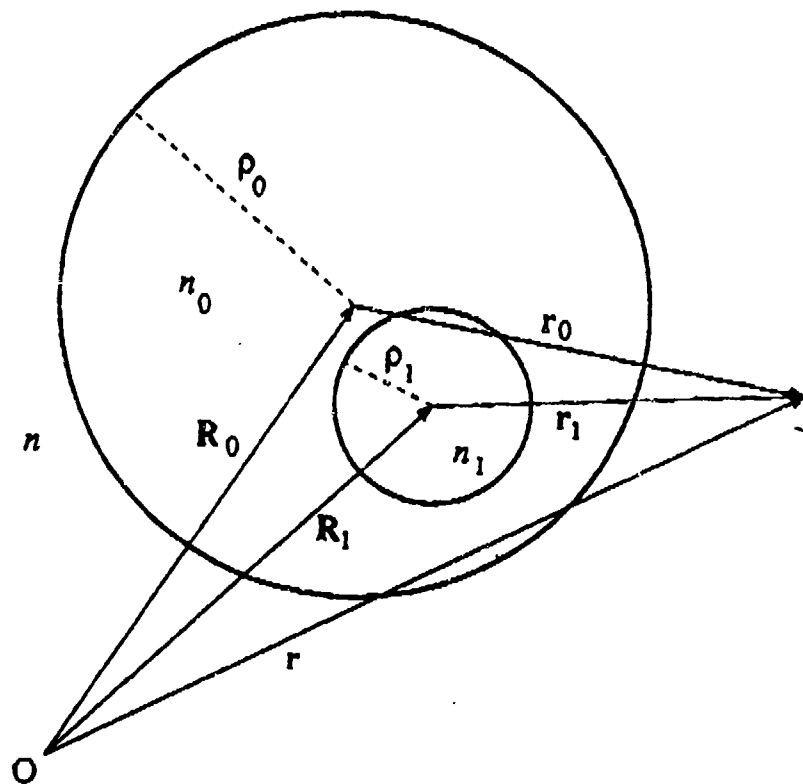
Figure 1. Sketch of the three regions into which the space is partitioned. In actual calculations the center of the external sphere coincides with the origin and the center of the inclusion lies on the z-axis.

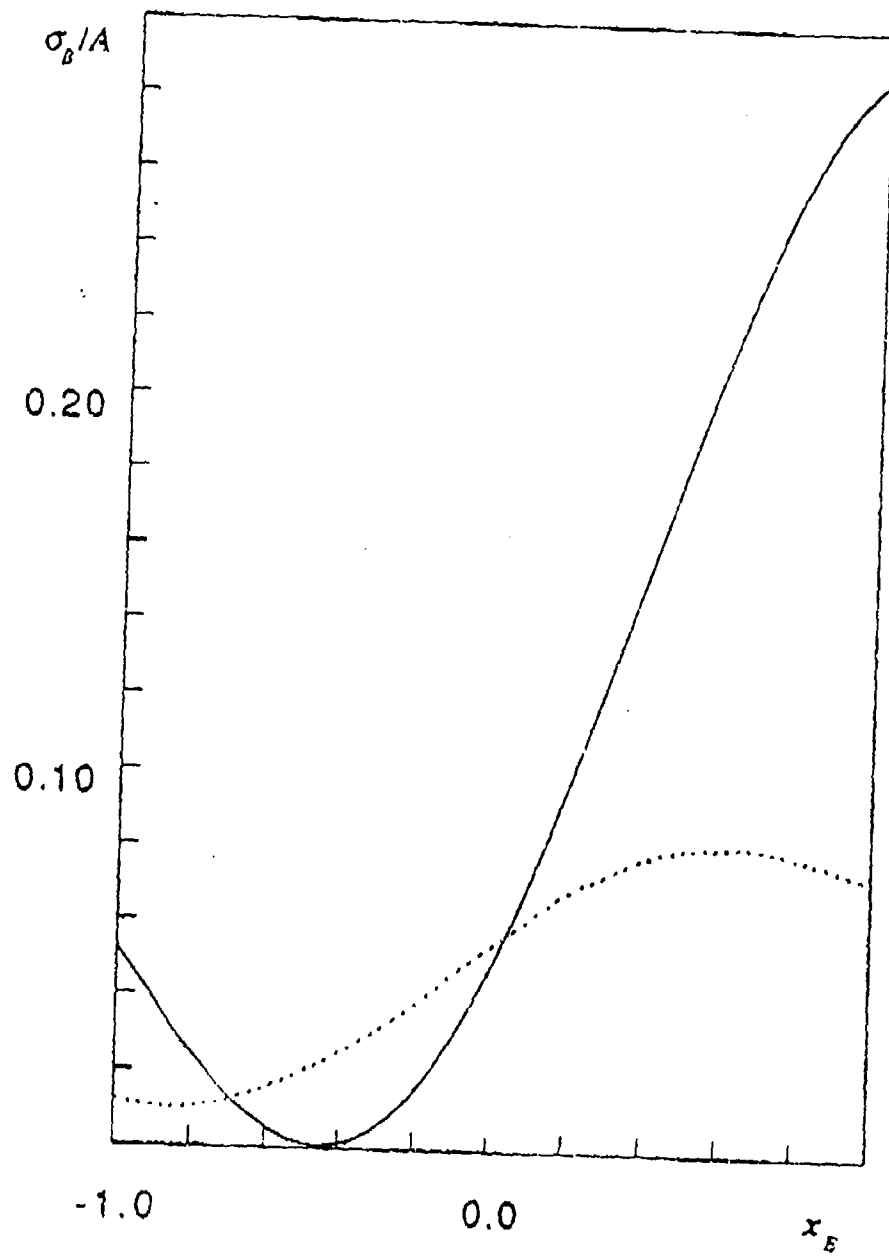
Figure 2. Backscattering efficiency, $\sigma_B/A = (4n^2/\rho_0^2) |f(\theta = \pi)|^2$, where $A = \pi\rho_0^2$ and θ is the angle of scattering, as a function of x_E . The dotted curve shows the approximate results of Fikioris and Uzunoglu (fig. 2 of ref.[5]), while the solid curve shows our results for the same scatterer.

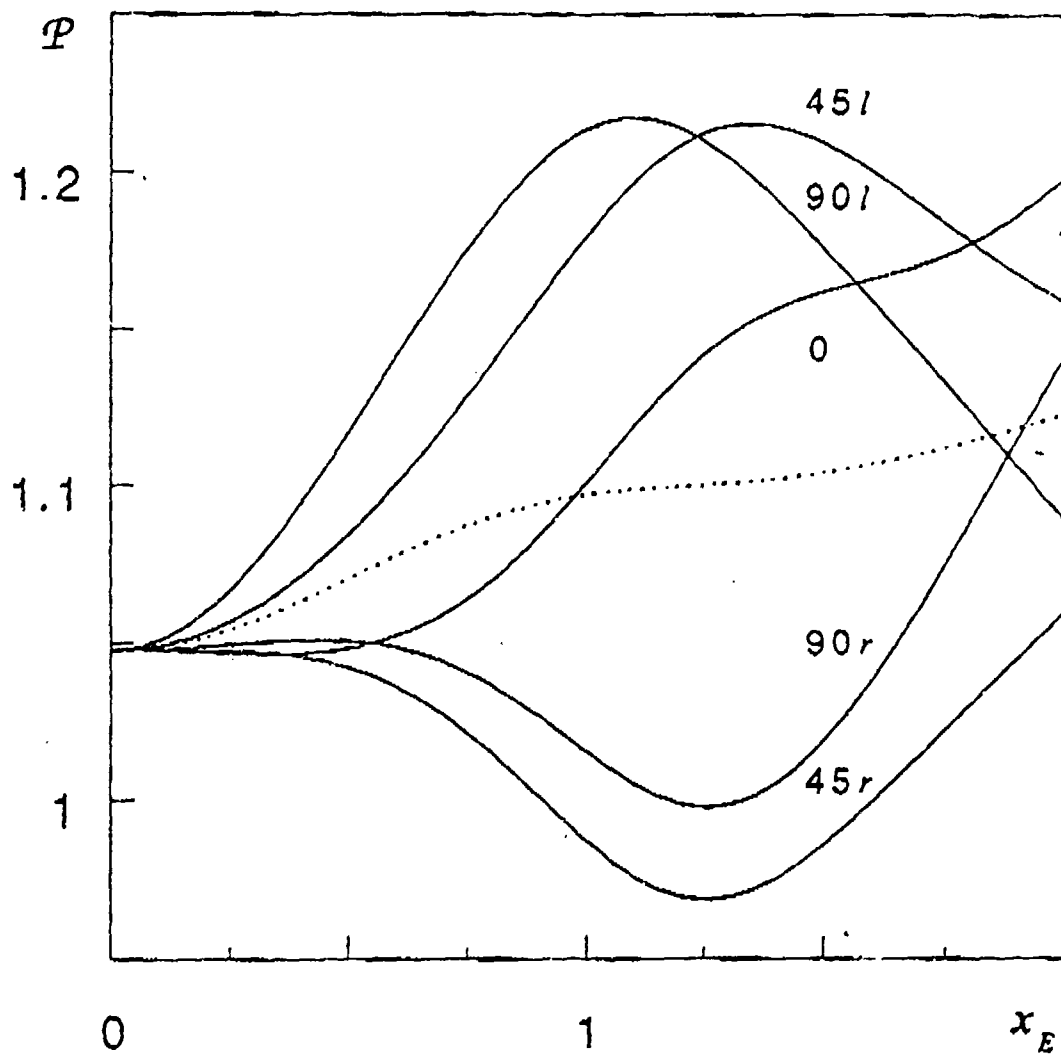
Figure 3. $P(\theta)$ (a) and $Q(\theta)$ (b) as a function of x_E for a dielectric sphere containing a metallic inclusion (solid curves). The curves are labelled by the values of θ_{inc} and, when necessary, it is also indicated whether the polarization vector is parallel (*l*) or perpendicular (*r*) to the scattering plane. The figures also show P^- fig. 3a. and Q^- , fig. 3b, as a function of x_E (dotted curve).

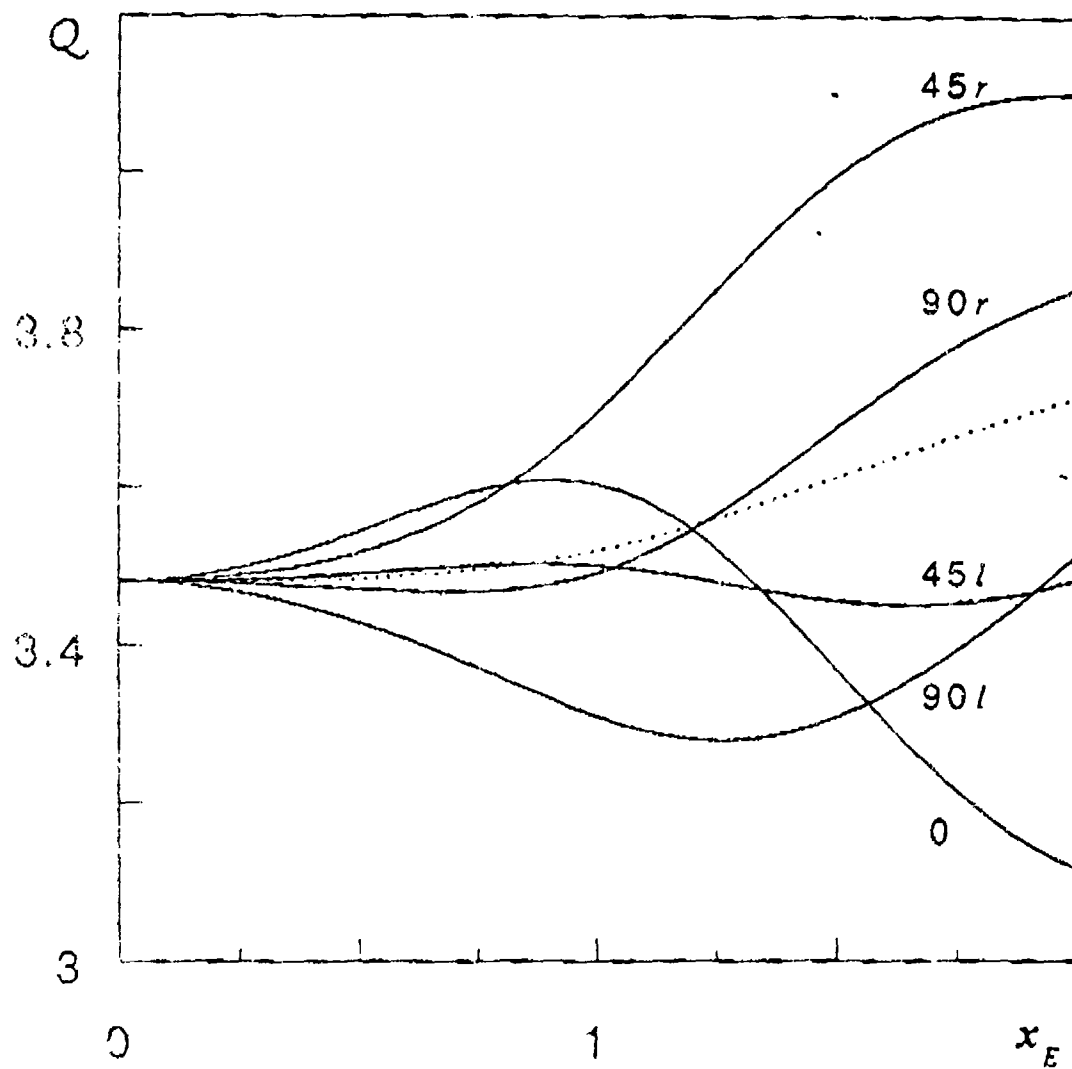
Figure 4. $P(\theta)$ vs. $Q(\theta)$ as a function of $\theta = 0$ (a), $\theta_{inc} = \pi/4$ (b) and $\theta_{inc} = \pi/2$ (c) for a dielectric sphere containing a metallic inclusion. The hollow circles mark a 30° increment of θ ; the forward scattering side is marked F. The solid curves are for $x_E = -2$ (B) and $x_E = 2$ (T), respectively. The dotted curve refers to $x_E = 0$ (centered inclusion). For the sake of comparison we also report $P_h(\theta)$ vs. $Q_h(\theta)$ (dashed curve).

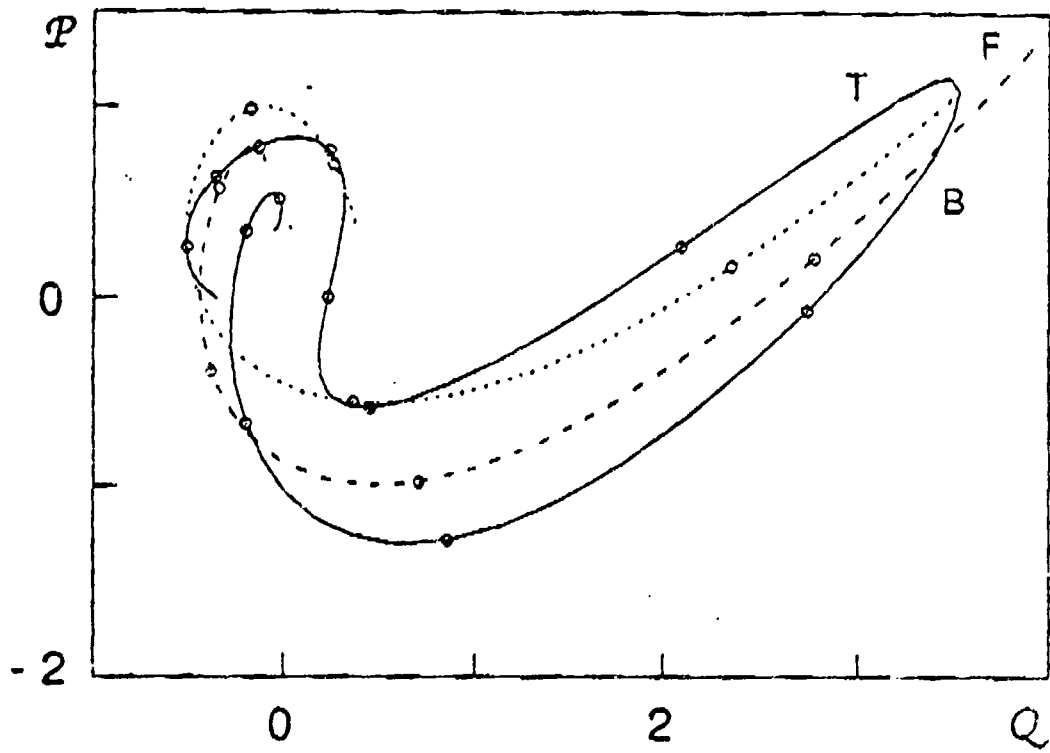
Figure 5. $P(\theta)$ and $Q(\theta)$ (b) as a function of x_E for a dielectric sphere containing an empty cavity (solid curves). The curves are labelled by the values of θ_{inc} and, when necessary, it is also indicated whether the polarization vector is parallel (*l*) or perpendicular (*r*) to the scattering plane. The figures also show P^- , fig. 5a and Q^- , fig. 5b as a function of x_E (dotted curve). The maximum value of the eccentricity is $x_E = 2.1705$.

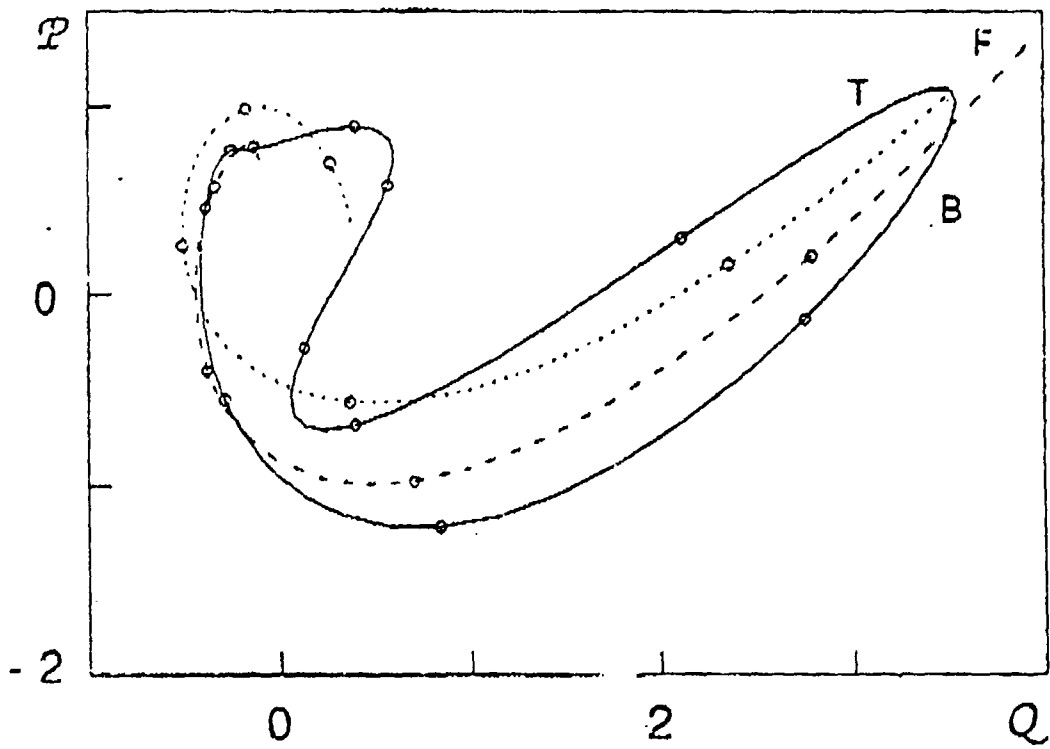


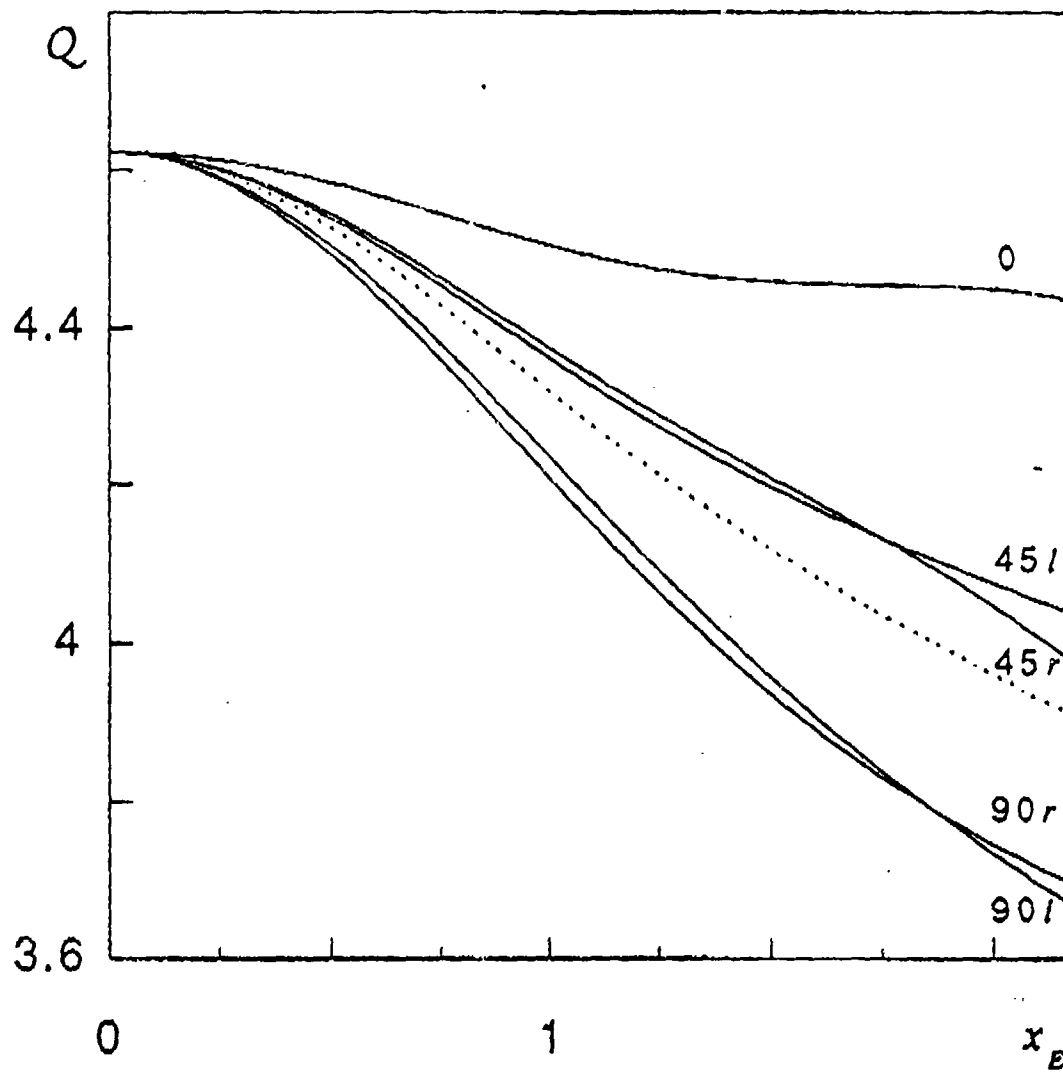












ELECTROMAGNETIC FIELD CALCULATIONS FOR A BEAM FOCUSED ON A LAYERED PARTICLE

J.P. Barton, S.A. Schaub, and D.R. Alexander
Center for Electro-Optics
College of Engineering
University of Nebraska-Lincoln
Lincoln, NE 68588-0656

RECENT PUBLICATIONS, SUBMITTALS FOR PUBLICATION, AND PRESENTATIONS:

- A.) J.P. Barton and D.R. Alexander, "The effects of particle nonsphericity on internal electromagnetic field distributions," Proceedings of the 1991 U.S. Army CRDEC Scientific Conference on Obscuration and Aerosol Research, Aberdeen Proving Ground, Maryland, 1991.
- B.) J.P. Barton and D.R. Alexander, "Electromagnetic fields for an irregularly-shaped, near-spherical particle illuminated by a focused laser beam," Journal of Applied Physics, Vol. 69(12), pp. 7973-7986, 1991.
- C.) J.P. Barton, W. Ma, S.A. Schaub, and D.R. Alexander, "Electromagnetic fields for a beam incident on two adjacent spherical particles," Applied Optics, Vol. 30(33), pp. 4706-4715, 1991.
- D.) J.P. Barton and D.R. Alexander, "Electromagnetic field calculations for a tightly focused beam incident upon a microdroplet: Applications to nonlinear optics," SPIE Proceedings, Nonlinear Optics and Materials, Vol. 1497, pp. 64-77, 1991.
- E.) J.P. Barton, D.R. Alexander, and S.A. Schaub, "Electromagnetic field calculations for a beam focused on a layered object," presentation at the 1992 U.S. Army CRDEC Scientific Conference on Obscuration and Aerosol Research, June 22-25, 1992, Aberdeen Proving Ground, Maryland.
- F.) J.P. Barton, "Theoretical studies of interaction of laser radiation with biological particles," Final Report, Delivery Order 2491, Contract No. DAAL03-86-D-0001, U.S. Army Research Office Scientific Services Program, 1991.
- G.) J.P. Barton and D.R. Alexander, "Recent progress concerning electromagnetic field calculations for a beam incident on an arbitrary particle," presentation at the 1991 U.S. Army CRDEC Scientific Conference on Obscuration and Aerosol Research, June 24-27, 1991, Aberdeen Proving Ground, Maryland.
- H.) J.P. Barton and D.R. Alexander, "Electromagnetic field calculations for a tightly-focused laser beam incident upon a microdroplet: Applications to nonlinear optics," presentation at SPIE's Optical Engineering SouthCentral'91 International Conference on Nonlinear Optics and Materials, May 8-10, 1991, Dallas, Texas.
- I.) S.A. Schaub, D.R. Alexander, and J.P. Barton, "Glare spot image calculations for a spherical particle illuminated by an arbitrary incident field," Journal of the Optical Society of America A, Vol. 9(2), pp. 316-330, 1992.
- J.) G.M. Holtmeier, D.R. Alexander, and J.P. Barton, "High intensity ultraviolet laser interaction with a metallic filament," Journal of Applied Physics, Vol. 71(2), pp. 557-563, 1992.
- K.) S.A. Schaub, D.R. Alexander, and J.P. Barton, "Theoretical model of the laser imaging of small aerosols: Applications to particle sizing," Applied Optics, Vol. 30(33), pp. 4777-4784, 1991.
- L.) D.R. Alexander, J.P. Barton, S.A. Schaub, and G. Holtmeier, "Nonlinear interactions of KrF laser radiation with small water droplets," Applied Optics, Vol. 30(12), pp. 1455-1460, 1991.
- M.) D.R. Alexander, S.A. Schaub, J. Stauffer, and J.P. Barton, "Femtosecond imaging and glare spot observations for small aerosol particles," presentation at the 1992 U.S. Army CRDEC Scientific Conference on Obscuration and Aerosol Research, June 22-25, 1992, Aberdeen Proving Ground, Maryland.
- N.) D.R. Alexander, R.D. Kubik, and E. Bahar, "Use of a new polarimetric optical bistatic scatterometer to measure the transmission and reflection Mueller matrix for arbitrary incident and scatter directions," presentation at the 1992 U.S. Army CRDEC Scientific Conference on Obscuration and Aerosol Research, June 22-25, 1992, Aberdeen Proving Ground, Maryland.
- O.) D.R. Alexander, S.A. Schaub, G.M. Holtmeier, and J.P. Barton, "Nonlinear laser interactions with saltwater droplets," SPIE Proceedings, Nonlinear Optics and Materials, Vol. 1497, pp. 90-97,

1991.

P.) J. Zhang, D.R. Alexander, and J.P. Barton, "Hybrid inelastic scattering models for particle thermometry: unpolarized emissions," *Applied Optics*, Vol. 31(24), 1992.

Q.) J. Zhang, D.R. Alexander, and J.P. Barton, "Hybrid inelastic scattering models for particle thermometry: polarized emissions," *Applied Optics*, Vol. 31(24), 1992.

R.) D.R. Alexander, J. Zhang, and J.P. Barton, "Hybrid inelastic scattering models for particle thermometry," poster presentation at the 1991 U.S. Army CRDEC Scientific Conference on Obscuration and Aerosol Research, June 24-27, 1991, Aberdeen Proving Ground, Maryland.

S.) D.R. Alexander, D.E. Poulain, S.A. Schaub, and J.P. Barton, "Nonlinear laser interactions with saltwater droplets," presentation at SPIE's Optical Engineering SouthCentral'91 International Conference on Nonlinear Optics and Materials, May 8-10, 1991, Dallas, Texas.

T.) S.A. Schaub, D.R. Alexander, and J.P. Barton, "Theoretical analysis of the effects of particle trajectory and structural resonances on the performance of a phase/Doppler particle analyzer," submitted for publication to *Applied Optics*, 1992.

U.) S.A. Schaub, D.R. Alexander, and J.P. Barton, "Analysis of the effects of particle trajectory on the performance of a phase/Doppler particle analyzer," presentation at the 5th Annual Conference on Liquid Atomization and Spray Systems, May 18-20, 1992, San Ramon, California.

V.) D.R. Alexander and J. Zhang, "Scattering models for Ramon and fluorescent particle temperature measurements," presentation at the 5th Annual Conference on Liquid Atomization and Spray Systems, May 18-20, 1992, San Ramon, California.

W.) R.M. Narayanan, E.D. von Rentzell, and D.R. Alexander, "Ti:sapphire laser reflectance measurements of natural and artificial targets," presentation at IGARSS'92 Symposium, May, 1992, Houston, Texas.

X.) D.R. Alexander, "Laser atomization for forming fine particles (Patent #5,044,565)," accepted for presentation at the American Association for Aerosol Research (AAAR) 1992 Annual Meeting, October 12-16, 1992, San Francisco, California.

ABSTRACT

Theoretical procedures are described for the determination of the electromagnetic fields for an arbitrary field (plane wave, focused beam, etc.) incident on layered particles of spherical, near-spherical, circular cylindrical, and near-circular cylindrical geometries. Presented calculations indicate that even a relatively thin layer around an otherwise homogeneous core can significantly affect the internal electromagnetic field distribution of the particle. Future work will include the use of spheroidal wave function solutions for the analysis of layered particles with appreciably elongated or appreciably flattened geometries.

I. INTRODUCTION

Procedures for the theoretical determination of the electromagnetic fields for an arbitrary field (plane wave, focused beam, etc.) incident on homogeneous particles of spherical¹ and near-spherical² geometries have been previously developed. In this paper, the homogeneous particle procedures have been extended to permit the analysis of layered particles. Applications include the modeling of laser interactions with biological particles (e.g., a bacteria modeled as a homogeneous core surrounded by a relatively thin cell wall) and laser interactions with layered aerosols.

II. GENERAL THEORY

The theoretical procedures for the determination of the electromagnetic fields for an arbitrary field incident on layered particles of spherical, near-spherical, circular cylindrical, and near-circular cylindrical geometries are described in detail in Ref. 3, only an overview of the development will be presented here.

A layered particle of general geometry consisting of a homogeneous "core" (material 1) enclosed by a homogeneous "layer" (material 2) is considered. The layered particle is surrounded by a homogeneous, nonabsorbing, infinite medium (the external material). A monochromatic field,

presumed known, is incident on the particle. Within each of these three homogeneous regions, the electric and magnetic field vectors satisfy the Helmholtz equation,

$$\nabla^2 \vec{E} + k^2 \vec{E} = 0 \quad (1)$$

and

$$\nabla^2 \vec{H} + k^2 \vec{H} = 0. \quad (2)$$

If Π_{lm} is a scalar eigenfunction of the Helmholtz equation,

$$\nabla^2 \Pi_{lm} + k^2 \Pi_{lm} = 0, \quad (3)$$

then corresponding vector eigenfunctions ($\vec{M}_{lm}, \vec{N}_{lm}$) of the Helmholtz equation can be determined from the operations

$$\vec{M}_{lm} = \vec{\nabla} \times \vec{r} \Pi_{lm} \quad (4)$$

and

$$\vec{N}_{lm} = \frac{1}{k} \vec{\nabla} \times \vec{M}_{lm}. \quad (5)$$

The electromagnetic fields of the core (w) and layer (l), and the electromagnetic field of the light scattered (s) from the particle are of interest. Each of these electromagnetic fields can be expressed in terms of expansions over the corresponding vector eigenfunctions.

CORE FIELD

$$\vec{E}^{(w)} = \sum_{l,m} [c_{lm} \vec{N}_{lm}^{(w)} + d_{lm} \vec{M}_{lm}^{(w)}] \quad (6)$$

$$\vec{H}^{(w)} = -i\sqrt{\epsilon_{ext}} \bar{n}_1 \sum_{l,m} [c_{lm} \vec{M}_{lm}^{(w)} + d_{lm} \vec{N}_{lm}^{(w)}] \quad (7)$$

LAYER FIELD

$$\vec{E}^{(l)} = \sum_{l,m} [e_{lm} \vec{N}_{lm}^{(l,1)} + f_{lm} \vec{N}_{lm}^{(l,2)} + g_{lm} \vec{M}_{lm}^{(l,1)} + h_{lm} \vec{M}_{lm}^{(l,2)}] \quad (8)$$

$$\vec{H}^{(l)} = -i\sqrt{\epsilon_{ext}} \bar{n}_2 \sum_{l,m} [e_{lm} \vec{M}_{lm}^{(l,1)} + f_{lm} \vec{M}_{lm}^{(l,2)} + g_{lm} \vec{N}_{lm}^{(l,1)} + h_{lm} \vec{N}_{lm}^{(l,2)}] \quad (9)$$

SCATTERED FIELD

$$\vec{E}^{(s)} = \sum_{l,m} [a_{lm} \vec{N}_{lm}^{(s)} + b_{lm} \vec{M}_{lm}^{(s)}] \quad (10)$$

$$\vec{H}^{(s)} = -i\sqrt{\epsilon_{ext}} \sum_{l,m} [a_{lm} \vec{M}_{lm}^{(s)} + b_{lm} \vec{N}_{lm}^{(s)}] \quad (11)$$

In spherical coordinates (r, θ, ϕ), the appropriate functional form of the corresponding scalar eigenfunctions for the core, layer, and scattered fields are

$$\Pi_{lm}^{(w)} = \psi_l(\bar{n}_1 \alpha \bar{r}) Y_{lm}(\theta, \phi), \quad (12)$$

$$\Pi_{lm}^{(l,1)} = \psi_l(\bar{n}_2 \alpha \bar{r}) Y_{lm}(\theta, \phi), \quad (13)$$

$$\Pi_{lm}^{(l,2)} = \chi_l(\bar{n}_2 \alpha \bar{r}) Y_{lm}(\theta, \phi), \quad (14)$$

and

$$\Pi_{lm}^{(s)} = \xi_l^{(1)}(\alpha \bar{r}) Y_{lm}(\theta, \phi) \quad (15)$$

where

$$\xi_l^{(1)} = \psi_l - i\chi_l \quad (16)$$

and ψ_l, χ_l are the Riccati-Bessel functions and Y_{lm} is the spherical harmonic function.

The expansion coefficients of the core (c_{lm}, d_{lm}), layer ($e_{lm}, f_{lm}, g_{lm}, h_{lm}$), and scattered (a_{lm}, b_{lm}) fields are determined by the application of the boundary condition of continuity of the tangential components of the electromagnetic fields at the layer/external and layer/core interfaces.

LAYER/EXTERNAL INTERFACE

$$\hat{n} \times (\vec{E}^{(i)} + \vec{E}^{(s)}) = \hat{n} \times \vec{E}^{(l)} \quad (17)$$

$$\hat{n} \times (\vec{H}^{(i)} + \vec{H}^{(s)}) = \hat{n} \times \vec{H}^{(l)} \quad (18)$$

LAYER/CORE INTERFACE

$$\hat{n} \times \vec{E}^{(l)} = \hat{n} \times \vec{E}^{(w)} \quad (19)$$

$$\hat{n} \times \vec{H}^{(l)} = \hat{n} \times \vec{H}^{(w)} \quad (20)$$

where \hat{n} is the unit vector normal to the interface and the incident electromagnetic field at the layer/external interface ($\vec{E}^{(i)}, \vec{H}^{(i)}$) is assumed known.

After substituting the series expansions of Eqs. (6)-(11) into Eqs. (17)-(20), the eight scalar equations associated with Eqs. (17)-(20) are multiplied by $Y_{l'm'}(\theta, \phi)$ and integrated over the respective interface surface. The result is a set of simultaneous linear, algebraic equations that can be solved for the expansion coefficients ($a_{lm}, b_{lm}, c_{lm}, d_{lm}, e_{lm}, f_{lm}, g_{lm}, h_{lm}$). Once the expansion coefficients are determined, the expansion coefficients are substituted into Eqs. (6)-(11) and the electromagnetic field can then be calculated anywhere inside or outside the particle. If the layered particle geometry is that of concentric spheres, then the boundary conditions can be matched mode-by-mode and explicit expressions can be derived for the series coefficients.

If a polar cylindrical coordinate system (r, θ) is chosen, then the procedure is similar to that just described except that the appropriate scalar eigenfunctions are of the form

$$\Pi_l^{(w)} = J_l(\bar{n}_1 \alpha \bar{r}) e^{il\theta}, \quad (21)$$

$$\Pi_l^{(l,1)} = J_l(\bar{n}_2 \alpha \bar{r}) e^{il\theta}, \quad (22)$$

$$\Pi_l^{(l,2)} = N_l(\bar{n}_2 \alpha \bar{r}) e^{il\theta}, \quad (23)$$

and

$$\Pi_l^{(s)} = H_l^{(1)}(\alpha \bar{r}) e^{il\theta} \quad (24)$$

where

$$H_l^{(1)} = J_l + iN_l \quad (25)$$

and J_l, N_l are the cylindrical Bessel functions.

III. CALCULATIONS

For the calculations that follow, all spatial quantities are nondimensionalized relative to a characteristic radius of the external particle surface (a) and all electromagnetic quantities are nondimensionalized relative to a characteristic electric field amplitude of the incident field (E_0). Important input parameters for the analysis include (1) the particle shape function, \hat{r} (A nondimensionalized single-valued function of the angular coordinates that defines the geometry of the external particle surface.), (2) the core/layer interface location parameter, \tilde{a}_{12} , (3) the particle size parameter, $\alpha = 2\pi a/\lambda_{ext}$, (4) the complex relative refractive index of the core, \tilde{n}_1 , (5) the complex relative refractive index of the layer, \tilde{n}_2 , (6) the propagation direction angle of the incident field, θ_{bd} , (7) the electric field polarization direction angle of the incident field, ϕ_{bd} , and, for focused beam incidence, (9) the beam waist radius, \tilde{w}_0 , and (10) the location of the beam focal point relative to the particle, $(\tilde{x}_0, \tilde{y}_0, \tilde{z}_0)$. For the spherical analysis, θ_{bd} is referenced to the y-z plane and ϕ_{bd} is reference to the x-z plane. For the cylindrical analysis, θ_{bd} is referenced to the x-z plane and ϕ_{bd} is referenced to the x-y plane.

Figure 1 presents the internal and near-surface normalized source function, $S = |\vec{E}/E_0|^2$, in the x-z plane for a homogeneous spherical particle ($\alpha = 30$, $\tilde{n} = 1.33 + 1.0 \times 10^{-6}i$) with an incident beam focused within the upper hemisphere of the particle ($\tilde{w}_0 = 0.2$, $\tilde{x}_0 = 0.7$, $\tilde{y}_0 = 0.0$, $\tilde{z}_0 = 0.0$). The beam propagates in the positive z axis direction ($\theta_{bd} = 0^\circ$) with electric field polarization perpendicular to the x-z plane ($\phi_{bd} = 90^\circ$). The Gaussian profile of the incident beam can be seen along the right-hand-side of Figure 1.

The conditions of Fig. 2 are identical to the conditions of Fig. 1, except the outer 30% of the sphere now consists of a layer of a second material ($\tilde{a}_{12} = 0.7$, $\tilde{n}_2 = 1.1 + 1.0 \times 10^{-6}i$). As can be observed by comparing Figs. 1 and 2, the presence of the layer significantly affects the electromagnetic field distribution. Figures 3 and 4 present the same data as Figs. 1 and 2, respectively, but in the form of a false contrast visualization (white \Rightarrow high, black \Rightarrow low).

The analysis is not restricted to purely spherical geometries. Figure 5 shows the internal normalized source function distribution in the x-z plane for a plane wave propagating in the positive x axis direction ($\theta_{bd} = 90^\circ$) with electric field polarization parallel to the x-z plane ($\phi_{bd} = 0^\circ$) incident on a homogeneous 1.3 to 1.0 axis ratio prolate spheroid ($\alpha = 10$, $\tilde{n} = 1.18 + 0.07i$). The conditions of Fig. 6 are identical to the conditions of Fig. 5, except that the outer 10% of the prolate spheroid has been replaced by a layer of a second material ($\tilde{a}_{12} = 0.9$, $\tilde{n}_2 = 1.48 + 0.0055i$). For this case, the presence of even a relatively thin layer significantly alters the internal field distribution of the particle.

The analysis can also be applied to cylindrical geometries. Figure 7 presents the internal source function distribution in the x-y plane for a plane wave propagating in the positive x axis direction ($\theta_{bd} = 0^\circ$) with electric field polarization perpendicular to the x-y plane ($\phi_{bd} = 90^\circ$) incident on a homogeneous circular cylinder ($\alpha = 10$, $\tilde{n} = 1.18 + 0.07i$). The conditions of Fig. 8 are identical to the conditions of Fig. 7, except the outer 10% of the cylinder has been replaced by a layer of a second material ($\tilde{a}_{12} = 0.9$, $\tilde{n}_2 = 1.48 + 0.0055i$). As was the case for the prolate spheroid particle, the presence of the relatively thin layer significantly affects the internal field distribution of the circular cylinder particle.

Figures 9 and 10 are identical to Figs. 7 and 8, respectively, except now (1) the particle geometry is that of a 1.3 to 1.0 axis ratio elliptic cylinder and (2) the incident plane wave propagates in the positive y axis direction ($\theta_{bd} = 90^\circ$) with electric field polarization parallel to the x-y plane ($\phi_{bd} = 0^\circ$).

IV. CONCLUSIONS AND FUTURE WORK

Theoretical procedures have been developed for the calculation of the electromagnetic fields for the interaction of an arbitrary incident field (plane wave, focused beam, etc.) on a layered particle of spherical, near-spherical, circular cylindrical, and near circular cylindrical geometries. Initial calculations indicate that even the presence of a relatively thin layer can alter the electromagnetic field distribution significantly from that of a corresponding homogeneous particle. Further systematic calculations will be performed in the future. In addition, spheroidal wave solutions will

be applied to enable the analysis of layered particles with appreciably elongated or appreciably flattened geometries.

ACKNOWLEDGEMENTS

The majority of this work was performed during the summers of 1991 and 1992 while Dr. Barton was at CRDEC supported under the auspices of the U.S. Army Research Office Scientific Services Program administrated by Battelle (1991: Delivery Order 2491, Contract No. DAAL03-86-D-0001, 1992: Task Control No. 92-140, Contract No. DAAL03-92-C-0034). Dr. Barton expresses his appreciation to his point-of-contact at CRDEC, Dr. S. Randolph Long, and to Dr. Orazio Sindoni for his assistance in the use of the computing and graphing facilities at CRDEC.

REFERENCES

1. J.P. Barton, D.R. Alexander, and S.A. Schaub, "Internal and near-surface electromagnetic fields for a spherical particle irradiated by a focused laser beam," *Journal of Applied Physics*, Vol. 64, pp. 1632-1639, 1988.
2. J.P. Barton and D.R. Alexander, "Electromagnetic fields for an irregularly-shaped, near-spherical particle illuminated by a focused laser beam," *Journal of Applied Physics*, Vol. 69(12), pp. 7973-7986, 1991.
3. J.P. Barton, "Theoretical studies of interaction of laser radiation with biological particles," Final Report, Delivery Order 2491, Contract No. DAAL03-86-D-0001, U.S. Army Research Office Scientific Services Program, 1991.

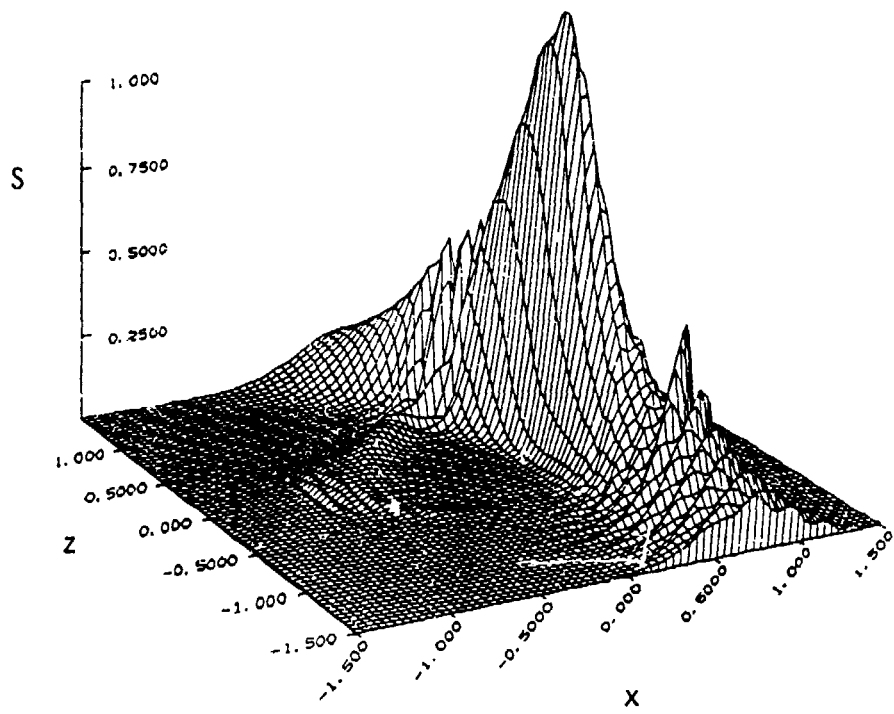


FIGURE 1. Normalized source function distribution in the x-z plane for a beam focused on a homogeneous sphere. ($\alpha = 30$, $\bar{n} = 1.33 + 1.0 \times 10^{-6}i$, $\bar{w}_0 = 0.2$, $\bar{x}_0 = 0.7$, $\bar{y}_0 = 0.0$, $\bar{z}_0 = 0.0$, $\theta_{bd} = 0^\circ$, $\phi_{bd} = 90^\circ$)

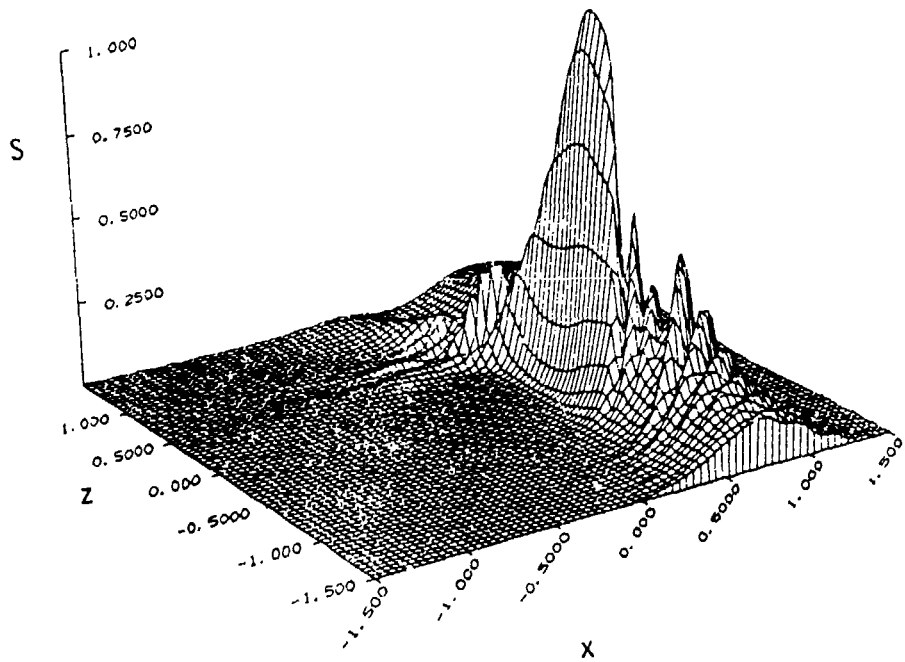


FIGURE 2. Normalized source function distribution in the x-z plane for a beam focused on a layered sphere. ($\alpha = 30$, $\bar{n}_1 = 1.33 + 1.0 \times 10^{-6}i$, $\bar{n}_2 = 1.1 + 1.0 \times 10^{-6}i$, $\bar{a}_{12} = 0.7$, $\bar{w}_0 = 0.2$, $\bar{x}_0 = 0.7$, $\bar{y}_0 = 0.0$, $\bar{z}_0 = 0.0$, $\theta_{bd} = 0^\circ$, $\phi_{bd} = 90^\circ$)

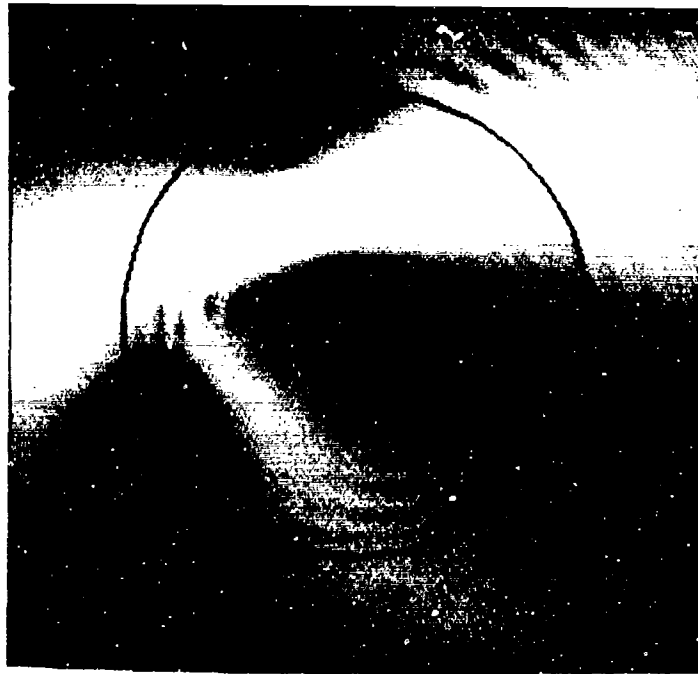


FIGURE 3. False contrast visualization of the normalized source function distribution in the x-z plane for a beam focused on a homogeneous sphere. ($\alpha = 30$, $\bar{n} = 1.33 + 1.0 \times 10^{-6}i$, $\tilde{w}_0 = 0.2$, $\tilde{x}_0 = 0.7$, $\tilde{y}_0 = 0.0$, $\tilde{z}_0 = 0.0$, $\theta_{bd} = 0^\circ$, $\phi_{bd} = 90^\circ$)



FIGURE 4. False contrast visualization of the normalized source function distribution in the x-z plane for a beam focused on a layered sphere. ($\alpha = 30$, $n_1 = 1.33 + 1.0 \times 10^{-6}i$, $\bar{n}_2 = 1.1 + 1.0 \times 10^{-6}i$, $\tilde{a}_{12} = 0.7$, $\tilde{w}_0 = 0.2$, $\tilde{x}_0 = 0.7$, $\tilde{y}_0 = 0.0$, $\tilde{z}_0 = 0.0$, $\theta_{bd} = 0^\circ$, $\phi_{bd} = 90^\circ$)

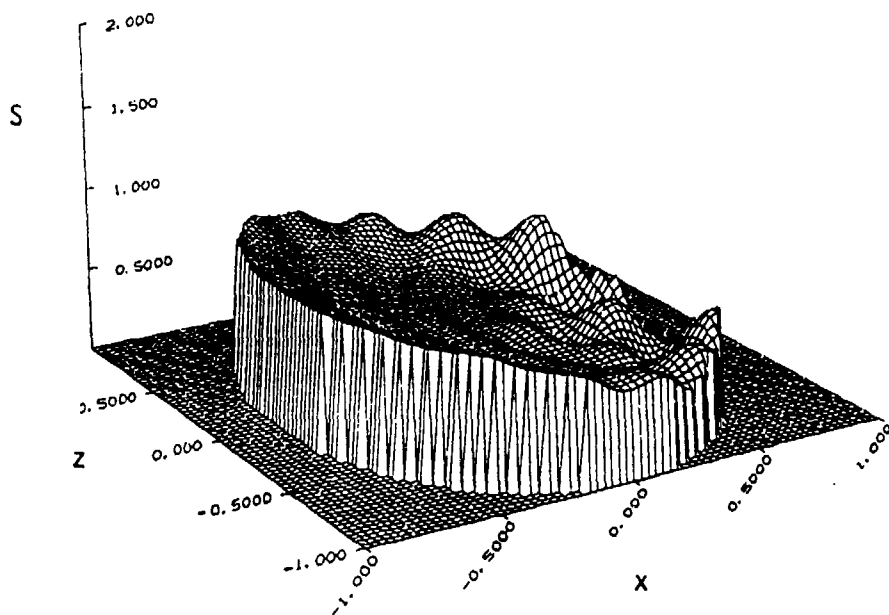


FIGURE 5. Internal normalized source function distribution in the x - z plane for a plane wave incident on a homogeneous 1.3 to 1.0 axis ratio prolate spheroid. ($\alpha = 10$, $\bar{n} = 1.18 + 0.07i$, $\theta_{bd} = 90^\circ$, $\phi_{bd} = 0^\circ$)

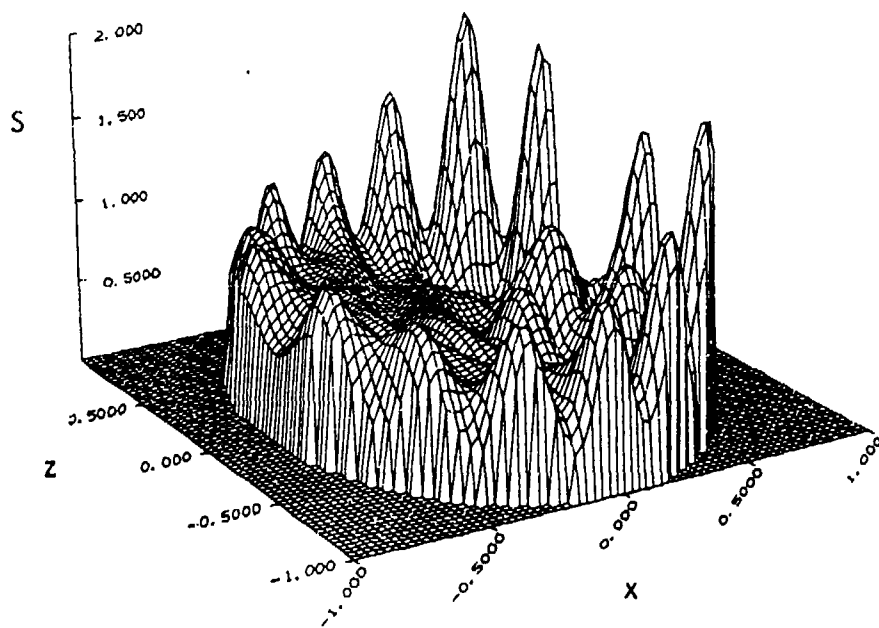


FIGURE 6. Internal normalized source function distribution in the x - z plane for a plane wave incident on a layered 1.3 to 1.0 axis ratio prolate spheroid. ($\alpha = 10$, $\bar{n}_1 = 1.18 + 0.07i$, $\bar{n}_2 = 1.48 + 0.0055i$, $\bar{a}_{12} = 0.9$, $\theta_{bd} = 90^\circ$, $\phi_{bd} = 0^\circ$)

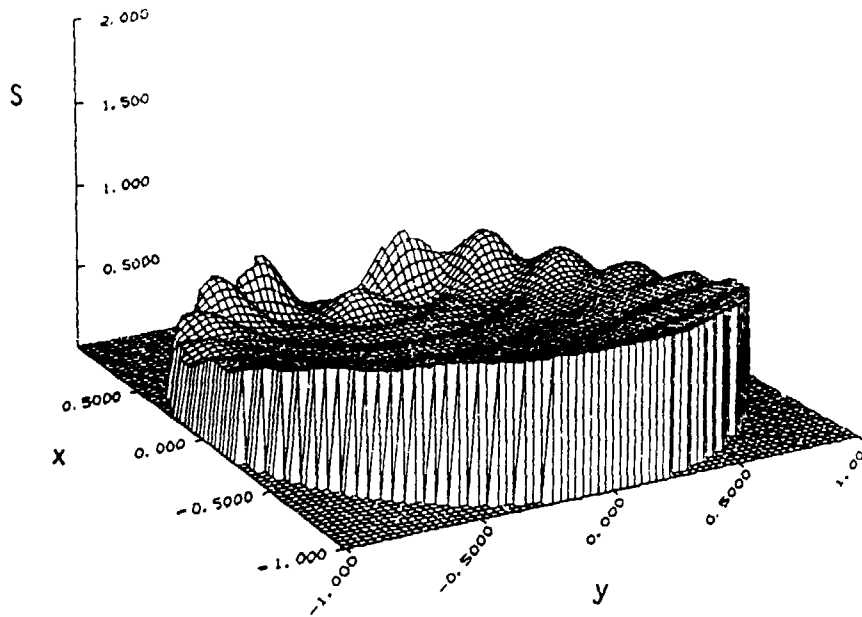


FIGURE 7. Internal normalized source function distribution in the x-y plane for a plane wave incident on a homogeneous circular cylinder. ($\alpha = 10$, $\bar{n} = 1.18 + 0.07i$, $\theta_{bd} = 0^\circ$, $\phi_{bd} = 90^\circ$)

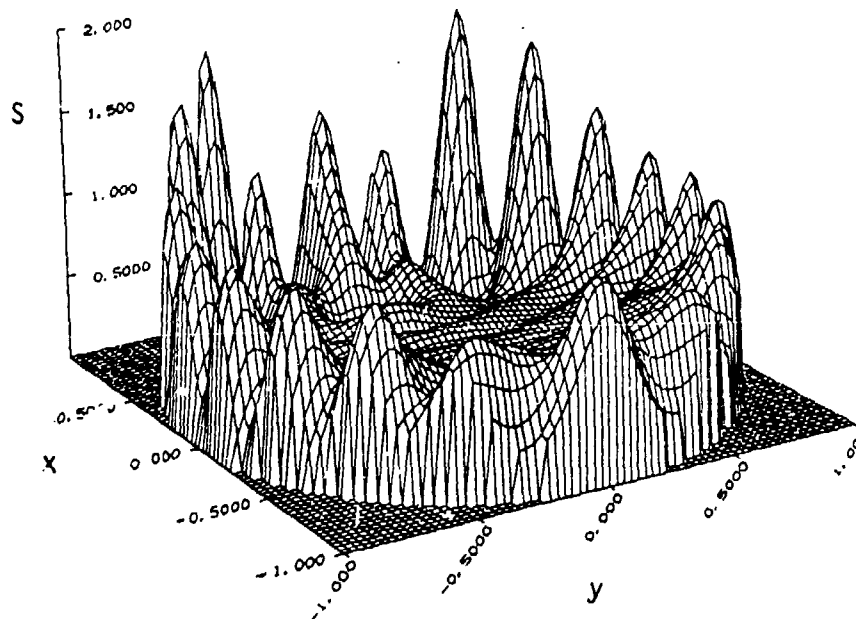


FIGURE 8. Internal normalized source function distribution in the x-y plane for a plane wave incident on a layered circular cylinder. ($\alpha = 10$, $\bar{n}_1 = 1.18 + 0.07i$, $\bar{n}_2 = 1.48 + 0.0055i$, $\bar{a}_{12} = 0.9$, $\theta_{bd} = 0^\circ$, $\phi_{bd} = 90^\circ$)

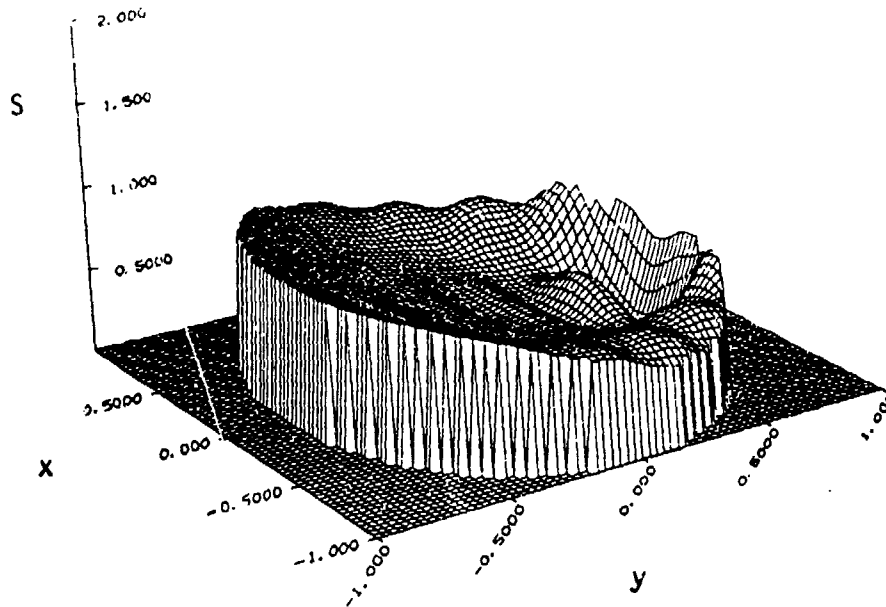


FIGURE 9. Internal normalized source function distribution in the x-y plane for a plane wave incident on a homogeneous 1.3 to 1.0 axis ratio elliptic cylinder. ($\alpha = 10$, $\bar{n} = 1.18 + 0.07i$, $\theta_{bd} = 90^\circ$, $\phi_{bd} = 0^\circ$)

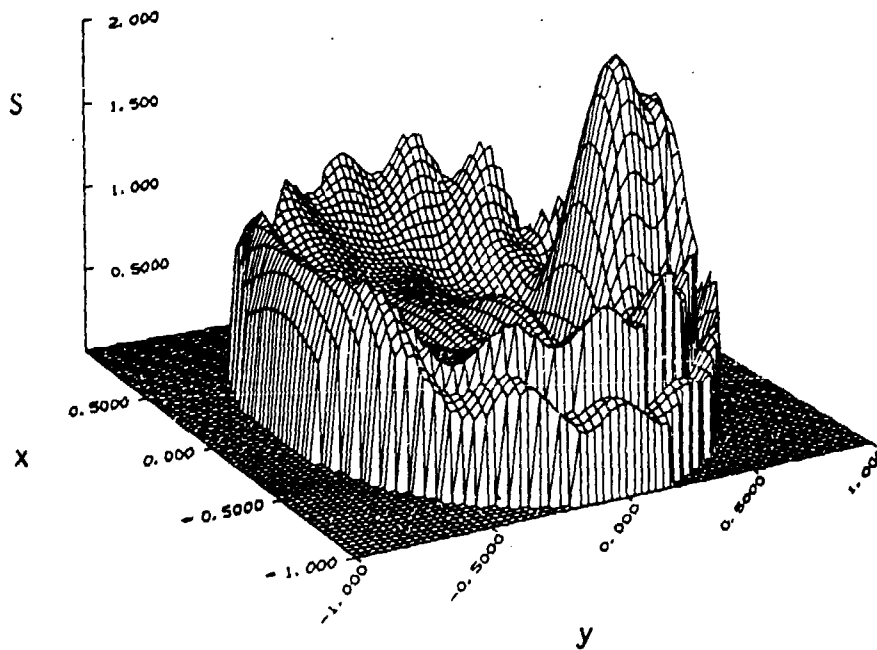


FIGURE 10. Internal normalized source function distribution in the x-y plane for a plane wave incident on a layered 1.3 to 1.0 axis ratio elliptic cylinder. ($\alpha = 10$, $\bar{n}_1 = 1.18 + 0.07i$, $\bar{n}_2 = 1.48 + 0.0055i$, $\bar{a}_{12} = 0.9$, $\theta_{bd} = 90^\circ$, $\phi_{bd} = 0^\circ$)

Blank

COMPARISONS BETWEEN THE DISCRETE DIPOLE APPROXIMATION AND THE EXACT SOLUTION FOR LIGHT SCATTERING BY TWO SPHERES

Piotr J. Flatau and Kirk A. Fuller

*Department of Atmospheric Science
Colorado State University
Fort Collins, CO 80523*

Recent Publications, Submittals for Publication, and Presentations

J. J. Goodman, B. T. Draine, and P. J. Flatau, "Application of fast Fourier transform techniques to the discrete dipole approximation," *Opt. Lett.* **16**, 1198-1200(1991).

P. J. Flatau, K. A. Fuller, and D. W. Mackowski, "Scattering by two spheres in contact: Comparisons between the discrete dipole approximation and modal analysis," submitted to *Applied Optics*.

Abstract

A comparison of the differential, scattering, and absorption cross sections of a bisphere obtained from the discrete dipole approximation (DDA) is made with those determined from modal analysis. The DDA is thus tested, for the first time to our knowledge, against an exact calculation of the scattering properties of a finite, nonspherical particle. The agreement with the exact solution is very good, even when the size parameter of the monomers is ≈ 8 (the largest size studied).

Introduction

The discrete dipole approximation (DDA) provides what is perhaps the best method available for modeling the scattering properties of particles with morphologies that do not allow for an exact solution. The DDA is obtained by replacing the particle with an array of N point dipoles on a cubic lattice. The polarization of each dipole is found by solving a self-consistent set of linear equations that accounts for the electric field of the incident radiation and of all other dipoles in the array. This is represented by

$$\mathbf{P} = \mathbf{A}^{-1} \mathbf{E}_i,$$

where \mathbf{P} is the $3N$ -dimensional polarization vector of the array, \mathbf{E}_i is a $3N$ -dimensional vector that describes the incident electric field of the plane wave at the position of each dipole, and \mathbf{A} is a $3N \times 3N$ symmetric matrix that relates the electric field of the j th dipole to the location of the k th dipole in the ensemble. Once \mathbf{P} has been determined, the scattered field of the

system can be calculated as the vector sum of the scattered fields of the dipoles. A more detailed description of this formalism is provided by Draine.¹

Computations have been greatly accelerated by applying the conjugate gradient method and the fast Fourier transform to the solution of the above equation. A description of these enhancements, along with comparison of the DDA technique to the exact solution for spheres with size parameters as large as 15 is provided in the paper of Goodman et al.² Results are also provided in that work for a cube having a volume equivalent to that of a sphere of size parameter 10. Application of the DDA to such optically large particles is unprecedented.

A comprehensive treatment of the DDA, along with a compendium of results of its application to cirrus cloud particles can be found in the dissertation of Flatau.³

Scattering by Two Pseudospheres

The scattering properties of a bisphere can be found exactly by modal analysis.^{4,5} In applying the DDA, the two spheres are replaced with pseudospheres, each comprised of about 33,000 dipole elements. This system is displayed in Fig. 1. A similar approach was taken by Kattawar and Humphreys,⁶ but the numerical techniques employed at that time did not allow for size parameters much greater than unity to be considered (pseudospheres of only 32 dipoles were used by those authors).

The monomers used in this study are chosen so that two of them would have a volume equal to that of a single sphere with a size parameter of either 5 or 10. In all cases, the wave vector of the incident radiation is taken to be parallel to the symmetry axis of the two-sphere system. Such a scattering geometry produces the strongest electrodynamic coupling between the principals and hence provides what is probably the most stringent test of the DDA. It is noted, however, that comparisons were made for other particle orientations and agreement with the modal analysis runs was at least as good as that seen in the case of end-on incidence.

Figures 2 and 3 display the phase functions of two pseudospheres that are made from the same amount of dielectric as would be required to construct a single sphere of size parameter 5 and 10, respectively. Orthogonal states of polarization of the incident beam are considered. The scattering plane is taken to be that which contains the symmetry axis of the particle and the wave vector of the scattered fields. The cases $\gamma = 0$ or $\pi/2$ correspond to an incident polarization that is parallel or perpendicular to this plane, respectively. The phase functions of the pairs of pseudospheres closely match those obtained for the corresponding bispheres. This is especially true in the case of Fig. 2, where the differences are negligible. The slight disagreements between modal analysis and DDA in Fig. 3 are due, of course, to a need for an increased number of dipolar subunits in the approximation. It is interesting that the agreement in Fig. 3 is better for $\gamma = 0$ than for $\gamma = \pi/2$, and that the reverse is true in Fig. 2.

In Figure 4, the efficiencies for extinction and absorption by a bisphere are plotted against the size parameter of an equivalent volume sphere. The efficiency factors of the bisphere are determined from the ratio of its respective cross sections to the cross sectional area of the equivalent-volume sphere. Agreement between the DDA and the exact calculation is outstanding.

Two pseudospheres
 $N=2 \times 32 \times 32 \times 32$

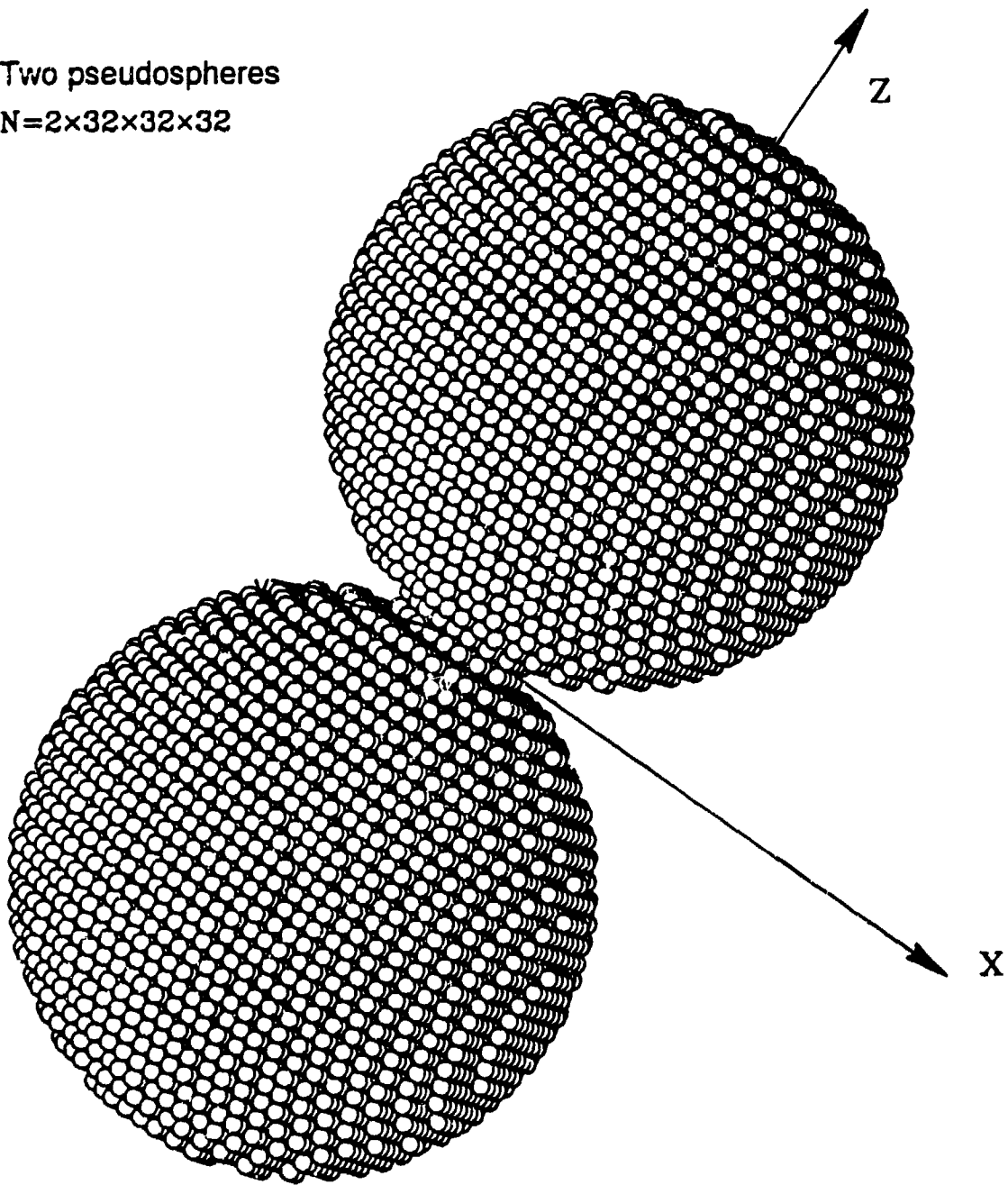


Figure 1. The scattering geometry for the pseudosphere calculations.

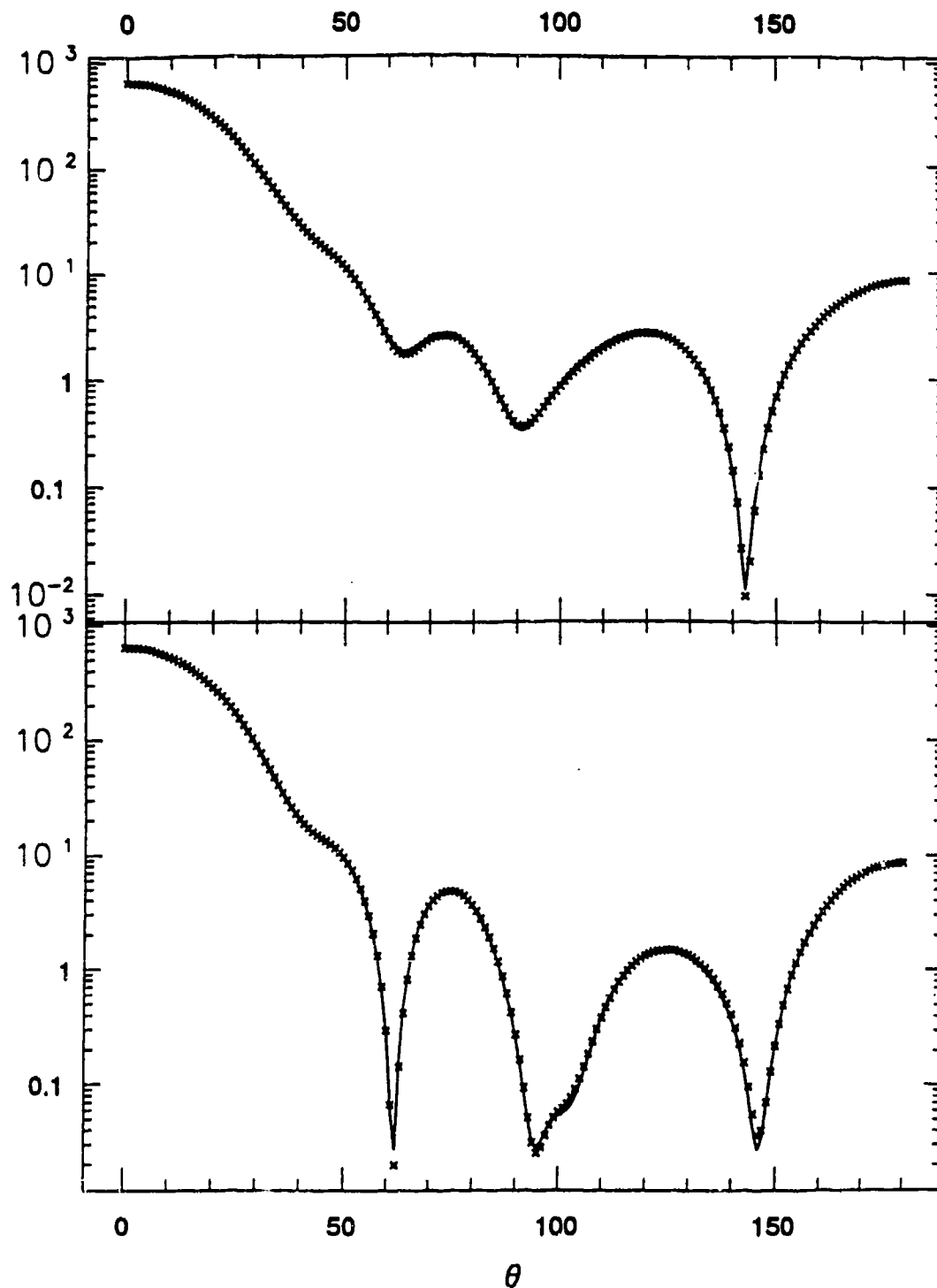


Figure 2. Phase function comparisons for a two-sphere system with a volume equivalent to that of a single sphere with size parameter 5. The solid line corresponds to the phase function of a bisphere illuminated at end-fire incidence as determined from modal analysis. The discrete points are the results of the DDA calculations based on the pseudospheres depicted in Fig. 1. The refractive index of the spheres is $1.33 + 0.01i$. The polarization angle, γ , is discussed in the text.

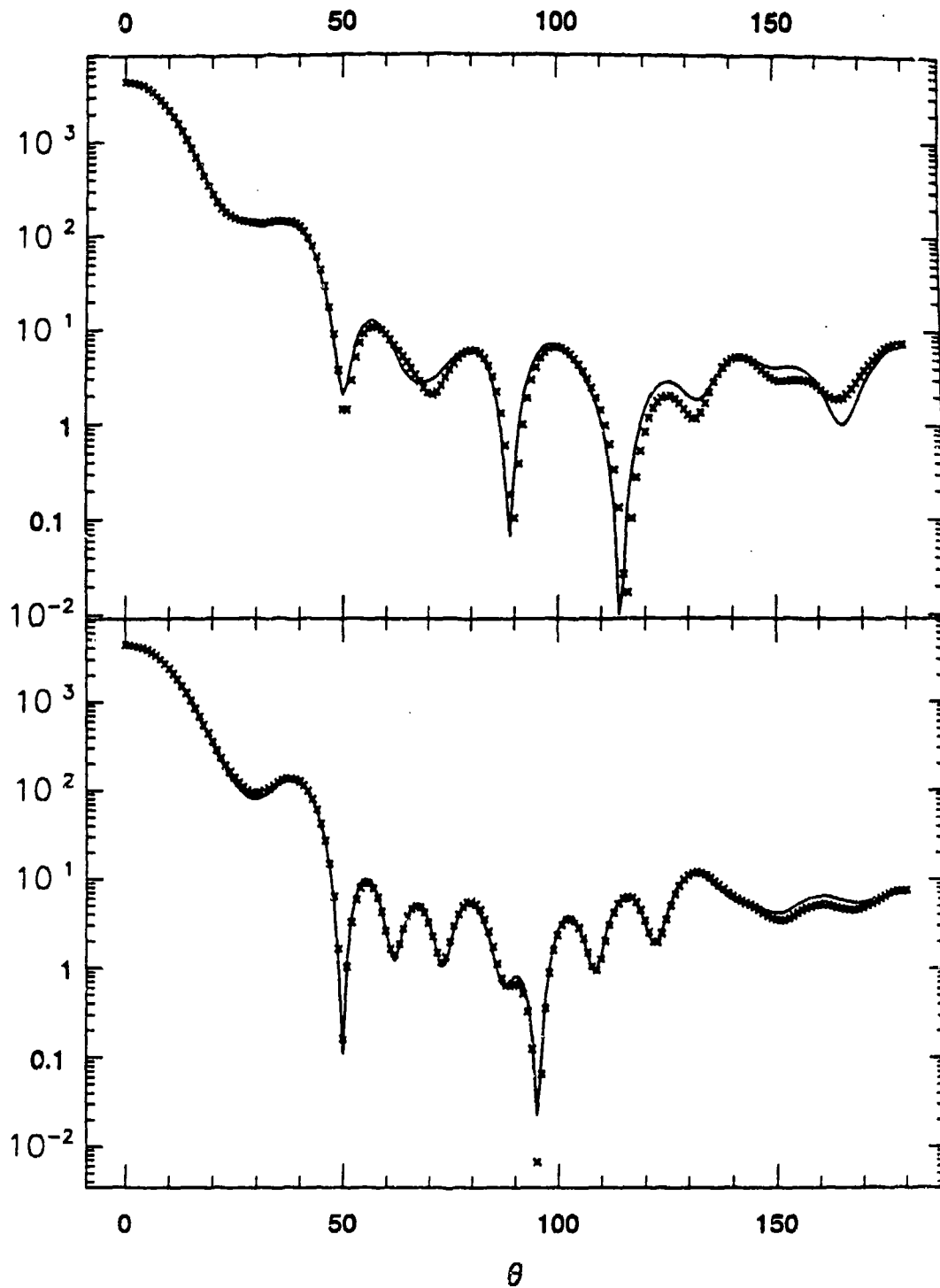


Figure 3. Same as Fig. 2, but for a bisphere having a volume equal to that of a single sphere of size parameter 10.

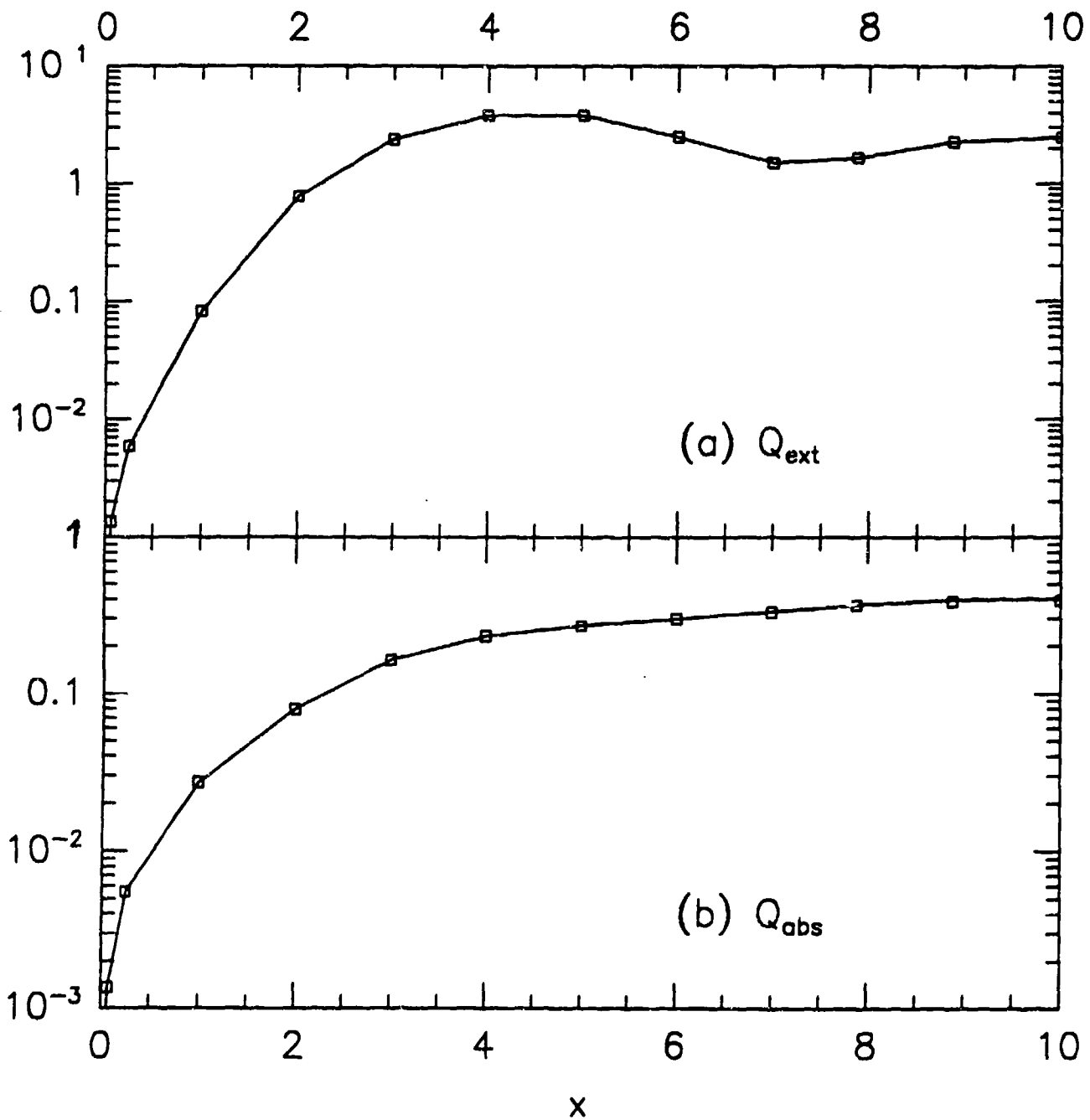


Figure 4. Comparison of extinction and absorption efficiencies of the particles discussed in Figs. 2 and 3 as a function of the size parameter of the equivalent-volume sphere. To obtain these efficiencies, the respective cross sections were normalized by the geometric cross section of the equivalent-volume sphere.

Acknowledgments

This work was supported in part by National Park Service grant #NA90RAH000077 and by National Science Foundation grant #ATM-88123353. One of the authors (KAF) also wishes to express his thanks to the Chemical Research, Development, and Engineering Command for supporting his travel and accommodations for the 1992 conference.

REFERENCES

1. B. T. Draine, "The discrete-dipole approximation and its application to interstellar graphite grains," *Astrophys. J.* **333**, 848-872(1988).
2. J. J. Goodman, B. T. Draine, and P. J. Flatau, "Application of fast Fourier transform techniques to the discrete dipole approximation," *Opt. Lett.* **16**, 1198-1200(1991).
3. P. J. Flatau, Ph.D. dissertation, Department of Atmospheric Science, Colorado State University, 1992
4. J. H. Bruning and Y. T. Lo, "Multiple scattering of em waves by spheres parts I & II," *IEEE Trans. Ant. Prop.* **AP-19**, 378-400 (1971), J. H Bruning and Y. T. Lo, "Multiple Scattering by Spheres," Antenna Laboratory Report No. 69-5, Antenna Laboratory, Department of Electrical Engineering, Engineering Experiment Station, University of Illinois, Urbana, Illinois.
5. K. A. Fuller, "Optical resonances and two-sphere systems," *Appl. Opt.* **30** 4716-4731 (1991)
6. G. W. Kattawar and T. J. Humphreys, "Electromagnetic Scattering from Two Identical Pseudospheres," in *Light Scattering by Irregularly Shaped Particles*, D. W. Schuerman, ed. (Plenum Press, New York, 1980).

Blank

ABSORPTION AND SCATTERING CROSS SECTIONS OF CARBON DISPERSION AEROSOLS

Kirk A. Fuller

*Department of Atmospheric Science
Colorado State University
Fort Collins, CO 80523*

Recent Publications, Submittals for Publication, and Presentations

K. A. Fuller, H. D. Downing, and M. R. Query, "Infrared optical properties of orthorhombic sulfur," *Appl. Opt.* 30, 4081-4093(1991).

K. A. Fuller, Scattering and Absorption Cross Sections of Colloidal Aggregates: A Tool for Studying Visibility and Climate in Polluted Environments, a seminar presented to the Department of Atmospheric Science, Colorado State University, February 27, 1992.

R. G. Pinnick, G. Fernandez, E. Martinez-Andazola, B. D. Hinds, A. D. A. Hansen, and K. A. Fuller, "Aerosol in the arid southwestern US: measurements of mass loading, volatility, size distribution, absorption characteristics, carbon content, and vertical structure to 7 km ASL," submitted to *Atmos. Env.*

K. A. Fuller, "Scattering and absorption cross sections of colloidal aggregates," in preparation for submission to *J. Opt. Soc. Am. A*.

Abstract

An outline is presented of the derivation of the cross section for total scattering by a cluster of spheres. The theory is then used to study the effects of scavenging and aggregation on the specific absorption of carbon. Results are presented for polarization- and orientation-dependent absorption cross sections of sulfate haze elements and cloud droplets with small carbon grains (spheres) attached to their surfaces. Comparisons between the absorption cross sections of free carbon, linear chains, and tightly clumped carbon spheres are also provided.

Introduction

The total scattering cross section, σ_s , of a particle is given by

$$\sigma_s = \int_{\Omega} \frac{\text{Energy scattered/unit time/unit solid angle}}{\text{Incident energy flux (energy/unit area/unit time)}} d\Omega. \quad (1)$$

For a spherical scatterer, this integral can be solved analytically.

The response of a *cluster* of spheres to em radiation derives from the natural modes of the individual spheres, but the modes of each sphere couple to those of all other spheres in the ensemble and the mathematical description of the scattered radiation is inherently more complicated than that for isolated spheres. With the use of the addition theorem for vector spherical harmonics, not only can the scattered fields of the cluster be determined; we have shown that the σ_s integral can once again be solved analytically. The cross section for total extinction, σ_e , can be found with relative ease from the optical theorem and the absorption cross section of the cluster is simply

$$\sigma_a = \sigma_e - \sigma_s. \quad (2)$$

Without an analytic solution for σ_s , the absorption cross sections of small, highly absorbing grains attached to (scavenged by) large, weakly absorbing haze elements or cloud droplets could not have been calculated.

Cross Sections for Spheres: Reduced Symmetry Case

The scattering geometry for the case of a single sphere is depicted in Fig. 1. Rather than restricting the wave vector of the incident radiation to be parallel to \hat{e}_z , we will require only that \mathbf{k}_0 lie in the xz -plane, oriented at an angle α from the z -axis. The angle γ specifies the polarization of the incident field \mathbf{E}_0 . The expansion, in vector spherical harmonics, of this field is then

$$\mathbf{E}_0 \exp(i\mathbf{k}_0 \cdot \mathbf{r}) = |\mathbf{E}_0| \sum_{n=1}^{\infty} \sum_{m=-n}^n \left(p_{mn} \mathbf{N}_{mn}^{(1)} + q_{mn} \mathbf{M}_{mn}^{(1)} \right), \quad (3)$$

where p_{mn} and q_{mn} are of the form

$$p_{mn} = -i^n \frac{2n+1}{n(n+1)} \frac{(n-m)!}{(n+m)!} \begin{bmatrix} -i\tau_{mn}(\cos \alpha) \\ \pi_{mn}(\cos \alpha) \end{bmatrix}, \quad \gamma = \begin{bmatrix} 0 \\ \pi/2 \end{bmatrix} \quad (4)$$

and

$$q_{mn} = i^n \frac{2n+1}{n(n+1)} \frac{(n-m)!}{(n+m)!} \begin{bmatrix} i\pi_{mn}(\cos \alpha) \\ -\tau_{mn}(\cos \alpha) \end{bmatrix}, \quad \gamma = \begin{bmatrix} 0 \\ \pi/2 \end{bmatrix}. \quad (5)$$

Radiation is scattered into an angle β , relative to the \mathbf{k}_0 direction, with polarization components $\mathbf{E}_{s\parallel}$ and $\mathbf{E}_{s\perp}$ that are, respectively, parallel and perpendicular to the plane swept out by the scattering angle. The scattered field can be expressed as

$$\mathbf{E}_s = |\mathbf{E}_0| \sum_{n=1}^{\infty} \sum_{m=-n}^n \left(AE_{mn} \mathbf{N}_{mn}^{(3)} + AH_{mn} \mathbf{M}_{mn}^{(3)} \right), \quad (6)$$

where

$$\begin{aligned} AE_{mn} &= p_{mn} a_n \\ AH_{mn} &= q_{mn} b_n \end{aligned} \quad (7)$$

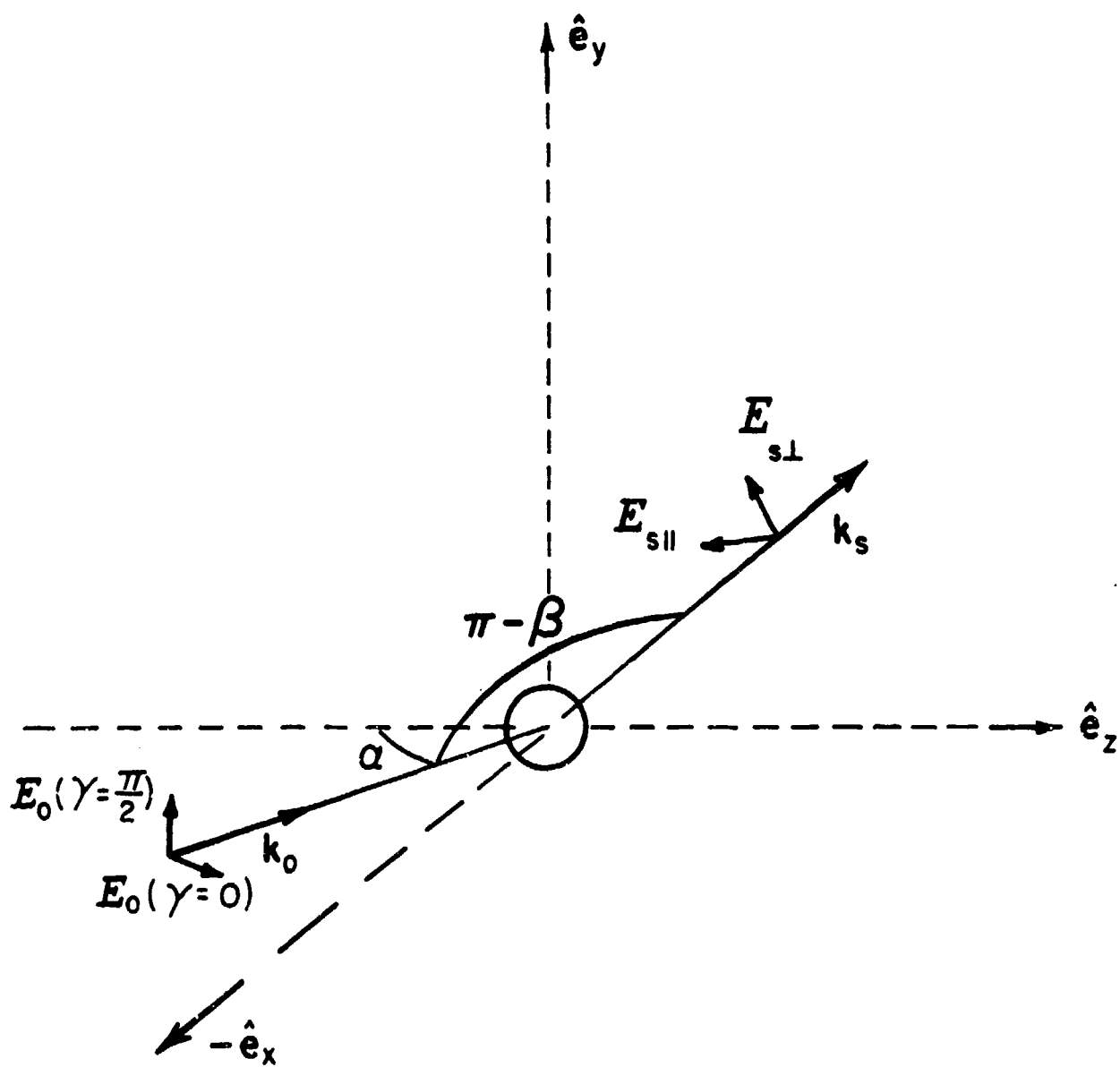


Figure 1. The reduced-symmetry geometry for light scattering by a sphere.

and a_n and b_n are the Lorenz Mie coefficients.

When \mathbf{k}_0 is parallel to $\hat{\mathbf{e}}_z$ and the incident field is polarized in the $\hat{\mathbf{e}}_z$ direction, then the more familiar¹ expression,

$$\mathbf{E}_s \rightarrow |\mathbf{E}_0| \sum_{n=1}^{\infty} i^n \frac{2n+1}{n(n+1)} \left(i a_n \mathbf{N}_{e1n}^{(3)} - b_n \mathbf{M}_{o1n}^{(3)} \right), \quad \begin{array}{l} \alpha \rightarrow 0 \\ \gamma = 0 \end{array} \quad (8)$$

is recovered.

The differential scattering cross section of a particle is defined as

$$\frac{d\sigma}{d\Omega} = \frac{\text{Energy scattered/unit time/unit solid angle}}{\text{Incident energy flux (energy/unit area/unit time)}} \quad (9)$$

Integrating the differential cross section over all solid angles yields the cross section for total scattering:

$$\sigma_s = \frac{1}{2|\langle \mathbf{S}_0 \rangle|} \text{Re} \int_0^{2\pi} \int_0^\pi \mathbf{S}_s \cdot \hat{\mathbf{e}}_r \, r^2 \sin \theta \, d\theta \, d\phi, \quad (10)$$

where $\mathbf{S}_0 = \langle \mathbf{E}_0 \times \mathbf{H}_0^* \rangle$ and $\mathbf{S}_s = \langle \mathbf{E}_s \times \mathbf{H}_s^* \rangle$ are, respectively, the time-averaged Poynting vectors of the incident and scattered radiation. From the optical theorem, the extinction cross section is simply

$$\sigma_e = \frac{4\pi}{k^2} \text{Re}(\mathbf{E}_s(\beta=0) \cdot \hat{\mathbf{e}}_\theta), \quad (11)$$

and the absorption cross section is, by conservation of energy,

$$\sigma_a = \sigma_e - \sigma_s. \quad (12)$$

For a single sphere and $\alpha = 0$

$$\sigma_s = \frac{2\pi}{k^2} \sum_{n=1}^{\infty} (2n+1)(|a_n|^2 + |b_n|^2). \quad (13)$$

When \mathbf{k}_0 is not parallel to $\hat{\mathbf{e}}_z$,

$$\begin{aligned} \sigma_s = & \int_0^{2\pi} \int_0^\pi r^2 \sin \theta \, d\theta \, d\phi \hat{\mathbf{e}}_r \cdot \\ & \text{Re} \left[i \sum_{n=1}^{\infty} \sum_{m=-n}^n \left(A E_{mn}(\mathbf{N}_{mn}^{(3)}) + A H_{mn}(\mathbf{M}_{mn}^{(3)}) \right) \times \right. \\ & \left. \sum_{n'=1}^{\infty} \sum_{m'=-n'}^{n'} \left(A H_{m'n'}^*(\mathbf{N}_{m'n'}^{(3)})^* + A E_{m'n'}^*(\mathbf{M}_{m'n'}^{(3)})^* \right) \right]. \end{aligned} \quad (14)$$

In carrying out the above integration, it is noted that

$$\oint (M_{m,n} \times M_{m',n'}^*) \cdot \hat{e}_r r^2 \sin \theta d\theta d\phi =$$

$$\oint (N_{m,n} \times N_{m',n'}^*) \cdot \hat{e}_r r^2 \sin \theta d\theta d\phi = 0$$
(15)

and

$$\oint (N_{m,n} \times M_{m',n'}^*) \cdot \hat{e}_r r^2 \sin \theta d\theta d\phi =$$

$$- \oint (M_{m',n'} \times N_{m,n}^*) \cdot \hat{e}_r r^2 \sin \theta d\theta d\phi = \mathcal{N}(m, n),$$
(16)

where

$$\mathcal{N}(m, n) = \frac{-4\pi i}{k^2} \frac{n(n+1)}{2n+1} \frac{(n+m)!}{(n-m)!} \xi_n^* \xi_n' \delta_{m,m'} \delta_{n,n'},$$
(17)

and ξ_n are Ricatti-Hankel functions. Now,

$$Re(i\xi_n^* \xi_n') = -1 \quad (\text{see Ref. 1}),$$
(18)

thus

$$\sigma_s = \frac{4\pi}{k^2} \sum_{n=1}^{\infty} \sum_{m=-n}^n \frac{n(n+1)}{(2n+1)} \frac{(n+m)!}{(n-m)!} \left(|AE_{mn}|^2 + |AH_{mn}|^2 \right)$$
(19)

Cross Sections for Sphere Aggregates

Having established the mathematical form of the total scattering cross section of a sphere with a scattering geometry that does not fully exploit the symmetry of a single sphere, one can more readily make the transition to scattering by clusters. The optical properties of clusters of spheres can be understood in terms of multiple scattering centers, and hence, multiple coordinate origins. The scattering geometry for such a system is shown in Fig. 2. The spheres in the cluster are centered about the ${}^{\ell}O$ origins, where ℓ is an index that identifies specific constituents of a set of L spheres. The quantities ${}^{\ell}\hat{e}_{\ell}$ are unit vectors in the ℓ th system. In the figure, the unit vectors associated with the ℓ' th origin have been displaced from the ${}^{\ell'}x^{\ell'}y$ -plane to the ${}^{\ell}x^{\ell}y$ -plane. The constituent spheres (with radii ${}^{\ell}a$) are now characterized by the size parameters $k^{\ell}a \equiv \zeta$ and complex refractive indices \hat{N} . The dimensionless center-to-center distance between spheres ℓ and ℓ' is denoted by $kd_{\ell,\ell'}$. The principal or primary coordinate system in which the integration of the Poynting flux is to be carried out corresponds to $\ell = 1$. It will be convenient in such instances to visualize ${}^{\ell}O$ in Fig. 2 as the origin of this system, and any other ${}^{\ell'}O$, $\ell' \neq 1$ as a secondary origin. The $L - 1$ secondary coordinate systems are related to the principal coordinate system by pure translations.

The coefficients of the plane wave expansion about an ℓ th secondary origin are obtained by simply multiplying ${}^1p_{mn}$ and ${}^1q_{mn}$ by the phase factor $\exp(i\mathbf{k}_0 \cdot \mathbf{d}_{1,\ell})$. In the theory developed

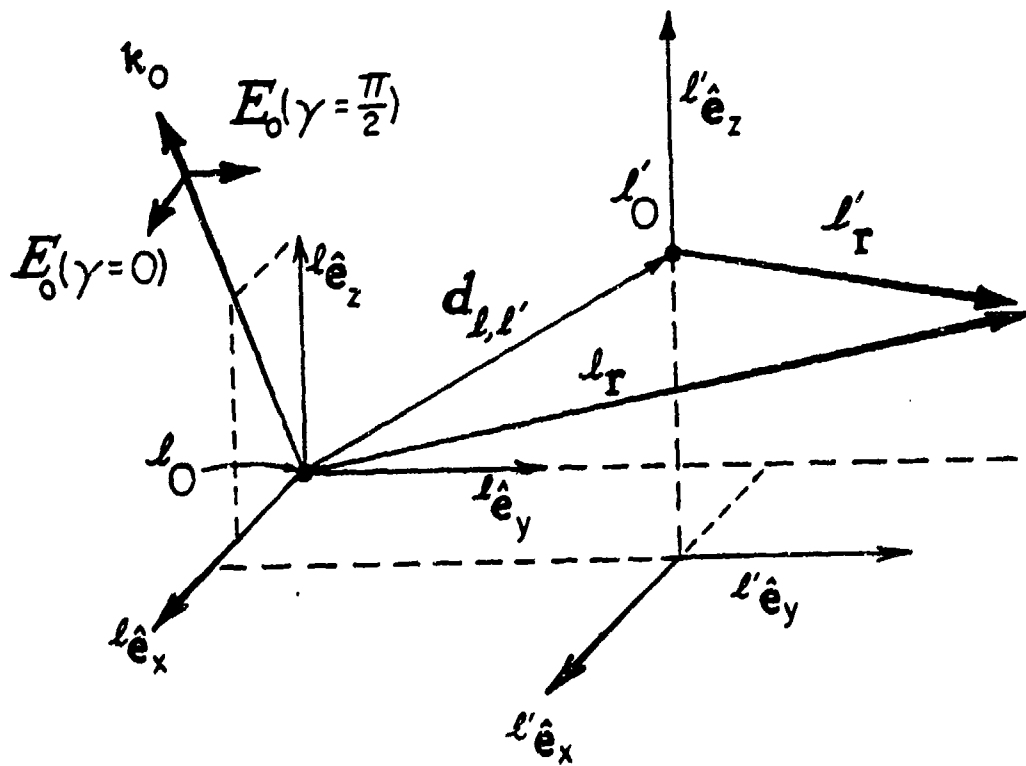


Figure 2. The scattering geometry for multiple scattering centers.

by Liang and Lo² and Bruning and Lo,³ as throughout this study, it is assumed that the scattered fields can be expanded as

$$\begin{aligned} \mathbf{E}_s &= \sum_{n=1}^{\infty} \sum_{m=-n}^n \sum_{\ell=1}^L \left({}^{\ell}A E_{mn} {}^{\ell}N_{mn}^{(3)} + {}^{\ell}A H_{mn} {}^{\ell}M_{mn}^{(3)} \right) \\ &= \sum_{\ell=1}^L {}^{\ell}\mathbf{E}_s, \end{aligned} \quad (20)$$

where the expansion coefficients ${}^{\ell}A E_{mn}$ and ${}^{\ell}A H_{mn}$ correspond, respectively, to the E- and H-type modes of the ℓ th sphere, and ${}^{\ell}N_{mn}^{(3)}$ and ${}^{\ell}M_{mn}^{(3)}$ are the vector spherical harmonics in the ℓ th coordinate system.

In order to apply boundary conditions successfully, one must be able to expand the fields scattered by the ℓ' th sphere about the center of any ℓ th constituent of the cluster. This can be accomplished through the use of the addition theorem for vector spherical harmonics.^{2,3,4-6} Applying boundary conditions, it can be shown that

$${}^{\ell}A E_{mn} = {}^{\ell}a_n \left[{}^{\ell}p_{mn} + \sum_{\ell' \neq \ell} \sum_{\nu} \sum_{\mu} \left({}^{\ell'}A E_{\mu\nu} A_{mn}^{\mu\nu}(kd_{\ell',\ell}) + {}^{\ell'}A H_{\mu\nu} B_{mn}^{\mu\nu}(kd_{\ell',\ell}) \right) \right] \quad (21)$$

$${}^{\ell}A H_{mn} = {}^{\ell}b_n \left[{}^{\ell}q_{mn} + \sum_{\ell' \neq \ell} \sum_{\nu} \sum_{\mu} \left({}^{\ell'}A H_{\mu\nu} A_{mn}^{\mu\nu}(kd_{\ell',\ell}) + {}^{\ell'}A E_{\mu\nu} B_{mn}^{\mu\nu}(kd_{\ell',\ell}) \right) \right], \quad (22)$$

where the quantities $A_{mn}^{\mu\nu}(kd_{\ell',\ell})$ and $B_{mn}^{\mu\nu}(kd_{\ell',\ell})$ are coefficients that are encountered in the addition theorem. These so-called translation coefficients are rather complicated functions of Clebsch-Gordan coefficients and of the geometry of the cluster.

Alternatively, the scattering coefficients may be found from the order-of-scattering_s (OS) method,^{7,8} which can be visualized as follows: First, plane wave radiation strikes one sphere which then scatters a field (as prescribed by the standard Lorenz-Mie theory) both to the field point and to the other sphere. This second sphere then responds to the field incident on it from the first sphere, scattering radiation to the field point and back to the first sphere. This process is continued indefinitely, and the total scattered field is obtained as a vector sum of these partial fields plus a sum of the partial fields which arise from plane wave radiation incident on the second sphere. For ease of visualization, the above description has been limited to just two spheres, but the extension to clusters of three or more is straightforward.

The total field scattered by the pair is thus

$$\sum_{j=0}^{\infty} \sum_{\ell=1}^L {}^{\ell}\mathbf{E}_s^{(j)}, \quad (23)$$

where the j th-order partial fields ${}^{\ell}\mathbf{E}_s^{(j)}$ are in turn expressed as

$${}^{\ell}\mathbf{E}_s^{(j)} = \sum_{n,m} \left({}^{\ell}a_{mn}^{(j)} {}^{\ell}N_{mn}^{(3)} + {}^{\ell}b_{mn}^{(j)} {}^{\ell}M_{mn}^{(3)} \right). \quad (24)$$

For the case of two spheres,

$$\begin{aligned}
 {}^1 a_{mn}^{(j)} &= {}^1 a_n \sum_{\nu} \sum_{\mu} \left({}^2 a_{\mu\nu}^{(j-1)} A_{mn}^{\mu\nu} + {}^2 b_{\mu\nu}^{(j-1)} B_{mn}^{\mu\nu} \right) \\
 {}^1 b_{mn}^{(j)} &= {}^1 b_n \sum_{\nu} \sum_{\mu} \left({}^2 b_{\mu\nu}^{(j-1)} A_{mn}^{\mu\nu} + {}^2 a_{\mu\nu}^{(j-1)} B_{mn}^{\mu\nu} \right) \\
 {}^2 a_{mn}^{(j)} &= {}^2 a_n \sum_{\nu} \sum_{\mu} \left({}^1 a_{\mu\nu}^{(j-1)} A_{mn}^{\mu\nu} + {}^1 b_{\mu\nu}^{(j-1)} B_{mn}^{\mu\nu} \right) \\
 {}^2 b_{mn}^{(j)} &= {}^2 b_n \sum_{\nu} \sum_{\mu} \left({}^1 b_{\mu\nu}^{(j-1)} A_{mn}^{\mu\nu} + {}^1 a_{\mu\nu}^{(j-1)} B_{mn}^{\mu\nu} \right).
 \end{aligned} \tag{25}$$

The expansion coefficients of the total scattered field are then given by

$$\begin{aligned}
 {}^{\ell} A E_{mn} &= \sum_{j=0}^{\infty} {}^{\ell} a_{mn}^{(j)} \\
 {}^{\ell} A H_{mn} &= \sum_{j=0}^{\infty} {}^{\ell} b_{mn}^{(j)}.
 \end{aligned} \tag{26}$$

The OS method is of particular importance in the efficient calculation of the scattering cross sections associated with large droplets that have small carbon grains attached to their surfaces.

In order to determine the total power, W , radiated from a surface Σ that encloses an ensemble of scatterers, the integral

$$\int_{\Sigma} \mathbf{S} \cdot \hat{\mathbf{r}} r^2 \sin \theta d\theta d\phi = \int_{\Sigma} (\mathbf{E} \times \mathbf{H}^*) \cdot \hat{\mathbf{r}} r^2 \sin \theta d\theta d\phi \tag{27}$$

must be evaluated, where, for a system of L particles,

$$\mathbf{E} = \mathbf{E}_0 + \sum_{\ell=1}^L {}^{\ell} \mathbf{E}_s \tag{28}$$

and

$$\mathbf{H} = \mathbf{H}_0 + \sum_{\ell=1}^L {}^{\ell} \mathbf{H}_s. \tag{29}$$

The radiated power is thus

$$\begin{aligned}
 W &= \sum_{\ell} \int_{\Sigma} (\mathbf{E}_0 \times {}^{\ell} \mathbf{H}_s^* + {}^{\ell} \mathbf{E}_s \times \mathbf{H}_0^*) \cdot \hat{\mathbf{e}}_r r^2 \sin \theta d\theta d\phi \\
 &+ \sum_{\ell} \int_{\Sigma} ({}^{\ell} \mathbf{E}_s \times {}^{\ell} \mathbf{H}_s^*) \cdot \hat{\mathbf{e}}_r r^2 \sin \theta d\theta d\phi \\
 &+ \sum_{\ell} \sum_{\ell' \neq \ell} \int_{\Sigma} ({}^{\ell} \mathbf{E}_s \times {}^{\ell'} \mathbf{H}_s^*) \cdot \hat{\mathbf{e}}_r r^2 \sin \theta d\theta d\phi,
 \end{aligned} \tag{30}$$

and the equation for the total scattering cross section becomes

$$|\langle S_0 \rangle|_{\sigma_s} = \frac{1}{2} \text{Re} \sum_{\ell} \sum_{\ell'} \int_0^{2\pi} \int_0^{\pi} ({}^{\ell} \mathbf{E}_s \times {}^{\ell'} \mathbf{H}_s^*) \cdot \hat{\mathbf{e}}_r r^2 \sin \theta d\theta d\phi. \quad (31)$$

It is noted that the integration is to be carried out in one set of coordinates, but ${}^{\ell} \mathbf{E}_s$ is referenced to a second coordinate system and ${}^{\ell'} \mathbf{H}_s^*$ is referenced to a yet another.

In principle, one could simply evaluate

$${}^{\ell} \sigma_s = \int_0^{2\pi} \int_0^{\pi} \left(\sum_{\ell} {}^{\ell} \mathbf{E}_s \times \sum_{\ell'} {}^{\ell'} \mathbf{H}_s^* \right) \cdot \hat{\mathbf{e}}_r r^2 \sin \theta d\theta d\phi \quad (32)$$

numerically, and calculate the total scattering cross section from

$$\sigma_s = \sum_{\ell} \sum_{\ell'} {}^{\ell} \sigma_s, \quad (33)$$

but, as will be made clear in the next section, this provides only a rather limited solution to the problem.

We once again make use of the addition theorem. In Eqs. (21) and (22) it is to be understood that the transformation of coordinates has been carried out at the surfaces of the scatterers and thus $k^{\ell} < kd_{\ell\ell'}$. In this case, the dependence of the translation coefficients on the distances between spheres is governed by spherical Hankel functions. When evaluating the integrals over a surface that contains all scatterers in the collection, $k^{\ell} > kd_{\ell\ell'}$. The dependence on $kd_{\ell\ell'}$ is, in this case, governed by spherical Bessel functions and the corresponding translation coefficients are here denoted as $\tilde{A}_{\mu\nu}^{mn}(kd_{\ell',\ell})$ and $\tilde{B}_{\mu\nu}^{mn}(kd_{\ell',\ell})$. The scattered fields of each sphere can then be expressed in terms of the basis functions of the principal origin, viz.,

$$\begin{aligned} {}^{\ell} \mathbf{E}_s = & \sum_{n=1}^{\infty} \sum_{m=-n}^n \\ & \left[{}^{\ell} A E_{mn} \sum_{\nu=1}^{\infty} \sum_{\mu=-\nu}^{\nu} \left({}^1 N_{\mu\nu}^{(3)} \tilde{A}_{\mu\nu}^{mn}(kd_{\ell,1}) + {}^1 M_{\mu\nu}^{(3)} \tilde{B}_{\mu\nu}^{mn}(kd_{\ell,1}) \right) \right. \\ & \left. + {}^{\ell} A H_{mn} \sum_{\nu=1}^{\infty} \sum_{\mu=-\nu}^{\nu} \left({}^1 N_{\mu\nu}^{(3)} \tilde{B}_{\mu\nu}^{mn}(kd_{\ell,1}) + {}^1 M_{\mu\nu}^{(3)} \tilde{A}_{\mu\nu}^{mn}(kd_{\ell,1}) \right) \right] \end{aligned} \quad (34)$$

and

$$\begin{aligned} {}^{\ell} \mathbf{H}_s^* = & \frac{ik}{\omega\mu_0} \sum_{n=1}^{\infty} \sum_{m=-n}^n \\ & \left[{}^{\ell} A H_{mn}^* \sum_{\nu=1}^{\infty} \sum_{\mu=-\nu}^{\nu} \left({}^1 N_{\mu\nu}^{(3)} \tilde{A}_{\mu\nu}^{mn}(kd_{\ell',1}) + {}^1 M_{\mu\nu}^{(3)} \tilde{B}_{\mu\nu}^{mn}(kd_{\ell',1}) \right)^* \right. \\ & \left. + {}^{\ell} A E_{mn}^* \sum_{\nu=1}^{\infty} \sum_{\mu=-\nu}^{\nu} \left({}^1 N_{\mu\nu}^{(3)} \tilde{B}_{\mu\nu}^{mn}(kd_{\ell',1}) + {}^1 M_{\mu\nu}^{(3)} \tilde{A}_{\mu\nu}^{mn}(kd_{\ell',1}) \right)^* \right]. \end{aligned} \quad (35)$$

The summations in the addition theorem are uniformly convergent and the series can therefore be integrated term-by-term, giving

$$\begin{aligned} \ell' \sigma_s = \frac{4\pi}{k^2} \text{Re} \sum_{m,n} \sum_{m',n'} \sum_{\mu,\nu} \frac{\nu(\nu+1)(\nu+\mu)!}{(2\nu+1)(\nu-\mu)!} \times \\ \left[\left({}^\ell A_{mn} {}^\ell A_{\mu\nu}^* + {}^\ell A_{mn} {}^\ell A_{\mu\nu}^* \right) \left(\tilde{A}_{\mu\nu}^{mn} (\tilde{A}_{\mu\nu}^{m'n'})^* + \tilde{B}_{\mu\nu}^{mn} (\tilde{B}_{\mu\nu}^{m'n'})^* \right) \right. \\ \left. + \left({}^\ell A_{mn} {}^\ell A_{\mu\nu}^* + {}^\ell A_{mn} {}^\ell A_{\mu\nu}^* \right) \left(\tilde{A}_{\mu\nu}^{mn} (\tilde{B}_{\mu\nu}^{m'n'})^* + \tilde{B}_{\mu\nu}^{mn} (\tilde{A}_{\mu\nu}^{m'n'})^* \right) \right]. \end{aligned} \quad (36)$$

These terms can then be rearranged to give

$$\sigma_s = \frac{4\pi}{k^2} \sum_{m,n} \frac{n(n+1)(n+m)!}{(2n+1)(n-m)!} (|A_{mn}|^2 + |B_{mn}|^2), \quad (37)$$

where

$$\begin{aligned} A_{mn} &= \sum_{\ell} \sum_{\mu,\nu} \left({}^\ell A_{\mu\nu} \tilde{A}_{mn}^{\mu\nu} + {}^\ell A_{\mu\nu} \tilde{B}_{mn}^{\mu\nu} \right) \\ B_{mn} &= \sum_{\ell} \sum_{\mu,\nu} \left({}^\ell A_{\mu\nu} \tilde{B}_{mn}^{\mu\nu} + {}^\ell A_{\mu\nu} \tilde{A}_{mn}^{\mu\nu} \right). \end{aligned} \quad (38)$$

It is to be noted that $\ell' \sigma_s = \ell' \sigma_s^*$ and thus

$$\ell' \sigma_s + \ell' \sigma_s = 2\text{Re}(\ell' \sigma_s). \quad (39)$$

This allows the total scattering cross section to be expressed as

$$\sigma_s = \sum_{\ell} \ell' \sigma_s + 2\text{Re} \sum_{\ell} {}^1 \ell' \sigma_s + 2\text{Re} \sum_{\ell > 1} \sum_{\ell' > \ell} \ell' \sigma_s, \quad (40)$$

B. Special cases

When coordinate translations are constrained to the z-axis we have

$$\ell' \mathbf{M}_{mn}^{(3)} = \sum_{\nu = \max(1, m)}^{\infty} \left({}^\ell \mathbf{M}_{m\nu}^{(3)} \tilde{A}_{m\nu}^{mn}(kd_{\ell}, \ell) + {}^\ell \mathbf{N}_{m\nu}^{(3)} \tilde{B}_{m\nu}^{mn}(kd_{\ell}, \ell) \right) \quad (41)$$

$$\ell' \mathbf{N}_{mn}^{(3)} = \sum_{\nu = \max(1, m)}^{\infty} \left({}^\ell \mathbf{N}_{m\nu}^{(3)} \tilde{A}_{m\nu}^{mn}(kd_{\ell}, \ell) + {}^\ell \mathbf{M}_{m\nu}^{(3)} \tilde{B}_{m\nu}^{mn}(kd_{\ell}, \ell) \right). \quad (42)$$

It can be shown that

$${}^{1\ell'}\sigma_s = \frac{4\pi}{k^2} \text{Re} \sum_{m,n} \frac{n(n+1)(n+m)!}{(2n+1)(n-m)!} \times \sum_{n'} \left[\left({}^1A_{mn} {}^{\ell'}A_{mn'}^* + {}^1A_{mn} {}^{\ell'}A_{mn'} \right) (\tilde{A}_{mn'}^{m'n'})^* + \left({}^1A_{mn} {}^{\ell'}A_{mn'} + {}^1A_{mn} {}^{\ell'}A_{mn'}^* \right) (\tilde{B}_{mn'}^{m'n'})^* \right] \quad (43)$$

and

$${}^{11}\sigma_s = \frac{4\pi}{k^2} \sum_{m,n} \frac{n(n+1)(n+m)!}{(2n+1)(n-m)!} (|{}^1A_{m,n}|^2 + |{}^1A_{m,n}|^2). \quad (44)$$

If $\ell = \ell'$ then

$${}^{\ell\ell}\sigma_s = \frac{4\pi}{k^2} \sum_{m,n} \frac{n(n+1)(n+m)!}{(2n+1)(n-m)!} (|{}^{\ell}A_{m,n}|^2 + |{}^{\ell}A_{m,n}|^2), \quad (45)$$

which it must if the solution obtained from Lorenz-Mie theory is to be recovered in cases where dependent scattering can be ignored.

From Eq. (36) we have, for $\ell = \ell'$,

$${}^{\ell\ell}\sigma_s = \frac{4\pi}{k^2} \text{Re} \sum_{m,n} \sum_{\mu,\nu} \frac{\nu(\nu+1)(\nu+\mu)!}{(2\nu+1)(\nu-\mu)!} \times \left[\left({}^{\ell}A_{mn} {}^{\ell}A_{\mu\nu}^* + {}^{\ell}A_{mn} {}^{\ell}A_{\mu\nu} \right) \sum_{m',n'} \left(\tilde{A}_{\mu\nu}^{mn} (\tilde{A}_{\mu\nu}^{m'n'})^* + \tilde{B}_{\mu\nu}^{mn} (\tilde{B}_{\mu\nu}^{m'n'})^* \right) + \left({}^{\ell}A_{mn} {}^{\ell}A_{\mu\nu} + {}^{\ell}A_{mn} {}^{\ell}A_{\mu\nu}^* \right) \sum_{m',n'} \left(\tilde{A}_{\mu\nu}^{mn} (\tilde{B}_{\mu\nu}^{m'n'})^* + \tilde{B}_{\mu\nu}^{mn} (\tilde{A}_{\mu\nu}^{m'n'})^* \right) \right]. \quad (46)$$

Comparing this last expression with Eq. (45) it can be inferred that

$$\sum_{m',n'} \left(\tilde{A}_{\mu\nu}^{mn}(kd_{\ell,1}) (\tilde{A}_{\mu\nu}^{m'n'}(kd_{\ell,1}))^* + \tilde{B}_{\mu\nu}^{mn}(kd_{\ell,1}) (\tilde{B}_{\mu\nu}^{m'n'}(kd_{\ell,1}))^* \right) = \delta_{m,\mu} \delta_{n,\nu} \quad (47)$$

and that

$$\sum_{m',n'} \left(\tilde{A}_{\mu\nu}^{mn}(kd_{\ell,1}) (\tilde{B}_{\mu\nu}^{m'n'}(kd_{\ell,1}))^* + \tilde{B}_{\mu\nu}^{mn}(kd_{\ell,1}) (\tilde{A}_{\mu\nu}^{m'n'}(kd_{\ell,1}))^* \right) = 0. \quad (48)$$

Applying the same argument to the case of an isolated sphere, displaced to the ℓ th origin,

$$\sum_{m,n} \frac{n(n+1)(n+m)!}{(2n+1)(n-m)!} \left(\tilde{A}_{\mu\nu}^{mn}(kd_{\ell,1}) (\tilde{A}_{\mu\nu}^{m'n'}(kd_{\ell,1}))^* + \tilde{B}_{\mu\nu}^{mn}(kd_{\ell,1}) (\tilde{B}_{\mu\nu}^{m'n'}(kd_{\ell,1}))^* \right) = \delta_{m,\mu} \delta_{n,\nu} \quad (49)$$

and

$$\sum_{m,n} \frac{n(n+1)(n+m)!}{(2n+1)(n-m)!} \left(\tilde{A}_{\mu\nu}^{mn}(kd_{\ell,1}) (\tilde{B}_{\mu\nu}^{m'n'}(kd_{\ell,1}))^* + \tilde{B}_{\mu\nu}^{mn}(kd_{\ell,1}) (\tilde{A}_{\mu\nu}^{m'n'}(kd_{\ell,1}))^* \right) = 0. \quad (50)$$

These relations provide valuable tests for convergence of the series expression of the scattering cross section of a cluster.

Gram-specific cross sections

It is popular (and, at times, useful) to use the efficiency factors

$$Q_e = \frac{\sigma_e}{G}, \quad Q_s = \frac{\sigma_s}{G}, \quad Q_a = \frac{\sigma_a}{G}, \quad (51)$$

where G is the geometric shadow of the particle. In view of the complex morphologies of aciniform colloids, a better choice for efficiency factors is the gram-specific cross section, A , the units of which are m^2/g .

$$A = \frac{\sigma}{m} = \frac{\sigma}{(\text{specific gravity})(\text{particle volume})} \quad (52)$$

It is noted that for a single sphere of radius $a \ll \lambda$,

$$\begin{aligned} A_a(\lambda) &= \frac{3k}{\rho} \text{Im} \left(\frac{N^2 - 1}{N^2 + 2} \right) \\ &= \frac{9k |N|^2 \sin(2 \tan^{-1} [\text{Im}(N) / \text{Re}(N)])}{\rho [|N|^4 + 4(1 + \text{Re}^2\{N\} - \text{Im}^2\{N\})]} \end{aligned} \quad (53)$$

At $\lambda = 5.5 \times 10^{-7}$ m this gives a specific absorption cross section for carbon of $\approx 3.654 m^2/g$, assuming the refractive index of carbon at this wavelength to be $1.8 + 0.5i$.

Results

Recent results from field measurements of atmospheric aerosols indicate that a significant fraction of haze elements can be comprised of sulfate particles with carbon grains dispersed internally or attached to their surfaces.⁹ In understanding the optical properties of clouds more fully it is necessary to understand the scattering properties of cloud droplets with inclusions or surface contaminants similar to those just described for haze particles. Results are presented in this section that illustrate the effects that the dispersion of carbon grains onto droplet surfaces may have on the mass-specific absorption efficiency of atmospheric carbon.

The scattering geometry for the surface dispersion calculations is shown in the inset of Fig. 3. At present, it is assumed that the concentration of the soot component of the aerosol or cloud

is low enough so that only single grains of carbon need be considered. Soot concentrations that would involve two or more grains per aerosol particle will be the subject of future research. Figs. 3-10 catalogue the calculated specific absorption cross sections of selected sizes of carbon grains attached to nonabsorbing sulfate particles with radii of 0.5 and 1.0 μm or to water droplets with radii of 3.0 and 5.0 μm . The variation in specific absorption with the orientation of the particle is displayed for orthogonal polarizations of the incident beam.

The basic features can be understood from geometric optics: An optically large sphere with a refractive index of ≈ 1.5 will focus light into a region near its surface. If the refractive index is ≈ 1.33 then light will be focused into a volume slightly less than half a radius from the sphere surface. The refractive effects of the sphere will prevent most of the incident radiation from reaching any other regions on the shadow side of the surface. Reflections from the shadow surface of the sphere will produce a secondary focal volume narrowly centered about the illuminated side of the droplet. Such features of a spherical lense are manifested in the behavior of the absorption cross sections of the carbon grains with particle orientation in each of Figs. 3-10. The larger the optical size of the host particle, the more accurate the geometric optics picture. Attention is also called to the second peak in A_a near $\alpha \approx 17^\circ$. This corresponds to the location of the so-called critical ring.¹⁰

Table I summarizes the orientation-averaged, polarization-dependent absorption efficiencies for the cases considered in Figs. 3-10. It appears that the more finely divided the carbon, the more efficient its absorption when residing on the surface of a sulfate host. This efficiency has not been found to be more than about a factor of two greater than that of free carbon. Carbon residing on the surface of cloud drops appears thus far to absorb slightly *less* than when it exists as isolated grains.

Also of interest are the optical properties of aggregates of carbon monomers. Two examples of such aggregates are considered here: A linear chain of five spheres and a tightly packed cluster of five spheres. The specific extinction and absorption cross sections for the linear chain as a function of orientation are shown in Fig. 11 for two polarizations. Similar results for the tightly packed cluster are provided in Fig. 12. For comparison, the cross sections for isolated monomers and for equivalent-volume spheres are also shown.

It is important that the numerical efficacy of Eqs. 37 and 40 compared to straightforward numerical integration be pointed out. The series expansion avoids the following four pitfalls:

- (1) The number of oscillations in the differential scattering cross section of a droplet increases dramatically with optical size, thereby requiring very high angular resolution of the integrand when hosts with large size parameters are involved.
- (2) When the carbon grains are very small relative to the host particle, the extinction cross section of the carbon/droplet system is dominated almost entirely by the scattering cross section of the host. The quantity $\sigma_e - \sigma_s$ can easily be of the order 10^{-6} or less and hence the integral must be evaluated with a very high precision.
- (3) For $\alpha \neq 0^\circ$ or 180° , azimuthal symmetry is lost and the integral over ϕ cannot be performed analytically.
- (4) The structure of the electric field at the surface of the host is quite complicated and therefore the absorption cross section of a small carbon grain is extremely sensitive to orientation. Orientation averages require a high resolution in α . (The

calculations summarized in the Table were based on a sampling frequency of 1° .) This makes it all the more imperative that the integrals over θ and ϕ be evaluated expeditiously.

An additional problem that will arise when large numbers of spheres are involved is that the interference between them will impose an additional oscillation in the differential cross sections of the clusters. The more monomers there are comprising the cluster, the greater the number of these interference fringes. (These oscillations are analogous to multiple slit diffraction patterns.)

A fuller discussion of these results will be provided in a future publication.¹¹

Acknowledgments

This work was supported in part by National Park Service grant #NA90RAH000077. The author also wishes to express his thanks to the Chemical Research, Development, and Engineering Command for supporting his travel and accommodations for the 1992 conference.

.05 μm C grain on 0.5 μm SO_4

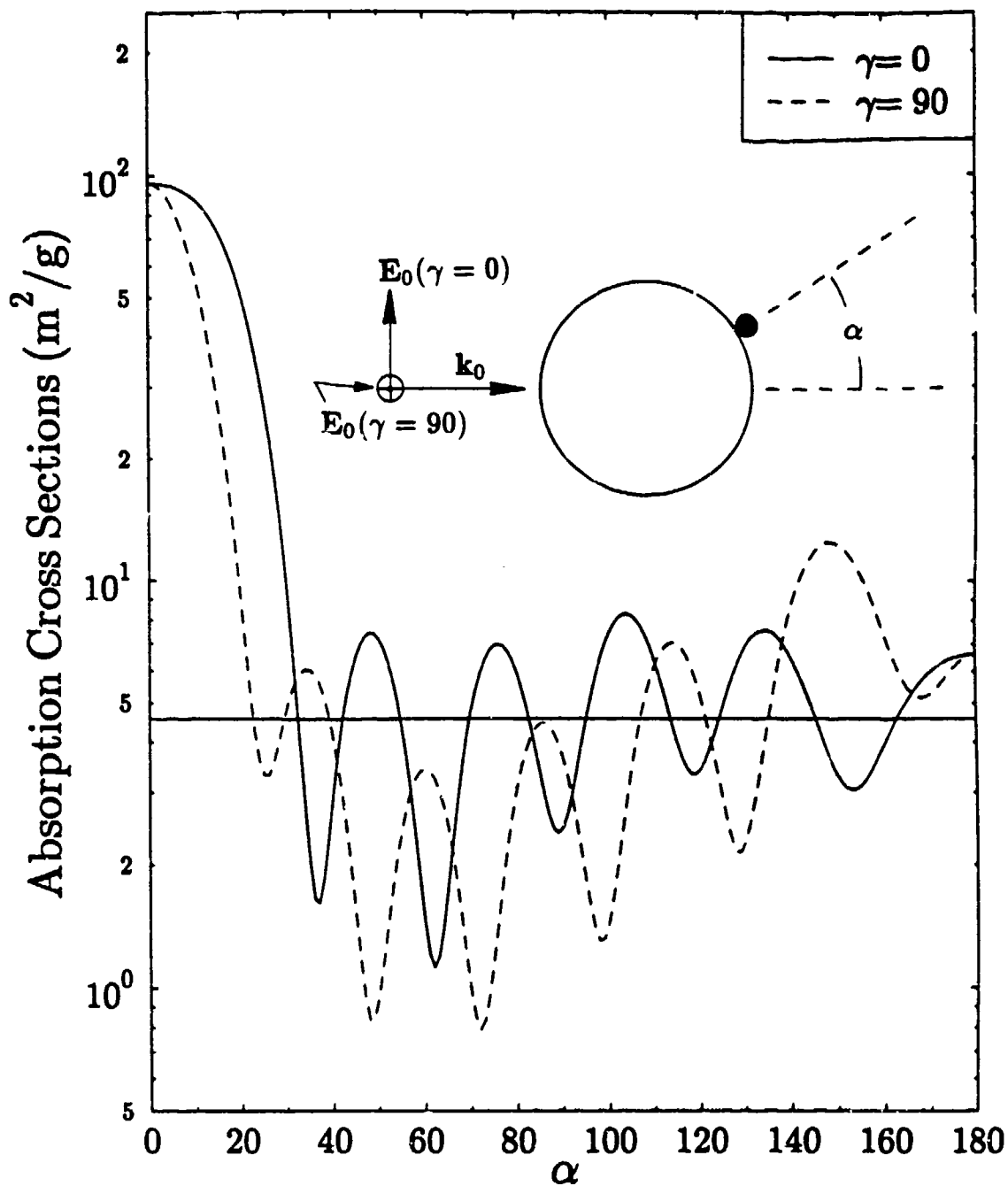


Figure 3. Gram-specific absorption cross sections for a carbon grain located on the surface of a spherical sulfate aerosol. The carbon particle has a radius of 0.05 μm and a refractive index of $1.80+0.5i$. The radius and refractive index of the sulfate particle are 0.50 μm and $1.52+0.0i$, respectively. The straight line corresponds to the gram-specific absorption cross section of an isolated carbon grain. In the inset, the size of the carbon particle relative to the sulfate aerosol is drawn to scale.

C grains on $0.5\mu\text{m SO}_4$

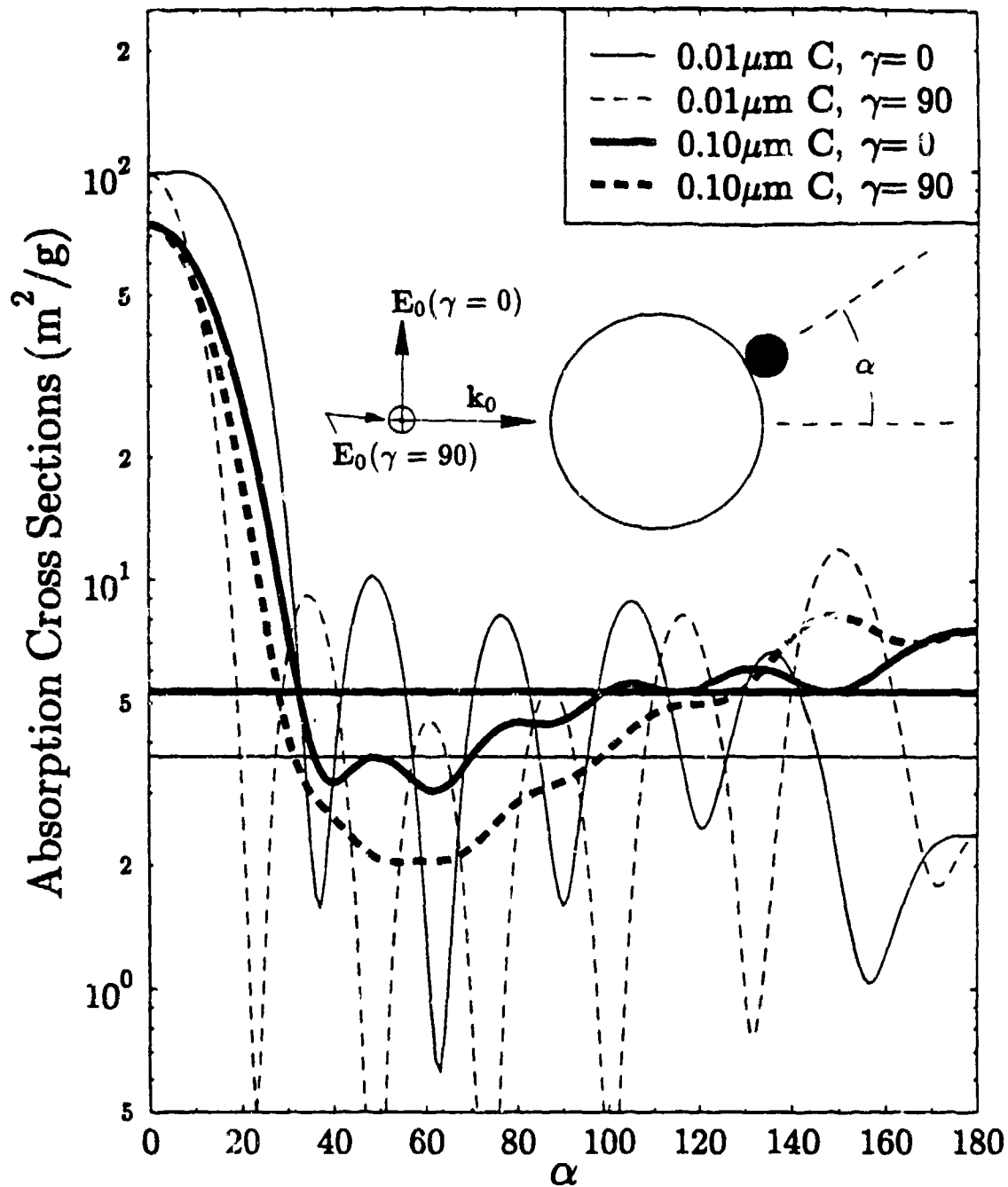


Figure 4. Same as Figure 3, but with either a 0.1 or $0.01 \mu\text{m}$ carbon grain. The heavy and light lines show the absorption cross sections of isolated 0.1 and $0.01 \mu\text{m}$ grains, respectively. The inset is drawn to scale for the $0.1\mu\text{m}$ carbon sphere.

.05 μm C grain on 1.0 μm SO_4

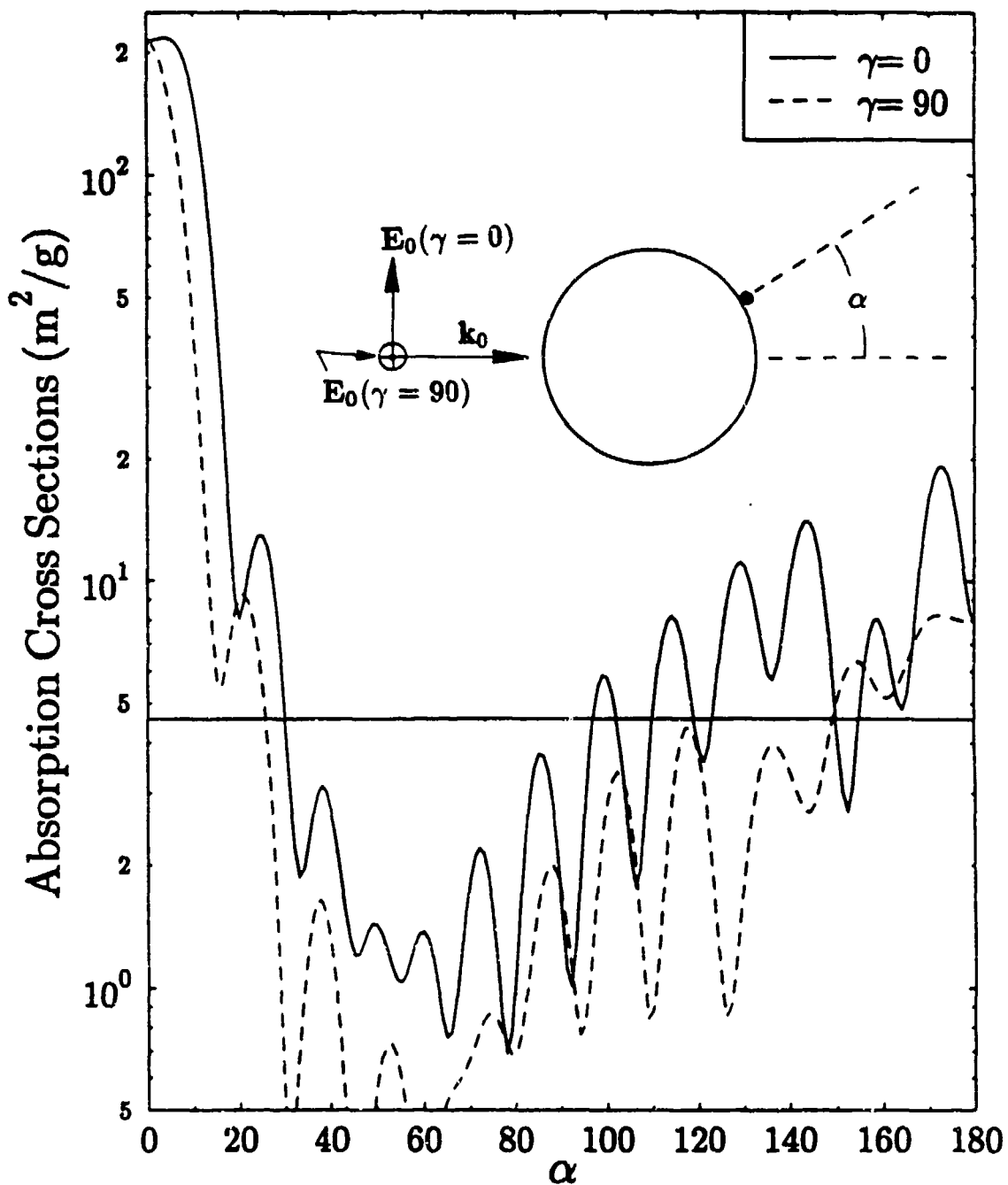


Figure 5. Same as Figure 3, but with a 1.0 μm sulfate particle.

C grains on 1.0 μm SO_4

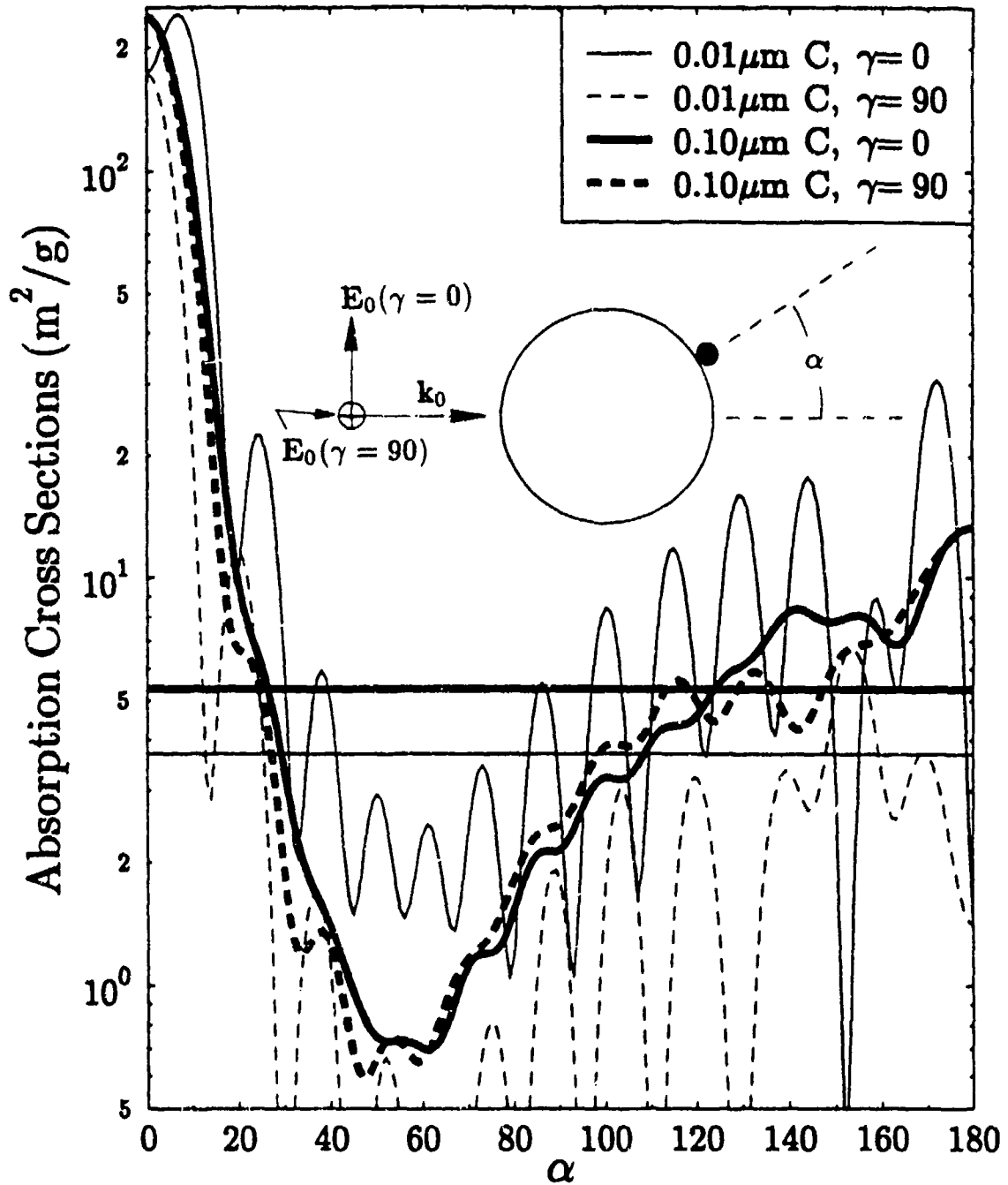


Figure 6. Same as Figure 4, but with a 1.0 μm sulfate particle.

.05 μm C grain on $3.0\mu\text{m}$ H_2O

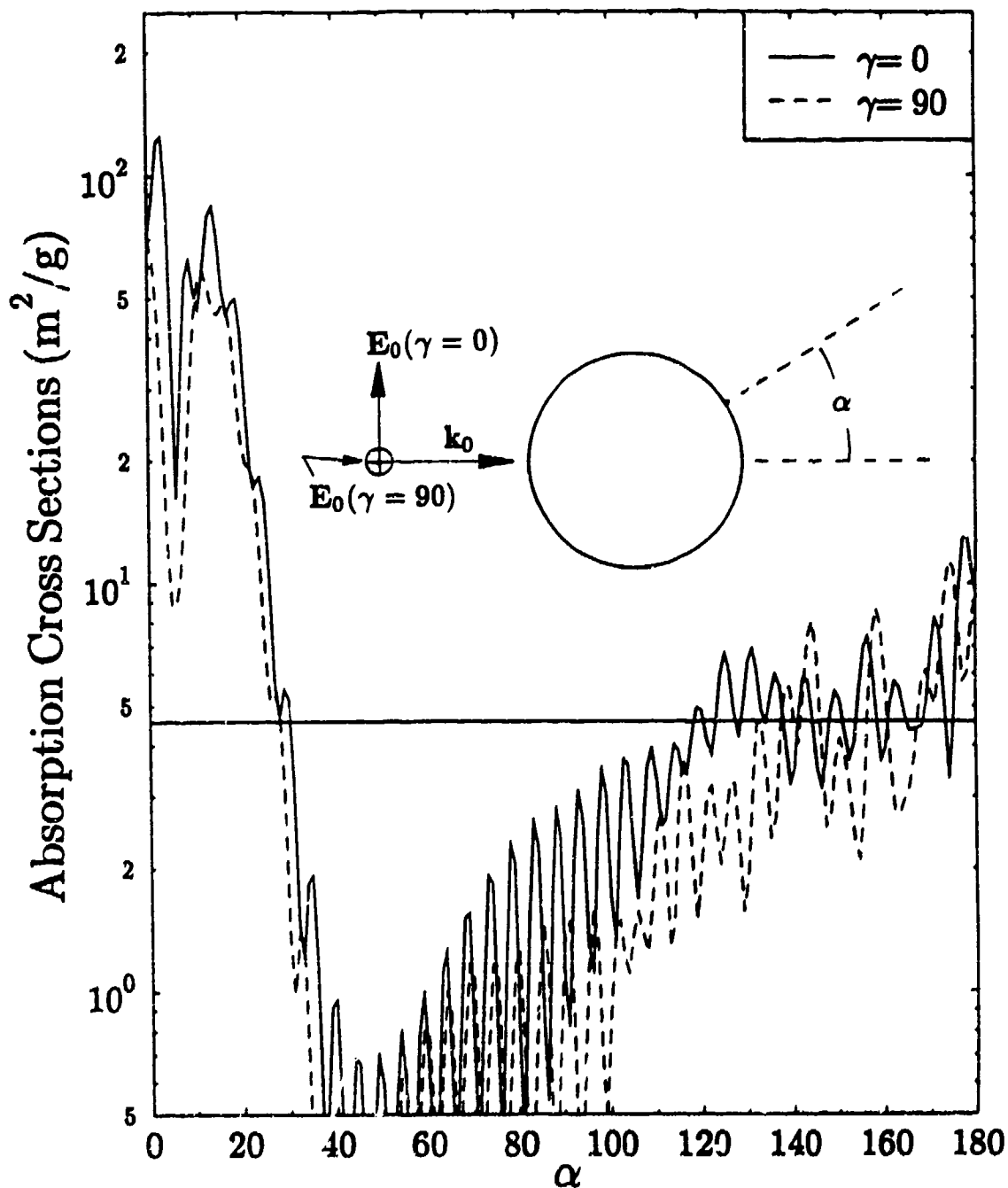


Figure 7. Same as Figure 3, but with a $3.0\ \mu\text{m}$ water droplet. The refractive index of water is taken to be $1.33 + 0.0i$.

C grains on $3.0\mu\text{m H}_2\text{O}$

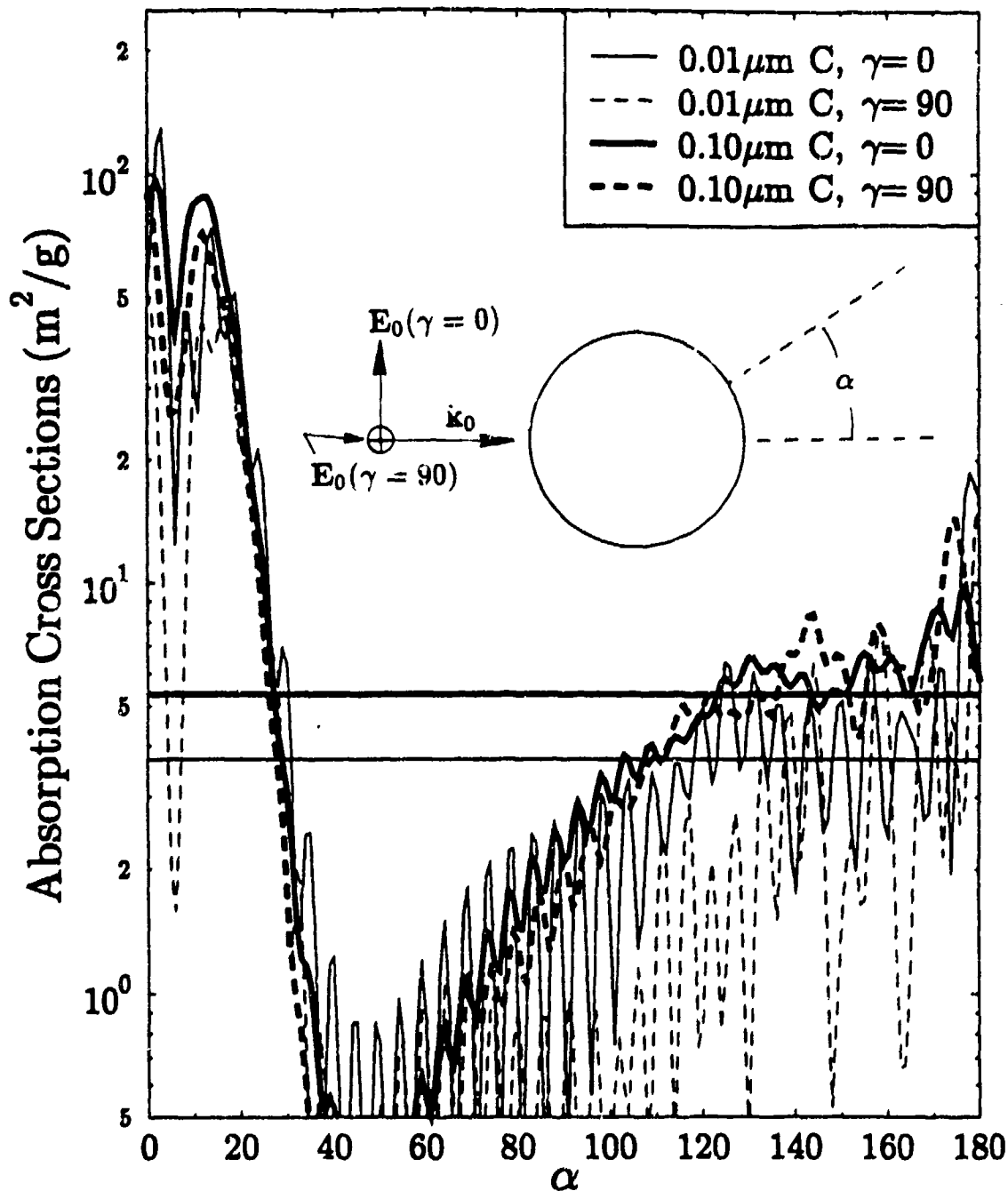


Figure 8. Same as Figure 4, but with a $3.0\mu\text{m}$ water droplet.

.05 μm C grain on 5.0 μm H₂O

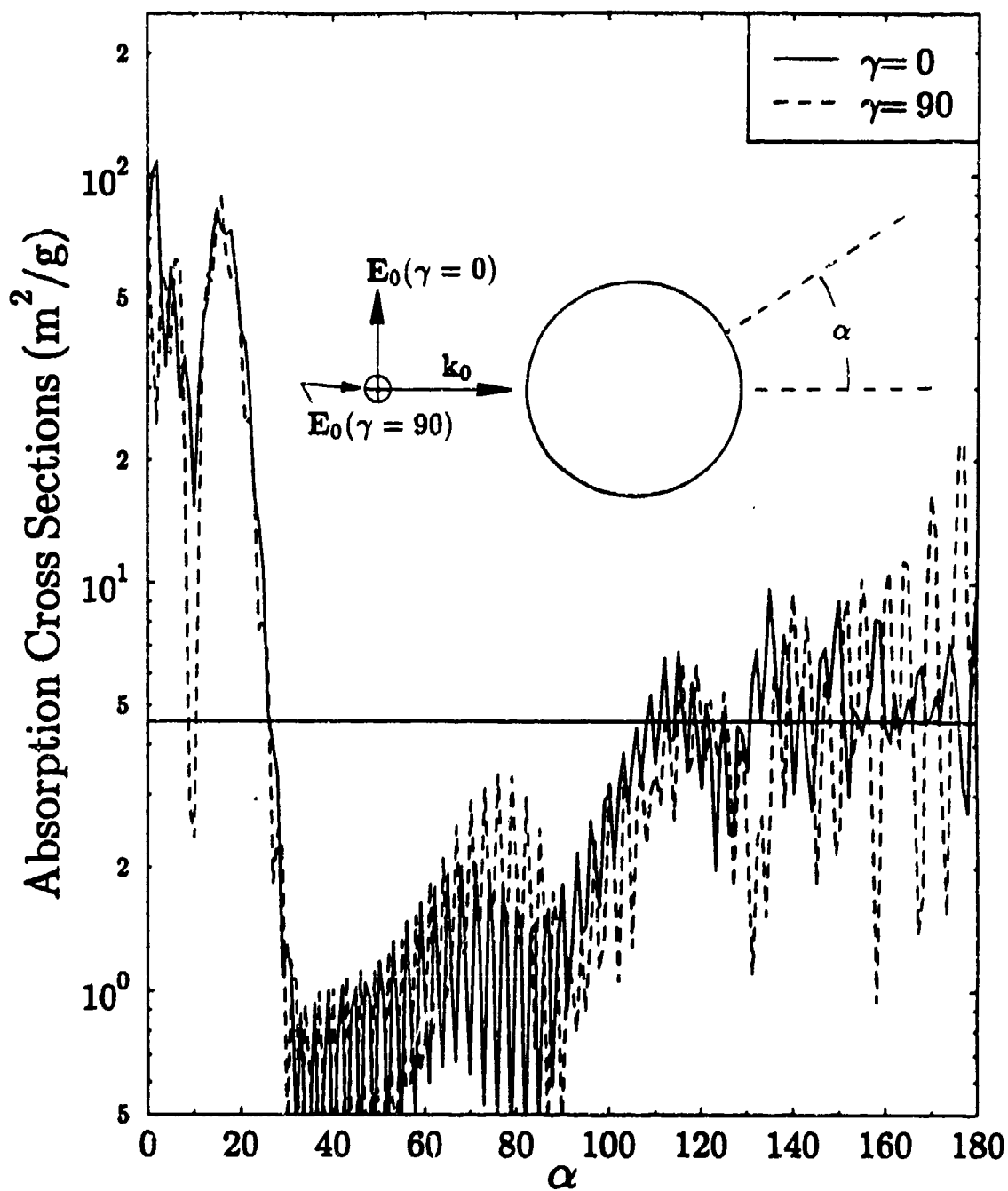


Figure 9. Same as Figure 3, but with a 5.0 μm water droplet.

C grains on $5.0\mu\text{m H}_2\text{O}$

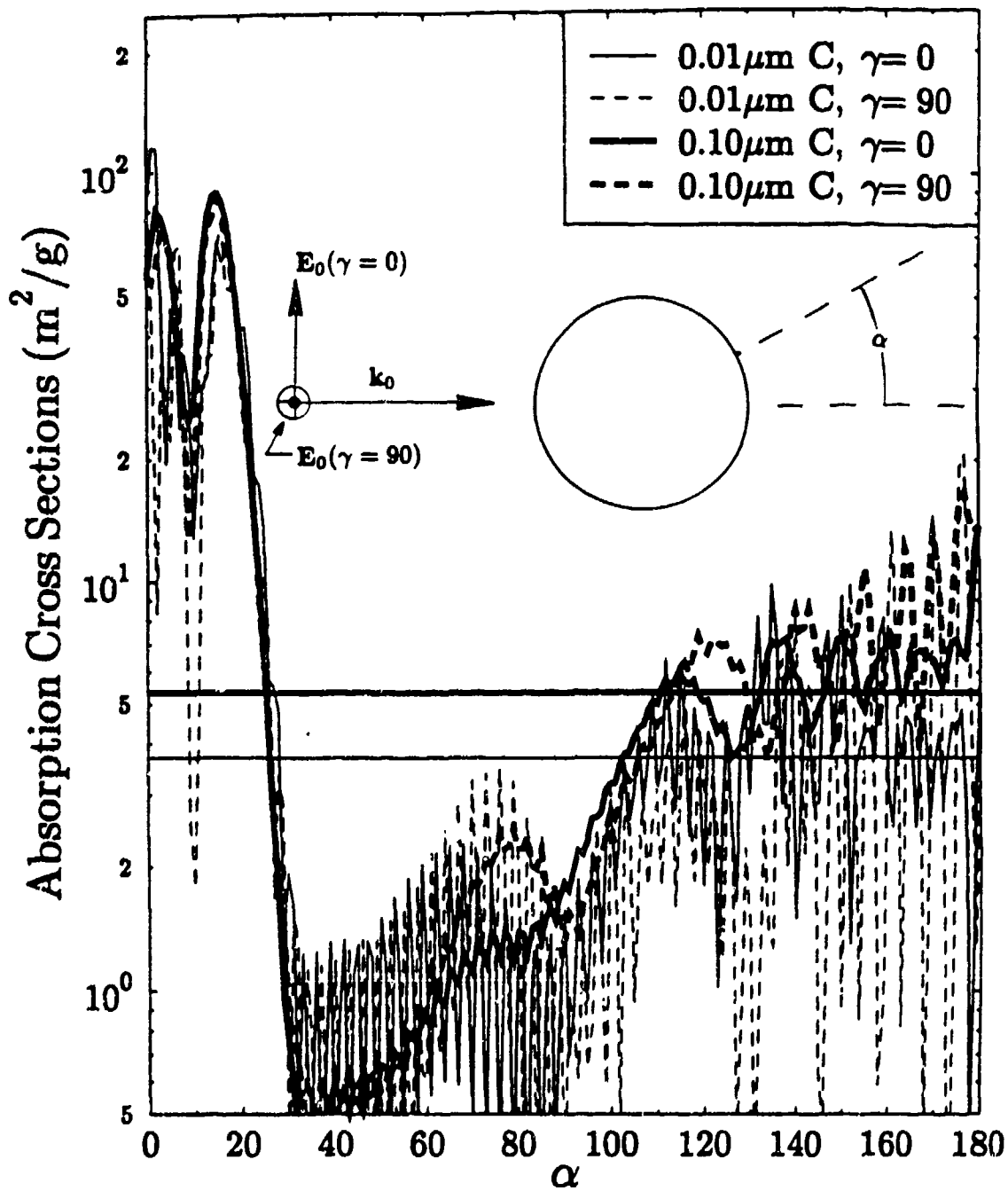


Figure 10. Same as Figure 4, but with a $5.0\mu\text{m}$ water droplet.

Table I

Orientation-averaged specific absorption cross sections of carbon grains on droplet surfaces

*** Specific Absorption of Scavenged Carbon ***

C Radius (microns)	$\gamma=0$	$\gamma=90$	
0.01	8.574244499	4.893493176	0.5 micron sulfate
0.05	7.896352768	5.202662468	
0.10	6.503396511	5.337140560	
0.01	8.816226959	2.266729116	1.0 micron sulfate
0.05	6.845155239	3.072171688	
0.10	5.319453716	4.746981621	
0.01	4.135703087	2.469252825	3.0 micron water
0.05	4.664968014	3.163699865	
0.10	5.213868141	4.424438477	
0.01	4.235696793	3.586464882	5.0 micron water
0.05	4.673493385	4.323986530	
0.10	5.013107300	5.192254543	

*** Ratio of Specific Absorption of Scavenged Carbon to Free Carbon ***

C Radius (microns)	$\gamma=0$	$\gamma=90$	$(\gamma=0 + \gamma=90) / 2$	
0.01	2.320	1.324	1.822	0.5 micron sulfate
0.05	1.730	1.140	1.435	
0.10	1.218	0.999	1.109	
0.01	2.386	0.613	1.500	1.0 micron sulfate
0.05	1.499	0.673	1.086	
0.10	0.996	0.889	0.943	
0.01	1.119	0.668	0.894	3.0 micron water
0.05	1.022	0.693	0.858	
0.10	0.976	0.828	0.902	
0.01	1.146	0.971	1.059	5.0 micron water
0.05	1.024	0.947	0.986	
0.10	0.939	0.972	0.956	

*** Specific Absorptions for Single Carbon Spheres ***

C Radius (microns)	Specific Absorption (m ² /g)
0.01	3.695
0.05	4.565
0.10	5.340

319

.05 μm C

Linear chain, 5 spheres, $ka=0.57$

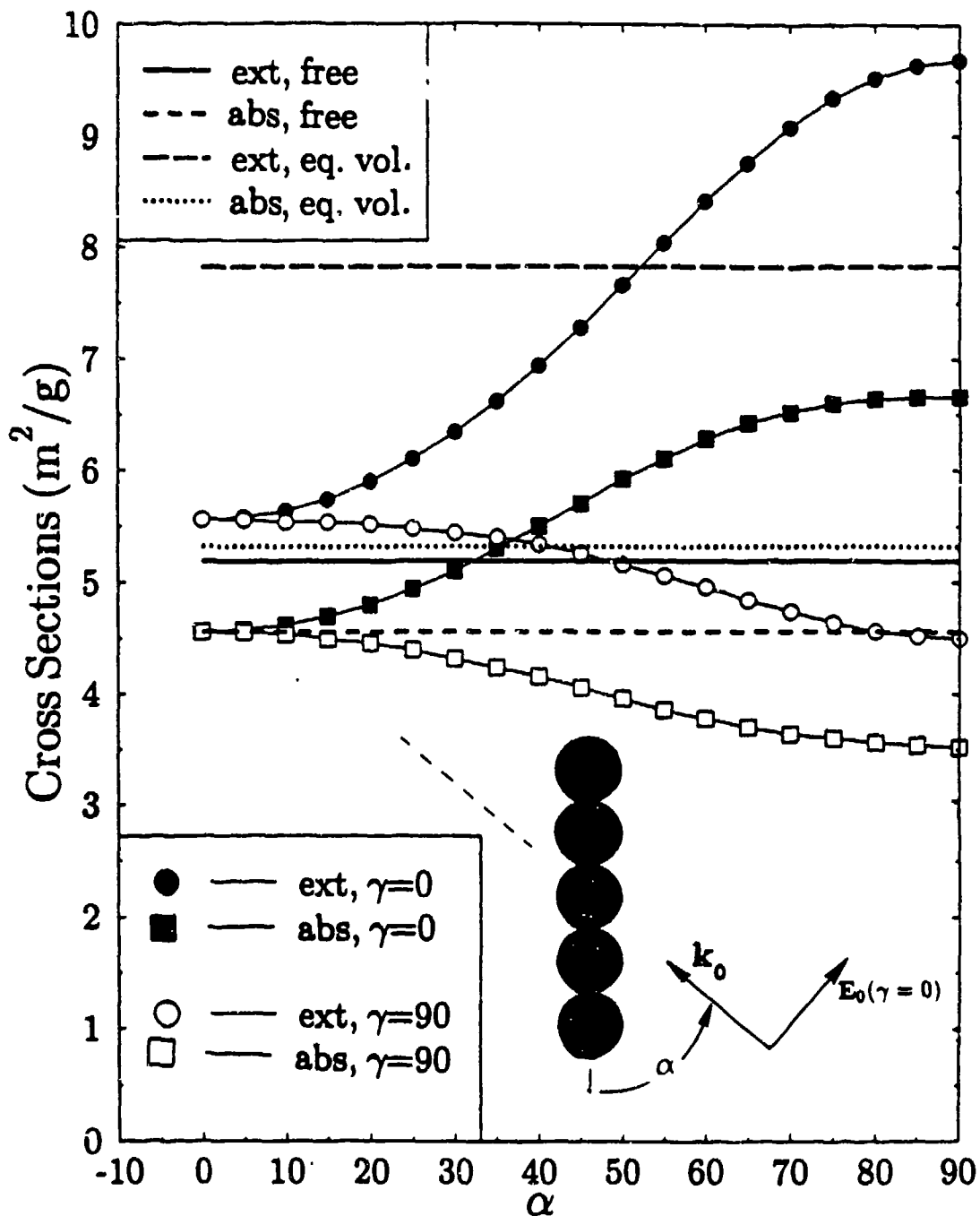


Figure 11. Extinction and absorption cross sections of a linear chain of five carbon spheres. Each of the monomers has a radius of $0.05 \mu\text{m}$ and a refractive index of $1.8 + 0.5i$.

Close-packed cluster, $ka=0.57$

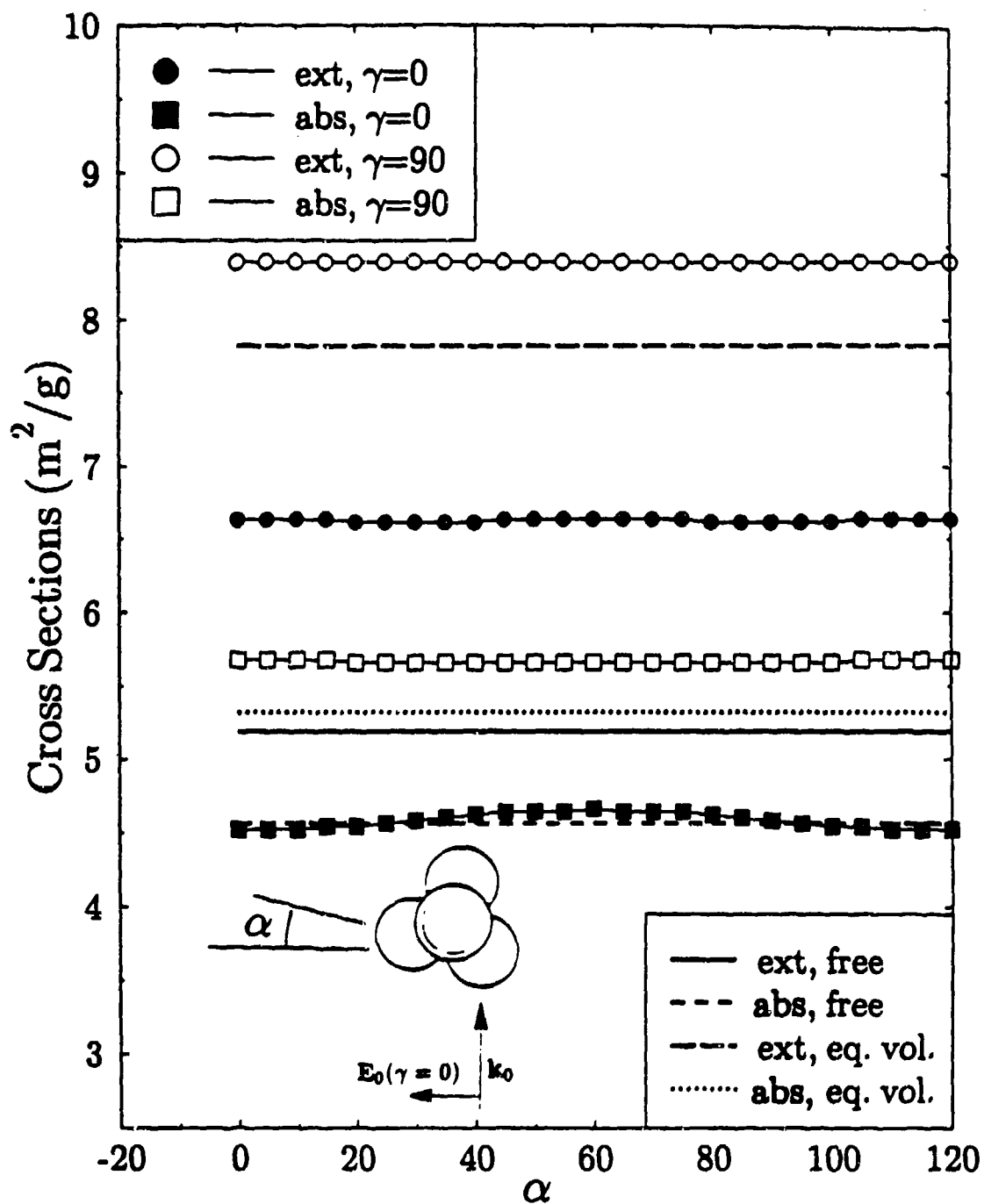


Figure 12. Same as Figure 11, but the monomers now form a close-packed hexahedron.

REFERENCES

1. C. F. Bohren and D. R. Huffman, *Absorption and Scattering of Light by Small Particles*, (John Wiley and Sons, New York, 1983).
2. C. Liang and Y. T. Lo, "Scattering by two spheres," *Radio Science* 2, 1481 (1967).
3. J. H. Bruning and Y. T. Lo, "Multiple scattering of em waves by spheres parts I & II," *IEEE Trans. Ant. Prop.* AP-19, 378 (1971), J. H Bruning and Y. T. Lo, "Multiple Scattering by Spheres," Antenna Laboratory Report No. 69-5, Antenna Laboratory, Department of Electrical Engineering, Engineering Experiment Station, University of Illinois, Urbana, Illinois.
4. S. Stein, "Addition theorems for spherical wave functions," *Quart. Appl. Math.* 19, 15 (1961).
5. O. R. Cruzan, "Translation addition theorems for spherical vector wave functions," *Quart. Appl. Math.* 20, 33 (1962).
6. K. A. Fuller, "Optical resonances and two-sphere systems," *Appl. Opt.* 30 4716-4731 (1991)
7. K. A. Fuller and G. W. Kattawar, "Consummate solution to the problem of classical electromagnetic scattering by ensembles of spheres. I: Linear Chains," *Opt. Lett.* 13, 90 (1988).
8. K. A. Fuller and G. W. Kattawar, "Consummate solution to the problem of classical electromagnetic scattering by ensembles of spheres. II: Clusters of arbitrary configuration," *Opt. Lett.* 13, 1063 (1988).
9. J. Podzimek, "Physical properties of coarse aerosol particles and haze elements in a polluted urban-marine environment," *J. Aerosol Sci.* 21, 299-308(1990).
10. M. A. Jarzembski and V. Srivastava, "Electromagnetic field enhancement in small liquid droplets using geometric optics," *Appl. Opt.* 28, 4962 (1989).
11. K. A. Fuller, "Scattering and absorption cross sections of colloidal aggregates: Part I, theory and Part II, numerical results," in preparation for submission to *J. Opt. Soc. Am. A*.

EXTINCTION AND ANGULAR SCATTERING BY ROUGH PARTICLES

Ru T. Wang

Space Astronomy Laboratory, Institute for Space Science and Technology, Inc.
Gainesville, FL 32609

RECENT PUBLICATIONS, SUBMITTALS FOR PUBLICATION AND PRESENTATIONS:

- A) H.C. van de Hulst and R.T. Wang, "Glare points," *Applied Optics* **30**, 4755-4763 (1991).
- B) R.T. Wang, "Scattering by Spheres of Narrow Size Distribution," submitted to the *Proc. of the 1991 CRDEC Scientific Conference on Obscuration and Aerosol Research*, Edgewood, MD (1991).
- C) R.T. Wang, in *Proc., 1984 CRDC Scientific Conference on Obscuration and Aerosol Research*, R. Kohl and D. Stroud, Eds. (Army CRDC-SP-85007, Aberdeen, MD, 1985).
(1): "Extinction by Rough Particles," pp. 315-326. (2): "Angular Scattering by Rough Particles," pp. 327-363.

ABSTRACT

This paper briefly summarizes the recent work on the subject title, as a continuation of the work reported in Refs. B) and C). All the 10 rough particles studied are comparable in size to the incident microwave wavelength λ ($= 3.1835$ cm), and are of 2 shapes resembling roughened spheres. The averaged scattering data over random particle orientations are compared to Mie calculations for independently scattering, size-distributed spheres of very narrow size spread. The comparison, shown both in tabulated and in graphical forms, is made on extinction and angular scattering, and also on $\overline{Q_{ext}}$, $\overline{Q_{sca}}$, $\overline{Q_{abs}}$, $\overline{Q_{pr}}$ (averaged efficiencies) and \overline{g} (averaged asymmetry factor of scattering). Aside from some minor mismatches at large scattering angles in the angular profile comparison, the good overall agreement between experiment and theory suggests the reasonableness of the theoretical modeling. This is a part of our continuing effort in the systematic analysis/catalogue of our existing microwave data.

I. INTRODUCTION

Almost all scattered light we see are from particles with rough surfaces. Scattering by very smooth particles, whose surface irregularity is very small compared to the wavelength λ of incident radiation, is rather exceptional. Not only the reflected light from a frosted glass is different from a smooth one, the reflection also depends on the glazing angle of incidence. For this, a simple ray optics rule known as the *Rayleigh Criterion* [Ref. 2] was widely employed in estimating the effective roughness of an object. This classical theory by Rayleigh, as well as most of the recent theoretical approaches [Refs. 1,7,10,11,14,18], assume that the scattering target is very large compared to λ , and few have discussed the case of moderately small sized rough particles (e. g., in the so-called *resonance* region).

Resonance-sized rough particles are abound, however, and indeed the extreme difficulty involed in solving the scattering problems led us to take an experimental approach for seeking

appropriate answers [Refs. 4,5]. We refer the detailed microwave analogue technique and the data analysis to in our earlier reports [Refs. C), 9,12,13,16] and describe in sec. II the mathematics and computational procedures for evaluating the Mie scattering by gamma-size-distributed spheres. The experiment-theory comparison is made in sec. III, and sec. IV contains the concluding discussion.

II. MIE CALCULATIONS FOR GAMMA-SIZE-DISTRIBUTED SPHERES

The gamma size distribution in this article is synonymous to the *Standard Size Distribution* by Hansen and Travis [Ref. 6], and represents a skewed Gaussian-like distribution of the sphere number density $n(x)$ as a function of the sphere size x :

$$n(x) = \text{const.} \cdot x^{(1-3b)/b} \exp\left[-\frac{x}{x_e b}\right] \quad (2.1)$$

where $x = 2\pi a/\lambda$ = sphere size parameter, b = effective variance of the distribution which gives a measure of the spread of $n(x)$ around the *effective size parameter*: $x_e = 2\pi a_e/\lambda$. a_e is the effective particle radius and corresponds to a certain mean radius of the sphere ensemble. The net scattering from the sphere ensemble is assessed by integrating the scattering contribution from each x over the particle size limits x_1 and x_2 , with $n(x)$ in Eq. (2.1) as the weighting factor.

(1) Single Sphere Mie Formulas

The needed Mie scattering functions for each x are copied from the literature [Refs. 3,8,15,17]. For example, the perpendicular and parallel components of the *complex scattering amplitudes* are:

$$S_1(x, m, \theta) = \sum_{n=1}^{n=n_{\max}} \frac{2n+1}{n(n+1)} \{a_n \pi_n(\mu) + b_n \tau_n(\mu)\} = |S_1(x, m, \theta)| \exp(i\sigma_1) \quad (2.2)$$

$$S_2(x, m, \theta) = \sum_{n=1}^{n=n_{\max}} \frac{2n+1}{n(n+1)} \{a_n \tau_n(\mu) + b_n \pi_n(\mu)\} = |S_2(x, m, \theta)| \exp(i\sigma_2) \quad (2.3)$$

where a_n, b_n = Mie expansion coefficients, with the maximum term at $n = n_{\max}$.

$$\mu = \cos\theta, \quad \pi_n(\mu) = dP_n(\mu)/d\mu, \quad \tau_n(\mu) = \mu\pi_n(\mu) - (1-\mu^2)d\pi_n(\mu)/d\mu,$$

and $P_n(\mu)$ = n -th order Legendre polynomial of μ .

The respective phase shifts suffered by the scattered wave for the two components are:

$$\varphi_1(x, m, \theta) = \pi/2 - \sigma_1(x, m, \theta) \quad (2.4)$$

$$\varphi_2(x, m, \theta) = \pi/2 - \sigma_2(x, m, \theta) \quad (2.5)$$

At the forward beam direction where $\theta = 0$, these formulas simplify to:

$$S_1(x, m, 0) = S_2(x, m, 0), \quad \text{and} \quad \varphi_1(x, m, 0) = \varphi_2(x, m, 0) \quad (2.6)$$

and the *complex extinction efficiencies* P and Q for the single sphere are found to be:

$$P = P_{ext}(x, m) = \frac{2}{x^2} \sum_{n=1}^{n=n_{max}} (2n+1) \text{Im}\{a_n + b_n\} \quad (2.7)$$

$$Q = Q_{ext}(x, m) = \frac{2}{x^2} \sum_{n=1}^{n=n_{max}} (2n+1) \text{Re}\{a_n + b_n\} \quad (2.8)$$

The perpendicular and parallel *scattering intensity components* are simply defined as

$$i_1(x, m, \theta) = |S_1(x, m, \theta)|^2 \quad (2.9)$$

$$i_2(x, m, \theta) = |S_2(x, m, \theta)|^2 \quad (2.10)$$

and similar to Eqs. (2.6), these two components are equal to each other at $\theta = 0$.

The single-sphere expressions for other efficiencies: Q_{sca} , Q_{abs} , and Q_{pr} , and also the asymmetry factor of scattering g can be written in terms of the Mie coefficients a_n , b_n alone [Refs. 3,8,15].

(2) Averaged Extinction/Scattering over the Sphere Ensemble

The complex extinction efficiency expressions for the gamma distribution are then

$$\overline{P}(x_e, m) = \int_{x_1}^{x_2} P(x, m) n(x) dx / \int_{x_1}^{x_2} n(x) dx \quad (2.11)$$

$$\overline{Q}(x_e, m) = \int_{x_1}^{x_2} Q(x, m) n(x) dx / \int_{x_1}^{x_2} n(x) dx \quad (2.12)$$

Similarly, the averaged angularscattering intensity components over the ensemble follow from Eqs. (2.9) & (2.10) as

$$I_1(x_e, m, \theta) = \int_{x_1}^{x_2} i_1(x, m, \theta) n(x) dx / \int_{x_1}^{x_2} n(x) dx \quad (2.13)$$

$$I_2(x_e, m, \theta) = \int_{x_1}^{x_2} i_2(x, m, \theta) n(x) dx / \int_{x_1}^{x_2} n(x) dx \quad (2.14)$$

The total scattering intensity for unpolarized incident light and the degree of linear polarization by the size distribution are respectively

$$S_{11} = (I_1 + I_2) / 2 \quad (2.15)$$

$$\text{Pol.} = (I_1 - I_2) / S_{11} \quad (2.16)$$

Notice that there is no cross-polarized scattering intensity component for the sphere case.

The ensemble average on other efficiencies Q_{sca} , Q_{abs} and Q_{pr} , and also on the asymmetry factor g can be evaluated, as in Eqs. (2.12)-(2.14), by taking in the proper integrands.

By virtue of the exponential dependence of $n(x)$ on x in Eq. (2.1), the integration limits x_1 and x_2 are chosen in such a way that both $n(x_1)$ and $n(x_2)$ fall off from $n(x_e)$ by 4 orders of magnitude,

thereby contributing little to the integral. The smaller the magnitude of b is, the more rapidly $n(x)$ drops off from $n(x_e)$ as x departs from x_e . The required number of divisions, n_{div} , between x_1 and x_2 for the numerical integration then decreases. For example, the value $b = 0.005$ employed in most cases represents a rather narrow size distribution so that $x_1 = 0.75x_e$ and $x_2 = 1.32x_e$. $n_{div} = 40$ was then found to give fairly good convergence for all the microwave target sizes. We took, however, $n_{div} = 160$ in this article to make sure the accuracy. Our stable and efficient Mie algorithm [Ref. 17] has allowed us to perform all computations via the 8-digit single-precision arithmetic on a VAX11/750 computer.

III. COMPARISON OF EXPERIMENT AND THEORY

Scattering from a rough particle differs strikingly from that of a smooth homogeneous sphere: the former is particle-orientation sensitive, but the latter is not. Yet, if we take the average of scattering data over all random particle orientations at each scattering angle θ , the angular pattern of the former is considerably smoother than the latter [Ref. C)]. Similar smoothing of the angular profiles seen as one goes from a single sphere to an ensemble of spheres [Ref. C)] motivated us to compare the scattering data for rough particles with Mie results for size-distributed spheres in [Refs. B) & C)], and, in a more detailed way, also in this article.

The target parameters of the 10 rough particles are listed in Table I, where the averaged microwave data over random particle orientations for each particle (marked Expt.) are compared to the sphere-ensemble-averaged data (marked Mie.). The microwave targets consist of two refractive-index groups: $m = 1.610 - i0.004$ (made of plexiglass) and $m = 1.36 - i0.005$ (made of expanded polystyrene). They were prepared either by machining or by molding into two shapes (see Table I inset) resembling roughened spheres but retaining certain cylindrical rotational symmetries.

The technical matters related to averaging the microwave data over random particle orientations were explained in Ref. C). Despite the microwave data were accumulated on a large number of scattering angles (plus ≈ 44 orientations at each angle), we had to skip the data taking at some non-important angles due to the time constraints. In evaluating \bar{g} , e. g., these missed data were filled in by the Lagrange-Aitken cubic spline technique. To compute the Mie data average over the size-distributed spheres, the mean radius of the ensemble x_e , Eq. (2.1), was taken equal to x , the size parameter of the corresponding rough-particle's equal-volume sphere.

The comparison in Table I is made on $\overline{Q_{ext}}$, $\overline{Q_{sca}}$, $\overline{Q_{abr}}$, and $\overline{Q_{pr}}$ (the averaged extinction, scattering, absorption and radiation pressure efficiencies); and also on \bar{g} , the averaged asymmetry factor of angular scattering. Except for the $\overline{Q_{abr}}$ comparison where the smallness of the imaginary part of refractive index results in measurement precision uncertainty, the agreement between experiment and theory is fairly close. The closest match is seen in the $\overline{Q_{ext}}$ and \bar{g} comparisons, which are also displayed in Figs. 1 & 2, respectively. For the Mie curves in Fig. 1, the effect of

the effective variance of the distribution, b , on $\overline{Q_{ext}}$ is shown for several values of b , from which we deduce that $b = 0.005$ appears to give the best fit.

Fig. 3 compares the detailed angular scattering profiles by experiment and theory, and is to supplement the similar comparisons made in Refs. B) and C). I_{11} and I_{22} denote respectively the scattering intensity when both the transmitter and receiver are vertically or horizontally polarized. S_{11} stands for the total scattering intensity for unpolarized incident wave, and Pol. is for the degree of linear polarization. Among the three values of b in Fig 3, $b = 0.005$ again seems to give the closest agreement between experiment and theory. The scattering intensity comparison is excellent at the forward angles, $\theta \leq 50^\circ$, where most of the scattering energy is directed. Indeed, the scattering in this angular range is the most dominant one in determining $\overline{Q_{ext}}$ and \bar{g} , and hence explains why the experiment & theory agreed best on these two quantities.

IV. CONCLUSION

We summarize below the findings on extinction & angular scattering by a *roughened-sphere-like particle whose volume-equivalent-sphere size is near the first resonance peak in extinction*:

- (1) The particle volume, rather than the particle surface area, controls the scattering.
- (2) Both the extinction and angular scattering depend on the particle orientation in the beam, but if the averages are taken over the random orientations, the patterns can be qualitatively predicted using Mie theory for the equal-volume sphere with same refractive index.
- (3) Further improvement on (2) is possible via averaging the Mie data over a gamma-size-distributed spheres whose effective mean size x_e is equal to the volume-equivalent size parameter of the rough particle, and whose effective variance of distribution is:
 $b \approx 0.005$. Quantitatively good experiment-theory agreements are then obtained, particularly on $\overline{Q_{ext}}$ and on \bar{g} .

Schade and Smith's work [Ref. 11] also agrees with our conclusions (2) & (3), in that they modeled by an ensemble of noninteracting spheres. Mukai and Mukai's scattering evaluation on *fine and coarse regoliths* [Ref. 14] also treat a *coarse regolith* as made of an independently scattering ensemble of spheres.

ACKNOWLEDGMENT

The author is indebted to Prof. J. M. Greenberg for the pioneering idea of modeling rough particles. He also thanks Drs. T. Mukai & S. Mukai for their recent reprints. Special thanks are due to Army Research Office, under whose contract to Univ. of Florida we were able to perform the experimental measurements.

REFERENCES

1. E. Bahar and M. A. Fitzwater, (1): "Enhancement of Backscattered Diffuse Specific Intensities from Random Distributions of Finitely Conducting Particles with Rough Surfaces," *J. Opt. Soc. Am. A-5*, 89-98 (1988); (2): "Depolarization and Backscatter Enhancement in Light Scattering from Random Rough Surfaces: Comparison of Full-Wave Theory with Experiment," *J. Opt. Soc. Am. A-6*, 33-43 (1989).
2. P. Beckmann and A. Spizzichino, *The Scattering of Electromagnetic Waves from Rough Surfaces*, Vol. 4 of the series on *Electromagnetic Waves*, V.A. Fock and J.R. Wait, Eds. (Pergamon-MacMillan, New York, 1963).
3. C.F. Bohren and D.R. Huffman, *Absorption and Scattering of Light by Small Particles*, (Wiley, New York, 1983).
4. J.M. Greenberg, R.T. Wang and L. Bangs, "Extinction by Rough Particles and the Use of Mie Theory," *Nature, Phys. Sci.* 230,110-112 (29 Mar. 1971).
5. J.M. Greenberg, "Interstellar Dust," in *Cosmic Dust*, J.A.M. McDonnell, Ed., (Wiley, New York, 1978), pp 187-294.
6. J.E. Hansen and L.D. Travis, "Light Scattering in Planetary Atmospheres," *Space Sci. Rev.* 16, 527-610(1974).
7. D.L. Jaggard and X. Sun, "Fractal surface scattering: A generalized Rayleigh solution," *J. Appl. Phys.* 68, 5456-5462 (1990).
8. M. Kerker, *The Scattering of Light and Other Electromagnetic Radiation* (Academic, New York, 1969).
9. A.C. Lind, R.T. Wang and J.M. Greenberg, "Microwave Scattering by Nonspherical Particles," *Appl. Opt.* 4, 1555-1561 (1965).
10. J. Peltoniemi, K. Lumme, K. Muinonen and W.M. Irvine, "Scattering of Light by Stochastically Rough Surfaces," *Appl. Opt.* 28, 4088-4095 (1989).
11. H. Schade and Z.E. Smith, "Mie Scattering and Rough Surfaces," *Appl. Opt.* 24, 3221-3226 (1985).
12. D.W. Schuerman, *Light Scattering by Irregularly Shaped Particles* (Plenum, New York, 1980).
13. D.W. Schuerman, R.T. Wang, B.A.S. Gustafson and R.W. Schaefer, "Systematic Study of Light Scattering: 1. Particle Shape," *Appl. Opt.* 20, 4039-4050 (1981).
14. T. Mukai and S. Mukai, (1): "Surface Albedo of Cometary Nucleus," *Adv. Space Res. (GB)* 9, (3)77-(3)80 (1989); (2): "Light Scattering by Rough Surfaces on Asteroidal/Lunar Regoliths," *Adv. Space Res. (GB)* 11, (12)137-(12)140 (1991).
15. H.C. van de Hulst, *Light Scattering by Small Particles*, (Wiley, New York, 1957; and Dover, New York, 1981).
16. R.T. Wang, "Status of the Microwave Scattering Facility (MSF) Upgrade," in *Proc., 1987 Scientific Conference on Obscuration and Aerosol Research*, Compiled by E.H. Engquist and K.A. Sitek, (Army CRDEC-SP-88031, Edgewood, MD, 1988) pp 323-339.
17. R.T. Wang and H.C. van de Hulst, "Rainbows: Mie Computations and the Airy Approximation," *Appl. Opt.* 30, 106-117 (1991).
18. M. Wolff, "Polarization of Light Reflected from Rough Planetary Surface," *Appl. Opt.* 15, 1395-1405 (1976).

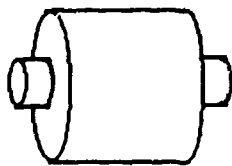
Table I

Averaged efficiencies $\overline{Q_{ext}}, \overline{Q_{sca}}, \overline{Q_{abs}}, \overline{Q_{pr}}$ and the asymmetry factor

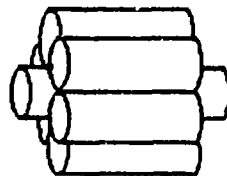
\overline{g} over random orientations of the 10 rough particles. The microwave data are compared with Mie calculations for gamma-size-distributed spheres around the equal-volume sphere of each particle, with an effective variance $b=0.005$.

ID	Target Shape	x	$m=m'-im''$	Data Source	$\overline{Q_{ext}}$	$\overline{Q_{sca}}$	$\overline{Q_{abs}}$	$\overline{Q_{pr}}$	\overline{g}
1	A	3.650	1.610- <i>i</i> 0.004	Expt.	3.78	3.58	0.208	1.32	0.690
				Mie	4.234	4.152	0.0818	1.373	0.6890
2	A	5.499	1.610- <i>i</i> 0.004	Expt.	2.51	2.04	0.476	1.48	0.506
				Mie	2.352	2.223	0.1284	1.287	0.4791
3	A	7.346	1.610- <i>i</i> 0.004	Expt.	2.49	2.13	0.358	1.20	0.604
				Mie	2.276	2.108	0.1690	1.013	0.5996
4	A	8.626	1.610- <i>i</i> 0.004	Expt.	2.89	2.56	0.334	1.13	0.689
				Mie	2.842	2.650	0.1918	0.8784	0.7409
5	A	3.592	1.256- <i>i</i> 0.003	Expt.	1.65	1.66	-0.01	0.340	0.788
				Mie	1.519	1.479	0.0394	0.2926	0.8288
6	A	5.184	1.388- <i>i</i> 0.005	Expt.	3.90	3.85	0.050	0.754	0.817
				Mie	3.918	3.804	0.1142	0.7996	0.8198
7	B	4.257	1.366- <i>i</i> 0.005	Expt.	3.22	3.02	0.192	0.636	0.853
				Mie	3.347	3.257	0.0900	0.6599	0.8250
8	B	6.069	1.367- <i>i</i> 0.005	Expt.	3.96	3.40	0.563	1.09	0.845
				Mie	3.840	3.709	0.1308	0.7768	0.8258
9	B	7.694	1.360- <i>i</i> 0.005	Expt.	3.43	2.95	0.476	1.09	0.791
				Mie	3.136	2.971	0.1644	0.8000	0.7861
10	B	12.882	1.353- <i>i</i> 0.005	Expt.	2.34	1.64	0.701	1.24	0.670
				Mie	2.232	1.970	0.2621	0.7463	0.7542

Note: x here denotes the volume-equivalent size parameter.



Shape A



Shape B

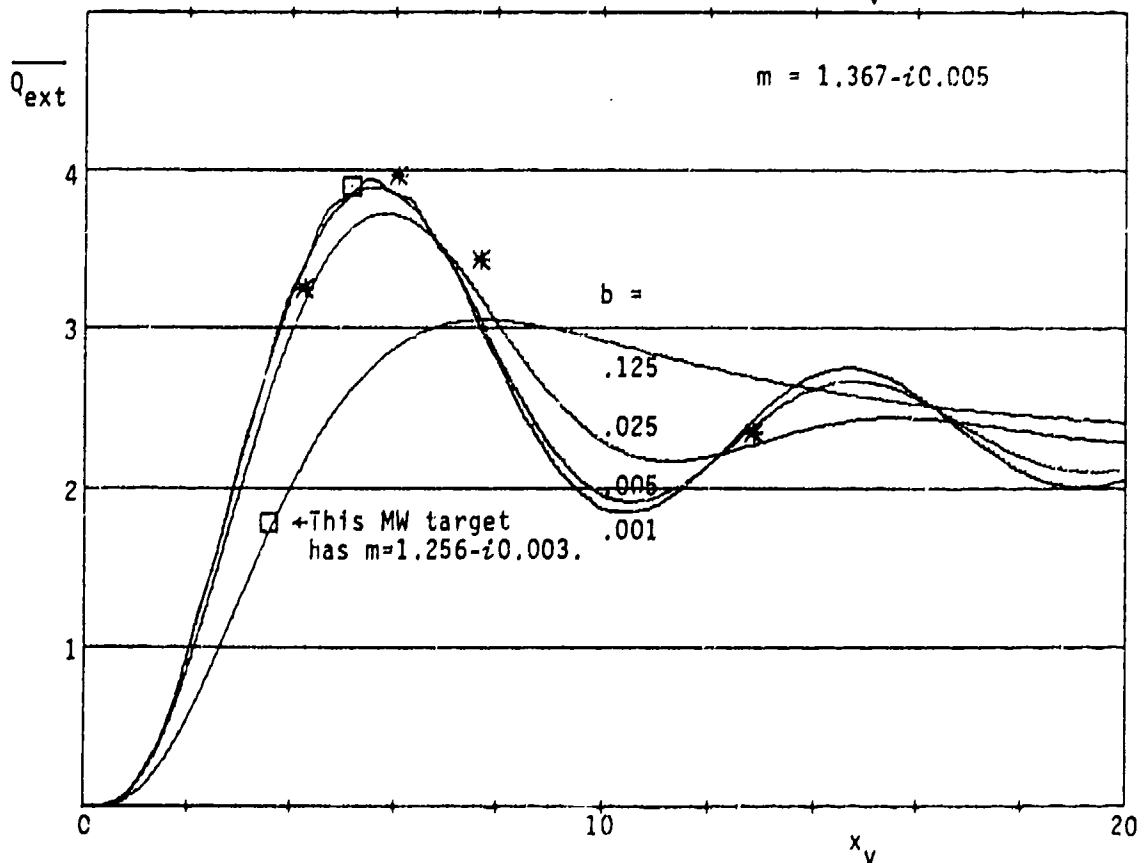
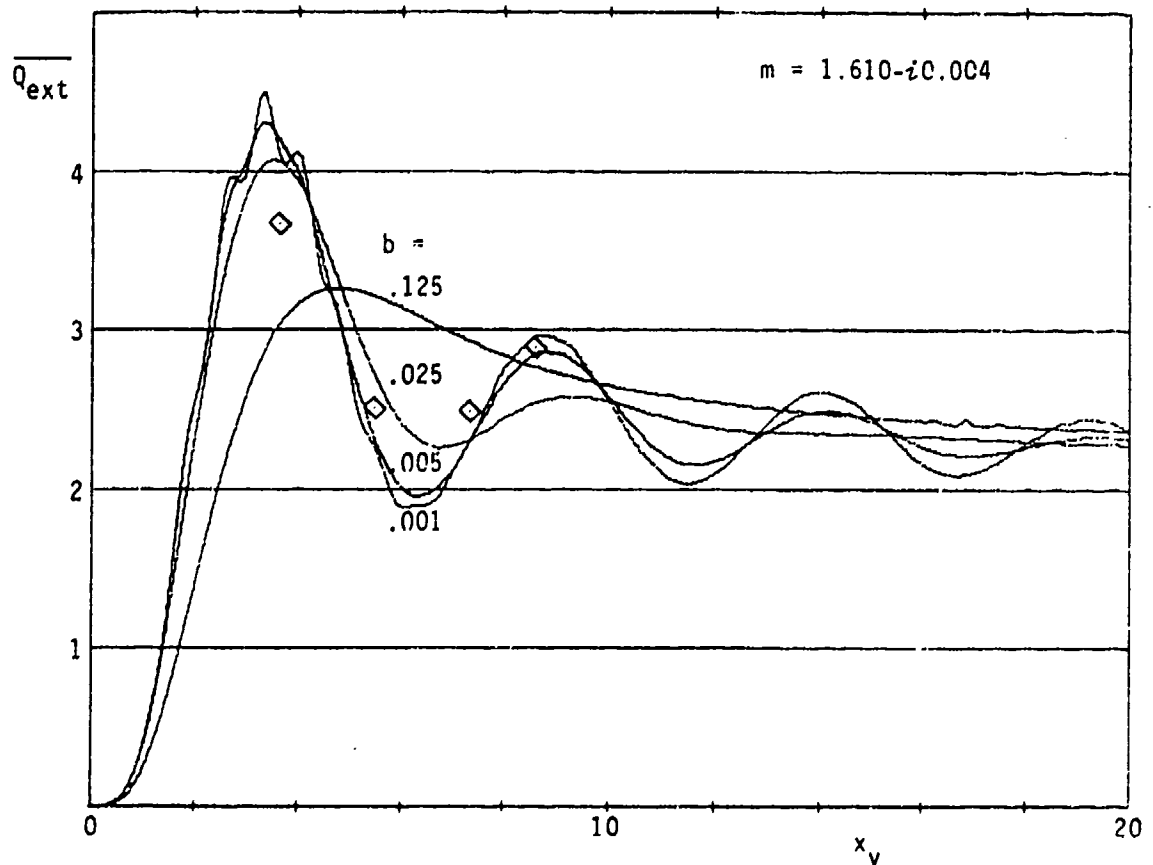


Figure 1 Extinction Efficiency $\overline{Q_{ext}}$ vs Volume-Equivalent Size Parameter x_v . The microwave data (symbols) are the averaged data over random orientations of each rough particle. Curves show the averaged Mie data over gamma-size-distributed spheres, several values of the effective variance b employed for the distributions are as shown.

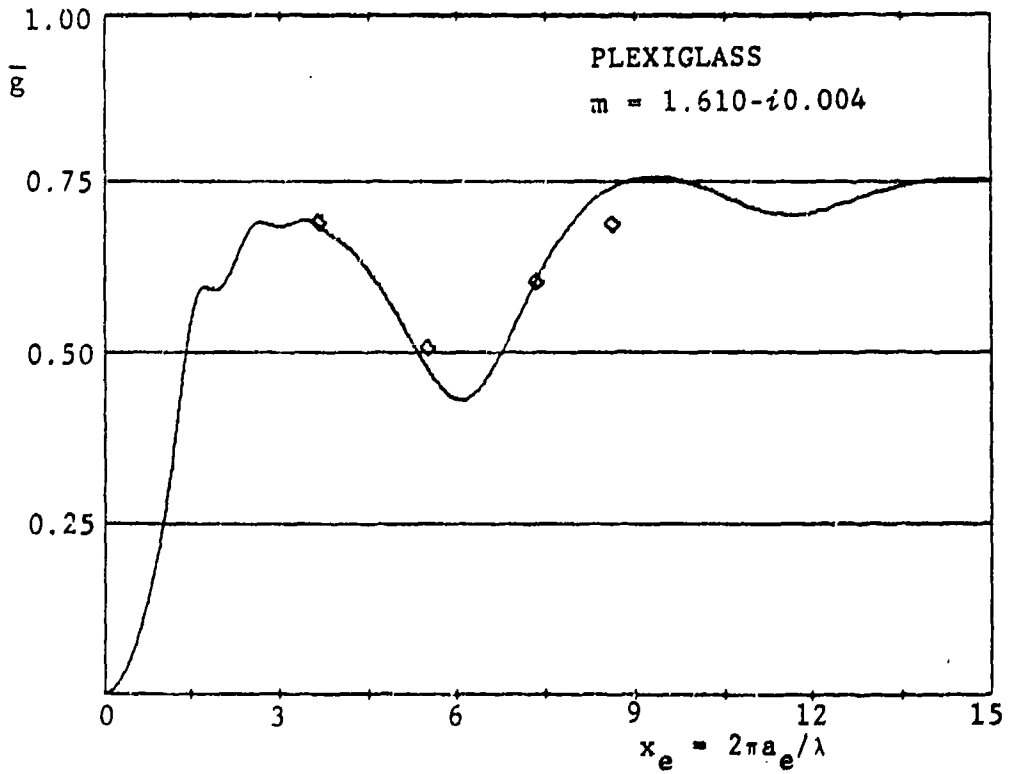
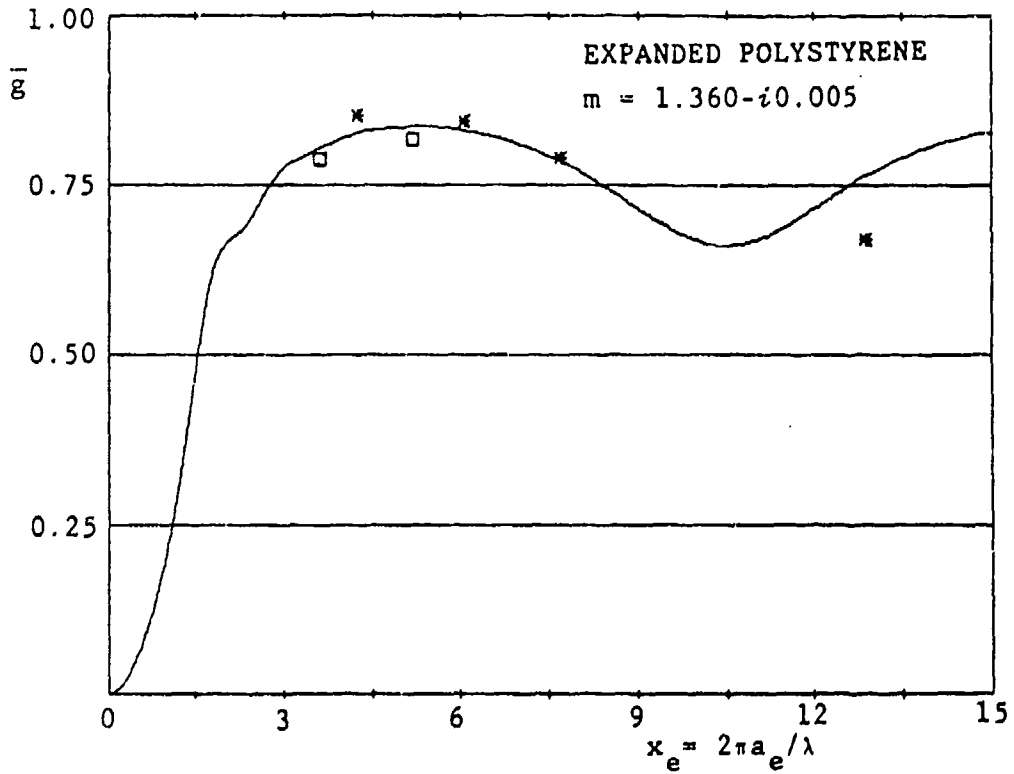


Figure 2 Asymmetry Factor \bar{g} vs Volume-Equivalent Size Parameter x_v
 The microwave data (symbols) are the averaged data over random orientations of each rough particle. Curves are the averaged Mie data over a gamma-size-distributed ensemble of spheres, whose effective variance of distribution is $b = 0.005$.

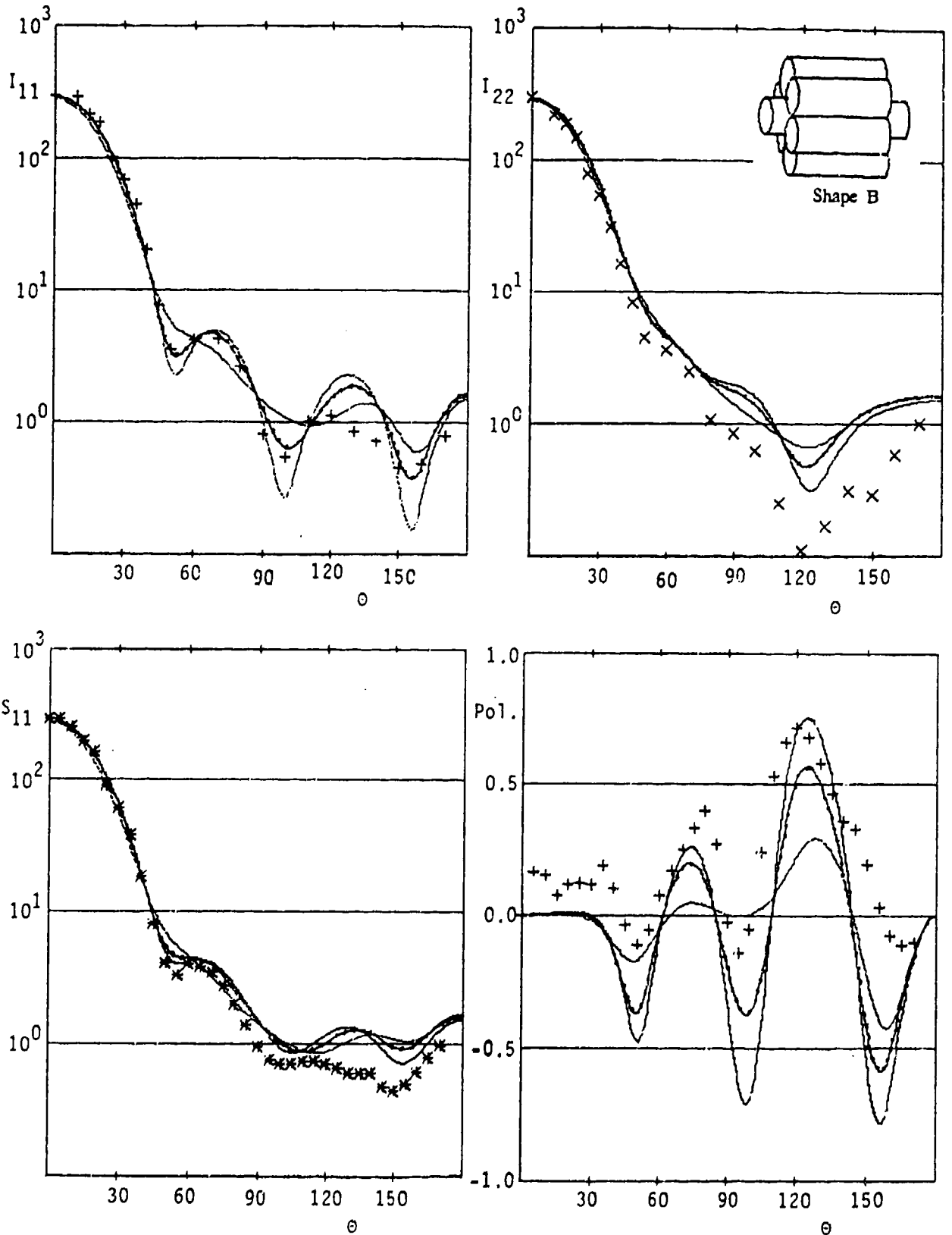


Figure 3 Microwave Angular Scattering Data (symbols) Averaged Over Random Orientations of a Rough Particle with $x = 4.257$ and $m = 1.366 - i0.005$. Curves show the averaged Mie data over gamma-size-distributed spheres. 3 effective variances of the distributions are employed: $b = 0.001$, $b = 0.005$ (marked as ----) and $b = 0.025$.

A THEORY OF HEATING OF VOIGT SOLIDS AND FLUIDS BY EXTERNAL ENERGY SOURCES AND FLAME THEORY

D. K. Cohoon
43 Skyline
Glen Mills, PA 19342

September 3, 1992

The purpose of this paper is to develop both (i) a theory of laser stimulated vaporization of droplets and (ii) a theory of internal heating resulting from vibration waves in linearly responding elastic material, and (iii) flame theory. There are applications to sending information through clouds on laser beams and to the control of temperature in ultrasonic welding, and improvement of the design of aircraft engines and the processes used for the destruction of toxic chemicals.

We develop a theory of thermal excursions resulting from ultrasonic welding in 3 and 7 dimensions, and interpret it as an elastic interaction with damping in a Voigt solid. It is hypothesized that with good control of temperature, one could achieve strong and uniform welds by this process and greatly reduce the cost of manufacture of aircraft, and other aluminum structures. We consider equations describing the conservation of mass, momentum, and energy coupled by an equation of state, and consider general mass, momentum, and energy transfer relationships in a compressible body subjected to external stimuli. For the Voigt solid theory, a linear elastic theory with damping forces, we show how some simple local time averaging gives us a dovetailed system consisting of the elastic wave equations whose solution provides the source term for an otherwise uncoupled heat equation. For the more general theory of droplet vaporization we illustrate a general nonlinear energy equation which includes a radiation energy conductivity term. We get a class of exact solutions for a nonlinear flame front boundary value problem.

Contents

- 1 INTRODUCTION
- 1.1 Vector Analysis

- 1.2 External Energy Sources
- 2 Mass Transfer
 - 2.1 Continuity Equation
- 3 Momentum Equations
 - 3.1 Voigt Solid Momentum Conservation
 - 3.2 Generalized Navier Stokes Equations
- 4 Energy Conservation
 - 4.1 A Heat Equation for Voigt Solids
 - 4.2 Droplet Explosion by Lasers
 - 4.3 EQUATION OF STATE
- 5 SUMMARY
- 6 FLAME THEORY
 - 6.1 Multicomponent Diffusion
 - 6.2 Conservation of Species and Energy
 - 6.3 Cylinder Flame Front Models and Homotopy

References

1 INTRODUCTION

We use this concept of a material derivative and fluxes of mass, momentum, kinetic energy, internal energy, temperature, and radiation to express the conservation of mass, momentum, and energy in a Voigt solid that is stimulated by an elastic wave energy source. Initially there are more dependent variables than there are equations. However, these equations are coupled by an equation of state which enables one to develop a semigroup formulation which will predict pressure, density, velocity, and temperature distributions in the interior of the stimulated solid. Local time averaging gives us a heat equation with an elastic energy source term.

1.1 Vector Analysis

The material derivative of a function f is defined by

$$\frac{Df}{Dt} = \frac{\partial f}{\partial t} + \frac{\partial f}{\partial x} \frac{\partial x}{\partial t} + \frac{\partial f}{\partial y} \frac{\partial y}{\partial t} + \frac{\partial f}{\partial z} \frac{\partial z}{\partial t} \quad (1.1.1)$$

Thus, the material derivative is, if we define,

$$\vec{v} = \frac{\partial x}{\partial t} \vec{e}_x + \frac{\partial y}{\partial t} \vec{e}_y + \frac{\partial z}{\partial t} \vec{e}_z \quad (1.1.2)$$

given by

$$\frac{D}{Dt} = \frac{\partial}{\partial t} + (\vec{v} \cdot \text{grad}) \quad (1.1.3)$$

where \vec{v} is the velocity of a point in the fluid.

1.2 External Energy Sources

Thermal energy is transferred by conductivity and internal radiation as well as radiation from the surface. We assume that the elastic material is electromagnetically polyanisotropic, a material more general than a bianisotropic material. The nonlinear Faraday Maxwell equation is given by

$$\text{curl}(\vec{E}) = \mathcal{F} \left(\vec{E}, \vec{H}, \dots, \left(\frac{\partial}{\partial t} \right)^k \vec{E}, \left(\frac{\partial}{\partial t} \right)^k \vec{H}, \dots \right) \quad (1.2.1)$$

while the nonlinear Ampere Maxwell equation has the form

$$\text{curl}(\vec{H}) = \mathcal{G} \left(\vec{E}, \vec{H}, \dots, \left(\frac{\partial}{\partial t} \right)^k \vec{E}, \left(\frac{\partial}{\partial t} \right)^k \vec{H}, \dots \right) \quad (1.2.2)$$

For a general material where we have continuity of tangential components of \vec{E} and \vec{H} across the boundary separating regions of continuity of electromagnetic properties the radiation source term is

$$\left(\frac{\partial}{\partial t} \right) Q_{in} = (1/2) \text{Re}(\text{div}(\vec{E} \times \vec{H}^*)) \quad (1.2.3)$$

The radiation source term which provides a thermal energy is for a linearly responding material given by

$$\begin{aligned} \left(\frac{\partial}{\partial t} \right) Q_{in} = & \\ & (1/2) \text{Re} \left\{ \vec{E}^* \cdot (i\omega \bar{\epsilon} + \bar{\sigma}) \vec{E} + \vec{E} \cdot \bar{\alpha} \vec{H}^* - \right. \\ & \left. \vec{H} \cdot (i\omega \bar{\mu} \vec{H}^*) + \vec{H} \cdot (\bar{\beta} \vec{E}^*) + \right. \\ & \left. \chi_{\partial\Omega}(\tau) \sigma_s |\vec{E}_{\text{tangential}}|^2 \right\} \quad (1.2.4) \end{aligned}$$

where if $\partial\Omega$ is the surface containing the impedance sheet, then

$$\int_{\Omega} \chi_{\partial\Omega} \sigma_s |\vec{E}_{\text{tangential}}|^2 dv = \int_{\partial\Omega} \sigma_s |\vec{E}_{\text{tangential}}|^2 dA \quad (1.2.5)$$

defines the characteristic function $\chi_{\partial\Omega}$ of the surface supporting the impedance sheet, ϵ is the permittivity, μ is the permeability, σ denotes conductivity, and $\bar{\alpha}$ and $\bar{\beta}$ are coupling tensors which appear in the linear Faraday and Ampere Maxwell equations, respectively.

Another internal source term is the Voigt solid damping term contribution which will be derived in the sections which follow. Another source of heat is the friction of a mechanical vibrator on the surface of the aluminum.

2 Mass Transfer

We consider that through melting or movement of a fluid that matter can flow across the boundary of a surface or that, in the case of an elastic medium, that it cannot, and examine the consequences and mathematical representation of these assumptions.

2.1 Continuity Equation

Assuming that in the Voigt solid or liquid interior that the rate at which mass is created or destroyed is given by Q_M and that the flux of mass across a surface is given by $\rho\vec{v}$ we see that

$$\frac{\partial\rho}{\partial t} + \text{div}(\rho\vec{v}) = Q_M \quad (2.1.1)$$

or if $Q_M = 0$ that

$$\text{div}(\rho\vec{v}) = -\frac{\partial\rho}{\partial t} \quad (2.1.2)$$

3 Momentum Equations

We examine the consequences of momentum conservation for the Voigt solid and for liquids permitting the derivation of generalizations of the elastic wave equations and the Navier Stokes equations.

3.1 Voigt Solid Momentum Conservation

In this section we derive the conservation of momentum by equating the rate of change of momentum to the work done by the fluid pressure and the viscous forces and the body forces and the flux of momentum across the boundaries of test volumes. We define the velocity as

$$\vec{v} = u\vec{e}_x + v\vec{e}_y + w\vec{e}_z \quad (3.1.1)$$

An important identity involving the dyadic product of two vectors \vec{A} and \vec{B} is

$$\text{div}(\vec{A}\vec{B}) = \text{div}(\vec{A})\vec{B} + (\vec{A} \cdot \text{grad})\vec{B} \quad (3.1.2)$$

Another important quantity is the tensor or dyadic quantity obtained by taking the gradient of a vector field given by

$$\text{grad}(\vec{A}) = \sum_{i=1}^n \left(\frac{\partial A_j}{\partial x_i} \right) \vec{e}_i \vec{e}_j \quad (3.1.3)$$

Using equation (3.1.3) we define the symmetric strain tensor in terms of the displacement \vec{U} of a point of a solid from its equilibrium position as

$$\bar{\epsilon} = \frac{\text{grad}(\vec{U}) + \text{grad}(\vec{U})^t}{2}$$

$$= \sum_{i=1}^n \sum_{j=1}^n \left(\frac{1}{2}\right) \left(\frac{\partial U_j}{\partial x_i} + \frac{\partial U_i}{\partial x_j}\right) \bar{e}_i \bar{e}_j \quad (3.1.4)$$

and cubical dilatation θ is given by

$$\theta = \text{div}(\bar{U}) = \sum_{i=1}^n \left(\frac{\partial U_i}{\partial x_i}\right) \quad (3.1.5)$$

The Voigt solid elastic stress tensor is defined by

$$\bar{S} = 2 \cdot \mu \bar{e} + \lambda \theta \bar{I} + 2 \cdot \bar{\mu} \frac{\partial \bar{e}}{\partial t} + \bar{\lambda} \frac{\partial \theta}{\partial t} \bar{I} \quad (3.1.6)$$

where

$$\bar{I} = \sum_{i=1}^n \sum_{j=1}^n (\delta_{(i,j)} \bar{e}_i \bar{e}_j) \quad (3.1.7)$$

If \bar{F} is the force per unit mass, and ρ is the mass per unit volume, then the generalized equations of elasticity for a stress tensor \bar{S} by Newton's force is equal to mass times acceleration law, or

$$\rho \frac{\partial^2 \bar{U}}{\partial t^2} = \rho \bar{F} + \text{div}(\bar{S}) \quad (3.1.8)$$

When the stress tensor \bar{S} is given by the Voigt solid relationship (3.1.6)

$$\rho \frac{\partial^2 \bar{U}}{\partial t^2} = \rho \bar{F} + (\lambda + \mu) \text{grad}(\theta) + \mu \Delta \bar{U} + (\bar{\lambda} + \bar{\mu}) \frac{\partial}{\partial t} \text{grad}(\theta) + \bar{\mu} \Delta \frac{\partial \bar{U}}{\partial t} \quad (3.1.9)$$

where in Cartesian coordinates the Laplacian Δ is defined by

$$\Delta \bar{U} = \left(\frac{\partial^2}{\partial x_1^2} + \frac{\partial^2}{\partial x_2^2} + \dots + \frac{\partial^2}{\partial x_n^2} \right) \bar{U} \quad (3.1.10)$$

When the material through which the elastic wave is propagating is three or seven dimensional, the displacement vector \bar{U} is necessarily a curl plus a gradient given by

$$\bar{U} = \text{grad}(\phi) + \text{curl}(\bar{\psi}) \quad (3.1.11)$$

This is true for any C^∞ function defined on an open set in \mathbb{R}^n with values in \mathbb{C}^n for n equal to three or seven, and can be seen from the following lemma ([19]).

Lemma 3.1 *If n is three or seven, then for every open set Ω in \mathbb{R}^n and for every vector field \bar{F} in $C^\infty(\Omega, \mathbb{C}^n)$ there is a vector field \bar{G} in the same space such that*

$$\bar{F} = \text{grad}(\text{div}(\bar{G})) + \text{curl}(\text{curl}(-\bar{G})) \quad (3.1.12)$$

where if n is equal to seven the curl is defined by the rule,

$$\begin{aligned} \text{curl}(\vec{E}) = & \\ & \sum_{i=1}^7 \left[\left(\frac{\partial E_{i+3}}{\partial x_{i+1}} - \frac{\partial E_{i+1}}{\partial x_{i+3}} \right) + \right. \\ & \left. \left(\frac{\partial E_{i+6}}{\partial x_{i+2}} - \frac{\partial E_{i+2}}{\partial x_{i+6}} \right) + \left(\frac{\partial E_{i+5}}{\partial x_{i+4}} - \frac{\partial E_{i+4}}{\partial x_{i+5}} \right) \right] \vec{e}_i \end{aligned} \quad (3.1.13)$$

where \vec{e}_i is the unit vector in the direction of the i th coordinate axis in 7 dimensional space and

$$E_{i+7} = E_i \quad (3.1.14)$$

If we then substitute equation (3.1.11) and equation (3.1.5) into (3.1.9) we deduce that

$$\begin{aligned} \text{grad} \left(\rho \frac{\partial^2 \phi}{\partial t^2} - (\lambda + 2\mu)\Delta\phi - (\bar{\lambda} + 2\bar{\mu})\Delta \frac{\partial \phi}{\partial t} \right) \\ = \text{curl} \left(\mu\Delta\vec{\psi} + \bar{\mu}\Delta \frac{\partial \vec{\psi}}{\partial t} - \rho \frac{\partial^2 \vec{\psi}}{\partial t^2} \right) \end{aligned} \quad (3.1.15)$$

where Δ is defined by (3.1.10). If we take the dot product of both sides of equation (3.1.15) with the gradient of any test function P with compact support and integrate over an open set containing the support of this test function, then the curl term disappears, since the curl of a gradient is the zero vector. We get two wave equations with damping terms and different wave speeds satisfied by ϕ and ψ . The ϕ wave equation is

$$\rho \frac{\partial^2 \phi}{\partial t^2} = (\lambda + 2\nu)\Delta\phi - (\bar{\lambda} + 2\bar{\mu})\Delta \frac{\partial \phi}{\partial t} \quad (3.1.16)$$

and

$$\rho \frac{\partial^2 \vec{\psi}}{\partial t^2} = \mu\Delta\vec{\psi} + \bar{\mu}\Delta \frac{\partial \vec{\psi}}{\partial t} \quad (3.1.17)$$

with Δ being defined by (3.1.10). Note that if we set $\bar{\mu}$ and $\bar{\lambda}$ equal to zero, then we get exactly the wave equations for the two types of observed Earthquake waves. If we Fourier transform all terms of equations (3.1.16) and (3.1.17) with respect to time we see that the Fourier transforms of both $\vec{\psi}$ and ϕ with respect to time satisfy a Helmholtz equation of the form,

$$\Delta V + k^2 V = 0 \quad (3.1.18)$$

where Δ is the Laplacian defined by (3.1.10) and k is a complex constant. Thus, except for the rather complex boundary conditions these equations might be solved by standard theories. The boundary conditions are highly mixed and require us to consider

- a region of welded contact between the plates where both the displacement and the stress tensor are continuous,
- a free surface where all the entries of the stress tensor are zero,

- a region of contact of the vibrator and the surface of the material being welded where the stress tensor is specified,
- the nonwelded contact region where the normal components of the stress and displacement are continuous, and
- the region of contact of the workpiece and the clamp, where the normal components of the stress are specified and the normal component of the displacement is fixed at zero.

3.2 Generalized Navier Stokes Equations

For compressible materials, the momentum conservation equations are nonlinear. The momentum flux is the dyad $\rho\vec{v}\vec{v}$ and using the concept of conservation of mass or equation (2.1.2) and equation (3.1.2) we see that

$$\begin{aligned} \text{div}(\rho\vec{v}\vec{v}) &= \text{div}(\rho\vec{v}) + \rho(\vec{v} \cdot \text{grad})\vec{v} \\ &= -\frac{\partial\rho}{\partial t}\vec{v} + \rho(\vec{v} \cdot \text{grad})\vec{v} \end{aligned} \quad (3.2.1)$$

If p is the pressure, then the total stress tensor Π is given by

$$\bar{\Pi} = -p(\vec{e}_x\vec{e}_x + \vec{e}_y\vec{e}_y + \vec{e}_z\vec{e}_z) + \bar{\tau} \quad (3.2.2)$$

The viscous stress tensor is given, using equation (3.1.1) for velocity, by the rule,

$$\begin{aligned} \bar{\tau} = & \mu \left(2\frac{\partial u}{\partial x} \right) \vec{e}_x\vec{e}_x + \mu \left(\frac{\partial v}{\partial x} + \frac{\partial u}{\partial y} \right) \vec{e}_y\vec{e}_x + \\ & \mu \left(\frac{\partial w}{\partial x} + \frac{\partial u}{\partial z} \right) \vec{e}_z\vec{e}_x + \mu \left(\frac{\partial u}{\partial y} + \frac{\partial v}{\partial x} \right) \vec{e}_x\vec{e}_y + \\ & + \mu \left(2\frac{\partial v}{\partial y} \right) \vec{e}_y\vec{e}_y + \mu \left(\frac{\partial w}{\partial y} + \frac{\partial v}{\partial z} \right) \vec{e}_z\vec{e}_y + \\ & \mu \left(\frac{\partial u}{\partial z} + \frac{\partial w}{\partial x} \right) \vec{e}_x\vec{e}_z + \mu \left(\frac{\partial v}{\partial z} + \frac{\partial w}{\partial y} \right) \vec{e}_y\vec{e}_z \\ & + \mu \left(2\frac{\partial w}{\partial z} \right) \vec{e}_z\vec{e}_z - \frac{2}{3}\mu \left(\frac{\partial u}{\partial x} + \frac{\partial v}{\partial y} + \frac{\partial w}{\partial z} \right) \vec{e}_x\vec{e}_x \\ & - \frac{2}{3}\mu \left(\frac{\partial u}{\partial x} + \frac{\partial v}{\partial y} + \frac{\partial w}{\partial z} \right) \vec{e}_y\vec{e}_y \\ & - \frac{2}{3}\mu \left(\frac{\partial u}{\partial x} + \frac{\partial v}{\partial y} + \frac{\partial w}{\partial z} \right) \vec{e}_z\vec{e}_z \end{aligned} \quad (3.2.3)$$

We have seen that the total stress tensor, equation (3.2.2) is given in terms of the pressure p and the viscous stress (3.2.3). The momentum equation is given by

$$\begin{aligned} \frac{\partial}{\partial t}(\rho \vec{v}) &= -\text{div}(\rho \vec{v} \vec{v}) \\ &+ \rho \vec{f} + \text{div}(\bar{\bar{\Pi}}) \end{aligned} \quad (3.2.4)$$

Using equation (3.2.1) we see that equation (3.2.4) and equations (3.2.2) and (3.2.3) we see that

$$\begin{aligned} \rho \frac{\partial \vec{v}}{\partial t} + \rho(\vec{v} \cdot \text{grad}(\vec{v})) &= \\ \rho \vec{f} - \text{grad}(p) + \text{div}(\bar{\bar{\tau}}) & \end{aligned} \quad (3.2.5)$$

Using the concept of material derivative, equation (1.1.1) and assuming that \vec{f} is the zero vector, equation (3.2.5) reduces to

$$\frac{D\vec{v}}{Dt} = -\frac{1}{\rho} \text{grad}(p) + \frac{1}{\rho} \text{div}(\bar{\bar{\tau}}) \quad (3.2.6)$$

4 Energy Conservation

There is internal energy, kinetic energy, work done by the viscous forces (equation 3.2.3), pressure, and work done by the external body forces. The energy is transferred from one region of the heated Voigt solid to another by thermal conduction, kinetic energy flux, and radiation conduction processes, and by the external elastic and thermal energy source. For boiling liquids we consider viscous dissipation functions and a radiation conductivity term.

4.1 A Heat Equation for Voigt Solids

We begin by considering the Voigt solid stress tensor and then go on to analysis of energy transfer where viscous dissipations functions are responsible for energy transfer.

We now consider specific energy per unit mass e within a stimulated Voigt solid, and we let the velocity \vec{V} of a point be defined by

$$\vec{V} = \frac{\partial \vec{U}}{\partial t} \quad (4.1.1)$$

where \vec{U} is the displacement from equilibrium. Then the total energy within a volume Ω is given by

$$\mathcal{E}_\Omega(t) = \int_\Omega \left\{ \rho(e + \vec{V} \cdot \vec{V}/2) \right\} dv \quad (4.1.2)$$

The time derivative of $\mathcal{E}_\Omega(t)$ is the rate of energy input into Ω by

- body forces,
- the stress system,

- the flux of kinetic energy across the boundaries,
- thermal heat conduction,
- internal heat generation,
- radiative transport, and
- internal energy flux.

The above means of energy transport are all important in fluid flow, but in elastic media, many of the terms may be ignored because there is no gross motion of material across boundaries. With our periodicity assumption, many of the terms which are conceptually small will be shown to vanish exactly when they are smoothed by using local time averages. This local smoothing may be thought of as a transition from a temporally microscopic to a temporally macroscopic theory.

To get to the final form of the equation that we consider we shall assume that the integral of the product of a slowly varying function and a highly oscillatory function is nearly zero. The rigorous energy equation may be expressed in the form,

$$\begin{aligned} \frac{d}{dt} \left(\int_{\Omega} (\rho(e + \vec{V} \cdot \vec{V}/2)) dv \right) = \\ \int_{\Omega} (\vec{F} \cdot \vec{V} + \text{div}(\vec{S} \cdot \vec{V}) - (\text{div}(\rho(\vec{V} \cdot \vec{V}/2)\vec{V})) \\ + \text{div}(\vec{K} \cdot \text{grad}(T)) + \frac{\partial Q}{\partial t} + \text{div}(q_r - e\rho\vec{V})) dv \end{aligned} \quad (4.1.3)$$

where the terms on the right side of (4.1.3) are respectively

- power transfer by body forces
- rate of kinetic energy transfer across the boundary
- the rate of energy transfer by thermal conduction
- the rate at which energy is created internally
- the rate at which energy is transferred into the body by radiation,
- the rate at which internal energy is transferred across the boundary by material motion.

From equation (4.1.3) we deduce an energy transfer equation,

$$\begin{aligned} \left(\frac{\partial \rho}{\partial t} \right) e + \rho \left(\frac{\partial e}{\partial t} \right) + \left(\frac{\partial \rho}{\partial t} \right) \left(\frac{\vec{V} \cdot \vec{V}}{2} \right) + \rho \vec{V} \cdot \left(\frac{\partial \vec{V}}{\partial t} \right) = \\ \vec{F} \cdot \vec{V} + \text{div}(\vec{S} \cdot \vec{V}) - \text{div}(\rho \left(\frac{\vec{V} \cdot \vec{V}}{2} \right) \vec{V}) + \text{div}(\vec{K} \cdot \text{grad}(T)) \end{aligned}$$

$$\frac{\partial Q}{\partial t} + \text{div}(q_r) - e \text{div}(\rho \vec{V}) - \rho \vec{V} \cdot \text{grad}(e) \quad (4.1.4)$$

If a slowly varying time envelope is riding on a rapidly varying oscillation, (e.g. very rapid vibrations and a periodic movement of the source of those vibrations or a steady increase in temperature resulting from those vibrations) then we can use the local time averaging operator

$$P_{T_p}(f)(t) = \bar{f}(t) = \left(\frac{1}{T_p} \right) \int_{t-T_p}^t f(\tau) d\tau \quad (4.1.5)$$

then it is clear that

Lemma 4.1 *If f is periodic with period T_p and if P_{T_p} is defined by (4.1.5) then for all real t*

$$P_{T_p}(f \cdot f') = 0 \quad (4.1.6)$$

This follows from the fact that

$$(f \cdot f')(t) = \frac{d}{dt} \left(\frac{f^2}{2} \right) (t) \quad (4.1.7)$$

and the fact that if f is periodic with period T_p that then

$$f^2(t + T_p) - f^2(t) = 0 \quad (4.1.8)$$

We shall use elementary vector analysis to reduce the energy equation (4.1.4) to a place where we can use the Lemma and the local time average operation P_{T_p} , defined by equation (4.1.5) to get a simplified heat equation.

We shall use the identity,

$$\begin{aligned} \text{div}((\vec{A} \cdot \vec{B})\vec{C}) &= (\vec{A} \cdot \vec{B})\text{div}(\vec{C}) + \vec{C} \cdot \text{grad}(\vec{A} \cdot \vec{B}) = \\ &(\vec{A} \cdot \vec{B})\text{div}(\vec{C}) + \vec{C} \cdot \{A \times \text{curl}(\vec{B}) + \vec{B} \times \text{curl}(\vec{A}) \\ &+ (\vec{A} \cdot \text{grad})\vec{B} + (\vec{B} \cdot \text{grad})\vec{A}\} \end{aligned} \quad (4.1.9)$$

which means that if we let \vec{A} be equal to \vec{B} be equal to \vec{C} be equal to $\rho \vec{V}$ to deduce a simplification of the divergence of ρ times half of the dot product of \vec{V} with itself times \vec{V} . We see that

$$\begin{aligned} \text{div}\left(\left(\rho \frac{\vec{V} \cdot \vec{V}}{2}\right)\vec{V}\right) &= \left(\frac{\vec{V} \cdot \vec{V}}{2}\right)\text{div}(\rho \vec{V}) + \vec{V} \cdot \text{grad}(\vec{V} \cdot \vec{V}) = \\ &\left(\frac{\vec{V} \cdot \vec{V}}{2}\right)\text{div}(\rho \vec{V}) + \rho \frac{\vec{V}}{2} \cdot \{\vec{V} \times \text{curl}(\vec{V}) + \\ &\vec{V} \times \text{curl}(\vec{V}) + (\vec{V} \cdot \text{grad})\vec{V} + (\vec{V} \cdot \text{grad})\vec{V}\} \end{aligned} \quad (4.1.10)$$

But since

$$\vec{V} \cdot (\vec{V} \times \text{curl}(\vec{V})) = 0, \quad (4.1.11)$$

we see that equation (4.1.10) reduces to

$$- \operatorname{div}\left(\rho \frac{\vec{V} \cdot \vec{V}}{2}\right) \vec{V} = \left(\frac{\vec{V} \cdot \vec{V}}{2}\right) \frac{\partial \rho}{\partial t} - \rho \vec{V} \cdot ((\vec{V} \cdot \operatorname{grad})\vec{V}) \quad (4.1.12)$$

The generalized momentum conservation equation,

$$\rho \frac{\partial \vec{V}}{\partial t} = -\rho(\vec{V} \cdot \operatorname{grad})\vec{V} + \vec{F} + \operatorname{div}(\vec{\bar{S}}) \quad (4.1.13)$$

Using the equation (4.1.12), which simplifies the divergence of the kinetic energy flux, and the result

$$\rho \vec{V} \cdot \frac{\partial \vec{V}}{\partial t} = -\rho \vec{V} \cdot (\vec{V} \cdot \operatorname{grad})\vec{V} + \vec{F} \cdot \vec{V} + \operatorname{div}(\vec{\bar{S}}) \cdot \vec{V} \quad (4.1.14)$$

of dotting all terms generalized momentum equation, (4.1.13), we deduce from (4.1.3) that

$$\begin{aligned} & \frac{\partial \rho}{\partial t} e + \rho \frac{\partial e}{\partial t} + \frac{\partial \rho}{\partial t} \left(\frac{\vec{V} \cdot \vec{V}}{2}\right) + \\ & \left\{ -\rho \vec{V} \cdot ((\vec{V} \cdot \operatorname{grad})\vec{V}) + \vec{F} \cdot \vec{V} + \operatorname{div}(\vec{\bar{S}}) \cdot \vec{V} \right\} \\ & = \vec{F} \cdot \vec{V} + \operatorname{div}(\vec{\bar{S}} \cdot \vec{V}) + \\ & \left\{ \left(\frac{\vec{V} \cdot \vec{V}}{2}\right) \frac{\partial \rho}{\partial t} - \rho \vec{V} \cdot ((\vec{V} \cdot \operatorname{grad})\vec{V}) \right\} + \\ & \operatorname{div}(\vec{\bar{K}} \cdot \operatorname{grad}(T)) + \frac{\partial Q}{\partial t} + \operatorname{div}(q_r) \\ & - e(\operatorname{div}(\rho \vec{V})) + \rho \vec{V} \cdot \operatorname{grad}(e) \end{aligned} \quad (4.1.15)$$

where the terms in energy equation (4.1.15) that differ from the original energy equation (4.1.3) are enclosed in curly brackets. We further simplify equation (4.1.15) by using the mass conservation equation (2.1.2) and cancelling out terms that appear on both sides of the equal sign of equation (4.1.15) to obtain,

$$\begin{aligned} & \rho \left(\frac{\partial \rho}{\partial t}\right) + \operatorname{div}(\vec{\bar{S}}) \cdot \vec{V} = \operatorname{div}(\vec{\bar{S}} \cdot \vec{V}) + \\ & \operatorname{div}(\vec{\bar{K}} \cdot \operatorname{grad}(T)) + \frac{\partial Q}{\partial t} + \operatorname{div}(q_r) - \rho \vec{V} \cdot \operatorname{grad}(e) \end{aligned} \quad (4.1.16)$$

We now make use of the dyadic identity

$$\operatorname{div}(\vec{\bar{S}} \cdot \vec{V}) - \operatorname{div}(\vec{\bar{S}}) \cdot \vec{V} = (\vec{\bar{S}} \cdot \operatorname{grad}) \cdot \vec{V} \quad (4.1.17)$$

Substituting equation (4.1.17) into equation (4.1.16) we obtain equation

$$\rho \frac{\partial e}{\partial t} = (\vec{\bar{S}} \cdot \operatorname{grad}) \cdot \vec{V} + \operatorname{div}(\vec{\bar{K}} \cdot \operatorname{grad}(T))$$

$$+ \frac{\partial Q}{\partial t} + \text{div}(q_r) - \rho \vec{V} \cdot \text{grad}(e) \quad (4.1.18)$$

We assume that ρ and the conductivity tensor $\overline{\overline{K}}$ are time independent and that the internal energy source Q and the radiative energy source q_r are both identically zero and apply the local time averaging operator P_T , defined by equation (4.1.5) to all terms of the simplified energy equation (4.1.18) ([41], p 17) to obtain equation

$$\rho \left(\frac{\partial e}{\partial t} \right) = \overline{(\overline{\overline{S}} \cdot \text{grad}) \cdot \vec{V}} + \text{div}(\overline{\overline{K}} \cdot \vec{T}) - \rho \overline{\vec{V} \cdot \text{grad}(e)} \quad (4.1.19)$$

We now use the oscillation theorem which says that if a is smaller than b and if f is continuous on $[a, b]$ then

$$\lim_{n \rightarrow \infty} \int_a^b \cos(nt) f(t) dt = 0 \quad (4.1.20)$$

to say that to a good approximation since \vec{V} is a rapidly varying function and e is a slowly varying function we may, in view of (4.1.20), say that to a good approximation,

$$\rho \vec{V} \cdot \text{grad}(e) = 0 \quad (4.1.21)$$

to obtain the first approximate heat equation,

$$\rho \frac{\partial e}{\partial t} = \overline{(\overline{\overline{S}} \cdot \text{grad}) \cdot \vec{V}} + \text{div}(\overline{\overline{K}} \cdot \text{grad}(T)) \quad (4.1.22)$$

We now are prepared to exploit equation (4.1.6) and the relation

$$e = cT \quad (4.1.23)$$

where e and T are respectively increases in energy density and temperature, and where c is the specific heat to obtain our final form of the heat equation with an elastic energy power density source term. We write for n equal to three or seven,

$$\overline{\overline{S}} = \sum_{i=1}^n \sum_{j=1}^n S_{(i,j)} \vec{e}_i \vec{e}_j \quad (4.1.24)$$

where

$$\begin{aligned} S_{(i,j)} = & \mu \left(\frac{\partial U_i}{\partial x_j} + \frac{\partial U_j}{\partial x_i} \right) + \tilde{\mu} \left(\frac{\partial^2 U_i}{\partial x_j \partial t} + \frac{\partial^2 U_j}{\partial x_i \partial t} \right) \\ & + \lambda \left(\sum_{k=1}^n \frac{\partial U_k}{\partial x_k} \right) \delta_{(i,j)} + \tilde{\lambda} \left(\sum_{k=1}^n \frac{\partial^2 U_k}{\partial x_k \partial t} \right) \delta_{(i,j)} \end{aligned} \quad (4.1.25)$$

We now take the dot product of both sides of equation (4.1.25) with \vec{V} obtaining,

$$\begin{aligned} (\overline{\overline{S}} \cdot \text{grad}) \cdot \vec{V} = & \\ & \left(\sum_{i=1}^n \sum_{j=1}^n \sum_{k=1}^n S_{(i,j)} \vec{e}_i \delta_{(j,k)} \frac{\partial}{\partial x_k} \right) \left(\sum_{l=1}^n \frac{\partial U_l}{\partial t} \vec{e}_l \right) \end{aligned}$$

$$= \left(\sum_{i=1}^n \sum_{j=1}^n \sum_{k=1}^n S_{(i,j)} \delta_{(i,j)} \delta_{(j,k)} \delta_{(i,\ell)} \frac{\partial^2 U_k}{\partial x_k \partial t} \right) \quad (4.1.26)$$

We apply the local time average operation defined by (4.1.5) to all terms of equation (4.1.26) making use of (4.1.6) and substitute into equation (4.1.22). Thus, from (4.1.4) we derive the heat equation,

$$\rho c \left(\frac{\partial T}{\partial t} \right) - \text{div}(\bar{\bar{K}} \cdot \text{grad}(T)) = \frac{\sum_{(i,j) \in \mathcal{J}(n)} \bar{\mu} \left(\frac{\partial^2 U_i}{\partial x_j \partial t} + \frac{\partial^2 U_j}{\partial x_i \partial t} \right)^2 + \bar{\lambda} \sum_{i=1}^n \left(\frac{\partial^2 U_i}{\partial x_i \partial t} \right)^2}{\quad} \quad (4.1.27)$$

where the index set is defined by

$$\mathcal{J}(n) = \{(i, j) : j \geq i \text{ and } \{i, j\} \in \{1, 2, \dots, n\}\} \quad (4.1.28)$$

and the internal energy density increase e that appeared in our original energy equation (4.1.4) is related to temperature increase by the relation (4.1.23), where c is the specific heat and T is the temperature increase, which means that since the right side source term of the heat equation (4.1.27) is positive that heat will be generated by vibrations in a Voigt solid.

4.2 Droplet Explosion by Lasers

We now consider energy transfer in a stimulated fluid. Using equation (3.2.3) we define the viscous dissipation function Φ by the rule,

$$\begin{aligned} \Phi = \mu \left[2 \left\{ \left(\frac{\partial u}{\partial x} \right)^2 + \left(\frac{\partial v}{\partial y} \right)^2 + \left(\frac{\partial w}{\partial z} \right)^2 \right\} + \right. \\ \left. \left(\frac{\partial v}{\partial x} + \frac{\partial u}{\partial y} \right)^2 + \left(\frac{\partial w}{\partial y} + \frac{\partial v}{\partial z} \right)^2 \right. \\ \left. + \left(\frac{\partial u}{\partial z} + \frac{\partial w}{\partial x} \right)^2 - \frac{2}{3} \left(\frac{\partial u}{\partial x} + \frac{\partial v}{\partial y} + \frac{\partial w}{\partial z} \right)^2 \right] \quad (4.2.1) \end{aligned}$$

In these terms the energy equation is given by (Anderson, Tannehill, and Pletcher [1], pages 188-189).

$$\begin{aligned} \frac{\partial}{\partial t} \left\{ \rho e + \frac{\rho \vec{v} \cdot \vec{v}}{2} \right\} = \\ - \text{div}(\rho e \vec{v}) + \vec{f} \cdot \vec{v} + \\ \text{div}(\bar{\bar{\Pi}} \cdot \vec{v}) - \text{div} \left(\left(\frac{\rho \vec{v} \cdot \vec{v}}{2} \right) \vec{v} \right) + \\ \text{div}(\bar{\bar{K}} \text{grad}(T)) + \left(\frac{\partial}{\partial t} \right) Q_{in} + \left(\frac{\partial}{\partial t} \right) Q_{out} \quad (4.2.2) \end{aligned}$$

We define the enthalpy h as (see Anderson [1], p 188)

$$h = e + \frac{p}{\rho} \quad (4.2.3)$$

where

$e =$ the internal energy including quantum states,
 $p =$ the pressure, and
 $\rho =$ the density.

To telescope the terms in the energy equation we make use of the vector identity

$$\begin{aligned} \text{grad}(\vec{A} \cdot \vec{B}) &= \vec{A} \times \text{curl}(\vec{B}) + \vec{B} \times \text{curl}(\vec{A}) + \\ &(\vec{B} \cdot \text{grad})\vec{A} + (\vec{A} \cdot \text{grad})\vec{B} \end{aligned} \quad (4.2.4)$$

to observe that

$$\begin{aligned} \rho \vec{v} \cdot \text{grad} \left(\frac{\vec{v} \cdot \vec{v}}{2} \right) &= \\ \rho \vec{v} \cdot \{ \vec{v} \times \text{curl}(\vec{v}) + \vec{v} \cdot \text{grad}(\vec{v}) \} \end{aligned} \quad (4.2.5)$$

Interchanging the dot and cross product in equation (4.2.5) we see that since for an arbitrary vector field \vec{v}

$$\vec{v} \cdot (\vec{v} \times \text{curl}(\vec{v})) = (\vec{v} \times \vec{v}) \cdot \text{curl}(\vec{v}) = \vec{0} \quad (4.2.6)$$

it follows that

$$\rho \vec{v} \cdot \text{grad} \left(\frac{\vec{v} \cdot \vec{v}}{2} \right) = \rho \vec{v} \cdot \{ (\vec{v} \cdot \text{grad})(\vec{v}) \} \quad (4.2.7)$$

We can then collapse terms in equation (4.2.2) by observing that the momentum equation implies that

$$\begin{aligned} \vec{v} \cdot \rho (\vec{v} \cdot \text{grad})\vec{v} &= \\ -\rho \frac{\partial \vec{v}}{\partial t} \cdot \vec{v} & \\ + \rho \vec{f} - \text{grad}(p) \cdot \vec{v} + \text{div}(\vec{\tau}) \cdot \vec{v} \end{aligned} \quad (4.2.8)$$

Thus, using equation (1.1.1) and equations (4.2.7) and (4.2.8) the energy equation (4.2.2) may be rewritten in the form,

$$\begin{aligned} \rho \frac{Dh}{Dt} &= \frac{Dp}{Dt} + \\ \left(\frac{\partial}{\partial t} \right) Q_{in} &+ \left(\frac{\partial}{\partial t} \right) Q_{out} + \\ \Phi - \text{div}(\vec{K} \text{grad}(T)) \end{aligned} \quad (4.2.9)$$

where $(\partial/\partial t) Q_{in}$ is given by equation (1.2.4) and Φ is the dissipation function representing the work done by the viscous forces of the fluid. The term representing the transfer by radiation from one part of the fluid to another is given by (Siegel and Howell [62], page 689)

$$\left(\frac{\partial}{\partial t} \right) Q_{out} = \text{div} \left(\frac{16\sigma T^3}{3a_R} \cdot \text{grad}(T) \right) \quad (4.2.10)$$

This equation may be interpreted as providing a radiation flux across a surface defined by

$$k_r = \frac{16\sigma T^3}{3a_R}, \quad (4.2.11)$$

where a_R is the Rosseland mean absorption coefficient (Siegel [62], p 504 and Rosseland) and where σ (Siegel [62], page 25) is the hemispherical total emissive power of a black surface into vacuum having a value of

$$\sigma = 5.6696 \times 10^{-8} \text{ Watts / (meters}^2 \text{ }^\circ\text{K)} \quad (4.2.12)$$

Using equation (4.2.10) and equation (4.2.2) we see that

$$\begin{aligned} \rho \frac{De}{Dt} = & \left(\frac{\partial}{\partial t} \right) Q_{in} + \left(\frac{\partial}{\partial t} \right) Q_{out} + \\ & (-p \operatorname{div}(\vec{v})) - \operatorname{div}(\overline{K} \operatorname{grad}(T)) + \Phi \end{aligned} \quad (4.2.13)$$

where Φ is the viscous dissipation function given by equation (4.2.1)

4.3 EQUATION OF STATE

In the energy equation (4.2.13) the perfect fluid assumption ([1], p 189) would yield

$$e = c_v T, \quad (4.3.1)$$

where c_v is the specific heat at constant volume, and if we define

$$\gamma = \frac{c_p}{c_v} \quad (4.3.2)$$

where c_p is the specific heat at constant pressure, then the pressure p , the internal energy e and the density ρ are related by ([1], p 189)

$$p = (\gamma - 1)\rho e \quad (4.3.3)$$

5 SUMMARY

Using the definition of velocity (equation 3.1.1) and the equation of state (4.3.3) we see that the number of equations is 5, allowing 3 equations for the three components of the momentum, and while the initial variables are ρ , u , v , w , p , e , and T , we see that since the temperature T is related to e and since pressure is a function of ρ and e , we see that there are now exactly 5 unknowns. This means that locally within the Voigt solid, we can describe the future state of the Voigt solid as a semigroup acting on the conditions at time t_0 . If we want to know the value at time t and \mathcal{S} is defined so that the solution at time t is

given by $\mathcal{S}(t - t_0)$ acting on the values at $t = t_0$ of the density ρ , the velocity components u , v , and w , and the temperature T . The semigroup relation,

$$\begin{pmatrix} \rho(t) \\ u(t) \\ v(t) \\ w(t) \\ T(t) \end{pmatrix} = \mathcal{S}(t - t_0) \begin{pmatrix} \rho(t_0) \\ u(t_0) \\ v(t_0) \\ w(t_0) \\ T(t_0) \end{pmatrix} \quad (5.0.1)$$

tells us how to get future values of the density ρ , the three velocity components, and the temperature at time t when the values at time t_0 are known.

6 FLAME THEORY

Flame theory can be considered as a system of partial differential equations ([43]) involving

- conservation of mass,
- species creation, diffusion, and transport,
- conservation of momentum,
- conservation of energy, and
- equations of state.

We need several definitions of terms for the formulation of the equations. The variables are

t	=	time
T	=	temperature
ρ	=	density of mixture
Y_k	=	concentration of species k
c_p	=	specific heat of the mixture
$c_{(p,k)}$	=	specific heat of species k
\vec{u}	=	velocity of mixture
$D_{(j,k)}$	=	(j,k) entry of species diffusion tensor
\vec{V}_k	=	diffusion velocity of species k
Ψ	=	$r^2 \cdot \vec{u}$ equals the stream function for transport down a tube described in cylindrical coordinates, where
r	=	the distance from the axis of the cylinder, and
$\frac{\partial \omega_k}{\partial t}$	=	molar rate of production of species k .

Here, the specific heat of species k and the specific heat of the mixture are related by ([36])

$$c_p = \sum_{k=1}^n \left(\frac{\rho_k}{\rho} \right) \cdot c_{(p,k)} \quad (6.0.1)$$

where ρ_k is the density of species k

6.1 Multicomponent Diffusion

One of the more recent developments are the concepts ([22], [43]) of mole fraction differential pressure gradients with the idea that even as a gas is moving along a pipe or a jet aircraft engine with velocity \vec{u} the species or molecular entities are diffusing with individual velocities \vec{V}_k as a result of weighted mole fraction pressure gradients \vec{d}_k and temperature gradients. If we suppose that

$$\begin{aligned} p &= \text{pressure} \\ X_k &= \text{mole fraction of species } k, \text{ and} \\ Y_k &= \text{mass fraction of species } k \end{aligned} \quad (6.1.1)$$

then the weighted mole fraction differential pressure gradient is ([43]) given by

$$\vec{d}_k = \text{grad}(\vec{X}_k) + (X_k - Y_k) \cdot \text{grad}(p) \quad (6.1.2)$$

and if we let

$$\begin{aligned} W_k &= \text{molecular weight of species } k \\ \bar{W} &= \text{mixture average molecular weight} \\ D_k^T &= \text{the species } k \text{ thermal diffusion coefficient} \end{aligned} \quad (6.1.3)$$

then the Dixon - Lewis species k diffusion velocity ([22], [43]) (for k running from 1 to N) is given by

$$\vec{V}_k = \left(\frac{1}{X_k \bar{W}} \right) \cdot \left(\sum_{j=1}^N W_j D_{(k,j)} \vec{d}_j \right) - \left(\frac{D_k^T}{\rho \cdot Y_k} \right) \left(\frac{\text{grad}(T)}{T} \right) \quad (6.1.4)$$

Then using equation (6.1.4) we see that the species k diffusion flux is given by

$$\vec{j}_k = \rho \cdot Y_k \cdot \vec{V}_k \quad (6.1.5)$$

The overall gas velocity contribution of the species k flux is given by

$$J_k = \rho \cdot Y_k \vec{u} \quad (6.1.6)$$

6.2 Conservation of Species and Energy

Using the species diffusion flux (6.1.5) and the species transport flux (6.1.6) and the idea that if the partial derivative with respect to time of ω_k is the molar rate of production of species k from chemical reactions that then the species conservation equation is

$$\rho \frac{\partial Y_k}{\partial t} = \text{div}(\vec{j}_k) + \text{div}(\rho \cdot Y_k \cdot \vec{u}) + \frac{\partial \omega_k}{\partial t} \quad (6.2.1)$$

where the species diffusion flux \vec{j}_k is given by equation (6.1.5)

The chemical kinetics and species creation processes are an integral part of flame modeling and can be used to describe soot particle nucleation and growth and to understand the

type and kind of dangerous materials that can be formed during burning processes (Frenklach and Wang, [29]); in particular we can describe the formation of the PAH, polycyclic aromatic hydrocarbons nucleation and coagulation or growth in premixed flames ([28], [30], [31], [33]). Microscopic equations can account for surface growth of soot particles; the soot formation mechanisms, in spite of intensive study have only recently come to be understood. As a consequence we better understand just how very dangerous to health these particles really are.

We now turn our attention to the development of energy flux using the concept of enthalpy which is defined by equation (4.2.3), the universal gas constant, R , and the concept of the partial pressure p_k of species k and the concept of the energy e_k possessed by species k to define the enthalpy of species k and the total stress tensor $\bar{\bar{\Pi}}$ defined by (3.2.2) to give an energy flux defined by

$$\begin{aligned} \vec{q} = & \sum_{j=1}^N (\vec{j}_j h_j) - \bar{K} \text{grad} T - \\ & \sum_{k=1}^N \left(\frac{RT}{W_k X_k} \right) D_k^T \cdot \vec{d}_k + \\ & (\rho \cdot e) \vec{u} + \left(\frac{\rho(\vec{u} \cdot \vec{u})}{2} \right) \vec{u} + \bar{\bar{\Pi}} \cdot \vec{u} \end{aligned} \quad (6.2.2)$$

Then if we define

$$\frac{\partial Q_{\text{internal}}}{\partial t} = \text{rate of chemical and radiative heat production}$$

to be the heat produced by chemical reactions and the electromagnetic radiation energy density term (1.2.3)

$$\frac{\partial Q_{\text{out}}}{\partial t} = \text{the rate of radiative transfer of heat to the outside}$$

which includes terms like the one on the right side of equation (4.2.10) describing radiation leaving from flames to all other parts of the reacting system. The energy equation is given by

$$\begin{aligned} \frac{\partial}{\partial t} \left\{ \rho e + \rho \left(\frac{\vec{u} \cdot \vec{u}}{2} \right) \right\} = \text{div}(\vec{q}) \\ + \frac{\partial Q_{\text{internal}}}{\partial t} + \frac{\partial Q_{\text{out}}}{\partial t} \end{aligned} \quad (6.2.3)$$

6.3 Cylinder Flame Front Models and Homotopy

Margolis and Sivashinsky ([49]) considered a flame front in a right circular cylinder whose boundary is the surface defined by

$$z = \Phi(r, \theta, t) \quad (6.3.1)$$

where Φ satisfies the nonlinear partial differential equation ([49], p 100)

$$\frac{\partial \Phi}{\partial t} + \frac{c}{2}(\text{grad}(\Phi) \cdot \text{grad}(\Phi)) + \Delta(\Phi) + 4 \cdot \Delta^2(\Phi) - W_0 = 0 \quad (6.3.2)$$

where the parameter c is equal to one and where ([49], p 100)

$$W_0 = -G \cdot (\Phi - \bar{\Phi}) \quad (6.3.3)$$

is a scaled diffusion velocity with G ([49]) denoting a scaled buoyancy parameter and with $\bar{\Phi}$ denoting the average value of Φ over the cross section of the cylinder defined by the formula

$$\bar{\Phi} = \left(\frac{1}{\pi R^2} \right) \int_0^{2\pi} \int_0^R \Phi(r, \theta, t) r dr d\theta \quad (6.3.4)$$

where R is the radius of the right circular cylinder, and we assume that on the sides of this cylinder the flame front Φ satisfies the boundary conditions

$$\frac{\partial \Phi}{\partial r} = 0 = \left(\frac{\partial}{\partial r} \right) \Delta \Phi \quad (6.3.5)$$

and since in cylindrical coordinates the laplacian Δ is given by

$$\Delta \Phi = \frac{\partial^2 \Phi}{\partial r^2} + \left(\frac{1}{r} \right) \cdot \frac{\partial \Phi}{\partial r} + \frac{1}{r^2} \left(\frac{\partial^2 \Phi}{\partial \theta^2} \right) + \frac{\partial^2 \Phi}{\partial z^2} \quad (6.3.6)$$

to see that if we remember that the Bessel function $J_n(z)$ satisfies

$$\left(\frac{d}{dz} \right)^2 J_n(z) + \left(\frac{1}{z} \right) \cdot \left(\frac{\partial}{\partial z} \right) J_n(z) + \left(1 - \frac{n^2}{z^2} \right) \cdot J_n(z) = 0 \quad (6.3.7)$$

and we choose

$$\Phi = \exp(i\nu\theta) J_\nu(\lambda r) \quad (6.3.8)$$

then the easily observed relations that

$$\Delta(\exp(i\nu\theta) \cdot J_\nu(\lambda r)) = -\lambda^2 \cdot \exp(i\nu\theta) \cdot J_\nu(\lambda r) \quad (6.3.9)$$

and

$$\Delta^2(\exp(i\nu\theta) \cdot J_\nu(\lambda r)) = \lambda^4 \cdot \exp(i\nu\theta) \cdot J_\nu(\lambda r) \quad (6.3.10)$$

enable us to find simple equations that must be satisfied by λ , G , and R in order to cause (6.3.8) to be a solution of equation (6.3.2) when c is equal to zero. For each value of the cylinder radius there are a discrete collection of λ which satisfy the boundary conditions (6.3.5) which are in view of (6.3.5) and (6.3.9) the condition that

$$J'_\nu(\lambda_m R) = 0 \quad (6.3.11)$$

If equation (6.3.11) is satisfied, both boundary conditions embodied in equation (6.3.5) are satisfied. If we select one of these values of λ we see that there is a simple relationship between R and G that must be satisfied in order that the expression (6.3.8) satisfy equation (6.3.2) and the boundary conditions (6.3.5). We can move along a path from these c equal

to zero solutions of (6.3.2) using a Maclaren series expansion about c equal to zero, that involves solving linear equations at each stage to move along a homotopy path from c equals zero to c equals one.

However, we give here a direct solution of the nonlinear problem by assuming that we can represent the stationary or nonstationary flame front Φ as a Fourier series of the form

$$\Phi = \sum_{k=1}^{\infty} (C_k(t) \cdot \exp(ik\nu\theta) \cdot F_k(r)) \quad (6.3.12)$$

Applying the Laplacian Δ defined by equation (6.3.6) to both sides of equation (6.3.12) we see that

$$\Delta\Phi = \sum_{k=1}^{\infty} \left(C_k(t) \cdot \exp(ik\nu\theta) \cdot \left[F_k''(r) + \frac{F_k'(r)}{r} + \left(\frac{F_k(r)}{r^2} \right) \cdot (-\nu^2 \cdot k^2) \right] \right) \quad (6.3.13)$$

As we also need to compute $\Delta^2\Phi$ we begin by observing that

$$\left[\left(\frac{\partial}{\partial r} \right)^2 + \frac{1}{r} \left(\frac{\partial}{\partial r} \right) \right] \cdot F_k''(r) = F_k''''(r) + \frac{F_k'''(r)}{r} \quad (6.3.14)$$

and then that

$$\left[\left(\frac{\partial}{\partial r} \right)^2 + \frac{1}{r} \left(\frac{\partial}{\partial r} \right) \right] \cdot \frac{F_k'(r)}{r} = \frac{F_k'''(r)}{r} - \frac{F_k''(r)}{r^2} + \frac{F_k'(r)}{r^3} \quad (6.3.15)$$

and also that

$$\left[\left(\frac{\partial}{\partial r} \right)^2 + \frac{1}{r} \left(\frac{\partial}{\partial r} \right) \right] \cdot \frac{F_k(r)}{r^2} = \frac{F_k''(r)}{r^2} - 3 \cdot \frac{F_k'(r)}{r^3} + 4 \cdot \frac{F_k(r)}{r^4} \quad (6.3.16)$$

Collecting terms using equations (6.3.14), (6.3.15), and (6.3.16) we see that since

$$\begin{aligned} & \Delta \left[\exp(-ik\nu\theta) \cdot \left\{ F_k''(r) + \frac{F_k'(r)}{r} + \frac{(-\nu^2 k^2) F_k(r)}{r^2} \right\} \right] = \\ & \left[\left(\frac{\partial}{\partial r} \right)^2 + \frac{1}{r} \left(\frac{\partial}{\partial r} \right) + (-\nu^2 k^2) \right] \cdot \left[\exp(-ik\nu\theta) \cdot \left\{ F_k''(r) + \frac{F_k'(r)}{r} + \frac{(-\nu^2 k^2) F_k(r)}{r^2} \right\} \right] \end{aligned} \quad (6.3.17)$$

that

$$\begin{aligned} & \Delta \left[\exp(-ik\nu\theta) \cdot \left\{ F_k''(r) + \frac{F_k'(r)}{r} + \frac{(-\nu^2 k^2) F_k(r)}{r^2} \right\} \right] = \\ & F_k''''(r) + 2 \cdot \left(\frac{F_k'''(r)}{r} \right) - (1 + 2 \cdot \nu^2 \cdot k^2) \cdot \left(\frac{F_k''(r)}{r^2} \right) + \\ & (1 + 2\nu^2 k^2) \cdot \left(\frac{F_k'(r)}{r^3} \right) - (4 \cdot \nu^2 \cdot k^2 - \nu^4 \cdot k^4) \cdot \left(\frac{F_k(r)}{r^4} \right) \end{aligned} \quad (6.3.18)$$

For a class of solutions we can see how to systematically make the transition from the solution of the problem for c equal to zero to the solution of the problem for c equal to one

or any other nonzero number by substituting the series under the assumption that ν is an integer which means that $\bar{\Phi}$ is zero. As a result of the substitution of (6.3.12) into (6.3.2) making use of equation (6.3.13) and equation (6.3.18) we find that the relationship between the coefficients is that of a nonhomogeneous linear parabolic equation that is exactly solvable in terms of a series of Bessel functions which satisfy the boundary conditions as at each stage the nonlinear terms in the equation involve previously computed functions which at the k th stage, for k larger than one, we expand using eigenfunctions $\mathcal{E}_{(k,j)}(r)$ associated with an eigenvalue $\lambda_{(k,j)}$ such that

$$\mathcal{E}'_{(k,j)}(r) = 0 = \frac{\partial}{\partial r} \left[\left(\frac{\partial}{\partial r} \right)^2 + \frac{1}{r} \left(\frac{\partial}{\partial r} \right) \right] \mathcal{E}_{(k,j)}(r) \quad (6.3.19)$$

We shall construct a fourth order differential operator with eigenfunctions satisfying (6.3.19) by considering the linear differential equation that enables us to solve the nonlinear problem by expressing new coefficients in terms of previously computed coefficients and previously computed functions is given as

$$\begin{aligned} & \sum_{k=1}^{\infty} (C'_k(t) \exp(i\nu k\theta) F_k(r)) = \\ & \frac{c}{2} \left\{ \sum_{k=2}^{\infty} \left[\sum_{j=1}^{k-1} (C_j(t) C_{k-j}(t) [F'_j(r) F'_{k-j}(r) - \nu^2 j \cdot (k-j) F_j(r) F_{k-j}(r)]) \exp(i\nu k\theta) \right] \right\} \\ & + \sum_{k=1}^{\infty} \left\{ C_k(t) \left[F''_k(r) + \frac{F'_k(r)}{r} + \frac{F_k(r)}{r^2} (-\nu^2 \cdot k^2) \right] \exp(i\nu k\theta) \right\} + \\ & \sum_{k=1}^{\infty} \left\{ 4C_k(t) \left[F'''_k(r) + \frac{2 \cdot F''_k(r)}{r} - (1 + 2 \cdot \nu^2 \cdot k^2) \left(\frac{F'_k(r)}{r^2} \right) \right. \right. \\ & \left. \left. + (1 + 2 \cdot \nu^2 \cdot k^2) \left(\frac{F_k(r)}{r^3} \right) - (4 \cdot \nu^2 \cdot k^2) \left(\frac{F_k(r)}{r^4} \right) \right] \exp(i\nu k\theta) \right\} + \\ & G \left(\sum_{k=1}^{\infty} C_k(t) \left[F_k(r) \cdot \exp(i\nu k\theta) - \left(\frac{1}{\pi R^2} \right) \int_0^{2\pi} \left(\int_0^R F_k(r) \cdot r \cdot dr \right) \exp(i\nu k\tilde{\theta}) d\tilde{\theta} \right] \right) \end{aligned} \quad (6.3.20)$$

We can get a representation of the $F_k(r)$ and the expansion coefficients $C_k(t)$ by solving nonhomogeneous linear equations. To solve this we introduce singular ordinary differential operators L_k by the rule

$$\begin{aligned} L_k &= 4 \cdot \left(\frac{d}{dr} \right)^4 + \frac{8}{r} \left(\frac{d}{dr} \right)^3 + \\ & \left\{ 1 - \left(\frac{1 + 2 \cdot \nu^2 \cdot k^2}{r^2} \right) \right\} \left(\frac{d}{dr} \right)^2 + \left(\frac{1}{r} + \frac{1 + 2 \cdot \nu^2 \cdot k^2}{r^3} \right) \left(\frac{d}{dr} \right) + \\ & \left\{ \left(\frac{-\nu^2 \cdot k^2}{r^2} \right) - \frac{(4 \cdot \nu^2 \cdot k^2 - \nu^4 \cdot k^4)}{r^4} + G \right\} \end{aligned} \quad (6.3.21)$$

We require that the eigenfunctions $\mathcal{E}_{(k,j)}$ satisfy, in addition to the boundary condition, (6.3.19), the relationship

$$L_k \mathcal{E}_{(k,j)} + \lambda_{(k,j)} \mathcal{E}_{(k,j)} = 0 \quad (6.3.22)$$

If we use the definition (6.3.21) we can simplify the differential equation (6.3.20) after using orthogonality to

$$\begin{aligned} C'_k(t)F_k(r) = & \\ \frac{c}{2} \left[\sum_{j=1}^{k-1} (C_j(t)C_{k-j}(t) [F'_j(r)F'_{k-j}(r) - \nu^2 j \cdot (k-j)F_j(r)F_{k-j}(r)]) \right] & \\ + C_k(t) \cdot L_k(F_k)(r) & \end{aligned} \quad (6.3.23)$$

Continuing we define a source term $\mathcal{S}_k(t, r)$ for our linear ordinary differential equation by the rule,

$$\mathcal{S}_k(t, r) = \left[\sum_{j=1}^{k-1} (C_j(t)C_{k-j}(t) [F'_j(r)F'_{k-j}(r) - \nu^2 j \cdot (k-j)F_j(r)F_{k-j}(r)]) \right] \quad (6.3.24)$$

which means that if we substitute (6.3.24) into (6.3.23) we obtain the relation

$$C'_k(t)F_k(r) = C_k(t)L_k F_k(r) + \frac{c}{2} \cdot \mathcal{S}_k(t, r) \quad (6.3.25)$$

for k that are two or larger. At this stage we use eigenfunctions $\mathcal{E}_{(k,j)}$ with eigenvalue $\lambda_{(k,j)}$ of the linear operator L_k which satisfy the boundary conditions (6.3.5) to write under the assumption that

$$\mathcal{S}_k(t, r) = \sum_{j=1}^{\infty} s_{(k,j)}(t) \cdot \mathcal{E}_{(k,j)}(r) \quad (6.3.26)$$

and

$$F_k(r) = \sum_{j=1}^{\infty} a_{(k,j)} \cdot \mathcal{E}_{(k,j)}(r) \quad (6.3.27)$$

to further reduce (6.3.25) to

$$C'_k(t) \cdot a_{(k,j)} = (-\lambda_{(k,j)})C_k(t) \cdot a_{(k,j)} + \frac{c}{2} \cdot s_{(k,j)}(t) \quad (6.3.28)$$

This is simply a first order linear ordinary differential equation in the time variable t which completely determines the functions

$$t \rightarrow C_k(t) \cdot a_{(k,j)} \quad (6.3.29)$$

and consequently, in view of (6.3.27) and (6.3.12) the flame front Φ satisfying (6.3.2) and in view of equation (6.3.19) the boundary conditions (6.3.5). This gives us a means of moving along a homotopy path from c equal to zero to c equal to one and to obtain exact solutions of the full nonlinear flame front equation (6.3.2).

References

- [1] Anderson, Dale A. *Computational Fluid Mechanics and Heat Transfer* New York: McGraw Hill (1984).
- [2] Armstrong, Robert L. and Andrew Zardecki. "Propagation of High Energy Laser Beams Through Metallic Aerosols" *Applied Optics*. Volume 29, Number 12 (April 20, 1990) pp 1786-1792
- [3] *Explosions in Air* Austin, Texas: University of Texas Press (1973)
- [4] Barton J. P., D. R. Alexander, and S. A. Schaub. "Internal fields of a spherical particle illuminated by a tightly focused laser beam: focal point positioning effects at resonance." *Journal of Applied Physics*. Volume 65 No. 8 (April 15, 1989) pp 2900-2906
- [5] Barton, J. P., D. R. Alexander, and S. A. Schaub. "Internal and near surface electromagnetic fields for a spherical particle irradiated by a focused laser beam" *Journal of Applied Physics*. Volume 64, no 4 (1988) pp 1632-1639.
- [6] Belts, V. A., O. A. Volkovitsky, A. F. Dobrovolsky, E. V. Ivanov, Y. V. Nasedkin, L. N. Pavlova. "Intensive CO₂ laser pulse transmission through droplet and ice crystal fogs" *IN Kaye, A. S. and A. C. Walker. Gas flow and chemical lasers. 1984. Proceedings of the Fifth International Symposium* Oxford, England: Gas Flow and Chemical Laser Symposium (August, 1984) pp 20-24
- [7] Benedict, Robert P. *Gas Dynamics* New York: John Wiley (1983)
- [8] Birkhoff, Garrett. *Hydrodynamics. A Study in Logic Fact, and Similitude* New York: Dover (1950)
- [9] Biswas, A., H. Latifi, R. L. Armstrong, and R. G. Pinnick. "Time resolved spectroscopy of laser emission from dye doped droplets" *Optics Letters*. Volume 14, No. 4 (February 15, 1989) pp 214-216
- [10] Bloembergen, N. *Nonlinear Optics* New York: W. A. Benjamin (1965)
- [11] Caledonia, G. E. and J. D. Teare. "Laser beam hygroscopic aerosol interactions" *Transactions of the ASME Journal of Heat Transfer*. Vol 99 (May, 1977) pp 281-286.
- [12] Carls, J. C. and J. R. Brock. "Explosive vaporization of single droplets by lasers: comparison of models with experiments." *Optics Letters*. Volume 13, No. 10 (October, 1988) pp 919-921
- [13] Chang, Randolph and E. James Davis. "Knudsen Aerosol Evaporation" *Journal of Colloid and Interface Science*. Volume 54, No. 3 (March, 1976) pp 352-363.
- [14] Chitanvis, Shirish M. "Explosion of Water Droplets" *Applied Optics*, Vol 25, No. 11 pp 1837-1839
- [15] Chow, S. N., J. Mallet-Paret, and J. A. Yorke. Finding zeros of maps: homotopy methods that are constructive with probability one. *Math. Comp.* Volume 32 (1978) pp 887-889.
- [16] Chevaillier, Jean Phillippe, Jean Fabre, and Patrice Hamelin. "Forward scattered light intensities by a sphere located anywhere in a Gaussian beam" *Applied Optics*, Vol. 25, No. 7 (April 1, 1986) pp 1222-1225.
- [17] Chevaillier, Jean Phillippe, Jean Fabre, Gerard Grehan, and Gerard Gousbet. "Comparison of diffraction theory and generalized Lorenz-Mie theory for a sphere located on the axis of a laser beam." *Applied Optics*, Vol 29, No. 9 (March 20, 1990) pp 1293-1298.
- [18] Chylek, Petr, Maurice A. Jarzembki, Vandana Srivastava, and Ronald G. Pinnick. "Pressure Dependence of the Laser Induced Breakdown Thresholds of Gases and Droplets" *Applied Optics* Volume 29, Number 15 (May 20, 1990) pp 2303-2306

- [19] Cohoon, D. K. On the uniqueness of Solutions of Electromagnetic Interaction Problems Associated with Scattering by Bianisotropic Bodies IN Rassias, George. *The Mathematical Heritage of C. F. Gauss* Singapore: World Scientific Publishing (1991) pp 119 - 132.
- [20] Cross, L. A. "High repetition rate, high resolution back lit, shadow, and schlieren photography of gaseous and liquid mass transport phenomena and flames" *International Congress on Instrumentation in Aerospace Simulation Facilities Dayton Ohio 1981* Dayton, Ohio: ICIASF 1981 Record (September 30, 1981)
- [21] Davis, E. James and Asit K. Ray. "Determination of diffusion coefficients by submicron droplet evaporation"
- [22] Dixon - Lewis, G. "Flame Structure and Flame Reaction Kinetics II. Transport Phenomena in Multi-component Systems" *Proceedings of the Royal Society A. Volume 307* (1968) pp 111 - 135.
- [23] Eringen, A. Cemal, and S. Suhubi S. Erdogan. *Elastodynamics. Volume I. Finite Motions* New York: Academic Press (1974)
- [24] Eringen, A. Cemal, and S. Suhubi S. Erdogan. *Elastodynamics. Volume II. Linear Theory* New York: Academic Press (1975)
- [25] Ewing, W., Maurice Wenceslas, S. Jardetzky, and Frank Press. *Elastic Waves in Layered Media* New York: McGraw Hill (1957)
- [26] Eyring, Henry, and Mu Shik Jhon. *Significant Liquid Structures* New York: John Wiley and Sons (1969)
- [27] Fisher, I. Z. *Statistical Theory of Liquids* Chicago: The University of Chicago Press(1961)
- [28] Frenklach, Michael and Hai Wang. "Detailed Modeling of Soot Particle Nucleation and Growth. *Twentythird Symposium (International) on Combustion. The Combustion Institute* (1990) pp 1559 -1556.
- [29] "On the driving force of PAH production" *Twenty Second Symposium (International) on Combustion /The Combustion Institute* (1988) pp 1075 - 1082.
- [30] Frenklach, Michael and Stephen J. Harris. "Aerosol Dynamics Modeling Using the Method of Moments" *Journal of Colloid and Interface Science, Volume 118, No. 1* (July, 1987) pp 252 -261
- [31] Frenklach, Michael. "Dynamics of Discret Distribution for Smoluchowski Coagulation Model" *Journal of Colloid and Interface Science, Volume 108, No. 1* (November, 1985) pp 237 - 242.
- [32] Frenklach, Michael. "Computer Modeling of Infinite Reaction Sequences: A Chemical Lumping" *Chemical Engineering Science, Volume 40, Number 10* (1985) pp 1843 - 1849.
- [33] Frenklach, Michael, David W. Clary, William Gardner, and Stephen Stein. "Detailed Kinetic Modeling of Soot Formation in Shock Tube Pyrolysis of Acetylene" *Twentieth Symposium (International) on Combustion /The Combustion Institute* (1984) pp 887 - 901
- [34] Garcia, C. B. and W. I. Zangwill. *Pathways to Solutions, Fixed Points, and Equilibria.* Englewood Cliffs, NJ: Prentice Hall(1981)
- [35] Glickler, S. L. "Propagation of a 10.6 μ laser through a cloud including droplet vaporization" *Applied Optics, Volume 10, No. 9* (March, 1971) pp 644-650
- [36] Gosman, A. D., W. M. Pun, A. K. Runchal, D. B. Spalding, and M. Wolfshtein (Eds) *Heat and Mass Transfer in Recirculating Flows* New York: Academic Press (1969)
- [37] Hochstadt, Harry. *The Functions of Mathematical Physics.* New York: Dover(1986).
- [38] Hörmander, Lars. *Linear Partial Differential Operators* New York: Academic Press (1963)

- [39] Hsu, Yih-Yun, and Robert W. Graham. *Transport Processes in Boiling and Two Phase Systems* New York: McGraw Hill(1976)
- [40] Incropera, Frank P. and David P. Dewitt. *Fundamentals of Heat Transfer* New York: John Wiley and Sons (1981)
- [41] Jaluria, Yogesh. *Natural Convection, Heat and Mass Transfer*. New York: Pergamon Press (1980)
- [42] Kogelnik, H. and T. Li. "Laser beams and resonators" *Applied Optics*. Volume 5, Number 10 (October, 1966) pp 1550-1566
- [43] Kee, R. J., and J. A. Miller. "A structured approach to the computational modeling of chemical kinetics and molecular transport in flowing systems" Albuquerque, NM 81185: Sandia National Laboratories (February, 1992)
- [44] Kozaki, Shogo. "Scattering of a Gaussian Beam by a Homogeneous Dielectric Cylinder" *Journal of Applied Physics*. Volume 53, No. 11 (November, 1982) pp 7195-7200
- [45] Liou, K. N., S. C. Ou Takano, A. Heymsfield, and W. Kreiss. "Infrared transmission through cirrus clouds: a radiative model for target detection" *Applied Optics*. Volume 29, Number 19 (May 1, 1990) pp 1886-1896
- [46] Luikov, A. V. and Yu A. Mikhailov. *Theory of Energy and Mass Transfer* New York: Pergamon Press (1965)
- [47] Mackowski, D. W., R. A. Altenkirch, and M. P. Menguc. "Internal absorption cross sections in a stratified sphere" *Applied Optics*, Volume 29, Number 10 (April 1, 1990) pp 1551-1559
- [48] Majda, Andrew. *The Stability of Multi Dimensional Shock Fronts* Providence, Rhode Island: Memoires of the AMS. Volume 41, Number 275 (January, 1983)
- [49] Margolis, Stephen L. and Gregory Sivashinsky. "On Spinning Propagation of Cellular Flames" *Combustion Science and Technology*. Volume 69 (1990) pp 99 - 131.
- [50] Margolis, Stephen B. and Bernard J. Matkowsky. "New Modes of Quasi Periodic Combustion Near a Degenerate Hopf Bifurcation Point" *SIAM Journal of Applied Mathematics*, Volume 48, No 4 (August, 1988) pp 828 - 853
- [51] Monson, B., Vyas Reeta, and R. Gupta. "Pulsed and CW Photothermal Phase Shift Spectroscopy in a Fluid Medium: Theory" *Applied Optics*. Volume 28, No. 19 (July, 1989) pp 2554-2561.
- [52] Mugnai, Alberto and Warren J. Wiscombe. "Scattering from nonspherical Chebyshev Particles. I. Cross Sections, Single Scattering Albedo, Asymmetry factor, and backscattered fraction" *Applied Optics*, Volume 25, Number 7 (April 1, 1986) pp 1235-1244.
- [53] Odishaw, Hugh. *Research in Geophysics. Volume II. Solid Earth and Interface Phenomena* Cambridge, Massachusetts: The MIT Press (1964).
- [54] Park, Bac-Sig, A. Biswas, and R. L. Armstrong. "Delay of explosive vaporization in pulsed laser heated droplets" *Optics Letters*. Volume 15, No. 4 (February 15, 1990) pp 206-208
- [55] Pinnick, R. G., Abhijit Biswas, Robert L. Armstrong, S. Gerard Jennings, J. David Pendleton, and Gilbert Fernandez. "Micron size droplets irradiated with a pulsed CO₂ laser: Measurement of Explosion and Breakdown Thresholds" *Applied Optics*. Volume 29, No. 7 (March 1, 1990) pp 918-925
- [56] Pinnick, R. G., S. G. Jennings, Petr Chylek, Chris Ham, and W. T. Grandy. "Backscatter and Extinction in Water Clouds" *Journal of Geophysical Research*. Vol 88, No. C11 (August 20, 1983) pp 6787-6796

- [57] Richardson, C. B., R. L. Hightower, and A. L. Pigg. "Optical measurement of the evaporation of sulfuric acid droplets" *Applied Optics*. Volume 25, Number 7 (April 1, 1986) pp 1226-1229
- [58] Rosseland, S. *Theoretical Astrophysics: Atomic Theory and the Analysis of Stellar Atmospheres and Envelopes* Oxford, England: Clarendon Press (1936)
- [59] Schaub, S. A., D. R. Alexander, J. P. Barton, and M. A. Emanuel. "Focused laser beam interactions with methanol droplets: effects of relative beam diameter" *Applied Optics*. Volume 28, No. 9 (May 1, 1989) pp 1666-1669
- [60] Schiffer, Ralf. "Perturbation approach for light scattering by an ensemble of irregular particles of arbitrary material" *Applied Optics*, Volume 29, Number 10 (April 1, 1990) pp 1536-1550
- [61] Siegel, R. "Radiative Cooling Performance of a Converging Liquid Drop Radiator." *Journal of Thermophysics and Heat Transfer*. Volume 3, Number 1 (January, 1989) pp 46-52.
- [62] Siegel, Robert, and John R. Howell. *Thermal Radiation Heat Transfer* New York: Hemisphere Publishing Company (1981)
- [63] Smoller, Joel. *Shock waves and reaction diffusion equations* New York: Springer Verlag (1983)
- [64] Svetyurov, D. E. "State of transfer of radiant energy accompanied by evaporation of a disperse medium" *Soviet J. Quantum Electronics* Volume 3, No. 1 (July August, 1973) pp 33-36
- [65] Temam, Roger. *Sur la Stabilité et la Convergence de la Méthode Des Pas Fractionnaires. Theses présentée a la faculté des sciences de L'Université de Paris pour obtenir le grade de docteur es sciences mathématiques* Paris, France: Institut Henri Poincaré (Juin, 1967)
- [66] Tsai, Wen Chung and Ronald J. Pogorzelski. "Eigenfunction solution of the scattering of beam radiation fields by spherical objects" *Journal of the Optical Society of America*. Volume 65. Number 12 (December, 1975) pp 1457-1463.
- [67] Trefil, J. S. *Introduction to the Physics of Fluids and Solids* New York: Pergamon Press, Inc. (1975)
- [68] Tzeng, H. M., K. F. Wall, M. B. Long, and R. K. Chang. "Laser emission from individual droplets at wavelengths corresponding to morphology dependent resonances" *Optics Letters*. Volume 9, Number 11 (1984) pp 499-501
- [69] Voikovitsky, O. A. "Peculiarities of light scattering by droplet aerosol in a divergent CO_2 laser beam" *Applied Optics*. Volume 26, Number 24 (December 15, 1987) pp 5307-5310
- [70] von Mises, Richard, Hilda Geiringer, and G. S. S. Ludford. *Mathematical Theory of Compressible Fluid Flow* New York: Academic Press (1958)
- [71] Wasow, Wolfgang. *Asymptotic Expansions for Ordinary Differential Equations* New York: John Wiley (1965)
- [72] White, J. E. *Seismic Waves, Radiation, Transmission, and Antennuation* New York: McGraw Hill (1965)
- [73] Whittaker, E. T. and G. N. Watson. *A Course of Modern Analysis* London: Cambridge University Press (1986).
- [74] Zardecki, A. and J. David Pendleton. "Hydrodynamics of water droplets irradiated by a pulsed CO_2 laser." *Applied Optics*. Volume 28, No. 3 (February 1, 1989) pp 638-640
- [75] Zel'dovich, Ya B. and Yu P. Raizer. *Physics of Shock Waves and High Temperature Thermodynamic Phenomena* New York: Academic Press (1966)

Globally Convergent Homotopy, Continued Fractions and the Eigenvalues of Spin Weighted Angular Spheroidal Harmonics

D. K. Cohoon

September 3, 1992

Contents

- 1 Introduction
- 2 Solving Maxwell's Equations
- 3 Spheroidal Coordinates
- 4 Rayleigh Ritz Procedures
- 5 Continued Fractions

References

1 Introduction

Prolate spheroids are cigars and footballs and oblate spheroids are falling raindrops and doorknobs. A spheroid is an ellipse rotated about an axis. If it is rotated about a major axis it is a prolate spheroid. If it is rotated about a minor axis, it is an oblate spheroid. In the halls of Congress a certain young representative had his desk in a most undesirable location; for some reason, however, he was able to rise instantly and give brilliant rebuttals of the arguments of his opposition. It turned out that the roof was a spheroid and his desk was at one of the focal points and the desk of the opposition was at the other focal point. He could hear the whispered planning of the opposition long before they got up to speak. Unlike the wedding guest described 2000 years ago, he refused to move up to a place of greater honor, and, his secret remaining with himself, others were content to allow him to remain in his more humble post.

Spheroid scattering is important because it provides challenges for general purpose codes, and because one is interested in the propagation of electromagnetic information through

clouds of spheroids, such as falling raindrops. The computer codes developed may also have a bearing on the design of liquid crystal devices, such as liquid crystal television sets and computer monitors which would, as they use natural room light, be far safer for the users, often young girls, than cathode ray tube (CRT) devices currently in use. Young children, in poor urban settings, often spend hours huddled close to television sets. If they are going to do this anyway, let us, for the sake of the children, make television screens safer with a liquid crystal design. The ability to remember sight together with sound, may provide a way to teach and make literate a larger segment of human society all over the world; we have many serious problems to solve, and no one knows from where the genius to create a solution may come.

There are at least two approaches to spheroid scattering. These use ordinary spheroidal harmonics ([44], [43], and [45]) and the more general spin weighted angular spheroidal harmonics (Fackerell [10] and Futterman [17]). The key to both methods is the determination of the eigenvalues of angular spheroidal harmonics. We have proposed a Rayleigh Ritz functional approach, the classical method of estimating eigenvalues for elliptic boundary value problems, and the solution of a transcendental equation involving continued fractions. The latter requires an efficient method of evaluating continued fractions.

2 Solving Maxwell's Equations

Spence and Wells ([46]) in their classic paper on vector wave functions considered the difficulties of describing scattering of electromagnetic radiation by spheroids. They considered the possibility that a general function vector valued function \vec{F} might give solutions of the vector Maxwell equations of the form

$$\vec{V} = \text{curl}(\vec{F}\Psi)$$

They show that if Ψ is a solution of the scalar Helmholtz equation, then \vec{F} must be a constant vector or else a scalar times the vector

$$\vec{r} = x\vec{e}_x + y\vec{e}_y + z\vec{e}_z$$

where (x, y, z) is the representation of a point in Cartesian coordinates and \vec{e}_x , \vec{e}_y , and \vec{e}_z are the unit vectors along the positive x , y , and z axes, respectively. When these are transferred to spheroidal coordinates we have a basis of solutions as a linear combination of the functions $\text{curl}(\vec{F}(r)\Psi)$ and $\text{curl}(\text{curl}(\vec{F}(r)\Psi))$, since

$$-\Delta(\text{curl}(\vec{F}(r)\Psi(r)))\text{curl}(\text{curl}(\text{curl}(\vec{F}(r)\Psi))) = \text{curl}(\text{grad}(\text{div}(\vec{F}(r)\Psi(r))) - \Delta\Psi(r)) \quad (2.1)$$

Since the curl of a gradient is the zero vector and since

$$\Delta(\Psi) = -k^2\Psi \quad (2.2)$$

we see that

$$\text{curl}(\text{curl}(\text{curl}(\vec{F}\Psi))) = k^2 \cdot \text{curl}(\vec{F}\Psi) \quad (2.3)$$

This idea is the basis of the solution of ([1]) and many others.

3 Spheroidal Coordinates

To solve the problem of spheroid scattering it is important to represent the Faraday and Ampere Maxwell equations in spheroidal coordinates.

Consider an ellipse with foci at $(0, -d/2)$ and $(0, d/2)$ on the z axis and if

$$r^2 = x^2 + y^2 \quad (3.1)$$

and (r, z) is a point on the generating curve for the spheroid, then if we define for r_1 being the distance between (r, z) and $(0, -d/2)$ and if r_2 is the distance between $(0, d/2)$ and (r, z) , and if we then define $\tilde{\xi}$ by the rule,

$$\tilde{\xi} = (r_1 + r_2)/(2 \cdot c) \quad (3.2)$$

and define $\tilde{\eta}$ by the relation,

$$\tilde{\eta} = (r_1 - r_2)/(2 \cdot c) \quad (3.3)$$

where c is a constant, we have a set of coordinates for describing points within a spheroid. We shall actually use a slightly different set of coordinates that are qualitatively the same. We can define points on the surface of the spheroid as all those points (ξ, η, ϕ) for which ξ is a constant, which since an ellipse is the locus of points such that the sum of the distances from fixed foci is a constant is embodied in the definition of ξ given by equation, (3.2). The other coordinate surface defined by setting η equal to a constant is a hyperbola, as this says simply that the difference of the distances between two foci is a constant. The third coordinate surface defined by setting ϕ equal to a constant is simply a plane passing through the axis of rotation. We give an alternative definition of the spheroidal coordinates and show that this definition is compatible with the more intuitive definitions of equations (3.2) and (3.3) The relations between spheroidal and Cartesian coordinates are given by

$$x = \frac{d}{2} [(1 - \eta^2)(\xi^2 + 1)]^{1/2} \cos(\phi) \quad (3.4)$$

and

$$y = \frac{d}{2} [(1 - \eta^2)(\xi^2 + 1)]^{1/2} \sin(\phi) \quad (3.5)$$

and

$$z = \frac{d}{2} \eta \xi \quad (3.6)$$

Going back to the equation for an oblate spheroid we have that

$$\begin{aligned} (x^2 + y^2)/A^2 + z^2/B^2 &= \\ \frac{(d^2/4)(1 - \eta^2)(\xi^2 + 1)}{A^2} + \frac{(d^2/4)\eta^2\xi^2}{B^2} &= \\ \frac{d^2}{4} \left[\frac{1 - \eta^2}{(d/2)^2} + \frac{\eta^2}{(d/2)^2} \right] &= 1 \end{aligned} \quad (3.7)$$

if we simply let A and B be defined by

$$A = \frac{d}{2} \sqrt{\xi^2 + 1} \quad (3.8)$$

and

$$B = \frac{d}{2} |\xi| \quad (3.9)$$

For the oblate spheroid, we have

$$A > B \quad (3.10)$$

and the foci of the ellipse may be thought to be on the x axis located at

$$x = C = \sqrt{A^2 - B^2} = d/2 \quad (3.11)$$

and the sum of the distances from a fixed point on the surface to the two foci is $2A$ which happens to be

$$2A = d\sqrt{\xi^2 + 1} = r_1 + r_2 \quad (3.12)$$

If we compare equation (3.12) with the earlier equation (3.2) we can see easily the connection between ξ and ζ and that setting either one of these equal to a constant defines a surface of a spheroid.

We now try to develop the unit vectors in the direction of the normals to the coordinate surfaces $\xi = \text{constant}$ or $\eta = \text{constant}$. Note that if we had a general coordinate transformation relationship

$$\begin{pmatrix} x \\ y \\ z \end{pmatrix} = \begin{pmatrix} x(u, v, w) \\ y(u, v, w) \\ z(u, v, w) \end{pmatrix} \quad (3.13)$$

and the unit vector in the direction of the normal to the coordinate surface

$$u = \text{constant} \quad (3.14)$$

is given by

$$\vec{e}_u = \frac{d\vec{R}}{du} / \left(\left\| \frac{d\vec{R}}{du} \right\| \right) \quad (3.15)$$

where

$$\vec{R} = x\vec{e}_x + y\vec{e}_y + z\vec{e}_z \quad (3.16)$$

If we imagine an arc in three dimensional space and try to describe it in Cartesian and spheroidal coordinate. Assume that the arc $\vec{R}(t)$ is defined as an orbit defined by a continuous parameter t . Let $s(t_2)$ minus $s(t_1)$ denote the arc length between $\vec{R}(t_2)$ and $\vec{R}(t_1)$ on this curve so that

$$\left(\frac{ds}{dt} \right)^2 = \left(\frac{dx}{dt} \right)^2 + \left(\frac{dy}{dt} \right)^2 + \left(\frac{dz}{dt} \right)^2 \quad (3.17)$$

In order to get values of parameters h_ξ , h_η , and h_ϕ so that we may express the Laplacian and curl operations in spheroidal coordinates we observe that equation (3.4) implies that

$$\frac{\partial x}{\partial \xi} = \frac{d}{2} [(1 - \eta^2)]^{1/2} \xi [(\xi^2 + 1)]^{-1/2} \cos(\phi) \quad (3.18)$$

From equation (3.5) we see that

$$\frac{\partial y}{\partial \xi} = \frac{d}{2} [(1 - \eta^2)]^{1/2} \xi [(\xi^2 + 1)]^{-1/2} \sin(\phi) \quad (3.19)$$

From equation (3.6) we see that

$$\frac{\partial z}{\partial \xi} = \frac{d}{2} \eta \quad (3.20)$$

Thus, using the unit vector equation (3.15) and equations (3.18) and (3.19) and (3.20) we see that the unit vector \vec{e}_ξ is given by

$$\begin{aligned} \vec{e}_\xi = & \sqrt{\frac{\xi^2 + 1}{\xi^2 + \eta^2}} \left[\xi \sqrt{\frac{1 - \eta^2}{\xi^2 + 1}} \cos(\phi) \vec{e}_x + \right. \\ & \left. \xi \sqrt{\frac{1 - \eta^2}{\xi^2 + 1}} \sin(\phi) \vec{e}_y + \eta \vec{e}_z \right] \end{aligned} \quad (3.21)$$

Thus, we see that the length factors In an analogous manner we write down the unit vector \vec{e}_η by the rule

$$\begin{aligned} \vec{e}_\eta = & \sqrt{\frac{1 - \eta^2}{\xi^2 + \eta^2}} \left[-\eta \sqrt{\frac{\xi^2 + 1}{1 - \eta^2}} \cos(\phi) \vec{e}_x + \right. \\ & \left. -\eta \sqrt{\frac{\xi^2 + 1}{1 - \eta^2}} \sin(\phi) \vec{e}_y + \xi \vec{e}_z \right] \end{aligned} \quad (3.22)$$

We observe from equations (3.4), (3.5), and (3.6) that

$$\frac{\partial x}{\partial \phi} = -\frac{d}{2} [(1 - \eta^2)(\xi^2 + 1)]^{1/2} \sin(\phi), \quad (3.23)$$

$$\frac{\partial y}{\partial \phi} = \frac{d}{2} [(1 - \eta^2)(\xi^2 + 1)]^{1/2} \cos(\phi) \quad (3.24)$$

and

$$\frac{\partial z}{\partial \phi} = 0 \quad (3.25)$$

Finally, again making use of the equation (3.15) and equations (3.23) and (3.24) and (3.25) we see that the unit vector \vec{e}_ϕ is given by

$$\vec{e}_\phi = -\sin(\phi) \vec{e}_x + \cos(\phi) \vec{e}_y \quad (3.26)$$

It is clear from the definition, equation (3.15) used in creating equations (3.21), (3.22), and (3.23) that there are scalar functions h_ξ , h_η , and h_ϕ of ξ and η that satisfy

$$h_\xi \vec{e}_\xi = \frac{\partial x}{\partial \xi} \vec{e}_x + \frac{\partial y}{\partial \xi} \vec{e}_y + \frac{\partial z}{\partial \xi} \vec{e}_z, \quad (3.27)$$

$$h_\eta \vec{e}_\eta = \frac{\partial x}{\partial \eta} \vec{e}_x + \frac{\partial y}{\partial \eta} \vec{e}_y + \frac{\partial z}{\partial \eta} \vec{e}_z \quad (3.28)$$

and

$$h_\phi \vec{e}_\xi = \frac{\partial x}{\partial \phi} \vec{e}_x + \frac{\partial y}{\partial \phi} \vec{e}_y + \frac{\partial z}{\partial \phi} \vec{e}_z \quad (3.29)$$

We notice that these vectors \vec{e}_ξ , \vec{e}_η , \vec{e}_ϕ are pairwise orthogonal in the sense that

$$\vec{e}_\eta \cdot \vec{e}_\xi = \vec{e}_\eta \cdot \vec{e}_\phi = \vec{e}_\xi \cdot \vec{e}_\phi = 0 \quad (3.30)$$

We can use these relationships to represent the vector \vec{R} defined by equation (3.16) in terms of \vec{e}_ξ , \vec{e}_η , and \vec{e}_ϕ . We see that

$$\vec{R} = (\vec{R} \cdot \vec{e}_\xi) \vec{e}_\xi + (\vec{R} \cdot \vec{e}_\eta) \vec{e}_\eta + (\vec{R} \cdot \vec{e}_\phi) \vec{e}_\phi \quad (3.31)$$

where

$$(\vec{R} \cdot \vec{e}_\xi) = \frac{x}{h_\xi} \cdot \frac{\partial x}{\partial \xi} + \frac{y}{h_\xi} \cdot \frac{\partial y}{\partial \xi} + \frac{z}{h_\xi} \cdot \frac{\partial z}{\partial \xi}, \quad (3.32)$$

$$(\vec{R} \cdot \vec{e}_\eta) = \frac{x}{h_\eta} \cdot \frac{\partial x}{\partial \eta} + \frac{y}{h_\eta} \cdot \frac{\partial y}{\partial \eta} + \frac{z}{h_\eta} \cdot \frac{\partial z}{\partial \eta}, \quad (3.33)$$

and

$$(\vec{R} \cdot \vec{e}_\phi) = \frac{x}{h_\phi} \cdot \frac{\partial x}{\partial \phi} + \frac{y}{h_\phi} \cdot \frac{\partial y}{\partial \phi} + \frac{z}{h_\phi} \cdot \frac{\partial z}{\partial \phi}, \quad (3.34)$$

First, substituting equations (3.18), (3.19), (3.20), (3.4), (3.5), and (3.6) into equation (3.32) we obtain

$$(\vec{R} \cdot \vec{e}_\xi) = \frac{d}{2} \cdot \xi \cdot \sqrt{\frac{\xi^2 + 1}{\xi^2 + \eta^2}} \quad (3.35)$$

Next, determining that

$$\frac{\partial x}{\partial \eta} = \frac{d}{2} [(\xi^2 + 1)]^{1/2} (-\eta) [(1 - \eta^2)]^{-1/2} \cos(\phi) \quad (3.36)$$

and that

$$\frac{\partial y}{\partial \eta} = \frac{d}{2} \left[\sqrt{\frac{\xi^2 + 1}{1 - \eta^2}} \right] (-\eta) \sin(\phi) \quad (3.37)$$

Equations (3.36), (3.37), and (3.4), (3.5), and (3.6) tell us that

$$(\vec{R} \cdot \vec{e}_\eta) = -\eta \frac{d}{2} \sqrt{\frac{1 - \eta^2}{\xi^2 + \eta^2}} \quad (3.38)$$

For a general coordinate transformation from an (x,y,z) frame to a (u,v,w) frame we have the relationship,

$$\begin{aligned} \left(\frac{dx}{dt} \right)^2 + \left(\frac{dy}{dt} \right)^2 + \left(\frac{dz}{dt} \right)^2 &= \left\{ \left[\left(\frac{\partial x}{\partial u} \right)^2 + \left(\frac{\partial y}{\partial u} \right)^2 + \left(\frac{\partial z}{\partial u} \right)^2 \right] \left(\frac{\partial u}{\partial t} \right)^2 + \right. \\ &\left[\left(\frac{\partial x}{\partial v} \right)^2 + \left(\frac{\partial y}{\partial v} \right)^2 + \left(\frac{\partial z}{\partial v} \right)^2 \right] \left(\frac{\partial v}{\partial t} \right)^2 + \left[\left(\frac{\partial x}{\partial w} \right)^2 + \left(\frac{\partial y}{\partial w} \right)^2 + \left(\frac{\partial z}{\partial w} \right)^2 \right] \left(\frac{\partial w}{\partial t} \right)^2 \end{aligned}$$

$$\begin{aligned}
& 2 \left[\frac{\partial x}{\partial u} \cdot \frac{\partial x}{\partial v} + \frac{\partial y}{\partial u} \cdot \frac{\partial y}{\partial v} + \frac{\partial z}{\partial u} \cdot \frac{\partial z}{\partial v} \right] \frac{du}{dt} \cdot \frac{dv}{dt} + \\
& 2 \left[\frac{\partial x}{\partial u} \cdot \frac{\partial x}{\partial w} + \frac{\partial y}{\partial u} \cdot \frac{\partial y}{\partial w} + \frac{\partial z}{\partial u} \cdot \frac{\partial z}{\partial w} \right] \frac{du}{dt} \cdot \frac{dw}{dt} + \\
& 2 \left[\frac{\partial x}{\partial v} \cdot \frac{\partial x}{\partial w} + \frac{\partial y}{\partial v} \cdot \frac{\partial y}{\partial w} + \frac{\partial z}{\partial v} \cdot \frac{\partial z}{\partial w} \right] \frac{dv}{dt} \cdot \frac{dw}{dt} \} \quad (3.39)
\end{aligned}$$

Making use of the orthogonality of the ξ , η , and ϕ coordinate system we see that with

$$(u, v, w) = (\xi, \eta, \phi) \quad (3.40)$$

that all of the terms in equation (3.39) with a factor of 2 vanish, and that

$$\left(\frac{dx}{dt} \right)^2 + \left(\frac{dy}{dt} \right)^2 + \left(\frac{dz}{dt} \right)^2 = h_\xi^2 \left(\frac{d\xi}{dt} \right)^2 + h_\eta^2 \left(\frac{d\eta}{dt} \right)^2 + h_\phi^2 \left(\frac{d\phi}{dt} \right)^2 \quad (3.41)$$

Thus, for oblate spheroidal coordinates we obtain upon making use of equation (3.41) the following expressions for h_ξ , h_η , and h_ϕ . From this equation and equations (3.18), (3.19), and (3.20) we see that

$$h_\xi = \frac{d}{2} \sqrt{\frac{\xi^2 + \eta^2}{\xi^2 + 1}} \quad (3.42)$$

Next observe that

$$h_\eta = \frac{d}{2} \sqrt{\frac{\xi^2 + \eta^2}{1 - \eta^2}} \quad (3.43)$$

Finally equations (3.23), (3.24), and (3.25) imply that

$$h_\phi = \frac{d}{2} \sqrt{(1 - \eta^2)(\xi^2 + 1)} \quad (3.44)$$

In order to carry out vector calculus in oblate spheroidal coordinates we need the following relations. Equations (3.42), (3.43), and (3.44) imply that

$$h_\xi h_\eta h_\phi = \frac{d^3}{8} (\xi^2 + \eta^2) \quad (3.45)$$

Also, equations (3.42), (3.43), and (3.44) imply that

$$\frac{h_\eta h_\phi}{h_\xi} = \frac{d}{2} (\xi^2 + 1) \quad (3.46)$$

The other two similar relations are

$$\frac{h_\xi \cdot h_\eta}{h_\phi} = \frac{d}{2} \left(\frac{\xi^2 + \eta^2}{(\xi^2 + 1)(1 - \eta^2)} \right) \quad (3.47)$$

and

$$\frac{h_\xi \cdot h_\phi}{h_\eta} = \frac{d}{2} (1 - \eta^2) \quad (3.48)$$

The above relations are needed to define the Helmholtz equation in oblate spheroidal coordinates. In order to define the *curl* operation in oblate spheroidal coordinates we need the product pairs as well Equations (3.42) and (3.43) imply that

$$h_\xi \cdot h_\eta = \frac{d^2}{4} \frac{\xi^2 + \eta^2}{\sqrt{(\xi^2 + 1)(1 - \eta^2)}} \quad (3.49)$$

Equations (3.42) and (3.44) imply that

$$h_\xi \cdot h_\phi = \frac{d^2}{4} \sqrt{(\xi^2 + \eta^2)(1 - \eta^2)} \quad (3.50)$$

Finally, equations (3.43) and (3.44) imply that

$$h_\eta \cdot h_\phi = \frac{d^2}{4} \sqrt{(\xi^2 + \eta^2)(\xi^2 + 1)} \quad (3.51)$$

The curl operator in a general orthogonal coordinate system of orthogonal u , v , and w coordinates is given by

$$\begin{aligned} \text{curl}(\vec{E}) = & \\ & \frac{1}{h_v h_w} \left[\frac{\partial}{\partial v} (h_w E_w) - \frac{\partial}{\partial w} (h_v E_v) \right] \vec{e}_u + \\ & \frac{1}{h_u h_w} \left[\frac{\partial}{\partial w} (h_u E_u) - \frac{\partial}{\partial u} (h_w E_w) \right] \vec{e}_v + \\ & \frac{1}{h_u h_v} \left[\frac{\partial}{\partial u} (h_v E_v) - \frac{\partial}{\partial v} (h_u E_u) \right] \vec{e}_w \end{aligned} \quad (3.52)$$

Equation (3.52) may be derived from combining the representation of Cartesian frame unit vectors in terms of \vec{e}_u , \vec{e}_v , and \vec{e}_w and using the *gradient* equation,

$$\text{grad}(\Psi) = \frac{1}{h_u} \frac{\partial \Psi}{\partial u} \vec{e}_u + \frac{1}{h_v} \frac{\partial \Psi}{\partial v} \vec{e}_v + \frac{1}{h_w} \frac{\partial \Psi}{\partial w} \vec{e}_w \quad (3.53)$$

since (3.53) can be used to express the curl of a vector field as the gradient cross this vector field. The divergence is given by

$$\begin{aligned} \text{div}(\vec{E}) = & \left(\frac{1}{h_u h_v h_w} \right) \left\{ \left(\frac{\partial}{\partial u} \right) (h_v h_w \cdot E_u) \right. \\ & \left. \left(\frac{\partial}{\partial v} \right) (h_w h_u \cdot E_v) + \left(\frac{\partial}{\partial w} \right) (h_v h_u \cdot E_w) \right\} \end{aligned} \quad (3.54)$$

It is easy to show that

$$\text{curl}(\text{curl}(\vec{E})) = \text{grad}(\text{div}(\vec{E})) - \Delta \vec{E} \quad (3.55)$$

where

$$\Delta \Psi = \frac{1}{h_u h_v h_w} \left\{ \frac{\partial}{\partial u} \left(\frac{h_v h_w}{h_u} \frac{\partial \Psi}{\partial u} \right) + \right.$$

$$\frac{\partial}{\partial v} \left(\frac{h_u h_w}{h_v} \frac{\partial \Psi}{\partial v} \right) + \frac{\partial}{\partial w} \left(\frac{h_u h_v}{h_w} \frac{\partial \Psi}{\partial w} \right) \quad (3.56)$$

The relationship (3.55) implies that

$$\Delta(\text{curl}(\vec{E})) = -\text{curl}(\text{curl}(\text{curl}(\vec{E}))) = \text{curl}(\Delta(\vec{E})) \quad (3.57)$$

since

$$\text{curl}(\text{grad}(\Psi)) = \vec{0} \quad (3.58)$$

4 Rayleigh Ritz Procedures

One method is to use separation of variables to obtain a solution of the scalar Helmholtz equation and then to use the fact that if we multiply the position vector by this single solution and repeatedly apply the curl operation, we only generate a basis for a finite dimensional vector space.

$$\begin{aligned} \Delta \Psi + k^2 \Psi = & \\ \left\{ \frac{\partial}{\partial \xi} \left((\xi^2 + 1) \frac{\partial \Psi}{\partial \xi} \right) + \frac{\partial}{\partial \eta} \left((1 - \eta^2) \frac{\partial \Psi}{\partial \eta} \right) \right. & \\ \left. + \frac{\xi^2 + \eta^2}{(\xi^2 + 1)(1 - \eta^2)} \frac{\partial^2 \Psi}{\partial \phi^2} \right\} & \\ + k^2 \frac{d^2}{4} (\xi^2 + \eta^2) \Psi = 0 & \quad (4.1) \end{aligned}$$

We now seek solutions of equation (4.1) of the form

$$\Psi = R(\xi)S(\eta)\exp(im\phi) \quad (4.2)$$

and substitute equation (4.2) into equation (4.1) and then divide all terms of this equation by the function Ψ defined by equation (4.2) after making use of the relationship

$$\begin{aligned} \frac{\xi^2 + \eta^2}{(\xi^2 + 1)(1 - \eta^2)} = & \\ \frac{1}{1 - \eta^2} - \frac{1}{\xi^2 + 1} & \quad (4.3) \end{aligned}$$

and making the substitution

$$c^2 = k^2 d^2 / 4 \quad (4.4)$$

we obtain the relation,

$$\begin{aligned} \left\{ \frac{\partial}{\partial \eta} \left((1 - \eta^2) \frac{\partial}{\partial \eta} S(c, \eta) \right) \right\} / S(c, \eta) & \\ - \frac{m^2}{1 - \eta^2} + c^2 \eta^2 = & \end{aligned}$$

$$- \left\{ \frac{\partial}{\partial \xi} \left((\xi^2 + 1) \frac{\partial R(c, \xi)}{\partial \xi} \right) \right\} / R(c, \xi) + \frac{m^2}{\xi^2 + 1} + c^2 \xi^2 = -\lambda_{(m,n)} \quad (4.5)$$

From equation (4.5) we obtain a kind of Rayleigh Ritz functional for the value of $\lambda_{(m,n)}$. Equation (4.5) tells us that

$$\lambda_{(m,n)} = \frac{\left\{ \int_{-1}^1 \left[(1 - \eta^2) \left(\frac{dS}{d\eta} \right)^2 + S^2 \cdot \left\{ (-c^2 \eta^2) + \frac{m^2}{1 - \eta^2} \right\} \right] d\eta \right\}}{\left\{ \int_{-1}^1 S^2 d\eta \right\}} \quad (4.6)$$

We note that when c is equal to zero, we are dealing with a sphere and that the angular functions are the associated Legendre functions $P_n^m(\eta)$ so it makes sense that we want S to behave like the function $P_n^m(\eta)$ when c is zero. We note that either $n - m$ is even or odd, and we know the initial conditions exactly in each case. We use partial derivative notation for functions $G(c, \eta)$ and note that

$$D_2 G(c, 0) = \lim_{\eta \rightarrow 0} \frac{\partial G}{\partial \eta} \quad (4.7)$$

and define the initial conditions for the second order ordinary differential equation satisfied by the functions $S(c, \eta)$. We find that if $n - m$ is an even integer

$$S_{(m,n)}(c, 0) = \left\{ (-1)^{(n-m)/2} (n+m)! \right\} / \left\{ 2^n \left(\frac{n-m}{2} \right)! \left(\frac{n+m}{2} \right)! \right\} \quad (4.8)$$

and

$$D_2 S_{(m,n)}(c, 0) = 0 \quad (4.9)$$

and when $n - m$ is an odd number that

$$S_{(m,n)}(c, 0) = 0 \quad (4.10)$$

and that

$$D_2 S_{(m,n)}(c, 0) = \left\{ (-1)^{(n-m-1)/2} (n+m+1)! \right\} / \left\{ 2^n \left(\frac{n-m-1}{2} \right)! \left(\frac{n+m+1}{2} \right)! \right\} \quad (4.11)$$

With these initial conditions we have completely specified S and its partial derivative and mixed partial derivative as a function of η , c , and λ and we also know that

$$\lambda(0) = n(n+1) \quad (4.12)$$

This gives us an initial value problem and an ordinary differential equation

$$\lambda'(c) = F(c, \lambda) \quad (4.13)$$

where the function F is determined by differentiating both sides of equation (4.6) with respect to c and collecting terms involving $\lambda'(c)$, and then dividing all terms by the coefficient

of $\lambda'(c)$ to get the first order ordinary differential equation (4.13). By the uniqueness of the Cauchy problem, different initial values cannot lead to the same eigenvalue at

$$c = k \cdot \frac{d}{2} \quad (4.14)$$

This is effective if c is real, but if k is complex, then we think of c as being a function of a parameter s defined by

$$c(s) = s \cdot k \cdot \frac{d}{2} \quad (4.15)$$

and with the same initial condition develop an ordinary differential equation of the form,

$$\lambda'(s) = G(s), \quad (4.16)$$

We can also use continued fraction relationships to get the values of λ . Separation of variables applied to the scalar Helmholtz equation in spheroidal coordinates yields the ordinary differential equation

$$\frac{\partial}{\partial \eta} \left((1 - \eta^2) \frac{\partial}{\partial \eta} \mathcal{S}(c, \eta) \right) + \left(\lambda + c^2 \eta^2 - \frac{m^2}{1 - \eta^2} \right) \mathcal{S}(c, \eta) = 0 \quad (4.17)$$

We seek a solution, $\mathcal{S}(c, \eta)$ which is bounded at η equal to plus and minus one only for a discrete set of eigenvalues λ . We obtain these solutions as one of two odd or even power series,

$$\mathcal{S}^{(o)}(\eta) = \eta \cdot (1 - \eta^2)^{m/2} \left[\sum_{k=0}^{\infty} C_{2k} (1 - \eta^2)^k \right] \quad (4.18)$$

or

$$\mathcal{S}^{(e)}(\eta) = (1 - \eta^2)^{m/2} \left[\sum_{k=0}^{\infty} C_{2k} (1 - \eta^2)^k \right] \quad (4.19)$$

Differentiating both sides of equation (4.18) with respect to η we find that

$$\begin{aligned} \frac{\partial \mathcal{S}^{(o)}}{\partial \eta} &= (1 - \eta^2)^{m/2} \cdot \left[\sum_{k=0}^{\infty} C_{2k} (1 - \eta^2)^k \right] + \\ &\eta \left\{ (m/2) (1 - \eta^2)^{(m/2-1)} \cdot (-2\eta) \right\} \cdot \left[\sum_{k=0}^{\infty} C_{2k} (1 - \eta^2)^k \right] + \\ &\eta (1 - \eta^2)^{m/2} \left[\sum_{k=0}^{\infty} \left\{ C_{2k} \cdot k \cdot (1 - \eta^2)^{k-1} \cdot (-2 \cdot \eta) \right\} \right] \end{aligned} \quad (4.20)$$

Similarly, differentiating both sides of equation (4.19) with respect to η we find that

$$\begin{aligned} \frac{\partial \mathcal{S}^{(e)}}{\partial \eta} &= (m/2) \cdot (1 - \eta^2)^{(m/2-1)} \cdot (-2\eta) \cdot \left[\sum_{k=0}^{\infty} \left\{ C_{2k} (1 - \eta^2)^k \right\} \right] \\ &+ (1 - \eta^2)^{m/2} \cdot \left[\sum_{k=0}^{\infty} \left\{ C_{2k} \cdot k \cdot (1 - \eta^2)^{k-1} \cdot (-2 \cdot \eta) \right\} \right] \end{aligned} \quad (4.21)$$

We can simplify the expression (4.20) obtained by taking derivatives with respect to η of the power series defined by equation (4.18) by making repeated use of the tautology

$$-A \cdot \eta^2 = (+A) \cdot (1 - \eta^2) - A \quad (4.22)$$

and, in fact, we deduce after collecting terms that

$$\begin{aligned} \frac{d}{d\eta} S^o(\eta) &= (1 - \eta^2)^{m/2} \sum_{k=0}^{\infty} C_{2k} [1 + m + 2 \cdot k] (1 - \eta^2)^k + \\ &\quad (1 - \eta^2)^{m/2} \sum_{k=0}^{\infty} C_{2k} [-m - 2k] (1 - \eta^2)^{k-1} \end{aligned} \quad (4.23)$$

A similar calculation involving the expression for the derivative of S^e given by equation (4.21) shows that

$$\frac{d}{d\eta} S^e(\eta) = \eta (1 - \eta^2)^{m/2} \sum_{k=0}^{\infty} C_{2k} [-m - 2 \cdot k] (1 - \eta^2)^{k-1} \quad (4.24)$$

Now we multiply both sides of equation (4.24) by $(1 - \eta^2)$ and differentiate with respect to η obtaining

$$\begin{aligned} \frac{\partial}{\partial \eta} \left((1 - \eta^2) \frac{\partial S^e}{\partial \eta} \right) &= (1 - \eta^2)^{m/2} \sum_{k=0}^{\infty} C_{2k} \left\{ [-m - 2 \cdot k] (1 - \eta^2)^k \right\} + \\ &\quad (-\eta^2) (1 - \eta^2)^{m/2} \left[\sum_{k=0}^{\infty} \left\{ C_{2k} [m \cdot (-m - 2 \cdot k)] (1 - \eta^2)^{(k-1)} \right\} \right] + \\ &\quad (-\eta^2) (1 - \eta^2)^{m/2} \left[\sum_{k=0}^{\infty} \left\{ C_{2k} [(2 \cdot k)(-m - 2 \cdot k)] (1 - \eta^2)^{(k-1)} \right\} \right] \end{aligned} \quad (4.25)$$

By combining equation (4.25) with equation (4.22) we deduce that

$$\begin{aligned} \frac{\partial}{\partial \eta} \left((1 - \eta^2) \frac{\partial S^e}{\partial \eta} \right) &= (1 - \eta^2)^{m/2} \left[\sum_{k=0}^{\infty} C_{2k} \left\{ [(1 + m + 2 \cdot k)(-m - 2 \cdot k)] (1 - \eta^2)^k \right\} \right] + \\ &\quad (1 - \eta^2)^{m/2} \left[\sum_{k=0}^{\infty} C_{2k} \left\{ [(-m - 2 \cdot k)(-m - 2 \cdot k)] (1 - \eta^2)^{k-1} \right\} \right] \end{aligned} \quad (4.26)$$

If we substitute the two power series given by (4.26) and (4.19) into the differential equation (4.17), we get a seemingly infinite set of recursion relations; a closer examination reveals that we can use continued fractions to eliminate the a priori unknown coefficients C_{2k} and get a single parameterized continued fraction expression for λ of the form

$$\mathcal{F}(\lambda(s), n, m, c(s)) = 0 \quad (4.27)$$

where if

$$c(0) = 0 \quad (4.28)$$

the equation is that of the associated Legendre function $P_n^m(\eta)$ which means that

$$\lambda(0) = n \cdot (n + 1) \quad (4.29)$$

Thus, the eigenvalues can be systematically determined, since $c(s)$ could be written as s times the actual value proportional to the distance between focal points of the spheroid, as the solution to the initial value problem

$$\lambda'(s) = \frac{D_4 F(\lambda, n, m, c) c'(s)}{D_1 F(\lambda, n, m, c)} \quad (4.30)$$

We simply solve the ordinary differential equation (4.30) to get to the eigenvalue, which then, because of the original recursion relationships gives us all the values of C_{2k} ; the spheroidal harmonics are systematically determined, even when the material properties are complex. Following this plan we see that the result of substituting equation (4.26) into the differential equation (4.17) is

$$\begin{aligned} \frac{\partial}{\partial \eta} \left((1 - \eta^2) \frac{\partial \mathcal{S}^e}{\partial \eta} \right) + \left((\lambda + c^2) - c^2 \cdot (1 - \eta^2) - \frac{m^2}{1 - \eta^2} \right) \mathcal{S}^e = \\ (1 - \eta^2)^{m/2} \left[\sum_{k=0}^{\infty} \left\{ C_{2k} \left\{ (\lambda + c^2) + [1 + m + 2 \cdot k](-m - 2k) \right\} (1 - \eta^2)^k \right\} \right] \\ + (1 - \eta^2)^{m/2} \left[\sum_{k=0}^{\infty} \left\{ C_{2k}(-c^2) \right\} (1 - \eta^2)^{k+1} \right] \text{space} + \\ (1 - \eta^2)^{m/2} \left[\sum_{k=0}^{\infty} \left\{ C_{2k} \left[-m^2 + (-m - 2 \cdot k)^2 \right] \right\} (1 - \eta^2)^{k-1} \right] = 0 \quad (4.31) \end{aligned}$$

Now equation (4.31) will give us a recursion relationship for the coefficients C_{2k} and will ultimately give us an expression for λ . Thankfully, the coefficient of the reciprocal of $(1 - \eta^2)$ in the series expansion in equation (4.31) is the $k = 0$ term of the third sum on the right side of equation (4.31) which is

$$C_{2,0} \left[-m^2 + (-m - 2 \cdot 0)^2 \right] = 0 \quad (4.32)$$

Making changes in indices using the formulae $j = (k + 1)$ and $j = (k - 1)$ in the second and third sums on the right side of equation (4.31) we obtain

$$\begin{aligned} 0 = \frac{\partial}{\partial \eta} \left((1 - \eta^2) \frac{\partial \mathcal{S}^e}{\partial \eta} \right) + \left((\lambda + c^2) - c^2 \cdot (1 - \eta^2) - \frac{m^2}{1 - \eta^2} \right) \mathcal{S}^e = \\ (1 - \eta^2)^{m/2} \left[\sum_{k=0}^{\infty} \left\{ C_{2k} \left\{ (\lambda + c^2) + [1 + m + 2 \cdot k](-m - 2k) \right\} (1 - \eta^2)^k \right\} \right] \\ + (1 - \eta^2)^{m/2} \left[\sum_{j=1}^{\infty} \left\{ C_{2(j-1)}(-c^2) \right\} (1 - \eta^2)^j \right] \\ (1 - \eta^2)^{m/2} \left[\sum_{j=0}^{\infty} \left\{ C_{2(j+1)} \left[-m^2 + (-m - 2 \cdot (j + 1))^2 \right] \right\} (1 - \eta^2)^j \right] = 0 \quad (4.33) \end{aligned}$$

Equation (4.33) after replacing the index j by k in the last two sums on the right side this equation gives us a three term recursion relationship involving the expansion coefficients

and the a priori unknown eigenvalue λ for indices k which are larger than 1. For $k = 0$, however, we have a vital relationship between C_0 , λ , and C_2 given by

$$C_0 \cdot [(\lambda + c^2 - m \cdot (1 + m))] + C_2 \cdot (-m^2 + (-m - 2)^2) = 0 \quad (4.34)$$

This tells us that

$$C_2 = \left(\frac{(\lambda + c^2) - m \cdot (m + 1)}{4 - 2m} \right) \cdot C_0 \quad (4.35)$$

If we set C_0 equal to zero when m is 2, then we can get a solvable relation for all values of m . Equation (4.35) tells us that

$$\frac{C_0}{C_2} = \frac{4 - 2m}{(\lambda + c^2) - m \cdot (m + 1)} \quad (4.36)$$

Looking at equation the three term relation determined by equating coefficients of powers of $(1 - \eta^2)^k$ in (4.33) for values of k larger than 0 we deduce that

$$C_{2k} \cdot [(\lambda + c^2) + [1 + m + 2 \cdot k] \cdot (-m - 2 \cdot k)] + C_{2 \cdot (k+1)} \left[-m^2 + \{-m^2 - 2 \cdot (k + 1)\}^2 \right] = C_{2 \cdot (k-1)} \cdot c^2 \quad (4.37)$$

By dividing all terms of the relation (4.37) by the middle term C_{2k} we get a series of continued fractions defined by

$$\frac{C_{2 \cdot (k-1)}}{C_{2 \cdot k}} = [(\lambda + c^2) + [1 + m + 2 \cdot k] \cdot (-m - 2 \cdot k)] + \frac{[-m^2 + \{(-m - 2 \cdot (k + 1))\}^2]}{c^2 \cdot [C_{2k}/C_{2 \cdot (k+1)}]} \quad (4.38)$$

The continued fraction relationship and a finite relationship based on repeated use of (4.38) and the initial condition (4.36) gives us a transcendental equation for the eigenvalues λ . In particular combine equation (4.38) for k equal to zero with the initial condition (4.36) then we get a functional relationship,

$$F(\lambda, c) = 0 \quad (4.39)$$

Differentiating both sides of equation (4.39) with respect to c we see that we can think of λ as a multivalued function of c

$$\left(\frac{\partial F}{\partial \lambda} \right) \cdot \lambda'(c) = \frac{\partial F}{\partial c} \quad (4.40)$$

This is a first order nonlinear ordinary differential equation. Let us imagine that a sphere is changing slowly into a spheroid by having c go from zero to a positive value. The solution of Maxwell's equations will change smoothly from the solution of the sphere scattering problem to the solution of the spheroid scattering problem. The eigenvalues for the associated Legendre functions which are $n \cdot (n + 1)$ will change systematically from those for the solution of the associated Legendre function equation

$$\frac{\partial}{\partial \eta} \left((1 - \eta^2) \frac{\partial}{\partial \eta} P_n^m(\eta) \right) + \left(n \cdot (n + 1) - \frac{m^2}{1 - \eta^2} \right) P_n^m(\eta) = 0 \quad (4.41)$$

to the corresponding solution of equation (4.17) by solving the differential equation (4.40) with initial value

$$\lambda'(0) = n \cdot (n + 1) \quad (4.42)$$

By the theory of continued fractions ([55]) we can show the convergence of the continued fractions used to represent the function $F(\lambda, c)$ mentioned in equation (4.39) to be the difference between the two representations of C_0/C_1 given by (4.38) for k equal to zero and (4.36), we can express the derivative by using Gaussian quadrature to help us evaluate the contour integrals

$$\frac{\partial F}{\partial \lambda}(\lambda, c) = \left(\frac{1}{2\pi i} \right) \cdot \int_C \left\{ \frac{F(\tilde{\lambda}, c)}{(\tilde{\lambda} - \lambda)^2} \right\} d\tilde{\lambda} \quad (4.43)$$

where C is a small contour in the complex plane surrounding λ inside of which $F(\lambda, c)$ is analytic. You simply move along solution paths from the $n \cdot (n + 1)$ initial values for the eigenvalues associated with equation (4.41) to the eigenvalues $\lambda_{(m,n)}$ associated with equation (4.17).

One problem with this approach is that the resulting vector functions that represent solutions of Maxwell equations are not orthogonal with respect to dot product and integration over the surface of the spheroid as they are with sphere scattering. One way to overcome this is to use a completely different concept. This is the concept of spin weighted angular spheroidal harmonics, solutions of a modification of the differential equation (4.17). The spin weighted angular spheroidal harmonics can be determined by a similar method.

A generalization of (4.17) is the ordinary differential equation for the spin weighted angular spheroidal functions ([10]) is given by

$$\frac{\partial}{\partial \eta} \left((1 - \eta^2) \frac{\partial}{\partial \eta} S(c, \eta) \right) + \left(\lambda + \gamma^2 \cdot \eta^2 - \frac{m^2 + s^2}{1 - \eta^2} - \frac{2 \cdot m \cdot s \cdot \eta}{1 - \eta^2} - 2 \cdot \gamma \cdot s \cdot \eta \right) S(c, \eta) = 0 \quad (4.44)$$

We note that we get the usual differential equation (4.17) simply by setting s equal to zero in equation (4.44). The method of using the spin weighted angular spheroidal harmonics to calculate scattering by spheroids is discussed in ([17]). The key to success is the determination of the eigenvalues. We attempt to find solutions of equation (4.17) of the form of equation (4.18) or equation (4.19). It appears at first glance that there would be a term involving the reciprocal of $(1 - \eta^2)$, but this term exactly cancels out, which means that if we can simply solve the resulting recursion relationship for some values of λ , we have our bounded solution. The values of λ for which we can find bounded solutions of equation (4.17) are eigenvalues and are determined by solving a transcendental equation in λ involving a continued fraction. A similar but more complex situation arises in determining the eigenvalues associated with the spin weighted angular spheroidal harmonics satisfying the more general equation (4.44).

The precise solution of a spheroid scattering problem will provide a convincing benchmark for the general surface or volume integral equation method.

5 Continued Fractions

The following theorems give us a practical means for evaluating continued fractions on a digital computer with a minimum of round off error.

Theorem 5.1 Let b_0, b_1, b_2, \dots and a_0, a_1, a_2, \dots be two sequences of complex numbers. Assume that W_0 is equal to b_0 and let

$$W_n = b_0 + \frac{a_1}{b_1 + \frac{a_2}{b_2 + \frac{a_3}{b_3 + \dots + \frac{a_n}{b_n}}}}$$
(5.1)

for all integers n greater than zero. Define initial values of a recursion by the relation,

$$(A_{-1}, B_{-1}, A_0, B_0) = (1, 0, b_0, 1)$$
(5.2)

Then define A_n and B_n for integers n larger than zero by the recursion

$$A_n = b_n A_{n-1} + a_n A_{n-2}$$
(5.3)

and the relation

$$B_n = b_n B_{n-1} + a_n B_{n-2}$$
(5.4)

Assume that b_n is nonzero and that for every positive integer n that

$$b_{n-1} \cdot b_n + a_n \neq 0$$
(5.5)

for all positive integers n . Then for all positive integers n we have

$$W_n = \frac{A_n}{B_n}$$
(5.6)

Proof: We proceed by induction on n . The statement (5.6) which we shall call proposition $\mathcal{P}(n)$ is true trivially if n is equal to zero and also for n equal to 1, since the initial conditions (5.2) and the recursion relations (5.3) and (5.4) imply that

$$\frac{A_1}{B_1} = \frac{b_1 \cdot b_0 + a_1 \cdot 1}{b_1 \cdot 1 + a_1 \cdot 0} = b_0 + \frac{a_1}{b_1} = W_1$$
(5.7)

Thus, assume that n is larger than one and that if m is a positive integer that is strictly smaller than n , then proposition $\mathcal{P}(m)$ or the statement,

$$W_m = \frac{A_m}{B_m},$$
(5.8)

is true. We now define a shorter continued fraction related to the W_n , which is defined by equation (5.1) by the rule,

$$W_n = W_n^*$$

where

$$W_n^* = b_0^* + \frac{a_1}{b_1^* + \frac{a_2^*}{b_2^* + \frac{a_3^*}{b_3^* + \dots + \frac{a_{n-1}^*}{b_{n-1}^*}}}} \quad (5.9)$$

where

$$b_{n-1}^* = b_{n-1} \cdot b_n + a_n, \quad (5.10)$$

$$a_{n-1}^* = a_{n-1} \cdot b_n, \quad (5.11)$$

and

$$a_j^* = a_j \quad (5.12)$$

and

$$b_j^* = b_j \quad (5.13)$$

for all j satisfying

$$j \in \{0, 1, \dots, n-2\} \quad (5.14)$$

Defining, as before,

$$A_{n-1}^* = b_{n-1} \cdot A_{n-2}^* + a_{n-3} \cdot A_{n-3}^* \quad (5.15)$$

and the relation

$$B_{n-1}^* = b_n \cdot B_{n-2}^* + a_n \cdot B_{n-3}^* \quad (5.16)$$

and realizing that

$$A_{n-2}^* = A_{n-2}, \quad (5.17)$$

$$A_{n-3}^* = A_{n-3}, \quad (5.18)$$

$$B_{n-2}^* = B_{n-2}, \quad (5.19)$$

and

$$B_{n-3}^* = B_{n-3}, \quad (5.20)$$

we see that by the inductive hypothesis

$$W_n = W_{n-1}^* = \frac{A_{n-1}^*}{B_{n-1}^*} = \frac{b_{n-1}^* \cdot A_{n-2} + a_{n-1}^* \cdot A_{n-3}}{b_{n-1}^* \cdot B_{n-2} + a_{n-1}^* \cdot B_{n-3}} \quad (5.21)$$

Substituting (5.10) and (5.11) into equation (5.21) and collecting coefficients of a_n and b_n we see that

$$W_n = \frac{(b_{n-1} \cdot b_n + a_n) \cdot A_{n-2} + (a_{n-1} \cdot b_n) \cdot A_{n-3}}{(b_{n-1} \cdot b_n + a_n) \cdot B_{n-2} + (a_{n-1} \cdot b_n) \cdot B_{n-3}} = \frac{b_n \cdot (b_{n-1} \cdot A_{n-2} + a_{n-1} \cdot A_{n-3}) + a_n \cdot A_{n-2}}{b_n \cdot (b_{n-1} \cdot B_{n-2} + a_{n-1} \cdot B_{n-3}) + a_n \cdot B_{n-2}} \quad (5.22)$$

Using the recursion relations (5.3) and (5.4) for A_n and B_n and substituting these into equation (5.22) we see that

$$W_n = \frac{b_n \cdot A_{n-1} + a_n \cdot A_{n-2}}{b_n \cdot B_{n-1} + a_n \cdot B_{n-2}} = \frac{A_n}{B_n} \quad (5.23)$$

In view of equation (5.23) and our original definition (5.1) the theorem is proven by induction on n .

With any fractional representation, one is always concerned about division by zero. If we regard the ground field to be the quotient field of the integral domain of functions which are holomorphic on some open set Ω of the field of complex numbers \mathbb{C} , then if each a_n is a constant function, and if each $b_n \cdot b_{n-1}$ and b_0 is nonzero, then b_n and $b_{n-1} \cdot b_n + a_n$ are nonzero meromorphic functions for all nonnegative integers, which means that under these hypotheses, all operations of the partial continued fractions W_n are defined for all but at most a countable collection of complex numbers.

The next theorem shows us how to eliminate some of the variables in the continued fractions.

Theorem 5.2 *Let us suppose that a continued fraction*

$$W_n = \frac{A_n}{B_n} \quad (5.24)$$

is defined by the initial conditions

$$(A_{-1}, A_0, B_{-1}, B_0) = (1, b_0, 0, 1) \quad (5.25)$$

and the recursion relations

$$A_n = b_n \cdot A_{n-1} + A_{n-2} \quad (5.26)$$

and

$$B_n = b_n \cdot B_{n-1} + B_{n-2} \quad (5.27)$$

where b_n and $b_n \cdot b_{n-1} + 1$ are nonzero for all nonnegative integers n . Then if for all nonnegative n we introduce a symbolic representation of a continued fraction by the relation

$$b_0 + \frac{1}{[b_1, b_2, \dots, b_n]} = [b_0, b_1, \dots, b_n] = W_n \quad (5.28)$$

then the A_n and B_n may be represented in terms of these continued fractions by the relations,

$$A_n = [b_0] \cdot [b_1, b_0] \cdot [b_2, b_1, b_0] \cdots [b_n, b_{n-1}, \dots, b_1, b_0] \quad (5.29)$$

for all nonnegative integers n and

$$B_n = [b_1] \cdot [b_2, b_1] \cdot [b_3, b_2, b_1] \cdots [b_n, b_{n-1}, \dots, b_2, b_1] \quad (5.30)$$

for all positive integers n

Proof of Theorem. We proceed by double induction on n . Let $\mathcal{P}(n)$ be the assertion that equation (5.29) is valid and let $\mathcal{Q}(n)$ be the assertion that equation (5.30) is valid, where n is a positive integer. Now if we set

$$A_{-2} = 0 \quad (5.31)$$

then $\mathcal{P}(0)$ is the statement

$$A_0 = [b_0] = \frac{A_0}{B_0} = \frac{b_0}{1} \quad (5.32)$$

follows simply from the initial conditions (5.25) and is also consistent with the recursion relation (5.26) which has the form,

$$A_0 = b_0 \cdot A_{0-1} + A_{0-2} \quad (5.33)$$

The statement $\mathcal{P}(1)$ is valid since

$$\begin{aligned} [b_0] \cdot [b_1, b_0] &= b_0 \cdot \left(b_1 + \frac{1}{b_0} \right) \\ &= b_0 \cdot b_1 + 1 = b_1 \cdot A_0 + A_{-1} \end{aligned} \quad (5.34)$$

in view of the initial conditions (5.25) and the recursion relation (5.26). This proves the validity of $\mathcal{P}(1)$. Now assume that $\mathcal{P}(m)$ is valid for m not exceeding n and attempt to prove $\mathcal{P}(n+1)$. We use the recursion relations (5.26) to define

$$A_{n+1} = b_{n+1} \cdot A_n + A_{n-1} \quad (5.35)$$

It follows from the inductive hypothesis and substituting the symbol product representation (5.29) of A_n and A_{n-1} into equation (5.35) that

$$\begin{aligned} A_{n+1} &= b_{n+1} \cdot ([b_0] \cdot [b_1, b_0] \cdot [b_2, b_1, b_0] \cdots [b_n, b_{n-1}, \cdots, b_1, b_0]) \\ &\quad + ([b_0] \cdot [b_1, b_0] \cdot [b_2, b_1, b_0] \cdots [b_{n-1}, b_{n-2}, \cdots, b_1, b_0]) \end{aligned} \quad (5.36)$$

Dividing both sides of equation (5.36) by the same quantity, A_{n-1} , we see that

$$\begin{aligned} \left(\frac{A_{n+1}}{[b_0] \cdot [b_1, b_0] \cdot [b_2, b_1, b_0] \cdots [b_{n-1}, b_{n-2}, \cdots, b_1, b_0]} \right) &= \\ [b_n, b_{n-1}, \cdots, b_1, b_0] \cdot \left(b_{n+1} + \frac{1}{[b_n, b_{n-1}, \cdots, b_1, b_0]} \right) \end{aligned} \quad (5.37)$$

But by the definition of continued fraction

$$\begin{aligned} [b_{n+1}, b_n, b_{n-1}, \cdots, b_1, b_0] &= \\ \left(b_{n+1} + \frac{1}{[b_n, b_{n-1}, \cdots, b_1, b_0]} \right) \end{aligned} \quad (5.38)$$

Substituting equation (5.38) into equation (5.37) and multiplying both sides of this rewritten equation by the symbol product in the denominator of (5.37) we see that

$$A_{n+1} =$$

$$\{[b_0] \cdot [b_1, b_0] \cdot [b_2, b_1, b_0] \cdots [b_{n-1}, b_{n-2}, \cdots, b_1, b_0]\} \cdot [b_n, b_{n-1}, \cdots, b_1, b_0] \{[b_{n+1}, b_n, \cdots, b_1, b_0]\} \quad (5.39)$$

This shows that $\mathcal{P}(n+1)$ is a consequence of $\mathcal{P}(n)$.

We now proceed to prove the validity of $\mathcal{Q}(n)$, or the assertion that (5.30) is valid for the positive integer n . Observe that even $\mathcal{Q}(0)$ is true if we assume that a product of an empty set of integers is 1 and the statement $\mathcal{Q}(1)$ is true since the recursion relation (5.27) says that

$$B_1 = b_1 \cdot B_0 + B_{-1} \quad (5.40)$$

which in view of the initial conditions (5.25) implies that

$$B_1 = b_1 = [b_1] \quad (5.41)$$

which proves that $\mathcal{Q}(1)$ is true. Now assume that $\mathcal{Q}(m)$ is true for all m not exceeding n and attempt to prove that $\mathcal{Q}(n+1)$ is valid. Note that the recursive definition (5.27) implies that

$$B_{n+1} = b_{n+1} \cdot B_n + B_{n-1} \quad (5.42)$$

and that by the inductive hypothesis we can substitute equations (5.30) and into equation (5.42) obtaining

$$\begin{aligned} B_{n+1} = & b_{n+1} \cdot ([b_1] \cdot [b_2, b_1] \cdot [b_3, b_2, b_1] \cdots [b_{n-1}, b_{n-2}, \cdots, b_2, b_1] [b_n, b_{n-1}, \cdots, b_2, b_1]) \\ & + ([b_1] \cdot [b_2, b_1] \cdot [b_3, b_2, b_1] \cdots [b_{n-1}, b_{n-2}, \cdots, b_2, b_1]) \end{aligned} \quad (5.43)$$

Dividing both sides of equation (5.43) by the product of the first $n-1$ symbols we have

$$\begin{aligned} \left(\frac{B_{n+1}}{[b_1] \cdot [b_2, b_1] \cdot [b_3, b_2, b_1] \cdots [b_{n-1}, b_{n-2}, \cdots, b_2, b_1]} \right) = \\ b_{n+1} ([b_n, b_{n-1}, \cdots, b_2, b_1]) + 1 = \\ [b_n, b_{n-1}, \cdots, b_2, b_1] \left(b_{n+1} + \frac{1}{[b_n, b_{n-1}, \cdots, b_2, b_1]} \right) \end{aligned} \quad (5.44)$$

Using the interpretation of the continued fraction in definition (5.28) which says that

$$[b_{n+1}, b_n, \cdots, b_2, b_1] = b_{n+1} + \left(\frac{1}{[b_n, b_{n-1}, \cdots, b_2, b_1]} \right) \quad (5.45)$$

Substituting (5.45) into (5.44) we see that

$$\begin{aligned} B_{n+1} = \\ [b_1] \cdot [b_2, b_1] \cdot [b_3, b_2, b_1] \cdots [b_n, b_{n-1}, \cdots, b_2, b_1] [b_{n+1}, b_n, \cdots, b_2, b_1] \end{aligned} \quad (5.46)$$

which completes the proof of the validity of $\mathcal{Q}(n)$ for all positive integers n . This completes the proof of the theorem.

We can use this to stabilize the numerical computation of any continued fraction by making transformations which reduce the continued fraction to the form where each a_n is equal to one by introducing new variables.

Theorem 5.3 Under the hypothesis that each b_n and a_n is nonzero and

$$b_{n-1} \cdot b_n + a_n \neq 0 \quad (5.47)$$

if we introduce the new variables

$$\tilde{b}_0 = b_0 \quad (5.48)$$

and

$$\tilde{b}_1 = \frac{b_1}{a_1} \quad (5.49)$$

and

$$\tilde{b}_{2n} = \left(\frac{\prod_{k=1}^n a_{2k-1}}{\prod_{k=1}^n a_{2k}} \right) \cdot b_{2n} \quad (5.50)$$

and if

$$\tilde{b}_{2n+1} = \left(\frac{\prod_{k=1}^n a_{2k}}{\prod_{k=1}^n a_{2k-1}} \right) \cdot \left\{ \frac{b_{2n+1}}{a_{2n+1}} \right\} \quad (5.51)$$

then if W_n is the general continued fraction defined by (5.1) it follows that

$$W_n = [\tilde{b}_0, \tilde{b}_1, \tilde{b}_2, \dots, \tilde{b}_n] \quad (5.52)$$

Proof of Theorem. We proceed by induction on n . Let $\mathcal{P}(n)$ be the statement that if we define W_n by (5.1) then (5.52) is valid, where the \tilde{b}_n are defined by equations (5.50) and (5.51). The validity of the assertion $\mathcal{P}(1)$ is simply the statement that

$$W_1 = \tilde{b}_0 + \frac{1}{\tilde{b}_1} = b_0 + \frac{1}{b_1/a_1} = b_0 + \frac{a_1}{b_1} \quad (5.53)$$

which is exactly equation (5.1) for n equal to 1. The assertion that $\mathcal{P}(2)$ is valid is, since the definition, (5.50), implies that

$$\tilde{b}_2 = \left(\frac{a_1}{a_2} \right) \cdot b_2 \quad (5.54)$$

equivalent to

$$W_2 = \tilde{b}_0 + \frac{1}{[\tilde{b}_1, \tilde{b}_2]} = \tilde{b}_0 + \frac{1}{(\tilde{b}_1 + 1/\tilde{b}_2)} = b_0 + \left(\frac{a_1}{a_1} \right) \cdot \frac{1}{\{(b_1/a_1) + 1/((a_1/a_2) \cdot b_2)\}} = b_0 + \frac{a_1}{b_1 + (a_2/b_2)} \quad (5.55)$$

which in view of equation (5.1) is true. We now assume that $\mathcal{P}(m)$ is true for m less than or equal to n and then attempt to prove the validity of $\mathcal{P}(n)$, thereby completing the proof

The lemma will be proven by induction on n . We prove (5.63) by observing that by definition,

$$\begin{aligned} \alpha \cdot [c_0, c_1, \dots, c_{2n}] &= \\ \alpha \cdot c_0 + \frac{\alpha}{[c_1, \dots, c_{2n}]} & \end{aligned} \quad (5.65)$$

We can then use the inductive hypothesis to show that

$$\begin{aligned} \alpha \cdot c_0 + \frac{1}{(1/\alpha) \cdot [c_1, \dots, c_{2n}]} &= \\ \alpha \cdot c_0 + \frac{1}{[c_1/\alpha, \alpha c_2, c_3/\alpha \dots \alpha c_{2n}]} &= \\ [\alpha c_0, c_1/\alpha, \alpha c_2, c_3/\alpha, \dots, \alpha c_{2n}] & \end{aligned} \quad (5.66)$$

which completes the proof of equation (5.63) by induction on n .

Next we use induction to establish equation (5.64) by assuming that n were equal to $2 \cdot m + 1$. Then by definition

$$\begin{aligned} \alpha \cdot [c_0, c_1, c_2, \dots, c_{2m+1}] &= \\ \alpha \cdot c_0 + \frac{1}{(1/\alpha) \cdot [c_1, c_2, \dots, c_{2m+1}]} & \end{aligned} \quad (5.67)$$

and by the inductive hypothesis we conclude that equation (5.67) implies that

$$\begin{aligned} \alpha \cdot [c_0, c_1, c_2, \dots, c_{2m+1}] &= \\ \alpha \cdot c_0 + \frac{1}{[c_1/\alpha, \alpha \cdot c_2, \dots, c_{2m+1}/\alpha]} & \end{aligned} \quad (5.68)$$

Applying the definition (5.62) to equation (5.68) we conclude that

$$\begin{aligned} \alpha \cdot [c_0, c_1, c_2, \dots, c_{2m+1}] &= \\ [\alpha \cdot c_0, c_1/\alpha, \alpha \cdot c_2, \dots, c_{2m+1}/\alpha] & \end{aligned} \quad (5.69)$$

which proves equation (5.64) and completes the proof of the Lemma.

By applying the lemma to equation (5.61) we see that

$$\begin{aligned} b_0 + \frac{a_1}{[\tilde{b}_1^{(t)}, \tilde{b}_2^{(t)}, \dots, \tilde{b}_n^{(t)}]} &= \\ b_0 + \frac{1}{[\tilde{b}_1, \tilde{b}_2, \dots, \tilde{b}_n]} & \end{aligned} \quad (5.70)$$

in view of equations (5.57) and (5.56). From equation (5.70) and (5.48) and it follows that (5.52) and the theorem are valid.

We can use these theorems to compute values of convergent continued fractions by numerically stable algorithms.

References

- [1] Asano, Shoji and Giichi Yamamoto. "Light Scattering by a Spheroidal Particle" *Applied Optics*. Volume 14, Number 1 (1975) pages 29 - 49.
- [2] Bjorkberg, Jonas, Gerhard Kristensson. "Electromagnetic Scattering by a Perfectly Conducting Elliptic Disk" *Canadian Journal of Physics*, Volume 65, No. 7 (July, 1987) pp 723 - 734.
- [3] Bouwkamp, C. J. "On Spheroidal Wave Functions of Order Zero" *Journal of Math. Phys.* Volume 26 (1947) pp 79-92
- [4] Cohoon, David K. "Free commutative semigroups of right invertible operators with decomposable kernels" *Journal of Mathematical Analysis and Applications*. Volume 19, Number 2 (August, 1970) pp 274-281.
- [5] Cooray, M. F. R. and I. R. Ciric. "Radar Cross Sections for Two Dielectric Spheroids in Arbitrary Configuration" Corporate S: University of Manitoba, Dept of EE, Winnipeg, Manitoba. *International Symposium Digest - Antennas and Propagation, 1989 AP - S International Symposium Digest Vol 2* pp 872 - 875.
- [6] Cooray, M. Francis R., Ioan R. Ciric. "Electromagnetic Wave Scattering by a System of Two Spheroids of Arbitrary Orientation" *IEEE Transactions on Antennas and Propagation*, V n M (1989) pp 608 - 618.
- [7] Ciarkowski, Adam. "Electromagnetic Plane Wave Diffraction by a Body of Revolution" *Bulletin de l'Academie Polonaise des Sciences, Serie des Sciences Techniques*, Volume 30, No. 1-2 (1982) pp 21 - 30
- [8] Elliott, Douglas F. and K. Ramamohan Rao. *Fast Transforms Algorithms, Analysis, and Applications* New York: Academic Press (1982).
- [9] Everitt, Brian. *Cluster Analysis* New York: Halsted Press (1980)
- [10] Fackerell, Edward D. and Robert G. Grossman. "Spin Weighted Angular Spheroidal Functions" *Journal of Mathematical Physics*, Volume 18, Number 9 (September, 1977) pp 1849 - 1854
- [11] Farafonov, V. G. "Scattering of Electromagnetic Waves by a perfectly conducting spheroid" *Radio Engineering and Electronic Physics*. Volume 29, No. 11 (November, 1984) pp 39 - 45.
- [12] Farafonov, V. G. "Scattering of a Plane Electromagnetic Wave by a Highly Prolate Perfectly Conducting Spheroid" *Soviet Journal of Communications Technology and Electronics*. Volume 34, Number 6 (June, 1989) pp 36 - 45.
- [13] Farafonov, V. C. "Optical Properties of Strongly Elongated Spheroidal Particles" *Transactions (Doklady) of the USSR Academy of Sciences: Earth Science Sections*, Vol 300 No. 3 (May - June, 1988) pp 48 - .
- [14] Fisher Keller, M. A., J. A. Friedman, and J. W. Tukey "PRIM-9 An Interactive Multidimensional Data Display System. Stanford Linear Accelerator Publication 1408" (1974)
- [15] Flammer, Carson. *Spheroidal Wave Functions* Stanford, California: Stanford University Press (1957)
- [16] Friedman, Avner. *Stochastic Differential Equations and Applications*. New York: Academic Press (1975)
- [17] Futterman, John A. H. and Richard A. Matzner. "Electromagnetic Wave Scattering by Spheroidal Objects Using a Method of Spin Weighted Harmonics" *Radio Science*, Volume 16, Number 6 (November - December, 1981) pp 1303 - 1313.
- [18] Garcia, C. B. and W. I. Zangwill. *Pathways to Solutions, Fixed Points, and Equilibria*. Englewood Cliffs, NJ: Prentice Hall(1981)

- [19] Gear, James. "Electromagnetic Scattering by a Slender Body of Revolution: Axially Incident Plane Wave." *SIAM Journal on Applied Mathematics*, Volume 38, Number 1 (February, 1980) pp 93 - 102
- [20] Grenander, Ulf. *Regular structures. Lectures in Pattern Theory. Volume III* New York: Springer (1980)
- [21] Jones, M. N. *Spherical Harmonics and Tensors for Classical Field Theory* Chichester, England: Research Studies Press Ltd (1985)
- [22] Hochstadt, Harry. *The Functions of Mathematical Physics*. New York: Dover(1986).
- [23] Hörmander, Lars. *Linear Partial Differential Operators* New York: Academic Press (1963)
- [24] Huber, Peter J. "Projection pursuit" *Annals of Statistics*. Vol. 13, No. 2(June, 1985) pp 435-525.
- [25] Jenkins, Gwilym M. and Donald G. Watts. *Spectral Analysis and its applications*. San Francisco: Holden Day (1969)
- [26] King, Ronald W. P. and Charles W. Harrison. *Antennas and Waves: A Modern Approach* Cambridge, Massachusetts: The M.I.T. Press (1969)
- [27] Kochmanova, L. V. "Field Scattered on a Small Spheroid Placed in a Conducting Half Space" *Radio Engineering and Electronic Physics*, Volume 24, No. 12 (December, 1979) pp 40 - 47
- [28] Koopmans, L. H. *The spectral analysis of time series* New York: Wiley (1974)
- [29] Liu, S. C., and D. K. Cohoon. "Limiting Behaviors of Randomly Excited Hyperbolic Tangent Systems". *The Bell System Technical Journal*, Volume 49, Number 4 (April, 1970) pp 543-560.
- [30] Lee, Kai Fong. *Principles of Antenna Theory* New York: John Wiley (1984)
- [31] Meixner, J. "Asymptotische Entwicklung der Eigenwerte und Eigenfunktionen der Differentialgleichungen der Spharoid Funktionen und der Mathieuschen Funktionen" *J. angew Math. Mech.* Volume 28 (1948) pp 304-310
- [32] Mittra, Raj and Richard K. Gordon. "Radar Scattering from Bodies of Revolution Using an Efficient Partial Differential Equation Algorithm" *IEEE Transactions on Antennas and Propagation*, Vol n M (1989) pp 538 - 545
- [33] Monzingo, Robert A. and Thomas W. Miller. *Introduction to Adaptive Arrays* New York: John Wiley and Sons (1980).
- [34] Moffatt, D. L. "Echo Area of a Perfectly Conducting Prolate Spheroid" *IEEE Transactions on Antennas and Propagation*. Vol. AP -17, No. 9 (May, 1969) pp 299 - 307
- [35] Milligan, Thomas A. *Modern Antenna Design* New York: McGraw Hill (1985)
- [36] Ogarcsyan, S. S. "Diffraction of a Plane Electromagnetic Wave by an Anisotropic Spheroid" *Radiophysics and Quantum Electronics*, Volume 25, No. 9 (September, 1982) pp 693 - 697
- [37] Patrick, Edward A., M.D., Ph.D. and James M. Fattu, M.D., Ph.D. *Artificial Intelligence with Statistical Pattern Recognition* Englewood Cliffs, N.J.: Prentice Hall(1986).
- [38] Ravey, J. C. and P. Mazon. "Light Scattering by Large Spheroids in the Physical Optics Approximation: Numerical Comparison with other Approximate and Exact Results" *Journal of Optics*, Vol 14, No. 1 (January - February) (1983) pp 29 - 41
- [39] Ravey, J. C. "Optical Anisotropy of Absorbing Particles: Light Scattering Depolarization, Electric and Flow Birefringence and Dichroism of Suspensions of Carbon Blacks." *Colloid and Polymer Science*, Vol 253, No. 4 (April, 1975) pp 292 - 305.

- [40] Schneider, John B. and Irene C. Pden. "Differential Cross Section of a Dielectric Ellipsoid by the T Matrix Extended Boundary Condition Method" *IEEE Transactions on Antennas and Propagation*, Vol 36, No. 9 (September, 1988) pp 1317 - 1321
- [41] Sebak, A. and L. Shafai. "Electromagnetic Scattering from Arbitrarily Shaped Imperfectly Conducting Bodies" University of Manitoba, Canada *Sixth International Conference on Antennas and Propagation ICAP 89, Coventry, England April 4 - 7, 1989 IEE Conference Publication Part 1, IEE London, England* (1989) pp 517 - 520
- [42] Siegel, K. M., F. V. Shultz, B. H. Gere, and F. B. Sleator. "The theoretical and numerical determination of the radar cross section of a prolate spheroid" *Electromagnetic Wave Theory Symposium: Antennas and Propagation 4* (1956) pp 266 - 276.
- [43] Sinha, Bateshwar P. and Robert H. MacPhie. "On Electromagnetic Plane Wave Scattering by a Prolate Spheroid" *Canadian Journal of Physics*, Vol 58, No. 1 (January, 1980) pp 25 - 30.
- [44] Sinha, Bateshwar P. and Robert H. MacPhie. "Electromagnetic scattering by prolate spheroids for plane waves with arbitrary polarization and angle of incidence" *Radio Science, Volume 12, Number 2* (March - April, 1977) pp 171 - 184.
- [45] Sinha, Bateshwar P., and Robert H. MacPhie. "Electromagnetic Scattering from Prolate Spheroids for Axial Incidence" *IEEE Transactions on Antennas and Propagation. Volume AP 23, Number 5* (September, 1975) pp 676 - 679.
- [46] Spence, R. D. and C. P. Wells "Vector Wave Functions" IN Courant, Richard and Lt. Col F. C. E. Oder (Editors) *The Theory of Electromagnetic Waves. A Symposium* New York: Interscience Publishers (1951) 159 - 168
- [47] Srinivasan, S. K. and R. Rasudevan. *Introduction to random differential equations and their applications* New York: American Elsevier (1971)
- [48] Stutzman, Warren L. and Gary A. Thiele. *Antenna Theory and Design* New York: Wiley (1981)
- [49] Takemoto - Hambleton, Randall M., W. J. Ross Dunseath, William T. Joines. "Electromagnetic Fields Induced in a Person Due to Devices Radiating in the 10 Hz to 100 KHz Range" *IEEE Transactions on Electromagnetic Compatibility. Volume 30, Number 4* (November, 1988) pp 529 - 537.
- [50] Uhlenbeck, G. E. and L. S. Ornstein. "On the theory of Brownian Motion" *Phys. Rev.* 36 (1930) pp 823-841
- [51] Uldrick, J. P. and J. Siekmann. "On the swimming of a flexible plate of arbitrary finite thickness" *Journal of Fluid Mechanics. Volume 20, Part 1* (1964) pp 1-33.
- [52] Vandenberghe, F. H., W. M. Boerner. "On the Inverse Problem of Scattering from a Perfectly Conducting Prolate Spheroid" *Canadian Journal of Physics, Volume 50, No. 8* (April, 1972) pp 754 - 759
- [53] Voshchinnikov, N. V., and V. G. Farafonov. "Characteristics of the Radiation Scattered by Prolate and Oblate Absolutely Conducting Spheroids" *Soviet Journal of Communications Technology and Electronics. Vol 33, Number 11* (November, 1988) pp 92 - 101.
- [54] Wait, James R. *Introduction to Antennas and Propagation* London: Peter Peregrinus (1986)
- [55] Wall, H. S. *Analytic Theory of Continued Fractions* New York: D. Van Nostrand Company, Inc. (1948)
- [56] Wang, Wan Xian and Ru T. Wang. Corrections and Developments on the Theory of Scattering by Spheroids - Comparison with Experiments *Journal of Wave Material Interaction* Volume 2 (1987) pages 227-241

- [57] Wang, W. X. "Higher Order Terms in the Expressions of Spheroidal Eigenvalues" *Journal of Wave Material Interactions. Volume 2* (1987) pp 217-226
- [58] Wang, W. X. "The Spheroidal Radial Functions of the Second Kind at High Aspect Ratio" *Journal of Wave Material Interaction. Volume 2* (1987) pp 207-216
- [59] Whittaker, E. T. and G. N. Watson. *A Course of Modern Analysis* London: Cambridge University Press (1986).

Blank

Scattering of Electromagnetic Radiation by Nonconnected, Heterogeneous Bianisotropic Structures

D. K. Cohoon

September 3, 1992

We consider in this paper powerful general methods for solving electromagnetic scattering problems that, while with presently used methods require 1000 human life times of time on an advanced computer, shall with the methods proposed in this paper require only one hour on the same computer. Furthermore, instead of guessing at the accuracy by requiring a certain sampling rate, the solution of the integral equation, using the exact finite rank integral equation methods described in this paper, is obtained to computing machine precision.

We consider a bounded three dimensional body with full tensor bianisotropy covered with impedance sheets.

As a specific and easily understood example, we consider the discretization of the integral equation of electromagnetic scattering for a magnetic, but penetrable structure delimited by parallel planes.

We conclude with a general surface integral equation formulation which will permit analysis of a complex of homogeneous structures whose regions of homogeneity of electromagnetic properties may be as general as the interiors of diffeomorphs of N handled spheres.

Contents

1 INTRODUCTION

- 1.1 Classes of Tensor Materials
- 1.2 Integral Equations and Bianisotropy

2 Exact Finite Rank Integral Equation Methods

- 2.1 Examples of Spaces of Approximation
- 2.2 The Standard but Nonoptimal Discretization

3 Exact Solutions of Integral Equations

- 3.1 Machine Precision in Integral Equation Methods

4 Layered Materials

- 4.1 Magnetic Slab Integral Equation

5 DISCRETIZATION

- 5.1 Piecewise Linear Approximation

6 Surface Integral Equation Methods

- 6.1 Combined Field Integral Equations

1 INTRODUCTION

We shall in this paper consider powerful new methods for formulating and solving integral equations describing the interaction of electromagnetic radiation with complex materials. Such interaction problems, for currently used methods, such as the method of moments, are beyond the capability of existing computers.

1.1 Classes of Tensor Materials

The most general linearly responding material is the bianisotropic material ([23], p 91) defined by the equations,

$$\text{curl} \begin{pmatrix} \vec{E} \\ \vec{H} \end{pmatrix} = i \cdot \omega \cdot \begin{pmatrix} 0 & -1 \\ 1 & 0 \end{pmatrix} \cdot \left[\begin{pmatrix} \bar{\epsilon} & \bar{\xi} \\ \bar{\zeta} & \bar{\mu} \end{pmatrix} \cdot \begin{pmatrix} \vec{E} \\ \vec{H} \end{pmatrix} + \begin{pmatrix} \vec{J} \\ \vec{J}_m \end{pmatrix} \right] \quad (1.1.1)$$

(It is easy to see which interchanges leave the above system of equations invariant; this gives us a way of checking complex codes) The bianisotropic relations are embodied in the relationship ([23], p 91)

$$\begin{pmatrix} \vec{D} \\ \vec{B} \end{pmatrix} = \begin{pmatrix} \bar{\epsilon} & \bar{\xi} \\ \bar{\zeta} & \bar{\mu} \end{pmatrix} \cdot \begin{pmatrix} \vec{E} \\ \vec{H} \end{pmatrix} \quad (1.1.2)$$

The biisotropic relations ([23], p 92) are

$$\vec{D} = \epsilon \vec{E} + ((\chi - i\kappa)\sqrt{(\mu_0 \cdot \epsilon_0)}) \cdot \vec{H} \quad (1.1.3)$$

and

$$\vec{B} = (\chi + i\kappa)\sqrt{(\mu_0 \cdot \epsilon_0)} \vec{E} + \mu \vec{H} \quad (1.1.4)$$

If in equations (1.1.3) and (1.1.4) the above two equations we set χ equal to zero, then we obtain the *Pasteur* medium.

The *gyroelectric* medium ([2], p 341) is a special case of an anisotropic medium where the permittivity tensor for a wave propagating in the direction of the z axis has the form

$$\bar{\epsilon} = \begin{pmatrix} \epsilon_{(x,x)} & \epsilon_{(x,y)} & 0 \\ \epsilon_{(y,x)} & \epsilon_{(y,y)} & 0 \\ 0 & 0 & \epsilon_{(z,z)} \end{pmatrix} \quad (1.1.5)$$

A different type of material is a general type of *gyrotropic* material ([2], page 342) where the permittivity has the form,

$$\bar{\epsilon} = \begin{pmatrix} \epsilon_{(x,x)} & \epsilon & 0 \\ \epsilon & \epsilon_{(y,y)} & \epsilon_{(y,z)} \\ 0 & \epsilon_{(x,y)} & \epsilon_{(x,z)} \end{pmatrix} \quad (1.1.6)$$

A third type of anisotropic material is ([2], p 344) are the *biaxial* and the *uniaxial* material where the permittivity tensors respectively have the form,

$$\bar{\bar{\epsilon}} = \begin{pmatrix} \epsilon_x & 0 & 0 \\ 0 & \epsilon_y & 0 \\ 0 & 0 & \epsilon_z \end{pmatrix} \quad (1.1.7)$$

and

$$\bar{\bar{\epsilon}} = \begin{pmatrix} \epsilon & 0 & 0 \\ 0 & \epsilon & 0 \\ 0 & 0 & \epsilon_z \end{pmatrix} \quad (1.1.8)$$

which serve to characterize the optical properties of many types of crystalline materials.

1.2 Integral Equations and Bianisotropy

Bianisotropic materials, because of their greater complexity, have greater potential for creating materials with prescribed or desired absorption, transmission, and reflection properties. Chiral properties are a special case of bianisotropic materials. With chiral materials there is a special scalar ξ_c (Jaggard and Engheta, p 173) such that

$$\vec{D} = \epsilon \cdot \vec{E} + i\xi_c \vec{B} \quad (1.2.1)$$

and

$$\vec{B} = \mu \cdot \vec{H} - i\xi_c \mu \cdot \vec{E} \quad (1.2.2)$$

With the more general bianisotropic materials described in (Lindell [23]) there are tensors $\bar{\bar{\xi}}$ and $\bar{\bar{\zeta}}$ such that \vec{D} and \vec{B} are related to \vec{E} and \vec{H} by the 6 by 6 matrix embodied in equation (1.1.2). Here the Faraday Maxwell equation has, for time harmonic radiation, the form

$$\text{curl}(\vec{E}) = -i\omega \vec{B} \quad (1.2.3)$$

while the Ampere Maxwell equation has the form

$$\text{curl}(\vec{H}) = i\omega \vec{D} + \bar{\bar{\sigma}} \cdot \vec{E} \quad (1.2.4)$$

Using these notions we make Maxwell's equations look like the standard Maxwell equations with complex sources by introducing the generalized electric and magnetic current densities by the relations,

$$\text{curl}(\vec{E}) = i\omega\mu_0\vec{H} - \vec{J}_m \quad (1.2.5)$$

and

$$\text{curl}(\vec{H}) = i\omega\epsilon_0\vec{E} + \vec{J}_e \quad (1.2.6)$$

where the \vec{J}_e appearing in equation (1.2.6) is defined by

$$\vec{J}_e = i\omega\bar{\epsilon} \cdot \vec{E} + i\omega\bar{\xi} \cdot \vec{H} - i\omega\epsilon_0\vec{E} \quad (1.2.7)$$

and the \vec{J}_m appearing in equation (1.2.5) is defined by

$$\vec{J}_m = i\omega[\bar{\mu} \cdot \vec{H} + \bar{\zeta} \cdot \vec{E} - \mu_0\vec{H}] \quad (1.2.8)$$

We can think of the current densities (1.2.7) and (1.2.8) as stimulators of radiation in ambient space and use the Maxwell equations (1.2.5) and (1.2.6) to formulate the resolution of the interaction problem as the solution of integral equations. We, however, need to use the current densities given by (1.2.7) and (1.2.8) to define electric and magnetic charge densities ρ_e and ρ_m by the relations,

$$\text{div}(\vec{J}_e) + \frac{\partial\rho_e}{\partial t} = 0 \quad (1.2.9)$$

and

$$\text{div}(\vec{J}_m) + \frac{\partial\rho_m}{\partial t} = 0 \quad (1.2.10)$$

We now use the electric and magnetic current densities given by (1.2.7) and (1.2.8) and the electric and magnetic charge densities given by (1.2.9) and (1.2.10), respectively, to develop a coupled system of integral equations describing the interaction of electromagnetic radiation with a bounded bianisotropic body Ω . The electric field integral equation is given by

$$\begin{aligned} \vec{E} - \vec{E}^i = & -\text{grad} \left(\int_{\Omega} \frac{\text{div}(\vec{J}_e)}{\omega\epsilon_0} G(r,s) dv(s) \right) \\ & + \frac{i}{\omega\epsilon_0} \text{grad} \left(\int_{\partial\Omega} (\vec{J}_e \cdot \vec{n}) G(r,s) da(s) \right) \end{aligned}$$

$$\begin{aligned}
& - i\omega\mu_0 \int_{\Omega} \vec{J}_e G(r, s) dv(s) + \\
& - \text{curl} \left(\int_{\Omega} \vec{J}_m G(r, s) dv(s) \right)
\end{aligned} \tag{1.2.11}$$

If the material is nonmagnetic, then there is no nonzero magnetic current density and we could derive a magnetic field integral equation directly from (1.2.11) simply using Maxwell's equations. The general magnetic field integral equation may be expressed as

$$\begin{aligned}
\vec{H} - \vec{H}^i = & - \text{grad} \left(\int_{\Omega} \frac{\text{div}(\vec{J}_m)}{\omega\mu_0} G(r, s) dv(s) \right) \\
& - \frac{i}{\omega\mu_0} \text{grad} \left(\int_{\partial\Omega} (\vec{J}_m \cdot \vec{n}) G(r, s) da(s) \right) \\
& - i\omega\epsilon_0 \int_{\Omega} \vec{J}_m G(r, s) dv(s) + \\
& + \text{curl} \left(\int_{\Omega} \vec{J}_e G(r, s) dv(s) \right)
\end{aligned} \tag{1.2.12}$$

where $G(r, s)$ is the rotation invariant, temperate fundamental solution of the Helmholtz equation,

$$(\Delta + k_0^2)G = \delta \tag{1.2.13}$$

given by

$$G(r, s) = \frac{\exp(-ik_0 |r - s|)}{4\pi |r - s|} \tag{1.2.14}$$

Substituting (1.2.7) and (1.2.8) into equations (1.2.11) and (1.2.12) we obtain, the coupled integral equations for bianisotropic materials. The electric field integral equation for a bianisotropic material is given by,

$$\begin{aligned}
\vec{E} - \vec{E}^i = & \\
& - \text{grad} \left(\int_{\Omega} \frac{\text{div}(i\omega [\bar{\epsilon} \cdot \vec{E} + \bar{\xi} \cdot \vec{H} - \epsilon_0 \vec{E}])}{\omega\epsilon_0} G(r, s) dv(s) \right) \\
& + \frac{i}{\omega\epsilon_0} \text{grad} \left(\int_{\partial\Omega} (i\omega [\bar{\epsilon} \cdot \vec{E} + \bar{\xi} \cdot \vec{H} - \epsilon_0 \vec{E}] \cdot \vec{n}) G(r, s) da(s) \right) \\
& - i\omega\mu_0 \int_{\Omega} i\omega [\bar{\epsilon} \cdot \vec{E} + \bar{\xi} \cdot \vec{H} - \epsilon_0 \vec{E}] G(r, s) dv(s) + \\
& - \text{curl} \left(\int_{\Omega} i\omega [\bar{\mu} \cdot \vec{H} + \bar{\zeta} \cdot \vec{E} - \mu_0 \vec{H}] G(r, s) dv(s) \right)
\end{aligned} \tag{1.2.15}$$

and the magnetic field integral equation for a bianisotropic material is given by

$$\begin{aligned} \vec{H} - \vec{H}^i = & -grad \left(\int_{\Omega} \frac{div(i\omega [\bar{\mu} \cdot \vec{H} + \bar{\zeta} \cdot \vec{E} - \mu_0 \vec{H}])}{\omega \mu_0} G(r, s) dv(s) \right) \\ & - \frac{i}{\omega \mu_0} grad \int_{\partial\Omega} (i\omega [\bar{\mu} \cdot \vec{H} + \bar{\zeta} \cdot \vec{E} - \mu_0 \vec{H}] \cdot \vec{n}) G(r, s) da(s) \\ & - i\omega \epsilon_0 \int_{\Omega} (i\omega [\bar{\mu} \cdot \vec{H} + \bar{\zeta} \cdot \vec{E} - \mu_0 \vec{H}]) G(r, s) dv(s) + \\ & + curl \left(\int_{\Omega} i\omega [\bar{\epsilon} \cdot \vec{E} + \bar{\xi} \cdot \vec{H} - \epsilon_0 \vec{E}] G(r, s) dv(s) \right) \end{aligned} \quad (1.2.16)$$

In the subsequent sections we shall explore methods of resolving these integral equations on existing computers using novel, powerful analytical methods of solution.

2 Exact Finite Rank Integral Equation Methods

While we have obtained exact solutions for layered materials, most of the problems are so complex that one must formulate the interaction problems using integral equations. The primary focus of this report is to describe the design of complex materials using an improvement of classical spline methods (Tsai, Massoudi, Durney, and Iskander, pp 1131-1139). This paper is unusual in that comparisons are made between internal fields predicted from moment method computations and Mie solution computations. Successful comparisons have been made for linear basis functions without enhancement by *exact finite rank integral equation* theory. However, as the scattering bodies become more complex the computational requirements become larger and larger. With *exact finite rank integral equation* theory if one has a discretization that enables one to closely approximate the solution, then refinements can be made by a convergent iterative process based on the concept that the norm of the difference between an approximate integral operator and the actual integral operator is simply smaller than one, not necessarily close enough to give answers of acceptable accuracy. Then the answer is improved by an iterative process to any desired precision without the use of additional computer memory.

2.1 Examples of Spaces of Approximation

Solving the electromagnetic transmission problem by finding solutions of Maxwell's equations inside and outside a penetrable scatterer which satisfy boundary conditions and radiation conditions requires functions on a continuum, the problem is from a practical point of view a discrete one and involves estimation of the values of induced and scattered electric and magnetic vectors in the interior and the exterior of the scattering body. Thus, it is important to understand methods of determining the accuracy with which a solution of a discrete approximation of an integral equation formulation of an electromagnetic interaction problem can be obtained. We specifically need to formulate a space of approximates and a projection operator onto this space of approximates and formulate a finite rank approximation of the original infinite rank integral equations (1.2.15) and (1.2.16) such that the precise solution of this approximate equation is exactly the projection onto the space of approximates of the solution of the original infinite rank integral equation. We further need to develop a means of correcting our solution so that we may exactly determine by iteration the difference $f - Pf$ between the solution f of the original equation and the projection Pf of this solution onto the space of approximates, possibly by an iterative scheme or a series expansion. In this section we illustrate (i) pulse basis function methods, (ii) linear interpolation, (iii) higher order spline interpolation, and (iv) a completely novel L^∞ norm method of approximating the field components with combinations of trigonometric functions of the local spatial variables using carefully selected frequencies.

We now explain linear interpolation. A common example would be to approximate the space V of functions which are continuous on $[a, b]$ by members of a set

$$S = \{[x_0, x_1], [x_1, x_2], \dots, [x_{n-1}, x_n]\} \quad (2.1.1)$$

where

$$a = x_0 < x_1 < \dots < x_n = b \quad (2.1.2)$$

and to define the projection operator of linear interpolation, for the partition defined by

equation (2.1.1) by the rule,

$$Pf(x) = f(x_{i-1}) \left(\frac{x_i - x}{x_i - x_{i-1}} \right) + f(x_i) \left(\frac{x - x_{i-1}}{x_i - x_{i-1}} \right) \quad (2.1.3)$$

if x belongs to the subinterval from x_{i-1} to x_i and we note that if this is the case then since

$$(Pf)(x_{i-1}) = f(x_{i-1}) \cdot 1 + 0 \quad (2.1.4)$$

and since

$$(Pf)(x_i) = 0 + f(x_i) \cdot 1 \quad (2.1.5)$$

it follows from equations (2.1.3), (2.1.4), and (2.1.5) that

$$P^2f = Pf \quad (2.1.6)$$

Another simple example is Fourier series or an eigenfunction expansion in the spatial variables. Suppose that V is a set of functions defined on \mathbb{R}^n which are square integrable with respect to Lebesgue measure ν multiplied by a positive function ρ and valued in a Hilbert space X with norm $|\cdot|_X$ with two measurable and square integrable functions f and g being equivalent on an open set,

$$\Omega \subset \mathbb{R}^n, \quad (2.1.7)$$

if and only if

$$\int_{\Omega} (|f - g(x)|_X^2) \rho(x) d\nu(x) = 0 \quad (2.1.8)$$

and where the square integrability with respect to the ordinary Lebesgue measure multiplied by ρ means that

$$\int_{\Omega} (|f(x)|_X^2) \rho(x) d\nu(x) < \infty \quad (2.1.9)$$

We say that two Hilbert space valued functions f and g are orthogonal if and only if

$$\int_{\Omega} \{f(x) \cdot g(x)\} \rho(x) d\nu(x) = 0 \quad (2.1.10)$$

where

$$(f(x), g(x))_X = f(x) \cdot g(x) \quad (2.1.11)$$

is the inner product of the Hilbert space elements $f(x)$ and $g(x)$ so that the square of the norm of the function f is

$$\|f\|_X^2 = \int_{\Omega} \{f(x) \cdot f(x)\} \rho(x) d\nu(x) \quad (2.1.12)$$

If

$$F = \{\phi_i : i \in \mathcal{I}\} \quad (2.1.13)$$

is a finite set of pairwise orthogonal functions in the space V of functions from Ω into the Hilbert space X , then

$$Pf(x) = \sum_{i \in \mathcal{I}} \left[\frac{\int_{\Omega} f(y) \cdot \phi_i(y) \rho(y) d\nu(y)}{\int_{\Omega} \phi_i(y) \cdot \phi_i(y) \rho(y) d\nu(y)} \right] \phi_i(x) \quad (2.1.14)$$

The projection operator defined by equation (2.1.14) yields a generalized Fourier series approximation of functions; which is the basis of Mie like solutions of electromagnetic problems.

The next approximation scheme that is often used in electromagnetic analysis is the pulse basis function method. The pulse basis function method has been used by Guru and Chen [13], Hagmann and Gandhi [14], Hagmann and Levine [16], and Livesay and Chen [24] to predict the results of electromagnetic radiation with complex structures by decomposing the body into cells within each of which the induced electric vector is assumed to be a constant and charge densities are also assumed to be piecewise constant. The pulse basis function method makes use of the concept of the partition of an open set Ω of \mathbb{R}^n .

We have defined for each x in \mathbb{R}^n and each positive number $r > 0$ the set

$$B(x, r) = \{y \in \mathbb{R}^n : |x - y| < r\} \quad (2.1.15)$$

to be the ball of radius r centered at x . We let Ω be an open set in \mathbb{R}^n whose closure is bounded.

Definition 2.1 A partition of Ω is a set $\mathcal{P}(\Omega)$ of pairs (V_i, x_i) where $i \in \mathcal{I}$ and the ball, $B(x_i, r)$ is contained in V_i for some positive number r ,

$$\bigcup_{i \in \mathcal{I}} V_i = \Omega \quad (2.1.16)$$

and

$$\mu_n(V_j \cap V_k) = 0 \quad (j \neq k) \quad (2.1.17)$$

whenever (V_i, x_i) and (V_j, x_j) are distinct members of the partition, $\mathcal{P}(\Omega)$ and μ_n is the standard Lebesgue measure on \mathbb{R}^n where we let

$$\mathcal{P}_1 = \{V_i : (V_i, x_i) \in \mathcal{P}(\Omega) \text{ for some } x_i \in V_i\} \quad (2.1.18)$$

and we define the characteristic functions,

$$\chi_{V_i}(x) = \begin{cases} 1 & x \in V_i \\ 0 & x \text{ is not a member of } V_i \end{cases} \quad (2.1.19)$$

to be the characteristic functions or pulse functions associated with the sets V_i in $\mathcal{P}(\Omega)_1$. The sets V_i are called cells in a cellular decomposition of Ω .

Next we define the projection operators associated with this partition of an open set in Euclidean n dimensional space.

Definition 2.2 We define the projection operator P associated with the partition,

$$\mathcal{P}(\Omega) = \{(V_i, x_i) : x_i \in V_i, i \in \mathcal{I}, V_i \subset \Omega\} \quad (2.1.20)$$

by the rule,

$$Pf(x) = \sum_{V_i \in \mathcal{P}(\Omega)_1} [\chi_{V_i}(x) \cdot f(x_i)] \quad (2.1.21)$$

for all functions,

$$f : \Omega \rightarrow \mathbb{C}^m \quad (2.1.22)$$

where \mathbb{C}^m denotes complex m dimensional space.

We prove the following.

Proposition 2.1 If $\mathcal{F}(\Omega, \mathbb{C}^m)$ is any topological vector space of functions from Ω into \mathbb{C}^m which includes all functions of the form,

$$x \rightarrow \chi_V(x)\vec{u} \quad (2.1.23)$$

where

$$V \in \mathcal{P}(\Omega)_1 \quad (2.1.24)$$

and

$$\vec{u} \in \mathbb{C}^m \quad (2.1.25)$$

then the mapping P defined by equation (2.1.21) is an endomorphism of this topological vector space which satisfies

$$PP = P \quad (2.1.26)$$

2.2 The Standard but Nonoptimal Discretization

Kun Mu Chen meticulously analyzed the electric field volume integral equation in the work he directed in ([24]) and correctly formulated the electric field volume integral equation for a nonmagnetic body as,

$$(\vec{E} - \vec{E}^i)(p, \omega) = \frac{i\omega^2}{c^2} \int_{\Omega} \left(\frac{(\epsilon - \epsilon_0) - i\sigma/\omega}{\epsilon_0} \right) \vec{G}(p, q) \cdot \vec{E}(q) dv(q) \quad (2.2.1)$$

where

$$\vec{G} = \left(\vec{I} + \left(\frac{1}{k_0^2} \right) \text{grad}(\text{grad}) \right) \left(\frac{\exp(ik_0 |p - q|)}{4\pi |p - q|} \right) \quad (2.2.2)$$

What is done in practice is to apply the projection operator to the a priori unknown field \vec{E} that appears under the integral and to also apply it also to both sides of the integral equation (2.2.1) to obtain the approximate equation

$$(P^x \vec{E} - P^x \vec{E}^i) = \frac{i\omega^2}{c^2} \int_{\Omega} \left(\frac{(\epsilon - \epsilon_0) - i\sigma/\omega}{\epsilon_0} \right) P^x \vec{G}(x, y) \cdot (P^y \vec{E}) dv(y) \quad (2.2.3)$$

where \vec{G} is defined by equation (2.2.2). The so called method of moments was developed in the early 1900s by mathematicians and is simply the weak topology approximation; as currently applied it is an attempt to do a better job of getting a more acceptable solution of the clearly nonoptimal approximation represented by equation (2.2.3). With the method of moments one obtains $3N$ equations for the $3N$ unknowns representing the electric vector in the N cells into which the scattering body Ω is decomposed by simply multiplying both sides of equation (2.2.3) by a function of x , often the characteristic function of the cell V_i , where i ranges from 1 to N , and integrating both sides of the new equation with respect to x

3 Exact Solutions of Integral Equations

We show in this section a method of creating a computerizable approximate to the original infinite rank integral equation. After multiplying all terms of the integral equation by the same invertible matrix, if necessary, we can reduce the coupled \vec{E} and \vec{H} integral equation to one of the form described in the following section.

3.1 Machine Precision in Integral Equation Methods

We show in this section how to correct our errors in an integral equation method, so that we can obtain, by doing more processing but not using excessive memory, an answer whose precision is close to that of the particular computing machine being used. Letting f be a vector valued function defined on an open set Ω of \mathbb{R}^3 and having values belonging to a Banach space, X , which represents the set of values of the electric and magnetic field vector within the scattering body and having enough regularity that boundary values are defined. Suppose that the functions f that we consider all satisfy the condition,

$$f \in \mathcal{E}(\Omega, X), \quad (3.1.1)$$

that they belong to a Banach space of functions from Ω into X . We further suppose that we define a projection operator,

$$P : \mathcal{E}(\Omega, X) \rightarrow \mathcal{E}(\Omega, X) \quad (3.1.2)$$

We let $\mathcal{B}(X)$ denote a Banach space of operators mapping X into itself and let K be a function,

$$K : \Omega \times \Omega \rightarrow \mathcal{B}(X) \quad (3.1.3)$$

which in practice will represent the integral operator acting on the values of the electric and magnetic field vectors in the interior and on the surface of the scattering body. One way this can be handled is to assume enough regularity in the space of functions, $\mathcal{E}(\Omega, X)$ in which we are seeking the solution (and in the space of approximations within which

we are attempting to find a solution that is reasonably close to actual solution), that the required boundary values are defined. Related to this basic projection operator, which may be defined in one of the ways described in the previous section, or in other ways, we define the operator Q^x on functions from Ω into X by the rule,

$$P \int_{\Omega} K(x, y)(Pf)(y)d\nu(y) = \int_{\Omega} Q^x K(x, y)(Pf)(y)d\nu(y) \quad (3.1.4)$$

We can reduce our original problem to that of solving an integral equation of the form,

$$f(x) - g(x) = \lambda Tf(x) \quad (3.1.5)$$

where

$$Tf(x) = \int_{\Omega} K(x, y)f(y)d\nu(y) \quad (3.1.6)$$

and f may represent a two tuple consisting of the electric and magnetic vectors and g represents the result of applying an invertible linear transformation two a two tuple consisting of the electric and magnetic vectors of the incoming radiation. We define the operator L by the rule

$$L = PTPf(x) \quad (3.1.7)$$

where P is a projection operator onto a space of approximates, and define the correction operator N by the rule,

$$Nf(x) = Tf(x) - Lf(x) \quad (3.1.8)$$

Normally we require that P is a good enough approximator that solving the equation (2.2.3) will give us a satisfactory solution. However, with *exact finite rank integral equation* theory we need only assume that P is good enough so that if N is defined by (3.1.8) that then the operator norm inequality,

$$\max \{ \|\lambda\| \|N\|_{\Omega}, \|\lambda\| \|(P - I)N\|_{\Omega} \} < 1 \quad (3.1.9)$$

Thus, it follows that

$$T = L + N \quad (3.1.10)$$

The usual approximate integral equation has the form

$$f_a = Pg = \lambda PTf_a \quad (3.1.11)$$

where f_a satisfies the condition,

$$f_a \in P(\mathcal{E}(\Omega, X)), \quad (3.1.12)$$

What is usually done is to assume that f_a is close enough to f to accurately represent the solution of the original infinite rank integral equation (3.1.5). We can, if inequality (3.1.9) is satisfied, define the bounded linear operator

$$G_\lambda = \sum_{k=1}^n \lambda^{k-1} N^k \quad (3.1.13)$$

so that it will follow that since formally and in fact,

$$(I - \lambda N) \cdot (I + \lambda N + \lambda^2 N^2 + \dots) f = f \quad (3.1.14)$$

that by combining equations (3.1.13) and (3.1.14) that

$$(I - \lambda N)(I + \lambda G_\lambda) f = f \quad (3.1.15)$$

in view of the the geometric series relationship and the identity

$$(I + \lambda G_\lambda) = (I + \lambda N + \lambda^2 N^2 + \dots) \quad (3.1.16)$$

for all functions f satisfying the relationship (3.1.1). Thus, we can in view of the relationship (3.1.10) deduce that

$$\lambda T = \lambda N + \lambda L \quad (3.1.17)$$

Equation (3.1.17) then means that we can express the original integral equation (3.1.5) in the form

$$f = g + \lambda N f + \lambda L f \quad (3.1.18)$$

Rearranging terms in equation (3.1.18) we see that

$$(I - \lambda N) f = g + \lambda L f \quad (3.1.19)$$

Combining equations (3.1.19) and (3.1.15) and equation (3.1.13) we deduce that

$$f = g + \lambda L f + \lambda G_\lambda (g + \lambda L f +) \quad (3.1.20)$$

Now if we simply combine equation (3.1.20) and equation (3.1.18) we deduce that

$$\lambda Nf = \lambda G_\lambda(g + \lambda Lf) \quad (3.1.21)$$

We would now like to apply the projection operator P to both sides of equation (3.1.20) making use of the fact that P is idempotent, equalling its square, and equation (3.1.7)

$$PL = L \quad (3.1.22)$$

to obtain the relation

$$Pf = Pg + \lambda Lf \lambda P(G_\lambda(g + \lambda Lf)) \quad (3.1.23)$$

Substituting equation (3.1.21) into equation (3.1.23) we see that

$$Pf = Pg + \lambda Lf + \lambda PNf \quad (3.1.24)$$

Thus, if we define

$$L_{(K,P)} = PT \quad (3.1.25)$$

then in view of equation (3.1.7) and (3.1.25) we see that

$$Lf = L_{(K,P)}Pf \quad (3.1.26)$$

Now we see that equations (3.1.24) and (3.1.26) imply that

$$Pf = Pg + \lambda PL_{(K,P)}Pf + \lambda PNf \quad (3.1.27)$$

While equation (3.1.27) is not a finite rank integral equation, it suggests that an approximate finite rank integral equation

$$Pf_a = Pg + \lambda PL_{(K,P)}Pf_a + \lambda PNf_a \quad (3.1.28)$$

might give a better approximation to the solution than the traditional approximation given by equation (3.1.11). We shall go much farther than this, however, and reduce the equation (3.1.24) to a true finite rank integral equation whose solution will be the projection Pf of the exact solution f of the original infinite rank integral equation (3.1.5) onto the space of approximates. This will permit us to achieve our ultimate objective of representing the

solution f exactly in terms of Pf and the stimulating fields g by an exact formula. Going back to equation (3.1.19) and making use of equation (3.1.14) we obtain

$$f = \sum_{k=0}^{\infty} [(\lambda N)^k (g + \lambda Lf)] \quad (3.1.29)$$

Operating on both sides of equation (3.1.29) with N and then applying λP to both sides of this equation, we see that

$$\lambda PNf = \sum_{k=0}^{\infty} [(\lambda N)^k (g + \lambda Lf)] \quad (3.1.30)$$

Now, simply substituting equation (3.1.30) into equation (3.1.27) we get the finite rank integral equation,

$$Pf = Pg + \lambda PL_{(K,P)}Pf + \lambda PN \left[\sum_{k=0}^{\infty} (\lambda N)^k (g + \lambda L_{(K,P)}Pf) \right] \quad (3.1.31)$$

Now collecting terms in equation (3.1.31) involving Pf and those involving g and Pg we obtain the relationship

$$Pf = Pg + \lambda PN \left[\sum_{k=0}^{\infty} (\lambda N)^k g \right] + \lambda P \left(L_{(K,P)} + N \left[\sum_{k=0}^{\infty} (\lambda N)^k \right] \lambda L_{(K,P)} \right) Pf \quad (3.1.32)$$

Our first objective is now achieved since equation (3.1.32) is a truly finite rank integral equation in the unknown member Pf of a finite dimensional vector space. The computer program giving a solution of equation (3.1.32) would provide us with coefficients of the basis vectors of this finite dimensional vector space that are needed to represent the solution Pf of equation (3.1.32). In other words, the linear combination of basis vectors of the vector space which is the image of the projector P is the exact value, Pf , of the projection of the exact value of the solution, f , of the original infinite rank integral equation, (3.1.5). From this point on we assume that Pf is known.

To finish off this section we use our exactly determined value of Pf that was obtained by solving equation (3.1.32) under the assumption that $I - \lambda L$ is invertible on the image of the projection operator P , where L is defined by equation (3.1.7). We begin by subtracting the right sides of equations (3.1.18) and (3.1.24) obtaining the relationship,

$$(f - Pf) = (g - Pg) + \lambda(I - P)Nf \quad (3.1.33)$$

Collecting the terms involving f in equation (3.1.33) and moving the known function Pf over on the right side, we obtain the equation,

$$[I - \lambda(I - P)N]f = (g - Pg + Pf) \quad (3.1.34)$$

The inequality (3.1.9) then enables us to invert the operator acting on the f in the left side of equation (3.1.34) by applying the geometric series operator

$$S = \sum_{k=0}^{\infty} (\lambda(I - P)N)^k \quad (3.1.35)$$

to both sides of equation (3.1.34). Thus, once we solve equation (3.1.32) for Pf we can correct ourselves by expressing the exact value of f as

$$f = \sum_{k=0}^{\infty} (\lambda(I - P)N)^k \{g - Pg + Pf\} \quad (3.1.36)$$

Thus, without using auxiliary memory we can with a good enough start and enough iteration correct our solution to within computer accuracy.

4 Layered Materials

We have formulated some one dimensional scattering problems associated with magnetic materials, and solutions obtained from the differential equation formulations have been substituted into the integral equations and have been shown to satisfy them exactly. For magnetic materials, a single integral equation was obtained and the significance of surface values of the derivative of the electric vector were shown to be important. For higher order splines all terms arising in a matrix representation of the integral equation formulation of the problem, and all iterates of the integrals could be computed exactly. Using distribution theory concepts, we have combined the electric and magnetic field integral equations for the case of a plane wave that is incident normally on the magnetic slab.

4.1 Magnetic Slab Integral Equation

We consider in this section radiation normally incident on a magnetic slab, and assume that the electric vector of the incident radiation has the form

$$\vec{E}^i = E_0 \exp(-ik_0 z) \vec{e}_x \quad (4.1.1)$$

so that the magnetic vector of the incident radiation defined by the Maxwell equation,

$$\begin{aligned} -i\omega\mu_0 H^i &= \text{curl}(\vec{E}^i) = \\ &= -\vec{e}_y \left(-\frac{\partial}{\partial z} \right) E_0 \exp(-ik_0 z) \\ &= -ik_0 E_0 \exp(-ik_0 z) \vec{e}_y \end{aligned} \quad (4.1.2)$$

is after dividing both sides of equation (4.1.2) by $-i\omega\mu$ is given by

$$H^i = \left(\frac{k_0 E_0}{\omega\mu_0} \right) \exp(-ik_0 z) \vec{e}_y \quad (4.1.3)$$

Within the magnetic slab, where the permittivity ϵ , the permeability μ , and the conductivity σ are diagonal tensors in Cartesian coordinates, the first Maxwell equation has the form,

$$\begin{aligned} \text{curl}(\vec{H}) &= (i\omega\epsilon_x + \sigma_x) E_x \vec{e}_x + (i\omega\epsilon_y + \sigma_y) E_y \vec{e}_y \\ &+ (i\omega\epsilon_z + \sigma_z) E_z \vec{e}_z \end{aligned} \quad (4.1.4)$$

However, if the stimulating electric vector has only an x component, then the same is true of the reflected, induced, and transmitted radiation, and, thus, we may assume that within the slab that this is also true. Hence, we assume that within the slab,

$$\vec{E} = g(z) \exp(-i\omega t) \vec{e}_x = E_x \vec{e}_x \quad (4.1.5)$$

Since then

$$\text{curl}(\vec{E}) = -\vec{e}_y \left(-\frac{\partial}{\partial z} \right) E_x = -i\omega\mu_y H_y \vec{e}_y \quad (4.1.6)$$

we conclude that

$$H_y = \frac{i}{\omega\mu_y} \frac{\partial E_x}{\partial z} \quad (4.1.7)$$

Using (3.4) we conclude that

$$\text{curl}(\vec{H}) = \vec{e}_x \left(-\frac{\partial}{\partial z} \right) H_y \quad (4.1.8)$$

which implies that

$$\begin{aligned} \text{curl}(\mathbf{H}) &= \\ \vec{e}_x \left[\left(\frac{i}{\omega \mu_y^2} \mu_y^{(1)}(z) \right) \frac{\partial E_x}{\partial z} - \frac{i}{\omega \mu_y} \frac{\partial^2 E_x}{\partial z^2} \right] \\ &= \vec{e}_x (i\omega \epsilon_x + \sigma_x) E_x \end{aligned} \quad (4.1.9)$$

Thus, multiplying all terms of this last equation by $i\omega \mu_y$ we see that

$$\begin{aligned} \frac{\partial^2 E_x}{\partial z^2} - \frac{\mu_y^{(1)}(z)}{\mu_y(z)} \frac{\partial E_x}{\partial z} \\ = (-\omega^2 \mu_y \epsilon_x + i\omega \mu_y \sigma_x) E_x \end{aligned} \quad (4.1.10)$$

We are, therefore, seeking an impulse response of the equation,

$$\begin{aligned} \frac{\partial^2 E_x}{\partial z^2} + \omega^2 \mu_0 \epsilon_0 E_x = \\ \frac{\mu_y^{(1)}(z)}{\mu_y(z)} \frac{\partial E_x}{\partial z} + (\omega^2 (\mu_0 \epsilon_0 - \mu_y \epsilon_x) + i\omega \mu_y \sigma_x) E_x \end{aligned} \quad (4.1.11)$$

We introduce the variable

$$\tau = \omega^2 \mu_y \epsilon_x - i\omega \mu_y \sigma_x - \omega^2 \mu_0 \epsilon_0, \quad (4.1.12)$$

where we agree that ϵ , μ , and σ take their free space values outside the slab, and assume that $E - E^i$ has the form,

$$\begin{aligned} E - E^i &= c \int_{-\infty}^{\infty} \tau E_x \exp(-ik_0 |z - \tilde{z}|) d\tilde{z} \\ &+ b \int_{-\infty}^{\infty} \frac{\mu_y^{(1)}(\tilde{z})}{\mu_y(\tilde{z})} \frac{\partial E_x}{\partial \tilde{z}} \exp(-ik_0 |z - \tilde{z}|) d\tilde{z} \end{aligned} \quad (4.1.13)$$

where we write the global magnetic permeability via the relationship

$$\mu_y(z) = (Y(z) - Y(z - L))(\tilde{\mu}_y - \mu_0) + \mu_0 \quad (4.1.14)$$

where

$$Y(z) = \begin{cases} 1 & \text{if } z \geq 0 \\ 0 & \text{if } z < 0 \end{cases} \quad (4.1.15)$$

is the Heaviside function and

$$Y^{(1)}(z) = \delta(z) \quad (4.1.16)$$

is the Dirac delta function and where we think of μ as the permeability at any point and think of $\bar{\mu}$ as the value of permeability inside the slab. Thus, with this definition and recognizing the tangential component of the magnetic field as being proportional to the reciprocal of the the magnetic permeability times the derivative of the electric vector with respect to z in view of the relationship

$$H_y = \frac{i}{\omega\mu_y} \frac{\partial E_x}{\partial z}$$

and seek a representation of the form,

$$\begin{aligned} E_x - E^i &= c \int_0^L \tau E_x \exp(-ik_0 |z - \bar{z}|) d\bar{z} \\ &+ b \int_0^L \frac{\mu_y^{(1)}(\bar{z})}{\mu_y(\bar{z})} \frac{\partial E_x}{\partial \bar{z}} \exp(-ik_0 |z - \bar{z}|) d\bar{z} \\ &+ b \left(1 - \frac{\mu_0}{\mu_y(0)}\right) \frac{\partial E_x}{\partial z}(0) \exp(-ik_0 z) \\ &- b \left(1 - \frac{\mu_0}{\mu_y(L)}\right) \frac{\partial E_x}{\partial z}(L) \exp(ik_0 z) \exp(-ik_0 L) \end{aligned} \quad (4.1.17)$$

Theorem 4.1 *If E_x satisfies (4.1.17) and E_x is twice continuously at points inside and outside the slab, then (a) outside the slab $E - E^i$ has the representation*

$$E - E^i = \begin{cases} C^r \exp(ik_0 z) & \text{for } z < 0 \\ C^t \exp(-ik_0 z) & \text{for } z > L \end{cases} \quad (4.1.18)$$

where C^r is the reflection coefficient, and C^t is the coefficient defining the transmitted radiation (c) if a function E_x that is differentiable inside and outside the slab satisfies the integral equation, then E_x is continuous on the entire real line, and furthermore, if $H - H^i$ is determined from (4.1.17) via the relationship

$$\begin{aligned} H - H^i &= \frac{-i}{2\omega\mu_0} \int_0^z \tau E_x \exp(-ik_0(z - \bar{z})) d\bar{z} \\ &+ \frac{i}{2\omega\mu_0} \int_z^L \tau E_x \exp(-ik_0(\bar{z} - z)) d\bar{z} \end{aligned}$$

$$\begin{aligned}
& + \frac{i}{2\omega\mu_0} \int_0^z \frac{\mu_y^{(1)}(z)}{\mu_y} \frac{\partial E_r}{\partial \bar{z}} \exp(-ik_0(z - \bar{z})) d\bar{z} \\
& + \frac{-i}{2\omega\mu_0} \int_z^L \frac{\mu_y^{(1)}(z)}{\mu_y} \frac{\partial E_s}{\partial \bar{z}} \exp(-ik_0(\bar{z} - z)) d\bar{z} \\
& + \frac{i}{2\omega\mu_0} \left(1 - \frac{\mu_0}{\mu_y(0)}\right) \frac{\partial E_x}{\partial z}(0) \exp(-ik_0z) \\
& + \frac{i}{2\omega\mu_0} \left(1 - \frac{\mu_0}{\mu_y(L)}\right) \frac{\partial E_x}{\partial z}(L) \exp(ik_0z) \exp(-ik_0L) \tag{4.1.19}
\end{aligned}$$

and $H - H^i$ is continuous across the boundaries of the magnetic slab. Furthermore, the classical solutions of the integral equation (4.1.17) are solutions of Maxwell's equations provided that

$$b = \frac{i}{2k_0} \tag{4.1.20}$$

and

$$c = -\frac{i}{2k_0} \tag{4.1.21}$$

Proof. Equations (4.1.20) and (4.1.21), which represent the evaluation of the parameters in the integral equation (4.1.17) follows by substituting (4.1.17) into Maxwell's equations. We begin by computing the first and second partial derivatives of E_x with respect to z from the integral equations and we then use these expressions to show that (4.1.20) and (4.1.21) are needed in order that Maxwell's equations be satisfied. We find, upon breaking up the integral from 0 to L into the integral from 0 to z plus the integral from z to L and differentiating, that

$$\begin{aligned}
& \frac{\partial E}{\partial z} - \frac{\partial E^i}{\partial z} = c\tau E_x - c\tau E_x \\
& c(-ik_0) \int_0^z \tau E_x \exp(-ik_0(z - \bar{z})) d\bar{z} + \\
& c(ik_0) \int_z^L \tau E_x \exp(-ik_0(\bar{z} - z)) d\bar{z} + \\
& b \frac{\mu_y^{(1)}}{\mu_y} \frac{\partial E_x}{\partial \bar{z}} \Big|_{\bar{z}=z} - b \frac{\mu_y^{(1)}}{\mu_y} \frac{\partial E_x}{\partial \bar{z}} \Big|_{\bar{z}=z} + \\
& (-ik_0)b \int_0^z \frac{\mu_y^{(1)}(\bar{z})}{\mu_y(\bar{z})} \frac{\partial E_x}{\partial \bar{z}} \exp(-ik_0(z - \bar{z})) d\bar{z} \\
& + (ik_0)b \int_z^L \frac{\mu_y^{(1)}(\bar{z})}{\mu_y(\bar{z})} \frac{\partial E_x}{\partial \bar{z}} \exp(-ik_0(\bar{z} - z)) d\bar{z} \\
& + (-ik_0)b \left(1 - \frac{\mu_0}{\mu_y(0)}\right) \frac{\partial E_x}{\partial z}(0) \exp(-ik_0 z) \\
& - (ik_0)b \left(1 - \frac{\mu_0}{\mu_y(L)}\right) \frac{\partial E_x}{\partial z}(L) \exp(ik_0 z) \exp(-ik_0 L) \tag{4.1.22}
\end{aligned}$$

We now take the derivative of both sides of this last equation with respect to z obtaining

$$\begin{aligned}
& \frac{\partial^2 E}{\partial z^2} - \frac{\partial^2 E^i}{\partial z^2} = \\
& c(-ik_0)^2 \int_0^z \tau E_x \exp(-ik_0(z - \bar{z})) d\bar{z} + (-ik_0)c\tau E_x \\
& - (ik_0)c\tau E_x + c(ik_0)^2 \int_z^L \tau E_x \exp(-ik_0(\bar{z} - z)) d\bar{z} + \\
& (-ik_0)b \frac{\mu_y^{(1)}(\bar{z})}{\mu_y(\bar{z})} \frac{\partial E_x}{\partial \bar{z}} \Big|_{\bar{z}=z} + (-ik_0)^2 b \int_0^z \frac{\mu_y^{(1)}(\bar{z})}{\mu_y(\bar{z})} \frac{\partial E_x}{\partial \bar{z}} \exp(-ik_0(z - \bar{z})) d\bar{z} + \\
& - (ik_0)b \frac{\mu_y^{(1)}(\bar{z})}{\mu_y(\bar{z})} \frac{\partial E_x}{\partial \bar{z}} \Big|_{\bar{z}=z} + (-ik_0)^2 b \int_z^L \frac{\mu_y^{(1)}(\bar{z})}{\mu_y(\bar{z})} \frac{\partial E_x}{\partial \bar{z}} \exp(-ik_0(\bar{z} - z)) d\bar{z} \\
& + (-ik_0)^2 b \left(1 - \frac{\mu_0}{\mu_y(0)}\right) \frac{\partial E_x}{\partial z}(0) \exp(-ik_0 z) \\
& - (ik_0)^2 b \left(1 - \frac{\mu_0}{\mu_y(L)}\right) \frac{\partial E_x}{\partial z}(L) \exp(ik_0 z) \exp(-ik_0 L) \tag{4.1.23}
\end{aligned}$$

We now make use of the fact that

$$-k_0^2(E - E^i) = -k_0^2 \left\{ c \int_0^L \tau E_x \exp(-ik_0 |z - \bar{z}|) d\bar{z} \right.$$

$$\begin{aligned}
& + b \int_0^L \frac{\mu_y^{(1)}(z)}{\mu_y} \frac{\partial E_x}{\partial \bar{z}} \exp(-ik_0 |z - \bar{z}|) d\bar{z} \\
& + b \left(1 - \frac{\mu_0}{\mu_y(0)}\right) \frac{\partial E_x}{\partial z}(0) \exp(-ik_0 z) \\
& - b \left(1 - \frac{\mu_0}{\mu_y(L)}\right) \frac{\partial E_x}{\partial z}(L) \exp(ik_0 z) \exp(-ik_0 L) \Big\} \quad (4.1.24)
\end{aligned}$$

and substitute it into our equation for the difference between the second partial derivatives of the stimulated and incident electric field vectors. Rewriting (4.1.23) to make this substitution transparent we see that

$$\begin{aligned}
& \frac{\partial^2 E}{\partial z^2} - \frac{\partial^2 E^i}{\partial z^2} = \\
& - (k_0)^2 \left\{ c \int_0^z \tau E_x \exp(-ik_0(z - \bar{z})) d\bar{z} \right. \\
& \quad + c \int_z^L \tau E_x \exp(-ik_0(\bar{z} - z)) d\bar{z} \\
& \quad + b \int_0^z \frac{\mu_y^{(1)}(\bar{z})}{\mu_y(\bar{z})} \frac{\partial E_x}{\partial \bar{z}} \exp(-ik_0(z - \bar{z})) d\bar{z} \\
& \quad + b \int_z^L \frac{\mu_y^{(1)}(\bar{z})}{\mu_y(\bar{z})} \frac{\partial E_x}{\partial \bar{z}} \exp(-ik_0(\bar{z} - z)) d\bar{z} \\
& \quad + b \left(1 - \frac{\mu_0}{\mu_y(0)}\right) \frac{\partial E_x}{\partial z}(0) \exp(-ik_0 z) \\
& \quad \left. - b \left(1 - \frac{\mu_0}{\mu_y(L)}\right) \frac{\partial E_x}{\partial z}(L) \exp(ik_0 z) \exp(-ik_0 L) \right\} \\
& - 2(ik_0)c\tau E_x + 2(-ik_0)b \frac{\mu_y^{(1)}(z)}{\mu_y(z)} \frac{\partial E_x}{\partial z} \quad (4.1.25)
\end{aligned}$$

Simplifying the above equation we find that

$$\begin{aligned}
& \frac{\partial^2 E}{\partial z^2} - \frac{\partial^2 E^i}{\partial z^2} = -k_0^2 (E_x - E_x^i) \\
& - 2cik_0\tau E_x - 2ik_0b \frac{\mu_y^{(1)}(z)}{\mu_y(z)} \frac{\partial E_x}{\partial z} \quad (4.1.26)
\end{aligned}$$

We next simplify this equation by making use of the fact that the electric vector, E_x^i , of the incident radiation satisfies the free space Helmholtz equation

$$\frac{\partial^2 E^i}{\partial z^2} + k_0^2 E^i = 0 \quad (4.1.27)$$

Substituting this into the previous equation we find that

$$\begin{aligned} \frac{\partial^2 E_x}{\partial z^2} + k_0^2 E_x = \\ - 2ck_0\tau E_x - 2ik_0b \frac{\mu_y^{(1)}(z)}{\mu_y(z)} \frac{\partial E_x}{\partial z} \end{aligned} \quad (4.1.28)$$

We now need to select c and b in the above equation so that the equation is identical to equation (4.1.11) where τ is given by

$$\begin{aligned} \tau &= \omega^2 \mu_y \epsilon_x - i\omega \mu_y \sigma_x - \omega^2 \mu_0 \epsilon_0 \\ &= k^2 - k_0^2 = k^2 - \omega^2 \mu_0 \epsilon_0 \end{aligned} \quad (4.1.29)$$

We see that we need

$$- 2ik_0b = 1 \quad (4.1.30)$$

and

$$2ik_0c = 1 \quad (4.1.31)$$

In order to define the operations we note here that, while it is true that we cannot in general multiply distributions, certain orders of distributions can act upon spaces larger than the infinitely differentiable functions. For example, order 0 distributions can act on the continuous functions with compact support, and order one distributions can act on the differentiable functions with compact support, et cetera which will enable us to define the product of an order 0 distribution u and a continuous function f by the rule,

$$(uf, \phi) = (u, f\phi) \quad (4.1.32)$$

where ϕ is a test function. However, the function uf is not a general distribution, but is a continuous linear functional on the space of continuous functions with compact support. The integral equation is then derived by recognizing that in view of equation (4.1.9) that

$$\begin{aligned} \frac{\partial^2 E_x}{\partial z^2} + k_0^2 E_x = \\ - i\omega \mu_y^{(1)}(z) H_y - \tau E_x \end{aligned} \quad (4.1.33)$$

By convolving the fundamental solution of the left side of this equation with the right side we obtain the integral equation. Since, as we have shown ([7], [22]), every solution

of the integral equation is a solution of Maxwell's equations and the solutions of the integral equation satisfy automatically the Silver Mueller radiation conditions and tangential components of the electric and magnetic vectors are automatically continuous across the boundaries, the solution of the integral equation is necessarily the solution of Maxwell's equations. Since the solution to this electromagnetic interaction problem is unique, the function space under consideration is the space of functions which are, along with their derivatives, continuous up to the boundaries. When the slab is nonmagnetic, then uniqueness may be proven in the function space ([22], pp 69-130) consisting of all vector valued functions ϕ such that

$$\int_{\Omega} |\phi|^2 dv + \int_{\Omega} |\text{curl}(\phi)|^2 dv < \infty \quad (4.1.34)$$

5 DISCRETIZATION

To approximate the integral equations on a computer with a finite memory, we divide the slab with which the radiation is interacting into thin wafers separated by planes whose normals are perpendicular to the planes defining the boundaries of the slab.

5.1 Piecewise Linear Approximation

We consider approximate integral equations of the form

$$\begin{aligned} \vec{E}(z) - \vec{E}^i(z) = & \\ & \sum_{j=1}^N \int_{z_{j-1}}^{z_j} \{A_j + B_j(y - z_j^*)\} K(z, y) dy + \\ & \sum_{j=1}^N \int_{z_{j-1}}^{z_j} B_j L(z, y) dy + \\ & F(z)B_1 - G(z)B_N \end{aligned} \quad (5.1.1)$$

where we suppose that the numbers z_j are defined by

$$0 = z_0 < z_1 < \dots < z_{j-1} < z_j < \dots < z_N = L \quad (5.1.2)$$

and that within the subinterval (z_{j-1}, z_j) , the electric vector is approximated by

$$\vec{E} = (A_j + B_j(z - z_j^*))\vec{e}_x, \quad (5.1.3)$$

where the constants A_j and B_j contain the $\exp(i\omega t)$ time dependence. We have a separate equation for each value of z . At this stage there are several methods to obtain a matrix equation from this continuum of approximate equations. One obvious method is point matching by selecting two points $\zeta_{2\ell-1}$ and $\zeta_{2\ell}$ in the subinterval $[z_{j-1}, z_j]$. This gives us a system of $2N$ equations in $2N$ unknowns, which have the form

$$\begin{aligned} E(\zeta_{2\ell-q+1}) - E^i(\zeta_{2\ell-q+1}) = \\ A_\ell + B_\ell(\zeta_{2\ell-q+1} - z_\ell^*) - E^i(\zeta_{2\ell-q+1}) = \\ \sum_{j=1}^N \int_{z_{j-1}}^{z_j} \{A_j + B_j(y - z_j^*)\} K(\zeta_{2\ell-q+1}, y) dy + \\ \sum_{j=1}^N \int_{z_{j-1}}^{z_j} B_j L(\zeta_{2\ell-q+1}, y) dy + \\ F(\zeta_{2\ell-q+1})B_1 - G(\zeta_{2\ell-q+1})B_N \end{aligned} \quad (5.1.4)$$

Defining

$$\delta_{(j,\ell)} = \begin{cases} 1 & j = \ell \\ 0 & j \neq \ell \end{cases} \quad (5.1.5)$$

We now use the delta function notation to rewrite the previous equation to make it look like a matrix equation. We find that

$$\begin{aligned} \sum_{j=1}^N \delta_{(j,\ell)} \{A_j + B_j(\zeta_{2\ell-q+1} - z_j^*)\} \\ - \sum_{j=1}^N \left\{ A_j \int_{z_{j-1}}^{z_j} K(\zeta_{2\ell-q+1}, y) dy + \right. \\ \left. B_j \int_{z_{j-1}}^{z_j} (y - z_j^*) K(\zeta_{2\ell-q+1}, y) dy \right\} - \\ \sum_{j=1}^N \delta_{(j,1)} B_j F(\zeta_{2\ell-q+1}) + \\ \sum_{j=1}^N \delta_{(j,1)} B_j G(\zeta_{2\ell-q+1}) = E^i(\zeta_{2\ell-q+1}) \end{aligned} \quad (5.1.6)$$

We now represent this last equation in the matrix form

$$T \begin{pmatrix} A_1 \\ B_1 \\ A_2 \\ B_2 \\ \cdot \\ \cdot \\ \cdot \\ A_N \\ B_N \end{pmatrix} = T\bar{\xi} = \begin{pmatrix} E^i(\zeta_1) \\ E^i(\zeta_2) \\ E^i(\zeta_3) \\ E^i(\zeta_4) \\ \cdot \\ \cdot \\ \cdot \\ E^i(\zeta_{2N-1}) \\ E^i(\zeta_{2N}) \end{pmatrix} \quad (5.1.7)$$

We now describe the entries of the matrix T . Note that if we define

$$\xi_{2j-1+p} = \begin{cases} A_j & p = 0 \\ B_j & p = 1 \end{cases} \quad (5.1.8)$$

that then the system of equations may be expressed more compactly in the form

$$\sum_{j=1}^N \left(\sum_{p=0}^1 T_{(2\ell-1+q, 2j-1+p)} \xi_{2j-1+p} \right) = E^i(\zeta_{2\ell-q+1}) \quad (5.1.9)$$

where $q \in \{0, 1\}$. If $p = 0$, then for each $q \in \{0, 1\}$ we have

$$T_{(2\ell-1+q, 2j-1+p)} = \delta_{(j,\ell)} - \int_{z_{j-1}}^{z_j} K(\zeta_{2\ell-q+1}, y) dy \quad (5.1.10)$$

On the other hand if $p = 1$, then again for each $q \in \{0, 1\}$ we have

$$\begin{aligned} T_{(2\ell-1+q, 2j-1+p)} &= \delta_{(j,\ell)} (\zeta_{2\ell-q+1} - z_j^*) \\ &- \int_{z_{j-1}}^{z_j} K(\zeta_{2\ell-q+1}, y) dy - \int_{z_{j-1}}^{z_j} L(\zeta_{2\ell-q+1}, y) dy \\ &- \delta_{(j,1)} F(\zeta_{2\ell-q+1}) + \delta_{(j,N)} G(\zeta_{2\ell-q+1}) \end{aligned} \quad (5.1.11)$$

Therefore, the solution of the matrix equation (5.1.7)

$$T\bar{\xi} = \vec{E}^i \quad (5.1.12)$$

then gives parameters in an approximate representation of the electric vector of the induced electromagnetic field.

6 Surface Integral Equation Methods

In this section we shall show how in the case where the irradiated structure consists of homogeneous regions which are delimited by diffeomorphisms of the interior of spheres in three dimensional space to represent the solution of the scattering problem as the solution of two combined field integral equations with integral operators formed from the Green's functions defined on opposite sides of the separating surfaces. The surface integral equation methods reduce the computational complexity in the sense that they require discretization electric and magnetic fields defined on a surface rather than on a region of three dimensional space.

6.1 Combined Field Integral Equations

Consider a set Ω in \mathbb{R}^3 with boundary surface $\partial\Omega$ on which are induced electric and magnetic surface currents \vec{J}_j and \vec{M}_j . If we have a simple $N + 1$ region problem, where we have N inside and a region outside all N bounded homogeneous aerosol particles corresponds to the region index j being equal to 1 and the region inside corresponds to j values ranging from 2 to $N + 1$, then if the propagation constant k_j in region j is defined also by a function k_j , naturally defined on a Riemann surface as the square root of,

$$k_j^2 = \omega^2 \mu \epsilon - i \omega \mu \sigma \quad (6.1.1)$$

For a Debye medium (Daniel, [10]) the branch cuts are along the imaginary ω axis. For a Lorentz medium particle (Brillouin, [3], [32]) the branch cuts are in the upper half of the complex ω plane parallel to the real axis. where μ , ϵ , and σ are functions of frequency that assure causality and that the radiation does not travel faster than the speed of light in vacuum. There are two Helmholtz equations, one for the interior of the particle and the other for the exterior, defined by

$$(\Delta + k_j^2)G_r = 4\pi\delta \quad (6.1.2)$$

where G_j is the temperate, rotationally invariant, fundamental solution ([19]) of the Helmholtz operator. We let

$$J_1 = J = -J_2 \quad (6.1.3)$$

and

$$M_1 = M = -M_2 \quad (6.1.4)$$

where we assume that the surface $S_{(1,2)}$ separates region 1 and region 2. We generalize equations (6.1.3) and (6.1.4) inductively by saying that for any surface $S_{(j,\tilde{j})}$ separating region j from region \tilde{j} where

$$j < \tilde{j} \quad (6.1.5)$$

we have

$$J_j = J = -J_{\tilde{j}} \quad (6.1.6)$$

and

$$M_j = M = -M_{\tilde{j}} \quad (6.1.7)$$

We define

$$\mathcal{I} = \left\{ (j, \tilde{j}) : S_{(j,\tilde{j})} \text{ is a separating surface} \right\} \quad (6.1.8)$$

where j is less than \tilde{j} . We get a single coupled, combined field integral equation which describes the interaction of radiation with the conglomerate aerosol particle or cluster given by

$$\begin{aligned} \vec{n} \times \vec{E}^{inc} = & \vec{n} \times \sum_{(j,\tilde{j}) \in \mathcal{I}} \left\{ \left(\frac{i\omega}{4\pi} \right) \int_{S_{(j,\tilde{j})}} \int \vec{J}(\vec{r}) \left(\mu_j \cdot G_j(r, \vec{r}) + \mu_{\tilde{j}} \cdot G_{\tilde{j}}(r, \vec{r}) \right) da(\vec{r}) \right. \\ & + \frac{i}{4\pi\omega} \text{grad} \left\{ \int_{S_{(j,\tilde{j})}} \int (\text{div}_s \cdot \vec{J}) \left[\frac{G_j(r, \vec{r})}{\epsilon_j} + \frac{G_{\tilde{j}}(r, \vec{r})}{\epsilon_{\tilde{j}}} \right] da(\vec{r}) \right\} + \\ & \left. \left(\frac{1}{4\pi} \right) \text{curl} \left(\int_{S_{(j,\tilde{j})}} \int \vec{M}(\vec{r}) \cdot (G_j(r, \vec{r}) + G_{\tilde{j}}(r, \vec{r})) da(\vec{r}) \right) \right\} \quad (6.1.9) \end{aligned}$$

In addition to equation (6.1.9) we need equation involving the magnetic vector H^{inc} of the stimulating electromagnetic field which is given by

$$\vec{n} \times \vec{H}^{inc} = \vec{n} \times \sum_{(j,\tilde{j}) \in \mathcal{I}} \left\{ \left(\frac{i\omega}{4\pi} \right) \int_{S_{(j,\tilde{j})}} \int \vec{M}(\vec{r}) \left(\epsilon_1 \cdot G_j(r, \vec{r}) + \epsilon_2 \cdot G_{\tilde{j}}(r, \vec{r}) \right) da(\vec{r}) \right\}$$

$$+ \left(\frac{i}{4\pi\omega} \right) \text{grad} \left\{ \int_{S_{(j,\tilde{j})}} \int (\text{div}_s \cdot \vec{M}) \left[\frac{G_j(r, \tilde{r})}{\mu_j} + \frac{G_{\tilde{j}}(r, \tilde{r})}{\mu_{\tilde{j}}} \right] da(\tilde{r}) \right\} + \frac{1}{4\pi} \text{curl} \left(\int_{S_{(j,\tilde{j})}} \int \vec{J}(\tilde{r}) \cdot (G_j(r, \tilde{r}) + G_{\tilde{j}}(r, \tilde{r})) da(\tilde{r}) \right) \quad (6.1.10)$$

Once the coupled combined field system (6.1.9) and (6.1.10) is solved for \vec{J} and \vec{M} , the surface electric and magnetic currents respectively and we define the surface electric charge density by ([11], p 7)

$$\rho^e(\tilde{r}) = \frac{i}{\omega} [\text{div}_s \cdot \vec{J}(\tilde{r})] \quad (6.1.11)$$

and the surface magnetic charge density

$$\rho^m(\tilde{r}) = \frac{i}{\omega} [\text{div}_s \cdot \vec{M}(\tilde{r})] \quad (6.1.12)$$

where div_s is the surface divergence. Now for each region index j we define

$$\mathcal{J}(j) = \{ \tilde{j} : (j, \tilde{j}) \in \mathcal{I} \} \quad (6.1.13)$$

where \mathcal{I} is the set of all indices of separating surfaces defined by (6.1.8). We now need to be able to express the electric and magnetic fields inside and outside the scattering body.

We first define the vector potentials \vec{A}_j and \vec{F}_j by the rules, ([11] [25])

$$\vec{A}_j = \sum_{\tilde{j} \in \mathcal{J}(j)} \left[\frac{\mu_{\tilde{j}}}{4\pi} \int_{S_{(j,\tilde{j})}} \int \vec{J}_{\tilde{j}}(\tilde{r}) \cdot G_j(r, \tilde{r}) da(\tilde{r}) \right] \quad (6.1.14)$$

$$\vec{F}_j = \sum_{\tilde{j} \in \mathcal{J}(j)} \left[\left(\frac{\epsilon_{\tilde{j}}}{4\pi} \right) \int_{S_{(j,\tilde{j})}} \int \vec{M}_{\tilde{j}}(\tilde{r}) \cdot G_j(r, \tilde{r}) da(\tilde{r}) \right] \quad (6.1.15)$$

The scalar potentials are defined in terms of the electric charge density (6.1.11) and magnetic charge density (6.1.12) by the rules,

$$\Phi_j(\tilde{r}) = \sum_{\tilde{j} \in \mathcal{J}(j)} \left[\left(\frac{1}{4\pi\epsilon_{\tilde{j}}} \right) \int_{S_{(j,\tilde{j})}} \int \rho_{\tilde{j}}^e(\tilde{r}) G_j(r, \tilde{r}) da(\tilde{r}) \right] \quad (6.1.16)$$

and

$$\Psi_j(\tilde{r}) = \sum_{\tilde{j} \in \mathcal{J}(j)} \left[\left(\frac{1}{4\pi\mu_{\tilde{j}}} \right) \int_{S_{(j,\tilde{j})}} \int \rho_{\tilde{j}}^m(\tilde{r}) G_j(r, \tilde{r}) da(\tilde{r}) \right] \quad (6.1.17)$$

We now can define the electric and magnetic vectors inside the region j in terms of these potentials (6.1.14), (6.1.15), (6.1.16), and (6.1.17) by the rules,

$$\vec{E}_j = -i\omega\vec{A}_j(r) - \text{grad}(\Phi_j(r)) + \frac{1}{\epsilon_j} \text{curl}(\vec{F}_j)(r) \quad (6.1.18)$$

and

$$\vec{H}_j = -i\omega\vec{F}_j(r) - \text{grad}(\Psi_j(r)) + \frac{1}{\mu_j}\text{curl}(\vec{A}_j)(r) \quad (6.1.19)$$

Similar equations apply outside the body, by there the fields represented are the differences \vec{E}_1^s and \vec{H}_1^s between the total electric and magnetic vectors and the electric vector \vec{E}^{inc} and the magnetic vector \vec{H}^{inc} of the incoming wave that is providing the stimulation. Thus ([11]) we see that outside the body,

$$\vec{E}_1^s = -i\omega\vec{A}_1(r) - \text{grad}(\Phi_1(r)) + \frac{1}{\epsilon_1}\text{curl}(\vec{F}_1)(r) \quad (6.1.20)$$

and

$$\vec{H}_1^s = -i\omega\vec{F}_1(r) - \text{grad}(\Psi_1(r)) + \frac{1}{\mu_1}\text{curl}(\vec{A}_1)(r) \quad (6.1.21)$$

These equations generalize the formulation of Glisson ([11]) to a three dimensional structure whose regions of homogeneity are diffeomorphisms of the interior of the sphere or a torus in \mathbb{R}^3 . If the scattering structure is not a body of revolution, then the region may be a diffeomorph of an N handled sphere.

References

- [1] Barber, P. W., Om P. Gandhi, M. J. Hagmann, Indira Chatterjee. "Electromagnetic Absorption in a Multilayer Model of Man" *IEEE Transactions on Biomedical Engineering*. Volume BME - 26, Number 7 (1979) pp 400-405
- [2] Barkeshi, S. "Eigenvalues and Eigenvectors of General Gyroelectric Media" *IEEE Transactions on Antennas and Propagation*. Volume 40, Number 3 (March, 1992) pp 340 - 344
- [3] Brillouin, Leon. *Wave Propagation and Group Velocity*. New York: Academic Press (1960).
- [4] Burr, John G., David K. Cohoon, Earl L. Bell, and John W. Penn. Thermal response model of a Simulated Cranial Structure Exposed to Radiofrequency Radiation. *IEEE Transactions on Biomedical Engineering*. Volume BME-27, No. 8 (August, 1980) pp 452-460.

- [5] Calderon, A. P. and A. Zygmund. "On the Existence of Certain Singular Integrals" *Acta Mathematica Volume 88* (1985) pp 85-139
- [6] Cohen, L. D., R. D. Haracz, A. Cohen, and C. Acquista. "Scattering of light from arbitrarily oriented finite cylinders." *Applied Optics. Volume 21* (1983) pp 742 - 748.
- [7] Cohoon, D. K. "Uniqueness of Solutions of Electromagnetic Interaction Problems Associated with Scattering by Bianisotropic Bodies Covered with Impedance Sheets" *IN Rassias, George M. (Editor) The Mathematical Heritage of C. F. Gauss* Singapore: World Scientific (1991) pp 119-132
- [8] Cohoon, D. K., J. W. Penn, E. L. Bell, D. R. Lyons, and A. G. Cryer. *A Computer Model Predicting the Thermal Response to Microwave Radiation SAM-TR-82-22* Brooks AFB, Tx 78235: USAF School of Aerospace Medicine. (RZ) Aerospace Medical Division (AFSC) (December, 1982).
- [9] Colton, David and Rainer Kress. *Integral Equation Methods in Scattering Theory* New York: John Wiley and Sons (1983)
- [10] Daniel, Vera V. *Dielectric Relaxation* New York: Academic Press (1967).
- [11] Glisson, A. K. and D. R. Wilton. "Simple and Efficient Numerical Techniques for Treating Bodies of Revolution" University of Mississippi: University, Mississippi USA 38677 *RADC-TR-79-22*
- [12] Gohberg, I. C. and I. A. Feldman. *Convolution Equations and Projection Methods for their Solution* Providence: American Mathematical Society (1974)
- [13] Guru, Bhag Singh and Kun Mu Chen. "Experimental and theoretical studies on electromagnetic fields induced inside finite biological bodies" *IEEE Transactions on Microwave Theory and Techniques. Volume MTT-24, No. 7* (1976).
- [14] Hagmann, M. J. and O. P. Gandhi. "Numerical calculation of electromagnetic energy deposition in man with grounding and reflector effects" *Radio Science Volume 14, Number 6* (1979) pp 23 -29

- [15] Hagmann, M. J. and O. P. Gandhi. "Numerical calculation of electromagnetic energy deposition for a realistic model of man." *IEEE Transactions on Microwave Theory and Techniques Volume MTT-27, Number 9* (1979) pp 804-809.
- [16] Hagmann, M. J. and R. L. Levin. "Nonlocal energy deposition - - problem in regional hyperthermia" *IEEE Transactions on Biomedical Engineering. Volume 33* (1986) pp 405 - 411.
- [17] Haracz, Richard, D. Leonard D. Cohen, and Ariel Cohen. "Scattering of linearly polarized light from randomly oriented cylinders and spheroids." *Journal of Applied Physics. Volume 58, Number 9* (November, 1958) pp 3322 - 3327.
- [18] Hochstadt, Harry. *The Functions of Mathematical Physics*. New York: Dover(1986).
- [19] Hörmander, Lars. *Linear Partial Differential Operators* New York: Academic Press (1963)
- [20] Jaggard, D. L. and N. Engheta. *ChirosorbTM* as an invisible medium. *Electronic Letters. Volume 25, Number 3* (February 2, 1989) pp 173-174.
- [21] Kleinman, R. E. "Low frequency electromagnetic scattering" In P. L. Uslenghi (Ed) *Electromagnetic Scattering* New York: Academic Press (1978)
- [22] Li, Shu Chen. Interaction of Electromagnetic Fields with Simulated Biological Structures. Ph.D. Thesis(Temple University, Department of Mathematics 038-16, Philadelphia, Pa 19122) (1986). 454 pages
- [23] Lindell, Ismo V. and Ari J. Viitanen. "Duality Transformations for General Bi-Isotropic (Nonreciprocal Chiral) Media" *IEEE Transactions on Antennas and Propagation, Volume 40, No. 1* (January, 1992) pp 91 -95
- [24] Livesay, D. E. and Kun-Mu Chen. "Electromagnetic fields induced inside arbitrarily shaped biological bodies" *IEEE Transactions on Microwave Theory and Techniques. Volume MTT-22, Number 12* (1974) pp 1273 - 1280.

- [25] Mautz, J. R. and R. F. Harrington. "Radiation and Scattering from bodies of revolution" *Applied Science Research. Volume 20* (June, 1969) pp 405-435.
- [26] Neittaanmaki, Pekka and Jukka Saranen. "Semi - discrete Galerkin approximation methods applied to initial boundary value problems for Maxwell's equations in anisotropic inhomogeneous media." *Proceedings of the Royal Society of Edinburgh. Volume 89 A* (1981) pp 125 - 133.
- [27] Ramm, A. G. "Numerical solution of integral equations in a space of distributions." *Journal of Mathematical Analysis and Applications. Volume 110* (1980) pp 384-390
- [28] Ramm, A. G. *Theory and applications of some new classes of integral equations* New York: Springer Verlag (1980)
- [29] Saranen, Jukka. "On generalized harmonic fields in domains with anisotropic homogeneous media." *Journal of Mathematical Analysis and Applications. Volume 88, Number 1* (1982) pp 104 - 182.
- [30] Saranen, Jukka. *Some remarks about the convergence of the horizontal line method for Maxwell's equations* Jyvaskyla 10, Finland: University of Jyvaskyla Department of Mathematics. Report 23 (1980)
- [31] Shepherd, J. W. and A. R. Holt. "The scattering of electromagnetic radiation from finite dielectric circular cylinders." *Journal of Physics A. Math. Gen. 16* (1983) pp 651-652.
- [32] Sherman, George C. and Kurt Edmund Oughston. "Description of pulse dynamics in Lorentz media in terms of energy velocity and attenuation of time harmonic waves." *Physical Review Letters, Volume 47, Number 20* (November, 1981) pp 1451 - 1454.
- [33] Shifrin, K. S. *Scattering of Light in a Turbid Medium*. Moscow - Leningrad: Gosudarstvennoye Izdatel'stvo Tekhniko - Teoreticheskoy Literatury Moscow Leningrad (1951)

- [34] Tsai, Chi-Taou, Habib Massoudi, Carl H. Durney, and Magdy F. Iskander. A Procedure for Calculating Fields Inside Arbitrarily Shaped, Inhomogeneous Dielectric Bodies Using Linear Basis Functions with the Moment Method. *IEEE Transactions on Microwave Theory and Techniques, Volume MTT-34, Number 11* (November, 1986) pp 1131-1139.
- [35] Uzunoglu, N. K. and N. G. Alexopoulos and J. G. Fikioris. "Scattering from thin and finite dielectric cylinders" *Journal of the Optical Society of America. Volume 68, Number 2* (1978) pp 194 - 197.
- [36] Uzunoglu, N. K. and A. R. Holt. "The scattering of electromagnetic radiation from dielectric cylinders" *Journal of Physics A. Math. Gen. Volume 10, Number 3*
- [37] Whittaker, E. T. and G. N. Watson. *A Course of Modern Analysis* London: Cambridge University Press (1986).

FORWARD SCATTERING AND SIZE PARAMETER IN LAYERED SPHERICAL AEROSOL PARTICLES

*Norman M. Witriol**
Crazio I. Sindoni

Louisiana Tech University
Ruston, LA 71272

USA CRDEC/ATTN:SMCCR-RSP-B
APG, MD 21010-5423

ABSTRACT

We investigate the scattering amplitude, phases, and Mueller Matrix Elements of polarized light scattering off a layered aerosol particle, with the goal of finding which combinations of the above quantities are most sensitive to the existence and thickness of a layer, the size of the particle, and the remaining optical parameters of the particle. Particle size parameters considered are 1 to 25; layer thickness 0 to particle size, indices of refraction from 1.33 to 2.50 and scattering angle from 0 to 180 degrees. Tunable lasers are proposed to enable scanning over the size parameter of a given aerosol droplet. Plots of the scattering amplitude, and Mueller Matrix elements for selected cases are shown, and conclusions are drawn.

KEYWORDS

layered aerosols, inverse scattering problem, forward scattering, intensity, Mueller matrix elements

INTRODUCTION

We have been investigating the information content in the scattering amplitude and Mueller matrix elements obtained from light scattering data. Our goal is to determine parametric quantities which will be used as input to reduce the inverse scattering problem. This problem is particularly difficult in real life as noise is present in the experimental data. At present the statistical decision method proposed by Hu and Lax (1992,1991,1990), has been shown to provide reasonable, albeit computationally intensive solutions. In their analysis all data is given equal weighting, and computations are performed on all possible values of the parameters in the system. The decision theory approach of Neyman and Pearson (1933), is used to determine the most probable parameters from maximum likelihood ratios. As all possible parameter space needs to be searched, the method is time intensive, due to the large number of unknowns for which a likely guess has to be made. Our goal is to consider whether a limited set of the data could be used to determine uniquely, or provide limit boundaries, on some of the parameters of the system. The number of unknowns, and therefore the computation time, will thereby significantly reduced, resulting in increased accuracy of the results. In plotting the scattering amplitude and the Mueller matrix elements

* NRC - Senior Research Associate USA CRDEC/ATTN:SMCCR-RSP-B APG, MD 21010-5423

as a function of various parameters of the system, with a fixed incident wavelength, due to interference effects, a unique inversion is not easily observed. However, by using variable wavelength lasers, and thereby scanning the size parameter for a fixed size particle, one can average over many of the short scale resonances, thereby readily obtaining unique information on the particle - specifically particle size, and a relationship between the other parameters of the system.

SCATTERING INTENSITY, AND MUELLER MATRIX ELEMENTS M_{12} , AND M_{34}

For illustration purposes, in this short report, we show the plots [Fig.1a-1d] for a homogenous sphere, index of refraction $n = (1.33, 0.0)$, and [Fig.2a-2d] for a layered sphere, $n_{core} = (1.33, 0.0)$, and $n_{layer} = (1.55, 0.0)$, with $r_{core}/r_{particle} = 0.8$. The 3D-plots [Figs. 1,2] are of the parallel [Figs. 1a,2a] and perpendicular [Figs.1b,2b] scattering amplitude and the Mueller matrix elements m_{12} [Figs.1c-2c], and m_{34} [Figs.1d,2d], for size parameter vs. scattering angle. A regular periodicity is readily observed, in all of the above figures. Fig.3 shows the forward (0°) scattering amplitude vs. size parameter for the above two cases. The dotted lines are an unweighted 9 pt. average (the center point, and 4 points on either side.) We observe that the relatively rapid oscillations are damped, and the linear and sinusoidal dependences are emphasized. The existence of sinusoidal dependences for homogenous spheres is well known (Bohren and Huffman, 1983). Similar sinusoidal dependences for layered spheres are observed. The period of the oscillations, in a manner similar to the homogenous case, is given by the phase difference due to the difference in the optical path lengths:

$$(2\pi/\lambda)(r_{particle}(n_{layer}-n_{external})-r_{core}(n_{layer}-n_{core}))=\pi$$

The linear dependence of the averaged amplitude with respect to size parameter is independent of the indices of refraction, and the existence (or lack thereof) of a layer. In Fig.4 the scattering amplitude of homogenous spheres of $n = (1.33, 0.0)$, $n = (1.55, 0.0)$ and $n = (2.50, 0.0)$, and of layered spheres of $n_{core} = (1.33, 0.0)$, with $n_{layer} = (1.55, 0.0)$ and $n_{layer} = (2.50, 0.0)$ are plotted. The mathematical model deriving this results will be presented in a forthcoming paper.

CONCLUSIONS

Using a tunable wavelength laser and looking at the forward scattering amplitude, we can i) obtain the size of the particle from the amplitude, and ii) obtain a relationship between the parameters of the particle from the period of the sinusoidal variation.

ACKNOWLEDGEMENT

We wish to thank Dr. John P. Barton (Univ. of Nebraska-Lincoln) for the use of one of his scattering codes which has been incorporated in the programs which produced the plots shown. This work was done while N.M. Witriol held a National Research Council-US Army CRDEC Research Associateship.

REFERENCES

- Craig F. Bohren and Donald R. Huffman, " *Absorption and Scattering of Light by Small Particles*," John Wiley & Sons, p.105 (1983).
- Po Hu and M. Lax (preprint,1992); *ibid.* Proceed. of the 1990 Scientific Conf. on Obscuration and Aerosol Research (CRDEC-SP-036); *ibid.* Proceed. of the 1991 Scientific Conf. on Obscuration and Aerosol Research (CRDEC-SP-037).

Amplitude vs size parameter

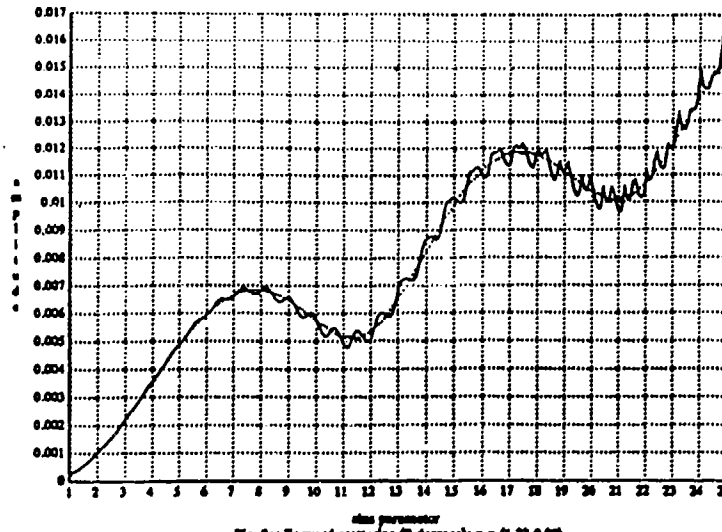


Fig. 3a: Forward scattering (0 degrees): $a = (1.33, 0, 0)$
 solid - original data, dashed - smoothed data (7 pt av)

Amplitude vs size parameter

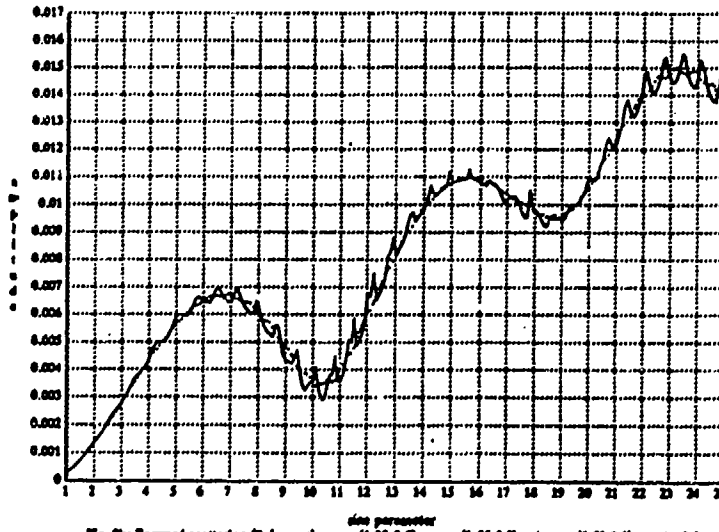


Fig. 3b: Forward scattering (0 degrees): $a_{hom} = (1.33, 0, 0)$, $a_{inh} = (1.55, 0, 0)$, $a_{inh} = (1.58, 0, 0)$, $\gamma_{inh} = 0.8$
 solid - original data, dashed - smoothed data (7 pt av)

Amplitude vs size parameter

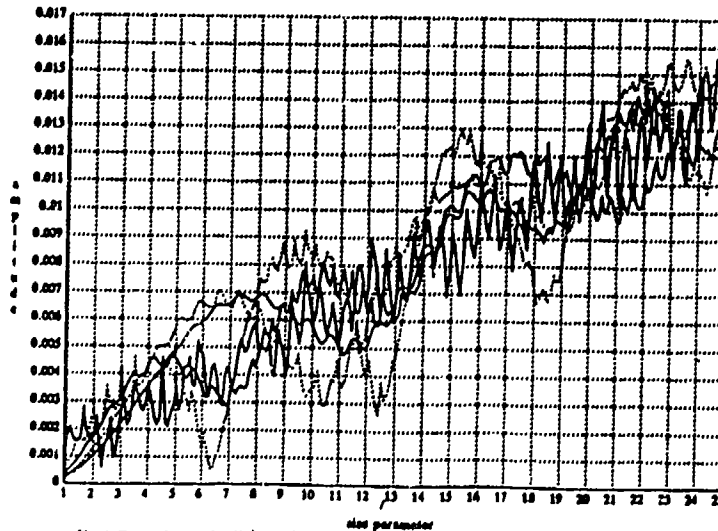
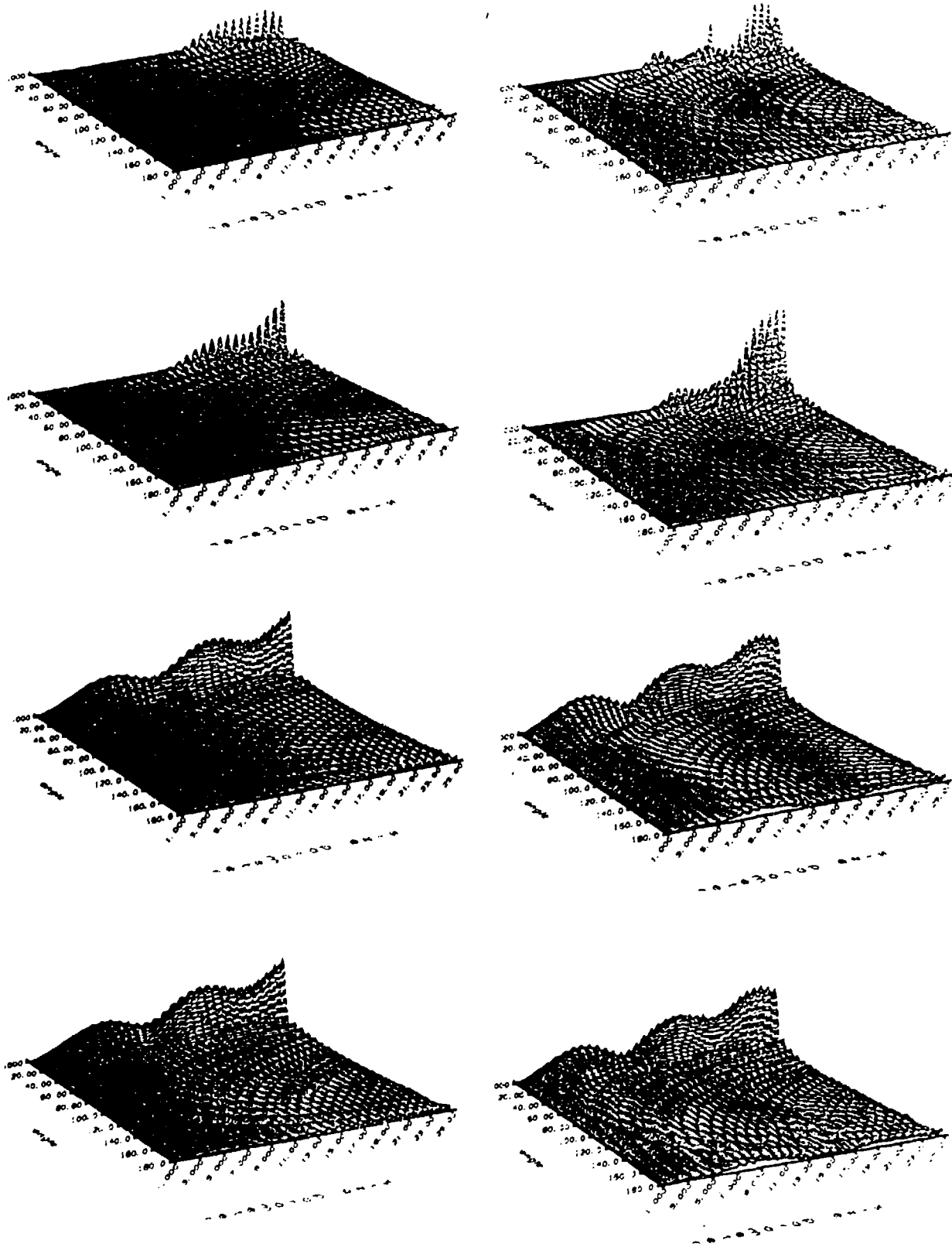


Fig. 4: Forward scattering (0 degrees): solid - homogeneous with: $a = (1.33, 0, 0)$, $a = (1.55, 0, 0)$, $a = (1.58, 0, 0)$
 dashed - layered with: $a_{hom} = (1.33, 0, 0)$, $a_{inh} = (1.55, 0, 0)$, $a_{inh} = (1.58, 0, 0)$, $\gamma_{inh} = 0.8$



Figs.[1-2] [Fig.1a-1d] for a homogenous sphere, index of refraction $n = (1.33, 0.0)$, and [Fig.2a-2d] for a layered sphere, $n_{core} = (1.33, 0.0)$, and $n_{layer} = (1.55, 0.0)$, with $r_{core}/r_{particle} = 0.8$. [Figs. 1,2] are of the parallel [Figs. 1a,2a] and perpendicular [Figs.1b,2b] scattering amplitude and the Mueller matrix elements m_{12} [Figs.1c-2c], and m_{34} [Figs.1d,2d], for size parameter vs. scattering angle.

QUASI-BINARY DECISION MAKING: AN UPDATE

Po Hu and Melvin Lax

Department of Physics, City College of the City University of New York, New York, New York 10031

RECENT PUBLICATIONS

^aP. Hu, M. Lax, "Quasi-Binary Decision Making Using Light Scattering", in Proceedings of the 1991 CRDEC Scientific Conference on Obscuration and Aerosol Research.

^bP. Hu, M. Lax, "Single Scattering Inversion Problem", in Proceedings of the 1990 CRDEC Scientific Conference on Obscuration and Aerosol Research.

^cB. Yudanin, M. Lax, "POST Adaptation for a Numerical Solution of the Spherically-Symmetric Riemann Problem," J. Mod. Phys. 4, 285-298 (1990).

^dB. Yudanin, P. Hu, M. Lax, "Numerical Solution of the Riemann Problem in the Presence of an External Energy Source", in Proceedings of the 1988 CRDEC Scientific Conference on Obscuration and Aerosol Research.

^eM. Lax, B. Yudanin, "Early-Time Hydrodynamic Response to Pulsed Laser Radiation," Digest - Intl. Conf. on Optical and Millimeter Wave Propagation and Scattering in the Atmosphere, Florence, Italy, 1986.

^fB. Yudanin, M. Lax, "Hydrodynamical Response to Uniform Laser Absorption in a Droplet," in Proceedings of the CRDC 1985 Scientific Conference on Obscuration and Aerosol Research, edited by R. H. Kohl and D. Stroud (1985).

ABSTRACT

Can a very limited number (5-20) of polarized light scattering measurements from spherical droplets be inverted to obtain a radially varying index of refraction $m(r)$? No! But if we are restricted to deciding between a uniform droplet and one with a shell-like structure (described by only two indices of refraction) the answer appears to be yes even in the presence of noise!

1. Introduction

The full inverse scattering problem requires that polarized light scattering from a spherical object be used to determine the complete dependence of the index of refraction $m(r)$ on radius r . This requires an enormous amount of highly accurate data. A more feasible question when only a small amount of (noisy) scattering intensities are available is this: are we observing a sphere or a shell?

This restricted problem is still non-trivial because one must *estimate* indices of refraction and radii before applying *decision* (or detection) theory to make the binary decision between sphere and shell. This problem falls into the area of pattern recognition. But it has the special difficulty that the light scattering data are highly nonlinear functions of the refractive indices and radii. Thus the relation between what is observed, and what is to be estimated, is much more indirect than say in character recognition.

Experiments involve experimental errors, that must be considered in our decision process. We shall treat the experimental error as a Gaussian noise.

The possibility of success depends on:

1. The amount of experimental inaccuracy and noise present.
2. The permissible range of parameters (radii and indices).
3. The number of measurements.

The logical procedure is to start with fairly restricted parameters and a small number of measurements. In this way, feasibility can be established with a modest amount of computer time. Then one can broaden the permitted range of parameters and determine how much the number of measurements must be increased to handle the larger number or range of parameters. In this paper, the outer radius of the shell is held fixed, so that the maximum number of parameters is three. We shall demonstrate feasibility over a fairly wide range of parameters.

Because of the nature of the audience, we shall skip a discussion of Mie scattering by a layered sphere, but we shall review some concepts in statistical decision theory even though some of these were originated by statisticians in the 1930's and carried over into communication theory in the 1960's.

2. Statistical Decision Method

We adopt the Neyman-Pearson statistical decision method^{1,2} which has also been used in communication theory^{3,4}. We have shown that this method can also be derived⁵ with the help of Bayes theorem. In the language of decision theory, the null hypothesis, H_0 will be identified with a spherical scatterer. The alternate process, H_1 will be identified with a shell (a signal). The Neyman-Pearson procedure, in the language of radar detection minimizes the probability P_M of a miss (choosing H_0 where a signal H_1 is present) subject to a fixed false alarm probability P_F (choosing a shell H_1 , when only H_0 , a sphere, is present). If R is an observed quantity (or a scalar combination of observations) and $P(R | H_0)$ is the conditional probability for R given hypothesis (or source) H_s , then the false alarm probability can be written

$$P_F = \int_{\lambda}^{\infty} P(R | H_0) dR = \alpha \quad (1)$$

and the value α is the constraint. Here λ , the threshold value for R above which a "hit" or H_1 is chosen, is determined using Eq. (1). The Neyman-Pearson decision criterion is simply

$$\text{if } \Lambda(R) > \lambda \text{ choose } H_1 \quad (2)$$

$$\text{if } \Lambda(R) < \lambda \text{ choose } H_0 \quad (3)$$

$$\text{when } \Lambda(R) = \frac{P(R | H_0)}{P(R | H_1)} \quad (4)$$

A choice for the statistic R follows in a natural way from our two-stage procedure of first estimating a parameter set η . [η^0 = radius r_s , index m for the sphere, η^1 = inner radius r_1 , outer radius r_2 , inner index m_1 , outer index m_2] and then making a binary choice. An estimate η^h is made for each hypothesis $h = 0, 1$ by using a least square fit:

$$\nu_h = \min[\eta^h] \sum_j^M [\tilde{i}(\theta_j, \eta^*) - i(\theta_j, \eta^h)]^2 \quad (5)$$

Here $i(\theta_j, \eta^h)$ represents the theoretical intensity at angle θ_j for parameters η^h . A polarization index has been suppressed. In the present paper, intensities at two polarizations are used. In the future, these Mueller scattering coefficients can be calculated (and measured) at each angle. Also, $\tilde{i}(\theta_j, \eta^*)$ represents the measured experimental intensity

$$\bar{i}(\theta_j, \eta^*) = i(\theta_j, \eta^*) + n_j \quad (6)$$

appropriate to an unknown parameter set η^* in the presence of the noise n_j . In this paper, the experimental results are emulated by a Monte Carlo procedure in which the parameters η^* are selected at random over the range of allowed parameters, and Gaussian noise n_i is added whose root-mean-square width is proportional to the intensity:

$$\sigma_j = k i(\theta_j, \eta^*) \quad (7)$$

with $k = 0.1$.

A natural choice for the statistical test parameter is

$$R = \log(v_0/v_1) \quad (8)$$

If a better fit is obtained with a sphere, v_0 will be small, v_1 will be large (hopefully) and $\log R$ will be negative. If a better fit is obtained with parameters η for a shell, then v_1 will be small and v_0 will be large (hopefully), and $\log R$ will be positive. Thus the Neyman-Pearson procedure, Eqs. (2-4), can be approximated by the simpler procedure

$$\text{if } R > 0 \text{ choose } H_1 ; \text{ if } R < 0 \text{ choose } H_0 \quad (9)$$

3. Monte Carlo Procedures

In order to establish the feasibility of our procedure, we shall perform Monte Carlo calculations to determine the distribution of values of R when the source is a sphere, and when the source is a shell. Before discussing the details, we would like to demonstrate the difficulties incurred in the minimization performed in Eq. (5). We shall plot the logarithm of the function that is to be minimized

$$F_h = \log \left[\sum_i \left[\bar{i}(\theta_i, \eta^*) - i(\theta_i, \eta^h) \right]^2 \right] \quad (10)$$

We use the source parameters in η^* : $m_s^* = 1.515$, $r_s^*/\lambda = 6.98$ where λ is the vacuum wavelength and plot F_0 for the spherical parameters over the range $m_s = [1.33, 1.8]$, $r_s/\lambda = [4, 8]$. The plot in Fig. 1 displays a large number of closely spaced minima and illustrates the difficulty of finding an absolute as opposed to a relative minimum. By splitting the range for each variable into 100 parts, we have obtained the plot for F and located the absolute minimum by brute force.

This calculation is feasible for one experimental point η^* and 10^4 choices of η for the spherical case. It is even feasible for the 10^6 choices of η for the three parameter shell case. However, we would like to choose $N = 1000$ experimental sources and 12 measurements. The number of calculations for the shell then involves at least $12 \times 1000 \times 10^6$ operations. Even if the Bessel functions have been precomputed and table look up is used, brute force becomes unacceptable.

If we use N_0 points (say 10^5) to sample the η space for the special case (2 parameters) and N_1 points (say 10^6) to sample the η space for the shell (4 parameters) the number of calculations is of order $N(N_0 + N_1)$. However, if we save intensities, we need not repeat the heavy Bessel function calculations. Then only the sum of squares need be performed $N(N_0 + N_1)$ times. Moreover, if we create an array of dimension N to hold N values of v , one for each η^* , then if a given η makes a best fit for a fixed η^* , store that η and $v(\eta^*, \eta)$ and discard all information regarding previously used η 's. By this procedure, the storage requirements again become reasonable.

4. Numerical Results

Bottiger's experimental apparatus⁶ has so far only been used on spheres, but we shall consider uniform spheres with indices in the range $m_s = [1.33, 1.8]$ and radii in the range $r_s/\lambda = [4, 8]$ and shells with indices in the range $m_1 = [1.33, 1.55]$ for the inner region and $m_2 = [1.6, 1.8]$ in the outer region. The inner shell radius is in the interval $r_1/\lambda = [4, 6]$ with a fixed outer radius, $r_2/\lambda = 8$. All calculations are performed with $N = 1000$ "experimental" points. Then the two spherical parameters are sampled with N_0 points and the three shell parameters are sampled with N_1 points. In Fig. 2, we choose $N_0 = N_1 = 100$. The left hand portion of Fig. 1 is the histogram $N(R)$ for the spherical case. The right hand portion is the histogram $N(R)$ for the shell case. The overlap region, near $R = 0$, is large because our trial points $N_0 = 100, N_1 = 100$ are insufficient to locate the best minima. A considerable improvement is shown with $N_0 = 10^4, N_1 = 10^5$ in Fig. 3 and even more in Fig. 4 with $N_0 = 10^5, N_1 = 10^6$. It can be seen that measurement of twelve pieces of scattering data (intensities at six angles and two polarizations) provide excellent discrimination in the present case of two spherical and three shell parameters.

¹J. Neyman and E. S. Pearson, "On the Problem of the Most Efficient Tests of Statistical Hypotheses," *Philosophical Trans. A*, 231, 289 (1933)

²M. G. Kendall and A. Stuart, *The Advanced Theory of Statistics, Volume 2* Hafner Publishing

Co, New York (1967)

³H. L. Van Trees, *Detection, Estimation, and Modulation Theory, Part I*, John Wiley and Sons, (1968)

⁴David Middleton, *Introduction to Statistical Communication Theory*, McGraw-Hill (1960)

⁵P. Hu and M. Lax, "Quasi-Binary Decision Making Using Light Scattering", in Proceedings of the 1991 CRDEC Scientific Conference on Obscuration and Aerosol Research.

⁶Jerold Bottiger, Proceedings, 1991 CRDEC Scientific Conference on Obscuration and Aerosol Research (to be published).

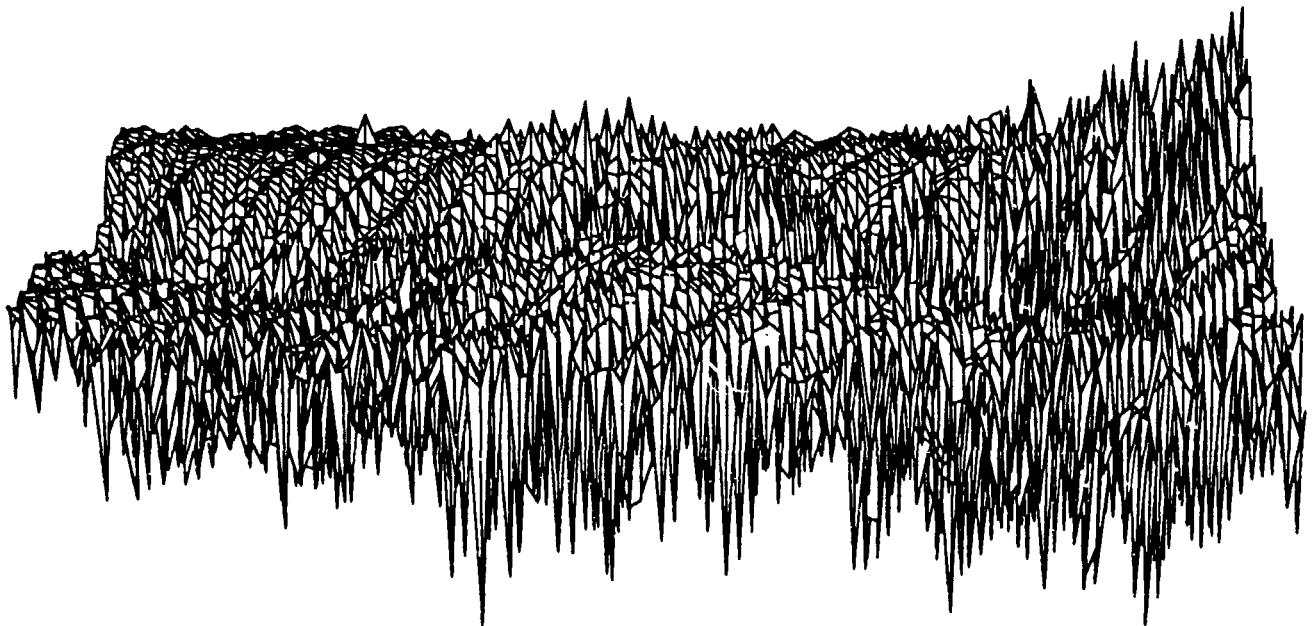
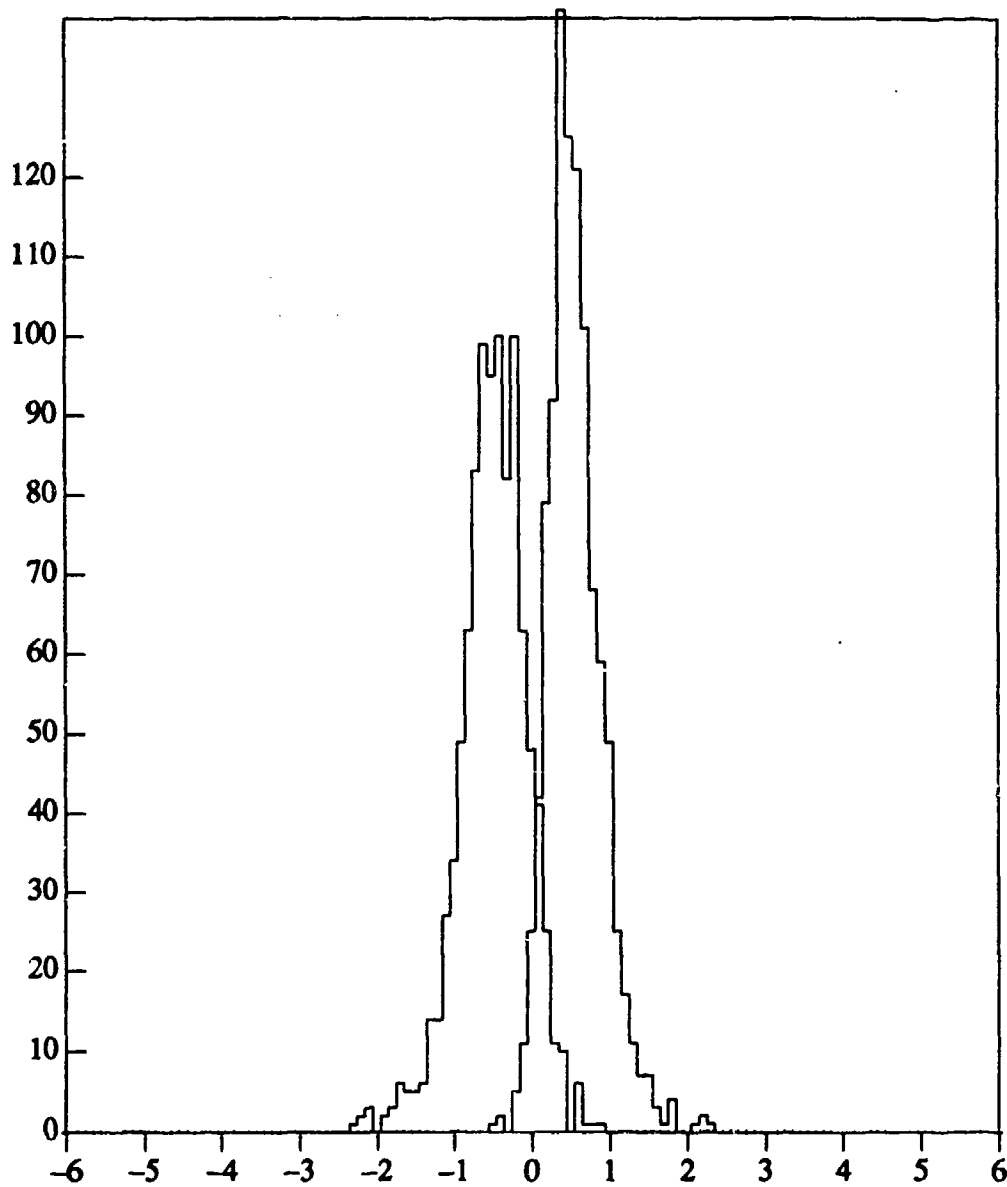


Fig. 1. Function $F = \ln(\sum_{i=1}^M [\tilde{i}(\theta_i, \eta^*) - i(\theta_i, \eta^0)]^2)$ is plotted over the permitted parameter space.

The source intensities $\tilde{i}(\theta_i, \eta^*)$ are generated from a parameter point for a uniform sphere $m^* = 1.515$ and $r^* = 6.98$. The fitting hypothesis is chosen as the correct hypothesis (uniform sphere), and the permitted parameter range is $m_s = [1.33, 1.8]$ and $r_s/\lambda = [4, 8]$. 100 mesh points are taken for both m_s and r_s . This figure displays the difficulty of finding a global minimum when large size parameters are permitted.



$\log_{10}(v_1/v_2)$

Fig. 2. The approximate distribution functions for both source cases. The numbers of points for the two hypotheses in the approximate least square fitting are $N_0=100$ and $N_1=100$. This plot is for 12 measurements of two polarizations at 6 angles at 75, 90, 115, 130, 145, 160 degrees and the noise level is 10 percent. The parameter ranges are: $m_s=[1.33,1.8]$, $r_s/\lambda=[4,8]$ for the uniform sphere and $m_1=[1.33,1.55]$, $m_2=[1.6,1.8]$, $r_1/\lambda=[4,6]$ for the layered scatterer while outer radius $r_2/\lambda=8$ is fixed here.

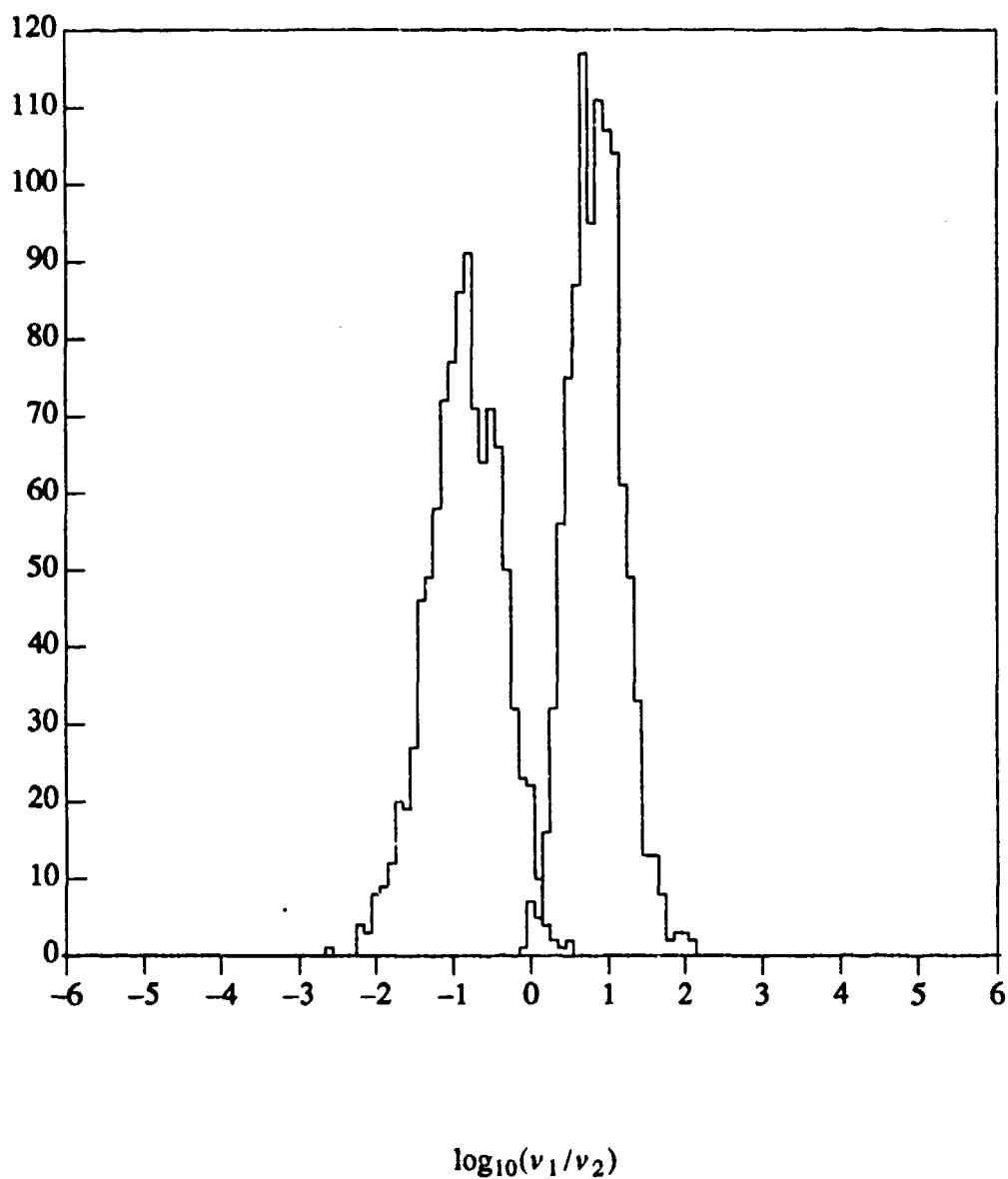
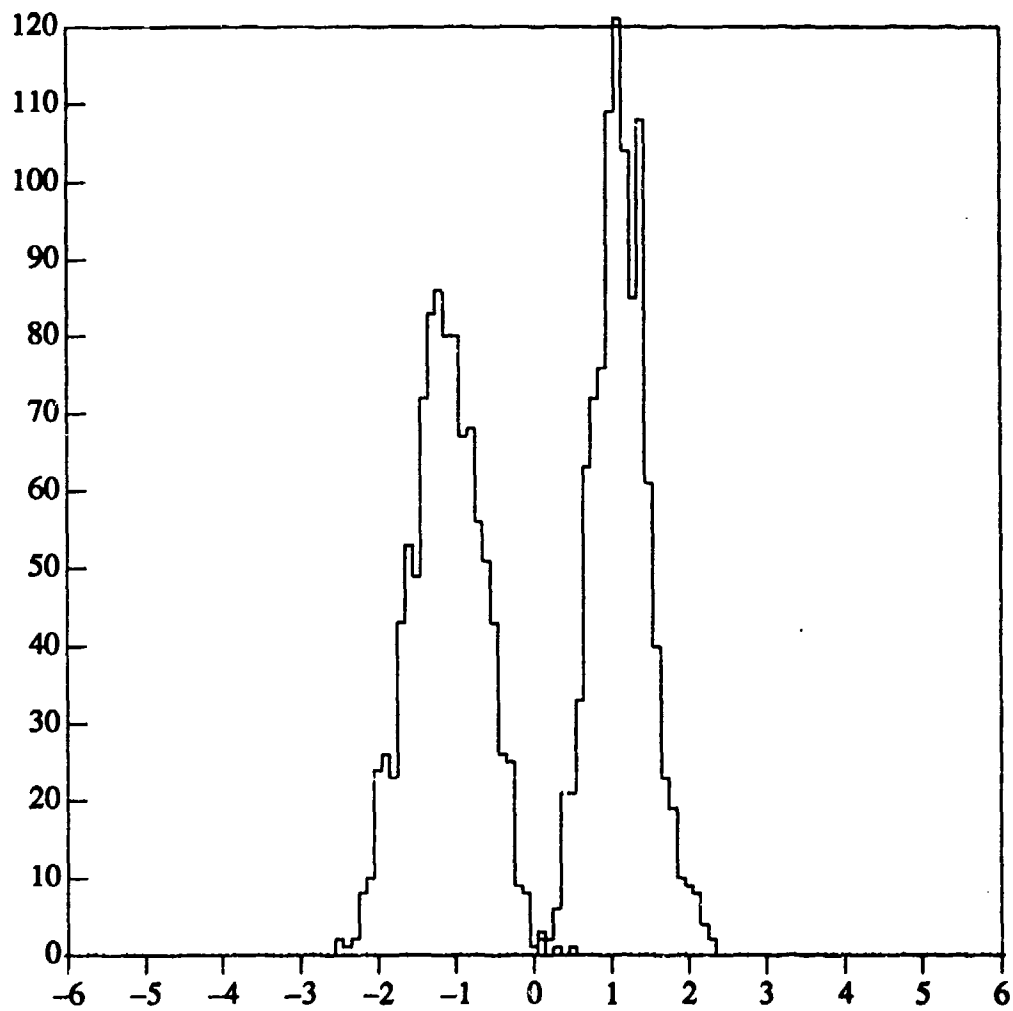


Fig. 3. The same distribution functions as Fig. 2 are plotted with a more accurate minimization process, using the increased number of points $N_0=10^4$ and $N_1=10^5$.



$\log_{10}(v_1/v_2)$

Fig. 4. The same distribution functions as Fig. 2 are plotted with a more accurate minimization process, using the increased number of points $N_0=10^5$ and $N_1=10^6$.

Blank

**LIGHT SCATTERING FROM A SLICED TARGET USING THE INTERNAL FIELD OF
INFINITE
CYLINDERS:
COMPARISON WITH MIE THEORY AND A SLICED SPHERE**

by

Ariel Cohen, R. D. Haracz* and L. D. Cohen*

Department of Atmospheric Sciences
The Hebrew University of Jerusalem, Israel
and

*Department of Physics and Atmospheric Science
Drexel University, Philadelphia

ABSTRACT

Light scattering from a particle that can be decomposed into circular slices is calculated by performing a coherent integration of the internal field over the volume of the target. The internal field in each slice is taken to be the internal field solution of an infinite cylinder of radius equal to the radius of the slice. It is shown that for a spherical scatterer, the integration leads to results that are in good agreement with those predicted by the Mie theory solution. The agreement is, in fact, significantly improved compared to previous approaches such as the Shrifrin approximation through the second order.

Introduction.

An integral equation for the scattered field intensities is used for target particles of size parameters up to $x=1.4$ and refractive indices $m=1.33$ or 1.55 . This integral equation uses the internal electric field to obtain the scattered field, and thus reduces the problem to a search for the internal field. The history of this approach begins with the work of Shifrin¹ and Acquista² - the first improving on the born approximation (internal field equal to the ambient field) by introducing the polarizability of the medium, and the latter iterates Shifrin's first approximation in a series involving the polarizability. Later work by our group extended Acquista's approach to a wider range of shapes by dividing the target into slices³ and to an attempt to evaluate the internal field by a direct evaluation of the relevant integral equations.⁴

The work of refs. 4 though guaranteeing success if the numerical evaluation is precise, leads to extremely time consuming computation and applications to realistic problems demands quick and accurate results to be able to deal with random orientations and multiple scattering effects.

The present work thus focuses on an approach that takes advantage of the fact that the internal electric field inside an infinite cylinder can be obtained to any degree of accuracy, and this field can be used for each of the disks that form the wide range of targets considered in the previous papers (including helices).

We will, in fact, use the internal field from an infinite cylinder two ways to show consistency and compare the resulting far-field results to the Mie theoretical results for spheres of size parameters ranging between 0.6 and 1.4 and indices of refraction 1.33 and 1.55. We will show that this approach is at least as good as the second-order Shifrin approximation with much quicker computational demands.

Integral equation for scattering.

A solution to Maxwell's equations¹ for the scattering of radiation from dielectric targets is

$$\mathbf{E}(\mathbf{r}) = \mathbf{E}_{inc}(\mathbf{r}) + \nabla \times \nabla \times \int dV' (m^2 - 1) / 4\pi \exp(ik_0 |\mathbf{r} - \mathbf{r}'|) / |\mathbf{r} - \mathbf{r}'| \mathbf{E}(\mathbf{r}') + (1 - m^2) \mathbf{E}(\mathbf{r}), \quad (1)$$

where the integration is over the volume of the scattering target. Introducing the effective field by

$$E_{\text{eff}}(r) = (m^2+2)/3 E(r) \quad (2)$$

and bringing the operators inside the integral⁵ gives

$$E_{\text{eff}}(r) = E_{\text{inc}}(r) + \alpha \int' dV' (\text{grad div} - k_0^2) \exp(ik_0|r-r'|)/|r-r'| E_{\text{eff}}(r'). \quad (3)$$

Here, the integral is over the target volume excluding an infinitesimal region surrounding the point $r=r'$, if the field point is within the target. The coefficient α is the polarizability

$$\alpha = (3/4\pi) (m^2-1)/(m^2+2). \quad (4)$$

When the field point is far from the target, eq.(3) reduces to

$$E_{\text{eff}}(r) = \alpha k_0^2 \exp(i k_0 r) \left[\int dV' \exp(-i k_0 r \cdot r') [E_{\text{eff}}(r')] \right]_{\text{per}} \quad (5)$$

where $r = r / r$, the integration is over the target volume with no singularity since r is outside the volume and $[..]_{\text{per}}$ indicates that the component of the vector within the square brackets is to be taken in a direction transverse to the direction toward the detector. Thus, the far field determined from eq. (4) depends on the effective field within the target, which by (2), depends on the effective internal electric field, and r' is the vector of an arbitrary point within the target.

Models for the evaluation of the integral equation.

As in our previous work, we treat targets that have a symmetry axis and possess a circular cross sectional area perpendicular to this axis. The target in this paper will be a sphere since Mie theory exists to test the model, and we will take the scattering plane (plane formed by the directions of incidence and scattering) to be parallel to the plane of the disks that form the sphere, as shown in Figures 1 and 2.

Two methods are used to calculate the scattered field. Method 1 is a calculation of the scattered field for a spherical target sliced into 19 disks (10 different sizes), each of which contains the direction of propagation of the incident wave. The polarization of the incident wave is taken to be either parallel or normal to the disk. The scattered electric field is then constructed from a coherent sum of the scattered fields from 19 infinite cylinders (intensities are per unit length) having radii corresponding to the 19 disks that form the target. It should be noted that the infinite cylinder theory for the scattered field has been used in this way in the past to predict the scattering of particles of helical shapes and the results were in good agreement with the measurements [3].

The second method is a calculation of the scattered field using the **internal** fields obtained from the infinite cylinder theory for each of the 19 disks and summing these using the above integral equation (5). A comparison is made with the results from method 1. The basic difference between the two approaches is that in method 1 the scattered field is derived from the far-field Eq values alone, whereas in method 2, $[E_{\text{eff}}(r')]_{\text{per}}$ inside the particle is dependent on the corresponding projections of E_{θ} and E_r inside the target in a direction perpendicular to r for polarization within the scattering plane. In the case of polarization perpendicular to the scattering plane, only the z component of the internal field need be taken.

The internal field that is used in eq. (5) when the incident electric field is linearly polarized parallel to the axis of a disk is (TM wave) :

$$E_{\text{int}}(r') = i \exp(i\omega t - k_0 z') \sum_{-\infty}^{+\infty} d_n (-i)^n \exp(in\theta') m k_0 / r' J_n'(k_0 m r') \mathbf{k}, \quad (6)$$

where for incidence perpendicular to the z axis⁶

$$d_n = [J_n(k_0 a) H_n^{(2)'}(k_0 a) - J_n'(k_0 a) H_n^{(2)}(k_0 a)] / [m J_n(k_0 m a) H_n^{(2)'}(k_0 a) - m J_n'(k_0 m a) H_n^{(2)}(k_0 a)].$$

The internal field when the incident electric field is linearly polarized perpendicularly to the axis of the disk is (TE wave):

$$E_{\text{int}}(r') = \exp(i\omega t - k_0 z') \sum_{-\infty}^{+\infty} c_n (-i)^n \exp(in\theta') [in/r' J_n(k_0 r') \mathbf{r}' - J_n'(k_0 m r') \boldsymbol{\theta}], \quad (7)$$

where

$$c_n = [J_n(k_0 a) H_n^{(2)'}(k_0 a) - J_n'(k_0 a) H_n^{(2)}(k_0 a)] / [m^2 J_n(k_0 m a) H_n^{(2)'}(k_0 a) - J_n'(k_0 m a) H_n^{(2)}(k_0 a)].$$

Here, r' and θ' are unit vectors in the plane of the disk as shown in Figure 2. All summations can be replaced by summations from 0 to infinity so that E_r will be dependent on $\sin(n\theta')$ and E_{θ} on $\cos(n\theta')$. The two methods discussed above were compared with the results of the Mie theory for the corresponding

spherical scatterers.

Conclusions.

The scattering intensities are defined by

$$I = k_0^2 r^2 / |E_0|^2 |E_{sc}|^2,$$

where E_{sc} is the scattered electric field. The scattering matrix elements

$$S_{11} = (I_{par} + I_{per})/2, \quad S_{12} = (I_{par} - I_{per})/2$$

are then calculated, where "par" and "per" refer to the direction of incident polarization being in and normal to the scattering plane, respectively. These are shown in figures 3 - 10. The first 6 are for $m=1.33$ and a size parameter $x = k_0 a = 0.6, 1.0$ and 1.4 , where "a" is the radius of the sphere. The final figure has $m= 1.55$ and a size parameter $x= 1$. We see that the agreement between the two methods of calculation is almost perfect, thus showing the consistency of the approach using the integral of eq. (4) and taking a coherent sum of the far field effects from all the disks that composed the spherical particle. The agreement with the results of the Mie theory is also quite good, where differences at the larger scattering angles begin to show for the larger size parameters.

The final figure is included to make a comparison with the Shrifrin method as extended by Acquista (Ref. 3). The scattering intensity S_{11} obtained by our present approach is significantly better than the second-order result contained in Reference 3.

The results of this approach, suggest that the angular scattered intensities can be calculated with a high accuracy for all particles of arbitrary shape which can be sliced into circular cylinder sections. For example, the scattering properties of rain droplets, whose shape is approximately that of a teardrop, by radar waves can be studied with the above theoretical tools.

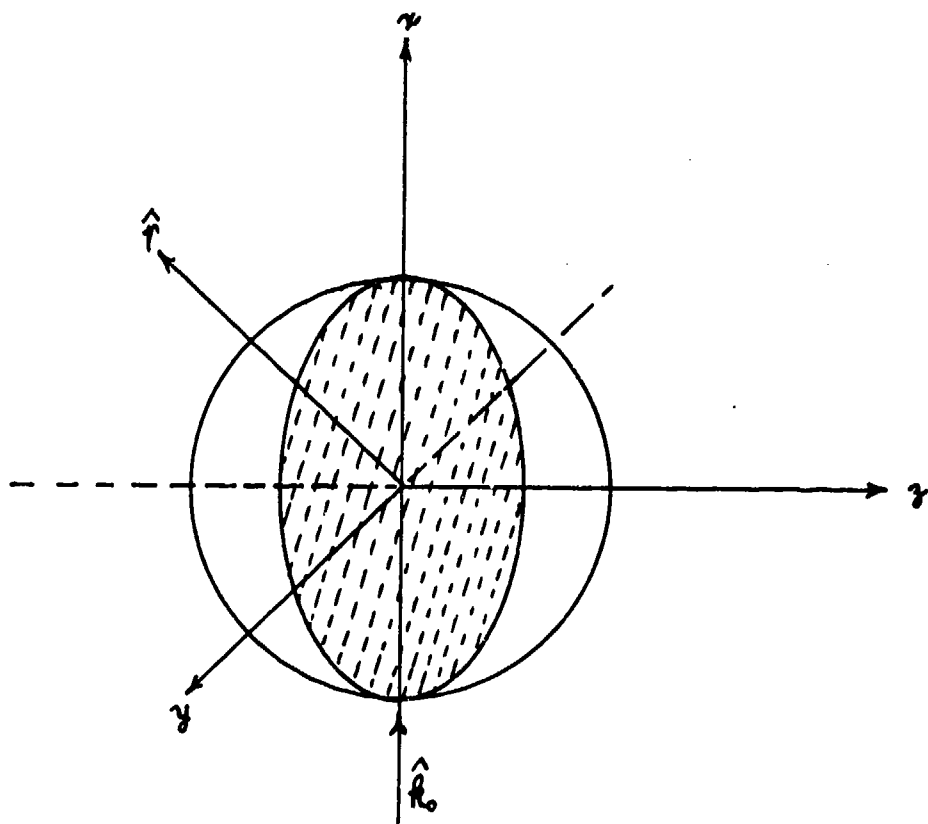
This research was partially supported by research grants from the US Army CRDEC at Aberdeen Proving Grounds.

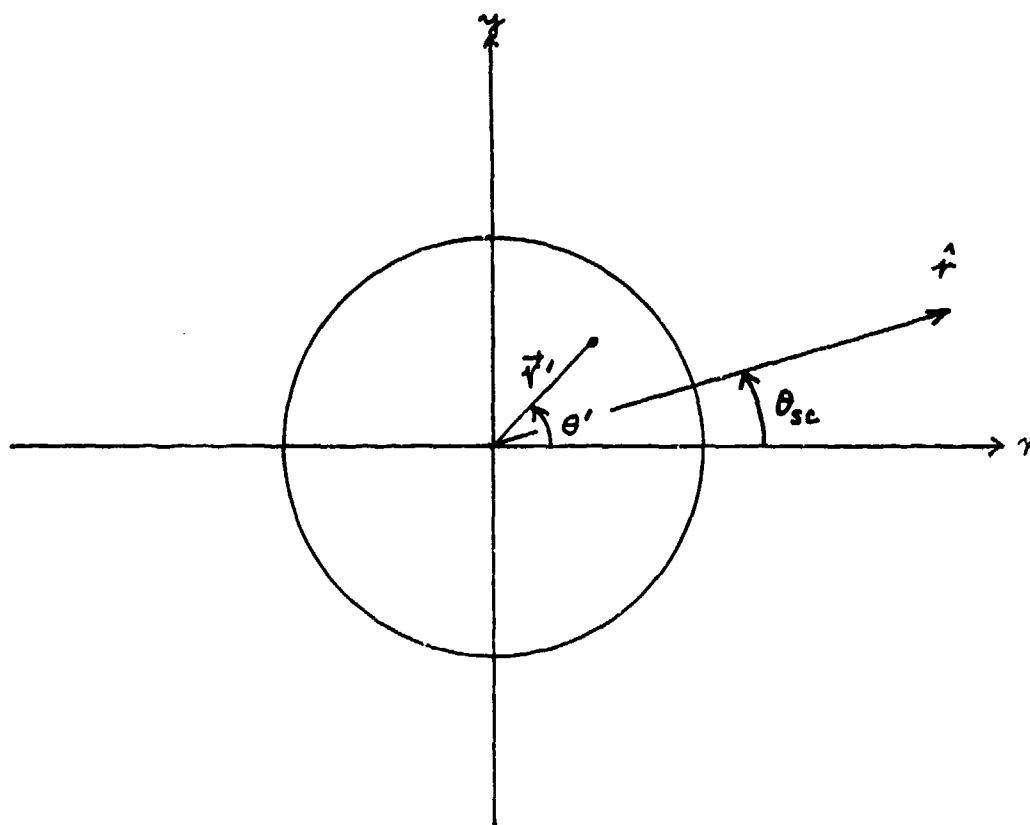
References

- [1] K. S. Shifrin, *Scatteing of Light in a Turbid Medium* (Moskow, 1951); or NASA document TT F-477, Washington, D.C. (1968).
- [2] C. Acquista, *Appl. Opt.* **15**, 2932 (1976).
- [3] R. D. Haracz, L.D. Cohen, A. Cohen and C. Acquista, *Oppl. Opt.* **25**, 4386 (1986) and A. Cohen, R.D. Haracz and L.D. Cohen, *J. Wave Mater. Inter.* **3**, 219 (1988).
- [4] R. D. Haracz, L.D. Cohen, A.R.W. Presley and A. Cohen, *Appl. Opt.* **28**, 1338m

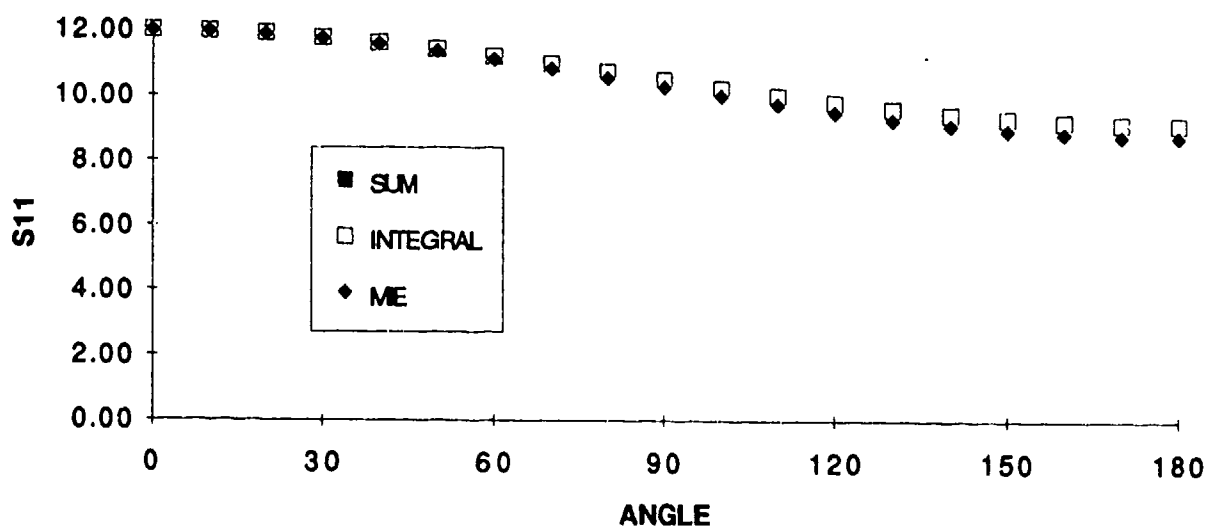
(1989).

- [5] M. Born and E. Wolf, *Principles of Optics*, 3rd. ed. (Pergamon Press, Oxford,)-
see Appendix 5.
- [6] H.C. van de Hulst, *Light Scattering by Small Particles* (John Wiley &
Sons, 1957) and M. Kerker, *The Scattering of Light and Other Small Particles*
(Academic Press, New York, 1969).

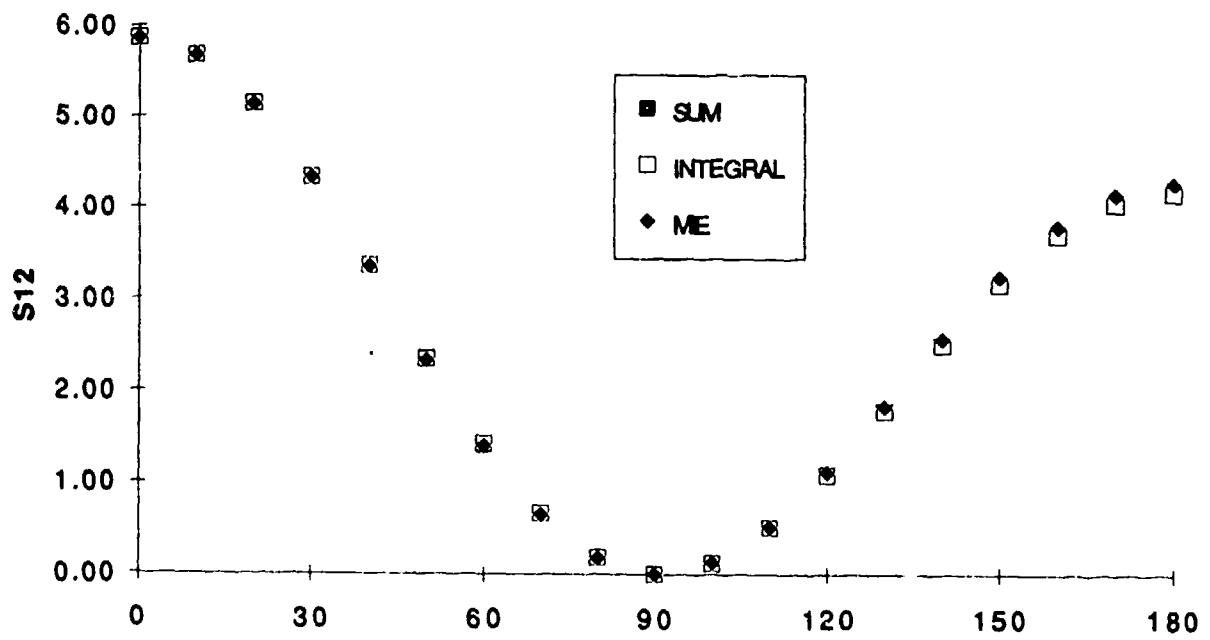




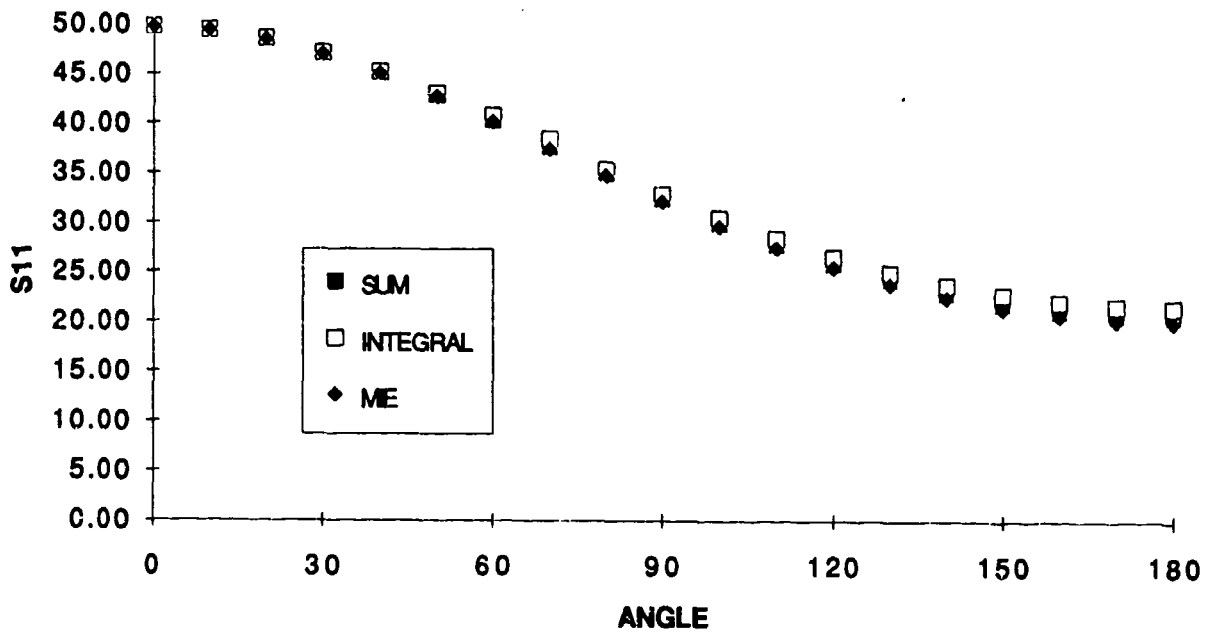
M=1.33, X=0.6



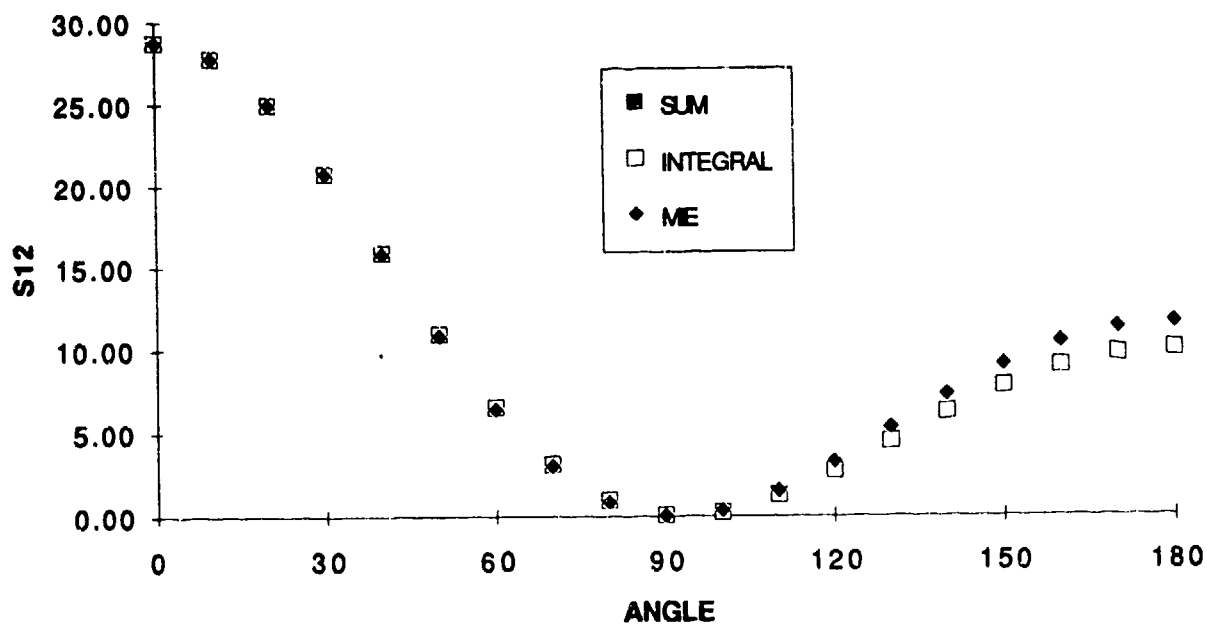
M=1.33, X=0.6



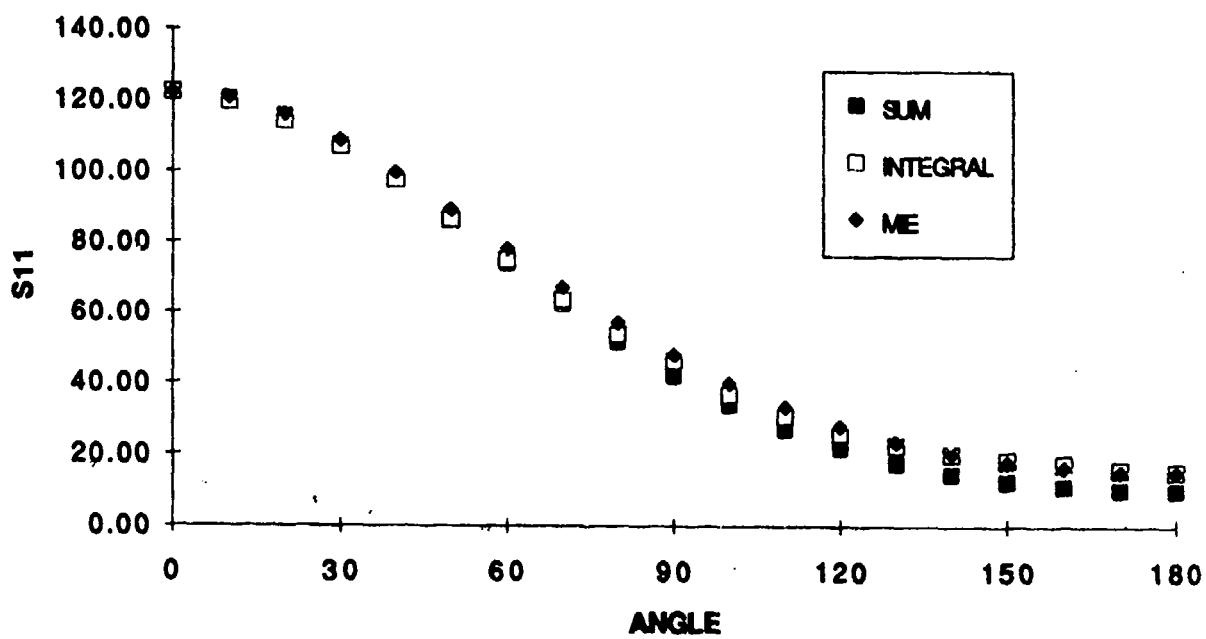
M=1.33, X=1.0



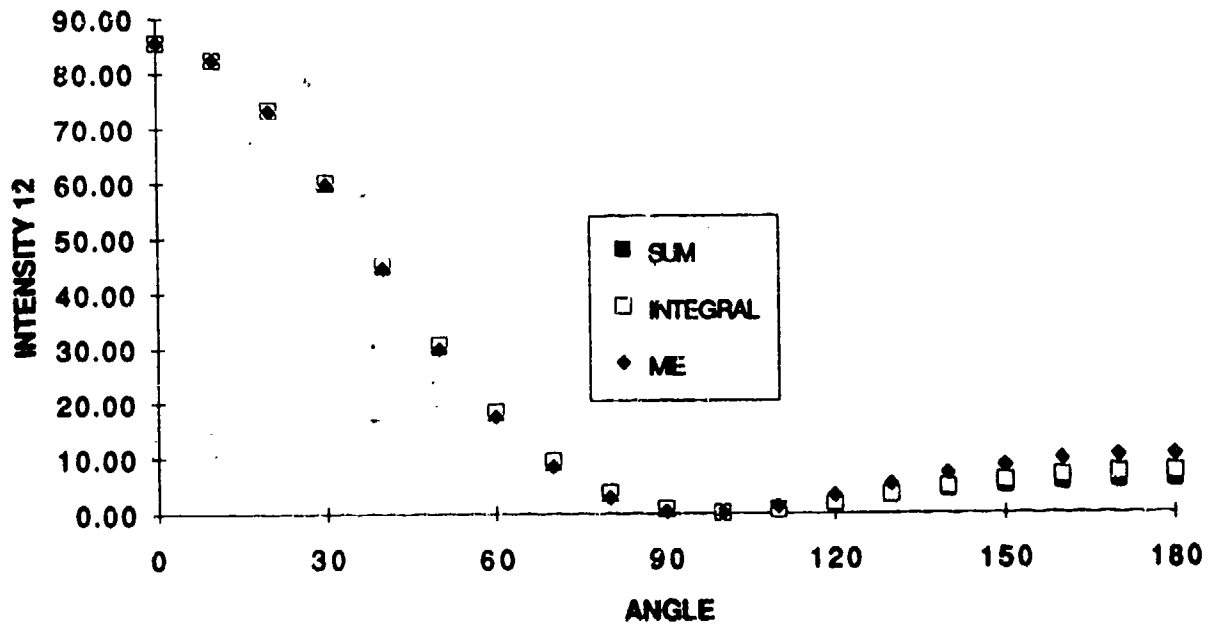
M=1.33, X=1.0



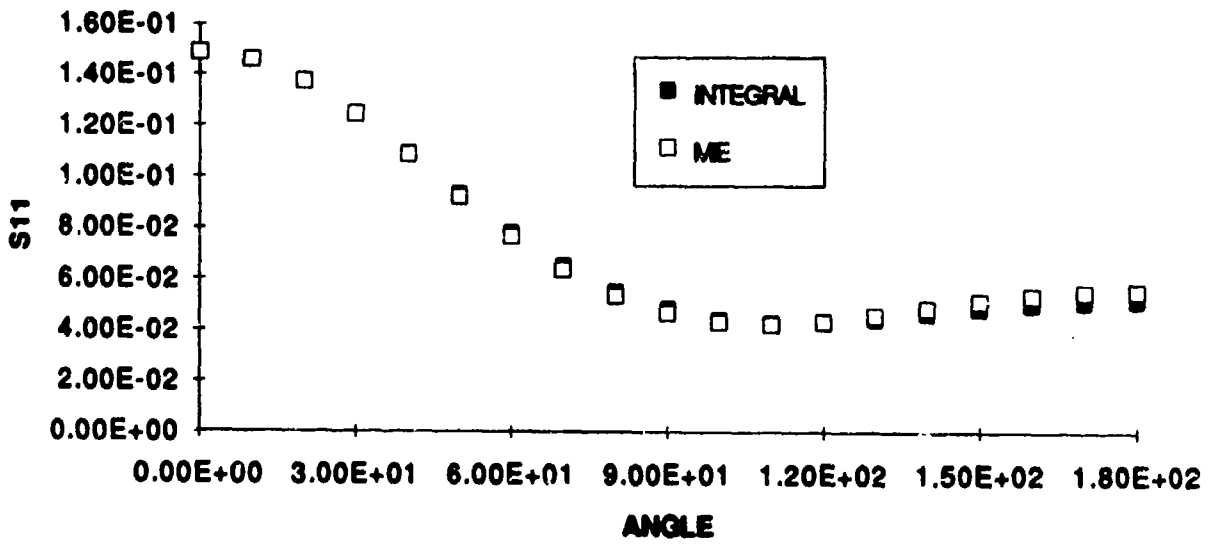
M=1.33, X=1.4



PARALLEL, M=1.33, X=1.4



M=1.55, X = 1.0



Blank

INDEX A

Index of Authors

Alexander, D.R.	61, 277	Curry, B.P.	77
Allison, E.E.	141	Denti, P.	255
Armstrong, R.L.	199	DeSha, M.S.	191
Arnold, S.	155	Essien, M.	199
Bahar, E	61	Evans, B.T.N.	239
Barnes, M.D.	155	Eversole, J.D.	145
Barton, J.P.	277	Flatau, P.J.	289
Borghese, F.	255	Fournier, G.R.	239
Bottiger, J.R.	97	Fry, E.S.	103
Brewster, M.Q.	77	Fuller, K.A.	289, 297
Brock, J.R.	37	Gillespie, J.B.	173, 199
Bronk, B.V.	141, 177	Hadad, A.	55
Butler, J.	191	Hameka, H.F.	97
Campillo, A. J.	145	Haracz, R.D.	437
Carrieri, A.H.	97	Hermann, G.	219
Cermak, J.E.	47, 55	Hu, P.	427
Choi, M.K.	37	Jensen, J.O.	97
Christesen, S.	191	Jones, M.R.	77
Clausen, C.A.	219	Kendall, B.R.F.	141
Cohen, A.	437	Kubik, R.D.	61
Cohen, L.D.	437	Lax, M.	427
Cohoon, D.K.	115, 333, 359, 387	Lee, M.H.	91

Leong, K.H.	77	Whitten, W.B.	155, 177
Lin, H-B.	145	Wilson, M.	191
Littman, H.	9	Witriol, N.M.	115, 423
Merrow, C.	191	Wong, A.	191
McLeod, W.	25	Zeroka, D.	97
Morgan III, M. H.	9	Zhou, Z.	25
Morgan, P.W.	219		
Oh, C.	103		
Padmabandu, G.G.	103		
Poreh, M.	47, 55		
Racine, T.R.	219		
Ramsey, J.M.	155, 177		
Reidy, D.	25		
Reinisch, L.	183		
Rosen, D.L.	173		
Rubel, G.O.	25, 31		
Saija, R.	255		
Schaub, S.A.	277		
Seaver, M.	31		
Shaffer, R.	25		
Sindoni, O.I.	115, 255, 423		
Stiassnie, M.	55		
Wang, R.T.	323		
Weyandt, D.S.	141		

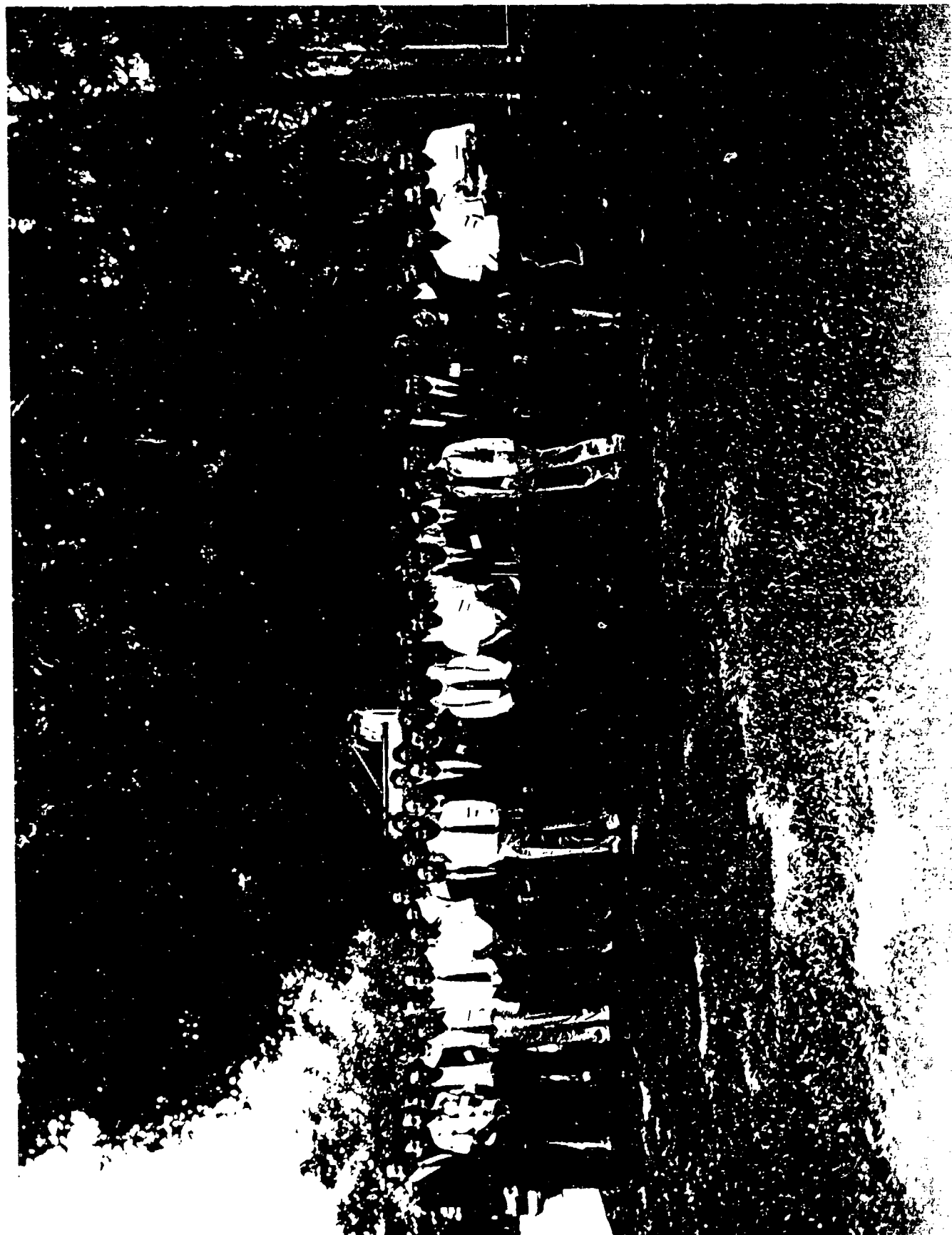
INDEX 8

Index of Authors' Organizations

- Argonne National Laboratory 77
- City College of the City University of New York 427
- Colorado State University
 Fluid Dynamics & Diffusion Laboratory, Engineering
 Research Center 47, 55
 Department of Atmospheric Science 289, 297
- Defense Research Establishment Valcartier 239
- Drexel University, Philadelphia,
 Department of Physics and Atmospheric Science 437
- Engineering Technology, Inc. 219
- GEO-Centers, Inc. 25
- The Hebrew University of Jerusalem, Israel
 Department of Atmospheric Sciences 437
- Institute for Space Science & Technology, Inc.,
 Space Astronomy Laboratory 323
- Lehigh University 97
- Louisiana Tech University 423
- Naval Research Laboratory 31, 145
- New Mexico State University,
 Department of Physics 199
- Oak Ridge National Laboratory,
 Analytical Chemistry Division 155, 177
- Pennsylvania State University,
 Department of Physics 141
- Polytechnic Institute of New York,
 Microparticle Photophysics Laboratory 155
- Potomac Photonics Inc. 145
- RPI, Department of Chemical Engineering 9

APPENDIX A

PHOTOGRAPH OF 1992 CONFERENCE ATTENDEES



1992 CRDEC SCIENTIFIC CONFERENCE ON
OBSCURATION AND AEROSOL RESEARCH

Pictured from left to right are:

First Row

Dipakbin Chowdhury

John Barton

Michael Smith

Gang Chen

H-B. Lin

Alfred Kwok

Second Row

Ed Stuebing

Esam Khaled

Ru Wang

Wei Cai

Matthew Jones

Blair Evans

Avi Ben-David

David Rosen

Stephen Arnold

Kirk Fuller

Lorcan Folan

M. Howard Lee

Orazio Sindoni

Jerold Bottiger

Norman M. Witriol

Janice Cheung

Mike Barnes

Mark Seaver

Third Row

Ron Pinnick

Dennis Garvey

Tom Giel

Ariel Cohen

James Brown

Dee Pack

Dennis Alexander

Bruce Kendall

Frank Poleski

Janon Embury

Grahame Poulson

Z. Joe Zhou

Robert Armstrong

Chris Swindal

Bill Whitter

Fourth Row

Steve Hill

Burt Bronk

Lou Reinisch

Robert Rubio

Bob Keesee

Melvin Lax

W. Michael Farmer

Tony Campillo

Marcelino Essien

ATTENDEES LIST

ALEXANDER, DENNIS R DR

CENTER FOR ELECTRO-OPTICS
248 WALTER SCOTT ENG. CENTER
UNIVERSITY OF NEBRASKA/LINCOLN
LINCOLN NE 68588 0656

ALLISON, E
APPLIED RESEARCH LAB
PENN STATE UNIVERSITY
UNIVERSITY PARK PA 16804

ARMSTRONG, ROBERT L PROF

DEPT OF PHYSICS
P O BOX 3D
NEW MEXICO STATE UNIVERSITY
LAS CRUCES NM 88003

ARNOLD, STEPHEN PROF

POLYTECHNIC UNIVERSITY
DEPT OF PHYSICS
6 METROTECH CENTER
BROOKLYN NY 11201

BARNES, MICHAEL D DR

ANALYTICAL CHEMISTRY DIVISION
OAK RIDGE NATIONAL LABORATORY
PO BOX 2008
OAK RIDGE TN 37831 6142

BARTON, JOHN P PROF

CENTER FOR ELECTRO-OPTICS
248 WALTER SCOTT ENG. CENTER
UNIVERSITY OF NEBRASKA/LINCOLN
LINCOLN NE 68588 0656

BEN-DAVID, AVISHAI

COMMANDER
US ARMY CRDEC
ATTN SMCCR RSL S/A BEN-DAVID
APG MD 21010

BOTTIGER, JEROLD

COMMANDER
US ARMY CRDEC
ATTN SMCCR RSP B/J BOTTIGER
APG MD 21010 5423

BROCK, JAMES R DR

UNIVERSITY OF TEXAS/AUSTIN
DEPT OF CHEMICAL ENGINEERING
AUSTIN TX 78712

BRONK, BURT DR

COMMANDER
US ARMY CRDEC
ATTN SMCCR RSP B/B BRONK
APG MD 21010 5423

BROWN, JAMES

COLORADO SCHOOL OF MINES
DEPT OF PHYSICS
GOLDEN CO 80401

CAI, WEI

CITY COLLEGE OF NY
NEW YORK NY 10031

CAMPILLO, ANTHONY

NAVAL RESEARCH LAB
ATTN CODE 6546/A CAMPILLO
WASHINGTON DC 20375 5000

CARLON, HUGH

COMMANDER
US ARMY CRDEC
ATTN SMCCR RSP P/H CARLON
APG MD 21010 5423

CARPIN, JOHN C DR

COMMANDER
US ARMY CRDEC
ATTN SMCCR RST I (CARPIN)
APG MD 21010 5423

CARRIERI, ARTHUR H DR

COMMANDER
US ARMY CRDEC
ATTN SMCCR DDT
APG MD 21010-5423

CHANG, YU-CHEN

UNIVERSITY OF MARYLAND
DEPT OF CHEMICAL ENGINEERING
COLLEGE PARK MD 20742

CHEN, PAUL G MR

YALE UNIVERSITY
DEPT OF APPLIED PHYSICS
P O BOX 2157 YALE STATION
NEW HAVEN CT 06520

CHEUNG, JANICE L.-C. MS

YALE UNIVERSITY
DEPT OF APPLIED PHYSICS
P O BOX 2157 YALE STATION
NEW HAVEN CT 06520

CHOWDHURY, DIPAKBIN Q DR

YALE UNIVERSITY
DEPT OF APPLIED PHYSICS
P O BOX 2157 YALE STATION
NEW HAVEN CT 06520

CLAUSEN III, CHRISTIAN A DR

UNIV OF CENTRAL FLORDIA
DEPT OF CHMEISTRY
ORLANDO FL 32816

COHEN, ARIEL

HEBREW UNIVERSITY
DEPT OF ATMOSPHERIC SCIENCES
JERUSALEM
ISRAEL

COHOON, DAVID K DR

43 SKYLINE
GLEN MILLS PA 19342

DESHA, SCOTT

COMMANDER
US ARMY CRDEC
ATTN SMCCR-DDT/S DESHA
APG MD 21014

EMBURY, JAY

COMMANDER
US ARMY CRDEC
ATTN SMCCR RSP-B/J EMBRY
APG MD 21010

ESSIEN, MARCELINO MR

DEPARTMENT OF PHYSICS
BOX 3D
NEW MEXICO STATE UNIVERSITY
LAS CRUCES NM 88003

EVANS, BLAIR DR

DEFENSE RESCH EST VALCARTIER
2459 PIE XI BLVD NORTH
PO BOX 8800
COURCELETTE QUEBEC
GOA 1R0

EVERSOLE, JAY DR

NAVAL RESEARCH LAB
ATTN CODE 6546/J EVERSOLE
WASHINGTON DC 20375 5000

FARMER, W MICHAEL DR

BIONETICS
500 S MAIN FNB SUITE 900
LAS CRUCES NM 88001

FLANIGAN, DENNIS MR

COMMANDER
US ARMY CRDEC
ATTN SMCCR RSP B/D FLANIGAN
APG MD 21010 5423

FOLAN, LORCAN M DR

POLYTECHNIC UNIVERSITY
DEPT OF PHYSICS
SIX METROTECH CENTER
BROOKLYN NY 11201

FRENKLACH, MICHAEL PROF

PENN STATE UNIVERSITY
DEPT MATERIALS SCIENCE & ENG
FUEL SCIENCE PROGRAM
202 ACADEMIC PROJECTS BUILDING
UNIVERSITY PARK PA 16802

FRICKEL, ROBERT H MR

1405 HARVARD CT
BEL AIR MD 21014

FRY, EDWARD

TEXAS A&M UNIVERSITY
DEPT OF PHYSICS
COLLEGE STATION TX 77843

FULLER, KIRK A DR

DEPT OF ATMOSPHERIC SCIENCE
COLORADO STATE UNIVERSITY
FT COLLINS CO 80523

GARVEY, DENNIS M

ARMY ATMOSPHERIC SCIENCES LAB
WHT SANDS MISSILE RNG NM 88002

GENOVESE, JAMES A

COMMANDER
US ARMY CRDEC
ATTN SMCCR MUS
APG MD 21010 5423

GENTRY, JAMES W

UNIVERSITY OF MARYLAND
DEPT OF CHEMICAL ENGINEERING
COLLEGE PARK MD 20742

GIEL, THOMAS V JR

UNIVERSITY OF TENNESSEE
SPACE INSTITUTE
MS-04
B H GOETHERT PARKWAY
TULLAHOMA TN 37388-8897

HAN, RUIJING

UNIVERSITY OF MARYLAND
DEPT OF CHEMICAL ENGINEERING
COLLEGE PARK MD 20742

HARACZ, DICK

DREXEL UNIVERSITY
DEPT OF PHYS & ATMOSPHERIC SCI
32ND & CHESTNUT STREETS
PHILADELPHIA PA 19104

HASHMONAY, RAM

7326 RUSKIN ROAD
PHILADELPHIA PA 19151

HILL, STEVEN

US ARMY ATMOS SCIENCES LAB
WHT SANDS MISSILE RNG NM 88002

HODGES, JOSEPH T DR

PROCESS MEASUREMENTS DIV
NIST
ROOM B306/BLDG 221
BAITHERSBURG MD 20899

JONES, MATHEW R

ARGONNE NATIONAL LABORATORY
BUILDING 207
9700 SOUTH CASS AVENUE
ARGONNE IL 60439

KEESE, ROBERT G PROF

EARTH SCIENCE 211
UNIVERSITY OF ALBANY
STATE UNIVERSITY OF NEW YORK
ALBANY NY 12203

KENDALL, BRUCE DR

PENNSYLVANIA STATE UNIVERSITY
DEPT OF PHYSICS
104 DAVEY LABORATORY
UNIVERSITY PARK PA 16802

KENEFICK, PETER

TITAN/SPECTRON
3535 HYLAND AVENUE
COSTA MESA CA 92626

KHALED, ESAM MR

CLARKSON UNIVERSITY
ECE DEPARTMENT
POTSDAM NY 13699 5720

KLEINMAN, RALPH E DR

UNIVERSITY OF DELAWARE
DEPT OF MATHEMATICAL SCIENCES
NEWARK DE 19716

KLETT, JAMES D

PAR ASSOCIATES
4507 MOCKINGBIRD ST
LAS CRUCES NM 88001

KWOK, ALFRED S MR

YALE UNIVERSITY
DEPT OF APPLIED PHYSICS
PO BOX 2157 YALE STATION
NEW HAVEN CT 06520

LAX, MELVIN PROF

CITY COLLEGE OF NEW YORK
PHYSICS DEPT
NEW YORK NY 10031

LEE, M HOWARD PROF

UNIVERSITY OF GEORGIA
DEPT OF PHYSICS
ATHENS GA 30602

LEONG, KENG H DR

ARGONNE NATIONAL LAB
BUILDING 207
9700 SOUTH CASS AVENUE
ARGONNE IL 60439

LETTIERI, THOMAS R DR

NATIONAL INSTITUTE OF
STANDARDS AND TECHNOLOGY
A55 MET
GAITHERSBURG MD 20899

LIN, H B

NAVAL RESEARCH LAB
ATTN CODE 6546/H B LIN
WASHINGTON DC 20375 5000

LITTMAN, HOWARD PROF

RENSSELAER POLYTECH INSTITUTE
DEPT OF CHEMICAL ENGINEERING
123 RICKETTS BUILDING
TROY NY 12180 3590

MILHAM, MERRILL MR

COMMANDER
US ARMY CRDEC
ATTN SMCCR RSP-B/M MILHAM
APG MD 21010

MORGAN, MORRIS H DR

RENSSELAER POLYTECH INSTITUTE
DEPT OF CHEMICAL ENGINEERING
131 RICKETTS BLDG
TROY NY 12180 3590

MORRIS, ROBERT

PSI
1515 J DAVIS HWY PH16
ARLINGTON VA 22202

PATEL, PARMANAND P

COMMANDER
US ARMY CRDEC
ATTN SMCCR QAO C
APG MD 21010 5423

PATERNO, DOROTHEA

COMMANDER
US ARMY CRDEC
ATTN SMCCR RSP-P/D PATERNO
APG MD 21010 5423

PEARCE, HORACE

COMMANDER
US ARMY CRDEC
ATTN SMCCR MUT
APG MD 21010 5423

PENSKI, ELWIN MR

COMMANDER
US ARMY CRDEC
ATTN SMCCR RSC-P/E PENSKI
APG MD 21010 5423

PINNICK, RONALD DR

ATMOSPHERIC SCIENCES LAB
ATTN SLCAS AR/R PINNICK
WHITE SANDS MISSILE RANGE
NM 88002 5501

POLESKI, FRANKLIN A MR

COMMANDER
USA FOREIGN SCIENCE & TECH CTR
220 7TH STREE NE
CHARLOTTESVILLE VA 22901 5396

POULSON, GRAHAME W. DR

DRA MILITARY DIVISION
RARDE FORT HALSTEAD BLDG R-47
SEVENOAKS KENT
TN14 7BP
UNITED KINGDOM

PRESSER, CARY DR

NATIONAL INSTITUTE OF
STANDARDS AND TECHNOLOGY -NIST
BLDG 221 RM B-306
GAITHERSBURG MD 20899

RAY, ASIT DR

UNIVERSITY OF KENTUCKY
DEPT OF CHEMICAL ENGINEERING
161 ANDERSON HALL
LEXINGTON KY 40502

REIDY, DENIS M

GEO-CENTER, INC.
7 WELLS AVENUE
NEWTON MA 02159

REINISCH, LOU PROF

VANDERBILT UNIV MEDICAL CNTR
DEPT OF OTOLARYNGOLOGY
S-2100 MEDICAL CENTER NORTH
NASHVILLE TN 37232-2559

RICHARDSON, ROBERT E

NAVAL SURFACE WEAPON CENTER
CODE J41
DAHLGREN VA 22448

RIN, CHUN-HSUN DR

COMMANDER
US ARMY CRDEC
ATTN SMCCR DDR (C H RIN)
APG MD 21010 5423

ROSEN, DAVID L

U.S. ARMY ATMOSPHERIC SCIENCES
ATTN SLCAS BW R/D ROSEN
WHT SANDS MISSILE RNG NM 88002

RUBEL, GLENN DR

COMMANDER
US ARMY CRDEC
ATTN SMCCR RSP-B/G RUBEL
APG MD 21010 5423

RUBIO, ROBERT

ATMOSPHERIC SCIENCES LAB
BLDG 1622
WHT SANDS MISSILE RNG NM 88002

SEAVER, MARK MR

NAVAL RESEARCH LAB
ATTN CODE 6540/M SEAVER
WASHINGTON DC 20375 5000

SHAFFER, ROY

GEO-CENTERS, INC.
7 WELLS AVENUE
NEWTON MA 02159

SINDONI, ORAZIO DR

COMMANDER
US ARMY CRDEC
ATTN SMCCR RSP-B/O SINDONI
APG MD 21010 5423

SITARSKI, MAREK A DR

KENTUCKY WESLEYAN COLLEGE
PHYSICS DEPARTMENT
3000 FREDERICA ST
P O BOX 1039
OWNESBORO KY 43202-1039

SMITH, MICHAEL J

COMMANDER
US ARMY CRDEC
P O BOX 49
GUNPOWDER BR
APG MD 21014

STUEBING, EDWARD DR

COMMANDER
US ARMY CRDEC
ATTN SMCCR RSP-B/E STUEBING
APG MD 21010

SWINDAL, J CHRISTIAN MR

YALE UNIVERSITY
DEPT OF APPLIED PHYSICS
P O BOX 2157 YALE STATION
NEW HAVEN CT 06520

VAN DE MERWE, WILLEM P

BIC USUHS
4301 JONES BRIDGE ROAD
BETHESDA MD 20814 4799

WANG, RU T DR

INSTITUTE OF SPACE SCIENCE
& TECHNOLOGY
SPACE ASTRONOMY LAB
1810 N W 6TH STREET
GAINSVILLE FL 32609

WHALLEY, CHRIS E

COMMANDER
US ARMY CRDEC
ATTN SMCCR RST E
APG MD 21010 5423

WHITE, JOHN R DR

COMMANDER
US ARMY CRDEC
ATTN SMCCR RSP-B/J R WHITE
APG MD 21010 5423

WITRIOL, NORMAN

COMMANDER
US ARMY CRDEC
ATTN SMCCR RSP B/O
APG MD 21010-5423

WONG, ANNA

COMMANDER
US ARMY CRDEC
ATTN SMCCR DDT
APG MD 21010 5423

ZHOU, ZHIXIANG

GEO-CENTER, INC.
7 WELLS AVENUE
NEWTON MA 02159

APPENDIX C

TECHNICAL AGENDA

MONDAY, 22 JUNE

9:00 Registration

9:50 Opening: *Dr. Edward W. Stuebing*, Coordinator, CRDEC

Welcome: *Dr. H. Dupont Durst*, Acting Chief Scientist, Research Directorate

Announcements: *Mr. Elmer H. Engquist*, Battelle Edgewood Operations

I. AEROSOL DYNAMICS - Moderator: Glenn Rubel

- 10:10 *M. Seaver*, R. Peele (NRL) and G. Rubel (CRDEC), The Dynamics of Water Drop Encapsulation by Octadecanol Monolayers
- 10:30 *J.R. Brock* (Univ. of TX/Austin), Quasi-Molecular Calculation of Complex Droplet Dynamics
- 10:50 *M. Sitariski* (Kentucky Wesleyan College), Co-condensation of Vapors of Large and Small Molecular Weights
- 11:10 *H. Littman* and M.H. Morgan III (RPI), The Effect of Electrostatic Forces on the Pneumatic Transport of Aerosols Flowing Through Pipes
- 11:30 *Z. Zhou*, R. Shafer, B. McCloud and D. Reidy (Geo-Centers, Inc.), Electrostatic Smoke Clearing in a Confined Volume
- 11:50 LUNCH (Sign up for dinner at Josef's)

II. AEROSOL CHARACTERIZATION METHODS

II A. NEPHELOMETRY AND INVERSION - Moderator: Jerold Bottiger

- 1:15 *A.H. Carrieri*, J. Jensen and J. Bottiger (CRDEC), Measured Characterization of Randomly Rough Surfaces by IR Mueller Matrix Scattering
- 1:35 *D.R. Alexander*, R.D. Kubik and E. Bahar (Univ. of NB/Lincoln), Use of a New Polarimetric Optical Bistatic Scatterometer to Measure the Transmission and Reflection Muller Matrix for Arbitrary Incident and Scatter Directions
- 1:55 *K.H. Leong*, D.J. Holdridge and M.R. Jones (Argonne), Performance of a Polar Nephelometer
- 2:15 *M.R. Jones*, K.H. Leong, B.P. Curry and Q. Brewster (Argonne), Inversion of Light Scattering Measurements for Size and Refractive Index
- 2:50 BREAK (Sign up for dinner at Josef's)
- 3:15 *E. Fry* (Texas A&M Univ.), Angular Scattering At and Near Zero Degrees
- 3:35 *M. Lax* and Po Hsu (CCNY), Quasi-Binary Decision Making: An Update

MONDAY, 22 JUNE (cont.)

II. AEROSOL CHARACTERIZATION METHODS (con't.)

II A. NEPHELOMETRY AND INVERSION - Moderator: Jerold Bottiger

- 3:55 **D. Cohoon** (Geo-Centers, Inc.), N.M. Witriol (LA Tech Univ., NRC Fellow @ CRDEC) and O.I. Sindoni (CRDEC), Determination of Layered Aerosol Particle Properties from Scattering Data
- 4:15 **M. H. Lee** (Univ. of Georgia), Kramers-Kronig Relations in Optic Data Inversion
- 4:35 **ADJOURN** (Suggested restaurant for dinner: Josef's)

TUESDAY, 23 JUNE

II B. IMAGING OF MICROPARTICLES - Moderator: Michael J. Smith

- 8:30 **D.R. Alexander**, S.A. Schaub, J. Stauffer and J. Barton (Univ. of NB/Lincoln), Femtosecond Imaging and Glare Spot Observations for Small Aerosol Particles
- 8:50 **S. Arnold** (Polytechnic Univ. of NY), Aerosol Particle Microphotography
- 9:10 **L.M. Folan** (Polytechnic Univ. of NY), Morphologically Dependent Imaging Using Enhanced Energy Transfer
- 9:30 **E. Allison**, B.R. Kendall (Penn State Univ.), B.V. Bronk (CRDEC) and D. Weyandt (Penn State Univ.), Manipulation of Microparticles in Multiphase Levitation Traps
- 9:50 **BREAK** (Sign up for Dinner at Hausners)

II C. SPECTROSCOPY OF SINGLE PARTICLES AND AEROSOLS - Moderator: Burt Bronk

- 10:10 **M. Essien**, R.L. Armstrong (NMSU) and J.B. Gillespie (ASL), Suppression of Morphology-Dependent Resonances of a Single Levitated Laser-Irradiated Microdroplet
- 10:30 **M.D. Barnes**, W.B. Whitten (ORNL), J.M. Ramsey and S. Arnold (Polytechnic Univ. of NY), Fluorescence Emission Rates in Levitated Droplets
- 10:50 **C.J. Swindal**, D.H. Leach, R.K. Chang and K. Young (Yale Univ.), Precession of Morphology-Dependent Resonances in Nonspherical Droplets
- 11:10 **S.D. Christesen**, M.S. DeSha, A. Wong (CRDEC), C.N. Merrow, M. Wilson and J. Butler (STC), UV Fluorescence Lidar Detection of Biological Aerosols
- 11:30 **B.V. Bronk**, M.J. Smith (CRDEC) and S. Arnold (Polytechnic Univ. of NY), Fluctuations in Scattering and Fluorescence Due to One or More Subparticles in Micron Size Droplets
- 11:50 **LUNCH** (Sign up for dinner at Hausners)

TUESDAY, 23 JUNE

*** WORKSHOP - CARBON PARTICLES FROM HYDROCARBON FEEDSTOCKS ***

- 1:15 *C. Clausen, III* (Univ. of Central Florida), P. Morgan (Environmental Technology, Inc.), G. Hermann and Teresa Resetar-Racine (CRDEC), Carbon Particles from Hydrocarbon Feedstocks
- 1:35 *J.R. Brock* (Univ. of TX/Austin), Problems in Generation of Carbon Smokes from Light Fuels
- 1:55 To be determined
- 2:15 To be determined
- 2:35 **BREAK** (Sign up for dinner at Hausners)

II. AEROSOL CHARACTERIZATION METHODS (cont.)

II C. SPECTROSCOPY OF SINGLE PARTICLES AND AEROSOLS - Moderator: Burt Bronk

- 3:15 *J.D. Eversole* (PPI), A.J. Campillo and H.B. Lin (NRL), CW Stimulated Raman Scattering in Microdroplets
- 3:35 *A.S. Kwok* and R.K. Chang (Yale Univ.), Fluorescence Seeding of Stimulated Raman Scattering
- 3:50 *P.G. Chen*, D.Q. Chowdhury and R.K. Chang (Yale Univ.), Lasing Emission from Descartes Ring with Multiple-100 ps Pulses
- 4:05 *J.L.C. Cheung*, K. Juvan, D. Leach and R.K. Chang (Yale Univ.), Stimulated Kerr-Broadened Scattering from Droplets
- 4:20 *D. Pack*, A. Pluchino and D. Masturzo (Aerospace Corp.), Emissivity of Single Levitated Particles
- 4:40 **ADJOURN** (Suggested restaurant for dinner: Hausners)

WEDNESDAY, 24 JUNE

II D. INTERNAL STRUCTURE - Moderator: Michael J. Smith

- 8:30 *R.G. Pinnick*, A. Biswas (ASL), J-G. Xie, T.E. Ruekgauer and R.L. Armstrong (NMSU), Scattering in Millimeter-Sized Glycerol Droplets
- 8:50 *R.L. Armstrong*, J-G. Xie, T.E. Ruekgauer (NMSU) and R.G. Pinnick (ASL), Energy Transfer in Microdroplet Lasers Seeded with Fluorescent Sol
- 9:10 *D.Q. Chowdhury*, M. Mazumder (Yale Univ.) and S.C. Hill (ASL & NMSU), Absorption and Gain Coefficient of Inhomogeneous Spheres
- 9:30 *A.J. Campillo*, H.B. Lin, A.L. Huston (NRL), P. Chylek (Dalhousie Univ.) and J.D. Eversole (PPI), Internal Scattering Effects on Microdroplet Resonant Emission Structure
- 10:00 **GROUP PHOTOGRAPH - BREAK**

WEDNESDAY, 24 JUNE

10:45 **OVERVIEW & DISCUSSION: DIRECTIONS FOR FUTURE RESEARCH IN THE CRDEC AEROSOL SCIENCE PROGRAM - E.W. Stuebing (CRDEC)**

11:50 LUNCH

III. **OPTICAL PROPERTIES OF AEROSOLS** - Moderator: Orazio I. Sindoni

1:15 *A. Ben-David* (STC) and M.L.G. Althouse (CRDEC), IR Lidar Returns from Cylindrical Graphite Aerosols

1:35 *D. Cohoon* (Geo-Centers, Inc.), Scattering of EM Radiation by Materials with Tensor Properties-- Predicting Scattering by Irregular Shapes with Error Correction to the Limit of the Machine's Precision

1:55 *J.R. Brock* and N.K. Choi (Univ. of TX/Austin), On Feasibility of Numerical Calculation of Light Scattering and Absorption by Particles

2:15 *J.P. Barton*, D.R. Alexander and S.A. Schaub (Univ. of NB/Lincoln), Electromagnetic Field Calculations for a Beam Focused on a Layered Object

POSTER PROGRAM

2:35 POSTER PREVIEWS (Auditorium)

W. Whitten, J.M. Ramsey (ORNL) and B.V. Bronk (CRDEC), Immunoassays Using Microparticles

D. Cohoon (Geocenters, Inc.), Nonlinear Interactions of Solids and Liquids with External Energy Sources

M. Milham (CRDEC), A Functional Scaling Approach to EM Scattering: Theory and Algorithms for Spheres and Cylinders

J.D. Eversole (PPI), A.J. Campillo and H.B. Lin (NRL), Aerosol Absorption Spectroscopy

N.M. Witriol and O.I. Sindoni (CRDEC), Mueller Matrix Elements for Layered Spheres

L. Reinisch (Vanderbilt Univ.), Computerized Fluorometer Analysis: Automated Identification of Particles

D.L. Rosen and J.B. Gillespie (ASL), Time and Wavelength Domain Algorithms for Chemical Analysis by Laser Radar

M.B. Ranade (Particle Technology, Inc.), R. Han and J.W. Gentry (Univ. of MD), Electronic Sorting of Fibers and Flakes by Aspect Ratio

A. Smart (Titan Spectrum), A New Remote Optical Measurement Technique for Aerosol Sizing from an Airborne Platform

E.E.M. Khaled, P.W. Barber (Clarkson Univ.) and S.C. Hill (ASL & NMSU), Scattering of a Gaussian Beam by a Layered Sphere

E.E.M. Khaled, D.Q. Chowdhury, P.W. Barber (Clarkson Univ.), and S.C. Hill (ASL & NMSU), Time-dependence of Internal and Scattered Intensity of Sphere Illuminated with a Gaussian Beam

5:30 **ADJOURN** (Beef & Burgundy Dinner at Edgewood Community Club)

POSTER PROGRAM (cont.)

8:30 **POSTER SESSION (cont.)**

II. OPTICAL PROPERTIES OF AEROSOLS (cont.)

9:20 **S.C. Hill** (ASL & NMSU), D.H. Leach, R.K. Chang (Yale Univ) and W.P. Acker (Texaco, Inc.), Third-Order Sum Frequency Generation in Droplets

9:40 **B.T.N. Evans** and G.R. Gournier (Defence Research Establishment, Valcartier), General Analytic Extinction Formula for Randomly Oriented Spheroids

10:00 **D. Cohoon** (Geo-Centers, Inc.), Scattering of EM Radiation by Multiple Layer Structures Separated by Confocal Spheroids

10:20 **BREAK**

10:40 **A. Cohen** (Hebrew Univ. of Jerusalem), R.D. Haracz and L.D. Cohen (Drexel Univ.), Light Scattering from Nonspherical Targets Using the Internal Fields from Infinite Cylinders

11:00 **K.A. Fuller** (Colorado State Univ.), Absorption and Scattering Cross Sections of Carbon Dispersion Aerosols

11:20 **O.I. Sindoni** (CRDEC), F. Borghese, P. Denti and R. Saija (Univ. of Messina, Messina, Italy), Optical Properties of a Dispersion of Spherical Scatterers Containing Off Axis Spherical Inclusions

12:00 **ADJOURN**

**END
FILMED**

DATE:

10-93

DTIC